

University of Windsor

## Scholarship at UWindor

---

Electronic Theses and Dissertations

Theses, Dissertations, and Major Papers

---

2018

### Multinuclear Solid-State NMR Investigation of Structure, Dynamics, and Formation of Porous Materials

Christopher Andrew O'Keefe  
*University of Windsor*

Follow this and additional works at: <https://scholar.uwindsor.ca/etd>

---

#### Recommended Citation

O'Keefe, Christopher Andrew, "Multinuclear Solid-State NMR Investigation of Structure, Dynamics, and Formation of Porous Materials" (2018). *Electronic Theses and Dissertations*. 7387.  
<https://scholar.uwindsor.ca/etd/7387>

This online database contains the full-text of PhD dissertations and Masters' theses of University of Windsor students from 1954 forward. These documents are made available for personal study and research purposes only, in accordance with the Canadian Copyright Act and the Creative Commons license—CC BY-NC-ND (Attribution, Non-Commercial, No Derivative Works). Under this license, works must always be attributed to the copyright holder (original author), cannot be used for any commercial purposes, and may not be altered. Any other use would require the permission of the copyright holder. Students may inquire about withdrawing their dissertation and/or thesis from this database. For additional inquiries, please contact the repository administrator via email ([scholarship@uwindsor.ca](mailto:scholarship@uwindsor.ca)) or by telephone at 519-253-3000ext. 3208.

**Multinuclear Solid-State NMR Investigation of Structure, Dynamics, and  
Formation of Porous Materials**

By

**Christopher Andrew O'Keefe**

A Dissertation  
Submitted to the Faculty of Graduate Studies  
through the Department of Chemistry and Biochemistry  
in Partial Fulfillment of the Requirements for  
the Degree of Doctor of Philosophy  
at the University of Windsor

Windsor, Ontario, Canada

2018

© 2018 Christopher Andrew O'Keefe

**Multinuclear Solid-State NMR Investigation of Structure, Dynamics, and  
Formation of Porous Materials**

by

**Christopher Andrew O'Keefe**

APPROVED BY:

---

J. Reimer, External Examiner  
University of California – Berkeley

---

R. Caron  
Department of Mathematics and Statistics

---

S. Loeb  
Department of Chemistry and Biochemistry

---

J. Wang  
Department of Chemistry and Biochemistry

---

R. Schurko, Advisor  
Department of Chemistry and Biochemistry

January 16, 2018

## **Declaration of Co-authorship/Previous Publications**

### **I. Co-Authorship**

I hereby declare that this thesis incorporates material that is result of joint research, as follows:

I am the primary author on two of the publications that have results, or will result from the work outlined in this thesis. I acknowledge my supervisor, Dr. Robert Schurko, as a co-author in this work and provided contributions to the writing and editing of this thesis

Chapter 2 “NMR-Assisted Powder X-Ray Diffraction for the Structural Characterization of a Zeolitic Imidazolate Framework Synthesized via Accelerated Aging Reactions” includes contributions from Dr. Cristina Mottillo who conducted the PXRD experiments and the initial syntheses. I assisted in the synthesis of the materials, collected and processed all SSNMR spectra and composed all sections of the unpublished manuscript relating to these experiments.

Chapter 3 “Monitoring the Formation of Cadmium-Containing Zeolitic Imidazolate Frameworks using a Combination of Powder X-ray Diffraction and Multinuclear Solid-State NMR” I am the primary author of this manuscript that is in preparation for publication. I acknowledge contributions from Dr. Cristina Mottillo for guidance in the initial mechanochemical reactions and Jacqueline Gemus for assisting with synthesis and the collection of SSNMR data. I conducted the majority of the SSNMR and PXRD experiments.

Chapter 4 “Observing Dynamics in Metal-organic Frameworks with Mechanically Interlocked Components using Solid-state NMR Spectroscopy” was conducted in collaboration with the following members of Dr. Stephen Loeb’s research group: Dr. Kelong Zhu, Dr. V. Nicholas Vukotic, Pablo Martinez-Bulit, and Christine To, who provided the materials that were studied and conducted X-ray diffraction experiments for the determination of their structures. I acquired and simulated all SSNMR data at 9.4 T and provided the written portions of the manuscripts pertaining to those experiments. Dr.

Kris Harris aided in the simulation of the SSNMR data. Dr. Victor Terskikh at the National Ultrahigh-Field NMR Facility for Solids acquired SSNMR data at 21.1 T.

Chapter 5 “Multinuclear Solid-State NMR Investigations of Platinum(II) trans-Dihydride Molecular Rotors” Samples were synthesized and provided by Dr. Ernest Prack and Dr. Ulrich Fekl from the University of Toronto at Mississauga and Dr. Salvador Conejero from the University of Seville, Spain. Dr. Jeremy Moore conducted the low temperature  $^2\text{H}$  SSNMR experiments, under the supervision of Dr. Conradi. A. Lai, A Lough, and Dr. P. M. MacDonald provided guidance in the interpretation of NMR data. Dr. Prack determined the energy landscape using DFT calculations. I acquired higher temperature  $^2\text{H}$  SSNMR data, processed and simulated all NMR data and assisted in writing the manuscript.

Chapter 6 “An investigation of chlorine ligands in transition-metal complexes via  $^{35}\text{Cl}$  SSNMR and DFT calculations” I acquired and processed all  $^{35}\text{Cl}$  SSNMR and NQR data, and performed the CASTEP DFT calculations. Dr. Karen Johnston from Windsor assisted with the interpretation of the NMR data and in editing the manuscript. Dr. Jochen Autschbach and K. Sutter at the State University of New York at Buffalo conducted the NLMO and NBO calculations. Dr. R. Gauvin, Dr. N Popoff and Dr. M. Taoufik synthesized the surface supported materials and Dr. L. Delevoy and Dr. J. Trébosc acquired the  $^{35}\text{Cl}$  SSNMR spectrum. Dr. Outdatchin from the NRC performed the PXRD experiments.

I am aware of the University of Windsor Senate Policy on Authorship and I certify that I have properly acknowledged the contribution of other researchers to my thesis, and have obtained written permission from each of the co-author(s) to include the above material(s) in my thesis.

I certify that, with the above qualification, this thesis, and the research to which it refers, is the product of my own work.

## II. Previous Publication

This thesis includes 6 original papers that have been previously published/submitted for publication in peer reviewed journals, as follows:

Thesis Chapter	Publication title/full citation	Publication status*
Chapter 4	Vukotic, V. N., <b>O’Keefe, C. A.</b> , Zhu, K., Harris, K. J., To, C., Schurko, R. W., Loeb, S. J., Mechanically Interlocked Linkers Inside Metal-Organic Frameworks: Effect of Ring Size on Rotational Dynamics, <i>J. Am. Chem. Soc.</i> , <b>2015</b> , <i>137</i> , 9643-9651	Published
Chapter 4	Zhu, K., <b>O’Keefe, C. A.</b> , Vukotic, V. N., Schurko, R. W., Loeb, S. J., A Molecular Shuttle that Operates Inside a Metal-Organic Framework, <i>Nat. Chem.</i> , <b>2015</b> , <i>7</i> , 514-519	Published
Chapter 4	Zhu, K., Vukotic, V. N., <b>O’Keefe, C. A.</b> , Schurko, R. W., Loeb, S. J. Metal-Organic Frameworks with Mechanically Interlocked Pillars: Controlling Ring Dynamics in the Solid State via a Reversible Phase Change, <i>J. Am. Chem. Soc.</i> , <b>2014</b> , <i>136</i> , 7403-7409	Published
Chapter 5	Prack, E., <b>O’Keefe, C. A.</b> , Moore, J. K., Lai, A., Lough, A. J., Macdonald, P. M., Conradi, M. S., Schurko, R. W., Fekl, U., A Molecular Rotor Possessing a H-M-H “Spoke” on a P-M-P “Axle”: a Platinum(II) trans-Dihydride Spins Rapidly Even at 75 K, <i>J. Am. Chem. Soc.</i> , <b>2015</b> , <i>137</i> , 13464-13467	Published

Chapter 6	<b>O’Keefe, C. A.</b> , Johnston, K. E., Sutter, K., Autschbach, J., Gauvin, R., Trébosc, J., Delevoye, L., Popoff, N., Taoufik, M., Oudatchin, K., Schurko, R. W. An Investigation of Chlorine Ligands in Transition-Metal Complexes via <sup>35</sup> Cl Solid-State NMR and Density Functional Theory Calculations, <i>Inorg. Chem.</i> , <b>2014</b> , <i>53</i> , 9581-9597	Published
-----------	--	-----------

I certify that I have obtained a written permission from the copyright owner(s) to include the above published material(s) in my thesis. I certify that the above material describes work completed during my registration as a graduate student at the University of Windsor.

### III. General

I declare that, to the best of my knowledge, my thesis does not infringe upon anyone’s copyright nor violate any proprietary rights and that any ideas, techniques, quotations, or any other material from the work of other people included in my thesis, published or otherwise, are fully acknowledged in accordance with the standard referencing practices. Furthermore, to the extent that I have included copyrighted material that surpasses the bounds of fair dealing within the meaning of the Canada Copyright Act, I certify that I have obtained a written permission from the copyright owner(s) to include such material(s) in my thesis.

I declare that this is a true copy of my thesis, including any final revisions, as approved by my thesis committee and the Graduate Studies office, and that this thesis has not been submitted for a higher degree to any other University or Institution.

## Abstract

The work described herein demonstrates the utility of solid-state nuclear magnetic resonance (SSNMR) spectroscopy for the characterization of molecular-level structure and dynamics in porous materials, including the determination of the reaction pathways involved in the formation of porous solids made via solid-state synthetic techniques, a study of the motion of dynamic components of metal-organic frameworks (MOFs) that are prototypes for future molecular machines, and the structural characterization of a surface-supported catalyst.

In Chapters 2 and 3, accelerated aging and mechanochemical reactions are used to synthesize cadmium-containing zeolitic imidazolate frameworks (ZIFs). These techniques provide a means for clean and efficient syntheses of these materials; however, little is known about the reaction kinetics and mechanisms underlying their production. First, the structure of a new cadmium-imidazolate framework (CdIF) is determined using a combination of powder X-ray diffraction (PXRD) and SSNMR, a methodology known as NMR-assisted crystallography. SSNMR experiments are also used to monitor the formation of ZIFs made using mechanochemical synthesis, providing information on the intermediates and products of the reactions. It is revealed that the initial mechanochemical ball milling provides the activation energy for the formation of ZIFs, but aging reactions within the milling jars drive the reaction to completion. As demonstrated here, milling times as short as five seconds provide enough energy for the initiation of the reactions, allowing for extremely low-energy synthesis of these materials.

In Chapter 4, series of metal-organic frameworks (MOFs) with dynamic, interlocked crown ether rings are investigated to determine the factors that influence the



motion of the rings. It is demonstrated that the size of the rings and the framework structure affect the motion.  $^{13}\text{C}$  variable temperature SSNMR is used to confirm the shuttling motion of rings between recognition sites on an axle that is incorporated into a MOF. Next, a study on a series of simple inorganic molecular rotors is described. It is shown that some of these compounds act as rotors with very low energy barriers that exhibit random rotational dynamics at temperatures below 75 K, while other structurally similar compounds do not display any motions over a wide range of temperatures. It is posited that steric and electronic effects from the coordinating ligands are responsible for the observed dynamics.  $^2\text{H}$  SSNMR is shown to be essential for classifying and understanding the dynamics of these low-energy molecular rotors

Finally,  $^{35}\text{Cl}$  SSNMR is used to elucidate the structure of a transition-metal compound bound to the surface of a porous silica material. It is demonstrated that ultra-wideline (UW)  $^{35}\text{Cl}$  SSNMR spectra for transition-metal complexes can be rapidly acquired using a combination of high magnetic fields and specialized pulse sequences. These spectra allow for the differentiation of different Cl bonding environments (*i.e.*, bridging, terminal axial, and terminal equatorial). Density functional theory (DFT) calculations and an accompany molecular-orbital analysis allow for an understanding of the origin of the observed  $^{35}\text{Cl}$  electric field gradient (EFG) parameters, which influence the  $^{35}\text{Cl}$  quadrupolar interactions. The structure of a surface-supported complex is then proposed, demonstrating the applicability of these techniques to the study of very dilute catalytic species.

## Dedication

In memory of:

Leonard N. Cohen

September 21<sup>st</sup>, 1934 – November 7<sup>th</sup>, 2016

and

Gordon E. Downie

February 6<sup>th</sup>, 1964 – October 17<sup>th</sup>, 2017

*Ring the bells that still can ring,*

*Forget your perfect offering,*

*There is a crack, in everything,*

*That's how the light gets in.*

“Anthem” by Leonard Cohen, 1992

## Acknowledgments

The completion of this thesis would not have been possible without the contributions (scientific or otherwise) many people. For those whom I have failed to mention, I offer my sincerest apologies.

First and foremost, I acknowledge my supervisor, Dr. Rob Schurko, for all the guidance he has provided through these past years. I first met Rob in his Physical Chemistry Class. The second time I met Rob was in the corridor of Essex Hall, where he convinced me to abandon the Physics Department and join his research group. Despite him (in)conveniently scheduling my orientation meeting at a time when he was in France for a conference, he has always been available to provide guidance on projects. I have had the opportunity to take several of his classes, and while his lectures can be sleep-inducing at times, he teaches with the utmost passion and enthusiasm. He has laid the foundation for my understanding of NMR and taught me to be an independent researcher. Through his gruelling 3+ hour-long practice talks for conferences presentations, he has taught me to present my ideas in a clear and succinct way. His rigorous editing of manuscripts, consisting of at least six versions, has taught me the skill of scientific writing; if the manifestation of this skill is not evident in this thesis, he is surely to blame. Lastly, he is well-versed in a wide range of topics, and so casual conversation in the lab is rarely dull. Working with Rob has been a truly rewarding experience, and for that, I am grateful.

To all members of the Schurko research group past and present, you are all thanked. A special thank you goes to Dr. Karen Johnston, who helped me develop as a young scientist. Dr. Johnston took a hands-on approach and was instrumental in my early

training. Dr. Kris Harris is acknowledged for taking the time to teach me about dynamics and NMR. The comic relief provided by Dr. Bryan Lucier certainly made the time in the lab more enjoyable. Dr. Stanislav Veinberg is acknowledged for all his help in troubleshooting spectrometer issues and his methodical approach to solving problems. Dr. Sean Holmes is thanked for his suggestions in regard to DFT calculations

David Hirsh and his better half, Steph Kosnik, are thanked for keeping me sane these past five years. The countless lunch-time gossip sessions and foggy nights at Sugar House will always be remembered (or will they?). Cameron Vojvodin is graciously thanked for agreeing to take over the coordination of Win.Chem. Austin Peach....is thanked....for....I don't know. I am certainly indebted to Jacqueline Gemus for all her assistance and ideas on the mechanochem project. You were a great student and I hope you learned something from me. Nathan Veinberg is thanked for being an easy target for jokes. Thankfully, Lucas Foster has taken his place. Adam and Derek are thanked, even though they don't say much.

My "posse" is also thanked. I am very grateful to have met these friends and I hope never lose contact with them, wherever we all end up. Habibi Manar, your dad jokes are unparalleled, and you always know how to make light of any situation. Akhil, you taught me that somehow, grad students can have expensive tastes. Gio, I rarely understand what you're saying, but I'm sure it makes sense in your head. A special thank you goes out to pinche Pablo Bulit, your assistance with chemistry, Microsoft Word, and life is greatly appreciated.

I would like to thank my committee members for agreeing to read this thesis, and participating in the several meetings through my academic career. Matt Revington is

acknowledged for his assistance in NMR experiments and Joe Lichaa is thanked for his help with numerous computer/technical issues.

Last, but certainly not least, a special thank you goes to my parents, Chris and Roseann, for all your love and support throughout my life. Now that I've submitted my thesis, you have nothing else to worry about.

# Table of Contents

<b>Declaration of Co-authorship/Previous Publications .....</b>	<b>iii</b>
<b>Abstract.....</b>	<b>vii</b>
<b>Dedication .....</b>	<b>ix</b>
<b>Acknowledgments .....</b>	<b>x</b>
<b>List of Tables .....</b>	<b>xx</b>
<b>List of Figures.....</b>	<b>xxiv</b>
<b>List of Schemes.....</b>	<b>xliv</b>
<b>List of Abbreviations .....</b>	<b>xlvi</b>
<b>Chapter 1: Introduction to NMR and Context of Research .....</b>	<b>1</b>
<b>1.1 Nuclear Magnetic Resonance Spectroscopy.....</b>	<b>1</b>
<b>1.2 NMR Interactions.....</b>	<b>3</b>
1.2.1 The Zeeman Interaction .....	3
1.2.2 The Radiofrequency Interaction.....	6
1.2.3 The Magnetic Shielding/Chemical Shift Interaction .....	9
1.2.4 The Quadrupolar Interaction.....	13
1.2.5 Direct Dipolar Coupling.....	20
1.2.6 Indirect spin-spin Coupling ( <i>J</i> -coupling).....	21
<b>1.3 Effects of Dynamics on SSNMR spectra .....</b>	<b>22</b>
<b>1.4 Acquisition Techniques.....</b>	<b>28</b>
1.4.1 Magic-Angle Spinning (MAS).....	29
1.4.2 Cross-Polarization (CP) .....	32

1.4.3	Quadrupolar Echo .....	34
1.4.4	Carr-Purcell Meiboom-Gill (CPMG) Pulse Sequence.....	35
1.4.5	Wideband Uniform-Rate Smooth-Truncation (WURST)-CPMG .....	36
1.4.6	Frequency-Stepped Acquisition .....	37
<b>1.5</b>	<b>Density Function Theory Calculations .....</b>	<b>38</b>
<b>1.6</b>	<b>Context of Research .....</b>	<b>39</b>
1.6.1	Into the Void(s) .....	40
1.6.2	“There’s plenty of room at the bottom” .....	42
<b>1.7</b>	<b>References .....</b>	<b>44</b>
<b>Chapter 2: NMR-Assisted Powder X-Ray Diffraction for the Structural</b>		
<b>Characterization of a Zeolitic Imidazolate Framework Synthesized via Accelerated</b>		
<b>Aging Reactions..... 54</b>		
<b>2.1</b>	<b>Overview.....</b>	<b>54</b>
<b>2.2</b>	<b>Introduction .....</b>	<b>54</b>
<b>2.3</b>	<b>Experimental Details .....</b>	<b>59</b>
2.3.1	Reagents .....	59
2.3.2	Accelerated Aging Reactions.....	59
2.3.3	Powder X-ray Diffraction .....	59
2.3.4	Solid-State NMR.....	59
2.3.5	$^1\text{H}$ - $^{111}\text{Cd}$ CP/MAS and CP static NMR.....	60
2.3.6	$^1\text{H}$ - $^{14}\text{N}$ BRAIN-CP/WURST-CPMG .....	61
2.3.7	Structure Refinement .....	62
<b>2.4</b>	<b>Results and Discussion .....</b>	<b>62</b>
2.4.1	Synthesis and Powder X-ray Diffraction .....	62
2.4.2	Solid-State NMR Studies .....	65

2.4.3	Structural Refinement .....	73
<b>2.5</b>	<b>Conclusions .....</b>	<b>74</b>
<b>2.6</b>	<b>References .....</b>	<b>76</b>
 <b>Chapter 3: Monitoring the Formation of Cadmium-Containing Zeolitic</b> <b>Imidazolate Frameworks using a Combination of Powder X-ray Diffraction and</b> <b>Multinuclear Solid-State NMR..... 83</b>		
<b>3.1</b>	<b>Overview.....</b>	<b>83</b>
<b>3.2</b>	<b>Introduction .....</b>	<b>84</b>
<b>3.3</b>	<b>Experimental Details.....</b>	<b>89</b>
3.3.1	Starting Materials .....	89
3.3.2	Mechanochemical Synthesis .....	89
3.3.3	Synthesis of $\alpha$ CdM.....	90
3.3.4	Synthesis of CdIF-1 .....	90
3.3.5	SSNMR Experiments.....	91
3.3.6	$^1\text{H}$ - $^{111}\text{Cd}$ CP/MAS NMR.....	91
3.3.7	$^{15}\text{N}$ MAS SSNMR.....	92
3.3.8	Powder X-ray Diffraction (PXRD).....	92
3.3.9	Void volume calculations.....	92
<b>3.4</b>	<b>Results and discussion.....</b>	<b>93</b>
3.4.1	General overview of syntheses .....	93
3.4.2	Reaction Set 1 (CdO + 2 eq. HMeIm, 4 mol% $\text{NH}_4\text{NO}_3$ , 100 $\mu\text{L}$ MeOH, room temperature). .....	95
3.4.3	Reaction Set 2 (CdO + 2 eq. HMeIm, 4 mol% $\text{NH}_4\text{NO}_3$ , 50 $\mu\text{L}$ MeOH, room temperature) .....	99



3.4.4	Reaction 3 (CdO + 2 eq. HMeIm, 4 mol% NH <sub>4</sub> NO <sub>3</sub> , 100 μL MeOH, cryomilling)	
		101
3.4.5	PXRD Analysis of Reaction Set 1 .....	103
3.4.6	Reaction 4 (amorphous framework + HMeIm + 4 mol% NH <sub>4</sub> NO <sub>3</sub> + 100 μL MeOH)	
		106
3.4.7	CdIF-1 .....	110
3.4.8	Identity of <i>i</i> CdM.....	112
3.4.9	Reaction pathways .....	114
3.4.10	Role of the salt .....	119
<b>3.5</b>	<b>Conclusions .....</b>	<b>121</b>
<b>3.6</b>	<b>References .....</b>	<b>123</b>

**Chapter 4: Observing Dynamics in Metal-organic Frameworks with  
Mechanically Interlocked Components using Solid-state NMR Spectroscopy ..... 129**

<b>4.1</b>	<b>Overview.....</b>	<b>129</b>
<b>4.2</b>	<b>Introduction .....</b>	<b>130</b>
<b>4.3</b>	<b>Experimental Details.....</b>	<b>136</b>
4.3.1	Synthetic procedures .....	136
4.3.2	SSNMR Studies at 9.4 T .....	136
4.3.3	<sup>13</sup> C SSNMR at 21.1 T.....	138
<b>4.4</b>	<b>Results and Discussion .....</b>	<b>139</b>
4.4.1	UWDM-1 Series .....	142
4.4.2	UWDM-2. ....	154
4.4.3	α-UWDM-3 .....	157
4.4.4	β-UWDM-3 .....	161
4.4.5	UWDM-P MOFs.....	165

4.4.6	UWDM-4 .....	173
<b>4.5</b>	<b>Conclusions .....</b>	<b>180</b>
<b>4.6</b>	<b>References: .....</b>	<b>182</b>
<b>Chapter 5: Multinuclear Solid-State NMR Investigations of Platinum(II) trans-</b>		
<b>Dihydride Molecular Rotors .....</b>		
<b>5.1</b>	<b>Overview.....</b>	<b>186</b>
<b>5.2</b>	<b>Introduction .....</b>	<b>187</b>
<b>5.3</b>	<b>Experimental Methodologies and Computational Details.....</b>	<b>190</b>
5.3.1	Synthesis .....	190
5.3.2	<sup>195</sup> Pt SSNMR.....	191
5.3.3	Low-temperature <sup>2</sup> H SSNMR.....	191
5.3.4	Variable-temperature <sup>2</sup> H SSNMR Experiments at 9.4 T .....	192
5.3.5	Simulation of <sup>2</sup> H SSNMR Data.....	193
5.3.6	Calculation of <sup>195</sup> Pt CS and <sup>2</sup> H EFG Tensor Parameters .....	193
5.3.7	DFT Calculations of Energy Landscapes.....	194
<b>5.4</b>	<b>Results and Discussion .....</b>	<b>194</b>
5.4.2	<i>trans</i> -D <sub>2</sub> Pt(P(NMe <sub>2</sub> ) <sub>3</sub> ) <sub>2</sub> (2) .....	208
5.4.3	<i>trans</i> -D <sub>2</sub> Pt(P(Cy) <sub>3</sub> ) <sub>2</sub> (3) .....	211
5.4.4	<i>trans</i> -D <sub>2</sub> Pt( <i>i</i> Pr) <sub>2</sub> (4) .....	212
5.4.5	<i>trans</i> -DPt( <i>i</i> Pr) <sub>2</sub> (5).....	213
<b>5.5</b>	<b>Conclusions .....</b>	<b>216</b>
<b>5.6</b>	<b>References .....</b>	<b>218</b>
<b>Chapter 6: An Investigation of Chlorine Ligands in Transition-metal</b>		
<b>Complexes via <sup>35</sup>Cl SSNMR and DFT Calculations .....</b>		
<b>6.1</b>	<b>Overview.....</b>	<b>222</b>

<b>6.2</b>	<b>Introduction .....</b>	<b>223</b>
<b>6.3</b>	<b>Experimental and Computational Details.....</b>	<b>227</b>
6.3.1	Sample Preparation .....	227
6.3.2	Synthesis of $\text{WCl}_6\text{-SiO}_2$ .....	227
6.3.3	Powder X-ray Diffraction (PXRD) .....	228
6.3.4	$^{35}\text{Cl}$ SSNMR Spectroscopy .....	228
6.3.5	$^{35}\text{Cl}$ NQR Spectroscopy .....	230
6.3.6	Plane-wave DFT Calculations .....	230
6.3.7	$^{35}\text{Cl}$ Natural Bond Orbital/Natural Local Molecular Orbital Analysis of $\text{NbCl}_5$ ...	231
<b>6.4</b>	<b>Results and Discussion .....</b>	<b>232</b>
6.4.1	Tungsten(VI) Chloride ( $\text{WCl}_6$ ) .....	237
6.4.2	Tetrachlorotungsten(VI) oxide ( $\text{WOCl}_4$ ) and tetrachloromolybdenum(VI) oxide ( $\text{MoOCl}_4$ ).....	244
6.4.3	Niobium(V) chloride ( $\text{NbCl}_5$ ) and tantalum(V) chloride ( $\text{TaCl}_5$ ).....	250
6.4.4	$^{35}\text{Cl}$ Transverse Relaxation Time ( $T_2$ ) measurements.....	255
6.4.5	LMO Analysis of the $^{35}\text{Cl}$ EFG Tensors .....	258
6.4.6	$^{35}\text{Cl}$ SSNMR of $\text{WCl}_6$ supported on silica .....	263
<b>6.5</b>	<b>Conclusions .....</b>	<b>265</b>
<b>6.6</b>	<b>References .....</b>	<b>268</b>
	<b>Chapter 7: Conclusions and Future Outlook.....</b>	<b>273</b>
<b>7.1</b>	<b>General Overview .....</b>	<b>273</b>
<b>7.2</b>	<b>Solid-state Synthesis of Cadmium-imidazolate Frameworks.....</b>	<b>274</b>
<b>7.3</b>	<b>Future Work – Monitoring the Formation of Porous Materials .....</b>	<b>275</b>
<b>7.4</b>	<b>Dynamics of Molecular Machines.....</b>	<b>278</b>
<b>7.5</b>	<b>Future Work – Molecular Machines .....</b>	<b>279</b>

7.6	Surface Supported Catalysts .....	283
7.7	Future Work – Ultra-wideline <sup>35</sup> Cl SSNMR .....	283
	Appendix A Supplementary Tables and Figures for Chapter 2.....	288
	Appendix B: Supplementary Tables and Figures for Chapter 3.....	295
	Appendix C Synthetic Information and Supplementary Tables and Figures for Chapter 4 .....	302
	Appendix D Supporting Tables and Figures for Chapter 5.....	314
	Appendix E Supplementary Information for Chapter 6.....	320
	Vita Auctoris.....	349

## List of Tables

<b>Table 2.1:</b> Experimentally measured cadmium chemical shift tensor parameters. ....	67
<b>Table 3.1:</b> Sample names and descriptions. ....	89
<b>Table 3.2:</b> Summary of the reagents and conditions used in the mechanochemical syntheses. ....	93
<b>Table 3.3:</b> Experimentally measured $^{111}\text{Cd}$ isotropic shifts, line widths, and $J$ -coupling constants. ....	97
<b>Table 4.1:</b> Rates and modes of motion used in the simulation of experimental VT $^2\text{H}$ SSNMR data for UWDM-1 <sub>(22)</sub> . ....	149
<b>Table 4.2:</b> Rates and modes of motion used in the simulation of experimental VT $^2\text{H}$ SSNMR data for UWDM-1 <sub>(B24)</sub> . ....	152
<b>Table 4.3:</b> Rates and modes of motion used in the simulations of experimental VT $^2\text{H}$ SSNMR data for UWDM-2. ....	156
<b>Table 4.4:</b> Rates and modes of motion used in the simulation of experimental VT $^2\text{H}$ SSNMR data for $\alpha$ -UWDM-3. ....	159
<b>Table 4.5:</b> Rates and modes of motion used in the simulation of experimental VT $^2\text{H}$ SSNMR data for $\alpha$ -UWDM-3. ....	162
<b>Table 4.6:</b> Rates and modes of motion used in the simulation of experimental VT $^2\text{H}$ SSNMR data for $\beta$ -UWDM-3. ....	164
<b>Table 4.7:</b> Unit cell parameters for the UWDM-P MOF series. ....	166
<b>Table 4.8:</b> Rates and modes of motion used in the simulation of experimental VT $^2\text{H}$ SSNMR data for UWDM-P1. ....	169

<b>Table 4.9:</b> Rates and modes of motion used in the simulation of experimental VT $^2\text{H}$ SSNMR data for UWDM-P1 <sub>d</sub> .....	169
<b>Table 4.10:</b> Rates and modes of motion used in the simulation of experimental VT $^2\text{H}$ SSNMR data for UWDM-P2.....	169
<b>Table 4.11:</b> Rates and modes of motion used in the simulation of experimental VT $^2\text{H}$ SSNMR data for UWDM-P2 <sub>d</sub> .....	169
<b>Table 5.1:</b> Calculated (DFT) and experimental platinum chemical shift (CS) tensor parameters for <b>1</b> . .....	196
<b>Table 5.2:</b> Calculated (DFT) and experimental $^2\text{H}$ EFG tensor parameters.....	200
<b>Table 6.1:</b> Experimentally measured $^{35}\text{Cl}$ NMR parameters for transition metal chlorides. ....	233
<b>Table 6.2:</b> Experimental and calculated (using CASTEP) $^{35}\text{Cl}$ EFG tensor parameters and comparison of predicted NQR frequencies obtained from $^{35}\text{Cl}$ SSNMR data to those reported in literature. Calculation of the NMR parameters was completed both prior to and post geometry optimization of the structure. ....	236
<b>Table 6.3:</b> LMO contributions to the $^{35}\text{Cl}$ EFG tensors of the various chlorine environments in <b>NbCl<sub>5</sub></b> .....	261
<b>Table B1:</b> $^1\text{H}$ - $^{111}\text{Cd}$ CP/MAS NMR contact times and recycle delays .....	295
<b>Table B2:</b> Calculated pore volumes for the Zn and Cd ZIFs. ....	295
<b>Table C1:</b> Optimized recycle delays and $90^\circ$ pulse lengths used in the acquisition of $^2\text{H}$ SSNMR spectra at 9.4 T. ....	303

<b>Table C2:</b> Shuttling rates obtained from the simulation of solution-state $^{13}\text{C}$ NMR data for the [2]rotaxane made from <b>A<sub>4</sub></b> and <b>CE<sub>4</sub></b> .	304
<b>Table D1:</b> Recycle delays used in the acquisition of VT $^2\text{H}$ SSNMR spectra at 9.4 T.	315
<b>Table D2:</b> Calculated hydrogen chemical shielding tensor parameters.	315
<b>Table E1:</b> Experimental times for the acquisition of $^{35}\text{Cl}$ SSNMR spectra at 9.4 and 21.1 T.	323
<b>Table E2:</b> WURST-CPMG acquisition parameters for $^{35}\text{Cl}$ SSNMR spectra acquired at 9.4 T for all samples.	325
<b>Table E3:</b> WURST-CPMG acquisition parameters for $^{35}\text{Cl}$ SSNMR spectra acquired at 21.1 T for all samples.	326
<b>Table E4:</b> Pseudopotential information for CASTEP calculations.	327
<b>Table E5:</b> Pre- and post-geometry optimization bond lengths.	328
<b>Table E6:</b> Initial and post-optimization atomic forces in the structures.	329
<b>Table E7:</b> Calculated (using CASTEP) $^{35}\text{Cl}$ CS tensor parameters. Calculation of the NMR parameters was completed both prior to and post geometry optimization of the structure.	334
<b>Table E8:</b> $T_2$ measurements made by placing the transmitter on each of the discontinuities of the $^{35}\text{Cl}$ SSNMR powder patterns.	335
<b>Table E9:</b> Structural parameters of $(\text{NbCl}_5)_2$ . Selected averaged XRD and optimized (OPT) <sup>a</sup> bond distances (Å) and bond angles (°).	336
<b>Table E10:</b> Comparison of experimental (EXP) and calculated $^{35}\text{Cl}$ EFG tensor parameters (using ADF and CASTEP (CSP)) on a geometry optimized structure of	

NbCl <sub>5</sub> , as well as ADF calculations performed on non-optimized crystal structures (XRD). .....	336
<b>Table E11:</b> LMO contributions to the $V_{33}$ component of equatorial (eq), bridging (br) and axial (ax) chlorides in the complex (NbCl <sub>5</sub> ) <sub>2</sub> . All values are in au. ....	337
<b>Table E12:</b> Bonds orders and compositions of selected chlorine-centered LMOs .....	338



## List of Figures

**Figure 1.1:** The effect of the Zeeman interaction on the energy levels for a spin-1/2 nucleus. The originally degenerate energy levels are split into two equally spaced energy levels when placed in an external magnetic field. .... 5

**Figure 1.2:** Vector representation of the effect of a radiofrequency pulse on the bulk magnetization. The coordinate system is a rotating reference frame that rotates about the direction of the external magnetic field at the transmitter frequency,  $\omega_{\text{rf}}$ . A rf pulse is applied along the  $x'$ -axis for a duration that tips the angle along the  $-y'$ -axis. After the pulse is turned off, the magnetization begins to precess about the  $z$ -axis ... 8

**Figure 1.3:** Schematic representation of the populations of spins at equilibrium (**A**). The application of  $\pi/2$  and  $\pi$  pulses create the conditions of (**B**) saturation and (**C**) inversion, respectively. .... 9

**Figure 1.4:** (**A**) Schematic representation of the MS tensor in its principal axis system (PAS) using an ellipsoid as a visual aid. The magnitudes of the components are  $\sigma_{11} \leq \sigma_{22} \leq \sigma_{33}$ . (**B**) Angles  $\theta$  and  $\varphi$  describe the relative orientations of  $\mathbf{B}_0$  and the MS tensor in its PAS. .... 11

**Figure 1.5:** Simulated CSA powder patterns showing the effects of the (**A**) span ( $\Omega$ ) and (**B**) skew ( $\kappa$ ) on the appearance of the spectra ..... 12

**Figure 1.6:** Schematic representation of the distribution of nuclear charge in a (**A**) spin-1/2 ( $Q = 0$ , spherical), (**B**) quadrupolar ( $Q > 0$ , prolate), and (**C**) quadrupolar ( $Q < 0$ , oblate) nuclides. .... 13

**Figure 1.7:** The relationship between the absolute magnitudes of  $C_Q$  and the spherical symmetry of the EFG tensor with its origin at the nucleus for a series of sodium

oxides, as described by Koller <i>et al.</i> As the degree of spherical symmetry increases, the magnitude of $C_Q$ decreases. Adapted from ref. 28.....	14
<b>Figure 1.8:</b> Relationships between the Cl bonding environment and typical magnitudes of $C_Q(^{35}\text{Cl})$ .....	16
<b>Figure 1.9:</b> Perturbation of the Zeeman energy levels by the first- and second-order quadrupolar interactions for a (A) spin-3/2 nuclide (e.g., $^{35}\text{Cl}$ ) and (b) spin-1 nuclide (e.g., $^2\text{H}$ ). The first-order quadrupolar interaction (FOQI) does not influence the central transition (CT, shown in red) but influences the satellite transitions (ST) to a great extent.....	18
<b>Figure 1.10:</b> Simulated central-transition second-order quadrupolar spectra for a spin-3/2 nucleus with (A) $\eta_Q = 0$ and values of $C_Q$ ranging from 15 to 35 MHz and (B) $C_Q = 25$ MHz and $\eta_Q$ values ranging from 0.2 to 1.0. ....	19
<b>Figure 1.11:</b> Appearance of a powder pattern in the spectrum of a spin-1 nuclide; such patterns are referred to as Pake doublets. Also shown are the frequency separations of the “horn”, “shoulder”, and “foot” discontinuities. ....	20
<b>Figure 1.12:</b> (A) A depiction of the rotation of a $^2\text{H}$ EFG tensor in its principal axis system (PAS) into the three sites of a $\text{CD}_3$ group in the crystallite-fixed frame (CFF). The $z$ -axis of the CFF is coincident with the $C_3$ rotation axis of the $\text{CD}_3$ group. (B) Simulated $^2\text{H}$ SSNMR spectra for the three-fold rotation of the $\text{CD}_3$ groups with different exchange rates ( $\nu_{\text{ex}}$ ). ....	29
<b>Figure 1.13:</b> Schematic representation of the orientation of an NMR rotor with respect to the external magnetic field ( $B_0$ ). $\theta_R$ is the experimentally adjusted angle between the rotor axis and $B_0$ , which is most commonly set to the magic angle ( $54.74^\circ$ ). The	

ellipsoid represents an interaction tensor whose largest component is oriented at angles $\beta$ with respect to the rotor axis and $\theta$ with respect to $B_0$ . .....	31
<b>Figure 1.14:</b> Diagrams depicting the (A) cross-polarization (CP), (B) quadrupolar echo (QE), and (C) Carr-Purcell-Meiboom-Gill (CPMG) pulse sequences. ....	34
<b>Figure 1.15 :</b> The (A) amplitude and (B) phase profiles of the WURST pulse. ....	36
<b>Figure 1.16:</b> The acquisition of a $^{35}\text{Cl}$ SSNMR spectrum using the variable offset cumulative spectra (VOCS) technique. WURST-CPMG spectra were acquired with 100 kHz increments of the transmitter frequency. ....	38
<b>Figure 2.1:</b> Experimental PXRD patterns for (A) 1:2 reaction aged for 12 days, (B) 1:2 reaction with $\text{NH}_4\text{NO}_3$ aged for 7 days, (C) 1:6 reaction with $\text{NH}_4\text{NO}_3$ aged for 6 days, (D) 1:6 reaction with $\text{NH}_4\text{NO}_3$ aged for 6 days, and (E) CdO. ....	63
<b>Figure 2.2:</b> Experimental $^1\text{H}$ - $^{111}\text{Cd}$ CP NMR spectra acquired under MAS (blue traces) and static (black traces) conditions, with accompanying simulations of the static spectra (red traces) for (A) dia-Cd[Im] $_2$ (2), (B) yqt1-Cd[MeIm] $_2$ (3), and (C) $[\text{Cd}(\text{HIm})_6]^{2+}[\text{CO}_3]^{2-} \cdot 3\text{H}_2\text{O}$ (4). ....	68
<b>Figure 2.3:</b> Experimental $^1\text{H}$ - $^{111}\text{Cd}$ CP NMR spectra under (A) MAS ( $v_{\text{rot}} = 5$ kHz) and (B) static conditions for compound 1, with an accompanying simulation of the static spectrum in (C). ....	70
<b>Figure 2.4:</b> (A) $^1\text{H}$ - $^{13}\text{C}$ CP MAS spectra of bulk HMeIm (green trace) and 1 (blue trace), (B) $^1\text{H}$ MAS spectrum of 1 and (C) $^1\text{H}$ - $^{14}\text{N}$ BRAIN-CP/WURST-CPMG spectra of HMeIm (green trace) and 1 (blue trace). ....	71

<b>Figure 2.5:</b> Depictions (adapted from the predicted crystal structure of <b>1</b> ) of (A) the coordination environment about the Cd atoms, and (B) a supercell showing the pores containing the HMeIm molecules (hydrogen atoms have been omitted for clarity).	72
<b>Figure 3.1.</b> $^1\text{H}$ - $^{111}\text{Cd}$ CP/MAS NMR spectra ( $v_{\text{rot}} = 5$ kHz) of the products of <b>1</b> (CdO + 2 eq. HMeIm + 4 mol% $\text{NH}_4\text{NO}_3$ + 100 $\mu\text{L}$ MeOH) milled for different time periods.	95
<b>Figure 3.2:</b> $^1\text{H}$ - $^{111}\text{Cd}$ CP/MAS NMR spectra ( $v_{\text{rot}} = 5$ kHz) for the products of the mechanochemical reaction between CdO, 2 eq. HMeIm, and 4 mol% $\text{NH}_4\text{NO}_3$ using (A) 25 $\mu\text{L}$ , (B) 50 $\mu\text{L}$ , and (C) 100 $\mu\text{L}$ of MeOH solvent. The reactions were milled for five minutes.	99
<b>Figure 3.3:</b> $^1\text{H}$ - $^{111}\text{Cd}$ CP/MAS NMR spectra ( $v_{\text{rot}} = 5$ kHz) of the products of <b>2</b> (CdO + 2 eq. HMeIm + 4 mol% $\text{NH}_4\text{NO}_3$ + 50 $\mu\text{L}$ MeOH) milled for different time periods.	100
<b>Figure 3.4:</b> $^1\text{H}$ - $^{111}\text{Cd}$ CP/MAS NMR ( $v_{\text{rot}} = 5$ kHz) spectra for the products of <b>3</b> (CdO + 2 eq. HMeIm + 4 mol% $\text{NH}_4\text{NO}_3$ + 100 $\mu\text{L}$ MeOH, 77 K). The spectra were acquired at different time intervals, as noted by the superscript on the reaction number (the spectra are non-cumulative).	102
<b>Figure 3.5:</b> (A) Experimental PXRD patterns for the products of <b>1</b> milled for different time periods. Simulated PXRD patterns for (B) CdO, (C) HMeIm, (D) CdIF-1, (E) $d\text{CdM}$ , and (F) $y\text{CdM}$ .	104
<b>Figure 3.6:</b> Experimental PXRD patterns for (A) <b>1</b> <sub>25m</sub> , (B) <b>1</b> <sub>25m-a1h</sub> , (C) <b>1</b> <sub>5s</sub> , (D) <b>1</b> <sub>5s-a1d</sub> . (E) Simulated PXRD pattern for $y\text{CdM}$ .	106

<b>Figure 3.7:</b> $^1\text{H}$ - $^{111}\text{Cd}$ CP/MAS NMR spectra of (A) <b>yCdM</b> obtained from mechanochemical synthesis and (B) the <b>aCdM</b> obtained by milling a dried sample of <b>yCdM</b> for three hours. ....	108
<b>Figure 3.8:</b> $^1\text{H}$ - $^{111}\text{Cd}$ CP/MAS NMR spectra ( $v_{\text{rot}} = 5$ kHz) for <b>4</b> ( <b>aCdM</b> + HMeIm + 4 mol% $\text{NH}_4\text{NO}_3$ + 100 $\mu\text{L}$ MeOH) acquired at different time intervals (the spectra are non-cumulative). ....	109
<b>Figure 3.9:</b> $^1\text{H}$ - $^{111}\text{Cd}$ CP/MAS NMR spectra ( $v_{\text{rot}} = 5$ kHz) for (A) <b>CdIF-1<sub>as</sub></b> , (B).....	111
<b>Figure 3.10:</b> (A) Unit cell of <b>CdIF-1</b> with the 002 lattice planes shown in red. ....	115
<b>Figure 3.11:</b> $^1\text{H}$ - $^{111}\text{Cd}$ CP/MAS NMR spectra ( $v_{\text{rot}} = 5$ kHz) of the products <b>1</b> conducted with (A) no salt, and (B) the addition of 4 mol% of $\text{NH}_4\text{NO}_3$ . ....	119
<b>Figure 3.12:</b> $^{15}\text{N}$ DP MAS NMR spectra of (A) $^{15}\text{NH}_4$ $^{15}\text{NO}_3$ and (B) <b>1<sub>30m</sub></b> . ....	121
<b>Figure 4.1:</b> General procedure for the synthesis of metal-organic frameworks with dynamic interlocked components. First, a [2]rotaxane is made from an organic axle molecule and a crown ether macrocycle. The [2]rotaxane is combined with an organic linker and a metal source to form the MOF. ....	132
<b>Figure 4.2:</b> (A) Experimental VT $^2\text{H}$ SSNMR powder patterns of UWDM-1 <sub>(24)</sub> , (B) simulated $^2\text{H}$ SSNMR powder patterns and, (C) accompanying depictions of the motional models used for the (i) motions that are too slow to influence the appearance of the Pake doublet ( <i>i.e.</i> , in the SML), (ii) the two-site jump with $\beta = 77^\circ$ , (iii) the two-site jump with $\beta = 60^\circ$ combined with partial rotation of the ring over $225^\circ$ in $45^\circ$ steps, and (iv) two-site jumps of $70^\circ$ combined with full rotation of the ring. ....	143

**Figure 4.3:** (A) Ball-and-stick representation of the [2]rotaxane ligand in UWDM-1<sub>(22)</sub>, which is composed of **A**<sub>1</sub> and **CE**<sub>2</sub> and coordinated to **SBU**<sub>1</sub> (colour key: C = black, O = red, N = blue, Cu = green. Hydrogen atoms are omitted for clarity). (B) View down the crystallographic c-axis of UWDM-1<sub>(22)</sub> depicting the hexagonal shaped channels (**A**<sub>1</sub> shown in blue, **CE**<sub>2</sub> in red, and Cu<sup>2+</sup> metal ions in green). It is noted that UWDM 1<sub>(B24)</sub> has the same structure, but with **CE**<sub>3</sub> rings..... 147

**Figure 4.4:** (A) Experimental VT <sup>2</sup>H SSNMR powder patterns for UWDM-1<sub>(22)</sub>, (B) simulated <sup>2</sup>H SSNMR powder patterns, and (C) accompanying depictions of the motional models used for the (i) motions that are too slow to influence the appearance of the Pake doublet (i.e., in the SML), (ii) two-site jumps with  $\beta = 65^\circ$  and rates in the FML, (iii) two-site jumps combined with the onset of partial rotation of the ring over 250° in 50° steps, and (iv) two-site jumps and partial rotation with rates in the FML..... 148

**Figure 4.5:** (A) Experimental VT <sup>2</sup>H SSNMR powder patterns for UWDM-1<sub>(B24)</sub>, (B) simulated <sup>2</sup>H SSNMR powder patterns, and (C) accompanying depictions of the motional model used for the (i) motions that are occurring too slowly to influence the appearance of the Pake doublet (i.e., in the SML), (ii) two-site jumps with  $\beta = 60^\circ$ , (iii) two-site jumps with  $\beta = 70^\circ$ , and (iv) two-site jumps with  $\beta = 75^\circ$ . ..... 151

**Figure 4.6:** (A) Ball-and-stick representation of UWDM-2 showing the three-fold interpenetration (colour key: **A**<sub>2</sub> = blue, **CE**<sub>1</sub> = red, **L**<sub>1</sub> = yellow). (B) Ball-and-stick representations showing the proximity of the rings (red) to one another and to the framework structure (green). ..... 155

**Figure 4.7:** (A) Experimental VT  $^2\text{H}$  SSNMR powder patterns for UWDM-2. (B) Simulated  $^2\text{H}$  SSNMR powder patterns using the two-site jump ( $\beta = 72(2)^\circ$ ) and partial rotation models. Rates used in the simulations are listed in Table 4.3. (C) Depiction of the motional model used. .... 157

**Figure 4.8:** (A) Ball-and-stick representation of  $\alpha$ -UWDM-3 showing the two-fold interpenetration (colour key:  $\text{A}_2$  = blue,  $\text{CE}_1$  = red,  $\text{L}_2$  = yellow). (B) Ball-and-stick representations showing the confinement of the  $\text{CE}_1$  ring (red) within the “square plane” of the framework (green). (C) Schematic depiction of the reversible phase change that occurs in UWDM-3. .... 158

**Figure 4.9:** (A) Experimental VT  $^2\text{H}$  SSNMR powder patterns for  $\alpha$ -UWDM-3. (B) Simulated  $^2\text{H}$  SSNMR powder patterns and (C) accompanying depictions of the motional model used for the (i) motions that are occurring too slowly to influence the appearance of the Pake doublet (i.e., in the SML), (ii) two-site jump with  $\beta = 75(2)^\circ$ , (iii) two-site jump with  $\beta = 75(2)^\circ$  combined with the onset of partial rotation of the ring over  $225^\circ$  in  $45^\circ$  steps and (iv) two-site jump and partial rotation combined with large amplitude ring flexing to positions  $30(3)^\circ$  above and below the “square plane” of the framework, and (v) the FML of all the above-mentioned motions. .... 160

**Figure 4.10:** (A) Experimental VT  $^2\text{H}$  SSNMR powder patterns for  $\beta$ -UWDM-3. (B) Simulated  $^2\text{H}$  SSNMR powder patterns and (C) accompanying depictions of the motional model used for the (i) motions that are too slow to influence the appearance of the Pake doublet (i.e., in the SML), (ii) two-site jump with  $\beta = 75(2)^\circ$ , (iii) two-site jump with  $\beta = 75(2)^\circ$  combined with the onset of partial rotation of the

ring over 225° in 45° steps, (iv) two-site jumps combined with partial rotation and jumps through the alkyl portion of the ring that are occurring at a rate slower than the rate of jumps between oxygen atoms, and (v) increased rate of jumps through the alkyl portion of the ring. .... 163

**Figure 4.11:** Crystal structures showing the two-fold interpenetration of (A) UWDM-P1, (B) UWDM-P2, and (C) UWDM-P2<sub>d</sub>. In each case, the CE<sub>1</sub> macrocycles sit above the square plane formed by the L<sub>3</sub> ligands. It is noted that a crystal structure of UWDM-P1<sub>d</sub> could not be determined, however; crystal lattice parameters were obtained (Table 4.6). .... 166

**Figure 4.12:** (A) Experimental VT <sup>2</sup>H SSNMR spectra for UWDM-P1 and corresponding simulations showing the (i) SML, (ii) onset of the two-site jump ( $\beta = 78^\circ$ ), (iii) FML of the two-site jump and onset of partial rotation, and (iv) FML of the two-site jump and partial rotation. (B) Experimental VT <sup>2</sup>H SSNMR spectra for UWDM-P1<sub>d</sub> and corresponding simulations showing the (i) SML, (ii) IMR for the two-site jump, (iii) FML of the two-site jump, (iv) onset of partial rotation, and (v) FML of the two-site jump and partial rotation. .... 167

**Figure 4.13:** (A) Experimental VT <sup>2</sup>H SSNMR spectra for UWDM-P2 and corresponding simulations showing the (i) SML, (ii) FML of the two-site jump ( $\beta = 78^\circ$ ) and the onset of partial rotation, (iii) FML of the two-site jump and partial rotation, and (iv) FML of the two-site jump and full rotation. (B) Experimental VT <sup>2</sup>H SSNMR spectra for UWDM-P2<sub>d</sub> and corresponding simulations showing the (i) SML, (ii) FML for the two-site jump ( $\beta = 70^\circ$ ), (iii) FML of the two-site jump ( $\beta = 75^\circ$ ) and



the onset of partial rotation, and (iv) FML of the two-site jump and partial rotation.

..... 168

**Figure 4.14:** (A) Schematic diagram of the [2]rotaxane used in the synthesis of UWDM-4. The positions of the  $^{13}\text{C}$  labels are marked with asterisks. (B) Depiction of the interpenetration in UWDM-4 where the [2]rotaxanes serve as “crossbars” that join together two lattices (green and yellow). (C) View along the crystallographic  $c$  axis showing the open channels in the framework..... 174

**Figure 4.15:** Variable temperature  $^1\text{H}$ - $^{13}\text{C}$  CP/MAS ( $\nu_{\text{rot}} = 14.4$  kHz) NMR spectra acquired for UWDM-4 at 21.1 T. .... 176

**Figure 4.16:**  $^1\text{H}$ - $^{13}\text{C}$  CP/EXSY MAS NMR spectra ( $\nu_{\text{rot}} = 14.4$  kHz) acquired at 0 °C and 21.1 T using mixing times of (A) 1 ms, and (B) 100 ms. .... 177

**Figure 4.17:** The Eyring plot generated from the simulation of the VT  $^{13}\text{C}$  SSNMR data. Rates used in the simulations and thermodynamic parameters extracted from the plot are shown in **Table 4.11** and **Table 4.12**, respectively. .... 179

**Figure 5.1:**(A) Platinum chemical shift, (B)  $^2\text{H}$  EFG, and (C) hydrogen chemical shielding tensor orientations for **1** determined by DFT calculations. .... 197

**Figure 5.2:** Experimental  $^{195}\text{Pt}$  WURST-CPMG NMR spectra (blue) and accompanying analytical simulations (red) for **1** acquired at (A) 133 K and (B) 298 K. The platinum CS tensor parameters are shown in **Table 5.1**. The dashed lines indicate the relative positions of  $\delta_{22}$  (black) and  $\delta_{33}$  (grey)..... 199

**Figure 5.3:** (A) VT  $^2\text{H}$  SSNMR spectra of **1-D** acquired at 4.75 T. (B) Accompanying simulations using the  $n$ :1:1 rotational model. The impurity peak that appears in the centre of the experimental spectra was not modeled. .... 202

<b>Figure 5.4:</b> (A) two-site, (B) three-site, (C) four-site, and (D) six-site rotation motional models used in the simulation of the $^2\text{H}$ SSNMR data. The red arrows in the schematic pictures represent the positions of the largest principal component of the $^2\text{H}$ EFG tensor ( $V_{33}$ ) which is collinear with the Pt–D bonds. ....	204
<b>Figure 5.5:</b> Simulated $^2\text{H}$ SSNMR spectra for the (A) $n:1:1$ , (B) $n:n':1$ , and (C) $n^2:n':1$ population models. The ratios represent the relative populations of the rotational states ( <i>i.e.</i> , the populations of the $0^\circ(180^\circ):60^\circ(240^\circ):120^\circ(300^\circ)$ states).....	206
<b>Figure 5.6:</b> (A) VT $^2\text{H}$ SSNMR spectra of <b>1-D</b> acquired at 9.4 T. (B) The accompanying simulations using the $n:1:1$ rotational model. The simulations include the effects of $^1\text{H}$ CSA. ....	207
<b>Figure 5.7:</b> The energy landscape for <b>1</b> as determined by DFT calculations. The hydride positions were rotated about the P–Pt–P axis. Global minima are observed at H–Pt–P–C torsion angles of $0^\circ$ and $180^\circ$ (hydrides eclipsed with the P-C9 bonds) and local minima are observed at positions where the deuterides are eclipsed with the P–C1 and P-C5 bonds. ....	209
<b>Figure 5.8:</b> VT $^2\text{H}$ SSNMR spectra acquired at 9.4 T for <b>2-D</b> . A simulation of the spectrum acquired at 273 K is shown as the red trace. The spectra do not change with temperature indicating that the motion is in the SML. ....	210
<b>Figure 5.9:</b> VT $^2\text{H}$ SSNMR spectra of <b>3-D</b> acquired at 9.4 T. A simulation of the spectrum acquired at 173 K is shown as the red trace. The spectra do not change with temperature, indicating that the motion is in the FML (see text for details) ..	212

- Figure 5.10:** VT  $^2\text{H}$  SSNMR spectra of **4-D** acquired at 9.4 T. An analytical simulation of the spectrum acquired at 223 K is shown in red. The spectra do not change with temperature, indicating that the motion is in the SML (see text for details). ..... 214
- Figure 5.11:** (A) VT  $^2\text{H}$  SSNMR spectra of 5-D acquired at 9.4 T. (B) Accompanying simulations using the four-site jump rotational model. .... 215
- Figure 6.1:** Comparison between the experimental and calculated values of (A)  $C_Q$  and (B)  $\eta_Q$  for all sites. All calculated values were obtained from  $^{35}\text{Cl}$  EFG tensor calculations completed on geometry optimized structures using CASTEP. The values of both  $C_Q$  and  $\eta_Q$  for the pseudo-bridging chlorine sites in **MoOCl<sub>4</sub>** were omitted due to poor correlation between experiment and calculation. .... 238
- Figure 6.2:** Static  $^{35}\text{Cl}$  SSNMR spectra acquired using frequency-stepped WURST-CPMG for (A)  $\alpha\text{-WCl}_6$  at 21.1 T and (B)  $\beta\text{-WCl}_6$  at 9.4 T with corresponding analytical simulations shown in red. (C) Hahn-echo experiments conducted on  $\beta\text{-WCl}_6$  at (i) the high and (ii) the low frequency discontinuities..... 240
- Figure 6.3:**  $^{35}\text{Cl}$  NQR spectra for (A)  $\alpha\text{-WCl}_6$  and (B)  $\beta\text{-WCl}_6$ . The NQR frequencies ( $\nu_Q^{\text{NQR}}$ ) for each of the sites are shown in the figure. The spectra were acquired with a transmitter frequency of 10.52 MHz. .... 242
- Figure 6.4:** Theoretical  $^{35}\text{Cl}$  EFG tensor orientations in the molecular frames for (A)  $\alpha\text{-WCl}_6$  and (B)  $\beta\text{-WCl}_6$ , as determined from  $^{35}\text{Cl}$  EFG tensor calculations completed on geometry-optimized structures using CASTEP. .... 244
- Figure 6.5:** Static  $^{35}\text{Cl}$  SSNMR spectra acquired at 21.1 T for (A) **WOCl<sub>4</sub>** and (B) **MoOCl<sub>4</sub>**. Analytical simulations representative of the entire powder patterns are

shown in red, while individual sites are shown in blue (Cl1), green (Cl2), black (Cl3) and orange (Cl4). ..... 246

**Figure 6.6:** Theoretical  $^{35}\text{Cl}$  EFG tensor orientations for (A)  $\text{WOCl}_4$  and (B)  $\text{MoOCl}_4$  with (i) the pseudo-bridging chlorine sites (Cl1), (ii) the terminal chlorine sites opposite the pseudo-bridging sites (Cl2) and (iii) the terminal chlorine sites adjacent to the pseudo-bridging chlorine sites (Cl3 and Cl4). All pictured orientations were determined from  $^{35}\text{Cl}$  EFG tensor calculations completed on geometry-optimized models using CASTEP. .... 248

**Figure 6.7:** Static  $^{35}\text{Cl}$  SSNMR spectra acquired at 21.1 T for (A)  $\text{NbCl}_5$  and (B)  $\text{TaCl}_5$ . Corresponding analytical simulations representative of the entire powder patterns are shown in red and simulations of the individual sites are shown in blue ( $\text{Cl}_{\text{br}}$ ), green ( $\text{Cl}_{\text{ax}}$ ), and orange ( $\text{Cl}_{\text{eq}}$ ). ..... 253

**Figure 6.8:** Theoretical  $^{35}\text{Cl}$  EFG tensor orientations in the molecular frame for the (A)  $\text{Cl}_{\text{br}}$ , (B)  $\text{Cl}_{\text{eq}}$ , and (C)  $\text{Cl}_{\text{ax}}$  environments in  $\text{NbCl}_5$ . Orientations were determined from  $^{35}\text{Cl}$  EFG tensor calculations completed on geometry-optimized models using CASTEP. Similar tensor orientations were found for the isostructural  $\text{TaCl}_5$  complex. .... 255

**Figure 6.9:**  $T_2$  relaxation time constants and corresponding CPMG echo trains from experiments on  $\alpha\text{-WCl}_6$  at (A) the high-frequency, (B) central and (C) low-frequency discontinuities. .... 257

**Figure 6.10:** (A) Atom numbering of the  $\text{Nb}_2\text{Cl}_{10}$  unit used in the LMO analysis. (B) Isosurface representations of the LMOs (1)  $\sigma(\text{Cl}_{\text{ax}}\text{-Nb})$ , (2)  $\sigma$  LP  $\text{Cl}_{\text{ax}}$ , (3)  $\pi_x$  LP  $\text{Cl}_{\text{ax}}$ , (4)  $\pi_y$  LP  $\text{Cl}_{\text{ax}}$ , (5)  $\sigma(\text{Cl}_{\text{eq}}\text{-Nb})$ , (6)  $\sigma$  LP  $\text{Cl}_{\text{eq}}$ , (7)  $\pi(\text{Cl}_{\text{eq}}\text{-Nb})$ , (8)  $\pi_z$  LP  $\text{Cl}_{\text{eq}}$ , (9)  $\pi_x$  LP

Cl <sub>br</sub> (with some μ-bonding character), (10) μ(Nb-Cl-Nb), (11) σ LP Cl <sub>br</sub> and (12) π <sub>z</sub> LP Cl <sub>br</sub> .....	260
<b>Figure 6.11:</b> Graphical representations (polar plots) of <sup>35</sup> Cl EFG tensors of NbCl <sub>5</sub> for (A) Cl <sub>ax</sub> , (B) Cl <sub>eq</sub> and (C) Cl <sub>br</sub> environments. The blue colour indicates a positive EFG while orange indicates a negative EFG. The values of <i>V</i> <sub>33</sub> are +0.71, +0.81 and -1.32 a.u., for (A) - (C) respectively. ....	262
<b>Figure 6.12:</b> Static <sup>35</sup> Cl SSNMR spectrum acquired using the WURST-CPMG pulse sequence at 18.8 T for WCl <sub>6</sub> -SiO <sub>2</sub> with corresponding analytical simulation shown in red. ....	265
<b>Figure A1:</b> Experimental PXRD patterns for (A) the dry-milled reaction mixture before aging and (B) CdO. (C) Simulated PXRD pattern for HMeIm. ....	290
<b>Figure A2:</b> Experimental PXRD patterns for the products of the aging reaction treated with either (NH <sub>4</sub> ) <sub>2</sub> (SO <sub>4</sub> ) after (A) one day and (B) seven days of aging, or HCafHSO <sub>4</sub> after (C) one day and (D) seven days of aging. Simulated PXRD patterns from the crystal structures (E) <b>1</b> and (F) <b>3</b> . ....	290
<b>Figure A3:</b> The coordination environment of the Cd atoms in <i>dia</i> -Cd[Im] <sub>2</sub> ( <b>2</b> ). ....	291
<b>Figure A4:</b> Coordination environment about (A) the Cd1 site, (B) the Cd2 site and atom labeling in thle <i>yqt1</i> -Cd[MeIm] <sub>2</sub> ( <b>3</b> ) framework. There is an apparent positional disorder of one of the MeIm- ligands at the Cd1 site. ....	291
<b>Figure A5:</b> Coordination environment about the Cd atom and atom labelling in the ...	292
<b>Figure A6:</b> <sup>1</sup> H MAS (νrot = 16 kHz) NMR spectra acquired at 9.4 T for (A) framework <b>2</b> , (B) framework <b>3</b> , and (C) compound <b>4</b> . ....	292

<b>Figure A7:</b> $^1\text{H}$ - $^{13}\text{C}$ CP/MAS (vrot = 10 kHz) NMR spectra acquired at 9.4 T of (A) framework <b>2</b> , (B) framework <b>3</b> , and (C) compound <b>4</b> . The asterisks (*) denoted spinning sidebands. ....	293
<b>Figure A8:</b> Proposed $^{111}\text{Cd}$ isotropic chemical shift ranges based on the compounds investigated herein and on studies conducted by Ellis <i>et al.</i> ....	293
<b>Figure A9:</b> $^1\text{H}$ - $^{14}\text{N}$ BRAIN-CP/WURST-CPMG spectrum of bulk HMeIm (blue trace) and simulation of the powder pattern (red trace). A deconvolution of the simulation into the two distinct powder patterns is also shown. The purple trace is the pattern corresponding to the N1 site ( $C_Q = 1.95(5)$ MHz, $\eta_Q = 0.44(2)$ ) and the green trace is the.....	294
<b>Figure B1:</b> (A) $^1\text{H}$ - $^{111}\text{Cd}$ CP/MAS NMR spectrum acquired for the products of <b>3</b> (twenty minute acquisition time). (B) $^{111}\text{Cd}$ NMR spectrum of the same sample acquired for an additional twenty minutes (the two spectra are non-cumulative). ....	296
<b>Figure B2:</b> $^1\text{H}$ - $^{111}\text{Cd}$ CP NMR spectra acquired under static conditions ( <i>i.e.</i> , no sample rotation) for products <b>3</b> at different time intervals (the spectra are non-cumulative). ....	297
<b>Figure B3:</b> Experimental PXRD patterns obtained for (A) <b>1<sub>85m</sub></b> and (B) <b>1<sub>25m-a<sub>1h</sub></sub></b> . ....	298
<b>Figure B4:</b> Experimental PXRD pattern acquired for <b>aCdM</b> that was synthesized by milling a sample of <b>yCdM</b> for three hours. The broad features confirm the amorphous nature of this material.....	299
<b>Figure B5:</b> (A) Experimental PXRD pattern obtained for <b>CdIF-1</b> . (B) Simulated PXRD pattern of <b>CdIF-1</b> from the crystal structure reported by Tian <i>et al.</i> .....	299

<b>Figure B6:</b> (A) Experimental PXRD pattern for <b>CdIF-1<sub>HMeIm</sub></b> . (B) Simulated PXRD pattern from the crystal structure of <b>dCdM</b> .....	300
<b>Figure B7:</b> Comparison of the peak widths in the <sup>111</sup> Cd NMR spectra of (A) <b>CdIF-1<sub>dried</sub></b> , (B) <b>CdIF-1</b> , and (C) <b>1<sub>30s</sub></b> . Experimental spectra are shown in blue and the corresponding simulations are shown as the red traces. ....	301
<b>Figure C1:</b> Simulation of a <sup>2</sup> H SSNMR powder pattern showing the positions of the three sets of discontinuities (horns, shoulders and feet) and their respective frequency separations ( $\Delta\nu_{11}$ , $\Delta\nu_{22}$ and $\Delta\nu_{33}$ ). Also shown are the relations between the positions of the discontinuities and the quadrupolar parameters ( $C_Q$ and $\eta_Q$ ). ....	304
<b>Figure C2:</b> (A) Orientation of the <sup>2</sup> H EFG tensor for the deuterons in the alkyl region of the macrocycles in the MOF systems. (B) Depiction of the two-site jump motional model. The CH <sub>2</sub> group jumps through an angle $\beta$ about an axis that is in the plane of the ring. (C) Simulated <sup>2</sup> H powder patterns for this motional model simulated in the FML with the corresponding values of $\beta$ . The powder patterns were simulated using a SML EFG tensor with $C_Q = 165$ kHz and $h_Q = 0.0$ .....	305
<b>Figure C3:</b> Simulated <sup>2</sup> H SSNMR powder patterns for the two-site jump model with $\beta = 77^\circ$ using rates within the three motional regimes. Rates in the SML are considered to be $\leq 10^3$ Hz, IMR rates are between $10^3$ and $10^7$ Hz and FML rates are $\geq 10^7$ Hz. ....	306
<b>Figure C4:</b> (A) Depiction of the partial rotation motional model. The $V_{33}$ component of the EFG tensor is depicted with the red arrows and jumps between $n$ sites separated by an angle $\gamma$ . Jumps can only occur to adjacent sites. The sites that the deuteron can visit are offset from the rotation axis by the angle $\alpha$ . (B) Simulated <sup>2</sup> H powder	

patterns for this motional model simulated in the FML as a function of the angles $\alpha$ and $\gamma$ and by considering six rotational steps. The powder patterns were simulated using a SML EFG tensor with $C_Q = 165$ kHz and $\eta_Q = 0.0$ . It is noted that the right-most column represents the special case of full rotation. ....	307
<b>Figure C5:</b> Simulated $^2\text{H}$ powder patterns using various rates ( $k$ ) for different two-site jump angles ( $\beta$ ). Simulations used a SML EFG tensor with $C_Q = 165$ kHz and $\eta_Q = 0.0$ .....	308
<b>Figure C6:</b> Simulated $^2\text{H}$ SSNMR powder patterns for a motional model consisting of two-site jumps through an angle of $72^\circ$ combined with partial rotation where the ring jumps through an angle $225^\circ$ in $45^\circ$ steps. ....	309
<b>Figure C7:</b> (A) Schematic diagram showing the sites used in the simulation of $\beta$ -UWDM-3. The numbered positions correspond to the rotational sites (1-6 are sites where the oxygen atoms on the ring form hydrogen bonds with the axle and sites 7 and 8 correspond to rotation through the alkyl portion of the ring). Sites $a$ and $b$ correspond to the two positions in the two-site jump model where the $\text{CD}_2$ groups rotate about an axis in the plane of the ring. (B) Kinetic matrix used in the simulation of the high-temperature data for $\beta$ -UWDM-3. $j$ is the rate constant for the two-site jump motion, $r$ is the rate constant for rotation between hydrogen-bonding positions and $a$ is the rate constant for rotation through the alkyl portion of the ring. ....	310
<b>Figure C8:</b> VT $^2\text{H}$ SSNMR spectra of UWDM-P2 with (A) no solvent, or the addition of (B) dimethylformamide, (C) mesitylene, (D) dioxane, (E) 1-butanol, (F) ethylene glycol, or (G) triethylene glycol within the pores of the framework.....	311



<b>Figure C9:</b> $^{19}\text{F}$ MAS NMR spectra acquired for (A) UWDM-4 ( $\nu_{\text{rot}} = 18$ kHz) and (B) UWDM-4• $\text{HBF}_4$ ( $\nu_{\text{rot}} = 9.5$ kHz). The blue shaded region shows signal from the $\text{BF}_4^-$ anion, † denote signal from the Teflon spacers and caps, and * denote spinning sidebands of the Teflon signal. ....	311
<b>Figure C10:</b> $^1\text{H}$ - $^{13}\text{C}$ CP/MAS ( $\nu_{\text{rot}} = 8$ kHz) acquired at 9.4 T for neutral UWDM-4. The resolution of these spectra is too low to observe chemical exchange.....	312
<b>Figure C11:</b> (A) Solution-state VT $^{13}\text{C}$ NMR data of the [2]rotaxane made from <b>A</b> <sub>4</sub> and <b>CE</b> <sub>4</sub> . (B) The Eyring plot is generated from the $^{13}\text{C}$ NMR data and used to calculate the thermodynamic parameters listed in <b>Table 4.12</b> . ....	313
<b>Figure D1:</b> Crystal structure of <b>1-H</b> showing the disorder of the hydride ligands. Atom numbering is shown for one of the phosphine ligands. ....	316
<b>Figure D2:</b> VT $^{195}\text{Pt}$ SSNMR spectra for <b>1-H</b> acquired at 4.75 T. The low S/N is due to the long $T_1(^{195}\text{Pt})$ at low temperatures and the experiments being run without $^1\text{H}$ decoupling. The spectrum at 40 K was acquired with significantly more scans. ...	316
<b>Figure D3:</b> $^2\text{H}$ SSNMR spectra acquired for <b>1-D</b> at 120 K with different values of the interpulse delay ( $\tau$ ). There are no appreciable differences in the spectra, indicating that the motion is occurring with rates in the FML. ....	317
<b>Figure D4:</b> Simulations of the experimental $^2\text{H}$ SSNMR for <b>1</b> pattern collected at 9.4 T and 298 K using $\Omega = 60$ and 13 ppm. The latter value was obtained from DFT calculations. The dashed lines show the relative positions of the low-frequency discontinuities. ....	318
<b>Figure D5:</b> View along the C–Pt–C rotation axis showing the relative positions of the hydrides in (A) <b>4-H</b> and (B) <b>5-H</b> . ....	319

<b>Figure E1:</b> Depections of the packing of atoms in the unit cell for $\alpha$ - $\text{WCl}_6$ with views along the crystallographic (A) $a$ -axis, (B) $b$ -axis, (C) $c$ -axis and (D) [111] plane.	338
<b>Figure E2:</b> Depections of the packing of atoms in the unit cell for $\beta$ - $\text{WCl}_6$ with views along the crystallographic (A) $a$ -axis, (B) $b$ -axis, (C) $c$ -axis and (D) [111] plane.	339
<b>Figure E3:</b> Depections of the packing of atoms in the unit cell for $\text{WOCl}_4$ with views along the crystallographic (A) $a$ -axis, (B) $b$ -axis, (C) $c$ -axis, and (D) the [111] plane. .....	339
<b>Figure E4:</b> Depections of the packing of atoms in a 2x2x2 supercell for $\text{MoOCl}_4$ with views along the crystallographic (A) $a$ -axis, (B) $b$ -axis, (C) $c$ -axis, and (D) [111] plane.....	340
<b>Figure E5:</b> Depections of the packing of atoms in the unit cell for $\text{NbCl}_5$ with views along the crystallographic (A) $a$ -axis, (B) $b$ -axis, (C) $c$ -axis, and (D) [111] plane.	340
<b>Figure E6:</b> Depections of the packing of atoms in the unit cell for $\text{TaCl}_5$ with views along the crystallographic (A) $a$ -axis, (B) $b$ -axis, (C) $c$ -axis, and (D) [111] plane.	341
<b>Figure E7:</b> Experimental PXRD pattern for $\text{WCl}_6$ shown as the black trace. Simulated patterns for $\alpha$ - $\text{WCl}_6$ (red trace) and $\beta$ - $\text{WCl}_6$ (blue trace). .....	341
<b>Figure E8:</b> Experimental (black trace) and simulated (red trace) PXRD patterns for $\text{WOCl}_4$ . .....	342
<b>Figure E9:</b> Experimental (black trace) and simulated (red trace) PXRD patterns for $\text{MoOCl}_4$ . .....	342
<b>Figure E10:</b> Experimental (black trace) and simulated (red trace) PXRD patterns for $\text{NbCl}_5$ . .....	343

<b>Figure E11:</b> Experimental (black trace) and simulated (red trace) PXRD patterns for <b>TaCl<sub>5</sub></b> .	343
<b>Figure E12:</b> Static <sup>35</sup> Cl SSNMR spectrum of <b>α-WCl<sub>6</sub></b> acquired at 9.4 T with corresponding analytical simulation (red trace).	344
<b>Figure E13:</b> Static <sup>35</sup> Cl SSNMR powder pattern for <b>WOCl<sub>4</sub></b> acquired at 9.4 T and corresponding analytical simulation (red trace).	344
<b>Figure E14:</b> Static <sup>35</sup> Cl SSNMR powder pattern for <b>MoOCl<sub>4</sub></b> acquired at 9.4 T. Analytical simulations for the individual sites are show in blue, green, black, and orange. The red trace is an analytical simulation representative of the entire powder pattern	345
<b>Figure E15:</b> Static <sup>35</sup> Cl SSNMR powder pattern for <b>NbCl<sub>5</sub></b> . Analytical simulations are shown in blue (bridging), green (terminal axial), and orange (terminal equatorial). The red trace is an analytical simulation representative of the entire powder pattern.	345
<b>Figure E16:</b> Static <sup>35</sup> Cl SSNMR powder pattern for <b>TaCl<sub>5</sub></b> . Analytical simulations are shown in blue (bridging), green (terminal axial), and orange (terminal equatorial). The red trace is an analytical simulation representative of the entire powder pattern.	346
<b>Figure E17:</b> Simulation of the <sup>35</sup> Cl SSNMR powder pattern for the terminal-equatorial site in <b>NbCl<sub>5</sub></b> including only the quadrupolar interaction (bottom trace) and both the quadrupolar and CSA interactions (top trace).	346
<b>Figure E18:</b> Dative (Cl→Nb) bonds in <b>NbCl<sub>5</sub></b> . Linear combinations of (A) $(v+vi)/\sqrt{2}$ and (B) $(v-vi)/\sqrt{2}$ of LMOs (v) and (vi) of <b>Figure 6.9(B)</b> .	347

**Figure E19:** Graphical representation of the EFG related to the  $sp^n$  set of hybrid orbitals of Eq. (3). Electron configuration  $(spn_1)^2(spn_2)^{1.8}(spn_3)^{1.8}(spn_4)^2$ . Angle  $\theta$  between  $spn_2$  and  $spn_3$ :  $102^\circ$ . The negative tensor component  $V_{33}$  (orange) is perpendicular to the plane spanned by the directional vectors of the two bonding hybrids with occupancy lower than two. .... 347

**Figure E20:** Analytical simulations of static  $^{35}\text{Cl}$  SSNMR spectra acquired at 18.8 T for  $\alpha\text{-WCl}_6$  (red trace) and  $\text{WCl}_6\text{-SiO}_2$  (blue trace)..... 348

## List of Schemes

- Scheme 2.1:** Proposed reaction pathways for the accelerated aging reactions of CdO and HMeIm with different protic salts. For the reaction with  $\text{NH}_4\text{NO}_3$ , 1:2, 1:3, and 1:6 Cd:HMeIm ratios were used. .... 64
- Scheme 3.1:** General synthetic procedure for the mechanochemical formation of ZIFs using cadmium oxide (CdO) and 2-methylimidazole (HMeIm) with the addition of a catalytic amount of ammonium nitrate ( $\text{NH}_4\text{NO}_3$ ) and a small amount of methanol (MeOH) solvent. .... 94
- Scheme 3.2:** Mechanochemical reaction pathways for (A) ZnO + HMeIm forming (i) 116
- Scheme 4.1:** Representations of the secondary building units (SBUs) used in MOF synthesis. (A) Cu paddlewheel ( $\text{SBU}_1$ ), (B) Zn paddlewheel ( $\text{SBU}_2$ ), and (C)  $\text{Zn}_4\text{O}$  cluster ( $\text{SBU}_3$ ). Colour key: C = black, O = red, N = blue, Cu = cyan, Zn = grey. 139
- Scheme 4.2:** Organic axle molecules for the rotaxanes used in the synthesis of (A) UWDM-1 ( $\text{A}_1$ ), (B) UWDM-2, UWDM-3, UWDM-P1 ( $\text{A}_2$ ), (C) UWDM-P2 ( $\text{A}_3$ ), and (D) UWDM-4 ( $\text{A}_4$ ). .... 140
- Scheme 4.3:** Schematic representation of the organic linkers used in the synthesis of pillared or mixed-linker MOFs. (A) 1,4-diazophenyl-dicarboxylic acid ( $\text{L}_1$ ), (B) 1,4-biphenyl-dicarboxylic acid ( $\text{L}_2$ ), and (C) tetracarboxyphenyl-porphyrin- $\text{Pd}^{2+}$  ( $\text{L}_3$ ). .... 140
- Scheme 4.4:** Schematic diagrams of the crown ether macrocycles used in the preparation the rotaxanes. (A) [24]crown-6 ( $\text{CE}_1$ ), (B) [22]crown-6 ( $\text{CE}_2$ ), (C) benzo[24]crown-6 ( $\text{CE}_3$ ), (D) [24]crown-8 ( $\text{CE}_4$ ). For the rings that were deuterated for dynamic studies, the positions of the D (=2H) labels are indicated. .... 141

**Scheme 5.1:** Representations of the structures of (A) *trans*-H<sub>2</sub>Pt(P<sup>t</sup>Bu<sub>3</sub>)<sub>2</sub> (**1**), (B) *trans*-H<sub>2</sub>Pt(P(NMe<sub>2</sub>)<sub>3</sub>)<sub>2</sub> (**2**), (C) *trans*-D<sub>2</sub>Pt(PCy<sub>3</sub>)<sub>2</sub> (**3-D**), (D) *trans*-D<sub>2</sub>Pt(*i*Pr)<sub>2</sub> (**4**), and (E) [*trans*-HPt(*i*Pr)<sub>2</sub>][BARF<sub>4</sub>] (**5**). For **1**, **2**, **4**, and **5**, ball-and-stick representations are derived from the crystal structures, whereas for **3-D**, no crystal structure has been reported. Non-hydride hydrogen atoms and the [BARF<sup>4-</sup>]<sup>-</sup> counterion have been omitted for clarity. Colour key: H/D = pink, C = black, N = blue, P = orange, Pt = grey. .... 190

**Scheme 6.1:** Schematic representations of (A) tungsten(VI) chloride (**WCl<sub>6</sub>**), (B) tetrachlorotungsten(VI) oxide (**WOCl<sub>4</sub>**) and tetrachloromolybdenum(VI) oxide (MoOCl<sub>4</sub>), (C) niobium(V) chloride (**NbCl<sub>5</sub>**) and tantalum(V) chloride (**TaCl<sub>5</sub>**).. 231

**Scheme 6.2:** Schematic representation of the different chlorine bonding environments in the bridging pentahalide species. Bridging chlorine atoms (Cl<sub>br</sub>) are shown in blue, terminal-axial (Cl<sub>ax</sub>) in green and terminal-equatorial (Cl<sub>eq</sub>) in orange..... 251

## List of Abbreviations

<b><i>aCdM</i></b>	Amorphous Cd[MeIm] <sub>2</sub>
ADC	Analog to digital controller
ADF	Amsterdam density function
BRAIN-CP	Broadband adiabatic Inversion cross-polarization
BRAIN-CP/WCPMG	Broadband adiabatic inversion with WCPMG
CASTEP	Cambridge serial total energy package
CCF	Crystallite-fixed frame
CdIF	Cadmium imidazolate framework
CdO	Cadmium oxide
CE	Crown ether
CP	Cross-polarization
CP/MAS	Cross-polarization/magic angle spinning
CPMG	Carr-Purcell-Meiboom-Gill
CS	Chemical shift
CSA	Chemical shift anisotropy
CSD	Cambridge Structural Database
CT	Central transition
<b><i>dCdM</i></b>	<i>dia</i> -Cd[MeIm] <sub>2</sub> •HMeIm
DFT	Density functional theory
DMF	Dimethylformamide
EFG	Electric field gradient
FID	Free induction decay

FML	Fast motion limit
FOQI	First-order quadrupolar interaction
FWHH	Full width half height
HMeIm	2-methylimidazole
<i>i</i> CdM	Intermediate Cd[MeIm] <sub>2</sub>
Im	Imidazole
IMR	Intermediate motion regime
MAS	Magic angle spinning
MeOH	Methanol
MO	Molecular orbital
MOF	Metal-organic framework
MQMAS	Multiple quantum magic angle spinning
MS	Magnetic shielding
NLMO	Natural localized molecular orbital
NMR	Nuclear magnetic resonance
o.d.	Outer diameter
PAS	Principal axis system
ppm	Parts per million
PXRD	Powder X-ray diffraction
QE	Quadrupolar echo
QI	Quadrupolar interaction
RAS	Relaxation-assisted separation
rf	Radiofrequency



rPBE	Revised Perdew, Burke, and Ernzerhof
S/N	Signal-to-noise
SBU	Secondary building unit
SCXRD	Single-crystal X-ray diffraction
SML	Slow motion limit
SOLA	Solid lineshape analysis
SOQI	Second-order quadrupolar interaction
SSNMR	Solid-state nuclear magnetic resonance
ST	Satellite transition
TMS	Trimethylsilane
UW	Ultra wideband
UWDM	University of Windsor Dynamic Material
UWDM-Pd	UWDM-P desolvated
UWDM-P	UWDM-porphyrin
UWNMR	Ultra-wideband NMR
VOCS	Variable offset cumulative spectra
WCPMG	WURST CPMG
WCPMG	WURST CPMG
WURST	Wideband Uniform-rate smooth truncation
XRD	X-ray diffraction
<i>yCdM</i>	<i>yqt1</i> -Cd[MeIm] <sub>2</sub>
ZIF	Zeolitic imidazolate framework
ZORA	Zeroth order regular approximation

# Chapter 1: Introduction to NMR and Context of Research

## 1.1 Nuclear Magnetic Resonance Spectroscopy

Since its discovery independently by the groups Purcell and Bloch in 1946,<sup>1,2</sup> nuclear magnetic resonance (NMR) spectroscopy has been an active area of research, and with advances in magnet technology, hardware, and pulse sequence design, has become one of the most powerful and widely-used analytical techniques across numerous scientific disciplines. NMR is routinely used by synthetic chemists to identify products and elucidate reaction mechanisms in solution, by biochemists to determine the structure and function of proteins and membranes, and by materials scientists to probe the surfaces of materials and to gain information on disordered systems. NMR spectra are sensitive to subtle differences and changes in both molecular-level structure and chemical environment, and since nearly every element on the periodic table has an NMR-active isotope, it provides a wealth of information on a variety of systems, which is often not available from other techniques. In addition, NMR spectra are influenced by motion and chemical exchange, and therefore, NMR is the only technique capable of studying motions with correlations times ranging from picoseconds to days.<sup>3-5</sup>

Most early applications of NMR spectroscopy focused on the study of systems in the solution state, due to the observation of fine structure arising from chemical shifts and *J*-couplings, which is of great diagnostic value for interpreting the structures of molecules in solution. Solid-state NMR was slower to develop, due to the relatively broad spectra (arising from orientation-dependent or *anisotropic* interactions, *vide infra*). Numerous technological advances<sup>6</sup> (*e.g.*, magic-angle spinning probes and linear high-power

amplifiers, *vide infra*) and the development of sophisticated pulse sequences have allowed for the development of solid-state NMR (SSNMR) and its application to various areas of chemistry, biochemistry, and physics.<sup>7-9</sup> This is particularly important since the majority of substances of interest encountered in the laboratory (and in day-to-day life) exist as solid forms. SSNMR provides a viable means for characterizing these materials and allows for the determination of the relationship between structure, dynamics, and chemical and physical properties, ultimately leading to the rational design of molecules and materials with finely-tuned properties and applications.

Despite the utility of NMR, the acquisition of spectra is often challenging. NMR is an inherently low-energy spectroscopy, which can lead to weak signals compared to those obtained from other forms of spectroscopy (*e.g.*, electronic, electron paramagnetic resonance, and IR spectroscopies). Many nuclides are also *unreceptive* to the NMR experiment as they have either (i) low gyromagnetic ratios, (ii) low natural abundances, (iii) unfavourable relaxation characteristics, or (iv) a combination of all of these factors. These issues are further exacerbated by dilution of the nucleus of interest. Further, SSNMR patterns are often very broad, due to anisotropic NMR interactions (*vide infra*), which further compromises the possibility of obtaining spectra with a high signal-to-noise ratio (S/N); therefore, the acquisition of SSNMR spectra often requires the use of specialized techniques and pulse sequences that have been carefully calibrated.

In the sections that follow, a brief discussion of the NMR interactions is presented, with a focus on those pertinent to this dissertation. Then, the use of NMR to study dynamics and chemical exchange is discussed. Finally, a brief overview and description of the acquisition techniques and pulse sequences used in all of the projects

described herein is presented. For a more comprehensive and detailed treatment of the NMR interactions, the reader is referred to a number of excellent texts on this subject.<sup>10-13</sup>

## 1.2 NMR Interactions

The NMR phenomenon, in both solution and the solid-state, is a result of the interaction of nuclear spins with an external applied magnetic field ( $\mathbf{B}_0$ ). Most nuclei possess spin angular momentum, an intrinsic property that is denoted by the spin quantum number,  $I$ . Therefore, NMR-active nuclei have non-zero spins, which may be either half-integer ( $I = 1/2, 3/2, 5/2, \text{etc.}$ ) or integer ( $I = 1, 2, 3, \text{etc.}$ ), whereas NMR-inactive nuclei have no intrinsic spin ( $I = 0$ ). The numerous spin interactions are divided into two categories: external and internal. External interactions are a result of the interaction of the nuclear spins with the applied static magnetic and oscillating radio-frequency fields, whereas internal interactions are defined as those between a nuclear spin and the magnetic and electric fields generated by other nuclei and electrons within the system. The general Hamiltonian describing these interactions is as follows:

$$\hat{\mathcal{H}}_{\text{NMR}} = \hat{\mathcal{H}}_{\text{Z}} + \hat{\mathcal{H}}_{\text{rf}} + \hat{\mathcal{H}}_{\text{Q}} + \hat{\mathcal{H}}_{\text{MS}} + \hat{\mathcal{H}}_{\text{DD}} + \hat{\mathcal{H}}_{\text{J}} \quad (1.1)$$

where  $\hat{\mathcal{H}}_{\text{Z}}$  and  $\hat{\mathcal{H}}_{\text{rf}}$  represent the external Zeeman and radio-frequency interactions, respectively. The internal interactions are denoted by  $\hat{\mathcal{H}}_{\text{Q}}$ ,  $\hat{\mathcal{H}}_{\text{MS}}$ ,  $\hat{\mathcal{H}}_{\text{DD}}$ , and  $\hat{\mathcal{H}}_{\text{J}}$  which represent the Hamiltonians for the quadrupolar, magnetic shielding, direct-dipolar coupling, and indirect spin-spin coupling interactions, respectively.

### 1.2.1 The Zeeman Interaction

The high-field approximation is often used when discussing the various NMR interactions. Under this approximation, the Zeeman interaction is the dominant NMR

interaction, with all others being treated as perturbations. It is the result of the interaction of nuclear spins with an externally applied magnetic field ( $\mathbf{B}_0$ ) and is expressed by the following Hamiltonian:<sup>14</sup>

$$\hat{\mathcal{H}}_Z = \gamma \hbar \mathbf{B}_0 I_z \quad (1.2)$$

where  $\gamma$  is the gyromagnetic ratio (in units of  $\text{rad T}^{-1} \text{s}^{-1}$ ), which is a distinct property of each nuclide,  $\hbar$  is the reduced Planck's constant, and  $I_z$  is the  $z$ -component of the nuclear spin angular momentum (the  $z$  direction is chosen such that it is parallel to  $\mathbf{B}_0$ ).

Nuclei which have intrinsic spin angular momentum ( $\mathbf{I}$ ) also have a magnetic dipole moment ( $\boldsymbol{\mu}$ ); these two quantities are related by:

$$\boldsymbol{\mu} = \gamma \hbar \mathbf{I} \quad (1.3)$$

When a nuclear spin is placed in an external magnetic field, it can only adopt certain orientations; therefore, spin angular momentum is said to be space quantized such that:

$$I_z = m_I \hbar \quad (1.4)$$

where the magnetic quantum number can have values of  $m_I = I, I-1, \dots, -I+1, -I$ . Each value of  $m_I$  corresponds to a distinct spin state, thus, a nucleus with spin  $I$  will have  $2I+1$  spin states, which are degenerate in the absence of an external magnetic field. The presence of the external magnetic field,  $\mathbf{B}_0$ , breaks the degeneracy of the spin states.

(**Figure 1.1**). The nuclear spin precesses about an axis which is parallel to the external magnetic field. The rate of precession of the nucleus about this axis is given by the

*Larmor frequency*:

$$\omega_0 = -\gamma \mathbf{B}_0 \quad (1.5)$$

The Larmor frequency,  $\omega_0$  is given in units of  $\text{rad s}^{-1}$  and follows a conical path about the axis of precession (the direction of  $\mathbf{B}_0$ ).

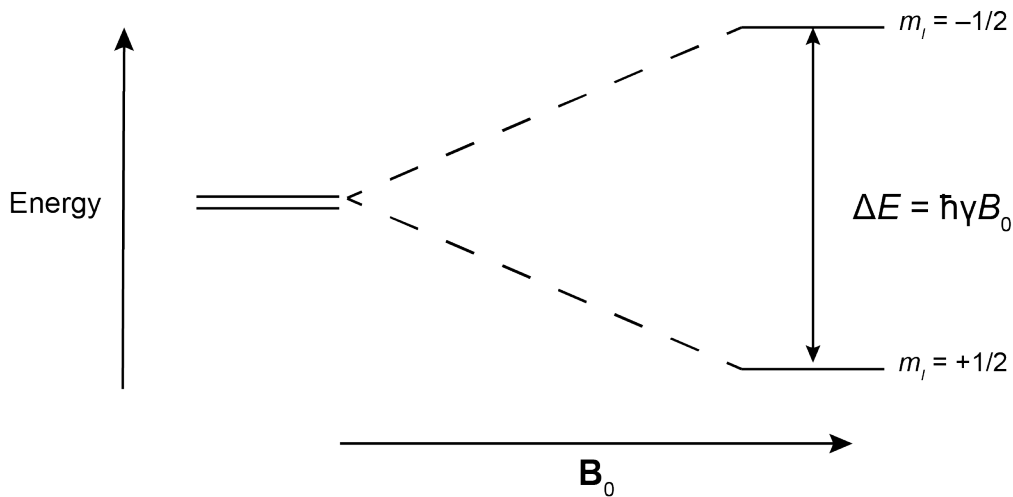


**Figure 1.1:** The effect of the Zeeman interaction on the energy levels for a spin-1/2 nucleus. The originally degenerate energy levels are split into two equally spaced energy levels when placed in an external magnetic field.

If considering only the Zeeman interaction, all spin states are evenly spaced and the energy difference between two spin states is given by:

$$\Delta E = \gamma \hbar B_0 \quad (1.6)$$

The discussion thus far has only taken into consideration the case of a single spin; however, an NMR experiment is performed on a sample that is best considered as an ensemble of spins. This enables the use of Boltzmann distributions to describe population differences between energy levels associated with different spin states. Since the energy difference between two states is dependent on the strength of the external field, increasing the magnetic field strength increases the energy difference and thus, the population difference between two energy states. The Boltzmann distribution describing this population difference for an ensemble of spin-1/2 nuclei with  $\gamma > 0$  is

$$\frac{N_\beta}{N_\alpha} = e^{\frac{-\Delta E}{kT}} \quad (1.7)$$

where  $N_\beta$  and  $N_\alpha$  are the populations of the higher and lower energy states, respectively,  $k$  is the Boltzmann constant, and  $T$  is the temperature of the sample measured in K. From

this equation, it is clear that decreasing the temperature also results in a larger population difference. The population differences between such nuclear spin states are significantly smaller than those in almost every other form of spectroscopy.

At thermal equilibrium, the lower energy level has a higher number of nuclear spins than the higher level. The positive population difference produces a bulk magnetization, denoted by the vector  $\mathbf{M}$ , which is orientated parallel to the external magnetic field  $\mathbf{B}_0$ . It can be shown that the magnitude of the bulk magnetization vector,  $M_0$ , can be defined as

$$M_0 = \frac{N\gamma^2\hbar^2B_0}{4kT}; \quad (1.7)$$

hence, the magnitude of  $M_0$  increases linearly with  $B_0$ , as the square of  $\gamma$ , and inversely proportional to temperature. Since  $\mathbf{M}$  is rotated into the transverse ( $xy$ ) plane for detection (*vide infra*), this implies that the signal intensity is dependent upon the population difference and magnitude of the bulk magnetization vector; however, since the energy difference between these states is so small, the population differences and bulk magnetization are also small – this means that NMR is a very insensitive technique in terms of signal. This can be remedied, in part, by the use of large samples sizes, isotopic enrichment, higher magnet fields, lower temperatures, and/or a variety of single- and double-resonance pulse sequences, all designed to optimize and maximize the magnetization detected by the NMR coil.

### 1.2.2 The Radiofrequency Interaction

In an NMR experiment, the sample is placed into a solenoid or Helmholtz coil, which is attached to the NMR probe that is placed within a strong external magnetic field,  $\mathbf{B}_0$ . An alternating current is passed through the coil, oscillating at a frequency known as

the transmitter frequency ( $\omega_{rf}$ ). The transmitter frequency is usually set to be equal to or near the nuclear Larmor frequency,  $\omega_0$ . This oscillating current generates an oscillating magnetic field,  $\mathbf{B}_1$ , within the coil that is normally directed perpendicular to  $\mathbf{B}_0$ . In order to understand the effect of  $\mathbf{B}_1$  on the bulk magnetization, it is helpful to utilize the *classical vector model* (**Figure 1.2**). Consider a reference frame rotating about the direction of  $\mathbf{B}_0$  at the transmitter frequency,  $\omega_{rf}$ , with transverse orthogonal axes labeled  $x'$  and  $y'$ ; this is the so-called *rotating frame*. If  $\omega_{rf}$  is set at the Larmor frequency,  $\omega_0$ , then the precessing spins that give rise to the bulk magnetization,  $\mathbf{M}$ , appear to be stationary in the rotating frame, meaning that the effective magnitude of  $\mathbf{B}_0$  is zero, and that  $\mathbf{B}_1$  is the only stationary, external magnetic field in the rotating frame. For the purposes of this discussion,  $\mathbf{B}_1$  is directed along the  $x'$  axis of the rotating frame. As a result, the stationary spins, and therefore  $\mathbf{M}$ , precess about  $\mathbf{B}_1$ , at a nutation frequency,  $\omega_1$ , which is defined as

$$\omega_1 = \gamma B_1 \quad (1.8)$$

If the pulse is applied for a finite amount of time,  $\tau_p$ ,  $\mathbf{M}$  is said to “tip” away from  $\mathbf{B}_0$  by an angle  $\theta_p$ ,

$$\theta_p = \tau_p \gamma B_1 = \omega_1 \tau_p \quad (1.9)$$

where  $B_1$  is the magnitude of  $\mathbf{B}_1$ .

At the termination of the pulse, there is no longer a stationary  $\mathbf{B}_1$  field in the rotating frame, and the individual spins return to precessing about  $\mathbf{B}_0$  at their respective Larmor frequencies. This precession of  $\mathbf{M}$  in the  $xy$  plane induces alternating current (AC) in the coil; the voltage of this signal is passed through an analog-to-digital converter (ADC) and stored as a time domain signal known as the free induction decay (FID). The precession of  $\mathbf{M}$  about  $\mathbf{B}_0$  does not continue indefinitely; rather, the bulk magnetization



undergoes two relaxation processes that simultaneously return the system to thermal equilibrium (longitudinal or  $T_1$  relaxation) and dephase the coherent magnetization in the  $xy$  plane (transverse or  $T_2$  magnetization). The value of the  $T_1$  time constant plays a role in determining the waiting period before the experiment can be repeated, known as the recycle delay. (To ensure complete relaxation back to thermal equilibrium, the recycle delay must be set equal to  $5T_1$ ).

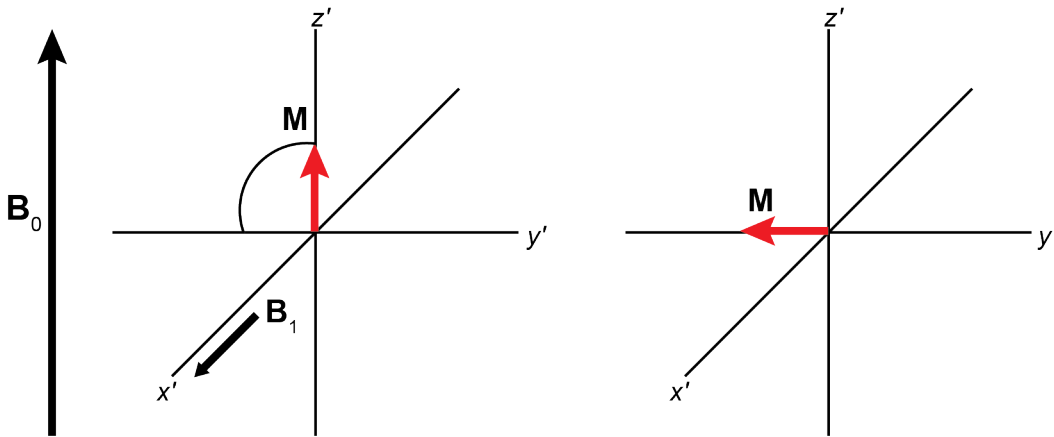


**Figure 1.2:** Vector representation of the effect of a radiofrequency pulse on the bulk magnetization. The coordinate system is a rotating reference frame that rotates about the direction of the external magnetic field at the transmitter frequency,  $\omega_{\text{rf}}$ . A rf pulse is applied along the  $x'$ -axis for a duration that tips the angle along the  $-y'$ -axis. After the pulse is turned off, the magnetization begins to precess about the  $z$ -axis

If the bulk magnetization along  $\mathbf{B}_0$  at thermal equilibrium arises from a positive population difference between the lower and upper states, then the populations of the two states are said to be equal or *saturated* when  $\mathbf{M}$  is located in the  $xy$ -plane. It is also possible to orient  $\mathbf{M}$  antiparallel to  $\mathbf{B}_0$ , which corresponds to a reversal of the populations at thermal equilibrium; this condition known as inversion. Pulses that create the saturation and inversion conditions are associated with  $\theta_p = 90^\circ$  and  $180^\circ$ , and are known as  $\pi/2$  and  $\pi$  pulses, respectively (**Figure 1.3**).

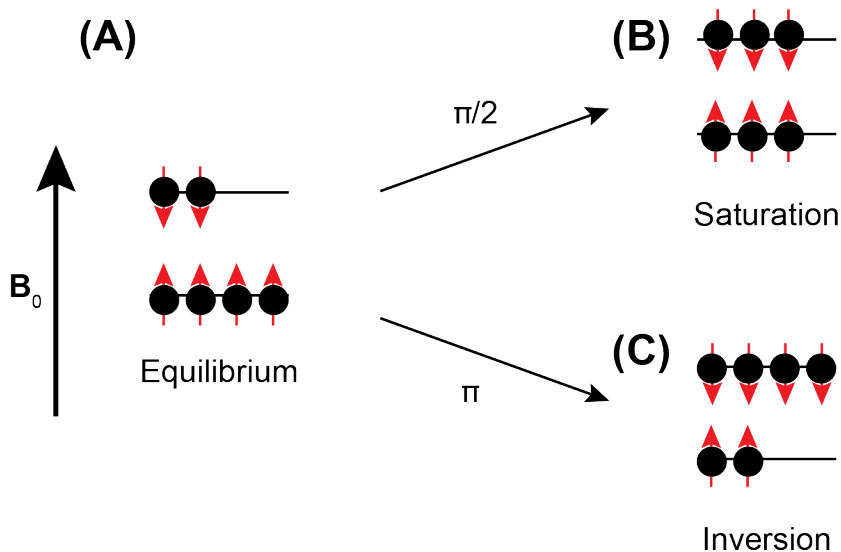


**Figure 1.3:** Schematic representation of the populations of spins at equilibrium (A). The application of  $\pi/2$  and  $\pi$  pulses create the conditions of (B) saturation and (C) inversion, respectively.

### 1.2.3 The Magnetic Shielding/Chemical Shift Interaction

The magnetic shielding (MS) interaction is frequently exploited by chemists for the differentiation of chemically and magnetically distinct environments within a molecule or unit cell of a crystal. The MS interaction arises from the external magnetic field, which induces the circulation of electrons in molecular orbitals. Electron circulation can occur within occupied molecular orbitals or as a mixing of occupied and virtual molecular orbitals; these are known as the diamagnetic and paramagnetic contributions to magnetic shielding, as originally described by Norman Ramsey.<sup>15-19</sup> The circulation of charged electrons produces small local magnetic fields ( $B_{loc}$ ) at the nuclear origins, which can be aligned either parallel or anti-parallel to  $B_0$ , resulting in a net deshielding or shielding of the nucleus, respectively. The primary source of deshielding arises from the paramagnetic shielding contribution. The deshielding and shielding increase and decrease the local fields, causing positive or negative frequency shifts for each magnetically distinct nucleus, respectively, according to

$$\omega_0 = -\gamma(\mathbf{B}_0 - \mathbf{B}_{loc}) \quad (1.10)$$

The Hamiltonian for the MS interaction can be written as:

$$\hat{\mathcal{H}}_{CS} = \gamma\hbar\mathbf{I}_z\ddot{\boldsymbol{\sigma}}\mathbf{B}_0 \quad (1.11)$$

where  $\ddot{\boldsymbol{\sigma}}$  is a second-rank, antisymmetric tensor describing the MS interaction. The MS tensor is defined by a  $3\times 3$  matrix:

$$\ddot{\boldsymbol{\sigma}} = \begin{pmatrix} \sigma_{xx} & \sigma_{xy} & \sigma_{xz} \\ \sigma_{yx} & \sigma_{yy} & \sigma_{yz} \\ \sigma_{zx} & \sigma_{zy} & \sigma_{zz} \end{pmatrix} \quad (1.12)$$

The MS tensor is asymmetric (*i.e.*,  $\sigma_{ij} \neq \sigma_{ji}$ ), but can be rewritten as a sum of symmetric and antisymmetric tensors with three and six independent elements, respectively; only the symmetric portion of the tensor makes contributions to frequency shifts in the NMR spectrum.<sup>20</sup> The symmetric tensor can be expressed in its own principal axis system (PAS) by diagonalization:

$$\ddot{\boldsymbol{\sigma}}_{PAS} = \begin{pmatrix} \sigma_{11} & 0 & 0 \\ 0 & \sigma_{22} & 0 \\ 0 & 0 & \sigma_{33} \end{pmatrix} \quad (1.13)$$

where the three orthogonal principal components are ordered  $\sigma_{11} \leq \sigma_{22} \leq \sigma_{33}$  (*i.e.*,  $\sigma_{11}$  and  $\sigma_{33}$  are the least and most shielded components, respectively). The orientation of the MS interaction with respect to the molecular frame is pictured in **Figure 1.4(A)**. For any given molecular orientation, and hence, orientation of the MS tensor with respect to  $\mathbf{B}_0$ , the magnitude of the MS interaction can be calculated as:

$$\hat{\mathcal{H}}_{CS}(\theta, \varphi) = \gamma B_0 (\sigma_{11} \sin^2 \theta \cos^2 \varphi + \sigma_{22} \sin^2 \theta \sin^2 \varphi + \sigma_{33} \cos^2 \theta) I_z \quad (1.14)$$

where  $\theta$  and  $\varphi$  are the tip and azimuthal polar angles, respectively, which describe the relative orientations of  $\mathbf{B}_0$  and the CS tensor (**Figure 1.4(B)**).

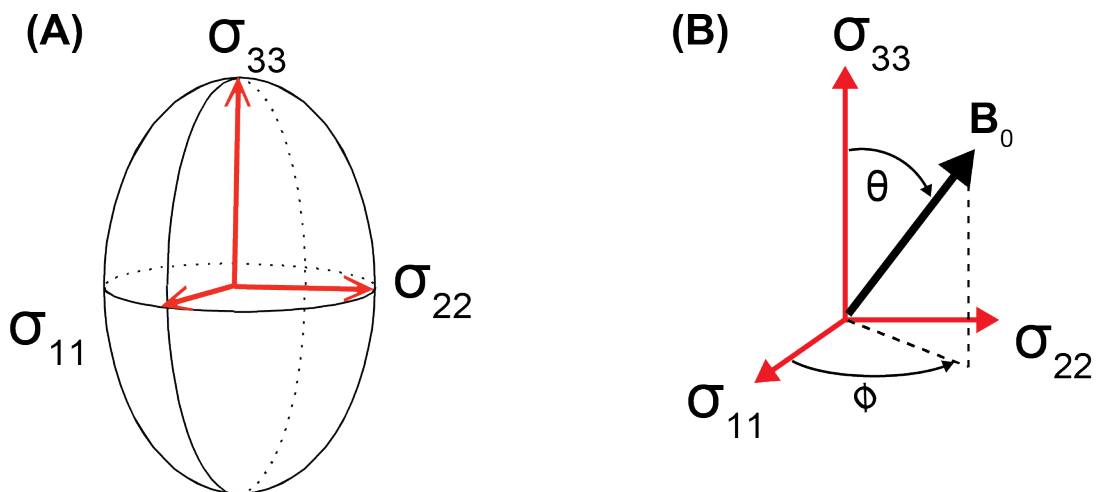


**Figure 1.4:** (A) Schematic representation of the MS tensor in its principal axis system (PAS) using an ellipsoid as a visual aid. The magnitudes of the components are  $\sigma_{11} \leq \sigma_{22} \leq \sigma_{33}$ . (B) Angles  $\theta$  and  $\phi$  describe the relative orientations of  $B_0$  and the MS tensor in its PAS.

MS values are reported in units of ppm with respect to a bare nucleus, which is said to have a chemical shielding of 0 ppm. The bare nucleus is not an appropriate experimental NMR standard; hence, values of chemical shifts (CS) are reported with respect to reference compounds. The conversion between MS and CS is as follows:

$$\delta = \frac{\sigma_{\text{ref}} - \sigma_{\text{sample}}}{1 - \sigma_{\text{ref}}} \approx \sigma_{\text{ref}} - \sigma_{\text{sample}} \quad (1.15)$$

Similarly, the CS is also represented as a second-rank tensor with components such that  $\delta_{11} \geq \delta_{22} \geq \delta_{33}$  ( $\delta_{11}$  and  $\delta_{33}$  correspond to the directions of least and most shielding). Aside from these three principal components, there is not a single, standard convention for describing the CS tensor.<sup>21</sup> Herein, the Herzfeld-Berger convention is utilized.<sup>22</sup> The *isotropic chemical shift* is given by,

$$\delta_{\text{iso}} = \frac{\delta_{11} + \delta_{22} + \delta_{33}}{3} \quad (1.16)$$

the *span* ( $\Omega$ ) is a measure of the magnitude of the chemical shift anisotropy (CSA), and determines the breadth of a powder pattern

$$\Omega = (\delta_{11} - \delta_{33}) \quad (1.17)$$

and the *skew* ( $\kappa$ ) is a measure of the axial symmetry of the CS tensor

$$\kappa = \frac{3(\delta_{22} - \delta_{iso})}{\Omega} \quad (1.18)$$

taking on values such that  $-1 \leq \kappa \leq +1$ , with the two outer limits representing cases of axial symmetry.

In solution, random, rapid molecular tumbling (with a correlation time,  $\tau_c$ , of *ca.*  $10^{-12}$  s) averages the anisotropic portion of the CS tensor to zero, such that only the isotropic chemical shift is observed. Conversely, in a microcrystalline solid, every molecular orientation gives rise to a unique CS tensor orientation with respect to  $\mathbf{B}_0$ , and therefore a distinct frequency shift (**Eq. 1.14**), resulting in a broad powder pattern said to be influenced by CSA. The centre of gravity of the powder pattern is located at a frequency corresponding to  $\delta_{iso}$ , and the values of  $\Omega$  and  $\kappa$  influence the breadth and shape of the pattern, respectively (**Figure 1.5**).

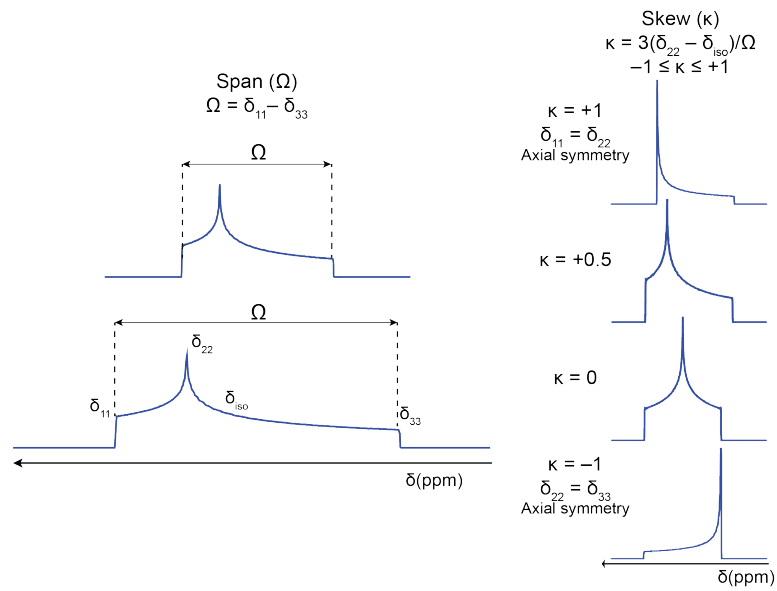


**Figure 1.5:** Simulated CSA powder patterns showing the effects of the (A) span ( $\Omega$ ) and (B) skew ( $\kappa$ ) on the appearance of the spectra

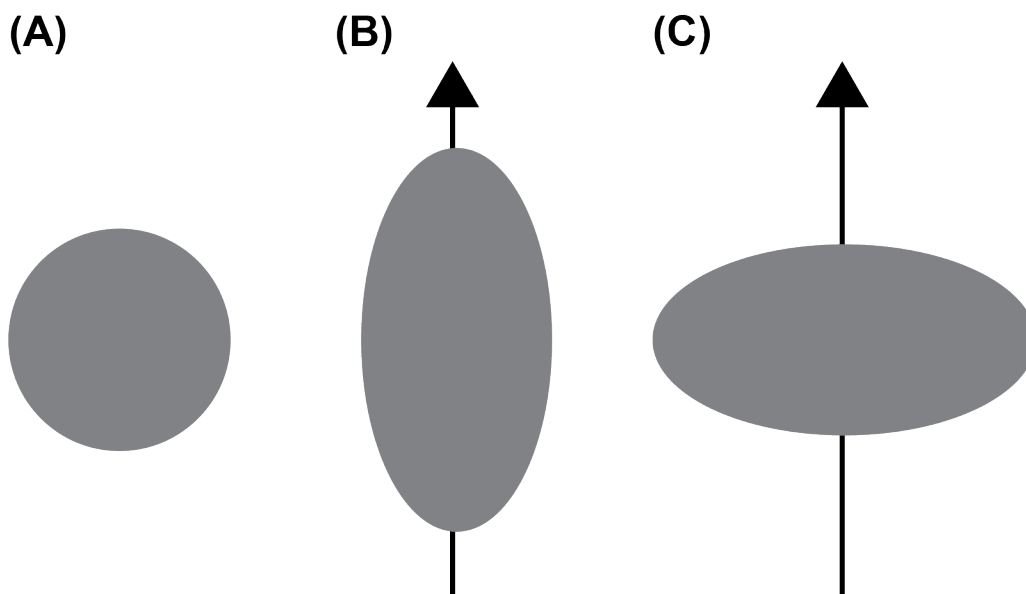


**Figure 1.6:** Schematic representation of the distribution of nuclear charge in a (A) spin- $1/2$  ( $Q = 0$ , spherical), (B) quadrupolar ( $Q > 0$ , prolate), and (C) quadrupolar ( $Q < 0$ , oblate) nuclides.

#### 1.2.4 The Quadrupolar Interaction

The *quadrupolar interaction* is only observed for quadrupolar nuclides (*i.e.*, those with  $I > 1/2$ ). Quadrupolar nuclides have spherically asymmetric nuclear charge distributions, as opposed to spin- $1/2$  nuclides, whose charge distributions can be visualized as spherical (**Figure 1.6**). The asymmetric distribution of charge is described by a scalar quantity known as the *nuclear quadrupole moment* ( $Q$ ),<sup>23</sup> measured in units of  $\text{fm}^2$ , and is an intrinsic property of the nucleus (the nuclear electric quadrupolar moment is often expressed as  $eQ$ ). The value of  $Q$  can be either negative or positive, corresponding to charge distributions of spherical oblate or spherical prolate symmetries, respectively. The nuclear quadrupolar moment interacts with the electric field gradients (EFGs) at the nucleus; non-zero EFGs result from a non-spherical distribution of ground state electronic charge and nuclear charges about the nucleus; this is known as the quadrupolar interaction,<sup>24</sup> which is described by<sup>23,25,26</sup>

$$\hat{\mathcal{H}}_Q = \frac{eQ}{2I(2I-1)} \mathbf{I} \cdot \ddot{\mathbf{V}} \cdot \mathbf{I} \quad (1.19)$$

where  $\mathbf{I}$  is the spin angular momentum operator,  $eQ$  is the nuclear electric quadrupole moment, and  $\ddot{\mathbf{V}}$  is the second-rank, symmetric  $3 \times 3$  EFG tensor:

$$\ddot{\mathbf{V}} = \begin{pmatrix} V_{xx} & V_{xy} & V_{xz} \\ V_{yx} & V_{yy} & V_{yz} \\ V_{zx} & V_{zy} & V_{zz} \end{pmatrix} \quad (1.20)$$

This tensor can be diagonalized to yield the EFG tensor in its own PAS

$$\ddot{\mathbf{V}}_{\text{PAS}} = \begin{pmatrix} V_{11} & 0 & 0 \\ 0 & V_{22} & 0 \\ 0 & 0 & V_{33} \end{pmatrix} \quad (1.21)$$

The principal components of the EFG tensor are defined such that  $|V_{11}| \leq |V_{22}| \leq |V_{33}|$ .

Unlike the CS tensor, the EFG tensor is traceless (*i.e.*,  $V_{11} + V_{22} + V_{33} = 0$ ), and there is no analog for the quadrupolar interaction to the isotropic chemical shift. Therefore, the EFG tensor can be described by only two parameters.

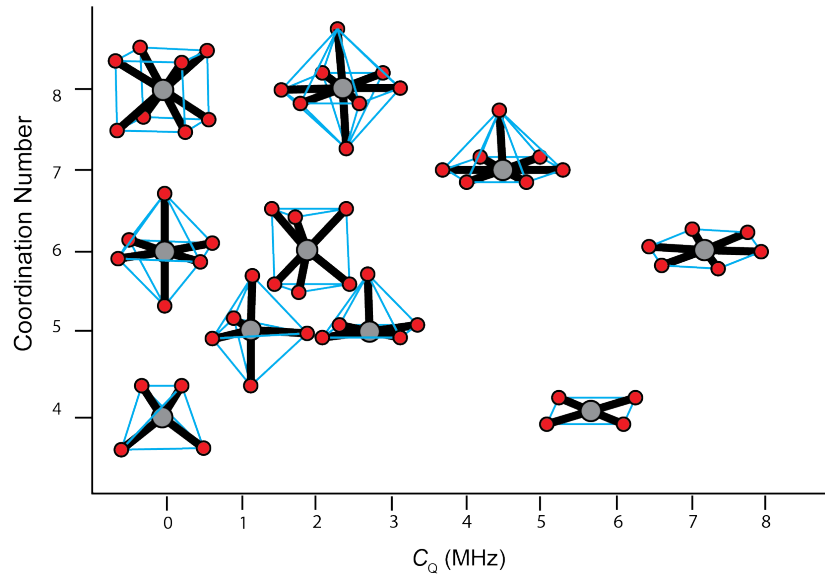


**Figure 1.7:** The relationship between the absolute magnitudes of  $C_Q$  and the spherical symmetry of the EFG tensor with its origin at the nucleus for a series of sodium oxides, as described by Koller *et al.* As the degree of spherical symmetry increases, the magnitude of  $C_Q$  decreases. Adapted from ref. 28.

The first of the parameters describes magnitude of the quadrupolar interaction and is called the *nuclear quadrupolar coupling constant*,  $C_Q$ , which is typically reported in units of kHz or MHz:

$$C_Q = \frac{eQV_{33}}{h} \quad (1.22)$$

The absolute magnitude of  $C_Q$  is related to the spherical symmetry of the ground-state electronic density around the nucleus.<sup>27</sup> An excellent demonstration of the simple relationship between the magnitude of  $C_Q$  and common structural motifs was demonstrated by Koller *et al.*<sup>28</sup> in the study of sodium oxides using  $^{23}\text{Na}$  SSNMR (**Figure 1.7**). If the quadrupolar nucleus is located at the centre of certain polyhedral arrangements of atoms (*i.e.*, the Platonic solids: cube, tetrahedron, octahedron, *etc.*), the EFG at the nuclear origin vanishes and  $C_Q = 0$ . Any deviation from spherical symmetry is reflected in an increase in the magnitude of  $C_Q$ . It is noted that  $C_Q$  can be positive or negative, depending on the relative signs of  $Q$  and  $V_{33}$ ; sign differences cannot be determined from NMR spectra of quadrupolar nuclides, but are readily available from first principles calculations. The relationships between structure and  $C_Q$  is particularly important in the  $^{35}\text{Cl}$  SSNMR studies described in **Chapter 6**. Briefly, for an isolated  $\text{Cl}^-$  anion with a perfectly spherical distribution of charge, the value of  $C_Q$  is 0; however, if the spherical symmetry of this charge distribution is perturbed by hydrogen bonds (*e.g.*, in HCl salts),<sup>29–31</sup> covalent bonding to a metal (*i.e.*, transition-metal chlorides),<sup>32–35</sup> or covalent bonds with carbon (*e.g.*, C–Cl bonds in organic compounds),<sup>36</sup> the values of  $C_Q$  increase (**Figure 1.8**).



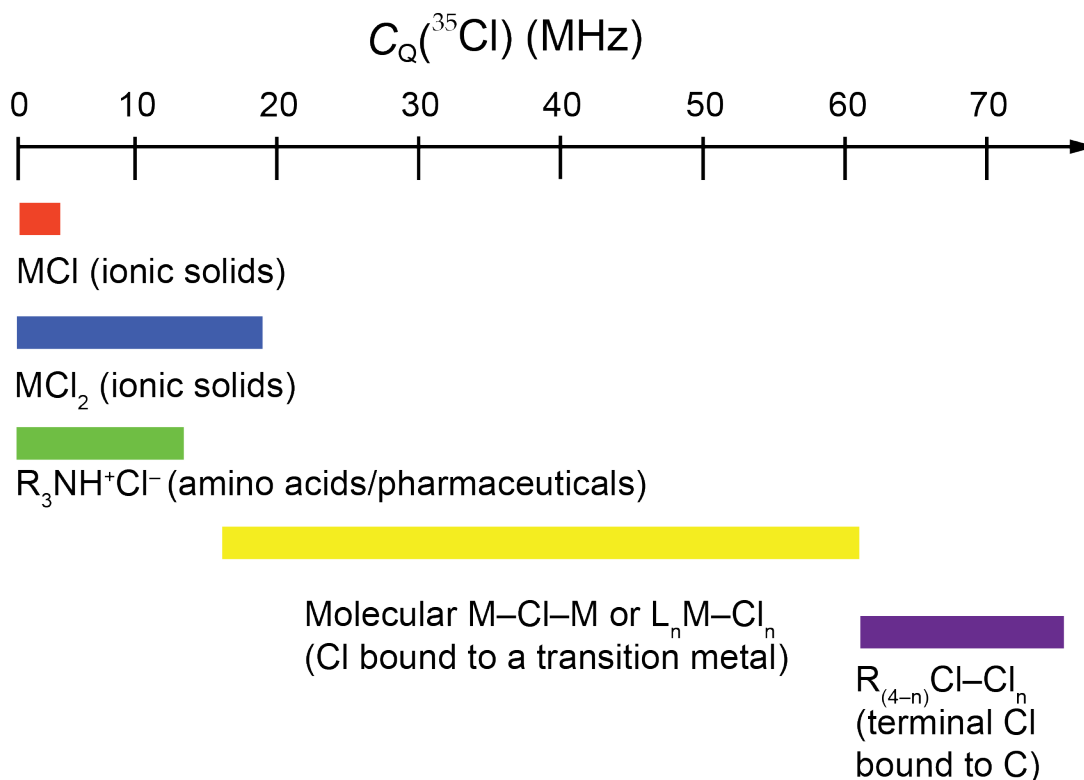


**Figure 1.8:** Relationships between the Cl bonding environment and typical magnitudes of  $C_Q(^{35}\text{Cl})$ .

The second parameter, referred to as the asymmetry parameter,  $\eta_Q$ , is a measure of the axial symmetry of the EFG tensor. This parameter is dimensionless and ranges from 0 to 1:

$$\eta_Q = \frac{V_{11} - V_{22}}{V_{33}} \quad (1.23)$$

The case of  $\eta_Q = 0$  ( $V_{11} = V_{22}$ ) denotes perfect axial symmetry of the EFG tensor and a cylindrically symmetric ground-state electron distribution around the nucleus. For  $\eta_Q = 1.0$ , the magnitude of  $V_{11} = 0$ , and  $V_{22} = -V_{33}$ .

Under the high-field approximation, the quadrupolar interaction Hamiltonian is treated as a perturbation on the Hamiltonian. **Eq. 1.19** is often expressed as

$$\hat{\mathcal{H}}_Q = \hat{\mathcal{H}}_Q^{[1]} + \hat{\mathcal{H}}_Q^{[2]} \quad (1.24)$$

where  $\hat{\mathcal{H}}_Q^{[1]}$  and  $\hat{\mathcal{H}}_Q^{[2]}$  are known and the *first-* and *second-order quadrupolar Hamiltonians*, respectively (full expressions for these Hamiltonians are found elsewhere).<sup>14,37,38</sup> These Hamiltonians have different effects on the spin states of a quadrupolar nucleus. For a spin-3/2 nuclide, there are  $2I + 1 = 4$  spin states and three possible transitions: the *central transition* (CT,  $m_1 = +1/2 \leftrightarrow m_1 = -1/2$ ) and the *satellite transitions* (ST,  $m_1 = +3/2 \leftrightarrow m_1 = +1/2$  and  $m_1 = -1/2 \leftrightarrow m_1 = -3/2$ ). While the first-order quadrupolar interaction (FOQI) perturbs all of the energy levels, it changes the  $m_1 = +1/2$  and  $m_1 = -1/2$  states by equal amounts, and therefore, the energy spacing for the CT is unaffected. However, the STs are affected; due to the orientation dependence of FOQI, powder patterns arising from STs are much broader than those associated with the CT (in many cases, they are broadened to such a degree that they are undetectable by conventional SSNMR experiments). The second-order quadrupolar interaction (SOQI), perturbs the energy levels such that the energy spacings of the CT and ST are influenced, albeit to a much smaller degree than the FOQI (**Figure 1.9(A)**). The orientation dependence of the SOQI is much more complex than that of the FOQI;<sup>16</sup> hence, CT patterns that are dominated by contributions from the SOQI are not as broad as the ST patterns, but have unusual shapes; they are colloquially described as *second-order quadrupolar patterns*. Fortunately, it is relatively facile to simulate these powder patterns, which enables the determination of  $C_Q$  and  $\eta_Q$ , (**Figure 1.10**), as well as  $\delta_{\text{iso}}$ , which is located near the centre of gravity of the patterns. When the broadening arising from the SOQI and CSA are comparable, it is possible to observe the simultaneous effects of these interactions in CT patterns. The simulation of such patterns is more complicated, because of their dependence on two sets of distinct tensor parameters, as

well as the relative orientation of these tensors, which are described by the Euler angles  $\alpha$ ,  $\beta$ , and  $\gamma$ .<sup>39</sup> Interestingly, the breadth of the CT patterns is often found to scale proportionally with the magnitude of  $B_0$  and inversely proportional to the magnitude of  $C_Q$  (depending on the values of the Euler angles); hence, simulations are aided by acquisition of these patterns at two different magnetic fields (or in some cases, by acquiring spectra for two different isotopes, when possible).

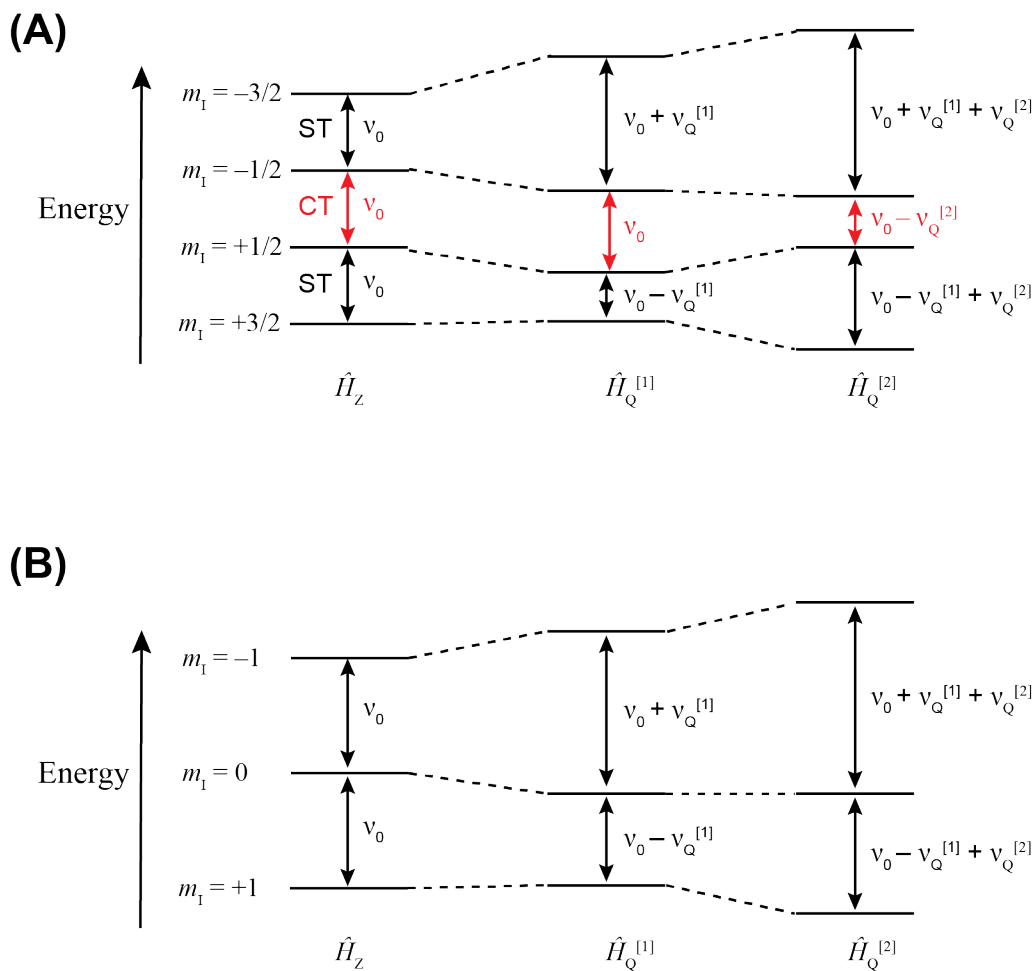


**Figure 1.9:** Perturbation of the Zeeman energy levels by the first- and second-order quadrupolar interactions for a (A) spin-3/2 nuclide (e.g.,  $^{35}\text{Cl}$ ) and (B) spin-1 nuclide (e.g.,  $^2\text{H}$ ). The first-order quadrupolar interaction (FOQI) does not influence the central transition (CT, shown in red) but influences the satellite transitions (ST) to a great extent

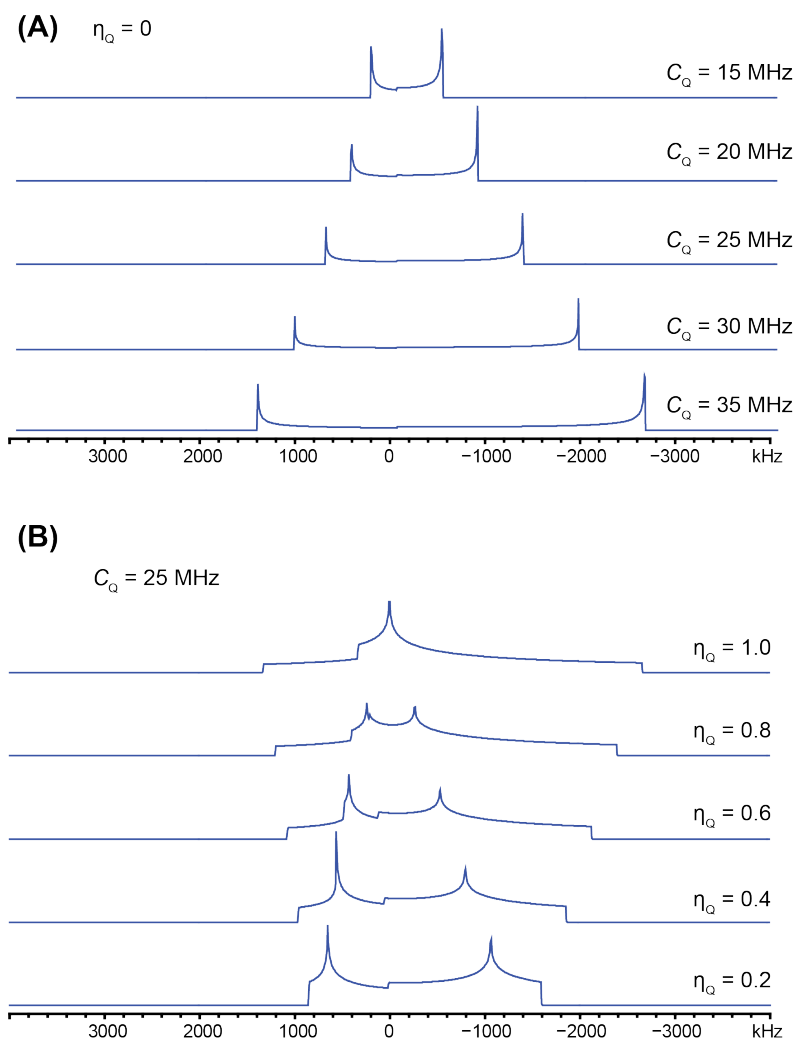


**Figure 1.10:** Simulated central-transition second-order quadrupolar spectra for a spin-3/2 nucleus with (A)  $\eta_Q = 0$  and values of  $C_Q$  ranging from 15 to 35 MHz and (B)  $C_Q = 25$  MHz and  $\eta_Q$  values ranging from 0.2 to 1.0.

For a spin-1 nucleus (e.g.,  $^2\text{H}$ ,  $^{14}\text{N}$ ), there are only STs ( $m_I = +1 \leftrightarrow m_I = 0$  and  $m_I = 0 \leftrightarrow m_I = -1$ ) (Figure 1.9(B)).<sup>40</sup> The powder patterns result from the two overlapping STs and are broad and mirror symmetric about the isotropic chemical shift, and are primarily influenced by the FOQI (i.e., the effects of the SOQI are negligible). These patterns, known as *Pake doublets*,<sup>41</sup> have three distinct sets of features: horns, shoulders and feet, separated by frequencies  $\Delta\nu_{11}$ ,  $\Delta\nu_{22}$ , and  $\Delta\nu_{33}$ , respectively (Figure 1.11). In cases where the broadening effects of the FOQI and CSA are similar, these patterns can

lose their mirror symmetries (see **Chapter 2** for examples in  $^2\text{H}$  SSNMR spectra of platinum-deuteride compounds acquired at 4.75 and 9.4 T).

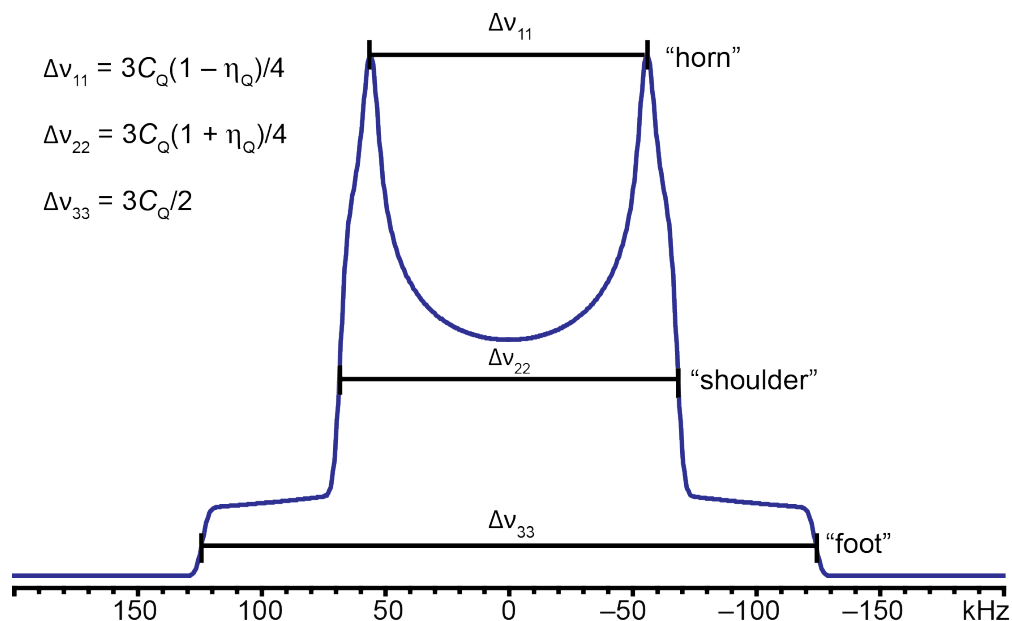


**Figure 1.11:** Appearance of a powder pattern in the spectrum of a spin-1 nuclide; such patterns are referred to as Pake doublets. Also shown are the frequency separations of the “horn”, “shoulder”, and “foot” discontinuities.

### 1.2.5 Direct Dipolar Coupling

The dipolar interaction arises from the mutual, through-space interaction of the magnetic dipole moments of two (or more) spins. The dipolar interaction between two spins  $I$  and  $S$  can be described by the dipolar Hamiltonian,

$$\hat{\mathcal{H}}_D = \mathbf{I} \cdot \hat{\mathbf{D}} \cdot \mathbf{S} \quad (1.25)$$

where the dipolar interaction tensor is given by

$$\hat{\mathbf{D}} = hR_{DD} = \begin{pmatrix} (r^2 - 3x^2)/r^2 & -3xy/r^2 & -3xz/r^2 \\ -3xy/r^2 & (1 - 3y^2)/r^2 & -3yz/r^2 \\ -3xy/r^2 & -3yz/r^2 & (1 - 3z^2)/r^2 \end{pmatrix} \quad (1.26)$$

This tensor is traceless (*i.e.*, no isotropic dipolar shift) and axially symmetric. The dipolar Hamiltonian can be expanded into the more familiar form

$$\hat{\mathcal{H}}_{\text{DD}} = R_{\text{DD}} \left[ \mathbf{I} \cdot \mathbf{S} - \frac{3(\mathbf{I} \cdot \mathbf{r})(\mathbf{S} \cdot \mathbf{r})}{r^2} \right] \quad (1.27)$$

where  $\mathbf{r}$  is the internuclear vector between spins  $I$  and  $S$ , and  $r$  is the internuclear distance.

The magnitude of the dipolar interaction is determined by the dipolar coupling constant:

$$R_{\text{DD}} = \frac{\mu_0 \gamma_I \gamma_S \hbar}{4\pi r^3} \quad (1.28)$$

In solution, rapid molecular tumbling averages the dipolar interaction (since  $\hat{\mathbf{D}}$  is traceless) and no secular effects (*i.e.*, frequency shifts) are manifested in the NMR spectra. However, the dipolar interaction has non-secular effects, and normally provides the dominant mechanism for nuclear relaxation in solution. In the solid state, the dipolar interaction is a significant source of broadening in SSNMR spectra. Fortunately, with the use of magic-angle spinning (MAS, *vide infra*) and decoupling pulse sequences, the effects of the dipolar interaction can be completely or partially averaged, depending upon its magnitude. Furthermore, the dipolar interaction is exploited in many SSNMR experiments for providing signal enhancements (*e.g.*, cross polarization, *vide infra*) or obtaining structural information through 1D experiments for measurements of internuclear distances<sup>42</sup> or 2D correlation experiments.<sup>43,44</sup>

### 1.2.6 Indirect spin-spin Coupling ( $J$ -coupling)

The indirect spin-spin coupling, or  $J$ -coupling, is a two-spin interaction resulting from the coupling of nuclear magnetic moments which is mediated by the electrons in chemical bonds. After the chemical shift, it is the most important interaction in most solution NMR experiments, since it provides information on bonding and connectivity.

The Hamiltonian describing the  $J$ -coupling interaction between spins  $I$  and  $S$  is:

$$\hat{\mathcal{H}}_J = \mathbf{I} \cdot \mathbf{J} \cdot \mathbf{S} \quad (1.29)$$

Where  $\mathbf{J}$  is a second-rank, non-traceless, antisymmetric tensor that describes the orientation dependence of the  $J$ -coupling interaction. The magnitude of the  $J$ -coupling interaction is expressed as the  $J$ -coupling constant,  $J_{IS}$ , which is equal to the average of the components of  $\mathbf{J}$ .

In solution, molecular tumbling averages the  $J$ -coupling to an isotropic value. For most nuclear pairs, the magnitude of the  $J$ -coupling is much smaller than that of the other interactions (*i.e.*,  $J_{IS}$  is usually on the order of a fraction of a Hz to several hundred Hz, though there are certain one-bond  $J$ -couplings involving heavy nuclides like  $^{195}\text{Pt}$  or  $^{199}\text{Hg}$  that have magnitudes of several thousand Hz).<sup>45</sup> In SSNMR spectra, the effects of  $J$ -coupling are more challenging to observe, due to broader line widths and powder patterns arising from larger anisotropic chemical shift and quadrupolar interactions, as well as phenomena such as magnetic susceptibility broadening. In cases where MAS experiments (*vide infra*) can yield sharp peak widths with breadths at half height less than the  $J$ -coupling (*i.e.*,  $\Delta\nu_{1/2} < J_{IS}$ ), the effects of  $J$ -coupling are manifested in the spectrum of nucleus  $I$  as a splitting of the signal into  $2nS + 1$  peaks, where  $n$  is the number of magnetically equivalent coupled nuclei with spin  $S$ .

### 1.3 Effects of Dynamics on SSNMR spectra

NMR spectra are extremely sensitive to a variety of molecular motions over a wide range of temperatures, and as such, reversible processes, which are described by dynamic equilibria, are readily detected. For example, SSNMR has been used to monitor the reorientation of chemical moieties,<sup>46–48</sup> diffusion of ions through porous media,<sup>49,50</sup> and rotational and translational motions of simple molecular machines.<sup>51,52</sup> N.B. This is

by no means a comprehensive list of dynamical systems studied with SSNMR, and there are several excellent resources that discuss these systems and many others in much great detail.<sup>4,10,37,53,54</sup>

The range of rates of motion that can be detected in NMR is dependent on the system (*i.e.*, structure, symmetry, and allowable motions or chemical exchange mechanisms), differences in frequency shifts ( $\Delta\nu$ , in cases where sharp peaks can be resolved, which correspond to magnetically distinct sites undergoing chemical exchange), and/or frequency distributions in anisotropic powder patterns ( $\Delta\Omega$ , arising from NMR interaction tensors that vary in orientation due to molecular motions or exchange). Three motional regimes are defined: (i) the slow-motion limit (SML), where motions are occurring at rates that are too slow to be manifested as changes in the NMR spectra (*i.e.*,  $\nu_{\text{ex}} \leq \Delta\nu$  or  $\Delta\Omega$ ), where  $\nu_{\text{ex}}$  is the rate of exchange between chemical sites,  $\Delta\nu$  and  $\Delta\Omega$  are as defined above, (ii) the intermediate motion regime (IMR), where  $\nu_{\text{ex}} \approx \Delta\nu$  or  $\Delta\Omega$ . (N.B. Motions with rates in the IMR result in NMR spectra that change drastically with temperature, and the simulation of these spectra yields detailed information on the rates and types of motion), and (iii) the fast-motion limit (FML),  $\nu_{\text{ex}} \geq \Delta\nu$  or  $\Delta\Omega$ , where spectra can be simulated by consideration of motionally averaged or *effective* values of isotropic chemical shifts, *J*-couplings, or in the case of anisotropic NMR interactions, tensor components (N.B., for most systems, once the FML limit is reached at higher temperatures, spectral appearance does not change – until the sample melts, decomposes, or undergoes a phase transition).

Very often, simulation of NMR spectra is required in order to extract dynamic information on the modes and rates of motion. Considering the simple case of exchange



between two chemical sites (A and B) with distinct isotropic shifts ( $\nu_A$  and  $\nu_B$ , in Hz), the motion of transverse magnetization for A,  $M_+^A$  is given by the Bloch equations:

$$\frac{dM_+^A}{dt} = i\nu_A M_+^A - \frac{M_+^A}{T_2^A} \quad (1.30)$$

where  $1/T_2^A$  is the natural line width (in Hz). An equivalent expression can be written for the transverse magnetization of site B. The effects of chemical exchange are taken into account with the following modifications to **Eq. 30**:

$$\begin{aligned} \frac{dM_+^A}{dt} &= i\nu_A M_+^A - \frac{M_+^A}{T_2^A} - k_{AB} M_+^A + k_{BA} M_+^B \\ \frac{dM_+^B}{dt} &= i\nu_B M_+^B - \frac{M_+^B}{T_2^B} - k_{BA} M_+^B + k_{AB} M_+^A \end{aligned} \quad (1.31)$$

where  $k_{AB}$  and  $k_{BA}$  are the rates of the motions that exchange site A with B and site B with A, respectively. It is more convenient to express the rate equations in matrix notation:

$$\frac{d\mathbf{M}_+}{dt} = \bar{\mathbf{A}} \cdot \mathbf{M}_+ \quad (1.32)$$

where  $\bar{\mathbf{A}}$  is a square matrix whose diagonal components contain the transition frequencies, linewidths, and exchanges rates and the off-diagonal components give the rates of exchange between connected sites

$$\bar{\mathbf{A}} = \begin{pmatrix} i\nu_A - \frac{1}{T_2^A} - k_{AB} & k_{BA} \\ k_{AB} & i\nu_B - \frac{1}{T_2^B} - k_{BA} \end{pmatrix} \quad (1.33)$$

and  $\mathbf{M}_+$  is a column vector

$$\mathbf{M}_+ = \begin{pmatrix} M_+^A \\ M_+^B \end{pmatrix} \quad (1.34)$$

The solution to **Eq. 1.32** has the general form:

$$\mathbf{M}_+ = e^{\bar{\mathbf{A}}t} \cdot M_+(0) \quad (1.35)$$

where  $M_+(0)$  is the initial magnetization, which is proportional to populations of sites A and B ( $p_A$  and  $p_B$ , respectively).

The effects of exchange on  $\mathbf{M}_+$ , and hence, on the appearance of the NMR spectrum, can be computed by determining an analytical expression for the spectrum (*i.e.*, an equation that describes the real absorption spectrum); however, solutions of such equations are both difficult and cumbersome in all but the simplest cases. The more common method is to generate a time-domain signal (*i.e.*, FID) using numerical calculations.

The general expression for the FID involving exchange between  $N$  sites with different populations is equal to the sum of the time evolutions of transverse magnetization of the individual sites  $j$

$$G(t) = \sum_j M_j(t) = \mathbf{1} \cdot e^{(i\bar{\omega} + \bar{\pi})t} \cdot \mathbf{W} \quad (1.36)$$

where  $\mathbf{1}$  is a unit row vector,  $\mathbf{W} = (W_1, \dots, W_N)$  is a column vector containing the *a priori* populations of the sites, and  $\bar{\omega}$  and  $\bar{\pi}$  are square matrices containing the frequency/linewidth and exchange information, respectively.<sup>10</sup> The FID is generated through diagonalization of the non-Hermitian  $(i\bar{\omega} + \bar{\pi})$  matrix, which can be easily accomplished using simple diagonalization routines to give:

$$G(t) = \mathbf{1} \cdot \mathbf{S} e^{\bar{\lambda}t} \mathbf{S}^{-1} \cdot \mathbf{W} \quad (1.37)$$

where  $\mathbf{S}$  is the diagonalization matrix.

**Eq. 1.37** is applicable for the cases where the exchange occurs between sites which each have single transition frequencies (i.e., chemical shifts) and can therefore be applied to study exchange processes in solution where the sites have distinct isotropic chemical shifts and changes in the exchange rate are usually caused by experimentally varying the temperature. When the exchange occurs with rates in the SML for a two-site systems with distinct shifts  $\nu_A$  and  $\nu_B$ , the spectrum has two peaks at  $\nu_A$  and  $\nu_B$  with widths proportional to  $(1/T_2) + k$ . Motions with rates in the IMR cause the peaks to merge together until they coalesce at a point defined by

$$\tau_{AB}^C = \frac{\sqrt{2}}{\pi} (\nu_A - \nu_B) \quad (1.38)$$

Finally, in the FML, a single peak is observed at an average frequency  $(p_A \nu_A + p_B \nu_B)$ .

In the solid state, the NMR interactions are anisotropic; therefore, each exchange site has a distribution of frequencies arising from all of the orientations of the interaction tensor with respect to  $\mathbf{B}_0$ . The frequency of a given crystallite is dependent on the polar angles  $\theta$  and  $\phi$  which describe the orientation of the interaction tensor with respect to  $\mathbf{B}_0$  (the special case of MAS is neglected here for simplicity); therefore, to obtain FID for a powdered sample, **Eq.1.34** must be averaged over all values of  $\theta$  and  $\phi$  and weighted by  $\sin \theta$ . Powder averaging is not discussed herein and the reader is referred to an excellent tutorial article by Edén for more information.<sup>55</sup>

In Chapters 4 and 5 of this dissertation, SSNMR is used extensively for probing the dynamics of a variety of systems. In particular,  $^2\text{H}$  SSNMR is valuable for dynamical studies, as the small quadrupole moment ( $Q = 0.286 \text{ fm}^2$ ) results in relatively narrow

patterns ( $140 \text{ kHz} \leq C_Q \leq 200 \text{ kHz}$  for most compounds) which are easily acquired. The  $^2\text{H}$  SSNMR spectra are sensitive to motions in the range from *ca.*  $10^3$  to  $10^6$  Hz, corresponding to motions that can be easily observed and analyzed in  $^2\text{H}$  SSNMR spectra acquired with standard equipment in most laboratories.

Simulations of  $^2\text{H}$  powder patterns are conducted by considering rotations of the EFG tensor ( $\ddot{V}$ ) through various geometries, which correspond to different magnetically distinct sites undergoing dynamical motions (*i.e.*, either chemical exchange or some other rotational, translation or torsional motions). The contribution to the spectral frequency from the FOQI for a crystallite in a given orientation is given by:

$$\omega_Q(\theta, \phi) = \frac{eQ}{4I(2I-1)\hbar} \mathbf{b}_{0,\text{PAS}} \ddot{V}_{\text{PAS}} \mathbf{b}_{0,\text{PAS}} \quad (1.39)$$

where  $\mathbf{b}_{0,\text{PAS}}$  is a unit vector in the PAS of the EFG tensor that points in the direction of  $\mathbf{B}_0$ :

$$\mathbf{b}_{0,\text{PAS}} = (\sin\theta\cos\phi, \sin\theta\sin\phi, \cos\theta) \quad (1.40)$$

A molecular reorientation described by a rotation through a set of Euler angles ( $\alpha, \beta, \gamma$ ) gives rise to an EFG tensor in a new orientation relative to the original PAS:

$$\ddot{V}_{\text{PAS}}^{\text{new}} = \mathbf{R}(\alpha, \beta, \gamma) \ddot{V}_{\text{PAS}} \mathbf{R}^{-1}(\alpha, \beta, \gamma) \quad (1.41)$$

where  $\mathbf{R}(\alpha, \beta, \gamma)$  is the rotation matrix. This new EFG orientation gives rise to a distinct spectral frequency that is calculated using **Eq. 1.36**. The PAS is relative to the molecular frame; therefore, chemical exchange results in a reorientation of the PAS. It is often more convenient to express EFG tensors for all of the exchanging sites relative to a frame in the crystallite that remains fixed during the exchange process, that is:

$$\ddot{V}_{i,\text{CFF}} = \mathbf{R}^{-1}(\alpha_i, \beta_i, \gamma_i) \ddot{V}_{i,\text{PAS}} \mathbf{R}(\alpha_i, \beta_i, \gamma_i) \quad (1.42)$$

where the  $\mathbf{R}(\alpha_i, \beta_i, \gamma_i)$  describes the rotation of the EFG PAS for site  $i$  into the crystallite-fixed frame ( $\ddot{\mathbf{V}}_{\text{CFF}}$ ). Similarly, the spectral contribution from the QI for each site is given by:

$$\omega_{\text{Q}}(\theta, \phi) = \frac{eQ}{4I(2I-1)\hbar} \mathbf{b}_{0,\text{CFF}} \ddot{\mathbf{V}}_{i,\text{CFF}} \mathbf{b}_{0,\text{CFF}} \quad (1.43)$$

where  $\mathbf{b}_{0,\text{CFF}}$  is given by an equivalent expression to that in **Eq. 1.30**, but with  $\theta$  and  $\phi$  now describing the orientation of  $\mathbf{B}_0$  in the CFF.

For molecular reorientations described by a rotation about an axis, it is easiest to define the  $z$ -axis of the CFF such that it coincides with the rotation axis. This procedure is illustrated in **Figure 1.12(A)** for the simple case of a  $\text{CD}_3$  group rotation. The EFG tensor in its PAS for a single deuteron is rotated into the three possible rotational sites ( $a$ ,  $b$ , and  $c$ ) in the CFF. The  $z$ -axis of the CFF is defined such that it is coincident with the  $C_3$  rotation axis of the methyl group. Rotation about the  $C_3$  axis causes the deuterons to exchange positions at a rate  $\nu_{\text{ex}}$ ; simulated spectra for this mode of motion are shown in **Figure 1.12(B)**.

## 1.4 Acquisition Techniques

In this section, a brief overview is given of the acquisition techniques and pulse sequences used in the projects described in this dissertation. Further modifications to and details regarding these methodologies are introduced on an *ad hoc* basis in **Chapters 2** through **6**.

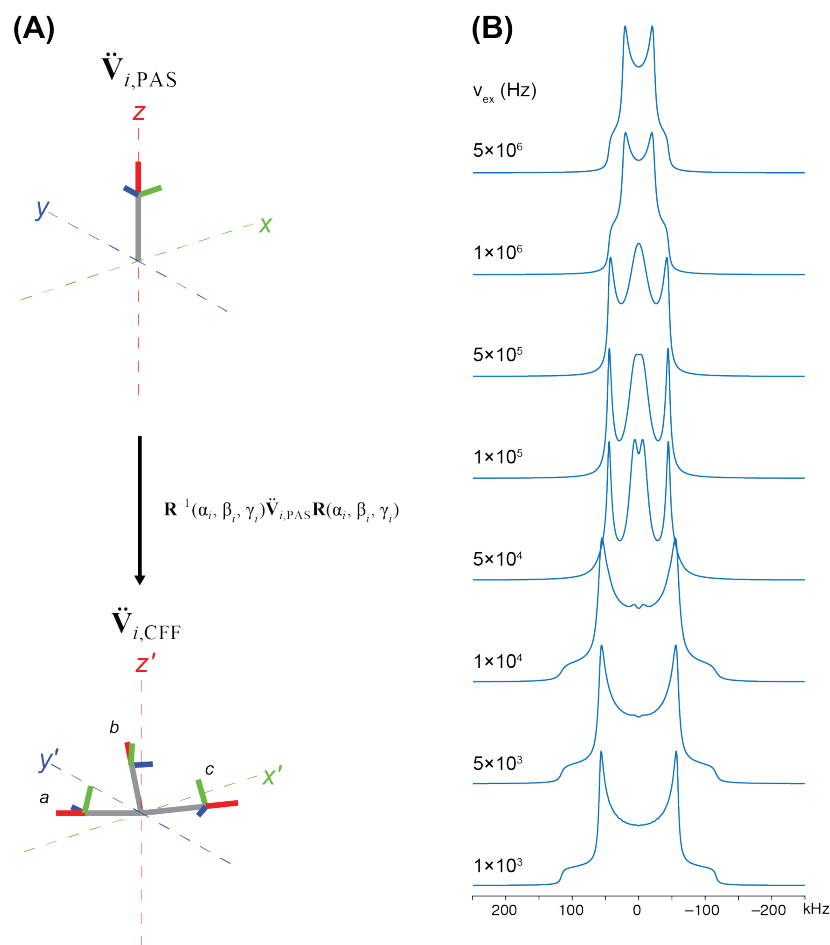


**Figure 1.12:** (A) A depiction of the rotation of a  $^2\text{H}$  EFG tensor in its principal axis system (PAS) into the three sites of a  $\text{CD}_3$  group in the crystallite-fixed frame (CFF). The  $z$ -axis of the CFF is coincident with the  $C_3$  rotation axis of the  $\text{CD}_3$  group. (B) Simulated  $^2\text{H}$  SSNMR spectra for the three-fold rotation of the  $\text{CD}_3$  groups with different exchange rates ( $v_{\text{ex}}$ ).

#### 1.4.1 Magic-Angle Spinning (MAS)

*Magic-angle spinning* (MAS) is possibly the most widely used technique for the acquisition of SSNMR spectra. The purpose of MAS is to acquire high-resolution NMR spectra analogous to those obtained for solution-state samples.<sup>56,57</sup> To first order, all NMR interactions have an orientation dependence which has a  $(3\cos^2\theta - 1)$  term, where  $\theta$  is the angle between the largest component of the interaction tensor and the external magnetic field,  $\mathbf{B}_0$ . In solution, rapid molecular tumbling reorients the interaction tensors

(on the order of  $10^{12}$  times per second) such that all of the possible values of  $\theta$  are sampled. This serves to average the anisotropic interactions to either zero (*i.e.*, the quadrupolar and dipolar interactions) or to their isotropic values (*i.e.*, the chemical shift and  $J$ -coupling interactions). Conversely, rapid isotropic reorientation does not occur for molecules in the solid state and every orientation of the tensor with respect to  $\mathbf{B}_0$  gives rise to a distinct frequency, resulting in broad patterns with the signal intensity spread over a large frequency range.

Spinning the sample about an axis oriented at the magic angle with respect to  $\mathbf{B}_0$  results in the orientation of the interaction tensor varying in time and the average orientation is given as:

$$\langle 3\cos^2\theta - 1 \rangle = \frac{1}{2}(3\cos^2\theta_R - 1)(3\cos^2\beta - 1) \quad (1.44)$$

where  $\theta_R$  is the experimentally controlled angle between the sample rotation axis and  $\mathbf{B}_0$  and  $\beta$  is the angle between the largest principal component of the interaction tensor and  $\mathbf{B}_0$  (**Figure 1.13**). If  $\theta_R$  is adjusted such that it is equal to the magic angle ( $\theta_R = 54.74^\circ$ ), the factor  $3\cos^2\theta_R - 1 = 0$ , thereby averaging the expectation value for  $\langle 3\cos^2\theta - 1 \rangle$  to 0, and resulting in an averaging of the terms responsible for the first-order anisotropic broadening of the SSNMR spectra. The first-order interactions can be completely averaged (*i.e.*, resulting in a single sharp peak) provided that the spinning frequency is sufficiently greater than the anisotropic frequency distribution of the SSNMR powder pattern.

During an MAS experiment, the magnetization is refocused at the end of a rotor period, resulting in the collection of a series of *rotational echoes* in the time domain signal. Fourier transformation of the FID gives rise to a series of spinning sidebands in

the frequency domain which are separated from the isotropic chemical shift at intervals equal to the spinning frequency. The signal intensity is concentrated into the spinning sidebands, resulting in an increase in signal-to-noise (S/N) in comparison to a spectrum acquired with no sample rotation. The number and intensities of the spinning sidebands are dependent on the magnitudes and orientation dependence of the anisotropic NMR interactions.

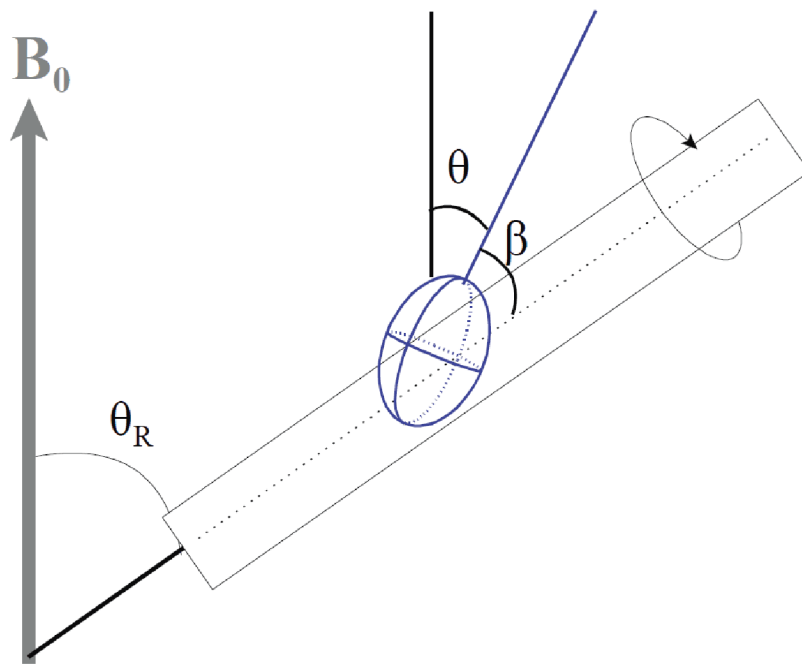


**Figure 1.13:** Schematic representation of the orientation of an NMR rotor with respect to the external magnetic field ( $B_0$ ).  $\theta_R$  is the experimentally adjusted angle between the rotor axis and  $B_0$ , which is most commonly set to the magic angle ( $54.74^\circ$ ). The ellipsoid represents an interaction tensor whose largest component is oriented at angles  $\beta$  with respect to the rotor axis and  $\theta$  with respect to  $B_0$ .

For quadrupolar nuclei, MAS can average the first-order interactions that influence the ST powder patterns, but only partially averages anisotropic contributions to the CT powder pattern, due to the distinct orientation dependence of the SOQI.<sup>58-60</sup> As a result, most half-integer quadrupolar nuclides have SSNMR spectra displaying distinct second-order MAS CT patterns. For spectra with one or two patterns arising from



magnetically distinct sites, it is facile to simulate these patterns and extract the values of  $C_Q$ ,  $\eta_Q$ , and  $\delta_{\text{iso}}$ . In cases where there are numerous overlapping patterns, such simulations can be challenging. Fortunately, there is a class of techniques that have been developed based on the 2D multiple-quantum MAS (MQMAS) method developed by Frydman and co-workers that enables separation of these patterns based upon their isotropic chemical shifts.<sup>61–64</sup> MQMAS methods can be applied to a handful of notable half-integer quadrupoles, including  $^{27}\text{Al}$ ,  $^{17}\text{O}$ ,  $^{11}\text{B}$ , and  $^{23}\text{Na}$ , but cannot be applied in circumstances where CT patterns are so broad that MAS cannot effectively separate the broad spinning sidebands from the central isotropic CT pattern.<sup>65</sup> In such instances, ultra-wideline (UW) NMR techniques must be applied for spectral acquisition under static conditions (*cf.* **Chapter 6**),<sup>38,66</sup> and several options are available for deconvolution of static patterns using relaxation-assisted spectroscopy (RAS) methods.<sup>67,68</sup> A full discussion of MAS of quadrupoles, MQMAS pulse sequences, and RAS methods is beyond the scope of this work; the reader is referred to the references above for further information.

#### 1.4.2 Cross-Polarization (CP)

Another commonly-employed acquisition technique in SSNMR is *cross polarization* (CP) which enhances the S/N of SSNMR spectra of unreceptive nuclei.<sup>69–72</sup> The signal enhancement in a CP experiment is a result of the transfer of spin polarization from abundant, high  $\gamma$  nuclei (*e.g.*,  $^1\text{H}$ ) to those that are dilute and/or have lower values of  $\gamma$  (*e.g.*,  $^{13}\text{C}$ ,  $^{111}\text{Cd}$ ). The maximum theoretical signal enhancement is determined by the ratio of the gyromagnetic ratios  $\gamma_I/\gamma_S$ , where  $I$  and  $S$  denote the abundant and dilute spins, respectively. The CP experiment is dependent on the  $T_1$  relaxation times of  $I$  which are

often short, therefore affording a reduction in experimental time. This is especially useful in the study of heavy spin-1/2 nuclei (*e.g.*,  $^{111}\text{Cd}$ , *cf.* **Chapters 2 and 3**) which can have extremely large  $T_1$  time constants, thereby necessitating prohibitively long experimental times using direct polarization (DP) experiments. The transfer of polarization occurs only for  $S$  spins that are spatially proximate and dipolar coupled to  $I$  spins, and is made possible by satisfying the Hartman-Hahn matching condition:

$$\omega_{1I} = \omega_{1S} \quad (1.45)$$

$$\gamma_I B_{1I} = \gamma_S B_{1S} \quad (1.46)$$

The CP pulse sequence is shown in **Figure 1.14(A)**. The sequence begins with the application of a  $90^\circ$  pulse on the  $I$  channel to create transverse magnetization.

Simultaneous spin-locking pulses are then applied on both the  $I$  and  $S$  channels, with powers chosen such that **Eq. 1.46** is satisfied. The duration of the spin-locking pulses is known as the contact time, during which  $S$  spin polarization builds up in the direction of the spin-locking pulse. At the end of the spin locking pulses, decoupling is applied on the  $I$  channel and signal is detected on the  $S$  channel.

CP can be combined with MAS (CP/MAS) to give high-resolution and high S/N spectra. It was demonstrated by Stejskal and Schaefer that the dipolar coupling is not averaged under MAS, but rather, is time dependent<sup>73</sup>. The Hartmann-Hahn condition is modified to

$$\omega_{1I} - \omega_{1S} = \pm n\omega_{\text{rot}} \quad (1.45)$$

which is the so-called *sideband match condition*.

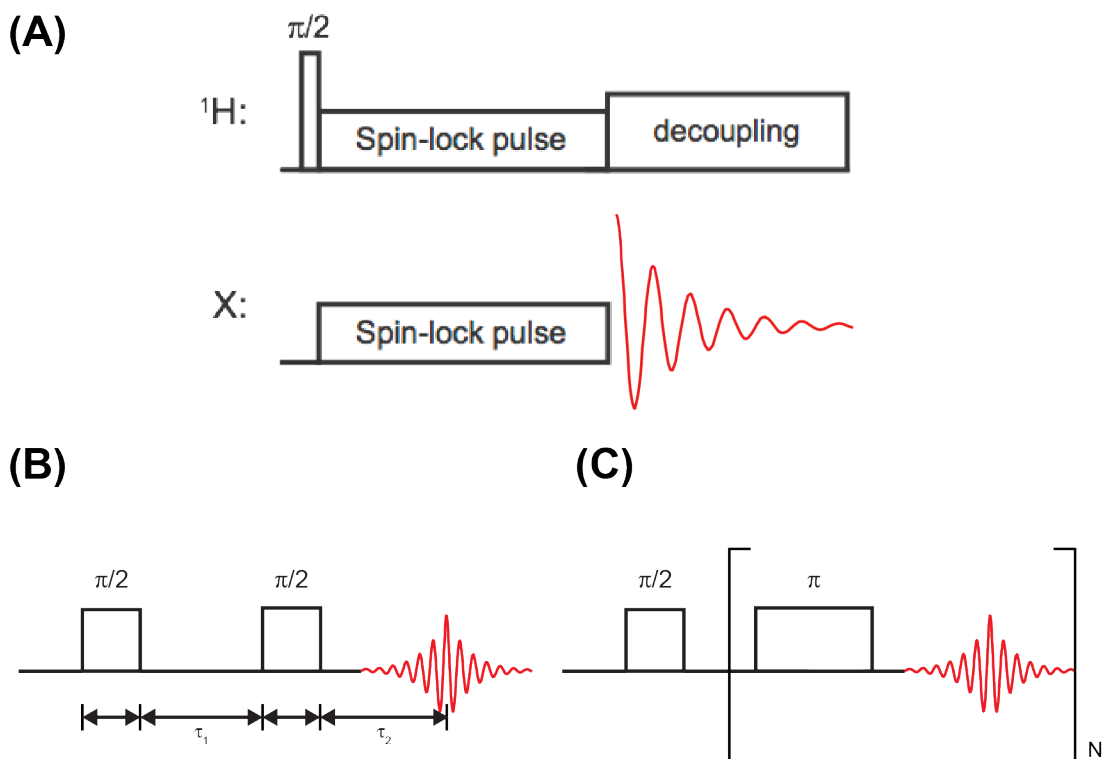


**Figure 1.14:** Diagrams depicting the (A) cross-polarization (CP), (B) quadrupolar echo (QE), and (C) Carr-Purcell-Meiboom-Gill (CPMG) pulse sequences.

### 1.4.3 Quadrupolar Echo

The acquisition of SSNMR spectra is often not possible using conventional Bloch-decay experiments (*i.e.*,  $90^\circ - \tau_D - \text{acquire}$ ). Efficient nuclear relaxation, especially for quadrupolar nuclei, causes rapid decay of the spin magnetization, and therefore the signal, during the dead time ( $\tau_D$ , *i.e.*, the delay to allow for dissipation of the pulse in the coil), resulting in severely distorted spectra or absence of signal altogether. The quadrupolar echo (QE, also known as the solid echo) pulse sequence (**Figure 1.14(B)**)<sup>74,75</sup> is often applied to avoid the spectral distortions resulting from traditional NMR experiments. In this sequence, a  $90^\circ$  pulse is applied to generate transverse magnetization. After the pulse, the spins evolve under the QI for a time period  $\tau_1$ , leading to a dephasing of the magnetization. A second  $90^\circ$  pulse is applied, and after a time  $\tau_2$ ,

the magnetization refocuses, resulting in the formation of an echo in the FID. The use of the QE sequence allows for the acquisition of undistorted powder patterns and significant enhancements in S/N compared to a Bloch decay experiment. The QE sequence is routinely used to study dynamics, especially in  $^2\text{H}$  SSNMR.<sup>40</sup> Dynamic processes which occur with rates in the IMR result in powder patterns that depend on the choice to  $\tau_1$ . Simulated powder patterns with different values of  $\tau_1$  can be used to extract additional information on the dynamic processes.

#### 1.4.4 Carr-Purcell Meiboom-Gill (CPMG) Pulse Sequence

The Carr-Purcell Meiboom-Gill (QCPMG) (**Figure 1.14(C)**) was originally designed for the purpose of measuring  $T_2$  relaxation times.<sup>76,77</sup> The experiment operates on the same principles as a Hahn-echo sequence ( $90^\circ - \tau_D - 180^\circ - \text{acquire}$ ),<sup>78</sup> except that a series of  $\pi$  pulses follow the original Hahn-echo block, and serve to refocus the magnetization. CPMG sequences have also been used to enhance S/N in inhomogeneously broadened patterns of spin-1/2<sup>79</sup> and quadrupolar nuclides,<sup>80</sup> by acquiring multiple FIDs as permitted by the  $T_2$  or effective  $T_2$  ( $T_2^{\text{eff}}$ ) relaxation times. These are generally much larger than the  $T_2^*$ , which is instrument dependent in the case of solution NMR or related to the inhomogeneous broadening in the case of SSNMR.

Signal is acquired in between each pair of refocusing pulses; therefore, multiple echoes are acquired in a single scan, thereby increasing the S/N in comparison to a standard Hahn-echo experiment. The echo train of the FID can be Fourier transformed to produce a series of spikelets whose manifold is representative of the lineshape of a classic powder pattern. The spikelet spacing (in Hz) is inversely proportional to the distance between echoes and the signal is localized under the spikelets, thus increasing S/N.<sup>81,80</sup>

FIDs containing trains of spin echoes can also be processed by shifting and co-adding the echoes, followed by subsequent FT, which yields a pattern free of spikelets and with resolution dependent upon the experimental dwell time; this is known as echo co-addition.<sup>82</sup>

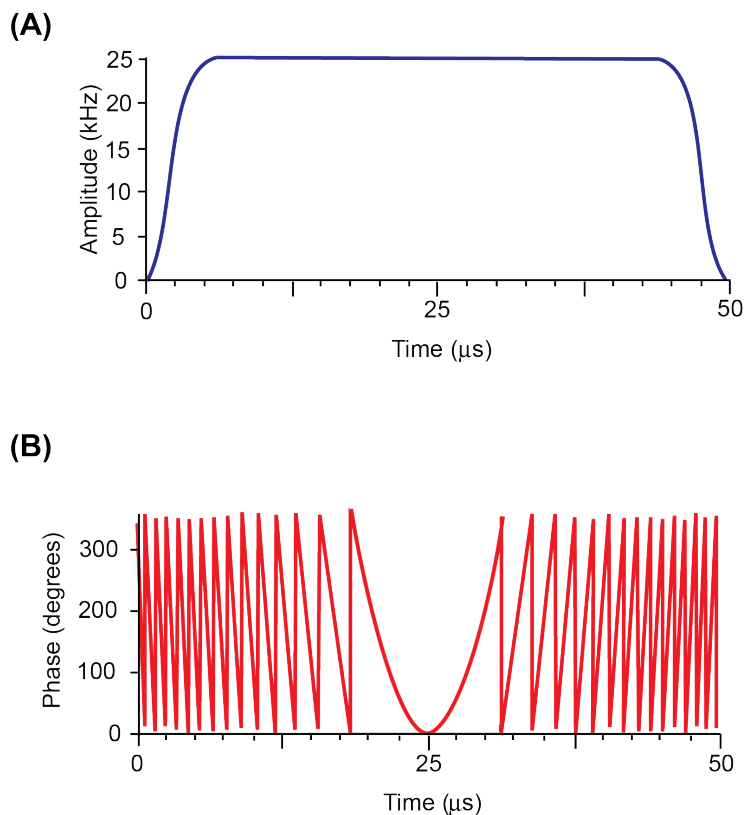


**Figure 1.15** : The (A) amplitude and (B) phase profiles of the WURST pulse.

#### 1.4.5 Wideband Uniform-Rate Smooth-Truncation (WURST)-CPMG

It is difficult to produce high-power rectangular pulses capable of achieving excitation bandwidths in excess of 250 kHz. In addition, the use of multiple high-power pulses in a CPMG-style acquisition, or long pulses in a CP experiment, can result in significant stress on the NMR probe. Bhattacharya and Frydman proposed using wideband uniform-rate smooth truncation WURST pulses,<sup>83</sup> which were originally developed by Kupče and Freeman, for the excitation of CT SSNMR powder patterns of

half-integer quadrupolar nuclides.<sup>84</sup> These pulses employ a quadratic phase modulation and gradually rounded amplitude profiles (**Figure 1.15**), and much lower rf fields than rectangular pulses. O'Dell *et al.* utilized WURST pulses in the context of a CPMG-style acquisition (WURST-CPMG).<sup>85-87</sup> This pulse sequence utilizes two identical WURST pulses, the first for broadband excitation and the subsequent pulses for broadband refocusing of magnetization. The use of the pulse sequence results in broad excitation bandwidths and substantial increases in S/N, and this technique is now routinely used for the acquisition of UWNMR spectra, since WURST pulses excite large bandwidths while using relatively low rf fields.

The number of echoes that can be acquired in a CPMG-style acquisition is dependent on the  $T_2$ . It was demonstrated that the use of high-power decoupling greatly increases the number of echoes that can be acquired, and therefore, the S/N of the resulting spectrum. The systems studies in **Chapter 6** do not have protons, and therefore, there is no source of efficient relaxation, resulting in the acquisition of numerous echoes. For example, using the WURST-CPMG pulse sequence, it was possible to acquire a high S/N  $^{35}\text{Cl}$  SSNMR spectrum with a breadth of  $\sim 650$  kHz in just 32 s (*vide infra*).

#### 1.4.6 Frequency-Stepped Acquisition

Despite the broadband excitation afforded by the use of WURST pulses, it is not possible to uniformly excite the entire breadth of ultra-wideline (UW) SSNMR patterns (*cf.* **Chapter 6**), and therefore, specialized techniques are required in order to acquire the powder patterns in their entirety. A method to overcome this challenge is to acquire a series of sub-spectra at evenly spaced transmitter frequencies followed by Fourier transformation and co-addition of the sub-spectra.<sup>88-90</sup> This method (known as the

variable offset cumulative spectrum, VOCS technique) allows for the acquisition of sub-spectra in large frequency increments and affords an increase in S/N (**Figure 1.16**).

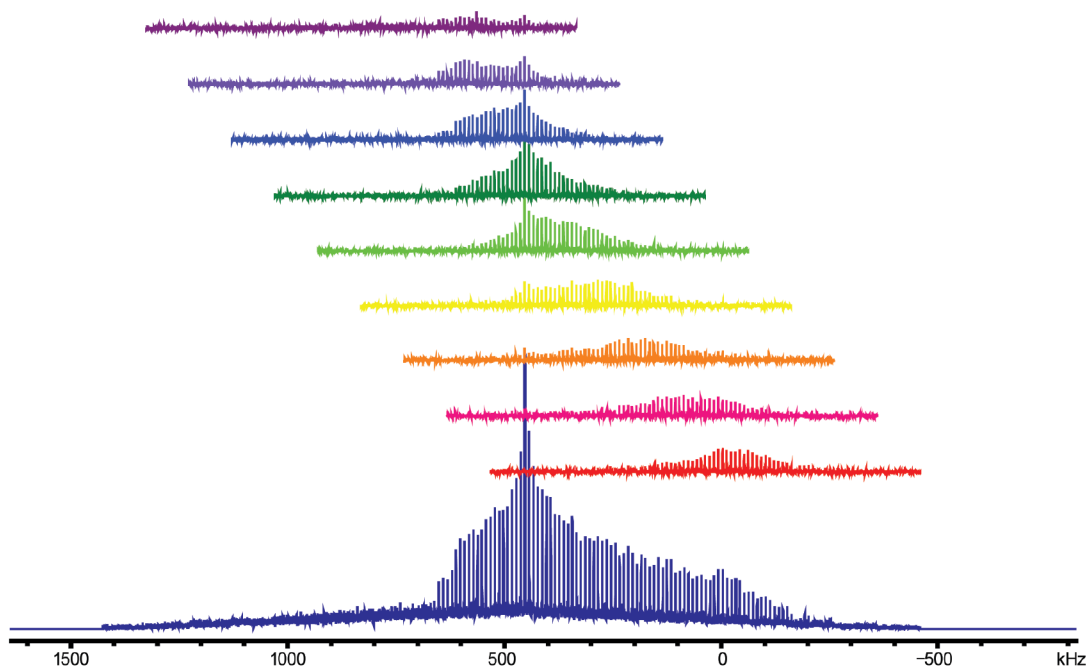


**Figure 1.16:** The acquisition of a  $^{35}\text{Cl}$  SSNMR spectrum using the variable offset cumulative spectra (VOCS) technique. WURST-CPMG spectra were acquired with 100 kHz increments of the transmitter frequency.

## 1.5 Density Function Theory Calculations

The assignment of NMR powder patterns to individual chemical environments in a molecule or material can often be challenging, especially in the case of multiple overlapping patterns. Additionally, knowledge of the orientation of the NMR interaction tensors with respect to the crystallite or molecular frames is essential in studies of molecular-level motions or chemical exchange, since the appropriate Euler angles ( $\alpha$ ,  $\beta$ ,  $\gamma$ ) are required to properly describe motional models. Often, tensor orientations can be inferred from the symmetry of the molecule; however, their exact determination is only possible through single-crystal NMR experiments. The use of quantum chemical

calculations allows for the predictions of NMR tensors (*i.e.*, their orientations and magnitudes), thus facilitating the assignment of NMR spectra and the establishment of motional models.

In this dissertation, density functional theory (DFT) calculations are performed using two software packages: Amsterdam Density Function (ADF)<sup>91</sup> and CASTEP.<sup>92-94</sup> In **Chapter 5**, calculations using ADF are performed on isolated molecules to predict the tensor orientations and assist in the determination of motional models. CASTEP calculations exploit the symmetry and periodicity of the extended solid system and are used in **Chapter 6** to aid in the assignment of <sup>35</sup>Cl SSNMR spectra. A full description of DFT in the context of molecular orbital (MO) theory and plane-wave orbitals is beyond the scope of this thesis; the reader is referred to a series of landmark papers and reviews.<sup>95-102</sup>

## 1.6 Context of Research

The NMR interactions discussed above are very sensitive to the chemical environments of the different nuclides, and as such, provide detailed structural information that cannot be obtained from any other spectroscopic method. Dynamical processes also influence the appearance of SSNMR spectra, and therefore, SSNMR is an ideal technique to study motions over a wide range of rates. The work in this dissertation makes use of SSNMR to provide information on the structure and formation of porous materials, to determine the motions occurring in simple molecular machines, and to provide a preliminary glimpse of the use of UWNMR to probe molecules on the surfaces of porous materials.



### 1.6.1 Into the Void(s)

The synthesis, development, and application of porous materials represents a burgeoning area in the fields of chemistry and materials science. A porous material is a three-dimensional solid consisting of a framework “skeleton” and large pores with well-defined volumes and surface areas. The high degree of functionalization, modularity, and selectivity of porous materials has allowed chemists to synthesize materials with finely-tuned pore sizes, geometries, and chemistries. This intimate control of the pore architecture has led to many potential applications for porous materials.<sup>103</sup> Perhaps the most widely exploited application is for molecular sieving<sup>104</sup> – the pores of the framework can allow for the separation of a mixture of molecules based on their size and chemistries (this has been especially useful for the drying of solvents and petroleum extracts). With increasing global concern about climate change and related environment hazards, porous materials are being designed for the purpose of gas absorption and storage.<sup>105</sup> Systems have been devised that can selectively contain carbon dioxide, showing promise for carbon sequestration from the atmosphere.<sup>106</sup> Furthermore, porous materials have shown potential for hydrogen fuel cells, as they may provide a safe, reliable means to store and transport large amounts of pressurized hydrogen gas. Another application of porous materials is in the field of catalysis<sup>107</sup> – the pores can provide a confined space, which can facilitate a reaction, and/or metals or functional groups on the framework structure can serve as catalytic active sites.

Metal-organic frameworks<sup>108</sup> (MOFs) are composed of metal or metal-cluster nodes that are joined together by organic ligands. There exist a wide variety of organic ligands, which are capable of coordinating several different metals, leading to an endless

cornucopia of possible MOF structures. Zeolitic Imidazolate Frameworks<sup>109</sup> (ZIFs) are a subclass of MOFs that use divalent metal nodes (*e.g.*, Zn<sup>2+</sup>, Cd<sup>2+</sup>, Co<sup>2+</sup>) and imidazole (Im) derivatives as the organic linkers; the Im-M-Im bond angle is analogous to the Si-O-Si bond angles found in zeolites, and therefore, these two classes have systems with very similar topologies.

Despite the great interest in MOFs and ZIFs, little research has been done into the development of new synthetic methodologies for their preparation. ZIFs are traditionally made using solvothermal synthetic techniques; however, these techniques are not desirable, as they use large amounts of solvent, require high energy inputs, and often involve toxic starting materials. The commercialization and anticipated increase in the industrial applications of MOFs and ZIFs necessitate the development of greener, more cost-effective synthetic techniques.<sup>110</sup> In addition, the development of new synthetic strategies should present the opportunity to generate new solid phases not accessible by traditional synthetic techniques, and an understanding of the mechanisms of the formation of MOFs will lead to the rational design of frameworks with specific topologies and functions.

SSNMR has been extensively applied to the study of MOFs and ZIFs.<sup>111,112</sup> As the organic linkers used in the synthesis of MOFs and ZIFs have many commonly-investigated NMR-active nuclides (*e.g.*, <sup>1</sup>H, <sup>13</sup>C, <sup>15</sup>N), SSNMR has been used to probe their framework structures and provide information on connectivities and bond lengths.<sup>113–120</sup> Characterization of the metal ions in secondary building units (SBUs) via SSNMR is more challenging, as the metals often have NMR-active nuclides that are classified as *unreceptive* (*i.e.*, low natural abundance, low gyromagnetic ratio, large

quadrupole moments, or a combinations of these factors), and therefore, only a few such studies exist in the literature.<sup>121–125</sup> Perhaps the most ubiquitous use of SSNMR is to observe the dynamics of guest molecules within the pores of the host frameworks.<sup>126–133</sup> The most promising applications of MOFs and ZIFs are for gas storage and separation; therefore, an intimate understanding of the locations, dynamics, and adsorption strengths of gas molecules within their pores is crucial for the design of materials with finely tuned properties for these specific applications. SSNMR is one of the only methods available for probing the rates and modes of motion of guest molecules; in particular, the wide range of motional rates that can be accessed surpass every other analytical technique. Despite the utility of SSNMR for the investigation of MOFs and ZIFs, there are only a few reports of the application of NMR-assisted crystallography for their structural elucidation.<sup>134,135</sup>

In **Chapters 2 and 3**, two solid-state synthetic approaches, *accelerated aging* and *mechanochemical synthesis*, are used to synthesize ZIFs. In **Chapter 2**, the structure of a new Cd imidazolate framework (CdIF) is determined using NMR-assisted crystallography. In **Chapter 3**, the formation of CdIF is monitored using a combination of SSNMR and PXRD. The detailed, molecular-level structural information afforded by the SSNMR experiments allows for the identification of intermediates and a reaction pathway is proposed. In **Chapter 6**, <sup>35</sup>Cl SSNMR is used to determine the structure of a transition-metal catalyst that is grafted onto a porous support material.

### **1.6.2 “There’s plenty of room at the bottom”**

In his seminal lecture delivered in 1959, Richard Feynman laid the foundation for the development of nanotechnology. One of the key principles he outlined was that of

molecular machines – tiny devices capable of performing work at the atomic level. In 2016 (nearly 60 years later), the Nobel Prize in Chemistry was awarded to J.P. Sauvage, J.F. Stoddard, and B.L. Feringa for the design and synthesis of molecular machines (*i.e.*, molecular switches and motors).<sup>136–139</sup> Molecular machines have been shown to undergo a variety of different motions in solution;<sup>140</sup> however, it can be envisioned that these devices could undergo spatially coherent motion if they were incorporated into solid-state materials. An intimate understanding of the dynamics exhibited by such devices is essential for the design of materials with finely-tuned motions and applications. As discussed above, SSNMR spectra are sensitive to a variety of different motions over a wide dynamical range, and as such, it is the premier technique for studying dynamics in the solid state. The simulation of SSNMR spectra acquired at different temperatures allows for the development of models that describe the dynamics of the rotators and the determination of the rates of their motions.

In **Chapter 4**, <sup>2</sup>H SSNMR is used to investigate the rotational dynamics of crown ether molecules that have been incorporated into the framework structures of MOFs. The factors that affect the dynamics of these simple molecular machines are investigated. In **Chapter 5**, the dynamics of inorganic molecular rotors are determined using SSNMR. These studies demonstrate that SSNMR, and in particular <sup>2</sup>H SSNMR, is an ideal technique for providing detailed information on dynamics and an intermediate understanding of the factors that govern motion at the molecular level.

## 1.7 References

- (1) Purcell, E.; Torrey, H.; Pound, R. *Phys. Rev.* **1946**, *69*, 37–38.
- (2) Bloch, F.; Hansen, W. W.; Packard, M. *Phys. Rev.* **1946**, *70*, 474–485.
- (3) Bryant, R. G. *J. Chem. Educ.* **1983**, *60*, 933.
- (4) Schmidt-Rohr, K.; Spiess, H. W. *Multidimensional Solid-State NMR and Polymers*; Academic Press: London, UK, 1994.
- (5) Steigel, A.; Spiess, H. W. In *NMR Basic Principles and Progress*; Springer-Verlag: Berlin, 1978.
- (6) Jonas, J.; Gutowsky, H. S. *Ann. Rev. Phys. Chem.* **1980**, *31*, 1–27.
- (7) Lesage, A. *Phys. Chem. Chem. Phys.* **2009**, *11*, 6875.
- (8) Ashbrook, S. E. *Phys. Chem. Chem. Phys.* **2009**, *11*, 6892–6905.
- (9) Schurko, R. W. *Acc. Chem. Res.* **2013**, *46*, 1985–1995.
- (10) Mehring, M. *Principles of High Resolution NMR in Solids*; Springer-Verlag: Berlin Heidelberg, 1983.
- (11) J Duer, M. *Solid-State NMR spectroscopy: Principles and Applications*; Blackwell: Oxford, UK, 2002.
- (12) Levitt, M. H. John Wiley and Sons: Chichester, UK 2006.
- (13) Keeler, J. *Understanding NMR Spectroscopy*; John Wiley and Sons: Chichester, UK, 2010.
- (14) Duer, M. J. *Introduction to Solid-State NMR Spectroscopy*; Blackwell: Oxford, 2004.
- (15) Ramsey, N. F. *Phys. Rev.* **1950**, *78*, 699–703.
- (16) Ramsey, N. F. *Phys. Rev.* **1952**, *86*, 243–246.

- (17) Pople, J. A. *Proc. R. Soc. A Math. Phys. Eng. Sci.* **1957**, 239, 541–549.
- (18) Pople, J. A. *Proc. R. Soc. A Math. Phys. Eng. Sci.* **1957**, 239, 550–556.
- (19) Widdifield, C. M.; Schurko, R. W. *Concepts Magn. Reson. Part A* **2009**, 91–123.
- (20) Anet, F. A. L.; O’Leary, D. J. *Concepts Magn. Reson.* **1991**, 3, 193–214.
- (21) Harris, R. K.; Becker, E. D.; De Cabral Menezes, S. M.; Granger, P.; Hoffman, R. E.; Zilm, K. W. *Pure Appl. Chem.* **2008**, 80, 59–84.
- (22) Herzfeld, J.; Berger, A. E. *J. Chem. Phys.* **1980**, 73, 6021–6030.
- (23) Lucken, E. A. C. *Nuclear Quadrupole Coupling Constants*; Academic Press: London, 1969.
- (24) Akitt, J. W.; McDonald, W. S. *J. Magn. Reson.* **1984**, 58, 401–412.
- (25) Das, T. P. *Nuclear Quadrupole Resonance Spectroscopy*; Academic Press: New York, 1958.
- (26) Weiss, A. *Nuclear Quadrupole Resonance*; Springer-Verlag: Berlin, 1972.
- (27) Kentgens, A. P. M. *Geoderma* **1997**, 80, 271–306.
- (28) Koller, H.; Engelhardt, G.; Kentgens, A. P. M.; Sauer, J. *J. Phys. Chem.* **1994**, 98, 1544–1551.
- (29) Hamaed, H.; Pawlowski, J. M.; Cooper, B. F. T.; Fu, R.; Eichhorn, S. H.; Schurko, R. W. *J. Am. Chem. Soc.* **2008**, 130, 11056–11065.
- (30) Namespetra, A. M.; Hirsh, D. A.; Hildebrand, M. P.; Sandre, A. R.; Hamaed, H.; Rawson, J. M.; Schurko, R. W. *CrystEngComm* **2016**, 18, 6213–6232.
- (31) Hirsh, D. A.; Rossini, A. J.; Emsley, L.; Schurko, R. W. *Phys. Chem. Chem. Phys.* **2016**, 18, 25893–25904.
- (32) Rossini, A. J.; Mills, R. W.; Briscoe, G. A.; Norton, E. L.; Geier, S. J.; Hung, I.;

- Zheng, S.; Autschbach, J.; Schurko, R. W. *J. Am. Chem. Soc.* **2009**, *131*, 3317–3330.
- (33) Chapman, R. P.; Bryce, D. L. *Phys. Chem. Chem. Phys.* **2009**, *11*, 6987–6998.
- (34) Johnston, K. E.; O’Keefe, C. A.; Gauvin, R. M.; Trébosc, J.; Delevoye, L.; Amoureux, J.-P.; Popoff, N.; Taoufik, M.; Oudatchin, K.; Schurko, R. W. *Chem. Eur. J.* **2013**, *19*, 12396–12414.
- (35) O’Keefe, C. A.; Johnston, K. E.; Sutter, K.; Autschbach, J.; Gauvin, R.; Trébosc, J.; Delevoye, L.; Popoff, N.; Taoufik, M.; Oudatchin, K.; Schurko, R. W. *Inorg. Chem.* **2014**, *53*, 9581–9597.
- (36) Perras, F. A.; Bryce, D. L. *Angew. Chem. Int. Ed.* **2012**, *51*, 4227–4230.
- (37) Ashbrook, S. E.; Duer, M. J. *Concepts Magn. Reson.* **2006**, *28A*, 183–248.
- (38) Wasylishen, R. E.; Ashbrook, S. E.; Wimperis, S. *NMR of Quadrupolar Nuclei in Solid Materials*; John Wiley and Sons: Chichester, UK, 2012.
- (39) Power, W. P.; Wasylishen, R. E.; Mooibroek, S.; Pettitt, B. A.; Danchura, W. J. *Phys. Chem.* **1990**, *94*, 591–598.
- (40) Chandrakumar, N. *Spin-1 NMR*; Springer: Berlin, 1996.
- (41) Pake, G. E. *J. Chem. Phys.* **1948**, *16*, 327–336.
- (42) Griffin, R. G. *Nat. Struct. Biol.* **1998**, *5 Suppl*, 508–512.
- (43) Laws, D. D.; Bitter, H. M. L.; Jerschow, A. *Angew. Chem. Int. Ed.* **2002**, *41*, 3096–3129.
- (44) Hong, M.; Griffin, R. G. *J. Am. Chem. Soc.* **1998**, *120*, 7113–7114.
- (45) Jameson, C. J.; Mason, J. In *Multinuclear NMR*; Plenum Press: New York; p 51.
- (46) Buchanan, G. W.; Morat, C.; Charland, J. P.; Ratcliffe, C. I.; Ripmeester, J. A.

- Can. J. Chem.* **1989**, *67*, 1212–1218.
- (47) Ratcliffe, C. I.; Ripmeester, J. A.; Buchanan, G. W.; Denikes, J. K. *J. Am. Chem. Soc.* **1992**, *114*, 3294–3299.
- (48) Buchanan, G. W.; Moghimi, A.; Ratcliffe, C. I. *Can. J. Chem.* **1996**, *74*, 1437–1446.
- (49) Böhmer, R.; Jeffrey, K. R.; Vogel, M. *Prog. Nucl. Magn. Reson. Spectrosc.* **2007**, *50*, 87–174.
- (50) Van Der Ven, A.; Bhattacharya, J.; Belak, A. A. *Acc. Chem. Res.* **2013**, *46*, 1216–1225.
- (51) Vukotic, V. N.; Harris, K. J.; Zhu, K.; Schurko, R. W.; Loeb, S. J. *Nat. Chem.* **2012**, *4*, 456–460.
- (52) Zhu, K.; O’Keefe, C. a; Vukotic, V. N.; Schurko, R. W.; Loeb, S. J. *Nat. Chem.* **2015**, *7*, 514–519.
- (53) Brown, S. P.; Spiess, H. W. *Chem. Rev.* **2001**, *101*, 4125–4155.
- (54) Bain, A. D. *Prog. Nucl. Magn. Reson. Spectrosc.* **2003**, *43*, 63–103.
- (55) Edén, M. *Concepts Magn. Reson. Part A Bridg. Educ. Res.* **2003**, *18A*, 24–55.
- (56) Andrew, E. R.; Bradbury, A.; Eades, R. G. *Nature* **1958**, *182*, 1695.
- (57) Andrew, E. R. *Philos. Trans. A* **1981**, *299*, 505.
- (58) Kundla, E.; Samoson, A.; Lippmaa, E. *Chem. Phys. Lett.* **1981**, *83*, 229–232.
- (59) Samoson, A.; Kundla, E.; Lippmaa, E. *J. Magn. Reson.* **1982**, *49*, 350.
- (60) Samoson, A.; Lippmaa, E. *Phys. Rev. B* **1983**, *28*, 6567–6570.
- (61) Frydman, L.; Harwood, J. S. *J. Am. Chem. Soc.* **1995**, *117*, 5367–5368.
- (62) A. Medek; J.S. Harwood; L. Frydman. *J. Am. Chem. Soc.* **1995**, *117*, 12779–



12787.

- (63) Rocha, J.; Morais, C. M.; Fernandez, C. 2005; pp 141–194.
- (64) ASHBROOK, S. *Prog. Nucl. Magn. Reson. Spectrosc.* **2004**, *45*, 53–108.
- (65) Marinelli, L.; Frydman, L. *Chem. Phys. Lett.* **1997**, *275*, 188–198.
- (66) Schurko, R. W. In *Encyclopedia of Magnetic Resonance*; John Wiley and Sons, 2012; pp 77–94.
- (67) Lupulescu, A.; Kotecha, M.; Frydman, L. *J. Am. Chem. Soc.* **2003**, *125*, 3376–3383.
- (68) Jaroszewicz, M. J.; Frydman, L.; Schurko, R. W. *J. Phys. Chem. A* **2017**, *121*, 51–65.
- (69) Hartmann, S. R.; Hahn, E. L. *Phys. Rev.* **1962**, *128*, 2042–2053.
- (70) Pines, A.; Gibby, M. G.; Waugh, J. S. *Chem. Phys. Lett.* **1972**, *15*, 373–376.
- (71) Pines, A.; Gibby, M. G.; Waugh, J. S. *J. Chem. Phys.* **1973**, *59*, 569–590.
- (72) Yannoni, C. S. *Acc. Chem. Res.* **1982**, *15*, 201–208.
- (73) Stejsal, E. O.; Schaefer, J.; Waugh, J. S. *J. Magn. Reson.* **1977**, *28*, 105.
- (74) Weisman, I. D.; Bennett, L. H. *Phys. Rev.* **1969**, *181*, 1341–1350.
- (75) Davis, J. H.; Jeffrey, K. R.; Bloom, M.; Valic, M. I.; Higgs, T. P. *Chem. Phys. Lett.* **1976**, *42*, 390–394.
- (76) Carr, H. Y.; Purcell, E. M. *Phys. Rev.* **1954**, *94*, 630–638.
- (77) Meiboom, S.; Gill, D. *Rev. Sci. Instrum.* **1958**, *29*, 688–691.
- (78) Hahn, E. L. *Phys. Rev.* **1950**, *80*, 580–594.
- (79) Shore, S. E.; Ansermet, J. P.; Slichter, C. P.; Sinfelt, J. H. *Phys. Rev. Lett.* **1987**, *58*, 953.

- (80) Larsen, F. H.; Jakobsen, H. J.; Ellis, P. D. *J. Phys. Chem. A* **1997**, *101*, 8597–8606.
- (81) Hung, I.; Schurko, R. W. *J. Phys. Chem. B* **2004**, *108*, 9060–9069.
- (82) Hung, I.; Gan, Z. *J. Magn. Reson.* **2010**, *204*, 256–265.
- (83) Kupce, E.; Freeman, R. *J. Magn. Reson.* **1995**, *115*, 273–276.
- (84) Bhattacharyya, R.; Frydman, L. *J. Chem. Phys.* **2007**, *127*, 194503/1-8.
- (85) O’Dell, L. A.; Schurko, R. W. *Chem. Phys. Lett.* **2008**, *464*, 117–130.
- (86) O’Dell, L. A.; Rossini, A. J.; Schurko, R. W. *Chem. Phys. Lett.* **2009**, *468*, 330–335.
- (87) O’Dell, L. A. *Solid State Nucl. Magn. Reson.* **2013**, *55–56*, 28–41.
- (88) Massiot, D.; Farnan, I.; Gautier, N.; Trumeau, D.; Trokiner, A.; Coutures, J. P. *Solid State Nucl. Magn. Reson.* **1995**, *4*, 241–248.
- (89) Medek, A.; Frydman, V.; Frydman, L. *J. Phys. Chem. A* **1999**, *103*, 4830–4835.
- (90) Tang, J. A.; Masuda, J. D.; Boyle, T. J.; Schurko, R. W. *ChemPhysChem* **2006**, *7*, 117–130.
- (91) Baerends, E. J. Z. T.; Autschbach, J. SCM, Theoretical Chemistry, Vrije Universiteit: Amsterdam.
- (92) Clark, S. J.; Segall, M. D.; Pickard, C. J.; Hasnip, P. J.; Probert, M. I. J.; Refson, K.; Payne, M. C. *Z. Krist.* **2005**, *220*.
- (93) Profeta, M.; Mauri, F.; Pickard, C. J. *J. Am. Chem. Soc.* **2003**, *125*, 541–548.
- (94) Yates, J. R.; Pickard, C. J.; Mauri, F. *Phys. Rev. B - Condens. Matter Mater. Phys.* **2007**, *76*, 1–11.
- (95) Ditchfield, R. *Chem. Phys.* **1973**, *2*, 400–406.
- (96) Ditchfield, R. *Mol. Phys.* **1974**, *27*, 789–807.

- (97) Cheeseman, J. R.; Trucks, G. W.; Keith, T. A.; Frisch, M. J. *J. Chem. Phys.* **1996**, *104*, 5497–5509.
- (98) Schreckenbach, G.; Ziegler, T. *J. Phys. Chem.* **1995**, *99*, 606–611.
- (99) Schreckenbach, G.; Ziegler, T. *Theor. Chem. Accounts Theory, Comput. Model. (Theoretica Chim. Acta)* **1998**, *99*, 71–82.
- (100) Pickard, C.; Mauri, F. *Phys. Rev. B Condens. Matter Mater. Phys.* **2001**, *63*, 245101/1-13.
- (101) Profeta, M.; Benoit, M.; Mauri, F.; Pickard, C. J. *J. Am. Chem. Soc.* **2004**, *126*, 12628–12635.
- (102) Bonhomme, C.; Gervais, C.; Babonneau, F.; Coelho, C.; Pourpoint, F.; Azaïs, T.; Ashbrook, S. E.; Griffin, J. M.; Yates, J. R.; Mauri, F.; Pickard, C. J. *Chem. Rev.* **2012**, *112*, 5733–5779.
- (103) Slater, A. G.; Cooper, A. I. *Science* **2015**, *348*, 988.
- (104) Lin, C. C. H.; Dambrowitz, K. A.; Kuznicki, S. M. *Can. J. Chem. Eng.* **2012**, *90*, 207–216.
- (105) Li, J.-R.; Kuppler, R. J.; Zhou, H.-C. *Chem. Soc. Rev.* **2009**, *38*, 1477.
- (106) Britt, D.; Furukawa, H.; Wang, B.; Glover, T. G.; Yaghi, O. M. *Proc. Natl. Acad. Sci. U. S. A.* **2009**, *106*, 20637–20640.
- (107) Perego, C.; Millini, R. *Chem. Soc. Rev.* **2013**, *42*, 3956–3976.
- (108) Kitagawa, S.; Kitaura, R.; Noro, S. *Angew. Chem. Int. Ed.* **2004**, *43*, 2334–2375.
- (109) Phan, A.; Doonan, C. J.; Uribe-Romo, F. J.; Knobler, C. B.; O’Keeffe, M.; Yaghi, O. M. *Acc. Chem. Res.* **2010**, *43*, 58–67.
- (110) Czaja, A. U.; Trukhan, N.; Müller, U. *Chem. Soc. Rev.* **2009**, *38*, 1284.

- (111) Sutrisno, A.; Huang, Y. *Solid State Nucl. Magn. Reson.* **2013**, *49–50*, 1–11.
- (112) Hoffmann, H. C.; Debowski, M.; Müller, P.; Paasch, S.; Senkovska, I.; Kaskel, S.; Brunner, E. *Materials (Basel)*. **2012**, *5*, 2537–2572.
- (113) Lawrence, M. C.; Schneider, C.; Katz, M. J. *Chem. Commun.* **2016**, *52*, 4971–4974.
- (114) Loiseau, T.; Serre, C.; Huguenard, C.; Fink, G.; Taulelle, F.; Henry, M.; Bataille, T.; Férey, G. *Chemistry* **2004**, *10*, 1373–1382.
- (115) Devautour-Vinot, S.; Maurin, G.; Serre, C.; Horcajada, P.; Paula Da Cunha, D.; Guillerm, V.; De Souza Costa, E.; Taulelle, F.; Martineau, C. *Chem. Mater.* **2012**, *24*, 2168–2177.
- (116) Haouas, M.; Volkringer, C.; Loiseau, T.; Férey, G.; Taulelle, F. *J. Phys. Chem. C* **2011**, *115*, 17934–17944.
- (117) Volkringer, C.; Loiseau, T.; Guillou, N.; Férey, G.; Haouas, M.; Taulelle, F.; Elkaim, E.; Stock, N. *Inorg. Chem.* **2010**, *49*, 9852–9862.
- (118) Morris, W.; Taylor, R. E.; Dybowski, C.; Yaghi, O. M.; Garcia-Garibay, M. A. *J. Mol. Struct.* **2011**, *1004*, 94–101.
- (119) Morris, W.; Stevens, C. J.; Taylor, R. E.; Dybowski, C.; Yaghi, O. M.; Garcia-Garibay, M. A. *J. Phys. Chem. C* **2012**, *116*, 13307–13312.
- (120) Rossini, A. J.; Zagdoun, A.; Lelli, M.; Canivet, J.; Aguado, S.; Ouari, O.; Tordo, P.; Rosay, M.; Maas, W. E.; Copéret, C.; Farrusseng, D.; Emsley, L.; Lesage, A. *Angew. Chem. Int. Ed.* **2012**, *51*, 123–127.
- (121) Sutrisno, A.; Terskikh, V. V.; Shi, Q.; Song, Z.; Dong, J.; Ding, S. Y.; Wang, W.; Provost, B. R.; Daff, T. D.; Woo, T. K.; Huang, Y. *Chem. Eur. J.* **2012**, *18*, 12251–

12259.

- (122) Volkringer, C.; Loiseau, T.; Férey, G.; Morais, C. M.; Taulelle, F.; Montouillout, V.; Massiot, D. *Microporous Mesoporous Mater.* **2007**, *105*, 111–117.
- (123) Mowat, J. P. S.; Miller, S. R.; Slawin, A. M. Z.; Seymour, V. R.; Ashbrook, S. E.; Wright, P. A. *Microporous Mesoporous Mater.* **2011**, *142*, 322–333.
- (124) Jiang, Y.; Huang, J.; Marx, S.; Kleist, W.; Hunger, M.; Baiker, A. *J. Phys. Chem. Lett.* **2010**, *1*, 2886–2890.
- (125) He, P.; Lucier, B. E. G.; Terskikh, V. V.; Shi, Q.; Dong, J.; Chu, Y.; Zheng, A.; Sutrisno, A.; Huang, Y. *J. Phys. Chem. C* **2014**, *118*, 23728–23744.
- (126) Wang, W.; Waang, W. D.; Lucier, B. E. G.; Terskikh, V. V.; Huang, Y. *J. Phys. Chem. Lett.* **2014**, *5*, 3360–3365.
- (127) Stallmach, F.; Gröger, S.; Künzel, V.; Kärger, J.; Yaghi, O. M.; Hesse, M.; Müller, U. *Angew. Chem. Int. Ed.* **2006**, *45*, 2123–2126.
- (128) Kong, X.; Scott, E.; Ding, W.; Mason, J. A.; Long, J. R.; Reimer, J. A. *J. Am. Chem. Soc.* **2012**, *134*, 14341–14344.
- (129) Lucier, B. E. G.; Zhang, Y.; Lee, K. J.; Lu, Y.; Huang, Y. *Chem. Commun.* **2016**, *52*, 7541–7544.
- (130) Li, J.; Li, S.; Zheng, A.; Liu, X.; Yu, N.; Deng, F. *J. Phys. Chem. C* **2017**, *121*, 14261–14268.
- (131) Xu, J.; Sinelnikov, R.; Huang, Y. *Langmuir* **2016**, *32*, 5468–5479.
- (132) Lucier, B. E. G.; Chan, H.; Zhang, Y.; Huang, Y. *Eur. J. Inorg. Chem.* **2016**, *2016*, 2017–2024.
- (133) Gul-E-Noor, F.; Mendt, M.; Michel, D.; Pöppel, A.; Krautscheid, H.; Haase, J.;

- Bertmer, M. J. *Phys. Chem. C* **2013**, *117*, 7703–7712.
- (134) Kobera, L.; Rohlicek, J.; Czernek, J.; Abbrent, S.; Streckova, M.; Sopcak, T.; Brus, J. *ChemPhysChem* **2017**, 1–8.
- (135) Taulelle, F.; Bouchevreau, B.; Martineau, C. *CrystEngComm* **2013**, *15*, 8613.
- (136) Stoddart, J. F. *Chem. Soc. Rev.* **2009**, *38*, 1802.
- (137) Coskun, A.; Banaszak, M.; Astumian, R. D.; Stoddart, J. F.; Grzybowski, B. A. *Chem. Soc. Rev.* **2012**, *41*, 19–30.
- (138) Browne, W. R.; Feringa, B. L. *Nat. Nanotechnol.* **2006**, *1*, 25–35.
- (139) Rapenne, G.; Joachim, C. *Top. Curr. Chem.* **2014**, *354*, 253–278.
- (140) Abendroth, J. M.; Bushuyev, O. S.; Weiss, P. S.; Barrett, C. J. *ACS Nano* **2015**, *9*, 7746–7768.

## Chapter 2: NMR-Assisted Powder X-Ray Diffraction for the Structural Characterization of a Zeolitic Imidazolate Framework Synthesized via Accelerated Aging Reactions

### 2.1 Overview

A new Cd-containing zeolitic imidazolate framework (**1**) was synthesized using accelerated aging reactions. Powder X-ray diffraction (PXRD) analysis of the products of the aging reaction show reflections corresponding to **1**, as well as characteristic reflections of the cadmium oxide (CdO) starting materials. By varying relative amounts of the CdO and 2-methylimidazole (**HMeIm**) starting materials, it was determined that the Cd:**MeIm** ratio in **1** is 1:3 as opposed to the typical 1:2 ratio expected for a ZIF. Multinuclear solid-state NMR (SSNMR) experiments were conducted on **1** to determine the nature of the Cd coordination environments, which in turn aids with the refinement of the molecular-level structure from the available PXRD data.  $^{111}\text{Cd}$  SSNMR spectra of **1** reveal that the Cd atoms in four-coordinate environments and multinuclear SSNMR (*i.e.*,  $^1\text{H}$ ,  $^{13}\text{C}$ ,  $^{14}\text{N}$ ,) experiments demonstrate that there is unbound HMeIm in this system. Refinement of the structure using this data determined that **1** is an open framework with a distorted diamondoid topology and unbound **HMeIm** within the pores of the framework.

### 2.2 Introduction

The design and synthesis of metal-organic frameworks (MOFs) represents an area of intense research within the field of materials chemistry.<sup>1-3</sup> The large void spaces present in these materials has led to their potential applications for gas storage and

separation,<sup>4,5</sup> catalysis,<sup>6,7</sup> and molecular sensing.<sup>8,9</sup> Furthermore, the wide array of available ligands and secondary building units (SBUs, *e.g.*, metal nodes, paddlewheels, and clusters)<sup>10</sup> allows for the synthesis of materials with varying topologies and finely tuned chemical and physical properties.

Zeolitic imidazolate frameworks (ZIFs) are a subclass of MOFs composed of divalent metal centres ( $M^{2+}$ , *e.g.*,  $Zn^{2+}$ ,  $Co^{2+}$ ,  $Cd^{2+}$ , etc.) that are connected together by imidazolate-derivative ligands ( $RIm^-$ ).<sup>11,12</sup> They are termed “zeolitic” because the  $M^{2+}-RIm^-$  bond angles are similar to the Si–O–Si bond angles found in zeolites, resulting in ZIFs having a high degree of topological diversity comparable to that of zeolites. ZIFs have attracted a lot of interest due to their high thermal and chemical stabilities, and have found uses for gas separation<sup>13</sup> and molecular sieving.<sup>14</sup> While  $Zn^{2+}$  is the most ubiquitous metal node employed in the synthesis of ZIFs, Cd-containing ZIFs (so-called CdIFs) have also been reported in literature.<sup>15,16</sup> The longer  $Cd^{2+}-N$  bond lengths can yield materials with larger void spaces, thereby allowing for the synthesis of frameworks with topologies not possible for analogous  $Zn^{2+}$ -containing systems.

Despite the great interest in MOFs and ZIFs, little research has been done into the development of new synthetic methodologies for their preparation. ZIFs are traditionally made using solvothermal synthetic techniques; however, these techniques are not desirable, as they use large amounts of solvent, require high energy inputs, and often involve toxic starting materials. The commercialization and anticipated increase in the industrial applications of MOFs and ZIFs necessitate the development of greener, more cost-effective synthetic techniques.<sup>17</sup> In addition, the development of new synthetic strategies should present the opportunity to generate new solid phases not accessible by



traditional synthetic techniques, and an understanding of the mechanisms of the formation of MOFs will lead to the rational design of frameworks with specific topologies and functions.

*Accelerated aging reactions*<sup>18–20</sup> are newly-introduced solid-state synthetic techniques that imitate the spontaneous formation of minerals in nature.<sup>21,22</sup> These reactions use no solvent, low energy inputs, and non-toxic starting materials; furthermore, they can afford quantitative yields, making them ideal alternatives to the traditional solvothermal synthesis of ZIFs. The general synthetic procedure for the formation of ZIFs using accelerated aging reactions is as follows: (i) a homogeneous reaction mixture of the solid starting materials (*i.e.*, a metal-oxide and the imidazole-based linker) is made, (ii) the mixture is placed inside a humidity chamber, and (iii) the aging reaction occurs at slightly elevated temperatures (*e.g.*, 45 °C), running to completion over the course of 2 to 7 days. To date, accelerated aging reactions have been used to synthesize a number of commercially relevant MOFs (*e.g.*, ZIF-8, ZIF-67, HKUST-1, and UiO-66/UiO-66-NH<sub>2</sub>) from a variety of metal-oxide starting materials (*e.g.*, ZnO, CdO, CuO, and ZrO, respectively).<sup>23,24</sup>

Accelerated aging reactions yield products as microcrystalline powders, precluding their characterization by single-crystal X-ray diffraction. Powder X-ray diffraction (PXRD) can be utilized to provide information on the completion of the reaction (*i.e.*, by observing the disappearance of signals from the starting materials, and even identifying impurity phases in some cases), and can also be used to identify and track the formation of a product, provided that its structure is known *a priori*. However, for the formation of new phases, the refinement of their structures from PXRD patterns is

challenging and often requires the use of complementary analytical techniques. The formation of amorphous or disordered phases further exacerbates this problem, as PXRD is of little utility for their characterization.

Solid-state NMR (SSNMR) is a powerful characterization technique, providing molecular-level information on structure and dynamics. It is also well-suited to the study of disordered and amorphous materials,<sup>25-27</sup> since it does not depend on long-range order. For crystalline samples, *NMR-assisted crystallography* combines the short-range, local structural information provided by SSNMR with the details on long-range order afforded by PXRD to elucidate the structures of materials.<sup>28-32</sup> In particular, the use of multinuclear SSNMR provides a high degree of specificity regarding the numbers and types of chemical environments, and can therefore greatly assist in the refinement of structures from PXRD data.

SSNMR has been extensively applied to the study of MOFs and ZIFs.<sup>33,34</sup> As the organic linkers used in the synthesis of MOFs and ZIFs have many commonly-investigated NMR-active nuclides (*e.g.*, <sup>1</sup>H, <sup>13</sup>C, <sup>15</sup>N), SSNMR has been used to probe their framework structures and provide information on connectivities and bond lengths.<sup>35-42</sup> Characterization of the metal ions in SBUs via SSNMR is more challenging as they often contain elements with NMR-active nuclides that are classified as *unreceptive* (*i.e.*, low natural abundance, low gyromagnetic ratio, large quadrupole moments, or a combinations of these factors) and therefore, only a few such studies exist in the literature.<sup>43-47</sup> Perhaps the most ubiquitous use of SSNMR is to observe the dynamics of guest molecules within the pores of the host frameworks.<sup>48-55</sup> The most promising applications of MOFs and ZIFs are for gas storage and separation; therefore, an intimate

understanding of the locations, dynamics, and adsorption strengths of gas molecules within their pores is crucial for the design of materials with finely tuned properties for these specific applications. SSNMR is one of the only methods available for probing the rates and modes of motion of guest molecules; in particular, the wide range of motional rates that can be accessed surpass every other analytical technique. Despite the utility of SSNMR for the investigation of MOFs and ZIFs, there are only a few reports of the application of NMR-assisted crystallography for their structural elucidation.<sup>29,56</sup>

In this chapter, data obtained from a combination of PXRD and multinuclear SSNMR experiments are used to describe the formation of ZIFs produced using accelerated aging reactions. In addition, the final structure of a new CdIF (**1**) was determined by NMR-assisted crystallography, as follows: First, PXRD data was used to verify the formation of a new phase (**1**) and indicate that the Cd:HMeIm ratio in this CdIF is 1:3. Next, a series of materials with known structures were characterized using <sup>111</sup>Cd SSNMR, in order to make correlations between the Cd chemical shift (CS) tensor parameters and the Cd coordination environments (four- and six-coordinate Cd sites). <sup>111</sup>Cd SSNMR experiments were conducted on the **1** to determine the Cd coordination environment, as informed by the Cd CS tensor data from known compounds. Then, a series of multinuclear (<sup>1</sup>H, <sup>13</sup>C, and <sup>14</sup>N) SSNMR experiments were utilized to gain information on the numbers and types of distinct chemical environments in the CdIF framework and species in the pores. Finally, all of this information was used to aid in the refinement of the structure from PXRD data and to propose a structure for **1**.

## 2.3 Experimental Details

### 2.3.1 Reagents

Cadmium oxide (CdO), 2-methylimidazole (HMeIm), and ammonium nitrate ( $\text{NH}_4\text{NO}_3$ ) were purchased from Sigma Aldrich and used without further purification.

### 2.3.2 Accelerated Aging Reactions

The reactants were dry-milled (*i.e.*, without the use of solvent) using a Retsch MM400 ball mill to produce a homogeneous mixture. The reagents were placed in 10 mL stainless steel milling jars with two 7 mm stainless steel ball-bearings and milled at a frequency of 30 Hz for five minutes. The homogeneous reagent mixtures were then placed in a beaker and put inside an acrylic hydration chamber with water. The hydration chamber was placed inside an incubation oven set to 45 °C.

Fractions of the aging reactions were taken at different times for analysis. Samples were finely ground and packed into 0.5 mm capillaries for PXRD analysis.

### 2.3.3 Powder X-ray Diffraction

PXRD patterns were collected using either a Bruker D2 Phaser benchtop diffractometer or a Bruker D8 Discovery diffractometer. Both diffractometers are equipped with  $\text{Cu-K}_\alpha$  ( $\lambda = 1.54056 \text{ \AA}$ ) sources operating at a power setting of 30 kV and 10 mA (D2 Phaser) or 40 kV and 40 mA (D8 Discovery). Powder patterns were collected in the range of  $2\theta = 4^\circ$  to  $40^\circ$ . Analyses of PXRD patterns were done using DASH 3.3.6 and CrystalDiffract 6.7.1 software packages.

### 2.3.4 Solid-State NMR

All SSNMR experiments were conducted on a Varian Infinity Plus console with an Oxford 9.4 T ( $\nu_0(^1\text{H}) = 400 \text{ MHz}$ ,  $\nu_0(^{111}\text{Cd}) = 84.86 \text{ MHz}$ ,  $\nu_0(^{13}\text{C}) = 100.58 \text{ MHz}$ ,

$\nu_0(^{14}\text{N}) = 28.91$  MHz) wide-bore magnet. Samples were finely ground with a mortar and pestle and packed into either 4 mm outer diameter (o.d.) zirconia rotors ( $^1\text{H}$ ,  $^{13}\text{C}$ ,  $^{111}\text{Cd}$  MAS NMR experiments) or 5 mm o.d. glass tubes ( $^{14}\text{N}$  static NMR experiments).

#### 2.3.4.1 $^1\text{H}$ MAS NMR

Experiments were conducted on a Chemagnetics 4 mm HX MAS probe. A Bloch decay pulse sequence with calibrated  $\pi/2$  pulse widths of  $3.56 \mu\text{s}$  ( $\nu_1 = 70$  kHz) was used for all experiments, which were conducted under MAS ( $\nu_{\text{rot}} = 16$  kHz). 4 K of points were collected with a dwell time of  $6.67 \mu\text{s}$  (spectral width of 150 kHz). The recycle delays were calibrated for each sample to maximize S/N and are shown in **Table A1**. Peaks were referenced to TMS using adamantane as a secondary reference ( $\delta_{\text{iso}} = 1.87$  ppm).

#### 2.3.4.2 $^1\text{H}$ - $^{13}\text{C}$ CP/MAS NMR

$^{13}\text{C}$  SSNMR experiments were conducted on the same spectrometer and probe using the variable-amplitude cross polarization (VACP) pulse sequence under MAS conditions<sup>57</sup> ( $\nu_{\text{rot}} = 10$  kHz). Optimized contact times and recycle delays are shown in **Table A2**. The  $\pi/2(^1\text{H})$  pulse width was  $7.4 \mu\text{s}$ . The spin locking powers were 34 kHz for  $^1\text{H}$  and 24 kHz for  $^{13}\text{C}$ . TPPM  $^1\text{H}$  decoupling was used, with  $\nu_2 = 46$  kHz. 8 K of points were collected with a dwell time of  $16.67 \mu\text{s}$  (spectral width of 60 kHz). Peaks were referenced to TMS using adamantane as a secondary reference ( $\delta_{\text{iso}} = 38.57$  ppm).

#### 2.3.5 $^1\text{H}$ - $^{111}\text{Cd}$ CP/MAS and CP static NMR

$^{111}\text{Cd}$  SSNMR experiments were conducted using the variable-amplitude cross polarization (VACP) pulse sequence under both MAS ( $\nu_{\text{rot}} = 5$  kHz) and static conditions.

Optimized contact times and recycle delays are shown in **Table A3**. The  $\pi/2(^1\text{H})$  pulse width was 3.5  $\mu\text{s}$ . The spinning locking powers were 52 kHz for  $^1\text{H}$  and 42 kHz for  $^{111}\text{Cd}$ . TPPM  $^1\text{H}$  decoupling was used, with  $\nu_2 = 58$  kHz. 2 K of points were collected with a dwell time of 20  $\mu\text{s}$  (spectral width of 50 kHz). Peaks were referenced to  $\text{Cd}[\text{ClO}_4]_2 \cdot 6\text{H}_2\text{O}$  using  $\text{Cd}[\text{NO}_3]_2 \cdot 4\text{H}_2\text{O}$  as a secondary reference ( $\delta_{\text{iso}} = -100$  ppm).

While  $^{113}\text{Cd}$  (n.a. = 12.22%,  $\gamma = -9.487$  MHz/T) is usually preferred over  $^{111}\text{Cd}$  (NA = 12.80 %,  $\gamma = -9.069$  MHz/T) for NMR experiments,  $^{113}\text{Cd}$  spectra acquired at 9.4 T are subject to interfering, semi-coherent signals from local FM radio stations. For this reason,  $^{111}\text{Cd}$  was chosen as the target nuclide, without incurring any significant losses in signal-to-noise.

### 2.3.6 $^1\text{H}$ - $^{14}\text{N}$ BRAIN-CP/WURST-CPMG

$^{14}\text{N}$  SSNMR experiments were conducted using the Broadband Adiabatic INversion Cross Polarization pulse sequence coupled with a WURST-CPMG echo train (BRAIN-CP/WURST-CPMG).<sup>58-61</sup> A 4.9  $\mu\text{s}$  (51 kHz)  $\pi/2$  excitation pulse was used on the  $^1\text{H}$  channel and 45 kHz of spin-locking power was applied on both channels for the optimized contact time. The WURST spin-locking pulse was swept over 1000 kHz on the  $^{14}\text{N}$  channel. The CPMG refocusing portion of the sequence used 50  $\mu\text{s}$  WURST-80 pulses, with  $\nu_1 = 28$  kHz and 1000 kHz sweep ranges. The spectral width was 2000 kHz (0.5  $\mu\text{s}$  dwell time). The acquisition period of a single echo was 100 points (50  $\mu\text{s}$ ).

Since the excitation bandwidths associated with the WURST pulses are insufficient to excite the entire breadth of the  $^{14}\text{N}$  powder patterns, the full  $^{14}\text{N}$  spectra were acquired using the frequency-stepped or variable-offset cumulative spectrum (VOCS) technique,<sup>62-64</sup> where a series of subspectra were acquired with transmitter steps

of 100 kHz over the low frequency half of the Pake-like doublet. The subspectra were processed by co-addition of the echoes in the FID into a single echo, application of 20 kHz of Gaussian broadening, Fourier transformation, and subsequent magnitude calculation. The subspectra were then co-added and mirrored about the  $^{14}\text{N}$  Larmor frequency to give the total spectrum.<sup>59,65–67</sup>

### 2.3.7 Structure Refinement

The PXRD pattern of **1** was indexed and the unit cell parameters were determined using the McMaille software package.<sup>68</sup> The initial structure solution was performed using DASH<sup>69</sup> and refined using EXPGUI/GSAS.<sup>70,71</sup>

## 2.4 Results and Discussion

### 2.4.1 Synthesis and Powder X-ray Diffraction

The reaction of solid cadmium oxide (CdO) and 2-methylimidazole (**HMeIm**) is the main accelerated aging reaction investigated herein, subject to a series of disparate reaction conditions, including different ratios of CdO:HMeIm and treatment with catalytic protic salts.

The first accelerated aging reaction that was investigated featured a 1:2 CdO:HMeIm ratio. The materials were added to a milling jar and milled for five minutes without any solvent (*i.e.*, dry-milling). The PXRD pattern of the resulting mixture shows reflections for only CdO and HMeIm (**Figure A1** in Appendix A), indicating that no reaction occurred during dry-milling and that a homogenous mixture of the reagents was obtained. The mixture was then placed in a chamber and exposed to 100% relative humidity at a temperature of 45 °C. The PXRD pattern (**Figure 2.1(A)**) of the mixture

after twelve days in the aging chamber shows reflections from an unknown crystalline phase (**1**), as well as characteristic reflections of CdO, indicating the incomplete conversion of CdO into **1**. It is noted that there are no reflections observed corresponding to unreacted HMeIm.

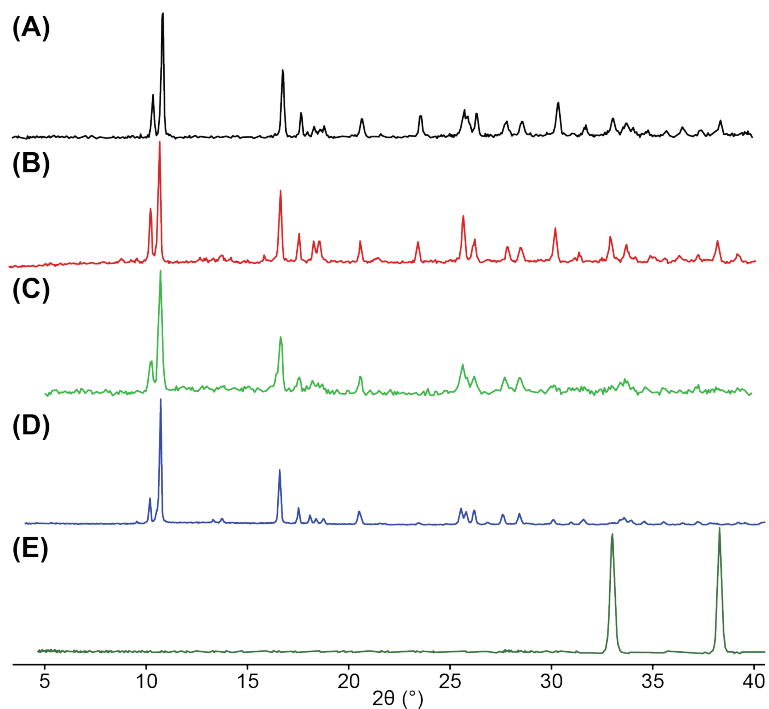
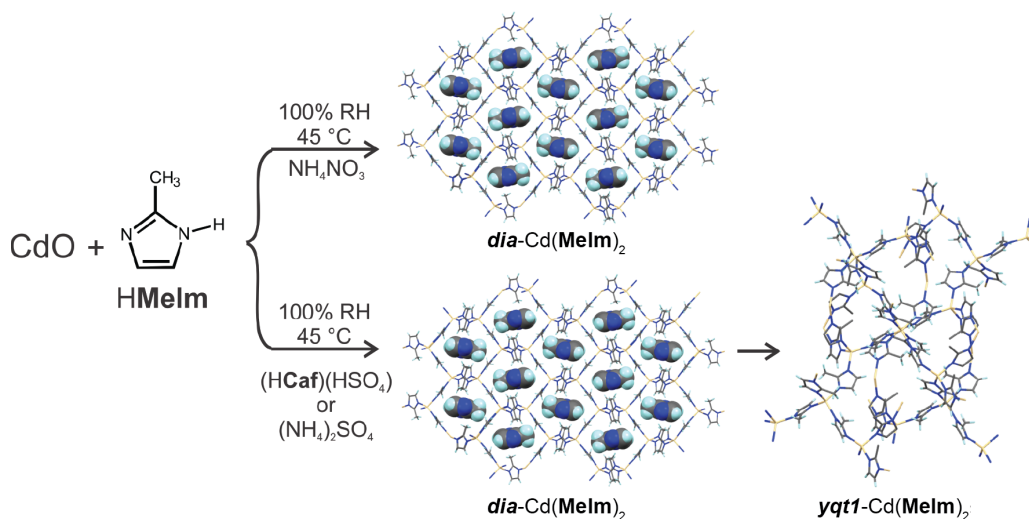


**Figure 2.1:** Experimental PXRD patterns for (A) 1:2 reaction aged for 12 days, (B) 1:2 reaction with  $\text{NH}_4\text{NO}_3$  aged for 7 days, (C) 1:6 reaction with  $\text{NH}_4\text{NO}_3$  aged for 6 days, (D) 1:6 reaction with  $\text{NH}_4\text{NO}_3$  aged for 6 days, and (E) CdO.

The aging reaction was repeated with the addition of a catalytic amount of a protic salt to attempt to obtain complete conversion of the 1:2 mixture into **1**. 4 mol% (with respect to CdO) of ammonium nitrate ( $\text{NH}_4\text{NO}_3$ ), ammonium sulfate ( $(\text{NH}_4)_2\text{SO}_4$ ), or caffeineium bisulfate ( $(\text{HCaf})\text{HSO}_4$ ) was added and the resulting mixtures were dry-milled for five minutes and then aged (**Scheme 2.1**). The PXRD pattern for the products of the reaction treated with  $\text{NH}_4\text{NO}_3$  and subjected to seven days of aging (**Figure 2.1(B)**) shows reflections from **1** and residual CdO, indicating an incomplete reaction. However,



the reactions using either  $(\text{NH}_4)_2\text{SO}_4$  or  $(\text{HCaf})\text{HSO}_4$  yielded **1**, followed by the formation of a ZIF with a *yqt1* topology and known structure (**2**, *yqt1*- $\text{Cd}(\text{MeIm})_2$ ). PXRD analysis of these reactions shows complete conversion to **2** after seven days of aging (**Figure A2**).



**Scheme 2.1:** Proposed reaction pathways for the accelerated aging reactions of  $\text{CdO}$  and  $\text{HMeIm}$  with different protic salts. For the reaction with  $\text{NH}_4\text{NO}_3$ , 1:2, 1:3, and 1:6  $\text{Cd}:\text{HMeIm}$  ratios were used.

The observation of reflections from  $\text{CdO}$  in the product mixture of the reaction conducted with  $\text{NH}_4\text{NO}_3$  suggests that the ratio of  $\text{Cd}:\text{MeIm}$  in **1** is different than the expected 1:2 ratio. The reaction was repeated with a 1:6  $\text{Cd}:\text{HMeIm}$  ratio to ensure the complete conversion of  $\text{CdO}$  into **1** by providing a large excess of  $\text{HMeIm}$ . The mixture was aged for six days, and the products were washed with methanol to remove any unreacted  $\text{HMeIm}$ . The powder diffraction pattern of the products showed no reflections from residual  $\text{CdO}$  (**Figure 2.1(C)**), indicating the complete conversion into **1**. A similar result was obtained using a 1:3 reaction (**Figure 2.1(D)**), indicating that the  $\text{Cd}:\text{HMeIm}$  ratio in **1** is 1:3.

In order to explain the 1:3 Cd:HMeIm ratio of **1**, two structural models were proposed: (i) **1** consists of a framework of four-coordinate tetrahedral Cd atoms connected by MeIm<sup>-</sup> ligands with the excess HMeIm in the pores of the framework, or (ii) the Cd atoms are coordinated to both MeIm<sup>-</sup> and HMeIm ligands, leading to a framework with five- and/or six-coordinate Cd centres.

#### 2.4.2 Solid-State NMR Studies

To determine which of the proposed structural models is correct, multinuclear SSNMR experiments (*i.e.*, <sup>111</sup>Cd, <sup>13</sup>C, <sup>1</sup>H, and <sup>14</sup>N) were conducted to aid in the refinement of the structure from the PXRD patterns collected for this sample.

Cd chemical shifts are known to be very sensitive to the Cd coordination number and the nature of the coordinating ligands.<sup>72,73</sup> Only a few Cd NMR studies of systems analogous to those discussed herein have been reported in the literature. Baxter *et al.* characterized the Cd-analogue of ZIF-8 (CdIF-1) using <sup>113</sup>Cd SSNMR.<sup>74</sup> The Cd atoms in CdIF-1 are coordinated by four MeIm ligands and the value of the Cd isotropic chemical shift,  $\delta_{\text{iso}}(^{113}\text{Cd})$ , was reported as 408.3 ppm. Mennitt *et al.* investigated two compounds with octahedral Cd environments, [Cd(HIm)<sub>6</sub>][NO<sub>3</sub>]<sub>2</sub> and [Cd(Him)<sub>6</sub>][OH][NO<sub>3</sub>] • 4H<sub>2</sub>O, reporting  $\delta_{\text{iso}}(^{113}\text{Cd})$  of 238 and 272 ppm, respectively.<sup>75</sup> In order to obtain correlations between the Cd coordination environments and their chemical shifts, more data is needed on four- and six-coordinate Cd environments with nitrogen-donor ligands. Hence, we conducted <sup>111</sup>Cd NMR experiments on the imidazolate frameworks *dia*-Cd(Im)<sub>2</sub> (2, CCDC code BAYQAU)<sup>16</sup> and *yqtl*-Cd(MeIm)<sub>2</sub> (3, CCDC code GUPBOJ),<sup>16</sup> which have four-coordinate Cd(II) sites, and the complex carbonate [Cd(HIm)<sub>6</sub>]<sup>2+</sup>[CO<sub>3</sub>]<sup>2-</sup> • 3H<sub>2</sub>O (4, CCDC code IMCDP01),<sup>76</sup> which has a six-coordinate Cd(II) site. Depictions of the

coordination environments of the Cd atoms (derived from the crystal structures) of compounds 2-4 are shown in **Figures A3-A5**, respectively.  $^1\text{H}$  MAS and  $^1\text{H}$ - $^{13}\text{C}$  CP/MAS NMR spectra of these compounds are shown in **Figures A6** and **A7**, respectively.

$^1\text{H}$ - $^{111}\text{Cd}$  cross-polarization (CP) experiments were conducted under both magic-angle spinning (MAS) and static (*i.e.*, no sample rotation) conditions. The MAS experiments allow for the accurate determination of ( $\delta_{\text{iso}}(^{111}\text{Cd})$ ), which can be correlated to the type of Cd coordination environment. Since the Cd chemical shift anisotropies (CSAs) are relatively small, they are challenging to accurately measure from most of the MAS NMR spectra. Hence, static  $^1\text{H}$ - $^{111}\text{Cd}$  CP experiments were conducted, which yield spectra that provide the chemical shift (CS) tensor parameters (**Table 2.1**), providing further information on the geometries and symmetries of the Cd environments.

The  $^{111}\text{Cd}$  NMR spectra of 2 are shown in **Figure 2.2(A)**. The MAS spectrum reveals a  $\delta_{\text{iso}}(^{111}\text{Cd}) = 436(1)$  ppm and a clearly resolved nonet coupling pattern corresponding to indirect spin-spin coupling of  $^{111}\text{Cd}$  to four  $^{14}\text{N}$  ( $I = 1$ ) nuclei, with  $^1J(^{111}\text{Cd}, ^{14}\text{N}) = 140(5)$  Hz. This  $\delta_{\text{iso}}(^{111}\text{Cd})$  is consistent with that reported by Baxter *et al.*,<sup>74</sup> as well as those in reports by Ellis *et al.* of Cd CS tensors of four-coordinate Cd centres with different geometries and mixed ligand types (**Figure A8**). The coordination environment of the Cd atom in 2 is significantly distorted from perfect tetrahedral symmetry (Tables A5 and A6), and this is manifested in the relatively large span ( $\Omega = 225$  ppm), which can be measured from both the MAS and static  $^{111}\text{Cd}$  spectra.

**Table 2.1:** Experimentally measured cadmium chemical shift tensor parameters.

Compound	$\delta_{\text{iso}}$ (ppm) <sup>a</sup>	$\Omega$ (ppm) <sup>b</sup>	$\kappa$ <sup>c</sup>
<b>1</b>	441(1)	40(3)	0.0(2)
<b>2</b>	436(2)	225(5)	-0.19(2)
<b>3</b>	437(1)	85(5)	-0.68(2)
	417(3)	280(5)	-0.51(2)
	437(1)	200(5)	-0.40(2)
<b>4</b>	251(2)	42(2)	0.55(2)

The principal components of the chemical shift tensor are defined as  $\delta_{11} \geq \delta_{22} \geq \delta_{33}$ .

<sup>a</sup> Isotropic shift:  $\delta_{\text{iso}} = (\delta_{11} + \delta_{22} + \delta_{33})/3$ ; <sup>b</sup> Span:  $\Omega = \delta_{11} - \delta_{33}$ ; <sup>c</sup> Skew:  $\kappa = 3(\delta_{22} - \delta_{\text{iso}})/\Omega$ . While the MAS spectra are useful for determining the values of  $\delta_{\text{iso}}(^{111}\text{Cd})$ , the full sets of tensor parameters are determined from the static spectra. Experimental uncertainties in the last digit(s) for each parameter are indicated in parentheses and were estimated using bidirectional variation of the parameters in the simulation software.

The MAS spectrum of **3** (**Figure 2.2(B)**) appears to exhibit two patterns arising from magnetically distinct <sup>111</sup>Cd nuclei, with  $\delta_{\text{iso}}(^{111}\text{Cd})$  of 437 and 417 ppm; again, both shifts are consistent with four-coordinate Cd environments with nitrogen-donor ligands. The peak at 437 ppm has a resolved nonet pattern ( $^1J(^{111}\text{Cd}, ^{14}\text{N}) = 125(5)$  Hz), and is much more intense than the peak at 417 ppm, which does not have any resolvable fine structure (though it is clearly broadened in a similar manner to the former peak). Interestingly, the static spectrum of **3** reveals *three* overlapping patterns arising from magnetically distinct Cd sites. Two of the sites have virtually identical values of  $\delta_{\text{iso}}(^{111}\text{Cd}) = 437$  ppm, but disparate CS tensor parameters; this almost certainly accounts for the broadening and increased intensity of the peak at 437 ppm in the MAS spectra, as noted above, and represents a rare case where distinct patterns are more easily resolved in static SSNMR patterns.

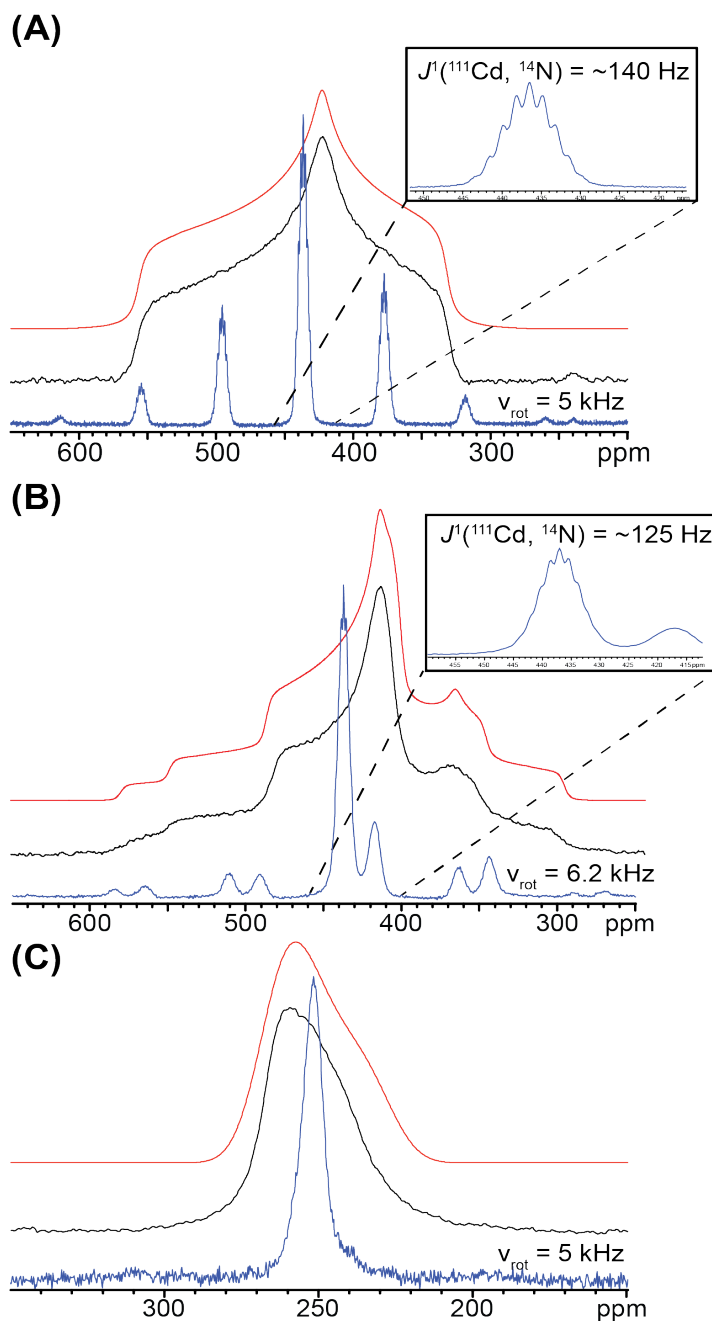


**Figure 2.2:** Experimental  $^1\text{H}$ - $^{111}\text{Cd}$  CP NMR spectra acquired under MAS (blue traces) and static (black traces) conditions, with accompanying simulations of the static spectra (red traces) for (A) dia- $\text{Cd}[\text{Im}]_2$  (**2**), (B) yqt1- $\text{Cd}[\text{MeIm}]_2$  (**3**), and (C)  $[\text{Cd}(\text{HIm})_6]^{2+}[\text{CO}_3]^{2-} \cdot 3\text{H}_2\text{O}$  (**4**).

The crystal structure of **3** has two crystallographically distinct Cd environments, with one of these having a positionally disordered MeIm ligand (Cd1). The positionally disordered Cd environment has a very distorted tetrahedral geometry; hence, the two

patterns with large spans (*i.e.*,  $\Omega = 200$  and  $280$  ppm) correspond to the Cd sites with the two possible orientations of the MeIm ligand. At this time, we are not able make assignments of the individual CS tensor parameter sets to different orientations of the MeIm ligand, even with the aid of *ab initio* DFT computations. Finally, the pattern with the smaller span value ( $\Omega = 85$  ppm) corresponds to the Cd site with a less distorted tetrahedral coordination environment, and no positionally disordered ligands.

The  $^{111}\text{Cd}$  MAS spectrum of 4 (**Figure 2.2(C)**) has a single peak with  $\delta_{\text{iso}}(^{111}\text{Cd}) = 251$  ppm, consistent with a Cd environment in an octahedral coordination environment with nitrogen donor ligands.<sup>77-84</sup> The span is relatively small with respect to those for the four-coordinate Cd sites above, indicating a near-octahedral symmetry. It is noted that the expected coupling pattern (thirteen peaks from coupling to six  $^{14}\text{N}$  nuclei) is not observed in the spectrum of this compound. This lack of resolution could arise from a distribution of  $^1J(^{14}\text{N}, ^{111}\text{Cd})$  coupling constants and/or efficient transverse relaxation of  $^{111}\text{Cd}$  caused by scalar relaxation of the second kind.

With the information above, and Cd chemical shift data from the literature, it is now possible to identify which of the structural models is more plausible. The  $^{111}\text{Cd}$  MAS NMR spectrum of 1 (**Figure 2.3(A)**) reveals a single peak with  $\delta_{\text{iso}}(^{111}\text{Cd}) = 441$  ppm, consistent with a crystallographically unique Cd species in a four-coordinate environment. There is no evidence for six-coordinate Cd species; therefore, model (ii) can be rejected, and consideration of model (i) can be pursued. In addition, the MAS spectrum has a relatively broad peak (significantly broader than those of the previously discussed four-coordinate Cd compounds) with no resolved *J*-couplings, indicating that there may be some disorder in this system (this is further substantiated by the  $^{111}\text{Cd}$  static

CP spectrum (**Figure 2.3(B)**) and accompanying simulation, **Figure 2.3(C)**, which do not show any clearly defined discontinuities). The disorder may be caused by the HMeIm guest molecules within the pores of the framework that assume random orientations at room temperature. Hence, further multinuclear SSNMR experiments were conducted to confirm the presence of HMeIm in the pores and to comment on the degree of ordering of these molecules.

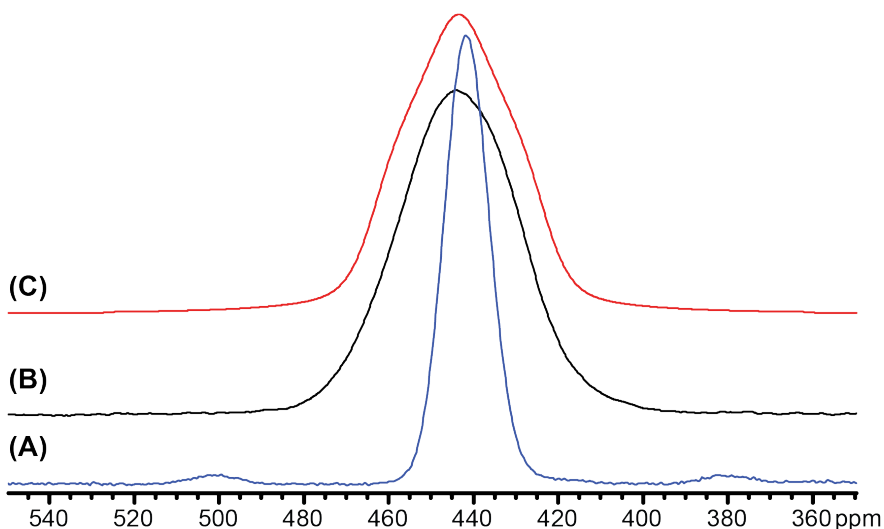


**Figure 2.3:** Experimental  $^1\text{H}$ - $^{111}\text{Cd}$  CP NMR spectra under (A) MAS ( $\nu_{\text{rot}} = 5$  kHz) and (B) static conditions for compound **1**, with an accompanying simulation of the static spectrum in (C).

The  $^1\text{H}$ - $^{13}\text{C}$  CP/MAS spectra of bulk HMeIm (green trace) and compound **1** (blue trace) are shown in **Figure 2.4(A)**. The spectrum of the bulk form has four peaks, corresponding to the four distinct carbon environments in HMeIm. The spectrum of **1** has many peaks matching those in the spectrum of bulk HMeIm, suggesting that there is unbound HMeIm in **1** (the remaining peaks arise from carbon atoms of the MeIm ligands in the framework). In addition, the  $^1\text{H}$  MAS NMR spectrum of **1** (**Figure 2.4(B)**) has a peak at ca. 13.3 ppm, corresponding to a proton bound to a nitrogen atom in the HMeIm

ring – this signal is observed only if there is unbound HMeIm in **1**, since all of the nitrogen atoms in the framework are coordinated to  $\text{Cd}^{2+}$  ions.

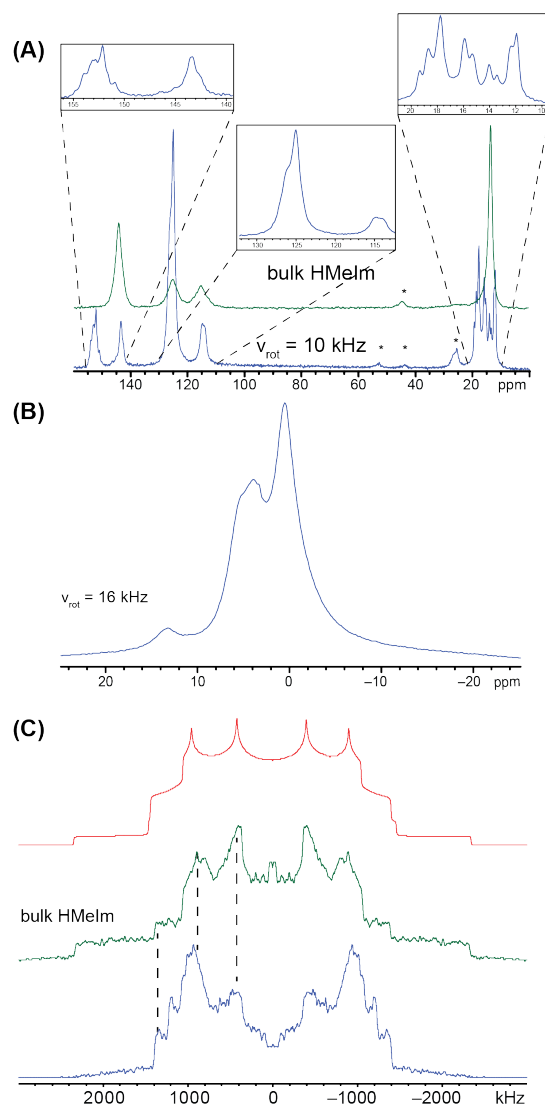


**Figure 2.4:** (A)  $^1\text{H}$ - $^{13}\text{C}$  CP MAS spectra of bulk HMeIm (green trace) and **1** (blue trace), (B)  $^1\text{H}$  MAS spectrum of **1** and (C)  $^1\text{H}$ - $^{14}\text{N}$  BRAIN-CP/WURST-CPMG spectra of HMeIm (green trace) and **1** (blue trace).



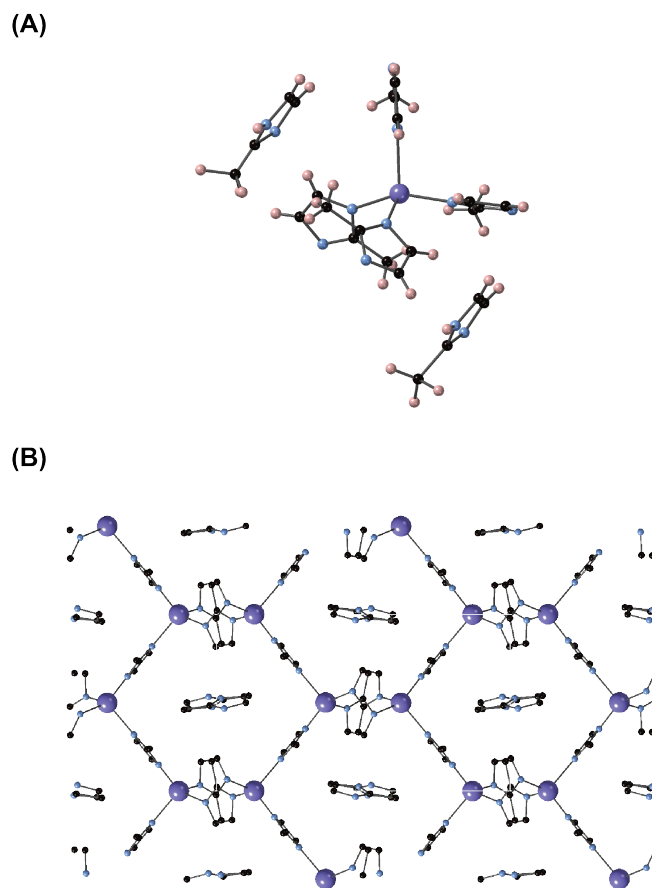


**Figure 2.5:** Depictions (adapted from the predicted crystal structure of **1**) of (A) the coordination environment about the Cd atoms, and (B) a supercell showing the pores containing the HMeIm molecules (hydrogen atoms have been omitted for clarity).

The  $^1\text{H}$ - $^{14}\text{N}$  static CP NMR spectra for bulk HMeIm (green) and compound **1** (blue) are shown in **Figure 2.4(C)**. Due to the enormous breadth of the  $^{14}\text{N}$  patterns (ca. 4.5 MHz), it is necessary to use the broadband adiabatic inversion CP (BRAIN-CP) for polarization transfer,<sup>58,59</sup> and the wideband uniform-rate smooth-truncation-CPMG (WURST-CPMG) pulse sequence for broadband excitation and refocusing.<sup>60,61,85</sup> The spectrum of the bulk HMeIm has two overlapping Pake-like doublet patterns corresponding to the two distinct nitrogen environments (**Figure A9**). The narrower pattern ( $C_Q = 1.95(5)$  MHz,  $\eta_Q = 0.44(2)$ ) is assigned to N1 (*i.e.*, the nitrogen with the

attached hydrogen atom) and the broader pattern ( $C_Q = 3.13(5)$ ,  $\eta_Q = 0.21(2)$ ) is assigned to N3. The spectrum of **1** has several broad features resulting from multiple overlapping Pake doublet patterns. Some of the features (*i.e.*, horns, shoulders and feet) in the spectrum of **1** occur at the same frequency as those in the spectrum of bulk HMeIm, supporting the hypothesis that there is unbound HMeIm present in **1**. Furthermore, the discontinuities in the spectrum of **1** are not as well defined as those in the spectrum of bulk HMeIm, suggesting that the guest HMeIm molecules are disordered in the former. Finally, there are discontinuities in the  $^{14}\text{N}$  spectrum of **1** that do not match those in the spectrum of HMeIm; these are assigned to nitrogen atoms of MeIm ligands in the framework of **1**.

### 2.4.3 Structural Refinement

The structural information obtained *via* SSNMR spectroscopy enabled the choice of a suitable model for structural characterization of **1** from PXRD data. Indexing of the PXRD pattern of **1** using McMaille<sup>68</sup> was only successful when allowing for the presence of impurity peaks and revealed an orthorhombic unit cell with parameters  $a = 10.102455(5)$  Å,  $b = 16.7887(11)$  Å and  $c = 9.54324(47)$  Å. Intensity statistics and cell volume considerations suggested *Ima2* as the most likely space group. Structure solution by DASH<sup>69</sup> produced a model with symmetry-imposed disorder of an imidazole ligand and an unusually short coordinative bond (1.96 Å). Consequently, structure determination was repeated using space group *Pna2*<sub>1</sub>, which is the maximal subgroup of *Ima2* that allows the ligands to reside in general positions. The resulting fit was slightly better with this space group and the model explained a minor peak (13.7°) that would be considered an impurity with the *Ima2* model. Even though the lower-symmetry model appears more

likely, it is important to note that some degree of disorder in the orientation of the coordinated imidazole rings cannot be excluded. The resolution of our PXRD data is not sufficient to resolve disorder. This caveat also applies to the voids present in the structure, which may contain disordered solvent molecules. The crystal structure, after successful refinement using EXPGUI/GSAS,<sup>70,71</sup> revealed a distorted *dia*-topology Cd(MeIm)<sub>2</sub> network. The cavities of the framework are populated by HMeIm molecules that are arranged into one-dimensional channels through short N··N contacts of 2.67 Å, indicative of NH··N hydrogen bonding (**Figure 2.5**).

## 2.5 Conclusions

We have demonstrated the synthesis of a new zeolitic imidazolate framework with a diamondoid topology from the accelerated aging reaction of cadmium oxide and 2-methylimidazole with catalytic amounts of NH<sub>4</sub>NO<sub>3</sub>; the synthesis of this material was not possible using traditional solvothermal techniques. The Cd:HMeIm ratio in this material was determined to be 1:3 and a combination of SSNMR and PXRD were used to refine and elucidate its structure. <sup>1</sup>H-<sup>111</sup>Cd CP SSNMR spectra of a series of Cd-containing compounds with known structures were acquired in order to obtain correlations between the <sup>111</sup>Cd CS tensor parameters and the types and geometries of the Cd coordination environments. The <sup>111</sup>Cd spectrum of the diamondoid framework suggests that the coordination environment about the Cd atoms is tetrahedral and multinuclear SSNMR experiments revealed that there is excess HMeIm in the pores of the framework that is likely disordered at room temperature. The information obtained from the multinuclear SSNMR experiments was used in the aid of the refinement of the structure from PXRD data. It was found that 1 consists of a distorted *dia*-Cd[MeIm]<sub>2</sub>

framework with one-dimensional channels that are populated by HMeIm molecules. Accelerated aging reactions provide an efficient, low-energy means for producing MOFs and ZIFs. The application of NMR crystallography for the structural elucidation of intermediates and products will allow for an understanding of the reaction pathways and mechanisms of accelerated aging reactions and aid in their rational design and optimization.

## 2.6 References

- (1) Furukawa, H.; Cordova, K. E.; O’Keeffe, M.; Yaghi, O. M. *Science* **2013**, *341*, 1230444.
- (2) Silva, P.; Vilela, S. M. F.; Tomé, J. P. C.; Almeida Paz, F. A. *Chem. Soc. Rev.* **2015**, *44*, 6774–6803.
- (3) Zhou, H.-C.; Kitagawa, S. *Chem. Soc. Rev.* **2014**, *43*, 5415–5418.
- (4) Li, J.-R.; Kuppler, R. J.; Zhou, H.-C. *Chem. Soc. Rev.* **2009**, *38*, 1477.
- (5) Li, J. R.; Ma, Y.; McCarthy, M. C.; Sculley, J.; Yu, J.; Jeong, H. K.; Balbuena, P. B.; Zhou, H. C. *Coord. Chem. Rev.* **2011**, *255*, 1791–1823.
- (6) Ma, L.; Abney, C.; Lin, W. *Chem. Soc. Rev.* **2009**, *38*, 1248.
- (7) Liu, J.; Chen, L.; Cui, H.; Zhang, J.; Zhang, L.; Su, C.-Y. *Chem. Soc. Rev.* **2014**, *43*, 6011–6061.
- (8) Chen, B.; Xiang, S.; Qian, G. *Acc. Chem. Res.* **2010**, *43*, 1115–1124.
- (9) Hu, Z.; Deibert, B. J.; Li, J. *Chem. Soc. Rev.* **2014**, *43*, 5815–5840.
- (10) Eddaoudi, M.; Moler, D. B.; Li, H.; Chen, B.; Reineke, T. M.; O’Keeffe, M.; Yaghi, O. M. *Acc. Chem. Res.* **2001**, *34*, 319–330.
- (11) Phan, A.; Doonan, C. J.; Uribe-Romo, F. J.; Knobler, C. B.; O’Keeffe, M.; Yaghi, O. M. *Acc Chem Res* **2010**, *43*, 58–67.
- (12) Zhang, J. P.; Zhang, Y. B.; Lin, J. Bin; Chen, X. M. *Chem. Rev.* **2012**, *112*, 1001–1033.
- (13) Pimentel, B. R.; Parulkar, A.; Zhou, E. K.; Brunelli, N. A.; Lively, R. P. *ChemSusChem* **2014**, *7*, 3202–3240.
- (14) Eum, K.; Jayachandrababu, K. C.; Rashidi, F.; Zhang, K.; Leisen, J.; Graham, S.;

- Lively, R. P.; Chance, R. R.; Sholl, D. S.; Jones, C. W.; Nair, S. *J. Am. Chem. Soc.* **2015**, *137*, 4191–4197.
- (15) Masciocchi, N.; Ardizzoia, G. A.; Brenna, S.; Castelli, F.; Galli, S.; Maspero, A.; Sironi, A. *Chem. Commun.* **2003**, No. 16, 2018–2019.
- (16) Tian, Y.-Q.; Yao, S.-Y.; Gu, D.; Cui, K.-H.; Guo, D.-W.; Zhang, G.; Chen, Z.-X.; Zhao, D.-Y. *Chem. Eur. J.* **2010**, *16*, 1137–1141.
- (17) Czaja, A. U.; Trukhan, N.; Müller, U. *Chem. Soc. Rev.* **2009**, *38*, 1284.
- (18) Cliffe, M. J.; Mottillo, C.; Stein, R. S.; Bučar, D.-K.; Frišćić, T. *Chem. Sci.* **2012**, *3*, 2495.
- (19) Mottillo, C.; Lu, Y.; Pham, M.-H.; Cliffe, M. J.; Do, T.-O.; Frišćić, T. *Green Chem.* **2013**, *15*, 2121.
- (20) Qi, F.; Stein, R. S.; Frišćić, T. *Green Chem.* **2014**, *16*, 121–132.
- (21) Adamo, P.; Violante, P. *Appl. Clay Sci.* **2000**, *16*, 229–256.
- (22) Jackson, T. A. *Geoderma* **2015**, *251–252*, 78–91.
- (23) Huang, X. C.; Lin, Y. Y.; Zhang, J. P.; Chen, X. M. *Angew. Chem. Int. Ed.* **2006**, *45*, 1557–1559.
- (24) Užarević, K.; Wang, T. C.; Moon, S.-Y.; Fidelli, A. M.; Hupp, J. T.; Farha, O. K.; Frišćić, T. *Chem. Commun.* **2016**, *52*, 2133–2136.
- (25) Ashbrook, S. E.; Dawson, D. M. *Acc. Chem. Res.* **2013**, *46*, 1964–1974.
- (26) Massiot, D.; Messinger, R. J.; Cadars, S.; Deschamps, M.; Montouillout, V.; Pellerin, N.; Veron, E.; Allix, M.; Florian, P.; Fayon, F. *Acc. Chem. Res.* **2013**, *46*, 1975–1984.
- (27) Moran, R. F.; Dawson, D. M.; Ashbrook, S. E. *Int. Rev. Phys. Chem.* **2017**, *36*, 39–

115.

- (28) Bryce, D. L. *IUCrJ* **2017**, *4*, 350–359.
- (29) Taulelle, F.; Bouchevreau, B.; Martineau, C. *CrystEngComm* **2013**, *15*, 8613.
- (30) Martineau, C.; Senker, J.; Taulelle, F. *NMR Crystallography*; 2014; Vol. 82.
- (31) Taulelle, F. *Solid State Sci.* **2004**, *6*, 1025–1037.
- (32) Ashbrook, S. E.; McKay, D. *Chem. Commun.* **2016**, *52*, 7186–7204.
- (33) Sutrisno, A.; Huang, Y. *Solid State Nucl. Magn. Reson.* **2013**, *49–50*, 1–11.
- (34) Hoffmann, H. C.; Debowski, M.; Müller, P.; Paasch, S.; Senkowska, I.; Kaskel, S.; Brunner, E. *Materials* **2012**, *5*, 2537–2572.
- (35) Lawrence, M. C.; Schneider, C.; Katz, M. J. *Chem. Commun.* **2016**, *52*, 4971–4974.
- (36) Loiseau, T.; Serre, C.; Huguenard, C.; Fink, G.; Taulelle, F.; Henry, M.; Bataille, T.; Férey, G. *Chemistry* **2004**, *10*, 1373–1382.
- (37) Devautour-Vinot, S.; Maurin, G.; Serre, C.; Horcajada, P.; Paula Da Cunha, D.; Guillerm, V.; De Souza Costa, E.; Taulelle, F.; Martineau, C. *Chem. Mater.* **2012**, *24*, 2168–2177.
- (38) Haouas, M.; Volkringer, C.; Loiseau, T.; Férey, G.; Taulelle, F. *J. Phys. Chem. C* **2011**, *115*, 17934–17944.
- (39) Volkringer, C.; Loiseau, T.; Guillou, N.; Férey, G.; Haouas, M.; Taulelle, F.; Elkaim, E.; Stock, N. *Inorg. Chem.* **2010**, *49*, 9852–9862.
- (40) Morris, W.; Taylor, R. E.; Dybowski, C.; Yaghi, O. M.; Garcia-Garibay, M. A. *J. Mol. Struct.* **2011**, *1004*, 94–101.
- (41) Morris, W.; Stevens, C. J.; Taylor, R. E.; Dybowski, C.; Yaghi, O. M.; Garcia-

- Garibay, M. A. *J. Phys. Chem. C* **2012**, *116*, 13307–13312.
- (42) Rossini, A. J.; Zagdoun, A.; Lelli, M.; Canivet, J.; Aguado, S.; Ouari, O.; Tordo, P.; Rosay, M.; Maas, W. E.; Copéret, C.; Farrusseng, D.; Emsley, L.; Lesage, A. *Angew. Chem. Int. Ed.* **2012**, *51*, 123–127.
- (43) Sutrisno, A.; Terskikh, V. V.; Shi, Q.; Song, Z.; Dong, J.; Ding, S. Y.; Wang, W.; Provost, B. R.; Daff, T. D.; Woo, T. K.; Huang, Y. *Chem. Eur. J.* **2012**, *18*, 12251–12259.
- (44) Volkringer, C.; Loiseau, T.; Férey, G.; Morais, C. M.; Taulelle, F.; Montouillout, V.; Massiot, D. *Microporous Mesoporous Mater.* **2007**, *105*, 111–117.
- (45) Mowat, J. P. S.; Miller, S. R.; Slawin, A. M. Z.; Seymour, V. R.; Ashbrook, S. E.; Wright, P. A. *Microporous Mesoporous Mater.* **2011**, *142*, 322–333.
- (46) Jiang, Y.; Huang, J.; Marx, S.; Kleist, W.; Hunger, M.; Baiker, A. *J. Phys. Chem. Lett.* **2010**, *1*, 2886–2890.
- (47) He, P.; Lucier, B. E. G.; Terskikh, V. V.; Shi, Q.; Dong, J.; Chu, Y.; Zheng, A.; Sutrisno, A.; Huang, Y. *J. Phys. Chem. C* **2014**, *118*, 23728–23744.
- (48) Wang, W.; Waang, W. D.; Lucier, B. E. G.; Terskikh, V. V.; Huang, Y. *J. Phys. Chem. Lett.* **2014**, *5*, 3360–3365.
- (49) Stallmach, F.; Gröger, S.; Künzel, V.; Kärger, J.; Yaghi, O. M.; Hesse, M.; Müller, U. *Angew. Chem. Int. Ed.* **2006**, *45*, 2123–2126.
- (50) Kong, X.; Scott, E.; Ding, W.; Mason, J. A.; Long, J. R.; Reimer, J. A. *J. Am. Chem. Soc.* **2012**, *134*, 14341–14344.
- (51) Lucier, B. E. G.; Zhang, Y.; Lee, K. J.; Lu, Y.; Huang, Y. *Chem. Commun.* **2016**, *52*, 7541–7544.



- (52) Li, J.; Li, S.; Zheng, A.; Liu, X.; Yu, N.; Deng, F. *J. Phys. Chem. C* **2017**, *121*, 14261–14268.
- (53) Xu, J.; Sinelnikov, R.; Huang, Y. *Langmuir* **2016**, *32*, 5468–5479.
- (54) Lucier, B. E. G.; Chan, H.; Zhang, Y.; Huang, Y. *Eur. J. Inorg. Chem.* **2016**, *2016*, 2017–2024.
- (55) Gul-E-Noor, F.; Mendt, M.; Michel, D.; Pöppel, A.; Krautscheid, H.; Haase, J.; Bertmer, M. *J. Phys. Chem. C* **2013**, *117*, 7703–7712.
- (56) Kobera, L.; Rohlicek, J.; Czernek, J.; Abbrent, S.; Streckova, M.; Sopcak, T.; Brus, J. *ChemPhysChem* **2017**, 1–8.
- (57) Peersen, O. B.; Wu, X. L.; Kustanovich, I.; Smith, S. O. *J. Magn. Reson, Sers A* **1993**, 334–339.
- (58) Harris, K. J.; Lupulescu, A.; Lucier, B. E. G.; Frydman, L.; Schurko, R. W. *J. Magn. Reson.* **2012**, *224*, 38–47.
- (59) Harris, K. J.; Veinberg, S. L.; Mireault, C. R.; Lupulescu, A.; Frydman, L.; Schurko, R. W. *Chem. Eur. J.* **2013**, *19*, 16469–16475.
- (60) O’Dell, L. A.; Schurko, R. W. *Chem. Phys. Lett.* **2008**, *464*, 117–130.
- (61) O’Dell, L. A.; Rossini, A. J.; Schurko, R. W. *Chem. Phys. Lett.* **2009**, *468*, 330–335.
- (62) Massiot, D.; Farnan, I.; Gautier, N.; Trumeau, D.; Trokiner, A.; Coutures, J. P. *Solid State Nucl. Magn. Reson.* **1995**, *4*, 241–248.
- (63) Medek, A.; Frydman, V.; Frydman, L. *J. Phys. Chem. A* **1999**, *103*, 4830–4835.
- (64) Tang, J. A.; Masuda, J. D.; Boyle, T. J.; Schurko, R. W. *ChemPhysChem* **2006**, *7*, 117–130.

- (65) Veinberg, S. L.; Friedl, Z. W.; Harris, K. J.; O'Dell, L. A.; Schurko, R. W. *CrystEngComm* **2015**, *17*, 5225–5236.
- (66) Veinberg, S. L.; Friedl, Z. W.; Lindquist, A. W.; Kispal, B.; Harris, K. J.; O'Dell, L. A.; Schurko, R. W. *ChemPhysChem* **2016**, *17*, 4011–4027.
- (67) Veinberg, S. L.; Johnston, K. E.; Jaroszewicz, M. J.; Kispal, B. M.; Mireault, C. R.; Kobayashi, T.; Pruski, M.; Schurko, R. W. *Phys. Chem. Chem. Phys.* **2016**, *18*, 17713–17730.
- (68) Le Bail, A. *Powder Diffr.* **2004**, *19*, 249–254.
- (69) David, W. I. F.; Shankland, K.; van de Streek, J.; Pidcock, E.; Motherwell, W. D. S.; Cole, J. C. *J. Appl. Crystallogr.* **2006**, *39*, 910–915.
- (70) Larson, A. C.; Von Dreele, R. *General Structure Analysis System (GSAS)*; 2004.
- (71) Toby, B. H. *J. Appl. Crystallogr.* **2001**, *34*, 210–213.
- (72) Summers, M. F. *Coord. Chem. Rev.* **1988**, *86*, 43–143.
- (73) Srikanth, K.; Schurko, R. W.; Hung, I.; Ramamoorthy, A. *Mater. Sci. Technol.* **2003**, *13*, 1191–1196.
- (74) Baxter, E. F.; Bennett, T. D.; Cairns, A. B.; Brownbill, N. J.; Goodwin, A. L.; Keen, D. A.; Chater, P. A.; Blanc, F.; Cheetham, A. K. *Dalt. Trans.* **2016**, *45*, 4258–4268.
- (75) Mennitt, P. G.; Shatlock, M. P.; Barluska, V. J.; Maciel, G. E. *J. Phys. Chem.* **1981**, *85*, 2087–2091.
- (76) Jian, F.; Zhao, P.; Wang, S.; Zhang, S. **2002**, *32*, 4–7.
- (77) Jakobsen, H. J.; Ellis, P. D.; Inners, R. R.; Jensen, C. F. *J. Am. Chem. Soc.* **1982**, *104*, 7442–7452.

- (78) Kennedy, M. A.; Ellis, P. D.; Jakobsen, H. J. *Inorg. Chem.* **1990**, *29*, 550–552.
- (79) Kennedy, M. A.; Sessler, J. L.; Murai, T.; Ellis, P. D.; Jakobsen, H. J. *Inorg. Chem.* **1990**, *29*, 1050–1054.
- (80) Rivera, E.; Kennedy, M. A.; Adams, R. D.; Ellis, P. D. *J. Am. Chem. Soc.* **1990**, *112*, 1400–1407.
- (81) Rivera, E.; Ellis, P. D. *Inorg. Chem.* **1992**, *11*, 2096–2103.
- (82) Lipton, A. S.; Mason, S. S.; Reger, D. L.; Ellis, P. D. *J. Am. Chem. Soc.* **1994**, *116*, 10182–10187.
- (83) Reger, D. L.; Myers, S. M.; Mason, S. S.; Darensbourg, D. J.; Holtcamp, M. W.; Reibenspies, J. H.; Lipton, A. S.; Ellis, P. D. *J. Am. Chem. Soc.* **1995**, *117*, 10998–11005.
- (84) Lipton, A. S.; Mason, S. S.; Myers, S. M.; Reger, D. L.; Ellis, P. D. **1996**, *2*, 7111–7117.
- (85) O'Dell, L. A. *Solid State Nucl. Magn. Reson.* **2013**, *55–56*, 28–41.

# Chapter 3: Monitoring the Formation of Cadmium-Containing Zeolitic Imidazolate Frameworks using a Combination of Powder X-ray Diffraction and Multinuclear Solid-State NMR

## 3.1 Overview

Chemical syntheses that adhere to the tenets of green chemistry (*i.e.*, reduce the amount of solvent, achieve higher yields, and require less energy input) are much sought after. Mechanochemistry is an attractive alternative to traditional solvothermal synthetic procedures, as it uses little solvent, affords quantitative yields, and has greatly reduced reaction times. Herein, we demonstrate the synthesis of cadmium-containing zeolitic imidazolate frameworks (ZIFs) from cadmium oxide and 2-methylimidazole using a combination of mechanochemical synthesis and accelerated aging reactions.  $^1\text{H}$ - $^{111}\text{Cd}$  CP/MAS NMR and PXRD are used in tandem to monitor the reactions and identify the products. The  $^{111}\text{Cd}$  NMR spectra show the presence of an intermediate (*iCdM*) that is converted into a framework of diamondoid topology, *dia*-Cd[MeIm]<sub>2</sub> • HMeIm (*dCdM*); this transformation is observed *in situ* during the course of the NMR experiment. To the best of our knowledge, this represents the first *in situ* observation of the formation of a ZIF from mechanochemical reactions using SSNMR. PXRD reveals that the intermediate corresponds to CdIF-1 with solvent and/or HMeIm molecules within the pores of the framework that cause slight distortions in the Cd coordination environments. Solvothermal syntheses demonstrate that CdIF-1 is converted to *dCdM* in the presence of excess HMeIm, thereby confirming its identity as the intermediate observed in the NMR

experiments. PXRD also shows that ball milling provides the activation energy to initiate the reactions, but that it is an aging process that drives the formation of ZIFs. It is demonstrated that CdIF formation is achieved with milling times as short as five seconds, followed by aging at room temperature, suggesting the potential for synthetic procedures that require very low energy inputs. A reaction pathway is proposed for the mechanochemical synthesis based on the results of the NMR and PXRD experiments. NMR experiments provide detailed information about the Cd coordination environments and distortions caused by the inclusion of guest molecules, whereas PXRD is useful for phase identification. This study demonstrates the great potential for the use of NMR and PXRD methods in concert for the characterization of structures and the elucidation of reaction pathways for a plethora of MOFs and ZIFs produced via solid-state syntheses. With the use of these two techniques in tandem, it is possible to probe reaction pathways for the mechanochemical synthesis of MOFs and ZIFs.

### 3.2 Introduction

Increasing global concern regarding climate change and environmental pollution has led to the development of the field of *green chemistry*,<sup>1</sup> which seeks to reduce the negative environmental impact associated with chemical reactions and syntheses, especially those that are conducted on an industrial scale. The *Twelve Principles of Green Chemistry*, proposed by Anastas and Warner in 1998,<sup>2</sup> provide a framework in which chemical syntheses can be designed such that the undesired effects of conventional syntheses can be mitigated. Generally, chemical processes should be designed so as to limit the amount of waste produced, maximize the atom economy of reagents, reduce the

amount of solvent, use less toxic starting materials, and afford high yields with minimal energy input.<sup>3-5</sup> Traditional solvothermal syntheses (*i.e.*, heating reagents that are dissolved in large amounts of solvent) clearly do not adhere to the Twelve Principles of Green Chemistry; therefore, the development of new synthetic methodologies is of paramount importance, and represents an enormous area of active research.

Mechanochemistry<sup>6,7</sup> is an ancient synthetic technique<sup>8</sup> that has experienced a renaissance in recent years.<sup>9</sup> Mechanochemistry uses mechanical forces (*e.g.*, grinding, shearing, and stretching) to provide the activation energy to initiate and propagate chemical transformations.<sup>10</sup> Modern mechanochemical syntheses often make use of a ball mill, a device which rapidly agitates reaction vessels containing the reagents and ball bearings, in order to produce the required mechanical forces. These synthetic procedures adhere to the principles of green chemistry, as they use little or no solvent, and make use of less toxic and readily-available starting materials that are usually considered inert under normal solvothermal synthetic conditions (*e.g.*, metal oxides). Furthermore, these reactions can afford quantitative yields in reduced experimental times (often on the order of minutes or hours), greatly reducing energy expenditure. There are several proposed general models for the reaction mechanisms that occur during mechanochemical syntheses, including the hot spot theory<sup>11,12</sup> and the magma-plasma model;<sup>12</sup> it is unlikely that there is one model that applies to all mechanochemical reactions, since these would be highly dependent upon the exact reaction type, reaction conditions, starting materials, and catalytic agents.

Mechanochemistry has found use in numerous industrial applications due to heightened interest in green chemistry. As such, there is an increasing amount of research

focused on the design of new, more efficient mechanochemical syntheses; however, there has only been limited research directed at understanding the mechanisms underlying these processes (*vide infra*). Extensive research is underway to develop new methodologies and access synthetic pathways that are not accessible via solvothermal procedures. To this end, mechanochemistry has been used to synthesize metal alloys<sup>13,14</sup> and oxides,<sup>15,16</sup> organic cocrystals,<sup>17–20</sup> and pharmaceuticals,<sup>21–25</sup> as well as in the formation of C–C and C–X bonds to facilitate organic transformations.<sup>26–30</sup>

Mechanochemistry has also been used to synthesize metal-organic frameworks (MOFs),<sup>7,31,32</sup> a class of materials that have garnered much attention for their potential applications for gas storage, separation,<sup>33–37</sup> catalysis,<sup>38,39</sup> and molecular sensing.<sup>40,41</sup> Mechanochemical synthesis provides a greener, more efficient route for the production of MOFs, often affording quantitative yields in a fraction of the time required for traditional solvothermal techniques (*i.e.*, minutes or hours compared to days or weeks). Furthermore, it has been demonstrated that the addition of a small amount of solvent (< 1 mL), as in liquid assisted grinding (LAG), or using a catalytic amount of ionic salt in addition to this solvent (*i.e.*, ion- and liquid-assisted grinding, ILAG) can greatly increase the rate of formation of MOFs and allow for a tuneable selection of the chemistries and topologies of the resulting products.<sup>42–44</sup>

It is suspected that many mechanochemical reactions have pathways and mechanisms that greatly differ from those of their solvothermal analogues, due to the distinct reaction conditions in each case; therefore, it is crucial to monitor mechanochemical reactions in order to gain insight into these pathways and mechanisms. The premier technique for monitoring mechanochemical reactions is powder X-ray

diffraction (PXRD), which can easily identify the solid phases of reactants, intermediates, products, and by-products, provided their structures are known *a priori* (if they are not known, searches of crystallographic databases and/or Rietveld refinements are possible). However, PXRD has limited application for the identification of solid phases that are in low concentrations or amorphous in nature. Since the products of mechanochemical syntheses are generally nano- or microcrystalline powders, the characterization of unknown phases using single-crystal X-ray diffraction is not usually possible. *In situ* PXRD investigations have been used to observe the formation of different phases,<sup>45–47</sup> and it was determined that these reactions proceed in stages that yield products with increasing density and thermodynamic stability.<sup>48</sup>

Solid-state NMR (SSNMR) is an ideal technique for characterizing MOFs, providing detailed, molecular-level information on structure and dynamics.<sup>49–54</sup> Despite the wealth of information offered by SSNMR, reports on its application for monitoring the mechanochemical synthesis of MOFs have focused mainly on the identification of products, and not on probing the underlying reaction pathways and mechanisms. Belcher *et al.* used <sup>13</sup>C SSNMR to confirm the formation of coordination polymers using mechanochemical ligand exchange reactions,<sup>55</sup> and Katsenis *et al.* used SSNMR and PXRD to prove that an amorphous phase of a zeolitic imidazolate framework (ZIF) was able to form during a mechanochemical synthesis.<sup>46</sup> Frišćić *et al.* used a combination of <sup>15</sup>N and <sup>23</sup>Na SSNMR to verify the inclusion of salt ions into the pores of frameworks made using ILAG reactions and suggested that the salts may act as templating agents that direct the topologies of the MOF products.<sup>56</sup> To date, SSNMR has not been used to monitor the mechanochemical formation of MOFs. In addition, there have been no



reports of the characterization of the metal centres in mechanochemically-synthesized MOFs with SSNMR, however; there are reports of the characterization of the metal centres in MOFs made from solvothermal techniques.<sup>49,57–60</sup> This is surprising, given that such studies have the potential to yield detailed information on metal coordination environments and the inclusion of guest molecules into the frameworks, as well as providing better routes to structural refinements and predictions for unknown products.

In this study, we use a combination of PXRD and  $^1\text{H}$ - $^{111}\text{Cd}$  cross-polarization/magic-angle spinning (CP/MAS) SSNMR to monitor the mechanochemical synthesis of a cadmium-containing zeolitic imidazolate frameworks (*i.e.*, **CdIF-1**, **dCdM**, **yCdM**, and **aCdM**, see **Table 3.1** for sample descriptions) made from cadmium oxide (CdO) and 2-methylimidazole (HMeIm), under ILAG conditions using a catalytic amount of ammonium nitrate ( $\text{NH}_4\text{NO}_3$ ) salt and methanol (MeOH) solvent. PXRD is used to identify bulk phases and products, and to track the depletion of the reagents.  $^1\text{H}$ - $^{111}\text{Cd}$  CP/MAS provides a direct probe of the Cd coordination environments in both crystalline and amorphous phases. In addition, the  $^1\text{H}$ - $^{111}\text{Cd}$  CP/MAS NMR spectra are not obscured by signals from the starting materials (in contrast to what is commonly observed in PXRD patterns), since  $^{111}\text{Cd}$  NMR signals resulting from CP can only arise from Cd-containing species having a spatially proximate source of protons. The use of these two techniques in tandem allows for the elucidation of a reaction pathway for CdIF formation. The results of these experiments suggest that aging reactions occur within the milling jars and NMR rotors, leading to framework formation. Milling times as short as five seconds provide sufficient energy to initiate the chemical transformations, and subsequent aging of the mixtures results in quantitative yields of the framework materials. The

characterizations of structures and reaction pathways herein demonstrate that the combination of milling and aging offers the possibility of truly low-energy syntheses that are in accordance with the Twelve Principles of Green Chemistry.

**Table 3.1:** Sample names and descriptions.

<b>Sample name</b>	<b>Description</b>
<i>i</i> CdM	Intermediate formed in the mechanochemical reactions. The Cd atoms are in a tetrahedral coordination environment with MeIm– ligands
<i>d</i> CdM	<i>dia</i> -Cd[MeIm] <sub>2</sub> • HMeIm
<i>y</i> CdM	<i>yqt1</i> -Cd[MeIm] <sub>2</sub>
<i>a</i> CdM	amorphous Cd[MeIm] <sub>2</sub> framework
CdIF-1	<i>sod</i> -Cd[MeIm] <sub>2</sub>
CdIF-1 <sub>dried</sub>	CdIF-1 that has been dried under vacuum to remove guest molecules from the pores of the framework
CdIF-1 <sub>HMeIm</sub>	CdIF-1 <sub>dried</sub> that has been soaked in a saturated solution of HMeIm

### 3.3 Experimental Details

#### 3.3.1 Starting Materials

Cadmium oxide (CdO) was purchased from Strem Chemicals. 2-methylimidazole (HMeIm), unlabeled ammonium nitrate (NH<sub>4</sub>NO<sub>3</sub>), and <sup>15</sup>N-labeled ammonium nitrate (<sup>15</sup>NH<sub>4</sub><sup>15</sup>NO<sub>3</sub>) were purchased from Millipore Sigma. All starting materials were used without further purification.

#### 3.3.2 Mechanochemical Synthesis

All reactions were carried out using a Retsch MM400 ball mill at a milling frequency of 30 Hz. The total mass of starting materials for each reaction (excluding that of the methanol solvent and the 4 mol% NH<sub>4</sub>NO<sub>3</sub>) was set at 200 mg. The materials were placed in a 10 mL stainless steel milling jar with two 7 mm stainless steel ball-bearings. Cryomilling reactions were performed by placing the materials in the milling jar, and then submersing the jar in liquid N<sub>2</sub> for five to ten minutes. To limit the effects of

frictional heating, cryomilling reactions were only performed for a maximum of two minutes; if longer milling times were required, the milling was stopped and the jar was resubmersed into liquid N<sub>2</sub>.

### 3.3.3 Synthesis of *a*CdM

A sample of *y*CdM was prepared by milling CdO and HMeIm in a 1:2 ratio with 4 mol% NH<sub>4</sub>NO<sub>3</sub> and 100 μL MeOH for 30 mins. The sample was then washed with MeOH to remove any unreacted HMeIm and dried under vacuum overnight. Following the procedure of Baxter *et al.*,<sup>61</sup> the dried sample was milled for three hours to form the amorphous framework, *a*CdM. The formation of *a*CdM was confirmed by PXRD and <sup>111</sup>Cd CP/MAS NMR.

### 3.3.4 Synthesis of CdIF-1

CdIF-1 was synthesized using the modified procedure of Tian *et al.*,<sup>62</sup> as proposed by Baxter *et al.*<sup>61</sup> A mixture of 0.267 g (1 mmol) of cadmium acetate dihydrate and 0.410 g (5 mmol) of HMeIm was dissolved in 15 mL 1-butanol and placed in a Teflon-lined autoclave. The mixture was allowed to react at 140 °C for 48 hours, followed by cooling to room temperature. The product was collected by vacuum filtration and washed three times with 10 mL of EtOH. CdIF-1<sub>dried</sub> was made by heating CdIF-1 in a vacuum oven for five hours at 200 °C. CdIF-1<sub>dried</sub> was stirred in a saturated methanol solution of HMeIm for three days to yield CdIF-1<sub>HMeIm</sub>.

### 3.3.5 SSNMR Experiments

All SSNMR experiments were conducted on a Bruker Avance III HD console with an Oxford 9.4 T ( $\nu_0(^1\text{H}) = 400$  MHz,  $\nu_0(^{111}\text{Cd}) = 84.86$  MHz,  $\nu_0(^{15}\text{N}) = 40.5$  MHz) wide-bore magnet. Samples were finely ground with a mortar and pestle and tightly packed into 4 mm outer diameter (o.d.) zirconia rotors. The TopSpin 3.5pl6 software package was utilized to control all experiments and spectra were simulated using the Solid Lineshape Analysis (SOLA) module.

### 3.3.6 $^1\text{H}$ - $^{111}\text{Cd}$ CP/MAS NMR

$^{111}\text{Cd}$  SSNMR experiments were conducted using a Chemagnetics 4 mm HX MAS probe. Spectra were acquired using the variable-amplitude cross polarization (VACP) experiment under MAS conditions ( $\nu_{\text{rot}} = 5$  kHz, unless otherwise noted).<sup>63</sup> Optimized contact times and recycle delays are shown in Appendix B, **Table B1**. The  $\pi/2(^1\text{H})$  excitation pulse width was 2.5  $\mu\text{s}$ . The spin locking powers were 50 kHz for  $^1\text{H}$  and 40 kHz for  $^{111}\text{Cd}$ . TPPM  $^1\text{H}$  decoupling was used, with  $\nu_2 = 100$  kHz. 2 K of points were collected with a dwell time of 20  $\mu\text{s}$  (spectral width of 50 kHz). Peaks were referenced to  $\text{Cd}[\text{ClO}_4]_2 \cdot 6\text{H}_2\text{O}$  using  $\text{Cd}[\text{NO}_3]_2 \cdot 4\text{H}_2\text{O}$  as a secondary reference ( $\delta_{\text{iso}} = -100$  ppm).

While  $^{113}\text{Cd}$  (NA = 12.22%,  $\gamma = -9.487$  MHz/T) is usually preferred over  $^{111}\text{Cd}$  (NA = 12.80 %,  $\gamma = -9.069$  MHz/T) for NMR experiments,  $^{113}\text{Cd}$  NMR spectra acquired at 9.4 T are subject to interfering, semi-coherent signals from local FM radio stations. For this reason,  $^{111}\text{Cd}$  was chosen as the target nuclide, without incurring any significant losses in signal-to-noise.

### 3.3.7 $^{15}\text{N}$ MAS SSNMR

$^{15}\text{N}$  SSNMR experiments were conducted using a Chemagnetics 4 mm HXY T3-style MAS probe. A MAS spinning rate of  $\nu_{\text{rot}} = 5$  kHz was used in all experiments. Spectra were acquired using a Bloch decay pulse sequence with an optimized  $90^\circ$  pulse length of  $5.25 \mu\text{s}$  and recycle delays of 300 s for  $^{15}\text{NH}_4^{15}\text{NO}_4$  and 120 s for  $\mathbf{1}_{30\text{m}}$ . Signal averaging was completed using 8 and 456 transients for  $^{15}\text{NH}_4^{15}\text{NO}_3$  and  $\mathbf{1}_{30\text{m}}$ , respectively. Chemical shifts were referenced to the  $\text{NO}_3^-$  of  $\text{NH}_4\text{NO}_3$  peak at  $-4.0$  ppm, relative to  $\text{CH}_3\text{NO}_2$  at 0.0 ppm.

### 3.3.8 Powder X-ray Diffraction (PXRD)

PXRD experiments were conducted using a Bruker Discover D8 diffractometer equipped with a  $\text{Cu-K}_\alpha$  source operating at 40 kV and 40 mA. A Bruker AXS HI-STAR area detector was used and patterns were collected using General Area Detector Diffraction System (GADDS) software with the detector positioned at  $2\theta = 18^\circ$  and  $48^\circ$ . Powder patterns were processed and simulated using Dash 3.3.6 and CrystalDiffract 6.7.1 software packages. Crystal structures and lattice planes were visualized using CrystalMaker 10.0.8.

### 3.3.9 Void volume calculations

The void volume and percentage of volume of the unit cell were calculated using Mercury 3.9. Calculations determine the volume accessible by solvent molecules using a  $1.2 \text{ \AA}$  probe (*i.e.*, the volume of spaces that are occupied by a fictitious molecule with a  $1.2 \text{ \AA}$  radius). Where applicable, atoms comprising guest molecules (*i.e.*, water or

HMeIm) were removed from the pores prior to the calculations. Calculations were completed on the following crystal structures found in the Cambridge Structural Database (CSD): *sod*-Zn[MeIm]<sub>2</sub> (CSD code: OFERUN03),<sup>64</sup> *kat*-Zn[MeIm]<sub>2</sub> (OFERUN08),<sup>46</sup> *dia*-Zn[MeIm]<sub>2</sub> (OFERUN01),<sup>65</sup> *sod*-Cd[MeIm]<sub>2</sub> (**CdIF-1**, GUPBUP),<sup>62</sup> *dia*-Cd[MeIm]<sub>2</sub> • HMeIm (**dCdM**, as determined in Chapter 2), *yqt1*-Cd[MeIm]<sub>2</sub> (**yCdM**, GUPBOJ).<sup>62</sup>

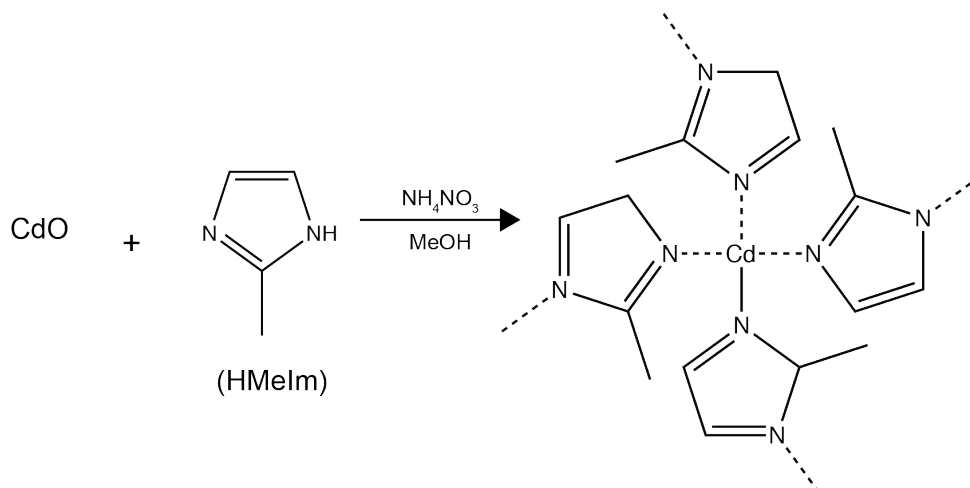
### 3.4 Results and discussion

#### 3.4.1 General overview of syntheses

The mechanochemical syntheses discussed herein involve the formation of cadmium-imidazolate frameworks (CdIFs) under different reaction conditions (**Table 3.2**). **1-3** involve the ILAG synthesis of CdIFs from cadmium oxide (CdO) and 2-methylimidazole (HMeIm) with 4 mol% (with respect to CdO) of ammonium nitrate (NH<sub>4</sub>NO<sub>3</sub>) and methanol as a solvent (**Scheme 3.1**). In **4**, an amorphous framework (**αCdM**) is reacted with one equivalent of HMeIm. The use of CdO (as opposed to ZnO) in CdIF synthesis has a twofold purpose: (i) the longer Cd–N bonds may allow for the formation of frameworks with topologies not found in analogous Zn-containing ZIFs,<sup>62</sup> and (ii) the <sup>111</sup>Cd nuclide is a far more receptive NMR nuclide than <sup>67</sup>Zn, and is therefore a much better spectroscopic tag for monitoring the mechanochemical formation of ZIFs.

**Table 3.2:** Summary of the reagents and conditions used in the mechanochemical syntheses.

Reaction	Summary
<b>1</b>	CdO + 2 eq. HMeIm + 4mol% NH <sub>4</sub> NO <sub>3</sub> + 100 μL MeOH, room temperature
<b>2</b>	CdO + 2 eq. HMeIm + 4mol% NH <sub>4</sub> NO <sub>3</sub> + 50 μL MeOH, room temperature
<b>3</b>	CdO + 2 eq. HMeIm + 4mol% NH <sub>4</sub> NO <sub>3</sub> + 100 μL MeOH, cryomilling
<b>4</b>	<b>αCdM</b> + 1 eq. HMeIm



**Scheme 3.1:** General synthetic procedure for the mechanochemical formation of ZIFs using cadmium oxide (CdO) and 2-methylimidazole (HMeIm) with the addition of a catalytic amount of ammonium nitrate ( $\text{NH}_4\text{NO}_3$ ) and a small amount of methanol (MeOH) solvent.

$^1\text{H}$ - $^{111}\text{Cd}$  CP/MAS NMR experiments were used to monitor the mechanochemical reactions in order to identify the intermediates and final products. Reagents were added to the milling jars, the mixture was milled for a set amount of time, and the sample was subsequently packed into an NMR rotor. For **1** and **2**, multiple NMR spectra were acquired of a reaction mixture corresponding to a unique milling time and a fresh set of reagents. For **3** and **4**, multiple NMR spectra were acquired for a single reaction mixture corresponding to a unique milling time, but over a longer time period in order to monitor the chemical transformations that occurs as a result of aging within the NMR rotor. The  $^1\text{H}$ - $^{111}\text{Cd}$  CP/MAS spectra have signals arising only from intermediates or products of the reactions that contain Cd and a spatially proximate source of protons as a CP source (*i.e.*, there are no signals from CdO, which has no protons, nor from HMeIm, which contains no Cd). This is in contrast to PXRD patterns, where the signals from reactants, intermediates and/or products may be observed (*vide infra*).

### 3.4.2 Reaction Set 1 (CdO + 2 eq. HMeIm, 4 mol% NH<sub>4</sub>NO<sub>3</sub>, 100 μL MeOH, room temperature).

The first reaction set (**1**) used two equivalents of HMeIm for every one equivalent of Cd, reflecting the typical 1:2 Cd:MeIm ratio found in ZIFs. The reactions were conducted at room temperature and utilized the addition of MeOH and NH<sub>4</sub>NO<sub>3</sub> (see **Experimental Section** for details). The product(s) associated with each reaction is(are) denoted by the reaction time (*i.e.*, the duration for which the reaction was milled prior to NMR experiments) as a subscript on the reaction number: *e.g.*, **1**, run for 25 minutes, is denoted as **1**<sub>25m</sub>; if run for 15 seconds, it is denoted as **1**<sub>15s</sub>.

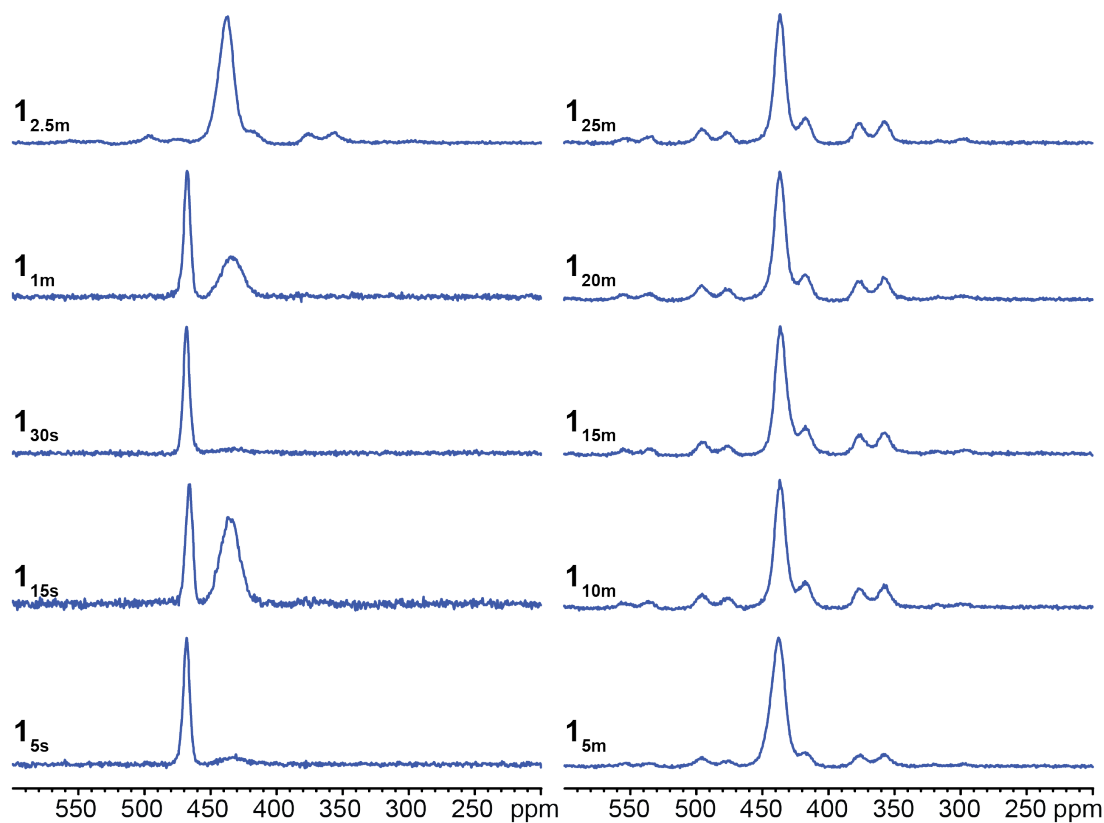


**Figure 3.1.** <sup>1</sup>H-<sup>111</sup>Cd CP/MAS NMR spectra ( $\nu_{\text{rot}} = 5$  kHz) of the products of **1** (CdO + 2 eq. HMeIm + 4 mol% NH<sub>4</sub>NO<sub>3</sub> + 100 μL MeOH) milled for different time periods.



The spectrum acquired for **1<sub>5s</sub>** (**Figure 3.1**) shows two peaks, a sharp, intense peak with isotropic chemical shift ( $\delta_{\text{iso}}(^{111}\text{Cd})$ ) of 466 ppm, and a broader, lower intensity peak at  $\delta_{\text{iso}}(^{111}\text{Cd}) = 434$  ppm (**Table 3.3**). The isotropic shift of the peak at 466 ppm is consistent with a cadmium in a four-coordinate environment with four nitrogen-donor ligands. The absence of spinning sidebands indicates a small chemical shift (CS) anisotropy, indicating an environment with a high degree of tetrahedral symmetry (*i.e.*, the Cd–N bond lengths and N–Cd–N angles are all very similar). The signal with  $\delta_{\text{iso}}(^{111}\text{Cd}) = 434$  ppm is very similar to that of the *dia*-Cd[MeIm]<sub>2</sub> • HMeIm (**dCdM**) framework (*cf.* Chapter 2). This CdIF has a 1:3 Cd:MeIm ratio as a result of unbound HMeIm molecules acting as framework guests. The isotropic shift is again indicative of a Cd atom in a four-coordinate environment with N-donor ligands. The broad peak width ( $\Delta\nu_{1/2} = 1330$  Hz) indicates a distribution of chemical shifts and *J*-coupling constants owing to a degree of disorder in this system, possibly due to the random orientation of the HMeIm molecules within the pores of the framework at room temperature. It is noted that there are slight differences in the values of  $\delta_{\text{iso}}(^{111}\text{Cd})$  and  $\Delta\nu_{1/2}$  reported for **dCdM** in the mechanochemical reactions described in this chapter and those obtained for the pure compound made through accelerated aging reactions (*cf.* Chapter 2), likely owing to slight differences in bond lengths and presence of guest molecules within the pores (*vide infra*).

**Table 3.3:** Experimentally measured  $^{111}\text{Cd}$  isotropic shifts, line widths, and  $J$ -coupling constants.

Compound	Site	$\delta_{\text{iso}}(^{111}\text{Cd})^a$ (ppm)	$\Delta\nu_{1/2}$ (Hz) <sup>b</sup>	$^1J(^{111}\text{Cd},^{14}\text{N})$ (Hz)
<b>Intermediate</b>	1	466(1)	485(20)	–
<b><i>dCdM</i></b> <sup>c</sup>	1	434(2)	1400(100)	–
<b><i>yCdM</i></b> <sup>c</sup>	1	437(2)	850(100)	–
	2	417(1)	1000(100)	–
	3	437(2)	850(100)	–
<b><i>aCdM</i></b>	1	433(3)	3800(400)	–
<b>CdIF-1</b>	1	475.0(2)	160(10)	140(5)
<b>CdIF-1<sub>dried</sub></b>	1	473.0(1)	75(5)	145(5)
<b>CdIF-1<sub>HMeIm</sub></b>	1	440(2)	1200(100)	–

<sup>a</sup> Isotropic shift:  $\delta_{\text{iso}} = (\delta_{11} + \delta_{22} + \delta_{33})/3$ . <sup>b</sup> Full peak width as measured at half the peak intensity. The experimental uncertainties in the last digit(s) are indicated in parenthesis. <sup>c</sup> Values obtained from reaction **1** (there are slight differences from the values obtained for the pure compounds synthesized using accelerated aging reactions described in Chapter 2, see text for details).

The  $^{111}\text{Cd}$  NMR spectrum of **1<sub>15s</sub>** has the same two peaks as that of **1<sub>5s</sub>**, but the intensity of the peak corresponding to ***dCdM*** has increased, while that of the peak at  $\delta_{\text{iso}}(^{111}\text{Cd}) = 466$  ppm appears unchanged. The spectrum of **1<sub>30s</sub>** has only the signal with  $\delta_{\text{iso}}(^{111}\text{Cd}) = 466$  ppm and no evidence of signal from ***dCdM***. This suggests that the species with  $\delta_{\text{iso}}(^{111}\text{Cd}) = 466$  ppm is possibly an intermediate (hereafter referred to ***iCdM***) in the formation of ***dCdM***.

The inconsistencies in the peak intensities of ***iCdM*** and ***dCdM*** in the early stages of **1** may be explained by three possible scenarios: (i) At the termination of the milling reaction, the sample must be transferred from the milling jar, packed into a rotor, and then placed in the NMR spectrometer. Variations in the timing of this procedure may result in the reaction being at different stages upon the start of the NMR experiment. (ii) The formation of ***iCdM*** and ***dCdM*** may be in competition after short milling times. (iii) There may be inconsistencies in the sample preparation; however, since great care was

taken in the preparation of all samples (*i.e.*, accurate measuring of all reagents and careful sample packing), we can eliminate this as a factor.

The spectrum of **1**<sub>2.5m</sub> shows the presence of **dCdM** as well as the onset of the formation of **yCdM**. The *yqtl*-framework gives rise to considerably broader patterns with larger spans ( $80 \leq \Omega \leq 280$  ppm) and  $\delta_{\text{iso}}(^{111}\text{Cd}) = 417$  and 437 ppm, indicating that the four-coordinate Cd atoms are in distorted tetrahedral environments. Longer milling times result in the complete conversion of **dCdM** into **yCdM**, as indicated by the spectrum of **1**<sub>25min</sub> that reveals signals arising only from **yCdM**.

**iCdM** (with  $\delta_{\text{iso}}(^{111}\text{Cd}) = 466$  ppm) is clearly a reactive species whose formation is occurring alongside of that of the more thermodynamically stable framework structures. The isotropic shift and cadmium CS tensor parameters of the **iCdM** do not match those reported for any known Cd-containing ZIF structure. The isolation and characterization of this intermediate is necessary for gaining mechanistic insight into the mechanochemical formation of the Cd-containing ZIFs (*vide infra*).

The solvent in a liquid-assisted grinding (LAG) reaction is known to accelerate the reaction compared to dry grinding, and the choice of solvent can also influence the topologies of the products. In an attempt to slow down the mechanochemical reaction and isolate **iCdM**, different amounts of MeOH solvent were used, and the reaction mixtures were milled for five minutes before acquiring <sup>111</sup>Cd SSNMR spectra (**Figure 3.2**). The spectra of the reactions with 25  $\mu\text{L}$  and 50  $\mu\text{L}$  of MeOH (**Figures 3.2(A)** and **2(B)**, respectively) show signals only from **dCdM**, whereas signals indicating the formation of **yCdM** are observed in the spectrum of the reaction using 100  $\mu\text{L}$  of MeOH. This

indicates that a decrease in the amount of solvent results in a decrease in the rate of the reaction.

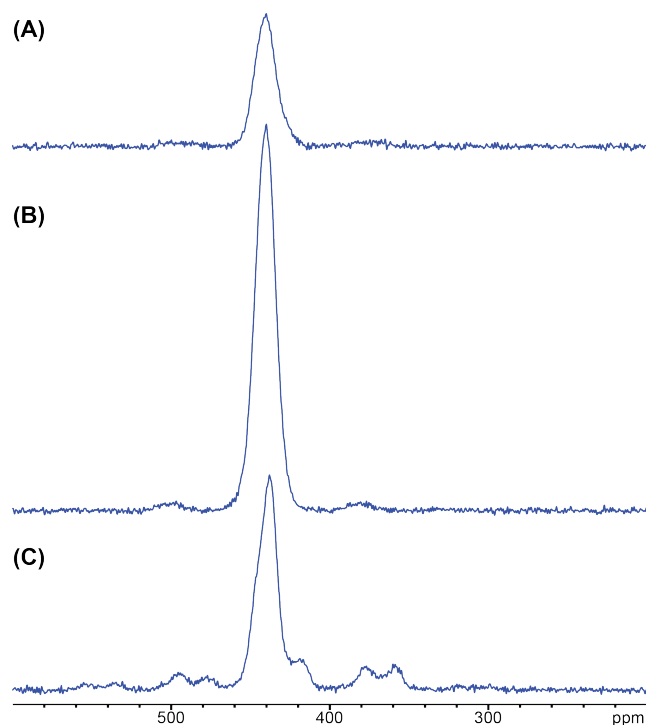


**Figure 3.2:**  $^1\text{H}$ - $^{111}\text{Cd}$  CP/MAS NMR spectra ( $\nu_{\text{rot}} = 5$  kHz) for the products of the mechanochemical reaction between CdO, 2 eq. HMeIm, and 4 mol%  $\text{NH}_4\text{NO}_3$  using (A) 25  $\mu\text{L}$ , (B) 50  $\mu\text{L}$ , and (C) 100  $\mu\text{L}$  of MeOH solvent. The reactions were milled for five minutes.

### 3.4.3 Reaction Set 2 (CdO + 2 eq. HMeIm, 4 mol% $\text{NH}_4\text{NO}_3$ , 50 $\mu\text{L}$ MeOH, room temperature)

Reaction set 2 was conducted in a similar manner to 1, except with less MeOH (50  $\mu\text{L}$  instead of 100  $\mu\text{L}$ ), in order to slow down the reaction rate and allow for the possible isolation of signals arising from *i*CdM in the final products. The spectrum of **2**<sub>15s</sub> shows signals from both *i*CdM and *d*CdM (Figure 3.3), and those of **2**<sub>30s</sub> and **2**<sub>45s</sub> again suggest that either the reactions are at different stages at the commencement of the NMR experiment or the formations of the *i*CdM and *d*CdM are in competition (*vide*

*supra*). The spectrum of **2**<sub>1m</sub> indicates the presence of *dCdM*, with no trace of the *iCdM* (in contrast to what is observed for **1**<sub>1m</sub>). Increasing the milling time results in the disappearance of the signal from *iCdM* and the formation of *dCdM* (**Figure 3.3**). Signals arising from *yCdM* are not observed until after ten minutes of milling (again in contrast to **1** where signal of *yCdM* is observed in the spectrum of **1**<sub>2.5m</sub>).

It is evident that the smaller amount of solvent results in a slower rate of formation of ZIFs in mechanochemical syntheses; however, for shorter milling times, there are inconsistencies in the intensities of the peaks corresponding *iCdM* and *dCdM*. The observation of the *iCdM* at shorter milling times suggests that this species is transient and that its isolation and identification may be difficult, unless the reaction rate can be further decreased.

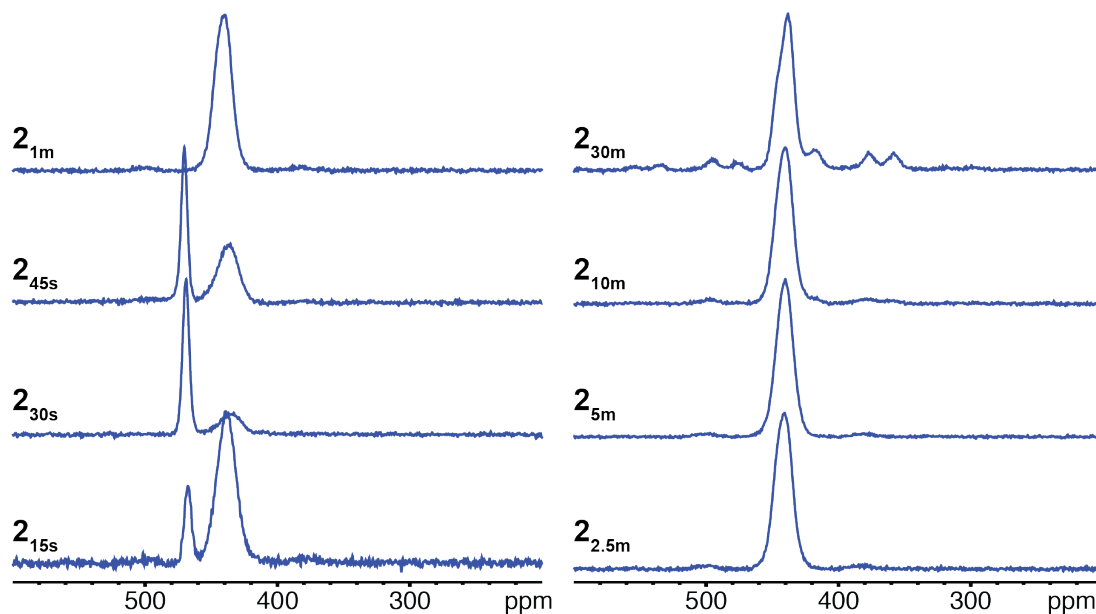


**Figure 3.3:**  $^1\text{H}$ - $^{111}\text{Cd}$  CP/MAS NMR spectra ( $\nu_{\text{rot}} = 5$  kHz) of the products of **2** ( $\text{CdO} + 2$  eq.  $\text{HMeIm} + 4$  mol%  $\text{NH}_4\text{NO}_3 + 50$   $\mu\text{L}$   $\text{MeOH}$ ) milled for different time periods.

### 3.4.4 Reaction 3 (CdO + 2 eq. HMeIm, 4 mol% NH<sub>4</sub>NO<sub>3</sub>, 100 μL MeOH, cryomilling)

A cryomilling reaction (**3**) was attempted to further slow down the reaction and isolate the intermediate. **3** used the same amounts of reagents as **1**, but was conducted at 77 K instead of room temperature. The reagents were placed in the milling jar, which was then submersed in liquid nitrogen for approximately five to ten minutes, and subsequently milled for five minutes. The products were collected and a <sup>1</sup>H-<sup>111</sup>Cd CP/MAS spectrum was acquired. It was observed that the relative intensities of the peaks corresponding to *i*CdM and *d*CdM changed over the course of the NMR experiment. First, signals corresponding to both *i*CdM and *d*CdM are present in the spectrum (**Figure B1(A)**), and at a later time, only signals from *d*CdM are observed (**Figure B1(B)**).

**3** was repeated and <sup>111</sup>Cd NMR spectra were acquired over a longer period of time in order to monitor the products of the reaction *in situ*. <sup>111</sup>Cd NMR spectra were acquired at the time intervals shown in **Figure 3.4**. The time interval is indicated by the superscript on the reaction number, *e.g.*, **3**<sup>64s</sup> denotes a spectrum for the products of **3** that was acquired for 64 s and **3**<sup>128s</sup> was acquired for an *additional* 64 s (the spectra are non-cumulative).

The spectrum of **3**<sup>64s</sup> has signals corresponding to both *i*CdM and *d*CdM. As time progresses, the signal corresponding to *i*CdM decreases in intensity and that of *d*CdM increases. The spectrum of **3**<sup>1024s</sup> shows only traces of the *i*CdM, and this signal is completely absent in the spectrum of **3**<sup>2048s</sup>. To eliminate the possibility that the conversion of *i*CdM into *d*CdM is caused by the frictional forces and heating induced by the MAS experiments, **Reaction 3** was repeated and the <sup>1</sup>H-<sup>111</sup>Cd CP experiment was

conducted under static (*i.e.*, stationary sample) conditions (**Figure B2**). The same phenomenon was observed: at the start of the experiment, signal is only observed for ***i*CdM** and signal for ***d*CdM** appears in spectra acquired after 512 seconds and longer.

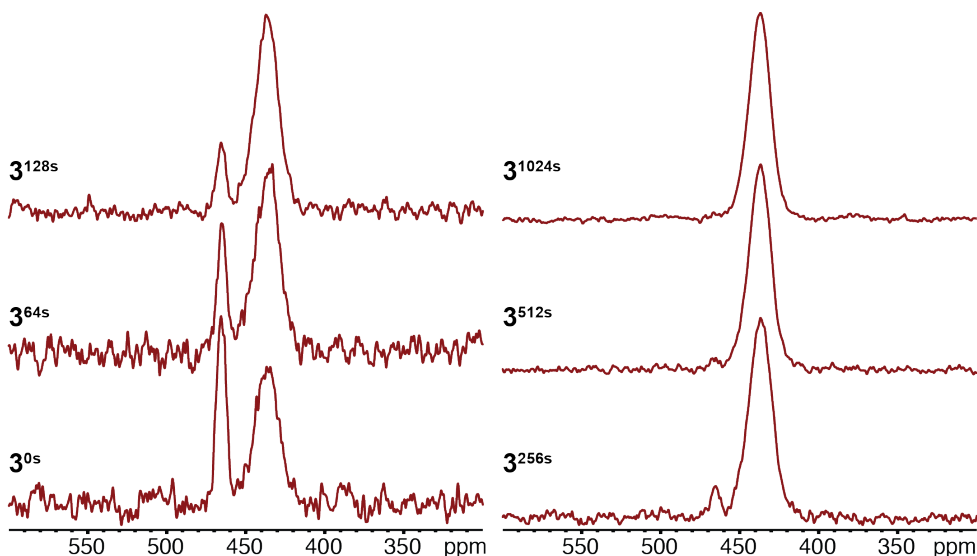


**Figure 3.4.** <sup>1</sup>H-<sup>111</sup>Cd CP/MAS NMR ( $\nu_{\text{rot}} = 5$  kHz) spectra for the products of **3** (CdO + 2 eq. HMeIm + 4 mol% NH<sub>4</sub>NO<sub>3</sub> + 100  $\mu$ L MeOH, 77 K). The spectra were acquired at different time intervals, as noted by the superscript on the reaction number (the spectra are non-cumulative).

There are several conclusions that can be made from the results of **3**. First, the NMR data suggest that ***i*CdM** is a reactive species that is being converted into ***d*CdM**. Second, chemical transformations continue to occur after the milling has ceased. This suggests that the milling provides the energy to initiate the reaction, but sustained milling is not required for the reaction to proceed (*vide infra*). Lastly, the NMR spectra of the products of the cryomilling reactions clearly indicate that the ***i*CdM** is transformed into ***d*CdM** and that no competition between their formations exists.

### 3.4.5 PXRD Analysis of Reaction Set 1

**1** was repeated and samples were analyzed with PXRD to determine if *iCdM* is a crystalline material and whether its PXRD pattern can be resolved from those of the starting materials and other products, thereby aiding in its identification (**Figure 3.5(A)**).

The PXRD patterns acquired for **1** show peaks at  $2\theta = 33$  and  $38^\circ$ , which match those in the pattern of CdO (**Figure 3.5(B)**), indicating that there is unreacted CdO in these samples. The intensities of the peaks of CdO decrease with increasing milling time, confirming that CdO is being consumed as the reaction mixture is milled for longer times. There are additional peaks in the patterns of **1** that do not correspond to either *dCdM* (**Figure 3.5(E)**) or *yCdM* (**Figure 3.5(F)**) (*i.e.*, the products of **1** as determined by  $^{111}\text{Cd}$  NMR). These peaks are present in all of the patterns of **Reaction 1**; however, they decrease in intensity as the reaction progresses. It is interesting to note that in all of the patterns of **1**, there is no evidence of the presence of *dCdM* or *yCdM*, which is in contrast to what is observed in the  $^{111}\text{Cd}$  NMR experiments.

The discrepancies between the results of the PXRD and NMR experiments (*i.e.*, the difference in the products and the completeness of the reactions) indicate that there is a fundamental difference between the samples. Despite the milling experiments being conducted under the same conditions (*i.e.*, amounts of reagents, temperature, and milling frequency), the manner in which the samples are prepared and for PXRD and NMR experiments differed. For PXRD, the products were loosely packed into glass capillaries that were left open to the atmosphere. Conversely, for the NMR experiments, the products were tightly packed into zirconia rotors that were then sealed with Teflon plugs. In addition, PXRD experiments were completed in thirty minutes whereas NMR spectra



for **1** were acquired in ninety minutes. It is possible that the different sample conditions and longer experimental times cause chemical processes to occur in the NMR rotors that do not take place in the PXRD capillaries (*vide infra*).

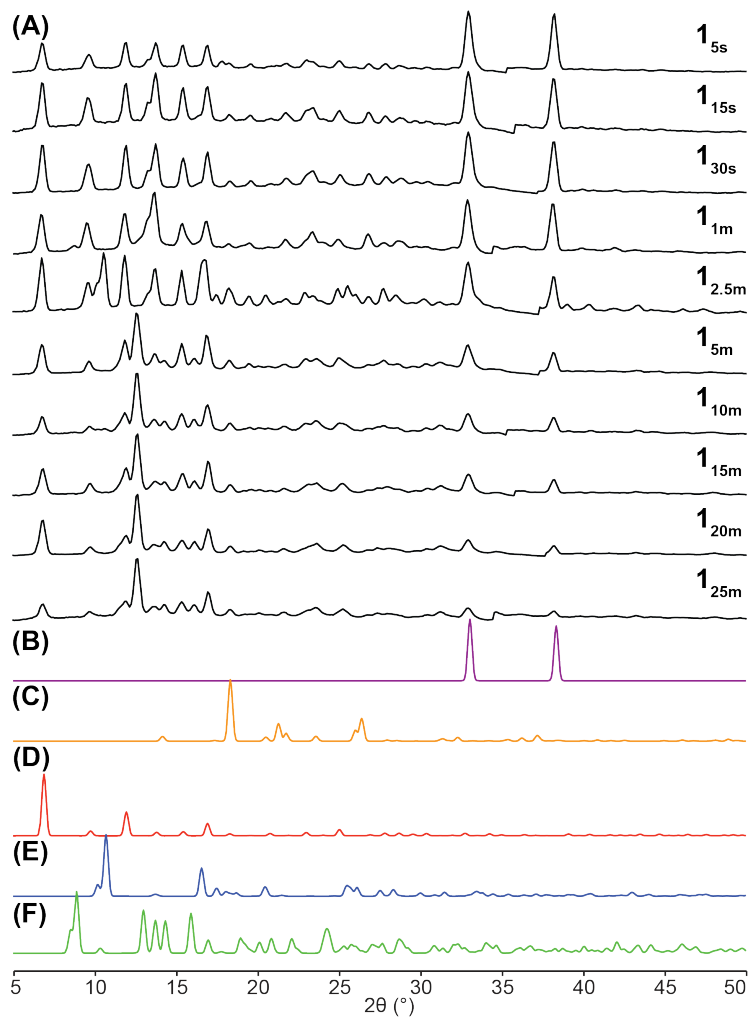


**Figure 3.5:** (A) Experimental PXRD patterns for the products of **1** milled for different time periods. Simulated PXRD patterns for (B) CdO, (C) HMeIm, (D) CdIF-1, (E) *d*CdM, and (F) *y*CdM.

The cryomilling experiments (*cf.* section 3.4.3) indicate that chemical transformations occur during the course of the NMR experiments (*i.e.*, *i*CdM is transformed into *d*CdM), whereas similar transformations are not observed in the PXRD

experiments. It is proposed that the ball milling provides the activation energy for CdIF formation to occur and that the NMR rotors act as miniature aging chambers that promote the chemical reactions. The tightly packed samples and sealed rotors do not allow for the facile evaporation of the MeOH solvent, in contrast to the loosely packed samples in the open capillaries.

To confirm the hypothesis that CdIF formation occurs after milling as a result of aging, the reaction to produce  $\mathbf{1}_{25m}$  was repeated, but the mixture was subsequently left in the milling jar for one hour (sample  $\mathbf{1}_{25m-a_{1h}}$ ) after the milling had stopped. The PXRD pattern for  $\mathbf{1}_{25m-a_{1h}}$  (**Figure 3.6(A)**) is drastically different than that of  $\mathbf{1}_{25m}$  (**Figure 3.6(B)**). The reflections corresponding to CdO and the intermediate phase have disappeared, and only reflections that match the pattern for  $\gamma\text{CdM}$  (**Figure 3.6(E)**) are present. It is also noted that the PXRD pattern for a reaction milled for 85 minutes (**Figure B3**) is almost identical to that obtained for  $\mathbf{1}_{25m-a_{1h}}$  (*i.e.*, the total amount of time that the reagents spent in the jar was the same, but the milling times were different). This effect was further demonstrated by repeating **Reaction 1** with a milling time of five seconds and allowing the products to sit in the milling jar for one day ( $\mathbf{1}_{5s-a_{1d}}$ ). The powder pattern for  $\mathbf{1}_{5s-a_{1d}}$  (**Figure 3.6(D)**) does not show any reflections corresponding to CdO, indicating that it is being consumed during the aging process. Furthermore, the pattern is similar to that simulated for  $\gamma\text{CdM}$ , suggesting that the reaction has gone to completion during aging. It is noted that there appears to be a broad, underlying feature in the PXRD patterns of  $\mathbf{1}_{5s}$  and  $\mathbf{1}_{5s-a_{1d}}$ , possibly due to an amorphous phase (*vide infra*). These results clearly demonstrate that while milling provides the activation energy required to initiate the formation of CdIFs, the reaction proceeds

without milling and is likely driven by residual solvent that has not evaporated in the NMR rotors.

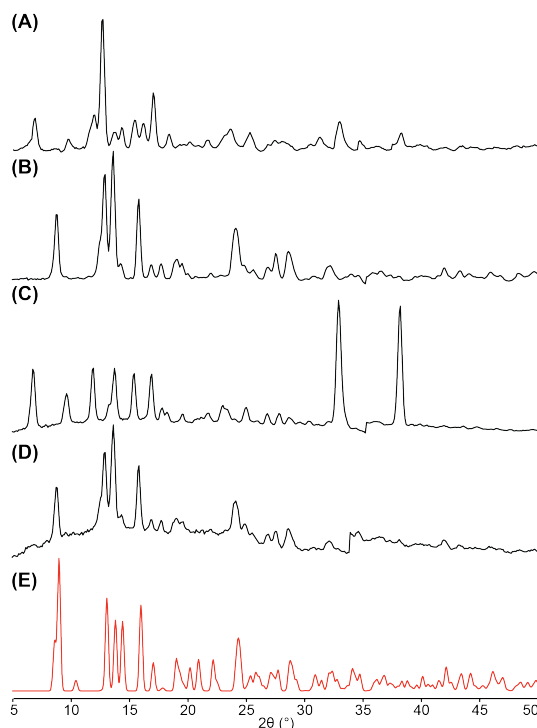


**Figure 3.6:** Experimental PXRD patterns for (A) **1<sub>25m</sub>**, (B) **1<sub>25m</sub>-a<sub>1h</sub>**, (C) **1<sub>5s</sub>**, (D) **1<sub>5s</sub>-a<sub>1d</sub>**. (E) Simulated PXRD pattern for **yCdM**.

### 3.4.6 Reaction 4 (amorphous framework + HMeIm + 4 mol% NH<sub>4</sub>NO<sub>3</sub> + 100 $\mu$ L MeOH)

The formation of ZIFs during mechanochemical synthesis and aging reactions is thought to proceed in a step-wise fashion, with structures of increased density and higher thermodynamic stability forming later during these processes. For example, the analogous mechanochemical reaction using ZnO as the starting material (**Scheme 3.2(A)**) yields first a ZIF with a sodalite topology (*sod*-Zn[MeIm]<sub>2</sub>, ZIF-8), followed by an amorphous phase (*a*-Zn[MeIm]<sub>2</sub>), then *kat*-Zn[MeIm]<sub>2</sub>, and finally, *dia*-Zn[MeIm]<sub>2</sub>.<sup>46</sup>

It is possible that an amorphous phase is being formed in the mechanochemical reaction with CdO, and upon further milling and aging, it is converted into a framework structure. Following the procedure of Baxter *et al.* for the amorphization of **CdIF-1**,<sup>61</sup> an amorphous framework (**aCdM**) was synthesized. First, **yCdM** was synthesized through a mechanochemical reaction, washed with MeOH to remove any unreacted HMeIm, dried under vacuum, then milled for three hours to generate **aCdM**. The PXRD pattern for final product (**Figure B4**) shows very broad, low-intensity signals, similar to those observed by Baxter *et al.*,<sup>61</sup> confirming the formation of an amorphous phase.

The <sup>111</sup>Cd spectra of **yCdM** and **aCdM** are shown in **Figures 3.7(A)** and **(B)**, respectively. The spectrum of **aCdM** has a single broad peak centered at  $\delta_{\text{iso}}(^{111}\text{Cd}) = 433$  ppm, with a breadth  $\Delta\nu_{1/2} = 3800$  Hz. When accounting for a difference in chemical shift referencing (*vide infra*), the isotropic shift is very similar to those observed by Baxter *et al.* This peak is consistent with a four-coordinate Cd environment, and its broad width indicates that there is a distribution of chemical shifts, likely resulting from a distribution of coordination environments with different bond lengths and angles (as is typical for the NMR spectra of many amorphous solids). The peak breadth is larger than those of any other species reported herein, and is similar to that in the <sup>113</sup>Cd NMR spectrum of the amorphous framework reported by Baxter *et al.* The signal from the amorphous framework does not correspond to that of the intermediate (both in terms of breadth and isotropic shift), precluding the description of the intermediate as an amorphous phase.

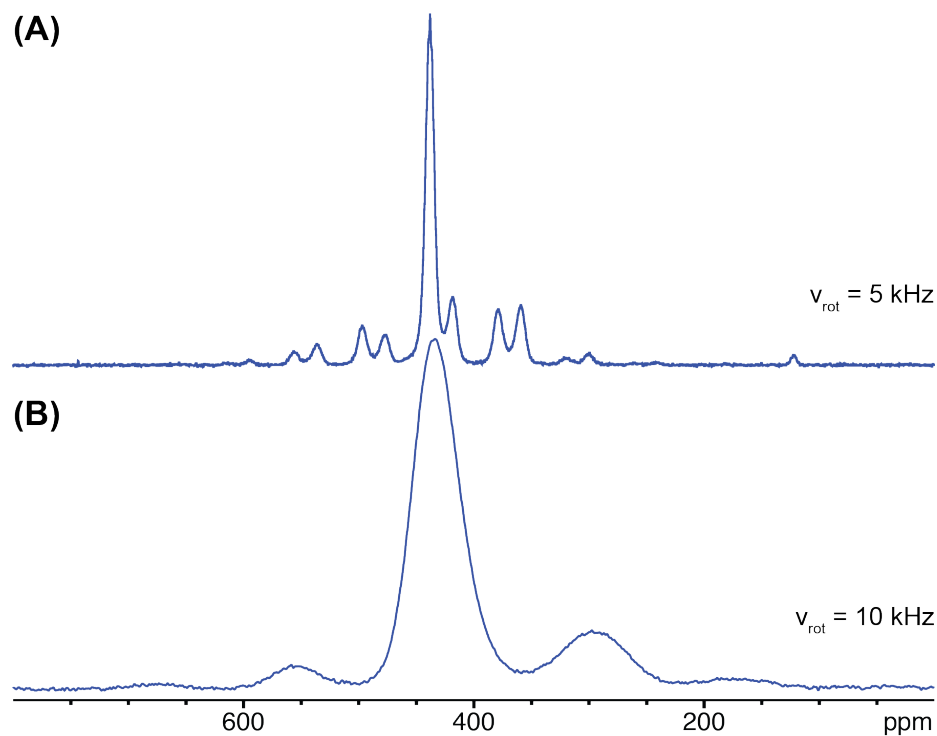


**Figure 3.7:**  $^1\text{H}$ - $^{111}\text{Cd}$  CP/MAS NMR spectra of (A)  $\gamma\text{CdM}$  obtained from mechanochemical synthesis and (B) the  $\alpha\text{CdM}$  obtained by milling a dried sample of  $\gamma\text{CdM}$  for three hours.

4 was conducted to determine if  $\alpha\text{CdM}$  is a reactive species (*i.e.*, whether it can be transformed into other framework structures), analogous to what was observed in the reaction with ZnO (*vide supra*). The amorphous framework was combined with one equivalent of HMeIm, 100  $\mu\text{L}$  of MeOH, and 4 mol%  $\text{NH}_4\text{NO}_3$ , and the mixture was milled for five minutes and subsequently packed in an NMR rotor.  $^{111}\text{Cd}$  NMR spectra were again acquired at different times to monitor reactivity (**Figure 3.8**) (N.B., the naming convention is analogous to that described above for **3**). The spectrum of  $\mathbf{4}^{1000\text{s}}$  shows the presence of the  $i\text{CdM}$ ,  $d\text{CdM}$ , and underlying, low-intensity signals from the amorphous phase. As the NMR experiment proceeds, the signals of  $i\text{CdM}$  and the

amorphous phase decrease in intensity while that of *dCdM* increases. The spectrum of **4**<sup>5000s</sup> indicates that *dCdM* is the predominant species.

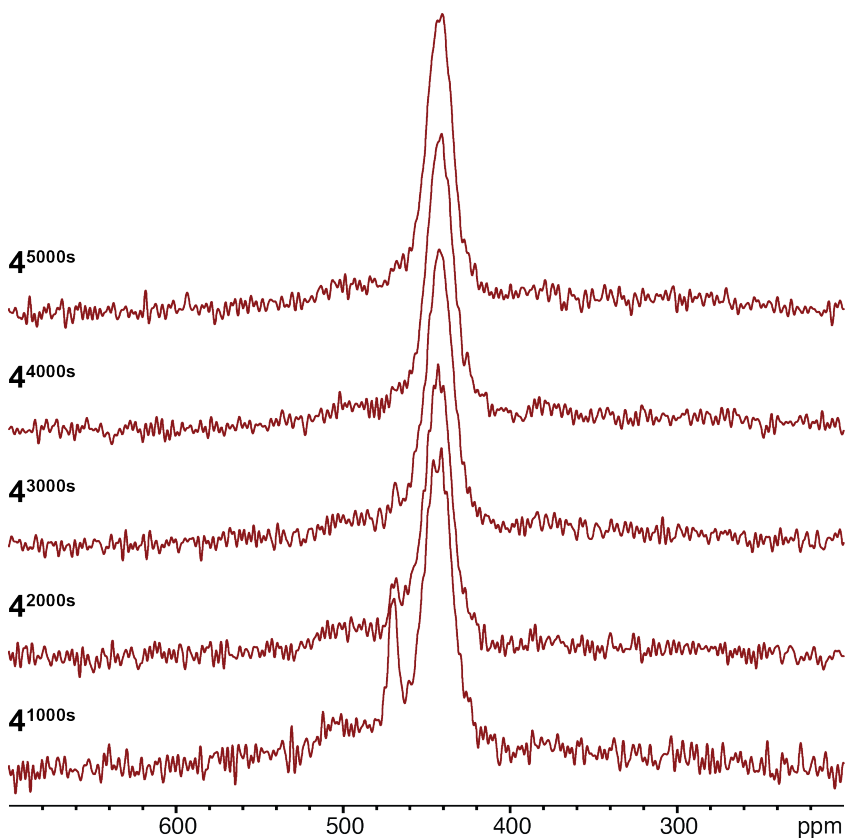


**Figure 3.8:** <sup>1</sup>H-<sup>111</sup>Cd CP/MAS NMR spectra ( $\nu_{\text{rot}} = 5$  kHz) for **4** (*aCdM* + HMeIm + 4 mol% NH<sub>4</sub>NO<sub>3</sub> + 100  $\mu$ L MeOH) acquired at different time intervals (the spectra are non-cumulative).

While there is no evidence for the formation of an amorphous phase in the <sup>111</sup>Cd NMR spectra of products from **1-3**, the PXRD patterns for **1**<sub>5s</sub> and **1**<sub>5s-a1d</sub> (Figures 3.6(C) and (D)) show a broad underlying feature that could be due to the presence of an amorphous species. As the amorphous phase can react to produce framework structures, it cannot be ruled out as an intermediate in the mechanochemical formation of ZIFs; it is possible that the amorphous phase is short-lived and therefore, is not observed in either the <sup>111</sup>Cd spectra or the PXRD experiments.

### 3.4.7 CdIF-1

The ***iCdM*** species observed in the  $^{111}\text{Cd}$  NMR spectra of products of **1-4** likely corresponds to the unknown phase identified in the PXRD experiments. A search of the Cambridge Structural Database (CSD) for cadmium-containing zeolitic imidazolate frameworks reveals that these signals correspond to **CdIF-1 (Figure 3.5(D))**, which was originally reported by Tian *et al.*<sup>62</sup> **CdIF-1** is a porous framework with a sodalite topology and Cd atoms in tetrahedral coordination environments. Baxter *et al.* reported the  $^{113}\text{Cd}$  spectrum of a sample of **CdIF-1** with a value of  $\delta_{\text{iso}}(^{113}\text{Cd}) = 408$  ppm.<sup>61</sup> The isotropic shift of ***iCdM*** reported in the current work ( $\delta_{\text{iso}}(^{111}\text{Cd}) = 466$  ppm) does not match this value (N.B., values of  $\delta_{\text{iso}}(^{113}\text{Cd})$  and  $\delta_{\text{iso}}(^{111}\text{Cd})$  in ppm are identical, provided that the same chemical shift reference is used).

A sample of **CdIF-1** was prepared using the modified synthesis of Tian *et al.*,<sup>62</sup> as proposed by Baxter *et al.*<sup>61</sup> The identity of the sample was confirmed by PXRD (**Figure B5**). The  $^{111}\text{Cd}$  spectrum of this **CdIF-1** sample (**Figure 3.9(A)**) has a single peak, corresponding to a single Cd environment (consistent with the crystal structure). The value of  $\delta_{\text{iso}}(^{111}\text{Cd}) = 475$  ppm is congruent with the tetrahedral coordination of Cd atoms by  $\text{MeIm}^-$  ligands. There is a relatively-well resolved nonet pattern arising from coupling to the four  $^{14}\text{N}$  nuclei of the HMeIm ligands ( $^1J(^{111}\text{Cd}, ^{14}\text{N}) = 140$  Hz). The absence of spinning sidebands (*i.e.*, very small CSA) reflects the near-perfect tetrahedral symmetry of the Cd coordination environment. The value of the isotropic shift reported herein is not the same as that reported by Baxter *et al.*; however, this is likely due to a difference in chemical shift referencing. Both studies reported the use of the same chemical shift scale with the primary reference, a 1 M aqueous solution of  $\text{Cd}(\text{ClO}_4)_2$ , set to 0 ppm, but differ

in the use of a secondary reference. Baxter *et al.* used a 4.5 M aqueous solution of  $\text{Cd}(\text{NO}_3)_2 \cdot 4\text{H}_2\text{O}$  ( $\delta_{\text{iso}}(^{113}\text{Cd}) = -49.41$  ppm) whereas solid  $\text{Cd}(\text{NO}_3)_2 \cdot 4\text{H}_2\text{O}$  ( $\delta_{\text{iso}}(^{111}\text{Cd}) = -100$  ppm) was used herein. We believe that the latter is more reliable as a secondary chemical shift standard, since it is not subject to changes in concentration resulting from evaporation.

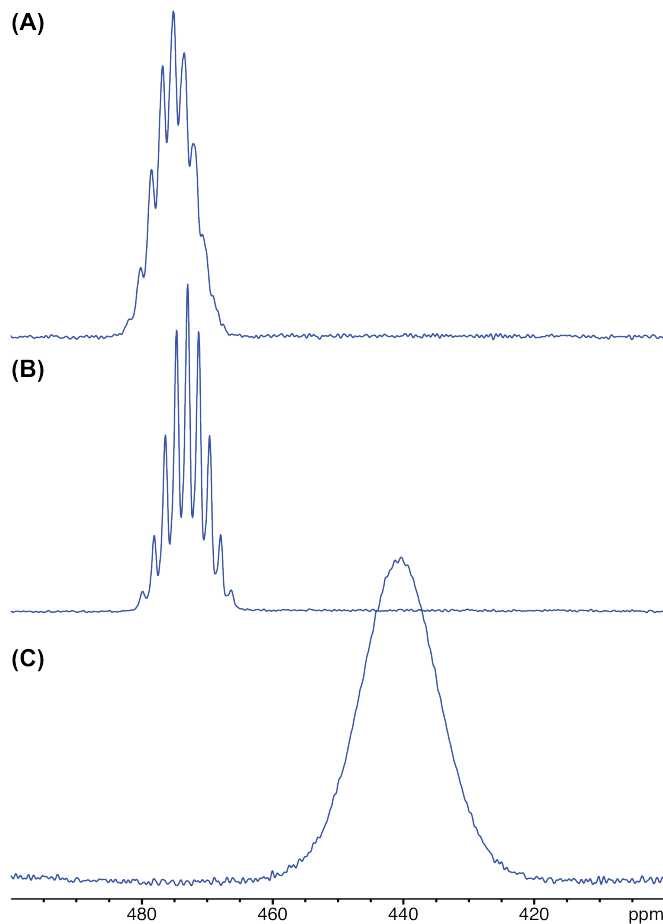


**Figure 3.9:**  $^1\text{H}$ - $^{111}\text{Cd}$  CP/MAS NMR spectra ( $\nu_{\text{rot}} = 5$  kHz) for (A) **CdIF-1<sub>as</sub>**, (B) **CdIF-1<sub>dried</sub>**, and (C) **CdIF-1<sub>HMeIm</sub>**.

**CdIF-1** was then dried under vacuum to remove any residual solvent molecules that may be trapped within the pores of the framework. The  $^{111}\text{Cd}$  spectrum of the dried sample (**CdIF-1<sub>dried</sub>**, **Figure 3.9(B)**) has a single peak with  $\delta_{\text{iso}}(^{111}\text{Cd}) = 473$  ppm and no



CSA. The nonet coupling pattern ( $^1J(^{111}\text{Cd}, ^{14}\text{N}) = 145 \text{ Hz}$ ) is better resolved than that of **CdIF-1**, indicating that the presence of guest molecules within the pores of the framework can influence the linewidth of the resulting  $^{111}\text{Cd}$  NMR spectra (*vide infra*).

The signals observed for **CdIF-1** and **CdIF-1<sub>dried</sub>** are the most similar to that reported for the intermediate in terms of both the observed isotropic shift and apparent absence of CSA. The differences in the  $^{111}\text{Cd}$  NMR spectra for these two compounds demonstrates that guest molecules in the pores of the framework can cause a change in the value of  $\delta_{\text{iso}}(^{111}\text{Cd})$  and increased in the peak widths. It is therefore possible that the intermediate is **CdIF-1** with an excess of imidazole molecules acting as framework guests. **CdIF-1<sub>dried</sub>** was stirred in a saturated methanolic solution of HMeIm to promote the inclusion of HMeIm molecules into the pores. The resulting sample (**CdIF-1<sub>HMeIm</sub>**) was filtered and then analyzed by PXRD and  $^{111}\text{Cd}$  NMR. Both  $^{111}\text{Cd}$  NMR (**Figure 3.9(C)**) and PXRD (**Figure B6**) indicate that the inclusion of HMeIm molecules into the pores of the framework of **CdIF-1** induces its transformation into ***d*CdM**.

#### 3.4.8 Identity of *i*CdM

Based on the above data, we propose that ***i*CdM**, observed in the  $^{111}\text{Cd}$  NMR spectra of **Reactions 1-4**, is **CdIF-1** with solvent and/or HMeIm molecules within the pores of the framework. The inclusion of guest molecules likely causes slight distortions of the Cd coordination environments, such that they are not perfectly tetrahedral. To summarize, this assignment is based on:

(i) The isotropic shift of ***i*CdM** ( $\delta_{\text{iso}}(^{111}\text{Cd}) = 466 \text{ ppm}$ ) is very close to those observed for **CdIF-1** ( $\delta_{\text{iso}}(^{111}\text{Cd}) = 475 \text{ ppm}$ ) and **CdIF-1<sub>dried</sub>** ( $\delta_{\text{iso}}(^{111}\text{Cd}) = 473 \text{ ppm}$ ).

Previous  $^{111}\text{Cd}$  NMR studies of ZIFs (*cf.* Chapter 2) revealed that the cadmium CS tensor

is very sensitive to differences in the coordination environment of the Cd atoms. The isotropic shift of **iCdM** is between that of **CdIF-1<sub>dried</sub>** (pores are empty) and **dCdM** (each pore contains a HMeIm molecule). Therefore, the distinct chemical shift of **iCdM** is likely caused by the inclusion of disordered guest molecules (either MeOH solvent, H<sub>2</sub>O product of the reaction, or unreacted HMeIm) within the pores of the framework, which cause slight differences in the Cd coordination environments.

(ii) The disorder of the Cd coordination environments is evidenced by the increased peak widths in the <sup>111</sup>Cd NMR spectrum of **iCdM** as compared to those of the more crystalline **CdIF-1** samples (**Figure B7**). The widths of the peaks (as measured from the centerband of the nonet coupling pattern) for **CdIF-1<sub>dried</sub>** and **CdIF-1** are  $\Delta\nu_{1/2} = 75$  and 160 Hz, respectively; therefore, inclusion of solvent molecules within the pores of the framework causes an increase in the width of the peaks in the <sup>111</sup>Cd spectra. The peak width for **iCdM** ( $\Delta\nu_{1/2} = 485$  Hz) indicates a significant degree of disorder (*i.e.*, a distribution of both chemical shifts and <sup>1</sup>J(<sup>111</sup>Cd, <sup>14</sup>N) *J*-couplings) due to the presence of guest molecules, which cause slight structural variations for each Cd environment.

(iii) The disorder of the Cd coordination environments is also confirmed by PXRD. The 002 lattice plane of the crystal structure of **CdIF-1** (**Figure 3.10(A)**) contains only cadmium atoms; therefore, the reflections in the PXRD patterns corresponding to this lattice plane should be broadened if the Cd positions are disordered. The peak width of the 002 reflection for **CdIF-1<sub>dried</sub>** (**Figure 3.10(B)**) is  $\Delta(2\theta) = 0.4^\circ$  whereas that for **1<sub>5s</sub>** is  $\Delta(2\theta) = 0.55^\circ$ . The peak widths of the reflection corresponding to the 011 plane, which does not contain any Cd atoms, are also compared (**Figure 3.10(C)**), and found to be the same ( $\Delta(2\theta) = 0.4^\circ$ ), indicating that the disorder is likely localized to the Cd atoms. It is

noted that while the 004 lattice planes also contain Cd atoms, the intensities of the 004 reflections are too low for reasonable estimations of the peak widths to be made.

(iv) Soaking **Cd-IF<sub>dried</sub>** in a saturated solution of HMeIm causes its transformation into **dCdM**. This demonstrates that the pores of **CdIF-1** are large enough, and the framework flexible enough, to accommodate HMeIm molecules.

(v) The <sup>111</sup>Cd NMR spectra show the *in situ* conversion of **iCdM** into **dCdM** upon aging in the NMR rotor (*cf.* **Figure 3.4**). This suggests that **CdIF-1** is formed first in the mechanochemical reactions, and upon aging, unreacted HMeIm enters the pores of the framework.

### 3.4.9 Reaction pathways

It is important to comment on the reaction pathway for the mechanochemical formation of CdIFs determined herein, and compare it to the analogous reaction for forming ZIFs from ZnO. We propose the following mechanism for the mechanochemical formation of ZIFs using CdO and HMeIm (**Scheme 3.2(B)**): (i) ball milling provides the activation energy to initiate the reactions and results in the formation of **CdIF-1** (and possibly an amorphous phase). The large void volume of **CdIF-1** allows for the incorporation of solvent molecules and/or unreacted HMeIm into the pores of the framework. (ii) The inclusion of HMeIm molecules into the pores induces the transformation of **CdIF-1** into **dCdM** during the aging process. (iii) Upon further aging, **dCdM** is transformed into **yCdM**.

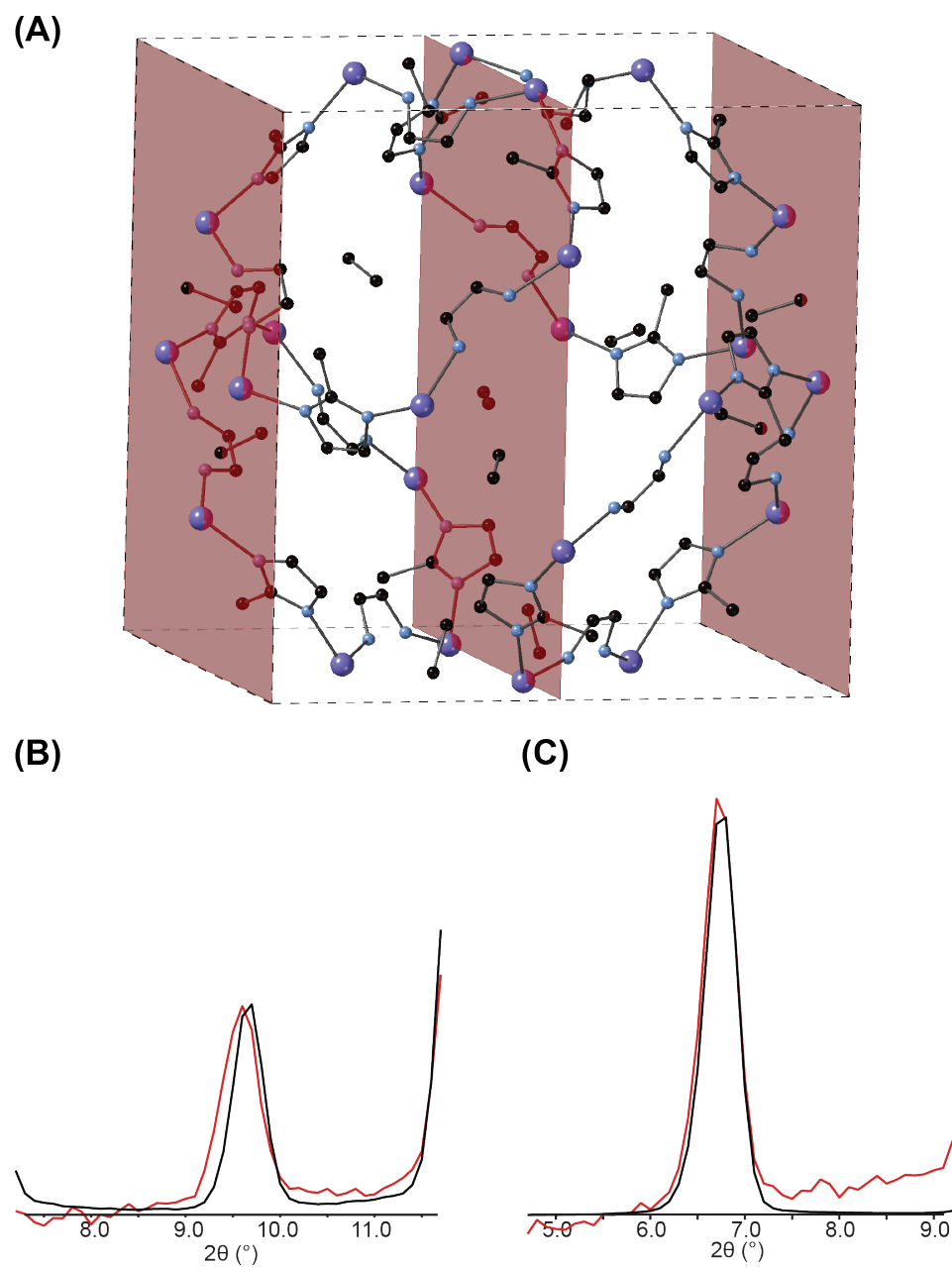
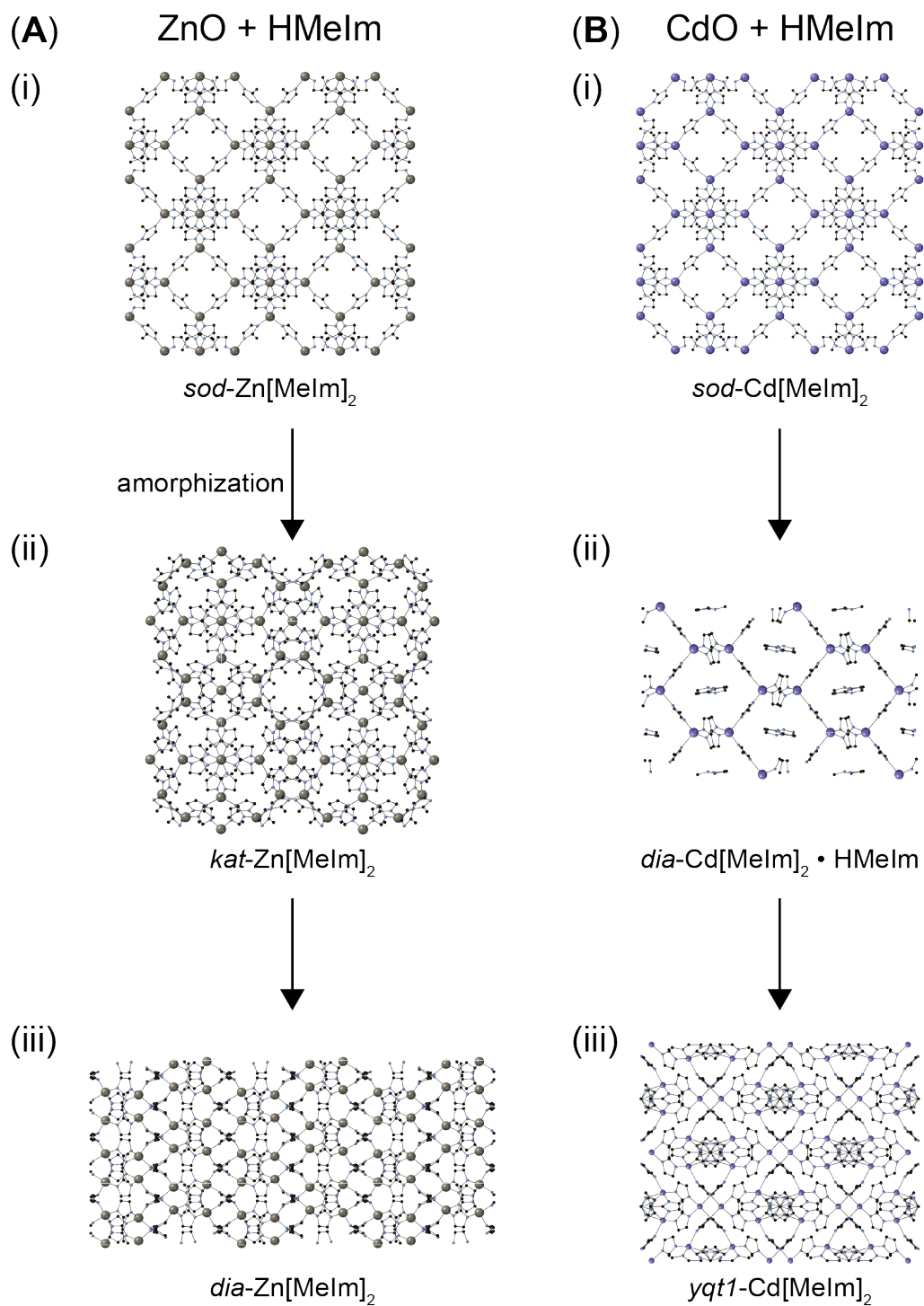


**Figure 3.10:** (A) Unit cell of CdIF-1 with the 002 lattice planes shown in red. Expansions of the PXRD patterns showing (B) the 002 reflection and (C) 011 reflection for CdIF-1<sub>dried</sub> (black trace) and 1<sub>5s</sub> (red trace).



**Scheme 3.2:** Mechanochemical reaction pathways for (A) ZnO + HMeIm forming (i) *sod-Zn[MeIm]<sub>2</sub>* (ZIF-8), (ii) *kat-Zn[MeIm]<sub>2</sub>*, and (iii) *dia-Zn[MeIm]<sub>2</sub>*. (B) CdO + HMeIm forming (i) *sod-Cd[MeIm]<sub>2</sub>*, (ii) *dia-Cd[MeIm]<sub>2</sub> · HMeIm*, and (iii) *yqt1-Cd[MeIm]<sub>2</sub>*.

The mechanochemical reaction of ZnO and HMeIm with an acetic acid solution as the solvent was previously monitored using *in situ* PXRD.<sup>46</sup> The reflections corresponding to HMeIm disappeared rapidly and those of ZnO disappeared much more slowly. The first product yielded by this reaction was *sod*-Zn[MeIm]<sub>2</sub> (also known as ZIF-8), a porous ZIF with a sodalite topology (**Scheme 3.2(A)**). Upon further milling, reflections from *sod*-Zn[MeIm]<sub>2</sub> disappeared and only those corresponding to ZnO were observed. The authors attributed this to the formation of an amorphous phase which is not visible in their PXRD patterns. Subsequent milling causes the disappearance of the reflections from ZnO and yields *kat*-Zn[MeIm]<sub>2</sub> (katsenite topology). Finally, the non-porous *dia*-Zn[MeIm]<sub>2</sub> framework is produced. It is noted that while the reaction conditions were different than those used herein (*i.e.*, acetic acid solution and no addition of salt), analogous reactions with ZnO, HMeIm, NH<sub>4</sub>NO<sub>3</sub>, and several different solvents yield only *sod*-Zn[MeIm]<sub>2</sub> as the final product.

The reaction with ZnO was determined to follow *Ostwald's Rule of Stages*, which states that in general, for a crystallization process, the least stable polymorph is formed first, followed by subsequent irreversible transformations to polymorphs of increasing thermodynamic stability.<sup>66–68</sup> In relation to MOFs and ZIFs, Ostwald's rule implies that the formation of products will proceed through a series of phases which are increasingly stable and dense (*i.e.*, the void volumes decrease as the reaction progresses). The void volumes (as determined from Mercury calculations) and the values of  $\Delta H_{\text{trans}}$  (*i.e.*, the enthalpic contributions for the transition of reactions to ZIFs arising from supramolecular interactions and pore formation) for the Zn[MeIm]<sub>2</sub> species were determined by Akimbekov *et al.*,<sup>48</sup> and are listed in **Table B2**. As the mechanochemical reaction

proceeds, the density of the products increases (*i.e.*, the void volume decreases) and the values of  $\Delta H_{\text{trans}}$  decrease, reflecting the formation of more stable phases.

The reaction studied herein has several similarities to that of ZnO and HMeIm. First, PXRD of **Reaction 1** reveals that the reflections corresponding to HMeIm disappear at a much faster rate than those of CdO, indicating that the former is consumed more readily. Second, the calculated void volumes of the CdIFs that are being formed decrease as the reaction proceeds (**Table B2**), suggesting that Ostwald's Rule of Stages applies to this synthesis. While a determination of the values of  $\Delta H_{\text{trans}}$  is beyond the scope of the current work, it is hypothesized that they will follow the same trend as those observed for the reaction with ZnO. Lastly, PXRD analysis of reactions at shorter milling times show broad, low intensity features that could be attributed to the formation of an amorphous phase. There is no evidence of an amorphous phase in the  $^{111}\text{Cd}$  NMR spectra acquired for the products of **1** and **2** with short milling times, nor in the spectra acquired for **3**, indicating that the formation of an amorphous phase may precede that of **CdIF-1**.

The main difference between the two reactions lies in the nature of the products that are formed. Both synthesis yield isostructural frameworks with sodalite topologies as the first product. The void volume of **CdIF-1** is much larger than that of *sod*-Zn[MeIm]<sub>2</sub>, likely due to the longer Cd–N bond lengths, thereby allowing for the inclusion of HMeIm molecules and subsequent transformation of **CdIF-1** into *dCdM*. The longer Cd–N bond lengths also allow for the formation of frameworks with topologies different than those of Zn ZIFs. The reactions progress in a similar fashion (*i.e.*, in stages of decreasing void volume) despite the different reaction conditions (*i.e.*, the use of a catalytic salt and different solvents). Lastly, it appears that ball milling provides the activation energy to

initiate the solid-state reaction, but aging drives the reaction towards its ultimate completion. This is demonstrated by the fact that chemical transformations occur when the product mixtures are either left in the milling jars or tightly packed into NMR rotors. At this time, it is not certain whether similar aging transformations occur in the reaction using ZnO.

#### 3.4.10 Role of the salt

Lastly, the role of the  $\text{NH}_4\text{NO}_3$  salt is discussed. The salt is believed to act as a catalyst and accelerate the formation of ZIFs in mechanochemical syntheses. The catalytic effect of the salt was demonstrated using  $^{111}\text{Cd}$  NMR to monitor two separate reactions (**Figure 3.11**). The  $^{111}\text{Cd}$  NMR spectrum of a 1:2 CdO:HMeIm reaction with 100 mL of MeOH and no  $\text{NH}_4\text{NO}_3$  that was milled for five minutes (**Figure 3.11(A)**) shows only a weak signal from  $d\text{CdM}$ . In contrast, the spectrum acquired for  $1_{5m}$  (**Figure 3.11(B)**) has much more intense signals and clearly shows the formation of  $y\text{CdM}$ .

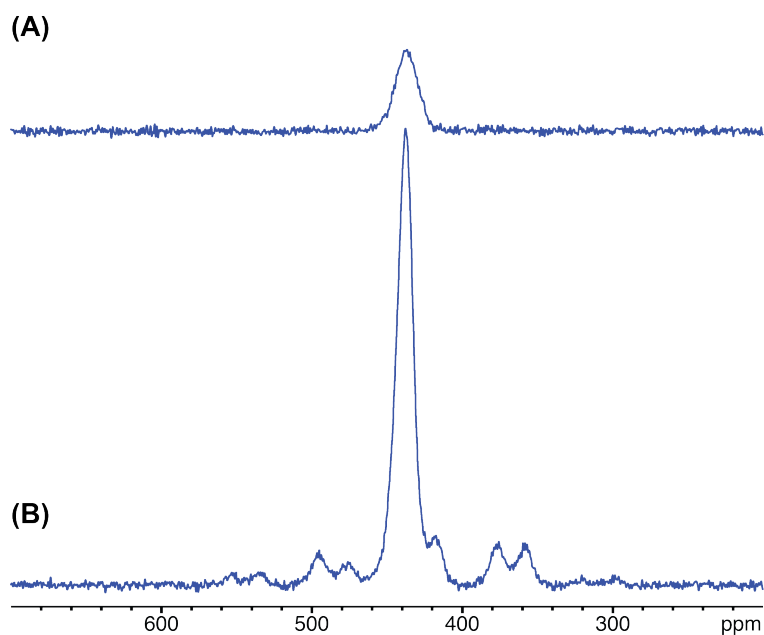


**Figure 3.11:**  $^1\text{H}$ - $^{111}\text{Cd}$  CP/MAS NMR spectra ( $\nu_{\text{rot}} = 5$  kHz) of the products **1** conducted with (A) no salt, and (B) the addition of 4 mol% of  $\text{NH}_4\text{NO}_3$ .



It has been demonstrated previously that the addition of a salt can guide the formation of products in mechanochemical reactions (*i.e.*, different salts can change the reaction pathways and produce different products). This suggests that components of the salt are included within the framework and can act as templating agents, though the mechanism of this templating effect is currently not understood.<sup>56</sup> To verify the inclusion of salt into the framework, <sup>15</sup>N direct polarization (DP) MAS NMR experiments were conducted on a sample of **1<sub>30m</sub>** using doubly-labelled <sup>15</sup>NH<sub>4</sub><sup>15</sup>NO<sub>3</sub> (**Figure 3.12**). The <sup>15</sup>N NMR spectrum of pure <sup>15</sup>NH<sub>4</sub><sup>15</sup>NO<sub>3</sub> has two peaks at  $\delta_{\text{iso}}(^{15}\text{N}) = -4$  and  $-357$  ppm, corresponding to the NO<sub>3</sub><sup>-</sup> and NH<sub>4</sub><sup>+</sup> ions, respectively (N.B. these shifts are with respect to neat CH<sub>3</sub>NO<sub>2</sub> at 0.0 ppm). The <sup>15</sup>N NMR spectrum of **1<sub>30m</sub>** has a single peak at  $-4$  ppm, corresponding to NO<sub>3</sub><sup>-</sup> ions; there is no evidence of signal arising from NH<sub>4</sub><sup>+</sup> ions (it is noted that the poor S/N in this spectrum is largely due to the low weight percentage of salt used in the reactions). The peak width in the spectrum of **1<sub>30m</sub>** is considerably broader than that of <sup>15</sup>NH<sub>4</sub><sup>15</sup>NO<sub>3</sub>, indicating that there might be a distribution of NO<sub>3</sub><sup>-</sup> ions within the pores of the framework. N.B. The distinct smell of NH<sub>3</sub>(g) was detected upon opening the milling jars for all reactions, suggesting that there is proton transferred from the NH<sub>4</sub><sup>+</sup> ions to another species resulting in the evolution of NH<sub>3</sub>(g); however, further studies are needed to identify the mechanism of this proton transfer.

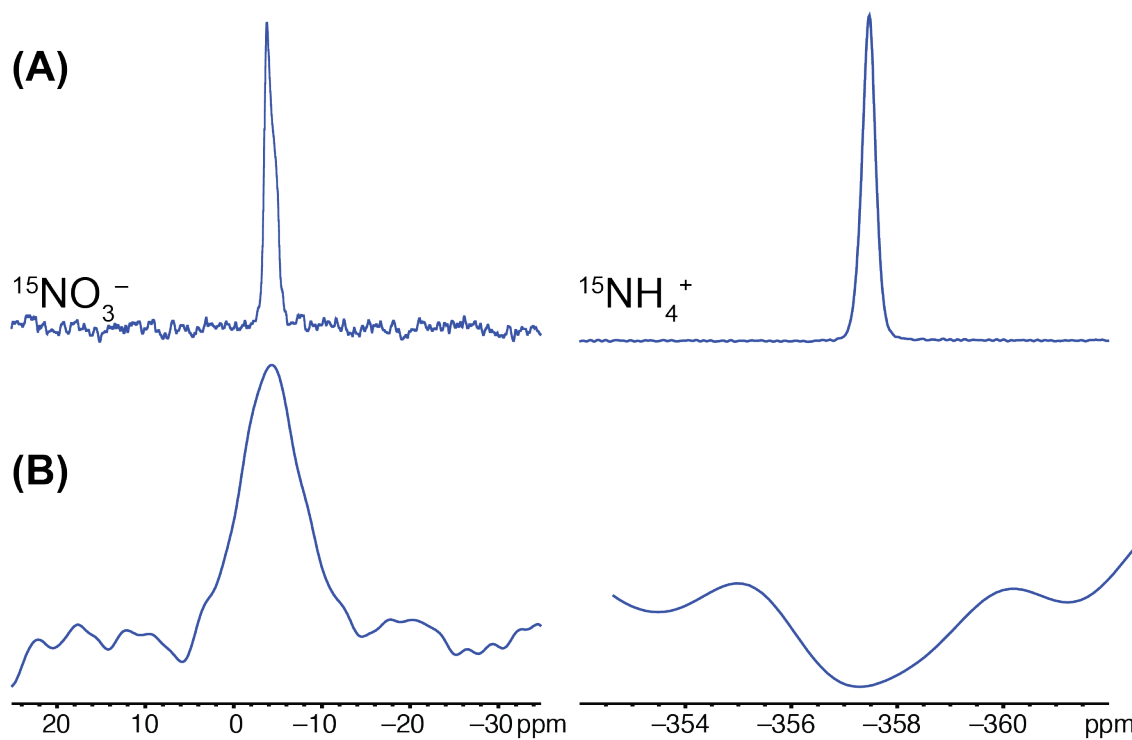


**Figure 3.12:**  $^{15}\text{N}$  DP MAS NMR spectra of (A)  $^{15}\text{NH}_4^+$   $^{15}\text{NO}_3^-$  and (B)  $^{130}\text{m}$ .

### 3.5 Conclusions

In this study, we have demonstrated that CdIFs can be easily made from readily available starting materials using mechanochemical synthesis and aging, offering an efficient, low energy alternative to traditional solvothermal synthetic methodologies.  $^{111}\text{Cd}$  NMR experiments identify the presence of *iCdM* and show its conversion into *dCdM*. PXRD analysis is used to identify the intermediate (**CdIF-1**) and confirm that aging effects are likely driving the chemical transformations observed in the NMR experiments. NMR and PXRD investigations also verify the presence of guest molecules within the pores of the frameworks, which cause slight distortions of the Cd coordination environments. It is proposed that the reaction proceeds through the following pathway: (i) ball milling provides the activation energy to initiate the reactions and results in the

formation of **CdIF-1** (and possibly an amorphous phase). The large void volume of **CdIF-1** allows for the incorporation of solvent molecules and/or unreacted HMeIm into the pores of the framework. (ii) The inclusion of HMeIm molecules into the pores induces the transformation of **CdIF-1** into **dCdM** during the aging process. (iii) Upon further aging, **dCdM** is transformed into **yCdM**. It is suggested that the chemical transformations follow Ostwald's Rule of Stages (*i.e.*, frameworks of increasing density and stability are being formed). Finally, the  $\text{NH}_4\text{NO}_3$  salt was demonstrated to have a catalytic effect on the reactions and  $^{15}\text{N}$  DP MAS NMR suggests the inclusion of  $\text{NO}_3^-$  ions into the framework. The use of NMR and PXRD in tandem will be useful for the continued study of the syntheses of MOFs, ZIFs, and other porous materials, via both mechanochemical synthesis and aging reactions, and provide detailed information on reaction pathways and mechanisms.

### 3.6 References

- (1) Cernansky, R. *Nature* **2015**, *519*, 379–380.
- (2) Anastas, P. T.; Werner, J. C. *Green Chemistry: Theory and Practice*; Oxford University Press: New York, 1998.
- (3) Poliakoff, M.; Licence, P. *Nature* **2007**, *450*, 810–812.
- (4) Clark, J. H. *Green Chem.* **1999**, *1*, 1–8.
- (5) Sanderson, K. *Nature* **2011**, *469*, 18–20.
- (6) James, S. L.; Adams, C. J.; Bolm, C.; Braga, D.; Collier, P.; Friščić, T.; Grepioni, F.; Harris, K. D. M.; Hyett, G.; Jones, W.; Krebs, A.; Mack, J.; Maini, L.; Orpen, A. G.; Parkin, I. P.; Shearouse, W. C.; Steed, J. W.; Waddell, D. C. *Chem. Soc. Rev.* **2012**, *41* (1), 413–447.
- (7) Friščić, T. *Chem. Soc. Rev.* **2012**, *41* (9), 3493.
- (8) Takacs, L. **2000**, No. January, 12–13.
- (9) Takacs, L. *Chem. Soc. Rev.* **2013**, *42* (18), 7649.
- (10) Kaupp, G. *CrystEngComm* **2003**, *5* (23), 117.
- (11) Fox, P. G. *J. Mater. Sci.* **1975**, *10* (2), 340–360.
- (12) Baláž, P. *Mechanochemistry in Nanoscience and Minerals Engineering*; Springer-Verlag: Berlin Heidelberg, 2008.
- (13) Arceo, L. D. B.; Cruz-Rivera, J. J.; Cabanas-Moreno, J. G.; Tsuchiya, K.; Umemoto, M.; Calderson, H. *Mater. Sci. Forum* **2000**, *343–346*, 641–646.
- (14) Karolus, M.; Jartych, E.; Oleszak, D. *Acta Phys. Pol., A.* **2002**, *102*, 253–258.
- (15) Fuentes, A. F.; Takacs, L. *J. Mater. Sci.* **2013**, *48* (2), 598–611.
- (16) Šepelák, V.; Düvel, A.; Wilkening, M.; Becker, K.-D.; Heitjans, P. *Chem. Soc.*

- Rev.* **2013**, *42* (18), 7507.
- (17) Bučar, D.-K.; Filip, S.; Arhangeliskis, M.; Lloyd, G. O.; Jones, W. *CrystEngComm* **2013**, *15* (32), 6289.
- (18) Friščić, T.; Childs, S. L.; Rizvi, S. A. A.; Jones, W. *CrystEngComm* **2009**, *11* (3), 418–426.
- (19) Braga, D.; Maini, L.; Grepioni, F. *Chem. Soc. Rev.* **2013**, *42* (18), 7638.
- (20) Friščić, T.; Jones, W. *CrystEngComm* **2009**, *9*, 1621–1637.
- (21) Descamps, M.; Willart, J. F. *Adv. Drug Deliv. Rev.* **2016**, *100*, 51–66.
- (22) Colombo, I.; Grassi, G.; Grassi, M. *J. Pharm. Sci.* **2009**, *98*, 3961–3986.
- (23) André, V.; Hardeman, A.; Halasz, I.; Stein, R. S.; Jackson, G. J.; Reid, D. G.; Duer, M. J.; Curfs, C.; Duarte, M. T.; Friščić, T. *Angew. Chemie - Int. Ed.* **2011**, *50* (34), 7858–7861.
- (24) Chow, E. H. H.; Strobridge, F. C.; Friščić, T. *Chem. Commun. (Camb)*. **2010**, *46*, 6368–6370.
- (25) Friščić, T.; Halasz, I.; Strobridge, F. C.; Dinnebier, R. E.; Stein, R. S.; Fábíán, L.; Curfs, C. *CrystEngComm* **2011**, *13* (9), 3125.
- (26) Rodríguez, B.; Bruckmann, A.; Rantanen, T.; Bolm, C. *Adv. Synth. Catal.* **2007**, *349* (14–15), 2213–2233.
- (27) Bruckmann, A.; Krebs, A.; Bolm, C. *Green Chem.* **2008**, *10* (11), 1131.
- (28) Kaupp, G. *Top. Curr. Chem.* **2005**, *254*, 95.
- (29) Kaupp, G. *CrystEngComm* **2009**, *11* (3), 388–403.
- (30) Stolle, A.; Szuppa, T.; Leonhardt, S. E. S.; Ondruschka, B. *Chem. Soc. Rev.* **2011**, *40* (5), 2317.

- (31) Friščić, T.; Halasz, I.; Štrukil, V.; Eckert-Maksić, M.; Dinnebier, R. E. *Croat. Chem. Acta* **2012**, *85* (3), 367–378.
- (32) Užarević, K.; Wang, T. C.; Moon, S.-Y.; Fidelli, A. M.; Hupp, J. T.; Farha, O. K.; Friščić, T. *Chem. Commun.* **2016**, *52* (10), 2133–2136.
- (33) Furukawa, H.; Cordova, K. E.; O’Keeffe, M.; Yaghi, O. M. *Science (80-. )*. **2013**, *341* (6149), 1230444–1230444.
- (34) Silva, P.; Vilela, S. M. F.; Tomé, J. P. C.; Almeida Paz, F. A. *Chem. Soc. Rev.* **2015**, *44* (19), 6774–6803.
- (35) Zhou, H.-C. “Joe”; Kitagawa, S. *Chem. Soc. Rev.* **2014**, *43* (16), 5415–5418.
- (36) Li, J.-R.; Kuppler, R. J.; Zhou, H.-C. *Chem. Soc. Rev.* **2009**, *38* (5), 1477.
- (37) Li, J. R.; Ma, Y.; McCarthy, M. C.; Sculley, J.; Yu, J.; Jeong, H. K.; Balbuena, P. B.; Zhou, H. C. *Coord. Chem. Rev.* **2011**, *255* (15–16), 1791–1823.
- (38) Ma, L.; Abney, C.; Lin, W. *Chem. Soc. Rev.* **2009**, *38* (5), 1248.
- (39) Liu, J.; Chen, L.; Cui, H.; Zhang, J.; Zhang, L.; Su, C.-Y. *Chem. Soc. Rev.* **2014**, *43* (16), 6011–6061.
- (40) Chen, B.; Xiang, S.; Qian, G. *Acc. Chem. Res.* **2010**, *43* (8), 1115–1124.
- (41) Hu, Z.; Deibert, B. J.; Li, J. *Chem. Soc. Rev.* **2014**, *43* (16), 5815–5840.
- (42) Wang, P.; Li, G.; Chen, Y.; Chen, S.; James, S. L.; Yuan, W. *CrystEngComm* **2012**, *14* (6), 1994.
- (43) Yuan, W.; Friščić, T.; Apperley, D.; James, S. L. *Angew. Chemie - Int. Ed.* **2010**, *49* (23), 3916–3919.
- (44) Beldon, P. J.; Fábíán, L.; Stein, R. S.; Thirumurugan, A.; Cheetham, A. K.; Friščić, T. *Angew. Chemie - Int. Ed.* **2010**, *49* (50), 9640–9643.

- (45) Friščić, T.; Halasz, I.; Beldon, P. J.; Belenguer, A. M.; Adams, F.; Kimber, S. A. J.; Honkimäki, V.; Dinnebier, R. E. *Nat. Chem.* **2012**, *5* (1), 66–73.
- (46) Katsenis, A. D.; Puškarić, A.; Štrukil, V.; Mottillo, C.; Julien, P. A.; Užarević, K.; Pham, M.-H.; Do, T.-O.; Kimber, S. A. J.; Lazić, P.; Magdysyuk, O.; Dinnebier, R. E.; Halasz, I.; Friščić, T. *Nat. Commun.* **2015**, *6*, 6662.
- (47) Julien, P. A.; Užarević, K.; Katsenis, A. D.; Kimber, S. A. J.; Wang, T.; Farha, O. K.; Zhang, Y.; Casaban, J.; Germann, L. S.; Etter, M.; Dinnebier, R. E.; James, S. L.; Halasz, I.; Friščić, T. *J. Am. Chem. Soc.* **2016**, *138* (9), 2929–2932.
- (48) Akimbekov, Z.; Katsenis, A. D.; Nagabhushana, G. P.; Ayoub, G.; Arhangel'skis, M.; Morris, A. J.; Friščić, T.; Navrotsky, A. *J. Am. Chem. Soc.* **2017**, *139* (23), 7952–7957.
- (49) Sutrisno, A.; Terskikh, V. V.; Shi, Q.; Song, Z.; Dong, J.; Ding, S. Y.; Wang, W.; Provost, B. R.; Daff, T. D.; Woo, T. K.; Huang, Y. *Chem. - A Eur. J.* **2012**, *18* (39), 12251–12259.
- (50) Sutrisno, A.; Huang, Y. *Solid State Nucl. Magn. Reson.* **2013**, *49–50*, 1–11.
- (51) He, P.; Lucier, B. E. G.; Terskikh, V. V.; Shi, Q.; Dong, J.; Chu, Y.; Zheng, A.; Sutrisno, A.; Huang, Y. *J. Phys. Chem. C* **2014**, *118* (41), 23728–23744.
- (52) Hoffmann, H. C.; Debowski, M.; Müller, P.; Paasch, S.; Senkowska, I.; Kaskel, S.; Brunner, E. *Materials (Basel)*. **2012**, *5* (12), 2537–2572.
- (53) Lucier, B. E. G.; Chan, H.; Zhang, Y.; Huang, Y. *Eur. J. Inorg. Chem.* **2016**, *2016* (13–14), 2017–2024.
- (54) Wang, W.; Waang, W. D.; Lucier, B. E. G.; Terskikh, V. V.; Huang, Y. *J. Phys. Chem. Lett.* **2014**, *5* (19), 3360–3365.

- (55) Belcher, W. J.; Longstaff, C. A.; Neckenig, M. R.; Steed, J. W. **2002**, *2* (13), 1602–1603.
- (56) Friščić, T.; Reid, D. G.; Halasz, I.; Stein, R. S.; Dinnebier, R. E.; Duer, M. J. *Angew. Chemie - Int. Ed.* **2010**, *49* (4), 712–715.
- (57) Volkringer, C.; Loiseau, T.; Férey, G.; Morais, C. M.; Taulelle, F.; Montouillout, V.; Massiot, D. *Microporous Mesoporous Mater.* **2007**, *105* (1–2), 111–117.
- (58) Mowat, J. P. S.; Miller, S. R.; Slawin, A. M. Z.; Seymour, V. R.; Ashbrook, S. E.; Wright, P. A. *Microporous Mesoporous Mater.* **2011**, *142* (1), 322–333.
- (59) Jiang, Y.; Huang, J.; Marx, S.; Kleist, W.; Hunger, M.; Baiker, A. *J. Phys. Chem. Lett.* **2010**, *1* (19), 2886–2890.
- (60) He, P.; Lucier, B. E. G.; Terskikh, V. V.; Shi, Q.; Dong, J.; Chu, Y.; Zheng, A.; Sutrisno, A.; Huang, Y. *J. Phys. Chem. C* **2014**, *118* (41), 23728–23744.
- (61) Baxter, E. F.; Bennett, T. D.; Cairns, A. B.; Brownbill, N. J.; Goodwin, A. L.; Keen, D. A.; Chater, P. A.; Blanc, F.; Cheetham, A. K. *Dalt. Trans.* **2016**, *45*, 4258–4268.
- (62) Tian, Y.-Q.; Yao, S.-Y.; Gu, D.; Cui, K.-H.; Guo, D.-W.; Zhang, G.; Chen, Z.-X.; Zhao, D.-Y. *Chem. - A Eur. J.* **2010**, *16* (4), 1137–1141.
- (63) Peersen, O. B.; Wu, X. L.; Kustanovich, I.; Smith, S. O. *Journal of Magnetic Resonance, Series A.* 1993, pp 334–339.
- (64) Fairen-Jimenez, D.; Moggach, S. A.; Wharmby, M. T.; Wright, P. A.; Parsons, S.; Düren, T. *J. Am. Chem. Soc.* **2011**, *133* (23), 8900–8902.
- (65) Shi, Q.; Chen, Z.; Song, Z.; Li, J.; Dong, J. *Angew. Chemie - Int. Ed.* **2011**, *50* (3), 672–675.



- (66) Ostwald, W. *Zeitschrift für Phys. Chemie* **1897**, 22 (1), 289–330.
- (67) Nývlt, J. *Cryst. Res. Technol.* **1995**, 30 (4), 443–449.
- (68) Burley, J. C.; Duer, M. J.; Stein, R. S.; Vrcelj, R. M. *Eur. J. Pharm. Sci.* **2007**, 31 (5), 271–276.

# **Chapter 4: Observing Dynamics in Metal-organic Frameworks with Mechanically Interlocked Components using Solid-state NMR Spectroscopy**

## **4.1 Overview**

The design and synthesis of molecular machines represents an intensely researched area in chemistry. Mechanically-interlocked molecules (MIMs) are components of molecular machines that have been shown to exhibit motion in solution, however this motion is random and hard to control. The inclusion of MIMs into metal-organic frameworks (MOFs) offers the possibility for the creation of controlled, coherent motion at the molecular level in the solid state. Solid-state NMR (SSNMR) spectroscopy is an ideal technique for studying dynamics in a wide array of solid materials, providing information on the modes and rates of motion. Herein, the dynamics of crown ether (CE) molecules which are incorporated into a series of MOFs are studied using SSNMR, and the factors that affect the motions of the CE rings are determined. First, the dynamics of the 24-crown-6 rings in UWDM-1 (University of Windsor Dynamic Material) are reviewed as they provide a framework in which to discuss the motion of the CEs in the MOFs that follow. The rings undergo three distinct types of motion: (i) a two-site jump, (ii) partial rotation, and (iii) full rotation. The effects on the rotational motion of CE rings of different sizes and structures in the UWDM-1 series (University of Windsor Dynamic Materials) of MOFs were then studied using variable-temperature (VT)  $^2\text{H}$  SSNMR; it was found that increasingly hindered ring motion occurs for CEs of smaller sizes or with increased steric interactions due to bulkier substituents. This is followed by studies of UWDM-2 and UWDM-3, which reveal that interpenetration of MOF structures leads to

unfavourable interactions of the rings with the framework structure, thereby reducing the rates of their motion or inducing large amplitude motions of the rings. Analysis of the UWDM-porphyrin (UWDM-P) MOF series reveals that desolvation of the MOFs induces slight structural changes, which greatly impact the motion of the CE rings. Finally,  $^{13}\text{C}$  SSNMR is used to verify the shuttling motion of the CE rings within UWDM-4, the first time that such motion has been observed in the solid state. A detailed understanding of the factors that affect dynamics is crucial for the design for materials with finely tuned properties.

## 4.2 Introduction

The 2016 Nobel Prize in Chemistry was awarded to J.P. Sauvage, J.F. Stoddard, and B.L. Feringa for the design and synthesis of molecular machines (*i.e.*, molecular switches and motors).<sup>1-4</sup> A key component in certain molecular machines are mechanically-interlocked molecules (MIMs),<sup>5-7</sup> which are defined as molecular architectures held together via non-covalent interactions and whose individual components cannot be separated without the breaking of covalent bonds. The design of MIMs has often drawn upon inspiration from the well-understood motions of macroscopic objects; some examples of these include: rotaxanes (axle and ring),<sup>8-10</sup> catenanes (chains),<sup>11-13</sup> molecular knots,<sup>14-16</sup> and Borromean rings.<sup>17</sup>

MIMs have been shown to undergo a variety of different motions in solution.<sup>18</sup> [2]catenanes (the value in brackets indicates the number of components in the MIM), which are composed of two interlocked ring-shaped molecules that exhibit rotational motion.<sup>19,20</sup> [2]rotaxanes, which are comprised of a macrocyclic *molecular ring* that is threaded onto or clipped around (*i.e.*, generating a ring from a linear molecule via a ring-

closing metathesis reaction) a dumbbell-shaped *molecular axle*, can undergo rotational motions similar to those of [2]catenanes.<sup>21,22</sup> [2]rotaxanes can also display translational motion of the macrocycle along the molecular axle, provided there are multiple recognition sites on the axle with which the ring can interact (*i.e.*, the ring shuttles between recognition sites, which may have different degrees of electronic charge, hydrogen bonds, or other non-covalent interactions with the ring).<sup>23,24</sup> The design of MIMs with components whose motions can be controlled via external stimuli (*e.g.*, thermal, chemical, or photochemical processes) is crucial for their incorporation into functional molecular machines.<sup>25–27</sup> The dynamics of MIMs are frequently observed in the solution state and the relative motion of the components is incoherent (*i.e.*, random and in all directions).<sup>28,29</sup>

The ordered organization of MIMs within a solid material could allow for coherent control of the motion of these components and aid in the design of materials with finely tuned properties for purposes of designing prototypes of molecular machines. The incorporation of MIMs into the periodic framework structure of metal-organic frameworks (MOFs) offers a viable means for their precise and predictable organization.<sup>30–32</sup> The large void volumes of the pores and channels of MOFs provide the requisite space for the large amplitude motions of the dynamic macrocyclic components.<sup>33–36</sup> Furthermore, the high thermal stabilities of MOFs allow for variety of different modes and rates of motion over wide temperature ranges.<sup>37–39</sup> To this end, rotaxanes have been designed with end groups that are able to coordinate to metals, which in turn can be used to form MOFs. The general synthetic procedure for producing such MOFs is as follows (**Figure 4.1**): a macrocyclic ring (usually a crown ether) is

either clipped around or threaded onto an axle molecule containing end groups that are suitable for coordination to metal ions (*e.g.*, carboxylic acids or pyridine functional groups) to generate a [2]rotaxane. The [2]rotaxane is then combined with a source of metal ions, and in the case of pillared or mixed-linker MOFs, an organic linker, and allowed to react to generate the MOFs. This procedure results in MOFs with dynamic components incorporated in a homogeneous and ordered manner.

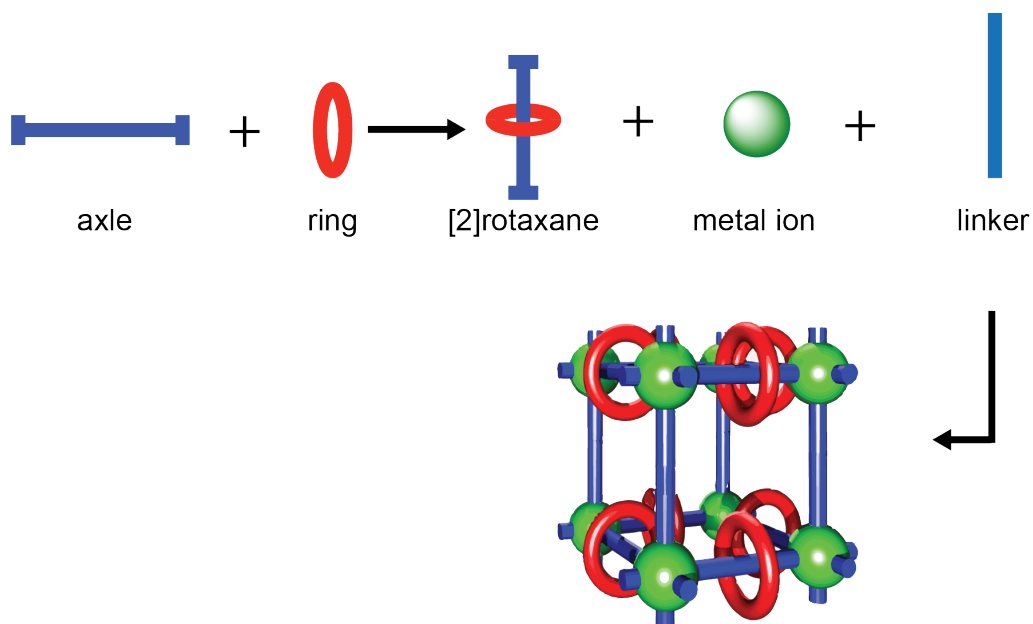


**Figure 4.1:** General procedure for the synthesis of metal-organic frameworks with dynamic interlocked components. First, a [2]rotaxane is made from an organic axle molecule and a crown ether macrocycle. The [2]rotaxane is combined with an organic linker and a metal source to form the MOF.

Structural characterization of the resulting MOFs is usually accomplished using single-crystal X-ray diffraction (SCXRD), which provides detailed information on the arrangement of atoms in the framework structure. However, in many cases the atoms in the dynamic macrocycles cannot be resolved and appear to be disordered, and virtually no information on the natures and rates of motions of these components is available.

Therefore, a reliable and unambiguous method is required for the elucidation of the types and rates of motion, as well as the various chemical and physical properties that affect these motions.

$^2\text{H}$  SSNMR is well suited to the study of molecular-level dynamics and can provide detailed information on the modes of motion and their respective rates.<sup>40,41</sup>

Deuterium is a quadrupolar nucleus ( $I = 1$ ) with a small nuclear quadrupole moment ( $Q = 0.286 \text{ fm}^2$ ).<sup>42</sup>  $^2\text{H}$  SSNMR powder patterns are strongly influenced by the quadrupolar interaction, which is the interaction of  $Q$  with the electric field gradients (EFG) at the nuclear origin. The EFG, which is dependent upon the local ground-state electron distribution about the nucleus, is described by a symmetric, traceless, second-rank tensor,  $\mathbf{\check{V}}$ , with principal components defined such that  $|V_{33}| \geq |V_{22}| \geq |V_{11}|$ . Since the EFG tensor is traceless, it can equivalently be described using just two parameters: the quadrupolar coupling constant ( $C_Q = eQV_{33}/h$ ) and the asymmetry parameter ( $\eta_Q = (V_{11} - V_{22})/V_{33}$ ).<sup>40</sup>

$^2\text{H}$  SSNMR powder patterns are characterized by two transitions that are equally displaced from the Larmor frequency, due to the first-order quadrupolar interaction (FOQI). These patterns, known as *Pake doublets*, are broad and mirror-symmetric about the isotropic chemical shift (N.B., the influences of chemical shift anisotropy (CSA) and the second-order quadrupolar interaction (SOQI) can break this mirror symmetry; however, in many cases, the magnitude of the FOQI outweighs contributions from these interactions, and the pattern appears to be symmetric).  $^2\text{H}$  SSNMR patterns of stationary samples (so-called *static patterns*) have three distinct sets of discontinuities: horns, shoulders, and feet, which are separated by frequencies  $\Delta\nu_{11}$ ,  $\Delta\nu_{22}$  and  $\Delta\nu_{33}$ , respectively (**Figure C1** in Appendix C).<sup>43</sup>  $^2\text{H}$  SSNMR powder patterns are sensitive to structural

differences that impact the EFG tensor (*i.e.*, the magnitudes of the principal components and the tensor orientation are very sensitive to different chemical structures and environments), as are most powder patterns arising from NMR experiments on quadrupolar nuclides. However,  $^2\text{H}$  SSNMR patterns are also particularly responsive to *motions* that alter the tensor components and orientations. In some cases, certain molecular-level motions result in rapid reorientations of the EFG tensor, which leads to the observation of motionally averaged principal components, and hence, a motionally averaged effective EFG tensor,  $\ddot{\mathbf{V}}^{\text{eff}}$ . The rates of motion that influence  $^2\text{H}$  SSNMR spectra are generally classified into three distinct regimes, which are based on the relative magnitudes of the exchange frequency ( $\nu_{\text{ex}}$ ) and the quadrupolar frequency ( $\nu_{\text{Q}} = 3C_{\text{Q}}/(2I(2I - 1))$ ): (1) the *slow motion limit* (SML) where  $\nu_{\text{ex}} \ll \nu_{\text{Q}}$ ; (2) the *intermediate motion regime* (IMR) where  $\nu_{\text{ex}} \approx \nu_{\text{Q}}$ ; and (3) the *fast motion limit* (FML) where  $\nu_{\text{ex}} \gg \nu_{\text{Q}}$ . Motions with rates within the SML and FML produce  $^2\text{H}$  NMR powder patterns that are relatively easily to model, since they are invariant to changes in echo spacing temperature (*i.e.*, increasing or decreasing the temperature, and hence the rate, produces no changes in the powder patterns in the FML or SML, respectively). Motions in the IMR can impact the appearance of  $^2\text{H}$  powder patterns in unusual ways, and are more challenging to model; however, careful consideration of motions in the SML and FML, and the use of an assortment of software packages for the simulation of dynamically-influenced SSNMR powder patterns, normally allow for the development of sound motional models.

$^2\text{H}$  SSNMR is ideal for the study of dynamics involving rotations, changes in torsional angles, and even chemical exchange. However, it is not suited for the

investigation of the  $^2\text{H}$ -labelled CE rings that act as molecular shuttles in MOFs, since their translational motion does not have a clearly defined impact on both the EFG tensor parameters and orientations. To observe the translational motion of molecular shuttles incorporated into MOFs, conventional NMR exchange experiments are used, where differences in the chemical shifts of a nucleus are observed as that nucleus experiences disparate chemical environments (*i.e.*, 1D and 2D exchange spectroscopy (EXSY) experiments). In the context of a [2]rotaxane molecular shuttle, the recognition site that is interacting with the macrocyclic ring has a different chemical shift than that of the non-interacting “empty” site. As the exchange rate of the shuttling motion increases, an average of the two chemical shifts is observed. The resulting NMR spectra can be simulated to extract information on the rates of the chemical exchange and the free energy of activation for the shuttling motion can be calculated using the Eyring equation:

$$\Delta G^\ddagger = -RT \ln \frac{kh}{k_b T}$$

where  $R$  is the ideal gas constant,  $T$  is temperature,  $k$  is the exchange rate,  $h$  is Planck’s constant, and  $k_b$  is Boltzmann’s constant. The comparison of free energies of activation between systems can be used to comment on the factors that affect the shuttling motion, such as ring size, axle length, steric effects, etc.

Herein, we use SSNMR to observe the thermally-driven dynamics of the crown ether molecules of [2]rotaxanes that have been incorporated into MOFs. A series of MOFs with different ring sizes, framework structures, and guest molecules within the pores are studied to determine how these factors affect ring dynamics. First,  $^2\text{H}$  SSNMR is used to study the University of Windsor Dynamic Material 1 (UWDM-1) series of MOFs to determine how the sizes and structures of the CE rings affect their motion. The



effects of framework structure on ring dynamics are investigated in a series of pillared, interpenetrated MOFs (UWDM-2 and UWDM-3). The influence of guest molecules within the pores of the framework is investigated with experiments on UWDM-porphyrin MOFs (UWDM-P1 and UWDM-P2).  $^{13}\text{C}$  VT CP/MAS and 2D CP/EXSY experiments are used to confirm shuttling motion in UWDM-4, representing the first time that shuttling motion has been observed to occur in a coherent fashion in the solid state. It is hoped that the SSNMR studies herein will provide an intimate understanding of the factors that affect the motion of MOFs with dynamic interlocked components, leading to the rational design of materials with finely-tuned properties and dynamics.

### **4.3 Experimental Details**

#### **4.3.1 Synthetic procedures**

The synthesis UWDM-1<sub>(22)</sub>,<sup>44</sup> UWDM-1<sub>(B24)</sub>,<sup>44</sup> UWDM-2,<sup>45</sup> UWDM-3,<sup>45</sup> and UWDM-4<sup>46</sup> have been reported in the literature. The synthetic procedures for UWDM-P1 and UWDM-P2 are outlined in Appendix C.

#### **4.3.2 SSNMR Studies at 9.4 T**

All SSNMR experiments were performed using either a Varian Infinity Plus or Bruker Avance III HD console, equipped with a 9.4 T Oxford magnet with resonance frequencies of:  $\nu_0(^1\text{H}) = 399.73$  MHz,  $\nu_0(^{19}\text{F}) = 376.76$  MHz,  $\nu_0(^{13}\text{C}) = 100.5$  MHz, and  $\nu_0(^2\text{H}) = 61.4$  MHz.

#### 4.3.2.1 $^2\text{H}$ SSNMR

$^2\text{H}$  SSNMR experiments for UWDM-1<sub>(22)</sub>, UWDM-1<sub>(B24)</sub>, UWDM-2- $\alpha$ , UWDM-2- $\beta$ , and UWDM-3 were conducted using a Varian Infinity Plus console and experiments for UWDM-P1, UWDM-P1<sub>d</sub>, UWDMP-2, UWDMP-2<sub>d</sub> were conducted using a Bruker Avance III HD console. A 5 mm double resonance (HX) static probe was used. Optimized  $90^\circ$  pulse lengths and recycle delays for each sample are listed in **Table C1** in Appendix C. Temperatures of the VT unit and probe were calibrated using the temperature-dependent chemical shift of  $\text{PbNO}_3$ .<sup>47,48</sup> The quadrupolar-echo pulse sequence ( $90^\circ$ - $\tau_1$ - $90^\circ$ - $\tau_2$ -acquire) was used with 30, 50, 60 or 90  $\mu\text{s}$  pulse spacings. The quadrupolar parameters of the SML spectra were determined with simulations using WSolids.<sup>49</sup> Simulations of the IMR and FML spectra were conducted using EXPRESS.<sup>50</sup>

#### 4.3.2.2 $^{19}\text{F}$ MAS Experiments

Experiments were conducted using a Varian Infinity Plus console and a Chemagnetics 2.5 mm HX MAS probe. The Hahn-echo pulse sequence was used with 5  $\mu\text{s}$   $90^\circ$  and 10  $\mu\text{s}$   $180^\circ$  pulses and a pulse spacing of 50  $\mu\text{s}$ . A 5 s cycle delayed was used for all experiments.  $^{19}\text{F}$  chemical shifts were referenced to  $\text{CFCl}_3$  (l) ( $\delta_{\text{iso}}(^{19}\text{F}) = 0.0$  ppm) using  $\text{C}_6\text{H}_5\text{F}$  (l) ( $\delta_{\text{iso}}(^{19}\text{F}) = -113.15$  ppm) as a secondary reference.

#### 4.3.2.3 $^{13}\text{C}$ SSNMR

$^{13}\text{C}$  CP/MAS SSNMR spectra for UWDM-4 were acquired using a Varian Infinity Plus console. Experiments were conducted using a Chemagnetics 4 mm HX MAS probe.

Experiments for UWDM-4 were conducted at a spinning speed of  $v_{\text{rot}} = 8$  kHz, using an optimized contact time of 2.5 ms and a recycle delay of 4 s.  $^{13}\text{C}$  chemical shifts were reference to TMS ( $\delta_{\text{iso}}(^{13}\text{C}) = 0.0$  ppm) using the high frequency peak of adamantane ( $\delta_{\text{iso}}(^{13}\text{C}) = 38.57$ ) as a secondary reference. Samples were packed into zirconia rotors and temperatures were calibrated using the  $^{207}\text{Pb}$  isotropic shift of  $\text{PbNO}_3$ .<sup>47,48</sup>

### 4.3.3 $^{13}\text{C}$ SSNMR at 21.1 T

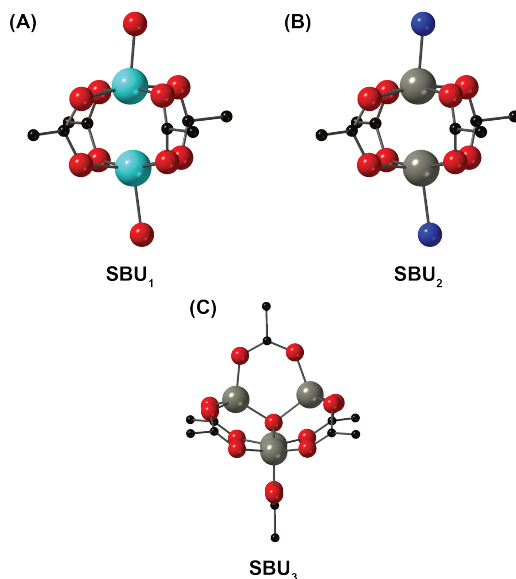
High-field VT 1D  $^1\text{H}$ - $^{13}\text{C}$  CP/MAS and  $^{13}\text{C}$  2D EXSY SSNMR spectra were acquired using a Bruker Avance II console and a 21.1 T (900 MHz) Bruker Ultra-Stabilized magnet at a resonance frequency of 226.1 MHz for  $^{13}\text{C}$ . A 4 mm H/C/N Bruker MAS probe using a MAS rate of 14.4 kHz was used for all experiments. Samples were packed into zirconia rotors and temperatures were calibrated using the  $^{79}\text{Br}$  isotropic shift of KBr.  $^1\text{H}$ - $^{13}\text{C}$  CP/MAS NMR experiments used a recycle delay of 5 s, an optimized contact time of 2.5 ms and 1024 scans. The 2D  $^{13}\text{C}$  CP/EXSY experiments were collected with 4096 points, 384 t1 increments, 64 scans and several different mixing time values.

Simulations of the spectra were performed using gNMR 5.0<sup>51</sup> to extract rates and thermodynamic parameters. Simulations used  $\nu_0(^{13}\text{C}) = 226.1$  MHz with exchange occurring between the nuclei corresponding to two signals centered at  $\delta = 152.7$  and 155.2 ppm. Gaussian lineshape functions were utilized and a static line width with a full-width at half-height (FWHH) of 180 Hz was used.

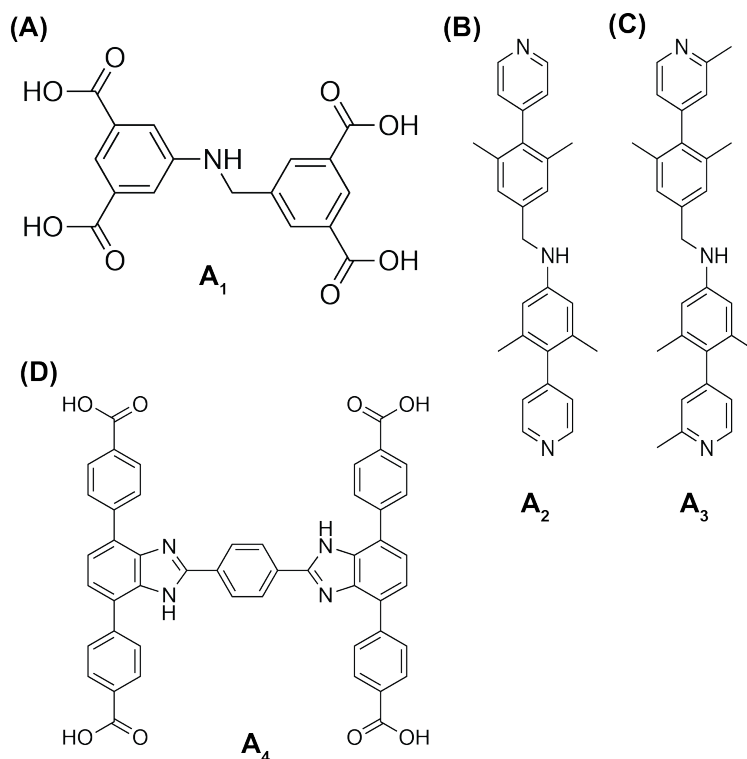
#### 4.4 Results and Discussion

The sections that follow describe the use of  $^2\text{H}$  and  $^{13}\text{C}$  SSNMR to study the dynamics of MOFs with mechanically interlocked components. The discussion first focuses on the use of VT  $^2\text{H}$  SSNMR to investigate the rotational dynamics of crown ether molecules incorporated into the framework structure of MOFs, followed by an example of how  $^{13}\text{C}$  SSNMR is used to observe shuttling motion within a MOF.

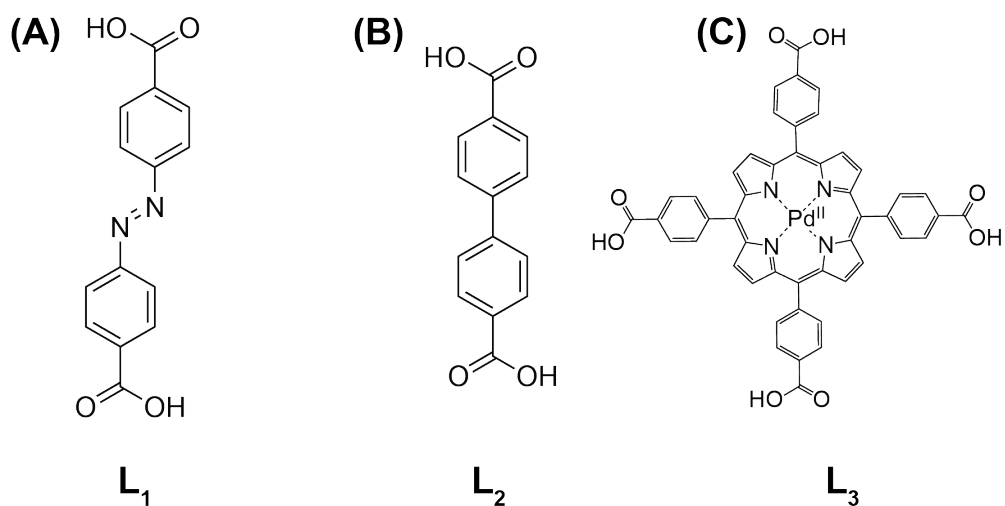
The MOFs discussed herein are very diverse in composition, structure, and topology. To facilitate the discussion, the different structural components are summarized in **Schemes 1-4**. **Scheme 1** shows the secondary building units (SBUs, *i.e.*, metal nodes or clusters) used in the MOF construction, **Scheme 2** shows the axles of the rotaxanes, **Scheme 3** shows the organic molecules for the pillared MOFs, and **Scheme 4** shows the different crown ether macrocycles.



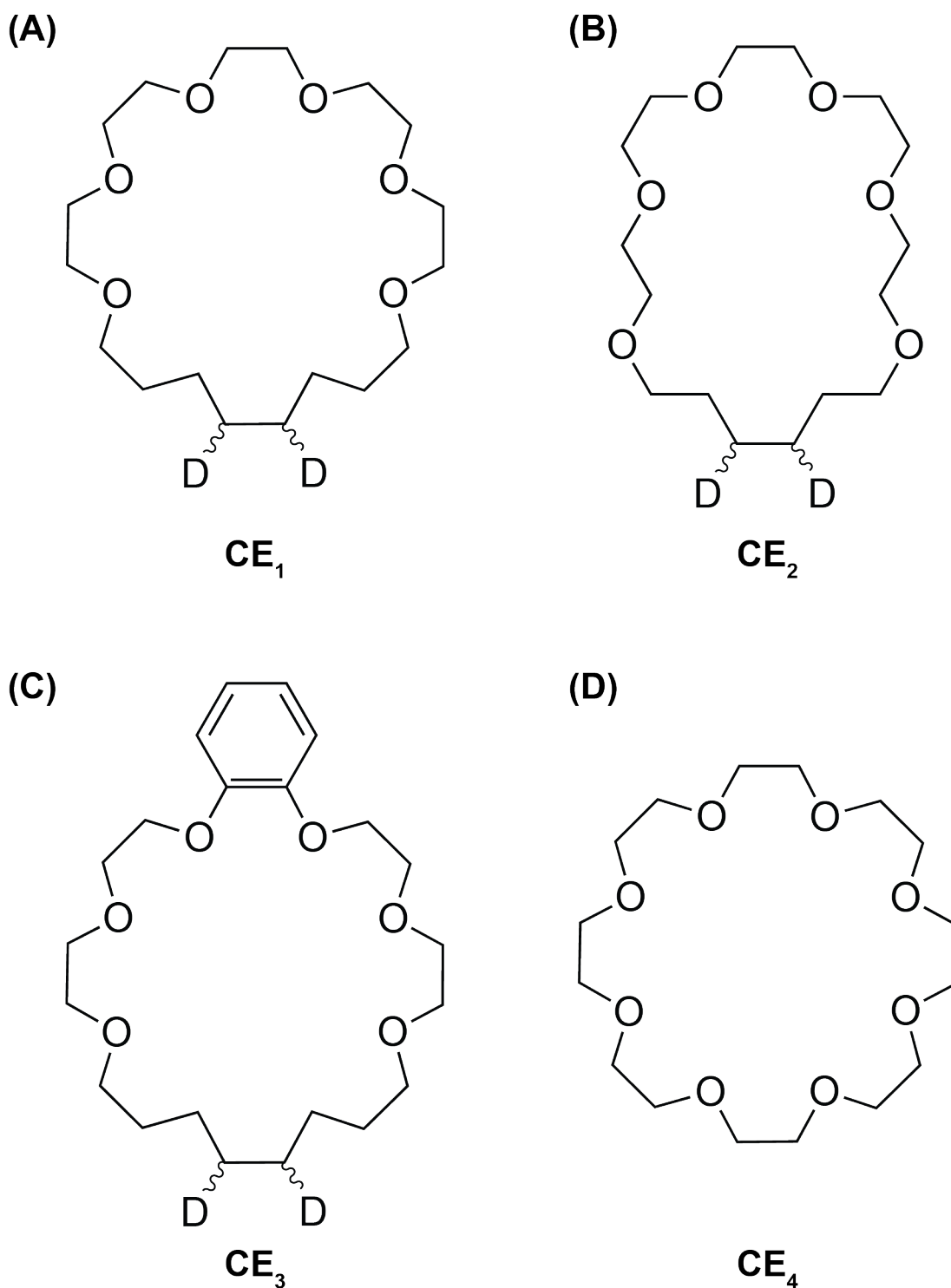
**Scheme 4.1:** Representations of the secondary building units (SBUs) used in MOF synthesis. (A) Cu paddlewheel (SBU<sub>1</sub>), (B) Zn paddlewheel (SBU<sub>2</sub>), and (C) Zn<sub>4</sub>O cluster (SBU<sub>3</sub>). Colour key: C = black, O = red, N = blue, Cu = cyan, Zn = grey.



**Scheme 4.2:** Organic axle molecules for the rotaxanes used in the synthesis of (A) UWDM-1 ( $A_1$ ), (B) UWDM-2, UWDM-3, UWDM-P1 ( $A_2$ ), (C) UWDM-P2 ( $A_3$ ), and (D) UWDM-4 ( $A_4$ ).



**Scheme 4.3:** Schematic representation of the organic linkers used in the synthesis of pillared or mixed-linker MOFs. (A) 1,4-diazophenyl-dicarboxylic acid ( $L_1$ ), (B) 1,4-biphenyl-dicarboxylic acid ( $L_2$ ), and (C) tetracarboxyphenyl-porphyrin- $Pd^{2+}$  ( $L_3$ ).



**Scheme 4.4:** Schematic diagrams of the crown ether macrocycles used in the preparation the rotaxanes. (A) [24]crown-6 ( $\text{CE}_1$ ), (B) [22]crown-6 ( $\text{CE}_2$ ), (C) benzo[24]crown-6 ( $\text{CE}_3$ ), (D) [24]crown-8 ( $\text{CE}_4$ ). For the rings that were deuterated for dynamic studies, the positions of the D (=2H) labels are indicated.

#### 4.4.1 UWDM-1 Series

##### 4.4.1.1 UWDM-1<sub>(24)</sub>

The dynamics of UWDM-1<sub>(24)</sub> have been characterized elsewhere,<sup>52</sup> but are reviewed here as they provide a framework in which to discuss the dynamics of the MOFs investigated herein. A detailed analysis of the rates of motion in UWDM-1<sub>(24)</sub> was not previously reported, but the distinct modes of motion are relevant to the present study. UWDM-1 is composed of **SBU**<sub>1</sub>, **A**<sub>1</sub> and **CE**<sub>1</sub>. The centre of the alkyl portion of the 24-crown-6 macrocycle was selectively deuterated upon reduction of the double bond with D<sub>2</sub> gas, producing both the *E* and *Z* isomers. The VT <sup>2</sup>H SSNMR spectra, analytical simulations, and depictions of the motional models are shown in **Figure 4.2**.

The low-temperature spectrum acquired at 160 K was simulated as a single site with quadrupolar parameters  $C_Q = 160(5)$  kHz and  $\eta_Q = 0.0(1)$ . These parameters are typical of a deuteron bonded to a carbon atom in an alkyl group. The fact that a single set of quadrupolar parameters is required to simulate the spectrum indicates that all deuterium environments are equivalent (within the limits of uncertainty). N.B. For all of the materials studied herein, the EFG tensor parameters and isotropic chemical shifts for individual deuterons cannot be differentiated in the <sup>2</sup>H SSNMR spectra; therefore, all simulations are conducted with a single set of NMR parameters and all deuterons undergoing the same motions. The spectrum was also simulated without the effects of any motion, indicating that if motion is occurring, it is at a rate that is too slow to affect the appearance of the <sup>2</sup>H SSNMR powder patterns (*i.e.*, motions are occurring at rates within the SML). Increasing the temperature to 225 K produces no appreciable changes in the powder patterns.

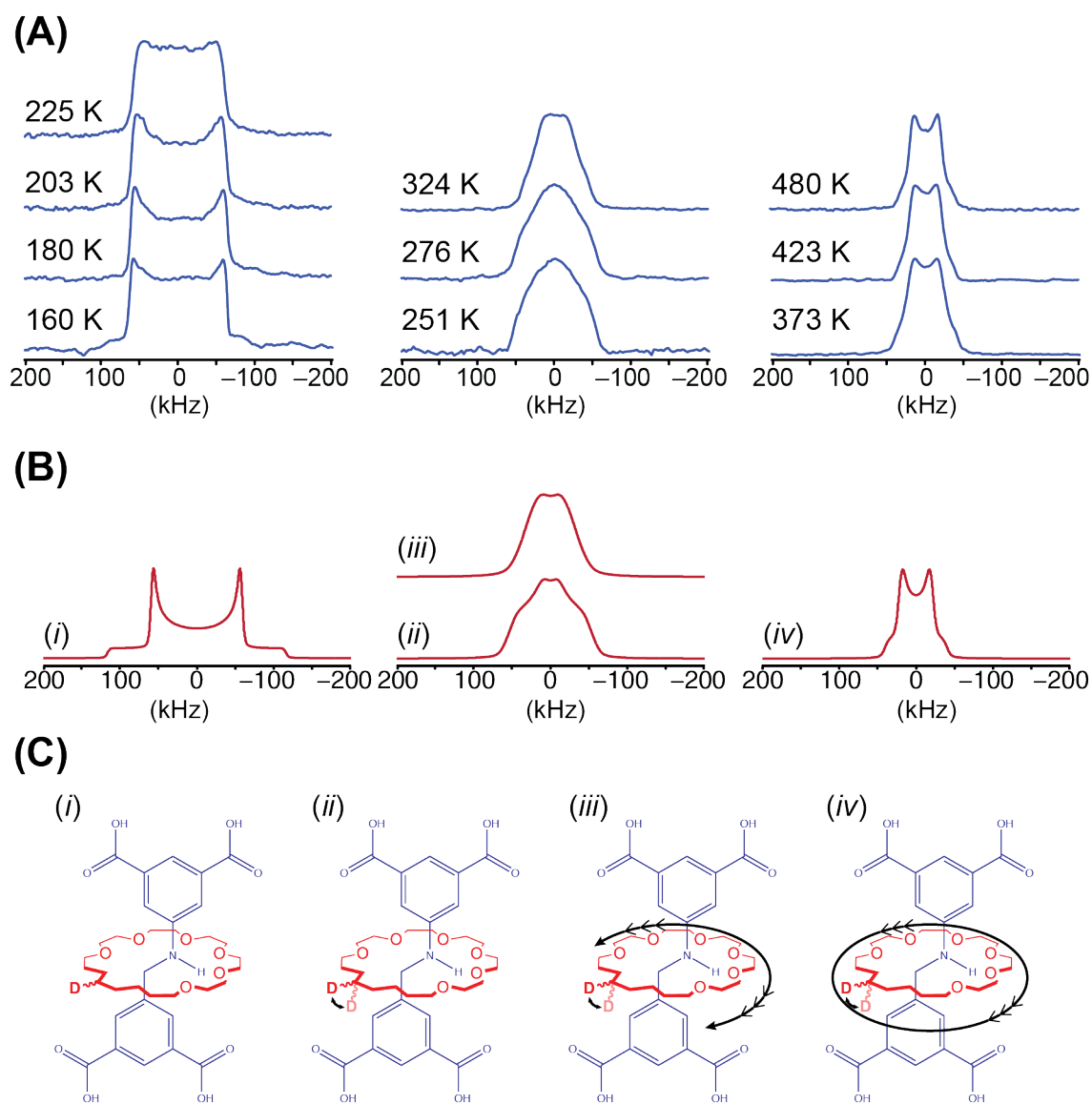


**Figure 4.2:** (A) Experimental VT  $^2\text{H}$  SSNMR powder patterns of UWDM-1<sub>(24)</sub>, (B) simulated  $^2\text{H}$  SSNMR powder patterns and, (C) accompanying depictions of the motional models used for the (i) motions that are too slow to influence the appearance of the Pake doublet (*i.e.*, in the SML), (ii) the two-site jump with  $\beta = 77^\circ$ , (iii) the two-site jump with  $\beta = 60^\circ$  combined with partial rotation of the ring over  $225^\circ$  in  $45^\circ$  steps, and (iv) two-site jumps of  $70^\circ$  combined with full rotation of the ring.

The spectrum acquired at 251 K is different than those acquired at lower temperatures and the presence of motion must be considered. This spectrum was simulated based upon a *two-site jump* of the deuterons through an angle of  $77^\circ$ . The two-



site jump mode of motion consists of the deuterons of the CD<sub>2</sub> groups moving between two positions that are related by a rotation through an angle  $\beta$  about an axis that is perpendicular to the plane of the CD<sub>2</sub> moiety (**Figure C2(B)**). This mode of motion results in powder patterns that are dependent on the jump angle,  $\beta$ , and the maximum amount of spectral narrowing that can occur is to half the width of the static spectrum in the SML. The spectra resulting from this mode of motion have one set of discontinuities that remains at the same frequencies for every value of  $\beta$ .<sup>53</sup> This set of features corresponds to the principal component of the EFG tensor that is parallel to the rotation axis (*cf.* **Figure C1**), as this component is not altered under this mode of motion (in **Figure C2**,  $V_{11}$ , which is parallel to the rotation axis of the two-site jump, is not averaged or altered by this motion). For the UWDM-1 systems, simulations featured a reorienting EFG tensor with  $V_{33}$  oriented along the C–D bond and  $V_{11}$  parallel to the rotation axis. While  $V_{11}$  is the smallest principal component of the static EFG tensor, the relative magnitudes of the components of the effective EFG tensor,  $\mathbf{V}^{\text{eff}}$ , are dependent on  $\beta$ , and average as follows:<sup>53,54</sup>

$$V_{ii}^{\text{eff}} = V_{11}$$

$$V_{jj}^{\text{eff}} = \left(\cos^2 \frac{\beta}{2}\right) V_{22} + \left(\sin^2 \frac{\beta}{2}\right) V_{33}$$

$$V_{kk}^{\text{eff}} = \left(\sin^2 \frac{\beta}{2}\right) V_{22} + \left(\cos^2 \frac{\beta}{2}\right) V_{33}$$

It is also noted that simulations of spectra under this mode of motion with rates in both the SML and IMR are not very different (**Figure C3**) aside from the presence of some additional intensity in the centres and loss of intensity on the outsides of the IMR

patterns. In many instances, the low intensities of the “feet” of the  $^2\text{H}$  powder patterns, perhaps resulting from low integrated signal intensity and a poor S/N ratio, make distinguishing spectra corresponding to the SML and IMR difficult; hence, there are large uncertainties associated with the rates estimated from these spectra.

The spectrum acquired at 324 K is considerably narrower than those acquired at lower temperatures and has a width that is less than half that of the static spectrum in the SML (**Figure 4.2(A)**). Therefore, the two-site jump model is no longer sufficient for describing the motion, and new modes of motion must be proposed. This spectrum was simulated using the *partial rotation* model, combined with two-site jumps with  $\beta = 60^\circ$ . The partial rotation model consists of the ring rotating about an axis that is perpendicular to the ring in steps separated by the angle  $\gamma$  (**Figure C4**). The jumps are made only to adjacent sites that allow for the interaction of the hydrogen bond donor on the axle with the oxygen atoms on the ring. The powder patterns resulting from partial rotation are dependent on the jump angle  $\gamma$ , as well as the angle between the rotation axis and the  $V_{33}$  component of the  $^2\text{H}$  EFG tensor (**Figure C4**). It is noted that the powder patterns resulting from partial rotation are not axially symmetric, except for the case where the product of the number of sites ( $n$ ) and the angle  $\gamma$ , is equal to  $360^\circ$ ; this is akin to *full rotation* (*vide infra*).<sup>55</sup>

The high-temperature spectrum collected at 480 K is axially symmetric, and therefore, cannot be described using the partial rotation model. This spectrum was simulated with the *full rotation model*, which consists of rotation of the crown ether about an axis with  $C_3$  symmetry of higher (**Figure C4(B)**, right-most column), which results in axially symmetric powder patterns (*i.e.*,  $\eta_Q = 0$ ). The ring is no longer constrained to

making jumps between adjacent oxygen atoms on the ring, but now has enough energy to make the full rotation in either direction. The full rotation is combined with two-site jumps with  $\beta = 60^\circ$ . The powder pattern is not influenced by changes in echo spacing, indicating that the motion is occurring at rates within the FML; however, it is difficult to comment on the relative rates of the full rotation and two-site jump motional modes. Nonetheless, it is postulated that the two-site jump motion is occurring at a higher rate than the full rotational model due to its significantly lower onset temperature.

The study of UWDM-1<sub>(24)</sub> described above is the basis on which all of the work of the UWDM series of MOFs is based. The two MOFs discussed in this section, UWDM-1<sub>(22)</sub> and UWDM-1<sub>(B24)</sub>, were made in a similar manner to UWDM-1<sub>(24)</sub> using **SBU**<sub>1</sub> and **A**<sub>1</sub> (therefore resulting in MOFs with same topology and structure (**Figure 4.3**)), but with the **CE**<sub>2</sub> and **CE**<sub>3</sub> macrocycles, respectively.

#### 4.4.1.2 UWDM-1<sub>(22)</sub>.

This system contains a smaller 22-crown-6 macrocycle (**CE**<sub>2</sub>) that was also selectively deuterated in a manner similar to the **CE**<sub>1</sub> rings in UWDM-1<sub>(24)</sub>. <sup>2</sup>H SSNMR VT experiments and analytical simulations (**Figure 4.4**) were undertaken to determine whether the smaller ring size would result in a more constrained (*i.e.*, less mobile) ring, or if the larger void volume resulting from the smaller ring size would in fact result in a less constrained (*i.e.*, more mobile) ring.

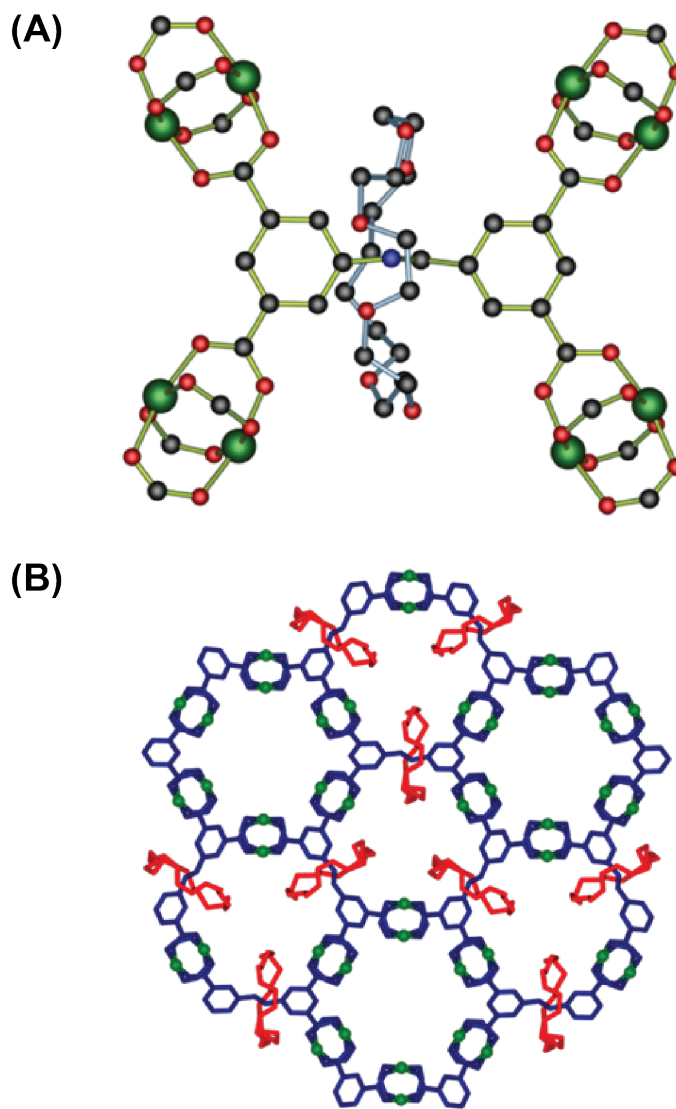


**Figure 4.3:** (A) Ball-and-stick representation of the [2]rotaxane ligand in UWDM-1<sub>(22)</sub>, which is composed of A<sub>1</sub> and CE<sub>2</sub> and coordinated to SBU<sub>1</sub> (colour key: C = black, O = red, N = blue, Cu = green. Hydrogen atoms are omitted for clarity). (B) View down the crystallographic c-axis of UWDM-1<sub>(22)</sub> depicting the hexagonal shaped channels (A<sub>1</sub> shown in blue, CE<sub>2</sub> in red, and Cu<sup>2+</sup> metal ions in green). It is noted that UWDM 1<sub>(B24)</sub> has the same structure, but with CE<sub>3</sub> rings.

The spectrum acquired at 192 K was simulated with typical quadrupolar parameters for an alkyl deuteron and as a single site, again indicating the equivalence of all the deuterons (within uncertainty limits). This spectrum was taken to be the static case

where motions are at rates within the SML, and therefore, have no effect on the appearance of the  $^2\text{H}$  SSNMR powder patterns. Increasing the temperature produces subtle changes in the powder patterns; this was simulated by considering the two-site jump mode of motion with  $\beta = 65(2)^\circ$  and rates within the IMR (**Table 4.1**). Again, it is noted that simulations for the two-site jump mode do not produce drastically different powder patterns when the rates are within the SML and IMR (**Figure C3**), and therefore, there are large uncertainties associated with these rates. The rates of the two-site jump continue to increase as the temperature is raised, with the onset of the FML at 318 K.

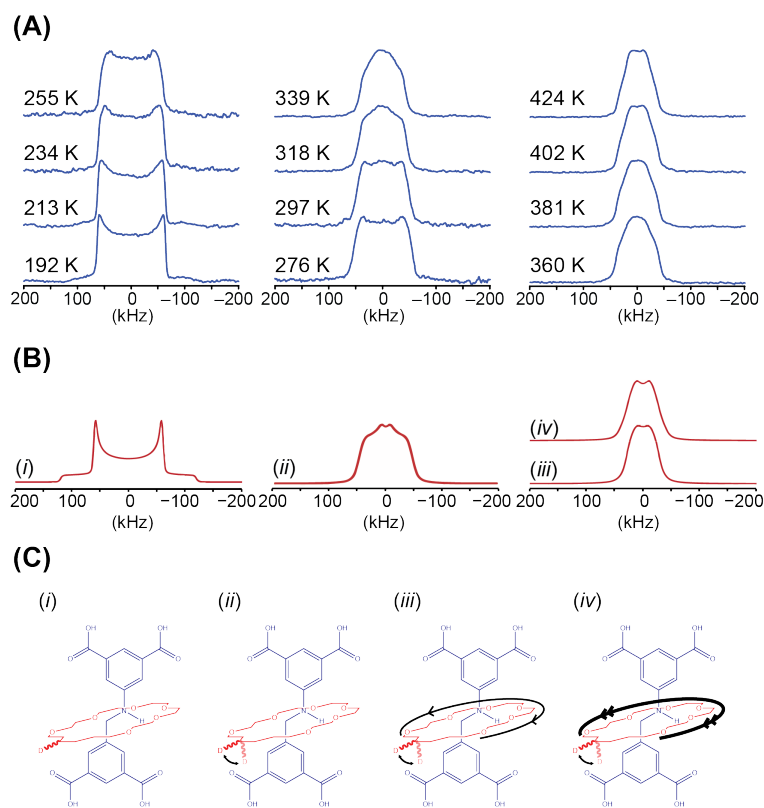


**Figure 4.4:** (A) Experimental VT  $^2\text{H}$  SSNMR powder patterns for UWDM-1<sub>(22)</sub>, (B) simulated  $^2\text{H}$  SSNMR powder patterns, and (C) accompanying depictions of the motional models used for the (i) motions that are too slow to influence the appearance of the Pake doublet (i.e., in the SML), (ii) two-site jumps with  $\beta = 65^\circ$  and rates in the FML, (iii) two-site jumps combined with the onset of partial rotation of the ring over  $250^\circ$  in  $50^\circ$  steps, and (iv) two-site jumps and partial rotation with rates in the FML.

**Table 4.1:** Rates and modes of motion used in the simulation of experimental VT  $^2\text{H}$  SSNMR data for UWDM-1<sub>(22)</sub>.

Temperature (K)	Two-site Jump Rate (kHz)	Partial Rotation Rate (kHz)
192	<500	0
213	<500	0
234	<500	0
255	<500	0
276	<500	1(1)
297	500(200)	5(2)
318	5000(1000)	10(5)
339	10000(1000)	50(10)
360	>10000	500(100)
381	>10000	5000(1000)
402	>10000	10000(1000)
424	>10000	>10000

Uncertainties in the rates are given in parentheses. The uncertainties are larger for faster rates of motion.

The spectra acquired at temperatures of 276 K and above begin to narrow appreciably and cannot be simulated by considering only two-site jumps; therefore, these spectra were simulated with the onset of partial rotation combined with the two-site jumps. The smaller ring size in this system means that the six rotation sites, corresponding to the hydrogen-bonding oxygen atoms, are separated by a larger angle with respect to the rotation axis (*i.e.*, the rotational sites are separated by  $50^\circ$  for UWDM-1<sub>(22)</sub> and  $45^\circ$  for UWDM-1<sub>(24)</sub>). The spectra acquired at 276 and 297 K were simulated with rates in the IMR for both the two-site jumps and partial rotation modes. The FML for the two-site jump is reached at 318 K, whereas the rates for the partial rotation continue to increase until the onset of the FML at 424 K. It is noted that there is no evidence for full rotation when the high-temperature limit is reached, as the spectrum is not axially symmetric at temperatures of 424 K or higher.

#### 4.4.1.3 UWDM-1<sub>(B24)</sub>.

This system incorporates a bulky benzo-24-crown-6 macrocycle, which is thought to have significantly hindered motion when functioning as an interlocked component in comparison to the 22-crown-6 and 24-crown-6 macrocycles. Ratcliffe *et al.* examined a similar system in their study of the dynamics in carboxybenzo-24-crown-8 and its KNCS complexes.<sup>54</sup> For this bulky ring, they found that rotation of the macrocycle is not possible, and that the only motion present is the familiar two-site jump. They also found that both the rate and amplitude of this motion increases with increasing temperature. A similar model was used in the simulation of the dynamics of UWDM-1<sub>(B24)</sub> herein.

The VT <sup>2</sup>H SSNMR spectra and analytical simulations are shown in **Figure 4.5** and the rates used in the simulations are shown in **Table 4.2**. The spectra acquired at 171 and 198 K were simulated with rates within the SML, where the motions are occurring too slowly to have any effect on the powder patterns. The spectrum acquired at 213 K shows subtle changes in comparison to the lower temperature spectra and was simulated with the onset of the two-site jump motion. It is noted that spectra simulated with rates between  $1 \times 10^3$  and  $5 \times 10^4$  Hz show no variation with jump angle, and therefore, the proposed rates and angles for simulations of the low temperature spectra have large associated uncertainties (**Figure C5**).

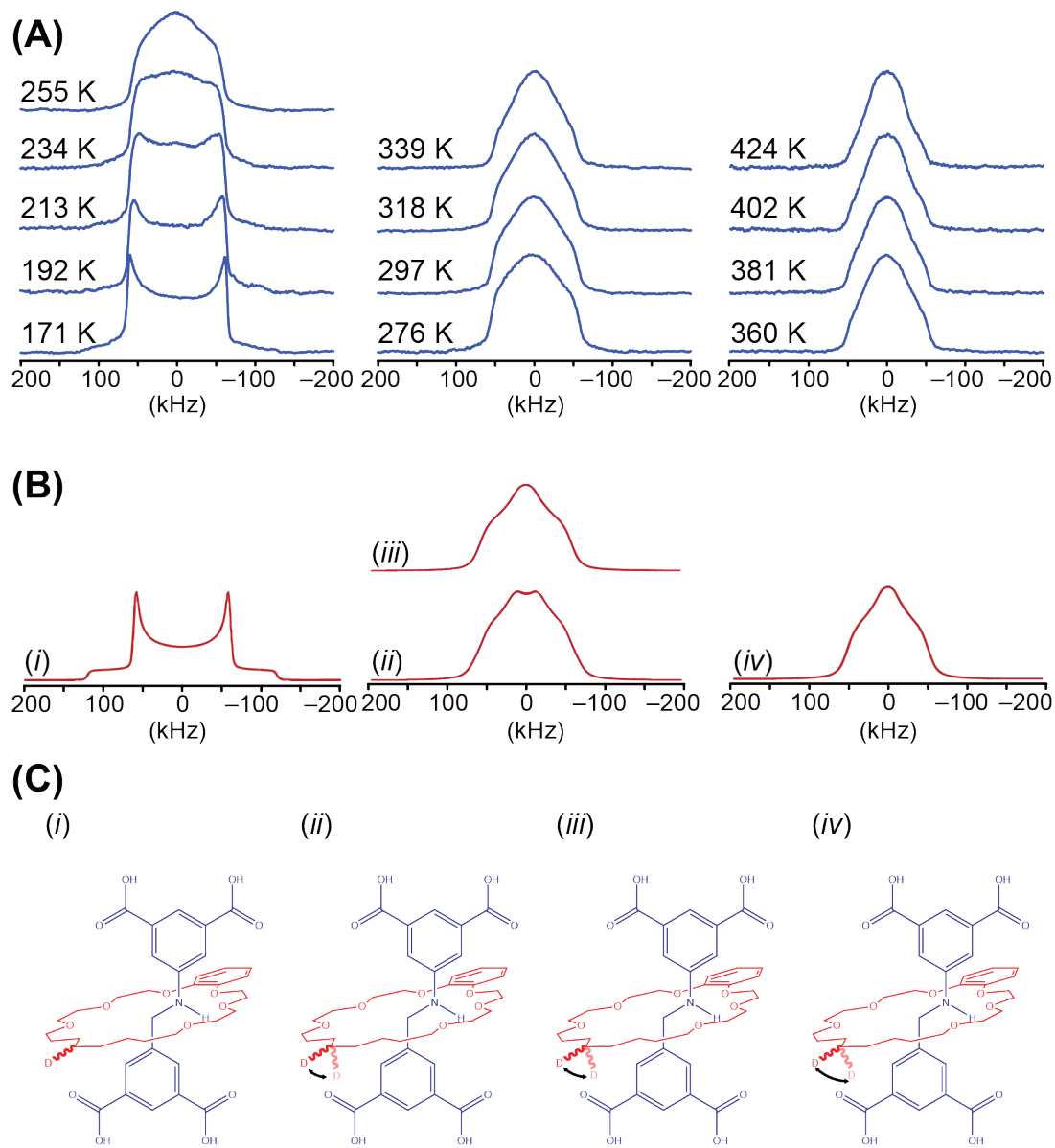


**Figure 4.5:** (A) Experimental VT  $^2\text{H}$  SSNMR powder patterns for UWDM-1<sub>(B24)</sub>, (B) simulated  $^2\text{H}$  SSNMR powder patterns, and (C) accompanying depictions of the motional model used for the (i) motions that are occurring too slowly to influence the appearance of the Pake doublet (i.e., in the SML), (ii) two-site jumps with  $\beta = 60^\circ$ , (iii) two-site jumps with  $\beta = 70^\circ$ , and (iv) two-site jumps with  $\beta = 75^\circ$ .



**Table 4.2:** Rates and modes of motion used in the simulation of experimental VT  $^2\text{H}$  SSNMR data for UWDM-1<sub>(B24)</sub>.

Temperature (K)	Jump Angle ( $^\circ$ ) <sup>a</sup>	Two-site Jump Rate (kHz)
171	-	<500
192	-	<500
213	-	<500
234	-	<500
255	60	500(100)
276	60	1000(200)
297	60	5000(1000)
318	65	5000(1000)
339	65	10000(1000)
360	70	>10000
381	70	>10000
402	75	>10000
424	75	>10000

<sup>a</sup>Uncertainties in the jump angles are  $\pm 5^\circ$ .

Increasing the temperature produces the characteristic powder patterns associated with the two-site jump model. The spectra up to 276 K were simulated with rates within the IMR and a jump angle of  $60^\circ$ . The FML for the two-site jump was reached at 297 K with a jump angle of  $60^\circ$ . Increasing the temperature further results in an increase in the jump angle and rate of motion, though the latter is not detectable, as the FML has been reached and further increases in the rate does not influence the powder patterns. The high-temperature spectrum acquired at 424 K was simulated with a jump angle of  $75^\circ$  and rates in the FML.

#### 4.4.1.4 Motions in the UWDM-1 series.

It is important to comment on the effect of ring size on the dynamics in the UWDM-1 system. The macrocycles in UWDM-1<sub>(24)</sub> are certainly the most mobile of the species studied, indicating that the 24-crown-6 macrocycle provides both ample free

volume and limited interactions with the axle. The FML for the two-site jump motion is reached at approximately 251 K, partial rotation at 324 K, and full rotation at 480 K.

The question to be answered in the study of UWDM-1<sub>(22)</sub> was whether the smaller ring would result in a more or less dynamic system in comparison to UWDM-1<sub>(24)</sub> (*i.e.*, would the same modes of motion be occurring at slower or faster rates, if at all). The FML for the two-site jump motion is reached at 318 K for UWDM-1<sub>(22)</sub>, which is almost 70 K higher than that for UWDM-1<sub>(24)</sub>. The higher onset temperature and smaller jump angle suggests the smaller ring in UWDM-1<sub>(22)</sub> is undergoing motion that is hindered in comparison that of the 24-crown-6 macrocycle. This claim is further substantiated when the partial rotation model is considered. The onset of partial rotation occurs at 276 K, similar to UWDM-1<sub>(24)</sub>, and the FML is reached by about 400 K. The spectrum acquired in the high-temperature limit (424 K) was also simulated using the partial rotation model and there is no evidence of full rotation. This is in contrast to UWDM-1<sub>(24)</sub> where evidence of full rotation is manifested in the spectrum acquired at 423 K. The hindered two-site jump motion, as well as no evidence of full rotation, clearly indicates that the larger free volume afforded by a smaller ring size is countered by the tighter fit of the ring around the axle.

The macrocycle in the UWDM-1<sub>(B24)</sub> species fits around the axle in a similar manner to that in UWDM-1<sub>(24)</sub>; however, the bulky phenyl substituent greatly reduces the free volume and increases interactions between the ring and the framework. Therefore, it was postulated that the motion in this species would be greatly encumbered, akin to what was observed by Ratcliffe *et al.* in their study of carboxybenzo-24-crown-8.<sup>54</sup> The only motion observed for this species is the two-site jump, with the onset of the FML at *ca.*

297 K. The higher temperature for the onset of the FML in comparison to that of UWDM-1<sub>(24)</sub> suggests that the bulkier ring hinders the conformational changes in the ring associated with the two-site jump. Furthermore, the absence of rotation (either partial or full) highlights the restricted nature of the motion of the crown ether ring in this MOF.

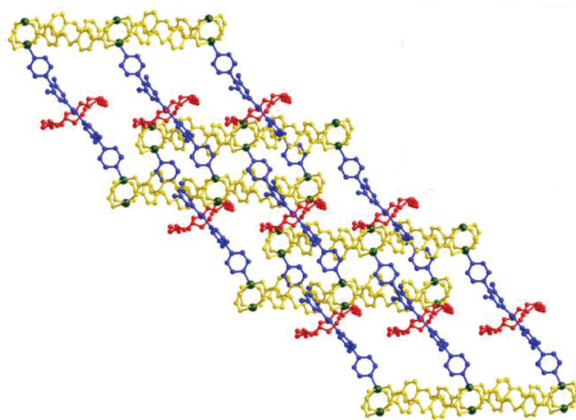
The three distinct motional modes in the UWDM-1 systems occur in sequential stages. While it may be desirable to calculate activation energies for each of the individual modes of motion, this is difficult for these systems due to the presence of multiple, simultaneous modes of motion occurring at different rates. The first mode of motion that occurs in all systems is the two-site jump, with the onset of the FML occurring at 251, 318, and 297 K for UWDM-1<sub>(24)</sub>, UWDM-1<sub>(22)</sub> and UWDM-1<sub>(B24)</sub>, respectively. The onset temperature of the two-site jump motion is dependent on both the fit of the macrocycle around the axle (*i.e.*, a tighter fit results in a higher onset temperature) and the overall steric bulk of the ring. Second, provided there is sufficient free volume, partial rotation occurs, and the jump angle depends on the size of the ring. This mode of motion occurs for both UWDM-1<sub>(24)</sub> and UWDM-1<sub>(22)</sub> with FML onset temperatures of 324 and 424 K, respectively. Finally, full rotation of the ring is possible only for the 24-crown-6 macrocycle in UWDM-1<sub>(24)</sub>, with the FML onset occurring at 423 K, indicating that the motion of this macrocycle is the least hindered of the series.

#### 4.4.2 UWDM-2.

UWDM-2 is an example of a pillared MOF with two-dimensional layers formed by coordination of **SBU**<sub>2</sub> by four molecules of **L**<sub>1</sub>. A rotaxane is made with **A**<sub>2</sub> and **CE**<sub>1</sub>, and is coordinated to **SBU**<sub>2</sub> through the pyridine donor groups, joining together the 2D layers to form a 3D MOF (**Figure 4.6(A)**). Contrary to the anticipated large void volume

from this MOF construction, UWDM-2 has three-fold interpenetration (*i.e.*, the framework lattice has two other lattices passing through it).<sup>56</sup> The interpenetration of the framework places the rings of two adjacent [2]rotaxanes in close proximity to each other and to the Zn-L<sub>1</sub> layers (**Figure 4.6(B)**). The effects of the interpenetration and the close proximity of the rings to one another on the ring dynamics was investigated with <sup>2</sup>H SSNMR.

**(A)**



**(B)**

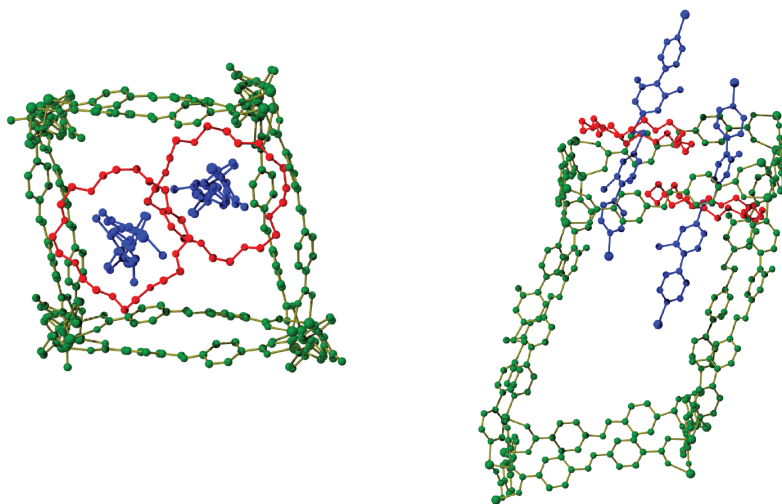


**Figure 4.6:** (A) Ball-and-stick representation of UWDM-2 showing the three-fold interpenetration (colour key: A<sub>2</sub> = blue, CE<sub>1</sub> = red, L<sub>1</sub> = yellow). (B) Ball-and-stick representations showing the proximity of the rings (red) to one another and to the framework structure (green).

The VT  $^2\text{H}$  SSNMR spectra, powder pattern simulations, and a depiction of the motional models used for UWDM-2 are shown in **Figure 4.7**. The static spectrum acquired at 171 K was simulated as a single site with typical quadrupolar parameters (*vide supra*). Increasing the temperature results in narrowing of the  $^2\text{H}$  powder patterns. The variations of powder patterns with temperature and echo spacing indicate that the motion is occurring at rates within the IMR. Therefore, the spectra were simulated using the two-site jump with an angle of  $72^\circ$  combined with the partial rotation model. A series of spectra were simulated as a function of the rates of the two types of motion (**Figure C6**). Examination of these simulations allowed for the isolation of approximate rates, which were then refined by direct comparison to the experimental spectra (**Table 4.3**). The rate of the two-site jump motion is lower than that of the partial ring rotation, unlike the cases discussed above. The reduced rate of motion for the two-site jump may arise from steric interactions between the rings that are in close proximity in UWDM-2.

**Table 4.3:** Rates and modes of motion used in the simulations of experimental VT  $^2\text{H}$  SSNMR data for UWDM-2

Temperature (K)	Two-site jump Rate (kHz)	Partial Rotation Rate (kHz)
171	0	0
255	25(5)	5000(500)
276	50(10)	6000(1000)
297	100(10)	7000(1000)
318	400(100)	8000(1000)
339	600(1000)	9000(1000)
360	800(100)	9000(1000)
381	900(100)	10000(1000)
402	1000(100)	30000(5000)
424	3000(1000)	50000(5000)

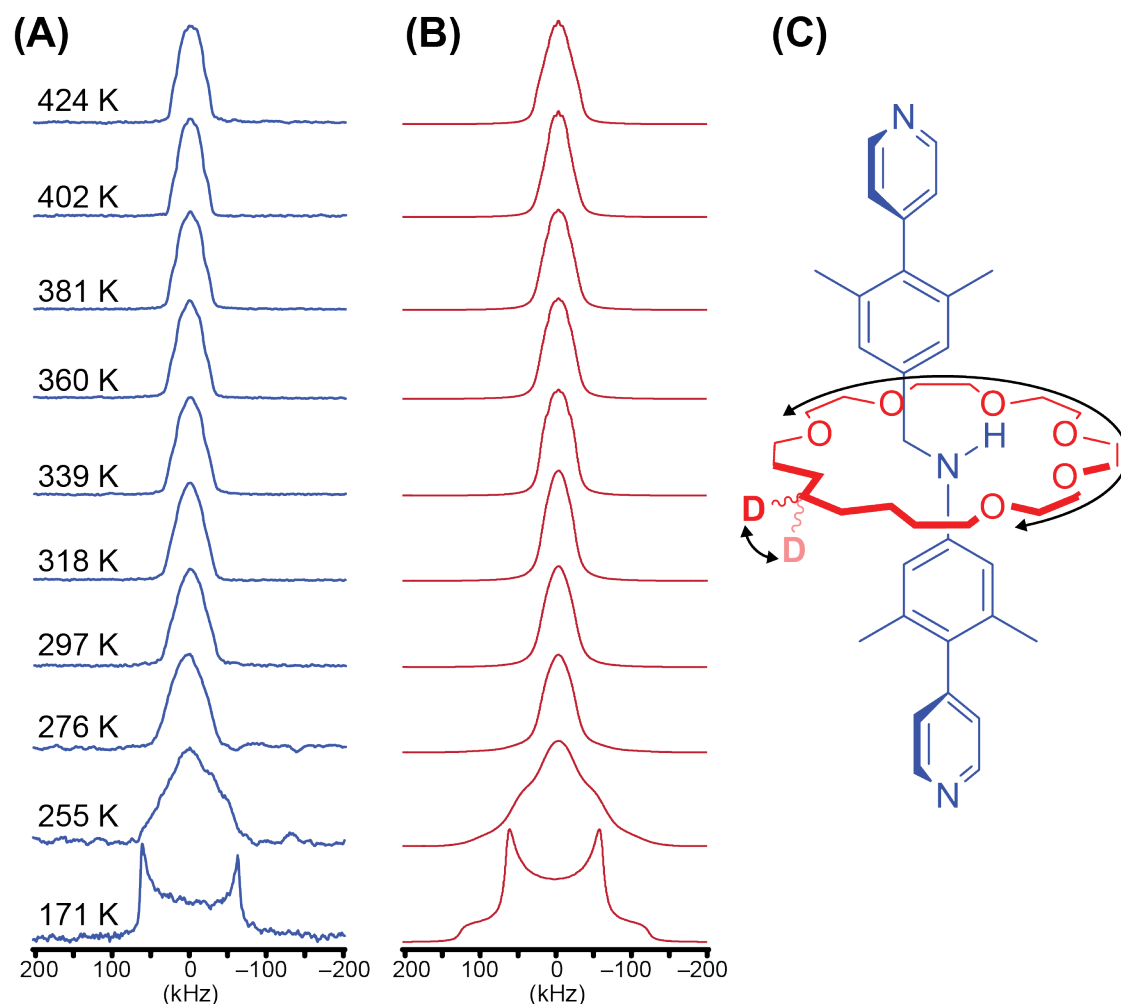


**Figure 4.7:** (A) Experimental VT  $^2\text{H}$  SSNMR powder patterns for UWDM-2. (B) Simulated  $^2\text{H}$  SSNMR powder patterns using the two-site jump ( $\beta = 72(2)^\circ$ ) and partial rotation models. Rates used in the simulations are listed in Table 4.3. (C) Depiction of the motional model used.

#### 4.4.3 $\alpha$ -UWDM-3

In an attempt to prevent the interpenetration observed in UWDM-2, a shorter linker ( $\text{L}_2$ ) was used to synthesize  $\alpha$ -UWDM-3 (**Figure 4.8(A)**), which has DMF solvent in the pores and two-fold interpenetration. The macrocyclic ring ( $\text{CE}_1$ ) lies within the “square planes” of the  $\text{SBU}_2\text{-L}_2$  layers (**Figure 4.8(B)**). It is postulated that the interactions between the ring and the framework might hinder the motion of the ring.

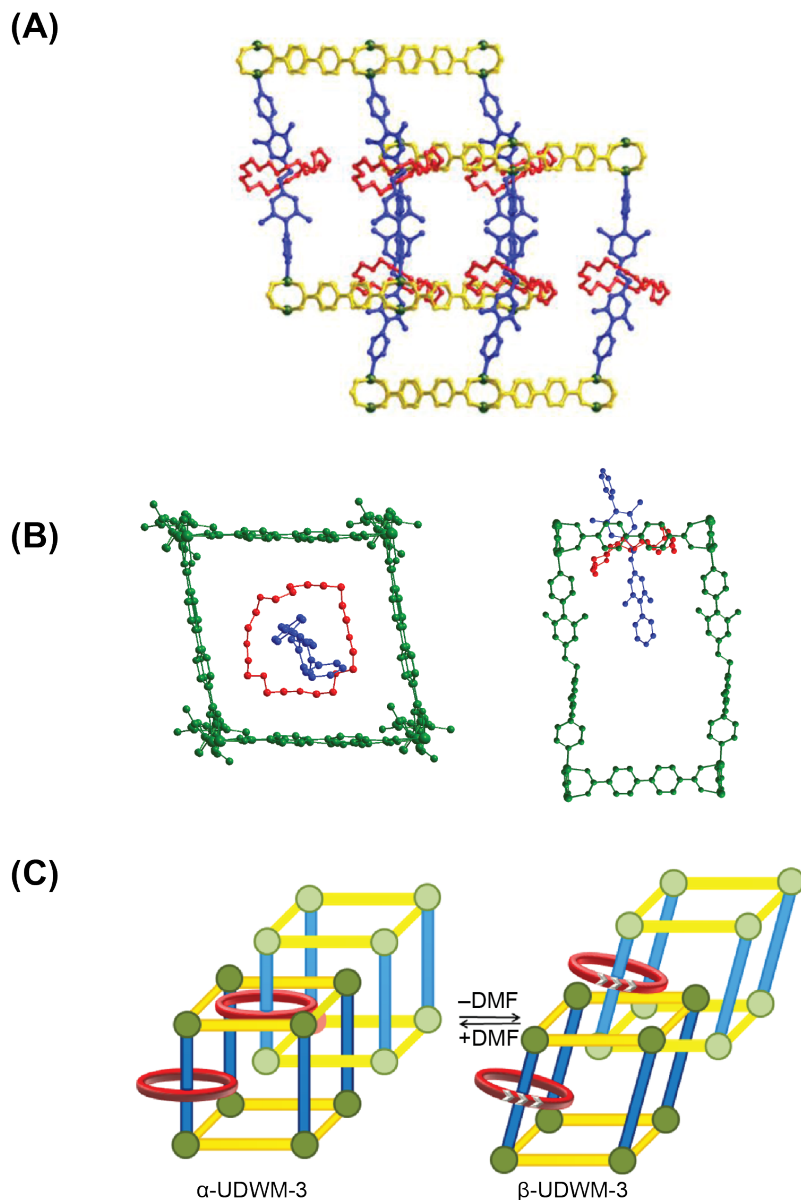


**Figure 4.8:** (A) Ball-and-stick representation of  $\alpha$ -UWDM-3 showing the two-fold interpenetration (colour key:  $A_2$  = blue,  $CE_1$  = red,  $L_2$  = yellow). (B) Ball-and-stick representations showing the confinement of the  $CE_1$  ring (red) within the “square plane” of the framework (green). (C) Schematic depiction of the reversible phase change that occurs in UWDM-3.

The VT  $^2H$  SSNMR spectra of  $\alpha$ -UWDM-3 are shown in **Figure 4.9** along with the accompanying simulations and depictions of the modes of motion. The rates used in

the simulation of experimental data are shown in **Table 4.4**. The low-temperature spectrum collected at 234 K was simulated with a single set of quadrupolar parameters (*vide supra*). This spectrum was simulated without the inclusion of any motions, indicating that the motion is in the SML. This SML spectrum of  $\alpha$ -UWDM-3 was obtained at a higher temperature than that of UWDM-1<sub>(24)</sub>; this suggests that the motions of the crown ethers in the former are more hindered.

The spectrum acquired at 247 K is distinct and was simulated using the two-site jump model with an angle of  $75(2)^\circ$ , and the onset temperature of this motion is comparable to those of UWDM-1<sub>(24)</sub> and benzo-24-crown-8.<sup>54</sup> The spectrum acquired at 255 K was simulated by considering the onset of partial rotation (*i.e.*, rotation of the ring through  $225^\circ$  in  $45^\circ$  steps), identical to that observed for UWDM-1<sub>(24)</sub>, in addition to the two-site jump of the CD<sub>2</sub> moieties. Collecting spectra at this temperature with different pulse spacings produces notable changes in the powder pattern; thus, it can be concluded that the rate of the new motions is within the IMR (motion occurring at a rate of approximately 10-100 kHz).

**Table 4.4:** Rates and modes of motion used in the simulation of experimental VT <sup>2</sup>H SSNMR data for  $\alpha$ -UWDM-3

Temperature (K)	Two-site Jump Rate (kHz)	Partial Rotation Rate (kHz)	Large Amplitude Jump Rate (kHz)
234	<100	--	--
247	5000(1000)	--	--
255	10000(1000)	10(5)	--
276	>10000	50(10)	5(1)
297	>10000	100(10)	50(10)
318	>10000	5000(1000)	1000(100)
339	>10000	10000(1000)	5000(1000)



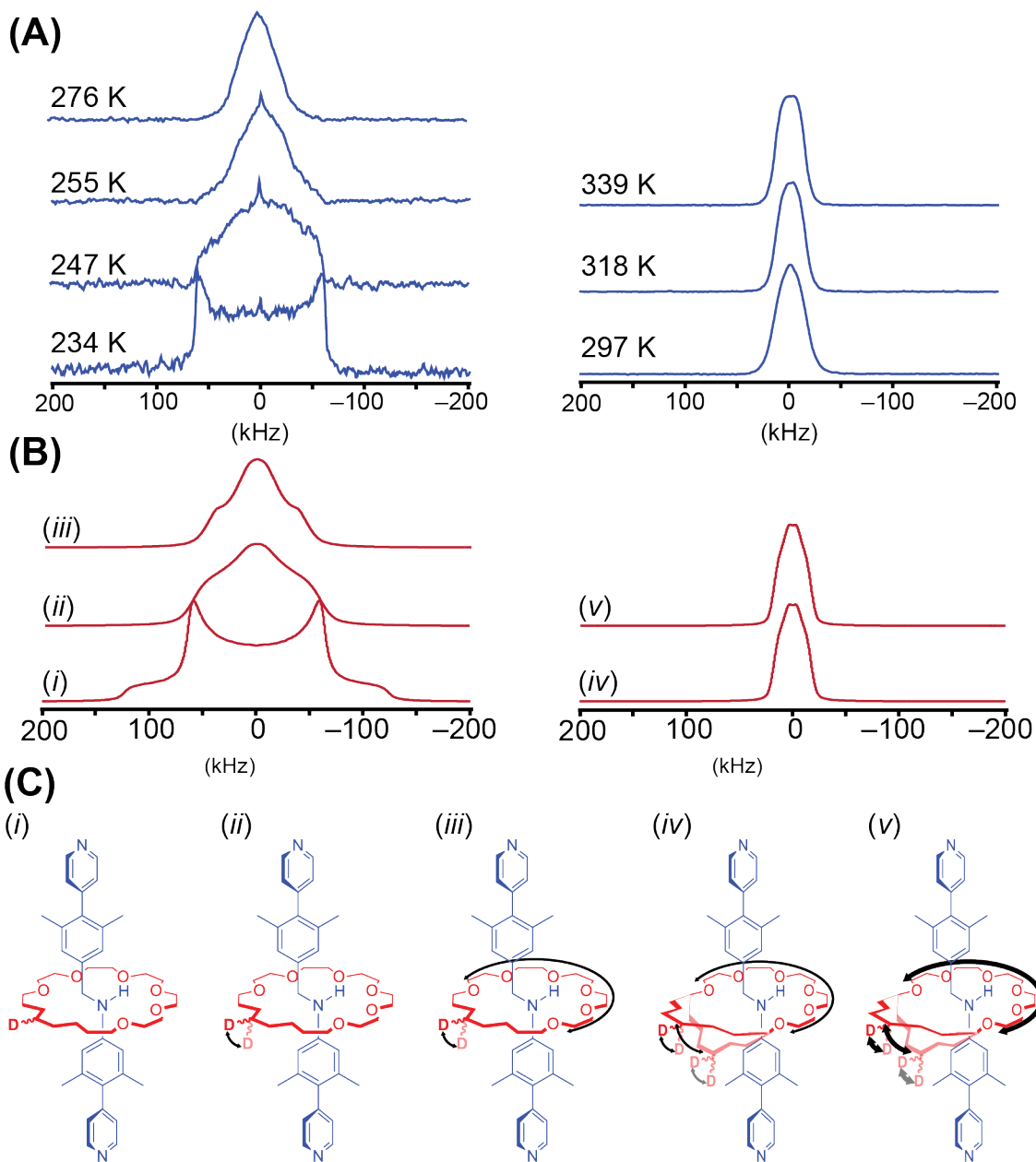


**Figure 4.9:** (A) Experimental VT  $^2\text{H}$  SSNMR powder patterns for  $\alpha$ -UWDM-3. (B) Simulated  $^2\text{H}$  SSNMR powder patterns and (C) accompanying depictions of the motional model used for the (i) motions that are occurring too slowly to influence the appearance of the Pake doublet (i.e., in the SML), (ii) two-site jump with  $\beta = 75(2)^\circ$ , (iii) two-site jump with  $\beta = 75(2)^\circ$  combined with the onset of partial rotation of the ring over  $225^\circ$  in  $45^\circ$  steps and (iv) two-site jump and partial rotation combined with large amplitude ring flexing to positions  $30(3)^\circ$  above and below the “square plane” of the framework, and (v) the FML of all the above-mentioned motions.

Further increasing the sample temperature produces patterns that have significantly narrower breadths. This degree of narrowing cannot be accounted for with the combination of the two-site jump and partial rotation. Hence, it is postulated that a third mode of motion is occurring. The  $^2\text{H}$  NMR spectra acquired at 318 K and 339 K were simulated with large amplitude jumps of the deuterons through an angle of  $60(5)^\circ$  about an axis in the plane of the ring, in combination with partial rotation and two-site jumps. This motion can be modeled in two distinct ways: the entire macrocycle is rotating between positions  $30(3)^\circ$  above and below the “square” of the framework, or the relatively flexible alkyl portion of the ring is moving above and below the constraining “square” of the metal-organic framework. While the latter process, denoted as *large-amplitude ring flexing*, is more likely due to the fact that it is much less energetically expensive, we note that both processes are simulated in the exact same manner (*i.e.*, using the same angles, parameters, and rates). Furthermore, this flexing also minimizes short-range interactions between the crown ether and the surrounding framework. Several other motional models were also explored; however, those with simulations which matched experimental data were not chemically sensible.

#### 4.4.4 $\beta$ -UWDM-3

PXRD analysis of  $\alpha$ -UWDM-3 indicates that a phase transition occurs in the temperature range of 100-125°C. The transition to  $\beta$ -UWDM-3 is attributed to the removal of the DMF solvent from the pores of the framework (this transition is reversible when  $\beta$ -UWDM-3 is exposed to DMF). This desolvation causes a change in the structure of the MOF, such that it is postulated that the ring no longer sits within the “square” of

the framework (**Figure 4.8(C)**). The “less constrained” environment suggests that the ring in the  $\beta$ -UWDM-3 is more mobile than that in the  $\alpha$ -UWDM-3.

The VT  $^2\text{H}$  SSNMR spectra, simulations, and depictions of the motional models are shown in **Figure 4.10** and the rates used in the simulations are shown in **Table 4.5**. The spectra are strikingly similar to those observed in the study of UWDM-1<sub>(24)</sub>, except for those acquired at high-temperature (*vide infra*), suggesting that the motions in these two systems are much the same at lower temperatures.<sup>52</sup> The static spectrum at 183 K was simulated as a single site with typical  $^2\text{H}$  quadrupolar parameters (*vide supra*). Increasing the temperature to 208 K results in no significant change in the powder pattern. The spectrum acquired at 234 K indicates the onset of motion, and the spectrum at 255 K was simulated using the familiar two-site jump of the  $\text{CD}_2$  groups through an angle of  $75(2)^\circ$ . Increasing the temperature of the sample further induces the onset of the partial rotation model of the ring through  $225^\circ$  in  $45^\circ$  increments, in addition to the aforementioned two-site jump motion. The spectrum at 318 K was simulated with rates in the FML for this combined motion (**Table 4.5**). The onset temperature of this mode of motion is similar to that of UWDM-1<sub>(24)</sub> (324 K), again validating the similar motions in these two systems.

**Table 4.5:** Rates and modes of motion used in the simulation of experimental VT  $^2\text{H}$  SSNMR data for  $\alpha$ -UWDM-3

Temperature (K)	Two-site Jump Rate (kHz)	Partial Rotation Rate (kHz)	Large Amplitude Jump Rate (kHz)
234	<100	--	--
247	5000(1000)	--	--
255	10000(1000)	10(5)	--
276	>10000	50(10)	5(1)
297	>10000	100(10)	50(10)
318	>10000	5000(1000)	1000(100)
339	>10000	10000(1000)	5000(1000)

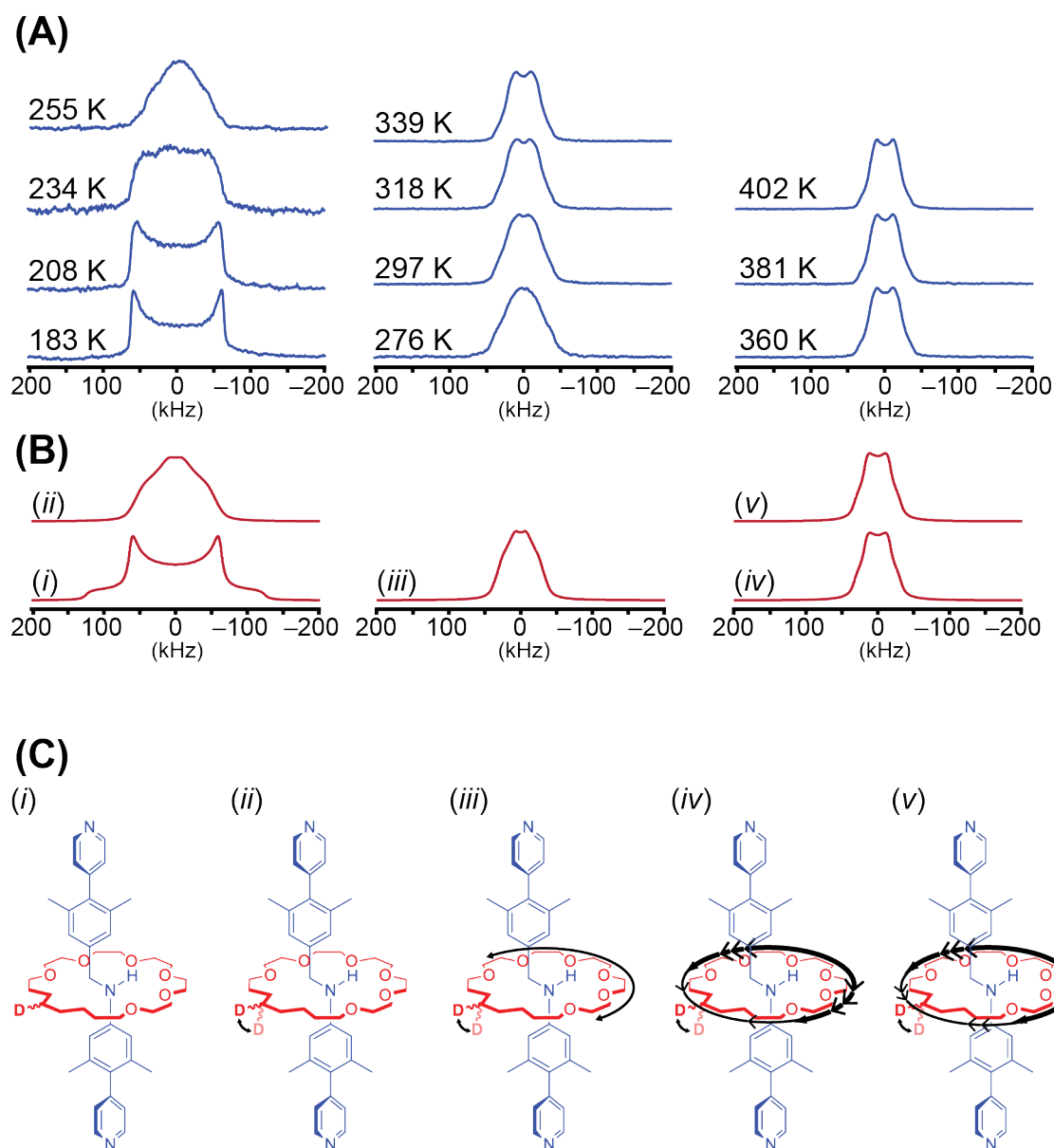


**Figure 4.10:** (A) Experimental VT  $^2\text{H}$  SSNMR powder patterns for  $\beta$ -UWDM-3. (B) Simulated  $^2\text{H}$  SSNMR powder patterns and (C) accompanying depictions of the motional model used for the (i) motions that are too slow to influence the appearance of the Pake doublet (i.e., in the SML), (ii) two-site jump with  $\beta = 75(2)^\circ$ , (iii) two-site jump with  $\beta = 75(2)^\circ$  combined with the onset of partial rotation of the ring over  $225^\circ$  in  $45^\circ$  steps, (iv) two-site jumps combined with partial rotation and jumps through the alkyl portion of the ring that are occurring at a rate slower than the rate of jumps between oxygen atoms, and (v) increased rate of jumps through the alkyl portion of the ring.

**Table 4.6:** Rates and modes of motion used in the simulation of experimental VT  $^2\text{H}$  SSNMR data for  $\beta$ -UWDM-3

Temperature (K)	Two-site Jump Rate (kHz)	Partial Rotation Rate (kHz)	Alkyl Jump Rate (kHz)
183	<500	--	--
208	<500	--	--
234	5000(1000)	--	--
255	10000(1000)	--	--
276	>10000	500(100)	--
297	>10000	1000(100)	--
318	>10000	5000(1000)	--
339	>10000	10000(1000)	50(10)
360	>10000	>10000	100(10)
381	>10000	>10000	500(100)
402	>10000	>10000	1000(100)

The spectra acquired at higher temperatures could not be simulated using the combined two-site jump and partial rotation model, nor could they be simulated with full rotation of the crown ether ring about an axis of  $C_{n \geq 3}$  symmetry (as such motion produces axially symmetry powder patterns). The simulation of the high-temperature spectra that matches experiment is achieved by considering an intermediate case between partial rotation and full rotation, combined with the two-site jump. Specifically, eight sites separated by  $45^\circ$  rotations were used, six corresponding to the hydrogen-bonding oxygen atom positions, and two corresponding to the alkyl portion of the ring (**Figure C7(A)**). A rate matrix was constructed (**Figure C7(B)**) where jumps between the oxygen atom positions are occurring at rates in the FML (*i.e.*,  $>10^7$  Hz) and jumps through the alkyl positions occur at a significantly slower rate (*i.e.*, 50-1000 kHz). The spectra acquired at 381 K and 401 K were simulated using this model, and excellent agreement with the experimental data is obtained. It is postulated that the ring does not undergo full rotation due to interactions between the ring and framework.

#### 4.4.5 UWDM-P MOFs

The studies of UWDM-2 and UWDM-3 reveal that interpenetration influences the motion of the rings; the more constrained environments cause by steric interactions with the framework and other rings greatly hinders their motion or induces new modes of motion so as to minimize these interactions. In an attempt to prevent interpenetration, a series of MOFs were synthesized with a large porphyrin-based organic linker (**L**<sub>3</sub>). The two MOFs consist of two-dimensional layers of **SBU**<sub>2</sub> and **L**<sub>3</sub> that are pillared by either **A**<sub>2</sub> (UWDM-P1) or **A**<sub>3</sub> (UWDM-P2). The two axes differ only by a methyl substituent on the pyridine functional group. Despite the inclusion of porphyrin linkers, both UWDM-P1 and P2 have a two-fold interpenetration (**Figure 4.11**). Similar to UWDM-3, UWDM-P1 and UWDM-P2 undergo reversible desolvation upon removal of the DMF from the pores of the framework to generate UWDM-P1<sub>d</sub> and UWDM-P2<sub>d</sub>. X-ray diffraction data indicates that the desolvation process induces slight structural changes (**Table 4.6**). It is noted that while structural changes induced by desolvation seem minor, the rings are in relatively encumbered environments and even slight changes (*e.g.*, tilting) of the framework could greatly alter their motions. Below, the VT <sup>2</sup>H SSNMR spectra are briefly discussed on a case-by-case basis. The spectra for UWDM-P1 and UWDM-P2, along with their desolvated forms, are shown in **Figures 4.12** and **4.13**, respectively, and the rates and modes of motion are summarized in **Tables 4.7** to **4.10**. This is followed by a discussion of the factors influencing the macrocyclic ring dynamics in the UWDM-P series. N.B. in all cases, the spectra acquired at 185 K were simulated with the absence of motions, or equivalently, motions occurring at rates within the SML.

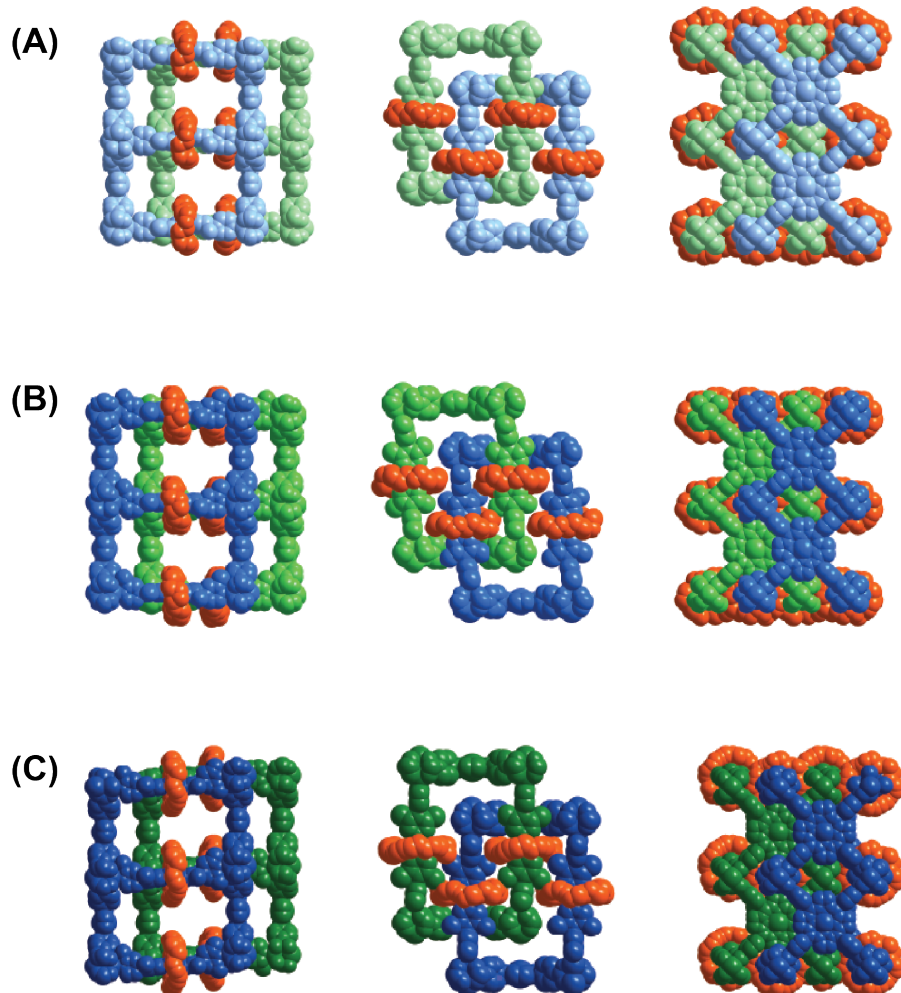


**Figure 4.11:** Crystal structures showing the two-fold interpenetration of (A) UWDM-P1, (B) UWDM-P2, and (C) UWDM-P2<sub>d</sub>. In each case, the CE<sub>1</sub> macrocycles sit above the square plane formed by the L<sub>3</sub> ligands. It is noted that a crystal structure of UWDM-P1<sub>d</sub> could not be determined, however; crystal lattice parameters were obtained (**Table 4.6**).

**Table 4.7:** Unit cell parameters for the UWDM-P MOF series.

MOF	$a$ (Å)	$b$ (Å)	$c$ (Å)	$\beta$ (°)	Space Group
UWDM-P1	17.052(4)	16.225(4)	24.722(6)	90.977(9)	$P2$
UWDM-P1 <sub>d</sub>	16.901(3)	16.390(3)	24.577(4)	92.421(7)	$P2$
UWDM-P2	16.8477(4)	16.4056(4)	24.7321(7)	94.16989(16)	$P2$
UWMD-P2 <sub>d</sub>	16.8219(6)	16.4164(6)	49.137(2)	91.786(3)	$P2/c$

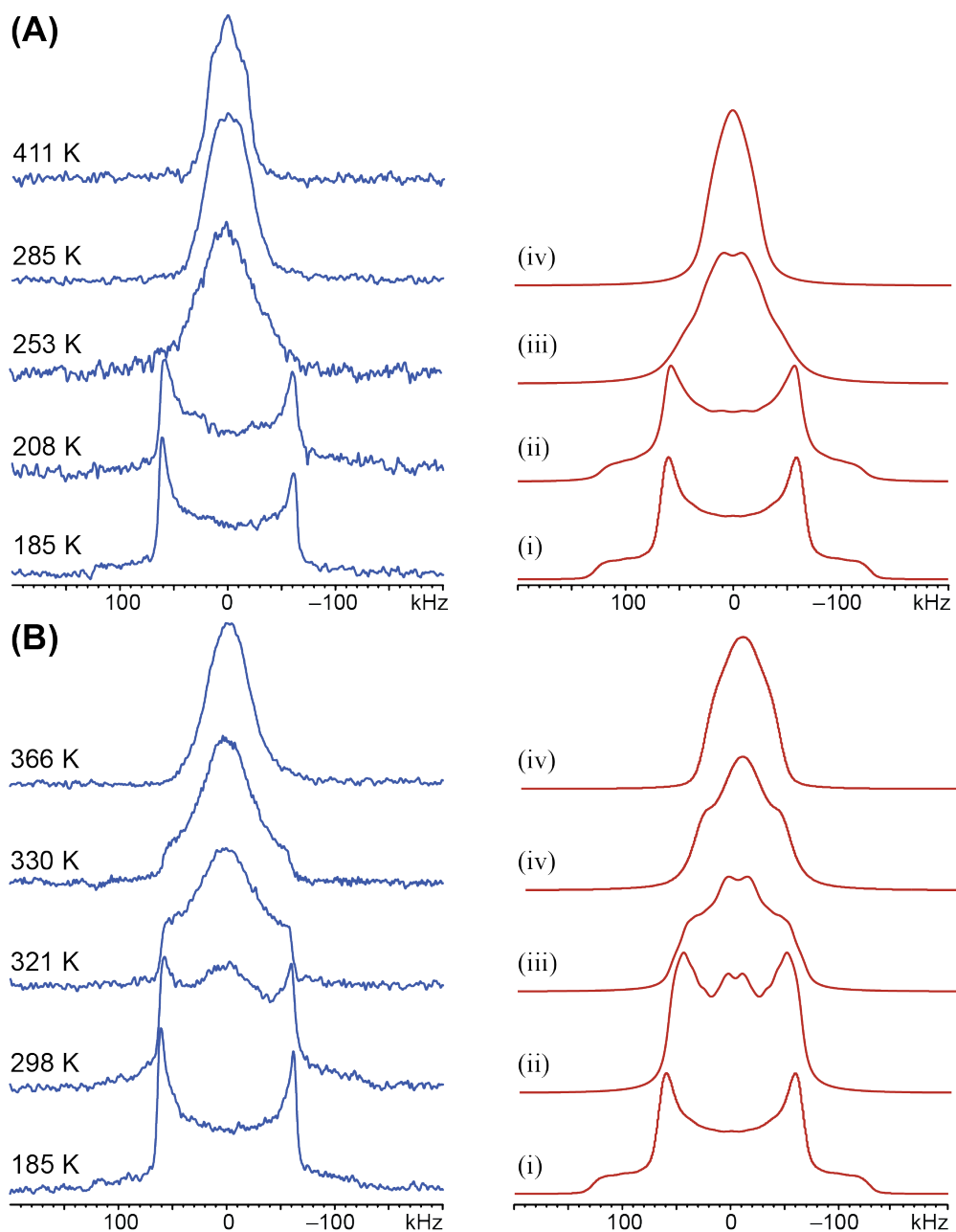


**Figure 4.12:** (A) Experimental VT  $^2\text{H}$  SSNMR spectra for UWDM-P1 and corresponding simulations showing the (i) SML, (ii) onset of the two-site jump ( $\beta = 78^\circ$ ), (iii) FML of the two-site jump and onset of partial rotation, and (iv) FML of the two-site jump and partial rotation. (B) Experimental VT  $^2\text{H}$  SSNMR spectra for UWDM-P1<sub>d</sub> and corresponding simulations showing the (i) SML, (ii) IMR for the two-site jump, (iii) FML of the two-site jump, (iv) onset of partial rotation, and (v) FML of the two-site jump and partial rotation.



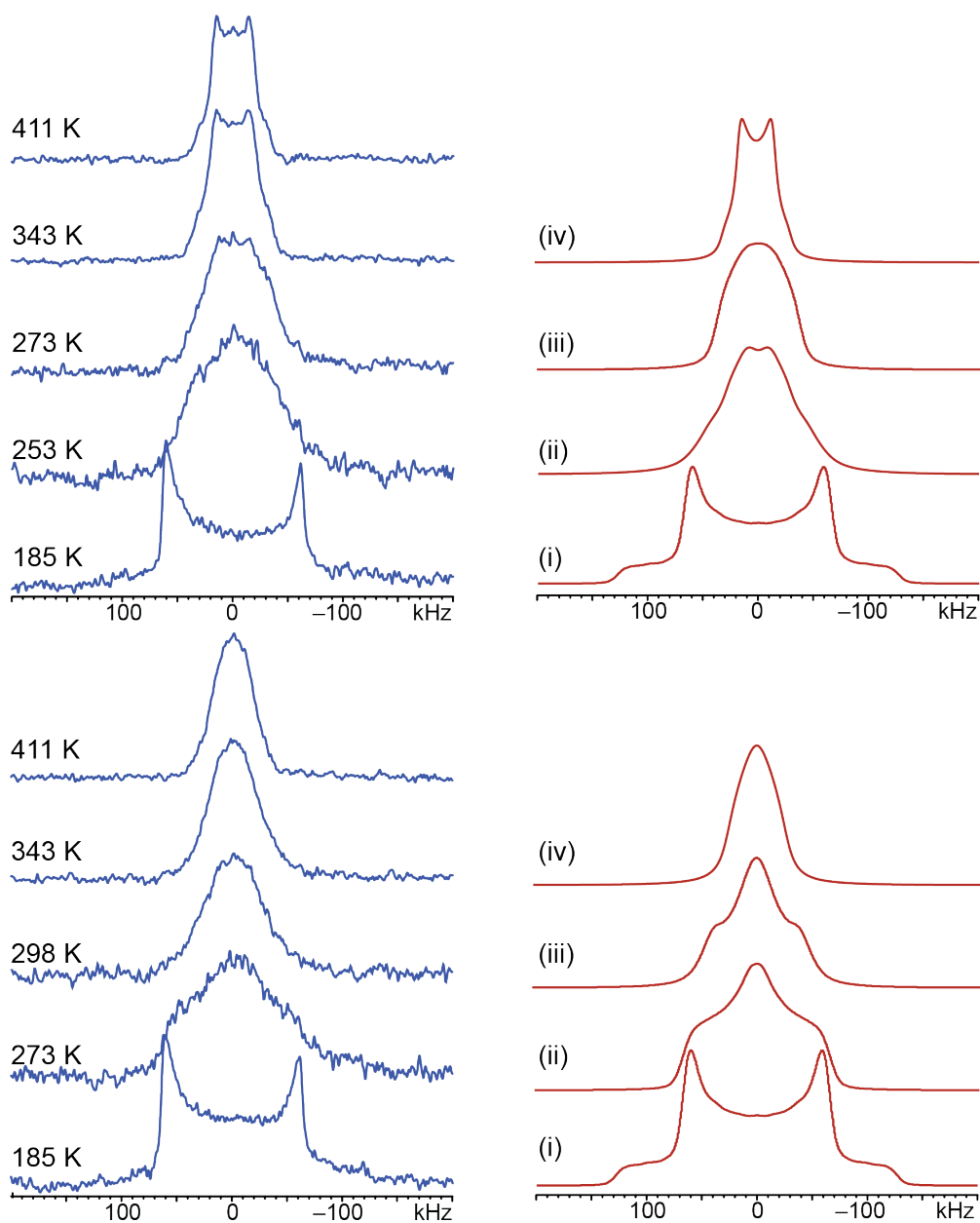


**Figure 4.13:** (A) Experimental VT  $^2\text{H}$  SSNMR spectra for UWDM-P2 and corresponding simulations showing the (i) SML, (ii) FML of the two-site jump ( $\beta = 78^\circ$ ) and the onset of partial rotation, (iii) FML of the two-site jump and partial rotation, and (iv) FML of the two-site jump and full rotation. (B) Experimental VT  $^2\text{H}$  SSNMR spectra for UWDM-P2<sub>d</sub> and corresponding simulations showing the (i) SML, (ii) FML for the two-site jump ( $\beta = 70^\circ$ ), (iii) FML of the two-site jump ( $\beta = 75^\circ$ ) and the onset of partial rotation, and (iv) FML of the two-site jump and partial rotation.

**Table 4.8:** Rates and modes of motion used in the simulation of experimental VT  $^2\text{H}$  SSNMR data for UWDM-P1.

Temperature (K)	Two-site Jump Rate (kHz)	Partial Rotation Rate
185	0	0
208	<500	0
253	>10000	10(5)
285	>10000	>10000
411	>10000	>10000

**Table 4.9:** Rates and modes of motion used in the simulation of experimental VT  $^2\text{H}$  SSNMR data for UWDM-P1<sub>d</sub>.

Temperature (K)	Two-site Jump Rate (kHz)	Partial Rotation Rate (kHz)
185	0	0
275	10(5)	0
285	50(10)	0
298	500(100)	0
311	5000(1000)	0
321	>10000	0
330	>10000	100(10)
366	>10000	>10000

**Table 4.10:** Rates and modes of motion used in the simulation of experimental VT  $^2\text{H}$  SSNMR data for UWDM-P2.

Temperature (K)	Two-site Jump Rate (kHz)	Partial Rotation Rate (kHz)	Full Rotation Rate (kHz)
185	0	0	0
253	>10000	10(5)	0
273	>10000	1000(500)	
343	>10000	>10000	>10000
411	>10000	>10000	>10000

**Table 4.11:** Rates and modes of motion used in the simulation of experimental VT  $^2\text{H}$  SSNMR data for UWDM-P2<sub>d</sub>.

Temperature (K)	Two-site Jump Rate (kHz)	Partial Rotation Rate (kHz)
185	0	0
273	>10000	0
298	>10000	100(10)
343	>10000	>10000
411	>10000	>10000

#### 4.4.5.1 UWDM-P1

The  $^2\text{H}$  SSNMR spectrum acquired at 208 K was simulated as two-site jump motion with a jump angle of  $\beta = 78^\circ$ . The onset of the partial rotational motion is observed in the spectrum acquired at 253 K. The spectrum collected at 285 K was simulated as the FML of the combined two-site jump and partial rotational motions. Increasing the temperature to 411 K (*i.e.*, the highest temperature to which the sample could be heated) does not produce any significant changes to the  $^2\text{H}$  powder patterns and therefore, no additional modes of motion are occurring in UWDM-P1.

#### 4.4.5.2 UWDM-P1<sub>d</sub>

$^2\text{H}$  SSNMR spectra acquired above 185 K were simulated as the two-site jump motion with rates in the IMR. The FML for the two-site jump motion occurs at 321 K. Increasing the temperature further results in the onset of the partial rotational motion and the spectrum acquired at 366 K was simulated as the FML of the combined two-site jump and partial rotational motions.

#### 4.4.5.3 UWDM-P2

Increasing the temperature above 185 K results in drastic changes in the  $^2\text{H}$  powder patterns, indicating the rapid onset of the two-site jump motion. The spectrum acquired at 253 K was simulated with the FML of the two-site jump and the onset of the partial rotational motion, the rate of which increases with temperature. At 343 K, an axially symmetric pattern is obtained, indicating the FML of the full rotational motion. Increasing the temperature further (up to 411 K) results in no further changes in the spectra.

#### 4.4.5.4 UWDM-P2<sub>d</sub>

The spectrum acquired at 273 K was simulated with the two-site jump motion with a jump angle of 70° and rates in the FML. Increasing the temperature to 298 K results in an increase in the jump angle ( $\beta = 75^\circ$ ) and the onset of partial rotation. The FML of the two-site jump and partial rotational motions occurs at 343 K and increasing the temperature does not result in any further changes in the <sup>2</sup>H powder patterns.

#### 4.4.5.5 Motions in the UWDM-P MOF series

In a similar manner to the UWDM-1 series (*vide supra*), it is important to summarize the factors that affect ring dynamics in the UWDM-P series. The UWDM-P series of MOFs are made using similar components and differ only in the presence of a methyl substituent on the pyridine group of the axle in UWDM-P2. The MOFs were found to have similar structures and XRD analysis suggests that desolvation does not produce drastic changes framework structure; however, the dynamics of the CE<sub>1</sub> macrocycles in these systems are very different.

The structural changes induced by desolvation have pronounced effects on the motion. For UWDM-P1, the onset temperature of the two-site jump motion is 208 K and the FML is reached by 253 K (similar to the onset temperature observed for UWDM-1<sub>(24)</sub>). Conversely, for UWDM-P1<sub>d</sub>, the FML of the two-site jump occurs at 321 K (a difference of almost 75 °C). An analogous observation is made for the partial rotational motion with FML temperatures of 285 and 366 K for UWDM-P1 and UWDM-P1<sub>d</sub>, respectively. The effect is less pronounced for UWDM-P2, where the FML for the two-site jump and partial rotation occur at same temperatures; however, increasing the

temperature further results in full rotation of the macrocyclic rings in UWDM-P2, but no additional motion for UWDM-P2<sub>d</sub>.

Desolvation results in a decrease in the rate(s) of motion of the rings in both UWDM-P1 and UWDM-P2, but it is unclear whether this is driven by structural changes, or is a consequence of the different chemical environments of the rings (*i.e.*, interactions with solvent molecules). To address this, solvent-exchange reactions were conducted on UWDM-P2, where solvents were chosen to reflect a variety of polarities and viscosities. VT <sup>2</sup>H SSNMR spectra were acquired and are shown in **Figure C8**. With the exception of some of the lower temperature spectra (with poor S/N), it appears that the motion of the rings in UWDM-P2 is the same (*i.e.*, full rotation occurs at higher temperatures) regardless of the solvent within the pores. Therefore, it is concluded while desolvation produces only minor changes in structure, this is sufficient to cause significant changes in the motion of the rings, and can be attributed to a tilting of the framework structure such that the rings of one [2]rotaxane molecule come into close contact with the axle of another [2]rotaxane.

In comparing UWDM-P1 and UWDM-P2, it is evident that the motion of the macrocyclic rings is more hindered in the former. The FML for partial rotation occurs at 343 K for UWDM-P2, which is comparable to other UWDM systems described herein (*vide supra*); however, increasing the temperature does not result in full rotation in UWDM-P2. It is proposed that the addition of the methyl group on **A<sub>3</sub>** (which is used in the synthesis of UWDM-P2) increases the rigidity of the pillars and reduces the possibility for thermally-induced structural transformations (*i.e.*, framework tilting) that

increase the steric interactions between the rings and the framework, thereby allowing for unhindered motions of the rings in comparison to those in UWDM-P1.

#### 4.4.6 UWDM-4

The systems discussed thus far consist of axles with a single recognition site (*i.e.*, a hydrogen bond donor that can interact with the O atoms of the CE rings). Previously, it has been demonstrated that the design of a [2]rotaxanes consisting of an axle with two recognition sites allows for translational motion (or *shuttling motion*) of the CE rings along the molecular axle in solution.<sup>57,58</sup> The incorporation of such a [2]rotaxane into a solid framework would allow for the coherent motion of the rings. UWDM-4, which consists of a [2]rotaxane made with the H-shaped **A**<sub>4</sub> and **CE**<sub>4</sub>, which is coordinated to **SBU**<sub>3</sub> (**Figure 4.14 (A)**), was synthesized and characterized in order to investigate the possibility of observing and controlling translation motions of the CE rings in the solid state. The carbon atoms in the 2-position of the benzimidazole groups of **A**<sub>4</sub> were labeled with <sup>13</sup>C to facilitate SSNMR experiments (*vide infra*). Coordination of the [2]rotaxane to **SBU**<sub>3</sub> results in an interpenetrated MOF with an ordered arrangement of the **CE**<sub>4</sub> rings (**Figure 4.14(B)**). Despite the interpenetration, the topology of UWDM-4 has channels with large void volumes that easily accommodate the [2]rotaxanes and provide ample space for the shuttling motion (**Figure 4.14(C)**).

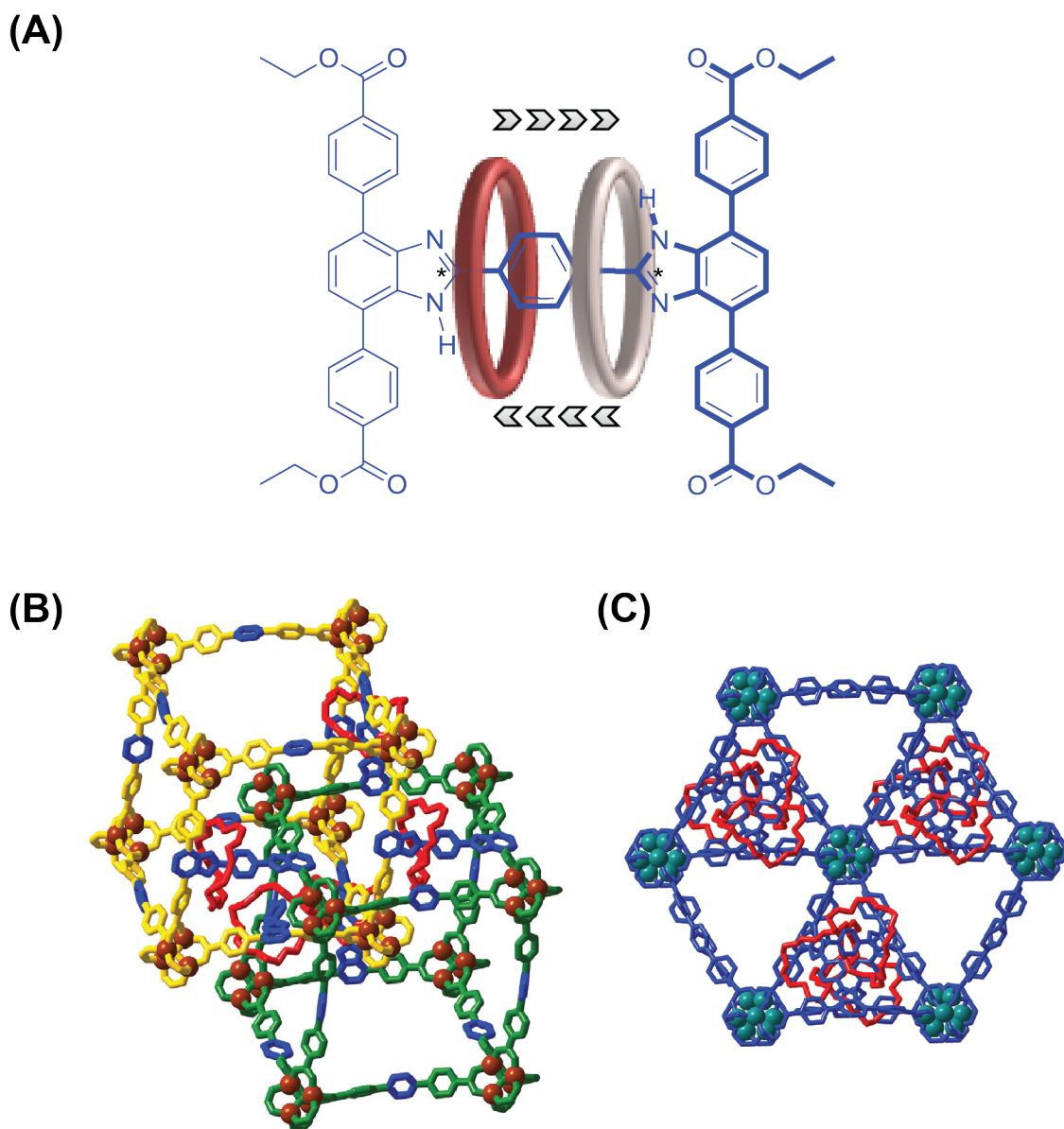


**Figure 4.14:** (A) Schematic diagram of the [2]rotaxane used in the synthesis of UWDM-4. The positions of the  $^{13}\text{C}$  labels are marked with asterisks. (B) Depiction of the interpenetration in UWDM-4 where the [2]rotaxanes serve as “crossbars” that join together two lattices (green and yellow). (C) View along the crystallographic  $c$  axis showing the open channels in the framework.

It was suspected that the addition of the  $\text{HBF}_4$  used in the synthesis of UWDM-4 results in protonation of the axle at one of the benzimidazole recognition sites (*i.e.*,  $\text{UWDM-4}\cdot\text{HBF}_4$ ). Such protonation is not desirable, as the interaction of  $\text{CE}_4$  with the

charged (+1) recognition site is significantly stronger than that with the neutral site;<sup>59,60</sup> if this is the case, the CE would preferentially interact with the charged recognition site and no shuttling would be observed. UWDM-4•HBF<sub>4</sub> was treated with Proton sponge<sup>®</sup> (*i.e.*, *N,N,N',N'*-tetramethylnaphthalene-1,8-diamine, a strong base) to deprotonate the axle; deprotonation was verified using <sup>19</sup>F MAS SSNMR (**Figure C9**). The <sup>19</sup>F NMR spectrum of UWDM-4•HBF<sub>4</sub> has a peak at -148 ppm corresponding to the BF<sub>4</sub><sup>-</sup> anion (thereby confirming the assertion that UWDM-4•HBF<sub>4</sub> is being made). The <sup>19</sup>F NMR spectrum of the sample treated with the proton sponge does not have this signal, confirming the successful deprotonation and production of neutral UWDM-4.

A preliminary set of VT <sup>1</sup>H-<sup>13</sup>C CP/MAS experiments were conducted at 9.4 T (**Figure C10**). The spectrum acquired at room temperature (RT) shows a single, broad peak centred at ~153 ppm. Decreasing the temperature results in a slight broadening of the peak and what might be a small splitting. However, the spectral resolution and S/N are insufficient to conclusively determine if chemical exchange is actually occurring.

The VT <sup>1</sup>H-<sup>13</sup>C CP/MAS ( $v_{\text{rot}} = 14.4$  kHz) experiments for neutral UWDM-4 were conducted at 21.1 T in order to improve spectral resolution and S/N (**Figure 4.15**). The spectrum acquired at 298 K clearly resolves two distinct resonances at 152.7 and 155.2 ppm; these signals are assigned to the open recognition site and one that is occupied by the CE<sub>4</sub> ring, respectively (N.B. These assignments are on similar observations for the [2]rotaxane in solution).<sup>46</sup> Increasing the temperature results in a broadening of the peaks, with coalescence is observed at 311 K. Increasing the temperature to 334 K gives a sharper, single peak centred at 154 ppm (the average of the



two chemical shifts observed in the spectrum at 298 K), indicating that chemical exchange is occurring (*i.e.*, the ring is shuttling between the two recognition sites).

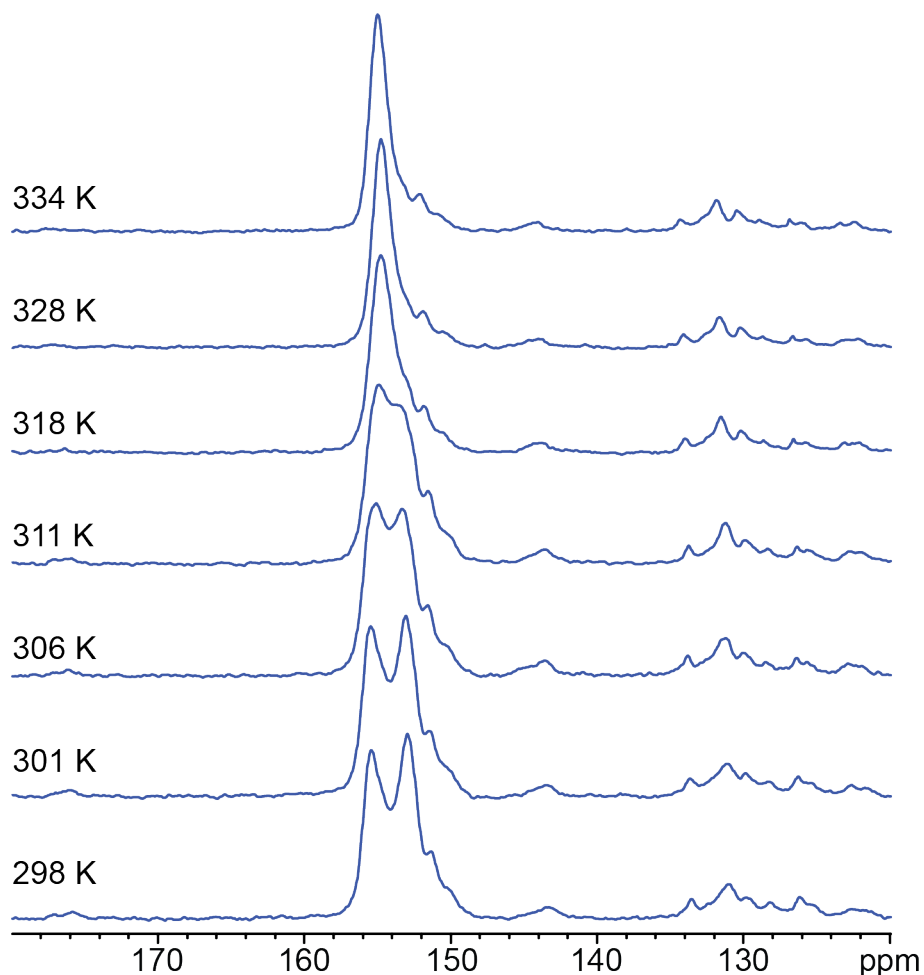


**Figure 4.15:** Variable temperature  $^1\text{H}$ - $^{13}\text{C}$  CP/MAS ( $\nu_{\text{rot}} = 14.4$  kHz) NMR spectra acquired for UWDM-4 at 21.1 T.

To provide further evidence that the shuttling motion is occurring within the MOF, two-dimension exchange spectroscopy (2D EXSY) experiments were conducted (**Figure 4.16**). EXSY spectra are used to identify chemical exchange phenomena in the slow-exchange regime, and therefore, the experiments were conducted at 273 K (*i.e.*, a temperature at which the two resonances are clearly resolved in the 1D  $^1\text{H}$ - $^{13}\text{C}$  CP/MAS

spectra). The spectrum acquired using a mixing time ( $\tau_m$ ) of 1 ms (Figure 4.16(A)) shows only diagonal peaks, as this mixing time is not sufficiently long to observe the cross peaks corresponding to chemical exchange. The spectrum acquired with  $\tau_m = 100$  ms shows intense cross peaks, indicating chemical exchange between the two environments.

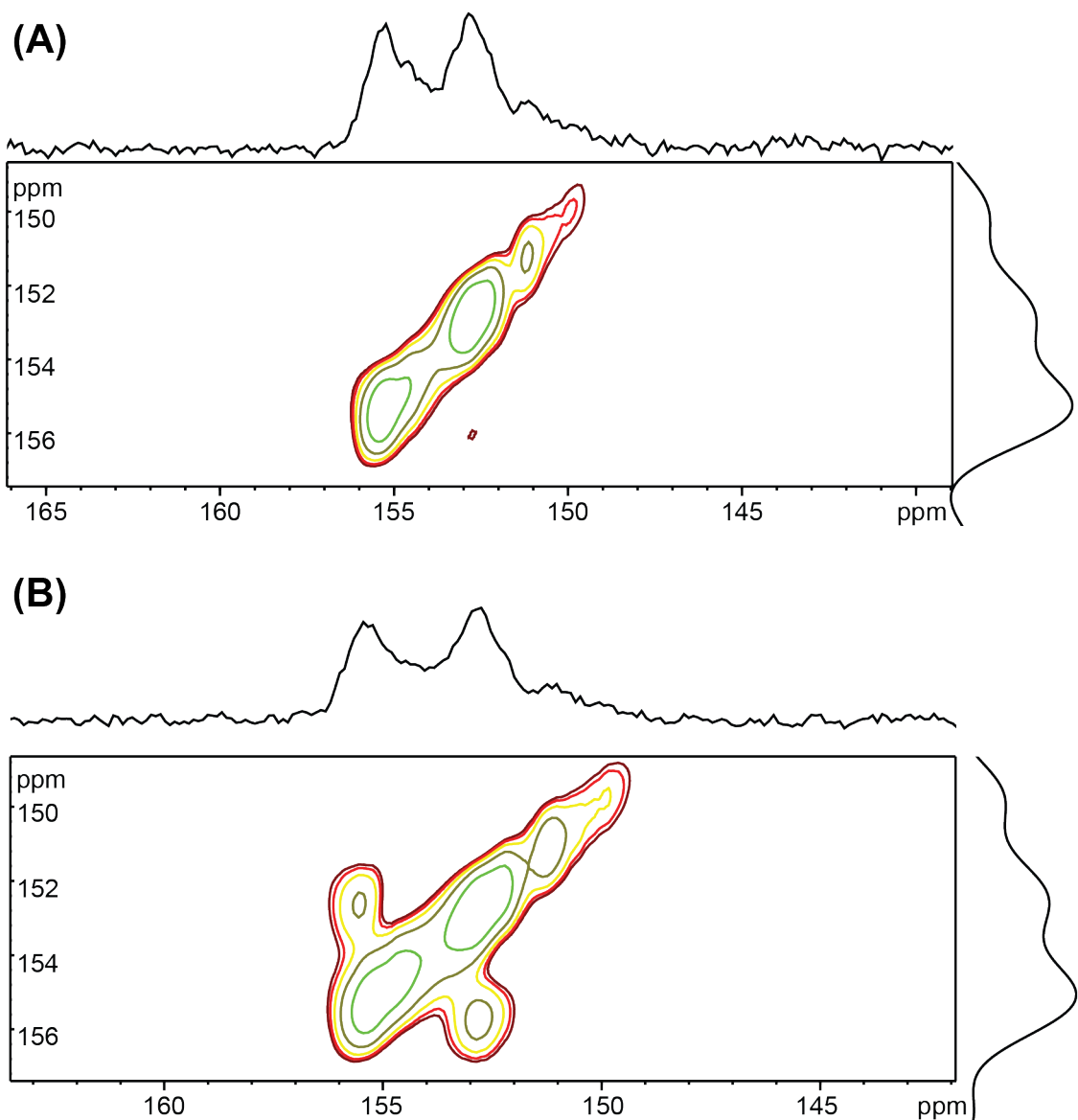


**Figure 4.16:** <sup>1</sup>H-<sup>13</sup>C CP/EXSY MAS NMR spectra ( $\nu_{\text{rot}} = 14.4$  kHz) acquired at 0 °C and 21.1 T using mixing times of (A) 1 ms, and (B) 100 ms.

The 1D  $^1\text{H}$ - $^{13}\text{C}$  CP/MAS data were simulated to extract information on the shuttling rates (**Table 4.11**). It was determined that the shuttling rate at room temperature is 283 Hz, and that this rate increases with temperature. A plot of  $\ln(kT)$  vs.  $(1/T)$  (**Figure 4.17**) was generated and fit using the Eyring equation to extract the barrier of activation for the shuttling motion ( $\Delta G^\ddagger$ ) and other thermodynamic quantities ( $\Delta H^\ddagger$  and  $\Delta S^\ddagger$ ) (**Table 4.12**). These values were compared to those obtained by simulation of the  $^{13}\text{C}$  solution-state NMR data for the [2]rotaxane in solution (**Table C2** and **Figure C11**). The activation barrier for UWDM-4 at room temperature is  $14.1 \text{ kcal mol}^{-1}$ , with  $\Delta H^\ddagger = 15.4(8) \text{ kcal mol}^{-1}$  and  $\Delta S^\ddagger = 4.31(40) \text{ cal K}^{-1} \text{ mol}^{-1}$ . The activation barrier for UWDM-4 is higher than that determined for the [2]rotaxane (made from **A<sub>4</sub>** and **CE<sub>4</sub>**) in solution ( $\Delta G^\ddagger = 7.7 \text{ kcal mol}^{-1}$ ). The higher value of  $\Delta G^\ddagger$  for UWDM-4 is likely due to an increase in enthalpic contributions due to steric and/or electrostatic interactions between the **CE<sub>4</sub>** rings and the framework structure. The lower value of  $\Delta S^\ddagger$  is a consequence of the lower number of configurations or states of the **CE<sub>4</sub>** molecules in the solid state (in contrast to in the solution state where the **CE<sub>4</sub>** molecules undergo a large number of collisions with solvent molecules and are not in any way restricted by other outside steric influences).

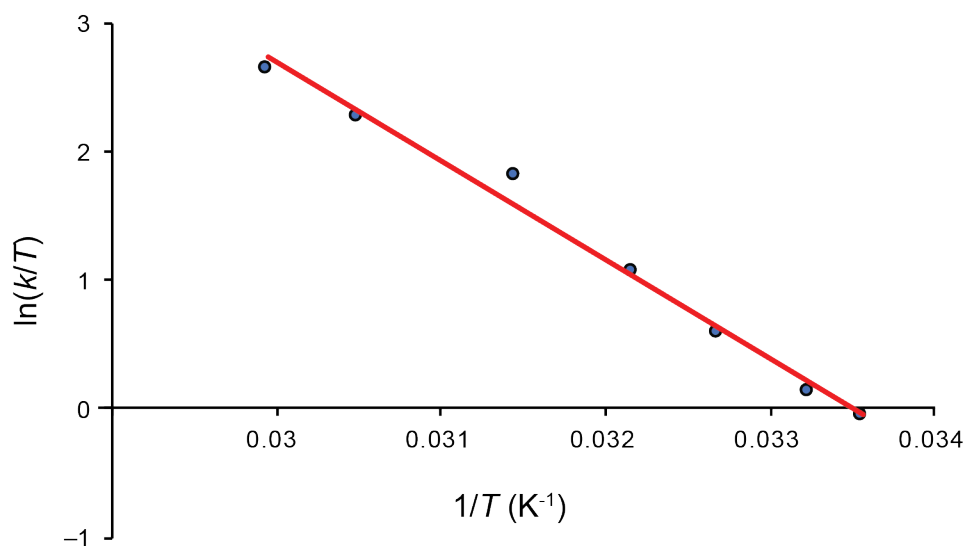


**Figure 4.17:** The Eyring plot generated from the simulation of the VT  $^{13}\text{C}$  SSNMR data. Rates used in the simulations and thermodynamic parameters extracted from the plot are shown in **Table 4.11** and **Table 4.12**, respectively.

In summary, an interpenetrated MOF was synthesized using a [2]rotaxane that has two recognition sites. VT  $^{13}\text{C}$  and 2D EXSY SSNMR experiments reveal that the  $\text{CE}_4$  molecules exhibit thermally-driven shuttling motion within the MOF. This represents the first case of a molecular shuttle incorporated into a solid-state structure, a crucial next step for the design of molecular machines with coherent motions.

**Table 4.11:** Shuttling rates obtained from simulations of the experiment VT  $^{13}\text{C}$  CP/MAS NMR spectra for UWDM-4.

Temperature (K)	Shuttling rate (Hz) <sup>a</sup>
298	280
301	340
306	550
311	910
318	1960
328	3170
334	4690

<sup>a</sup>Uncertainties in the shuttling rates are  $\pm 10$  Hz.

**Table 4.12:** Thermodynamic parameters determined from the Eyring plot generated by simulation of the  $^{13}\text{C}$  NMR data.

Parameter	[2]rotaxane	UWDM-4
$k$ (Hz)	$1.4 \times 10^7$ <sup>a</sup>	283
$\Delta G^\ddagger$ (kcal mol <sup>-1</sup> )	7.7	14.1
$\Delta H^\ddagger$ (kcal mol <sup>-1</sup> )	13.0	15.4
$\Delta S^\ddagger$ (cal K <sup>-1</sup> mol <sup>-1</sup> )	17.7	4.3
$-T\Delta S^\ddagger$ (kcal mol <sup>-1</sup> )	-5.3	-1.3

<sup>a</sup>Value extrapolated from the Eyring plot, **Figure 4.17**.

## 4.5 Conclusions

A series of MOFs that incorporate dynamic interlocked components (*i.e.*, [2]rotaxanes) into their framework structures were synthesized.  $^2\text{H}$  and  $^{13}\text{C}$  SSNMR experiments were conducted to provide information on the modes and rates of motions of the macrocyclic rings that are occurring within these MOFs, and determine the factors (*i.e.*, ring size, framework structure, and guest molecules) that affect the ring dynamics. Comparison of the UWDM-1 series featuring an assortment of different ring sizes demonstrates that the use of a smaller CE molecule results in more hindered motion, and a bulky ring limits rotational motion. Interpenetration of the MOF structures was shown to greatly restrict the motion of the CE rings (UWDM-2), or to induce large amplitude motions (UWDM-3). Studies of the UWDM-P MOF series reveal that the structural changes induced by desolvation can greatly hinder the motion of the CE rings, and that the nature of the solvent (*i.e.*, polarity and viscosity) does not have a substantial influence on these dynamics. Lastly,  $^{13}\text{C}$  SSNMR was used to demonstrate that shuttling motion occurs in a MOF made from a [2]rotaxane with two recognition sites. The rates and activation barrier of the shuttling motion were determined and the latter was found to be greater than the [2]rotaxane in solution. The data obtained from SSNMR experiments

provide a detailed understanding of the factors that affect ring dynamics, offering insight into the design of future molecular machines with a variety of components capable of undergoing a complex range of rotational, torsional, and/or translational motions.

#### 4.6 References:

- (1) Stoddart, J. F. *Chem. Soc. Rev.* **2009**, *38*, 1802.
- (2) Coskun, A.; Banaszak, M.; Astumian, R. D.; Stoddart, J. F.; Grzybowski, B. A. *Chem. Soc. Rev.* **2012**, *41*, 19–30.
- (3) Browne, W. R.; Feringa, B. L. *Nat. Nanotechnol.* **2006**, *1*, 25–35.
- (4) Rapenne, G.; Joachim, C. *Top. Curr. Chem.* **2014**, *354*, 253–278.
- (5) Lewis, J. E. M.; Galli, M.; Goldup, S. M. *Chem. Commun.* **2017**, *53*, 298–312.
- (6) Haussmann, P. C.; Stoddart, J. F. *Chem. Rec.* **2009**, *9*, 136–154.
- (7) Kim, K. *Chem. Soc. Rev.* **2002**, *31*, 96–107.
- (8) Durola, F.; Heitz, E.; Reviriego, F.; Roche, C. E.; Sauvage, J.-P. *Acc. Chem. Res.* **2014**, *47*, 633–645.
- (9) Ma, X.; Tian, H. *Chem. Soc. Rev.* **2010**, *39*, 70–80.
- (10) Tian, H.; Wang, Q.-C. *Chem. Soc. Rev.* **2006**, *35*, 361.
- (11) Sauvage, J.-P. *Acc. Chem. Res.* **1998**, *31*, 611–619.
- (12) Fujita, M. *Acc. Chem. Res.* **1999**, *32*, 53–61.
- (13) Nepogodiev, S. A.; Stoddart, J. F. *Chem. Rev.* **1998**, *98*, 1959–1976.
- (14) Lukin, O.; Vögtle, F. *Angew. Chem. Int. Ed.* **2005**, *44*, 1456–1477.
- (15) Fielden, S. D. P.; Leigh, D. A.; Woltering, S. L. *Angew. Chem. Int. Ed.* **2017**, *56*, 11166–11194.
- (16) Forgan, R. S.; Sauvage, J.-P.; Stoddart, J. F. *Chem. Rev.* **2011**, *111*, 5434–5464.
- (17) Cantrill, S. J.; Chichak, K. S.; Peters, A. J.; Stoddart, J. F. *Acc. Chem. Res.* **2005**, *38*, 1–9.
- (18) Abendroth, J. M.; Bushuyev, O. S.; Weiss, P. S.; Barrett, C. J. *ACS Nano* **2015**, *9*,

7746–7768.

- (19) Leigh, D. A.; Wong, J. K. Y.; Dehez, F.; Zerbetto, F. *Nature* **2003**, *424*, 174–179.
- (20) Hernandez, J. V. *Science* **2004**, *306*, 1532–1537.
- (21) Nishimura, D.; Oshikiri, T.; Takashima, Y.; Hashidzume, A.; Yamaguchi, H.; Harada, A. *J. Org. Chem.* **2008**, No. 2, 2496–2502.
- (22) Schalley, C. A.; Beizai, K.; Vögtle, F. *Acc. Chem. Res.* **2001**, *34*, 465–476.
- (23) Anelli, P. L.; Spencer, N.; Fraser Stoddart, J. *J. Am. Chem. Soc.* **1991**, *113*, 5131–5133.
- (24) Saha, S.; Flood, A. H.; Stoddart, J. F.; Impellizzeri, I.; Silvi, S.; Venturi, M.; Credi, A. *J. Am. Chem. Soc.* **2007**, *129*, 12159–12171.
- (25) Bermudez, V.; Capron, N.; Gase, T.; Gatti, F. G.; Kajzar, Ě.; Leigh, D. A.; Zerbetto, F.; Zhang, S.; Gco, D. S. P. E.; Saclay, C. E.; Ciamician, C. G.; Selmi, V. *Nature* **2000**, *406*, 608–611.
- (26) Serreli, V.; Lee, C.-F.; Kay, E. R.; Leigh, D. A. *Nature* **2007**, *445*, 523–527.
- (27) Bissell, R. A.; Córdova, E.; Kaifer, A. E.; Stoddart, J. F. *Nature* **1994**, *369*, 133–137.
- (28) Kay, E. R.; Leigh, D. A.; Zerbetto, F. *Angew. Chem. Int. Ed.* **2007**, *46*, 72–191.
- (29) Choi, J. W.; Flood, A. H.; Steuerman, D. W.; Nygaard, S.; Braunschweig, A. B.; Moonen, N. N. P.; Laursen, B. W.; Luo, Y.; Delonno, E.; Peters, A. J.; Jeppesen, J. O.; Xu, K.; Stoddart, J. F.; Heath, J. R. *Chem. Eur. J.* **2005**, *12*, 261–279.
- (30) Zhu, K.; Loeb, S. J. *Top. Curr. Chem.* **2014**, *345*, 213–251.
- (31) Loeb, S. J. *Chem. Soc. Rev.* **2007**, *36*, 226–235.
- (32) Zhao, Y. L.; Liu, L.; Zhang, W.; Sue, C. H.; Li, Q.; Miljanić, O. Š.; Yaghi, O. M.;



- Fraser Stoddart, J. *Chem. Eur. J.* **2009**, *15*, 13356–13380.
- (33) Zhou, H.-C.; Kitagawa, S. *Chem. Soc. Rev.* **2014**, *43*, 5415–5418.
- (34) Eddaoudi, M. *Science* **2002**, *295*, 469–472.
- (35) Hupp, J. T. *Science* **2005**, *309*, 2008–2009.
- (36) Furukawa, H.; Cordova, K. E.; O’Keeffe, M.; Yaghi, O. M. *Science* **2013**, *341*, 1230444–1230444.
- (37) Howarth, A. J.; Liu, Y.; Li, P.; Li, Z.; Wang, T. C.; Hupp, J. T.; Farha, O. K. *Nat. Rev. Mater.* **2016**, *1*, 15018.
- (38) Burtch, N. C.; Jasuja, H.; Walton, K. S. *Chem. Rev.* **2014**, *114*, 10575–10612.
- (39) Bennett, T. D.; Keen, D. A.; Tan, J. C.; Barney, E. R.; Goodwin, A. L.; Cheetham, A. K. *Angew. Chem. Int. Ed.* **2011**, *50*, 3067–3071.
- (40) Chandrakumar, N. *Spin-1 NMR*; Springer: Berlin, 1996.
- (41) Schmidt-Rohr, K.; Spiess, H. W. *Multidimensional Solid-State NMR and Polymers*; Academic Press: New York, 1994.
- (42) Pyykkö, P. *Mol. Phys.* **2001**, *99*, 1617–1629.
- (43) Ratcliffe, C. I.; Ripmeester, J. A.; Buchanan, G. W.; Denikes, J. K. *J. Am. Chem. Soc.* **1992**, *114*, 3294–3299.
- (44) Vukotic, V. N.; O’Keefe, C. A.; Zhu, K.; Harris, K. J.; To, C.; Schurko, R. W.; Loeb, S. J. *J. Am. Chem. Soc.* **2015**, *137*, 9643–9651.
- (45) Zhu, K.; Vukotic, V. N.; O’Keefe, C. A.; Schurko, R. W.; Loeb, S. J. *J. Am. Chem. Soc.* **2014**, *136*, 7403–7409.
- (46) Zhu, K.; O’Keefe, C. A.; Vukotic, V. N.; Schurko, R. W.; Loeb, S. J. *Nat. Chem.* **2015**, *7*, 514–519.

- (47) van Gorkom, L. C. M.; Hook, J. M.; Logan, M. B.; Hanna, J. V.; Wasylishen, R. E. *Magn. Reson. Chem.* **1995**, *33*, 791–795.
- (48) Bielecki, A.; Burum, D. P. *J. Magn. Reson.* **1995**, *220*, 215–220.
- (49) Eichele, K.; Wasylishen, R. E. **2001**, WSolids.
- (50) Vold, R. L.; Hoatson, G. L. *J. Magn. Reson.* **2009**, *198*, 57–72.
- (51) Adept Scientific Inc.: Bethesda, Maryland 2003.
- (52) Vukotic, V. N.; Harris, K. J.; Zhu, K.; Schurko, R. W.; Loeb, S. J. *Nat. Chem.* **2012**, *4*, 456–460.
- (53) Wittebort, R. J.; Olejniczak, E. T.; Griffin, R. G. *J. Chem. Phys.* **1987**, *86*, 5411–5420.
- (54) Buchanan, G. W.; Moghimi, A.; Ratcliffe, C. I. *Can. J. Chem.* **1996**, *74*, 1437–1446.
- (55) Meirovitch, E. *J. Phys. Chem.* **1985**, *89*, 2385–2393.
- (56) Gong, Y.-N.; Zhong, D.-C.; Lu, T.-B. *CrystEngComm* **2016**, *18*, 2596–2606.
- (57) Gholami, G.; Zhu, K.; Baggi, G.; Schott, E.; Zarate, X.; Loeb, S. J. *Chem. Sci.* **2017**, *8*, 7718–7723.
- (58) Vukotic, V. N.; Zhu, K.; Baggi, G.; Loeb, S. J. *Angew. Chem. Int. Ed.* **2017**, *56*, 6136–6141.
- (59) Zhu, K.; Vukotic, V. N.; Loeb, S. J. *Angew. Chem. Int. Ed.* **2012**, *51*, 2168–2172.
- (60) Noujeim, N.; Zhu, K.; Vukotic, V. N.; Loeb, S. J. *Org. Lett.* **2012**, *14*, 2484–2487.

# Chapter 5: Multinuclear Solid-State NMR Investigations of Platinum(II) trans-Dihydride Molecular Rotors

## 5.1 Overview

The design and synthesis of solid-state molecular rotors with low energy barriers of rotation represents an important step in the fabrication of molecular machines. An understanding of the factors that affect rotation is crucial for the design of systems with controlled dynamics, and for the future inclusion of unidirectional motion. Herein, we provide a detailed analysis of *trans*-D<sub>2</sub>Pt(P<sup>t</sup>Bu<sub>3</sub>)<sub>2</sub> (**1-D**), an inorganic random rotor (*i.e.*, in which rotational motions occur in both directions) that functions in the solid state. Single-crystal X-ray diffraction (SCXRD) and <sup>195</sup>Pt solid-state NMR (SSNMR) indicate the presence of motion, but are insufficient to elucidate the exact nature of the dynamics. Variable-temperature (VT) <sup>2</sup>H SSNMR is used to study the motion over a wide range of temperatures, and several different models are proposed. Simulation of the VT <sup>2</sup>H SSNMR spectra indicate that the deuterides exhibit a three-fold rotational motion with rates in the fast motion limit (FML) at temperatures as low as 75 K. The SSNMR results are confirmed by the DFT computation of the energy landscape associated with the rotational motion, revealing a low energy barrier to rotation. A preliminary investigation of a series of structurally similar platinum-deuteride compounds is also presented, and their VT <sup>2</sup>H SSNMR spectra were simulated using the motional models developed for **1-D**. These studies reveal that the nature of the coordinating ligands greatly affects the motion of the deuterides and rotational barriers. It is hoped that the information provided herein, and the use of SSNMR and DFT calculations in tandem, will allow for the

rational design of solid-state rotors with tuneable, low-energy barriers and controlled motions.

## 5.2 Introduction

The design of molecular machines draws influence from analogous macroscopic devices.<sup>1</sup> This design principle has led to the fabrication of molecular elevators,<sup>2</sup> muscles,<sup>3</sup> and nano-cars.<sup>4</sup> A key component in these devices are *molecular rotors*, which feature an axis of rotation that allows for the rotation of the mobile part, the *rotator*, with respect to the static part, the *stator*.<sup>5</sup> The motion of molecular rotors can be broadly categorized as either random or unidirectional. Random motion involves the rotator moving in both directions with thermal energy as the driving force, whereas unidirectional motion occurs in a single direction, akin to a ratchet, and requires a source of free energy.<sup>5-7</sup> For the design of random rotors, a key challenge is to lower the activation barrier for the rotational motion; properly designed molecules or materials may have applications as molecular gyroscopes.<sup>8-15</sup> It is envisaged that a low activation-barrier random rotor can be modified such that unidirectional motion can be achieved (*e.g.*, with careful control of both steric and electronic interactions between the stator and the rotator).

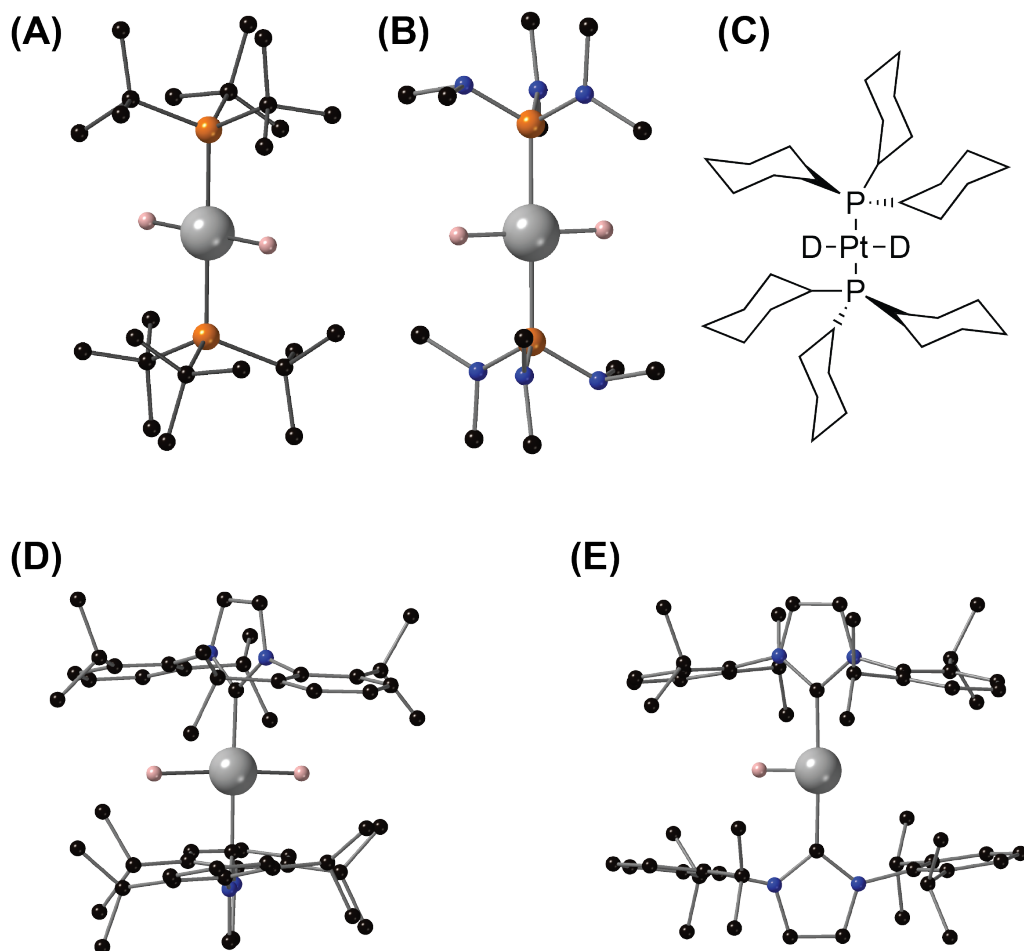
The first intensely studied class of molecular rotors, reported by Mislou *et al.*,<sup>16</sup> functioned only in the solution state. Efforts were later made to design molecular rotors that would operate in the solid state, and to understand the factors that govern their mobilities.<sup>17-20</sup> It was determined that the size, shape, and symmetry of the components of the rotor affect the overall dynamics. The design of functional solid-state rotors has

proven to be difficult, with the limitations resulting from the synthesis of stators that provide enough void space to allow for the free rotation of the rotator.<sup>21,22</sup> Most of the current examples of molecular rotors in the solid state consist of large organic stators and organic rotators; however, the design of inorganic rotators has shown promise.<sup>23</sup> Despite the elegant syntheses reported for these inorganic rotors, most have suffered from high activation barriers to the rotational motions, greatly hindering their further development and application.<sup>24,25</sup> Therefore, molecular rotors that are easily synthesized and have low barriers to rotation are highly sought after.

A detailed understanding of the factors that determine the rates and modes of motions in solid-state rotors is crucial for the design of systems with low barriers and controlled dynamics. The dynamics of the rotators are usually evidenced by the apparent disorder of the rotator components in crystal structures determined by X-ray diffraction (XRD); however, XRD is limited in the information that it can provide on the exact nature of the dynamics. Solid-state NMR (SSNMR) spectra are sensitive to a variety of different motions over a wide dynamical range, and as such, it is the premier technique for studying dynamics in the solid state. The simulation of SSNMR spectra acquired at different temperatures allows for the development of models that describe the dynamics of the rotators and the determination of the rates of their motions.

In this chapter, SSNMR is used to study the dynamics of a series of platinum hydride compounds that show potential as molecular rotors (**Scheme 5.1**). A detailed analysis of *trans*-D<sub>2</sub>Pt(P<sup>t</sup>Bu<sub>3</sub>)<sub>2</sub> (**1-D**) is provided, and several motional models are proposed, providing a framework in which to discuss the compounds that follow. SCXRD data and <sup>195</sup>Pt SSNMR spectra indicate that the hydrides in **1** are dynamic, but

these techniques are insufficient for developing detailed motional models. Variable-temperature (VT)  $^2\text{H}$  SSNMR experiments reveal that the deuterides in **1-D** are in motion at temperatures as low as 75 K. Simulation of the  $^2\text{H}$  SSNMR powder patterns indicates that the deuterides are undergoing a three-site rotation with rates in the fast motion limit (FML), and that the relative populations of the rotational states are changing with temperature. An energy landscape for the rotational motion of **1** was determined using DFT calculations and is in excellent agreement with the results obtained from  $^2\text{H}$  SSNMR. Experiments conducted on *trans*- $\text{D}_2\text{Pt}(\text{P}(\text{NMe}_2)_3)_2$  (**2-D**) indicate that the deuterides are static within a temperature range from 273 to 373 K. Conversely, the  $^2\text{H}$  SSNMR spectra of *trans*- $\text{D}_2\text{Pt}(\text{PCy}_3)_2$  (**3-D**) indicate motional averaging with very fast rates and equal populations of the states, even at low temperatures, suggesting a very low barrier to rotation. *Trans*- $\text{D}_2\text{Pt}(i\text{Pr})_2$  (**4-D**) and [*trans*- $\text{DPt}(i\text{Pr})_2$ ][ $\text{BAr}^{\text{F}}_4$ ] (**5-D**), while structurally and chemically very similar, exhibit very different dynamics.  $^2\text{H}$  SSNMR is an ideal technique for probing the motions of these inorganic rotors, and the complementary use of DFT calculations allows for an understanding of the structural features that affect their motions, which we believe will ultimately lead to the rational design of rotors with very low energy barriers.



**Scheme 5.1:** Representations of the structures of (A) *trans*-H<sub>2</sub>Pt(P<sup>t</sup>Bu<sub>3</sub>)<sub>2</sub> (**1**), (B) *trans*-H<sub>2</sub>Pt(P(NMe<sub>2</sub>)<sub>3</sub>)<sub>2</sub> (**2**), (C) *trans*-D<sub>2</sub>Pt(PCy<sub>3</sub>)<sub>2</sub> (**3-D**), (D) *trans*-D<sub>2</sub>Pt(*i*Pr)<sub>2</sub> (**4**), and (E) [*trans*-HPt(*i*Pr)<sub>2</sub>][BARF<sub>4</sub>] (**5**). For **1**, **2**, **4**, and **5**, ball-and-stick representations are derived from the crystal structures, whereas for **3-D**, no crystal structure has been reported. Non-hydride hydrogen atoms and the [BARF<sub>4</sub>]<sup>-</sup> counterion have been omitted for clarity. Colour key: H/D = pink, C = black, N = blue, P = orange, Pt = grey.

### 5.3 Experimental Methodologies and Computational Details

#### 5.3.1 Synthesis

The synthesis of **1-H** and **1** are outlined in Appendix D. Compounds **2-D** and **3-D** were provided by Dr. Fekl from the University of Toronto at Mississauga. Compounds **4-D** and **5-D** were provided by Dr. Salvador Conejero from the University of Seville,

Spain. Details of syntheses and crystal structures will be detailed in forthcoming publications by these research groups.

### 5.3.2 $^{195}\text{Pt}$ SSNMR

A Varian Infinity Plus spectrometer equipped with a wide-bore Oxford 9.4 T magnet ( $\nu_0(^1\text{H}) = 400$  MHz and  $\nu_0(^{195}\text{Pt}) = 85.59$  MHz) was used for the acquisition of static (*i.e.*, stationary samples)  $^{195}\text{Pt}$  SSNMR spectra. The experiments were conducted on a Varian Chemagnetics 5 mm triple-resonance (HXY) T3 MAS NMR probe.  $^{195}\text{Pt}$  chemical shifts were referenced with respect to 1.0 M aqueous  $\text{Na}_2\text{PtCl}_6$  ( $\delta_{\text{iso}} = 0$  ppm). The  $^{195}\text{Pt}$  powder patterns were too broad to excite with a single, high-powered rectangular pulse; therefore, the WURST-CPMG pulse sequence was used.<sup>26–28</sup> These experiments made use of 50  $\mu\text{s}$  WURST-80 pulses swept over 2000 kHz (sweep rate of 40 MHz/ms). Echoes were composed of either 200 or 400 points and experiments used 44 kHz of rf power, 40 kHz of proton decoupling, and a 5 s recycle delay.

$^{195}\text{Pt}$  WCPMG spectra were processed using the NUTS program from Acorn software. FIDs were processed with digital filtering, followed by Fourier transformation and a magnitude calculation. The SSNMR spectra were simulated using the WSolids<sup>29</sup> program to extract the  $^{195}\text{Pt}$  CS tensor parameters. Errors in the values of the parameters were estimated by bidirectional variation and visual inspection of the resulting simulated powder patterns.

### 5.3.3 Low-temperature $^2\text{H}$ SSNMR

Low temperature (*i.e.*, 30 – 295 K)  $^2\text{H}$  SSNMR experiments for **1** were acquired using a homebuilt spectrometer equipped with a Bradley 4.75 T magnet ( $\nu_0(^1\text{H}) = 200$  MHz and  $\nu_0(^2\text{H}) = 32.02$  MHz) at Washington University, St. Louis, MO. A homebuilt



probe was used for the acquisition of the static spectra. Temperatures were controlled using Lakeshore temperature controller equipped with both platinum and carbon-glass resistance thermometers and a Kadel Research helium dewar. Temperatures in the probe were measured using a platinum resistance thermometer.

Experiments were conducted using the quadrupolar echo ( $90^\circ - \tau_1 - 90^\circ - \tau_2 -$  acquire) pulse sequence.<sup>30</sup> Experimentally optimized  $90^\circ$  pulse lengths of  $3.8 \mu\text{s}$  and interpulse delays ( $\tau$ ) of  $75 \mu\text{s}$  were used.  $^2\text{H}$  chemical shifts were referenced with respect to a sample of liquid  $\text{D}_2\text{O}$  (0 ppm). 16 K of data points were acquired with a dwell time of  $1 \mu\text{s}$ .

Low-temperature  $^2\text{H}$  SSNMR spectra were processed using MatLab. The FID was left-shifted to the top of the echo and zero-filled once. 1500 Hz of exponential apodization was applied before subsequent Fourier transform and phase correction.

#### **5.3.4 Variable-temperature $^2\text{H}$ SSNMR Experiments at 9.4 T**

$^2\text{H}$  SSNMR experiments were conducted using a Bruker Avance III HD console equipped with a wide-bore 9.4 T Oxford magnet ( $\nu_0(^1\text{H}) = 399.73 \text{ MHz}$ ,  $\nu_0(^2\text{H}) = 61.4 \text{ MHz}$ ). A 5 mm double-resonance (HX) static probe was used. The quadrupolar echo pulse sequence was used with 30 or  $100 \mu\text{s}$  pulse spacings. Optimized  $90^\circ$  pulse lengths of  $3 \mu\text{s}$  were used and the recycle delays are listed in **Table D1**. 1 K of data points were acquired using a  $1 \mu\text{s}$  dwell time. Spectra were processed using TopSpin 3.5pl6. FIDs that were left-shifted to the top of the echo were processed using one zero fill and 2000 Hz of exponential apodization, followed by Fourier transform and phase correction. FIDs that were not left-shifted were processed with 2000 Hz of Gaussian apodization, followed by

a Fourier transform and a magnitude calculation. Temperatures of the VT unit and probe were calibrated using the temperature-dependent chemical shift of  $\text{PbNO}_3$ .<sup>31,32</sup>

### 5.3.5 Simulation of $^2\text{H}$ SSNMR Data

The SSNMR spectra acquired at all temperatures were simulated to extract the slow motion limit (SML)  $^2\text{H}$  EFG tensor parameters using either WSolids,<sup>29</sup> or the Solid Lineshape Analysis (SOLA) tool in TopSpin. The EXPRESS software package<sup>33</sup> was used to simulate the  $^2\text{H}$  SSNMR spectra affected by motions in the intermediate motional regime (IMR) and FML, for purposes of extracting motional rates and site populations.

### 5.3.6 Calculation of $^{195}\text{Pt}$ CS and $^2\text{H}$ EFG Tensor Parameters

DFT calculations of the platinum chemical shielding and  $^2\text{H}$  EFG tensor parameters were conducted with the Amsterdam Density Functional (ADF) software package.<sup>34,35</sup> The calculations used the revised Perdew-Burke-Ernzerhof (rPBE) functional and the all-electron quadruple-zeta quadruply polarized (QZ4P) basis sets from the ADF basis set library.<sup>36,37</sup> Relativistic effects were included at the spin-orbit level using the zeroth-order regular approximation (ZORA) formalism.<sup>38</sup> A criterion of  $10^{-4}$  a.u. was applied to remove the linearly dependent basis function combinations.

Calculations were performed on cluster models derived from the reported crystal structures. The clusters consisted of a single  $\text{PtH}_2\text{L}_2$  molecule and the positions of the protons were geometry optimized before computation of the CS tensor parameters.

To compare the calculated tensors to experimental values, the platinum chemical shielding values were converted to chemical shifts through calculations on a reference compound ( $\text{PtCl}_6^{2-}$ ).

### 5.3.7 DFT Calculations of Energy Landscapes

Calculations were conducted on GAMESS(US),<sup>39,40</sup> using the B3LYP functional, the 6-31G\*\* basis set for C, H, and P, and the 6-31G\*\* basis set with LANL2DZ effective core potentials for Pt. Heavy atom coordinates were taken from X-ray crystal structure of **1** and not geometry optimized, the Pt–H distance was set to DFT-optimized value of 1.657 Å, all P–Pt–H angles were set to 90°. The energies were calculated for different molecular conformations in which the H–Pt–H unit was rotated in 10° increments and only the *tert*-butyl methyl group atoms were relaxed.

## 5.4 Results and Discussion

In this work, a series of square-planar platinum(II) deuteride compounds (**Scheme 5.1**) were studied to determine if they behave as solid-state molecular rotors. The compounds consist of Pt(II) centres that are coordinated by two donor ligands (*i.e.*, phosphines or carbenes) that are positioned *trans* to one another. Compounds **1-4** have two *trans* hydrides and **5** has a single hydride (and a [BArF<sub>4</sub>]<sup>−</sup> anion to balance the positive charge of the Pt(II) centre). The steric bulk afforded by the donor ligands results in thermodynamically stable compounds; in addition, some of these ligands allow for uninhibited motion of the comparatively small deuteride ligands. The structures of the compounds were originally determined for the hydride forms (*i.e.*, **1**, **2**, **4**, and **5**), but the following discussion pertains mostly to the deuteride forms (*i.e.*, **1-D**, **2-D**, **3-D**, **4-D**, and **5-D**).

VT <sup>195</sup>Pt and <sup>2</sup>H SSNMR experiments were conducted to observe the motion (or lack thereof) of the deuteride ligands. A detailed analysis of the VT NMR data and

motional models is provided for **1-D**, providing a framework in which preliminary descriptions of the motions within the other compounds are discussed. A brief comment is made on the factors that affect the motion of the deuterides in each of the compounds.

#### 5.4.1 *trans*-H<sub>2</sub>Pt(P(<sup>t</sup>Bu)<sub>3</sub>)<sub>2</sub> (**1**) and *trans*-D<sub>2</sub>Pt(P(<sup>t</sup>Bu)<sub>3</sub>)<sub>2</sub> (**1-D**)

Compound **1** consists of a Pt(II) centre coordinated by staggered *trans-tert*-butylphosphine ligands and *trans*-hydride ligands. Inspection of the crystal structure of **1** indicates an unusually short Pt–H bond length of 1.35 Å.<sup>41</sup> Previous X-ray diffraction (XRD) studies revealed apparent Pt–H bond lengths between 1.5-1.8 Å;<sup>42-44</sup> we use “apparent” since the precise location of hydrogen atom positions with XRD techniques is known to be challenging. The short Pt–H bond length observed in **1** is likely the result of motion “smearing” the electron density over a circular path within the plane perpendicular to the P–Pt–P molecular axis. The refined crystal structure could only be obtained by implementing model in which each hydride occupies three positions, each with one-third occupancy (*i.e.*, a total of six positions, **Figure D1**). Therefore, the XRD data suggest that the hydrogen atoms are mobile, but provide limited information on the nature of these motions, and no information on the motional rates.

SSNMR is the premier technique for studying molecular-level dynamics in the solid-state and providing detailed information on the rates and modes of motion over a wide range of temperatures. NMR investigations were conducted on **1** and **1-D** to complement the XRD data and provide more detailed information on the nature of the dynamics of the hydrides/deuterides.

### 5.4.1.1 VT $^{195}\text{Pt}$ SSNMR of **1**

The platinum chemical shift (CS) range is approximately 15,000 ppm, due to the extreme sensitivity of the platinum CS to the electronic environment about the Pt atom.<sup>45</sup>  $^{195}\text{Pt}$  SSNMR powder patterns yield information on both the isotropic chemical shift ( $\delta_{\text{iso}}$ ) and the chemical shift anisotropy (CSA, which can be described by two parameters: the span ( $\Omega$ ) and the skew ( $\kappa$ ), see **Table 5.1** for definitions). Predicting the orientation of the CS tensor in the molecular frame using DFT calculations is useful for considering relationships between structure and chemical shift,<sup>46</sup> as well as for considering how molecular motion can produce an *effective CS tensor*, whose principal components represent motional averages of the components of the original tensor.

**Table 5.1:** Calculated (DFT) and experimental platinum chemical shift (CS) tensor parameters for **1**.

Method	$\delta_{11}$ (ppm)	$\delta_{22}$ (ppm)	$\delta_{33}$ (ppm)	$\delta_{\text{iso}}$ (ppm) <sup>a</sup>	$\Omega$ (ppm) <sup>b</sup>	$\kappa$ <sup>c</sup>
Calculated <sup>d</sup>	-3930	-5526	-5630	-5029	1700	-0.88
Experimental (298 K)	-4701	-5698	-5750	-5383	1050	-0.90
Experimental (133 K)	-4735	-5690	-5785	-5403	1050	-0.82

<sup>a</sup> Isotropic chemical shift:  $\delta_{\text{iso}} = (\delta_{11} + \delta_{22} + \delta_{33})/3$ . <sup>b</sup> Span:  $\Omega = \delta_{11} - \delta_{33}$ . Skew:  $\kappa = 3(\delta_{22} - \delta_{\text{iso}})/\Omega$ . Uncertainties in the experimental values are indicated in parentheses and were determined by bidirectional variation and visual inspection of the simulated powder patterns. Platinum chemical shieldings were converted to chemical shifts through calculations on a reference compounds ( $\text{PtCl}_6^{2-}$ ).

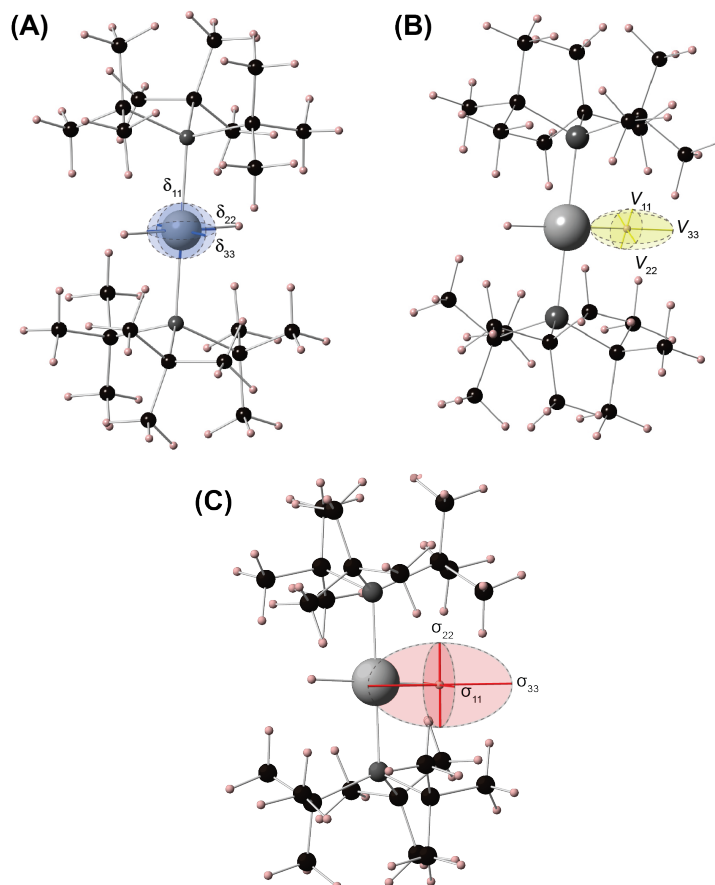


**Figure 5.1:**(A) Platinum chemical shift, (B)  $^2\text{H}$  EFG, and (C) hydrogen chemical shielding tensor orientations for **1** determined by DFT calculations.

The experimental spectrum acquired at 133 K (**Figure 5.2(A)**) has values of  $\delta_{22}$  and  $\delta_{33}$  of  $-5690$  and  $-5785$  ppm, respectively, whereas the spectrum acquired at 298 K (**Figure 5.2(B)**) has values of  $-5698$  and  $-5750$  ppm. Both sets of parameters indicate that the CS tensor is orientated such that  $\delta_{11}$  is along the direction of the P–Pt–P, and that  $\delta_{22}$  and  $\delta_{33}$  are perpendicular to this axis. It appears that the values of  $\delta_{22}$  and  $\delta_{33}$  approach each other as the temperature is increased; however, the small changes in these components relative to the overall span of the powder pattern does not allow for the determination of an accurate motional model. Lower-temperature  $^{195}\text{Pt}$  SSNMR experiments were attempted in order to extract more information on the motion and the

associated rates (**Figure D2**). These spectra have very poor signal-to-noise (S/N) ratios and are not of high enough quality to be of value for simulations of dynamics, due to the long  $T_1(^{195}\text{Pt})$  times at low temperatures and the inability to apply  $^1\text{H}$  decoupling on the low-temperature probe.

The  $^{195}\text{Pt}$  chemical shielding tensor parameters and orientation were predicted for **1** using DFT calculations within the ADF software package (see *Section 5.3.5* for computational details). The calculated  $^{195}\text{Pt}$  chemical shielding tensor parameters are shown in **Table 5.1**. For comparison to experimental chemical shift tensors, the chemical shielding tensor parameters have been converted to a chemical shift scale (see *Section 5.3.6*); hereafter, all discussion is framed in terms of chemical shift tensors. The calculated values of  $\delta_{22}$  and  $\delta_{33}$  are in fair agreement with the experimental values, but there are large discrepancies in the values of  $\delta_{11}$  (**Table 5.1**). For heavy elements like Pt, it is often difficult to obtain accurate CS tensor parameters, due deficiencies in the basis sets or unsuitable correlation functionals being used.<sup>47,48</sup> These problems arise from the (i) large number of electrons in the Pt atom (and possible need for electron correlation) and (ii) the requirement for a relativistic approach for the calculation of CS tensor parameters.<sup>49</sup> It is the components of the CS tensor representing the directions of least shielding (in this case,  $\delta_{11}$ ) that are the most challenging to calculate, since their accurate calculations are highly dependent upon accurate modeling of the virtual orbitals.

The principal component indicating the direction of least shielding,  $\sigma_{11}$ , which corresponds to the highest frequency component of the CS tensor,  $\delta_{11}$ , is oriented along the Pt-P bond (**Figure 5.1(A)**).  $\delta_{22}$  is oriented along the Pt-H bond and  $\delta_{33}$  is perpendicular to the P-Pt-H plane. A rotor-like motion of the H-Pt-H unit is therefore

expected to average (or partially average) the values of the  $\delta_{22}$  and  $\delta_{33}$  components, while having no effect on  $\delta_{11}$ .

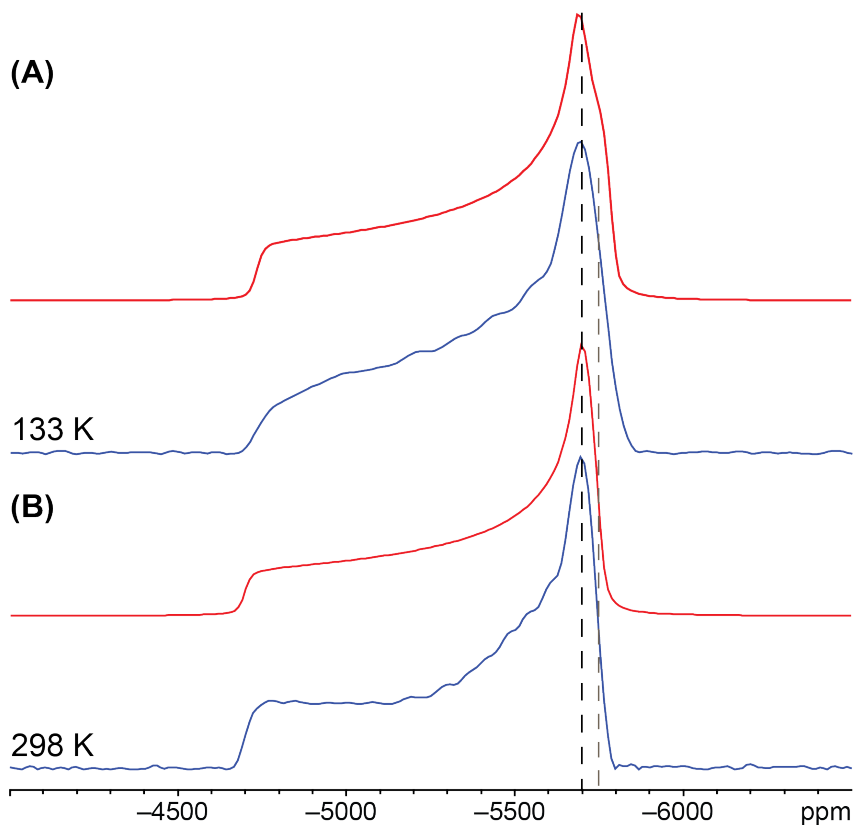


**Figure 5.2:** Experimental  $^{195}\text{Pt}$  WURST-CPMG NMR spectra (blue) and accompanying analytical simulations (red) for **1** acquired at (A) 133 K and (B) 298 K. The platinum CS tensor parameters are shown in **Table 5.1**. The dashed lines indicate the relative positions of  $\delta_{22}$  (black) and  $\delta_{33}$  (grey)

#### 5.4.1.2 $^2\text{H}$ SSNMR of 1-D

$^2\text{H}$  SSNMR is an established technique for the study of molecular-level dynamics, providing detailed information on both the rates and modes of motion.<sup>50,51</sup> Molecular motions can produce drastic changes in the appearance of  $^2\text{H}$  powder patterns if they dynamically alter the magnitudes of the principal components or orientation of the  $^2\text{H}$  EFG tensor. The extent to which the components of the EFG tensor are changed and how



their *effective* (*i.e.*, motionally averaged) values manifest in a  $^2\text{H}$  SSNMR powder pattern are dependent on the modes and rates of the motion. Three motional regimes are defined based on the relative magnitudes of the exchange rate ( $\nu_{\text{ex}}$ ) and the quadrupolar frequency ( $\nu_{\text{Q}} = 3C_{\text{Q}}/(2I(2I - 1))$ ), where  $C_{\text{Q}}$  is the quadrupolar coupling constant and is defined in **Table 5.2**): the slow-motion limit (SML), where  $\nu_{\text{ex}} \ll \nu_{\text{Q}}$ ; the intermediate motion regime (IMR), where  $\nu_{\text{ex}} \approx \nu_{\text{Q}}$ ; and, the fast motion limit (FML), where  $\nu_{\text{ex}} \gg \nu_{\text{Q}}$ . Motions occurring at rates in the SML (typically  $\nu_{\text{ex}} < 10^3$  Hz for the systems herein) are too slow to produce observable changes in the  $^2\text{H}$  SSNMR powder patterns, and the line shapes are invariant to changes in the interpulse delays ( $\tau$ ) in the quadrupolar echo pulse sequence. Motions occurring at rates in the IMR ( $10^3 \text{ Hz} \leq \nu_{\text{ex}} \leq 10^7 \text{ Hz}$ ) produce complex powder patterns that are dependent on both temperature and interpulse delay, and typically require detailed numerical simulations. Spectra influenced by motions occurring in the FML ( $\nu_{\text{ex}} > 10^7 \text{ Hz}$ ) can be simulated by utilizing the effective EFG tensor parameters, whose values depend on the motional model. Spectra acquired in the FML are independent of temperature and interpulse delays.

**Table 5.2:** Calculated (DFT) and experimental  $^2\text{H}$  EFG tensor parameters.

Compound	Calculated		Experimental <sup>a</sup>	
	$C_{\text{Q}}$ <sup>b</sup>	$\eta_{\text{Q}}$ <sup>c</sup>	$C_{\text{Q}}$	$\eta_{\text{Q}}$
1	61.0	0.07	88(2)	0.0(1)
2	72.7	0.01	79(3)	0.0(1)
3	-- <sup>d</sup>	--	42(1) <sup>e</sup>	0.0(1)
4	74.0	0.02	77(4)	0.0(1)
5	112.0	0.06	105(5)	0.0(1)

<sup>a</sup> Experimental values were obtained from simulations of the spectra acquired at the lowest temperature for each compound. <sup>b</sup>  $C_{\text{Q}} = eQV_{33}/h$ , <sup>c</sup>  $\eta_{\text{Q}} = (V_{11} - V_{22})/V_{33}$ . <sup>d</sup> No reported crystal structure for **3**. <sup>e</sup> Values reflect an motionally-averaged effective EFG tensor (see text for details). Errors in the experimental values are shown in parentheses and were determined by bidirectional variation and visual inspection of the simulated powder patterns.

To study the motion of **1**, a deuterated sample, **1-D**, was prepared where the hydrides were replaced by deuterides. Variable-temperature (VT)  $^2\text{H}$  SSNMR spectra were acquired (**Figure 5.3(A)**). *N.B.* A sharp feature is observed in some of the spectra of **1-D** (and the compounds that follow), which corresponds to signal from an impurity; this feature was not considered in the simulations of the spectra. The spectrum acquired at 30 K was simulated with a value of  $C_Q = 88(2)$  kHz and a value of  $\eta_Q = 0.0(1)$  (a definition of  $\eta_Q$  is given in **Table 5.2**). These values are in good agreement with those determined by DFT calculations (**Table 5.2**). The predicted  $^2\text{H}$  EFG tensor orientation is shown in **Figure 5.1(B)**. The largest component of the EFG tensor,  $V_{33}$ , is oriented along the direction of the Pt–D bond, with  $V_{11}$  nearly parallel to the P–Pt–P rotation axis. A rotor-like motion of the deuterides at a fast enough rate (*i.e.*, in the IMR or FML) has two effects: (i) it produces *effective* values of all of the principal components and (ii) it can result in elongation of the Pt–D bond, resulting in a decrease in the absolute magnitude of  $V_{33}$ . The latter effect is negligible in this system, as there are no apparent changes in  $V_{33}$  with changing temperature, since all of the simulations were conducted with values of  $C_Q = 88$  kHz and  $\eta_Q = 0.0$ . However: (i) as the temperature is increased, motional averaging of  $V_{33}$  manifests as decreases in the breadths of the powder patterns (*i.e.*,  $V_{33}^{\text{eff}} < V_{33}$ ), and (ii)  $V_{11}$  and  $V_{22}$  produce patterns with variations in the effective  $\eta_Q$  values (*i.e.*,  $V_{11}^{\text{eff}}$  and  $V_{22}^{\text{eff}}$  are of equal magnitude in the SML and FML, such that  $\eta_Q^{\text{eff}} = 0.0$ , but not in the IMR, where  $\eta_Q^{\text{eff}} \neq 0.0$ , as manifested by changes in the relative positions of the sharp discontinuities). A detailed description follows:

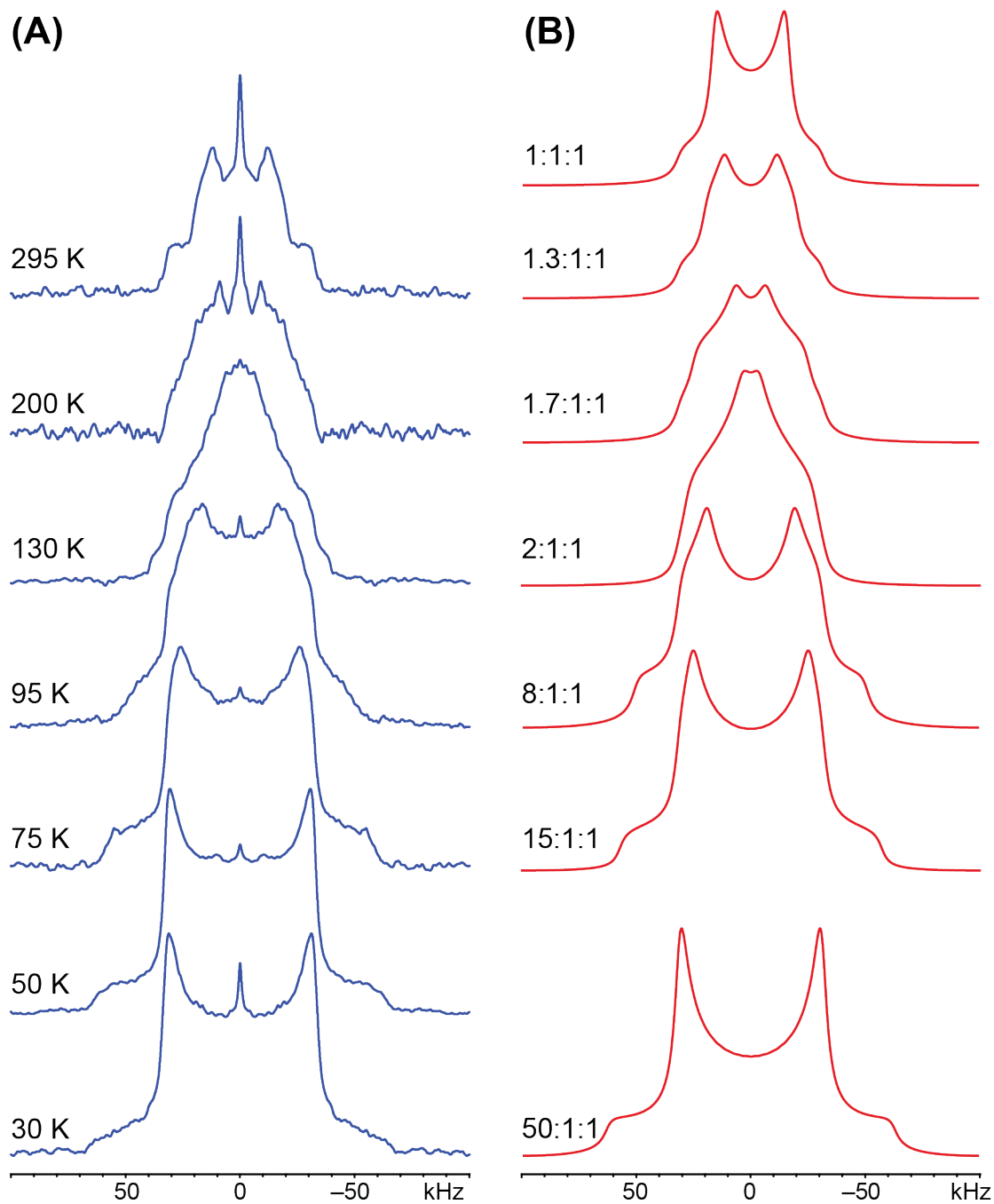


**Figure 5.3:** (A) VT  $^2\text{H}$  SSNMR spectra of **1-D** acquired at 4.75 T. (B) Accompanying simulations using the  $n:1:1$  rotational model. The impurity peak that appears in the centre of the experimental spectra was not modeled.

The spectrum acquired at 30 K indicates that the motion is occurring at rate within the SML (the same is observed in the spectrum acquired at 50 K). Increasing the

temperature to 75 K results in a narrowing of the powder pattern and an increase in the value of  $\eta_Q^{\text{eff}}$ . Increasing the temperature above 75 K results in further narrowing of the pattern and an increase in the value of  $\eta_Q^{\text{eff}}$  until 130 K, where the value of  $\eta_Q^{\text{eff}}$  begins to decrease. The spectrum acquired at 295 K has a width that is half that of the static spectrum and an  $\eta_Q^{\text{eff}}$  value of 0.15(5).

Several different models were used to attempt to simulate the effects of the motion of **1** on the  $^2\text{H}$  SSNMR powder pattern (**Figure 5.4**), each taking into account the symmetry of the molecule and the nature of the rotor-like motion suggested by the SCXRD data. The models involve two-, three-, four- and six-fold rotations of the deuterides by angles of  $180^\circ$ ,  $120^\circ$ ,  $90^\circ$  and  $60^\circ$ , respectively, and the assumption that the populations of the exchanging deuterons are equal. A two-fold rotation does not average the principal components of the  $^2\text{H}$  EFG tensor, producing simulations that disagree with the experimental data (**Figure 5.4(A)**). A three-site rotational model positions the deuterides as shown in **Figure 5.4(B)**. The width of the FML spectrum for this model is half that of the SML spectrum, consistent with experimental observation; however, the spectra simulated with rates in the IMR do not agree with the intermediate temperature spectra. A four-site model yields similar results, producing simulated patterns that do not correspond to intermediate temperature experimental spectra (**Figure 5.4(C)**). Finally, a six-site rotational model (**Figure 5.4(D)**) yields the same results as those obtained for the three-site rotational model. Due to the three-fold rotational symmetry of **1**, three- and six-fold rotations are indistinguishable.

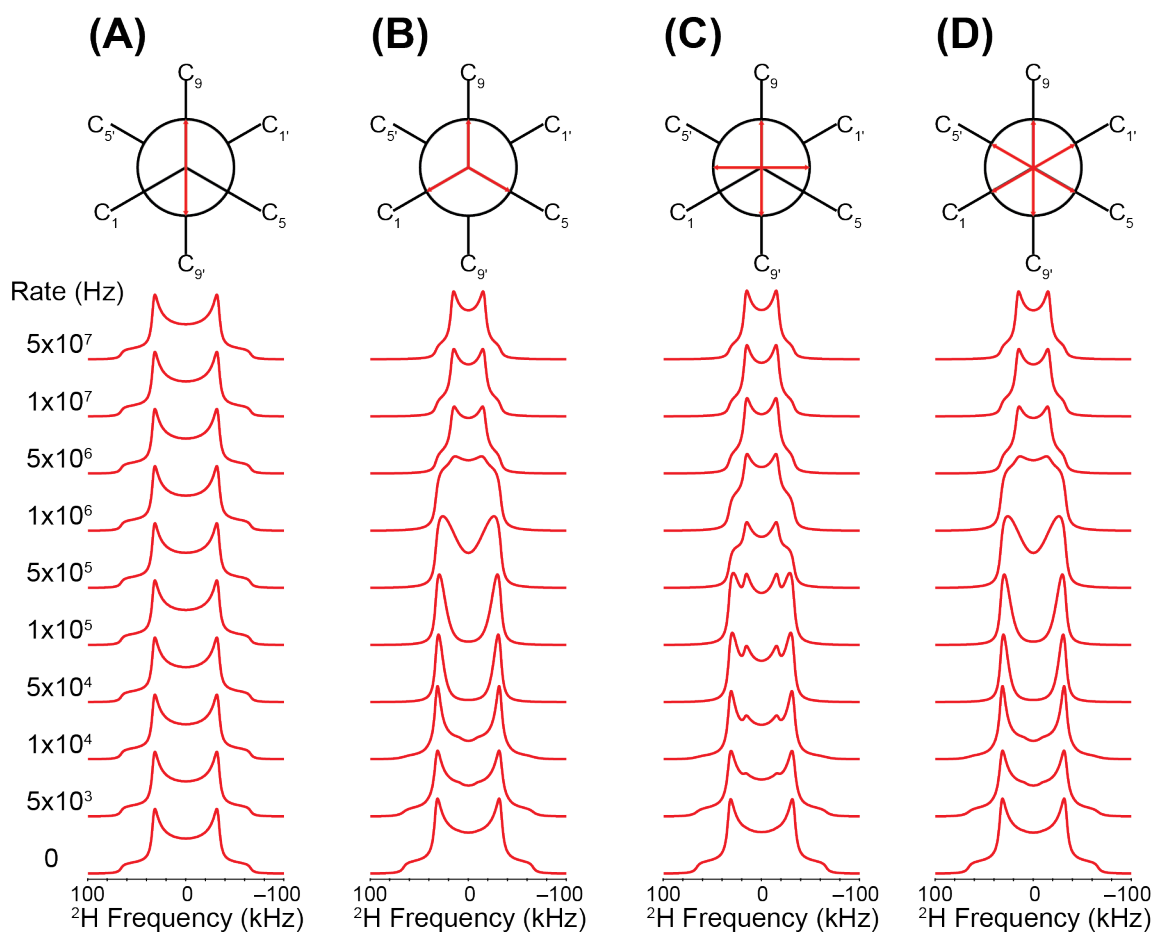


**Figure 5.4:** (A) two-site, (B) three-site, (C) four-site, and (D) six-site rotation motional models used in the simulation of the  $^2\text{H}$  SSNMR data. The red arrows in the schematic pictures represent the positions of the largest principal component of the  $^2\text{H}$  EFG tensor ( $V_{33}$ ) which is collinear with the Pt–D bonds.

Since the experimental data do not match any of the above rotational models, they may be influenced by the relative populations of the different deuterium sites in addition to the rates of motion. Therefore, additional spectra were acquired at 120 K with different interpulse delays ( $\tau$ ) (**Figure D3**). There are no appreciable differences in these spectra, indicating that the motion present at 120 K is occurring with rates in the FML. The motional model is therefore not based on increasing rates with increasing temperature, but rather, different populations of the various *rotational states*. The effects of

populations were taken into account by considering a three-site (or equivalently, a six-site) rotational model, as discussed above. The  $0^\circ$  site is assigned to a position where the deuteride is eclipsed with the P–C9 bond (**Figure D1**, this was chosen as first-principles calculations suggest that this configuration corresponds to an energy minimum, *vide infra*). The other two sites, rotated  $60^\circ$  and  $120^\circ$  from the first, correspond to the deuteride being eclipsed with the P–C1 and P–C5 bonds, respectively. All simulations were conducted with rates in the FML (*i.e.*,  $\nu_{\text{ex}} = 10^9$  Hz)

Since **1-D** has a three-fold rotational symmetry axis, it is likely that a three- or six-fold rotational motion is the most appropriate for modeling (*vide supra*) the impact of these dynamics on the  $^2\text{H}$  SSNMR spectra. Therefore, several models were tested incorporating six-fold rotation and varying the relative populations  $n$ ,  $n'$ , and  $n''$  for the  $0^\circ(180^\circ)$ ,  $60^\circ(240^\circ)$ , and  $120^\circ(300^\circ)$  rotational states, respectively (**Figure 5.5**). The models, expressed as ratios  $n:n':n''$ , include  $n:1:1$ ,  $n:n':1$ , and  $n^2:n':1$ . In each model, states separated by a  $180^\circ$  rotation are viewed as degenerate (*vide infra*).

Of these, only the  $n:1:1$  model (**Figure 5.5(A)**) is successful in modelling the effects of rotational motion on the  $^2\text{H}$  SSNMR spectra. In this model,  $n$  corresponds to the relative population of the  $0^\circ(180^\circ)$  state, which is assumed to be the lowest in energy, and is assigned a value greater than 1. As the temperature is increased, the  $60^\circ(240^\circ)$  and  $120^\circ(300^\circ)$  states, which are higher in energy and degenerate, become increasingly populated. At low temperatures, the  $0^\circ(180^\circ)$  state is the most populated, and the

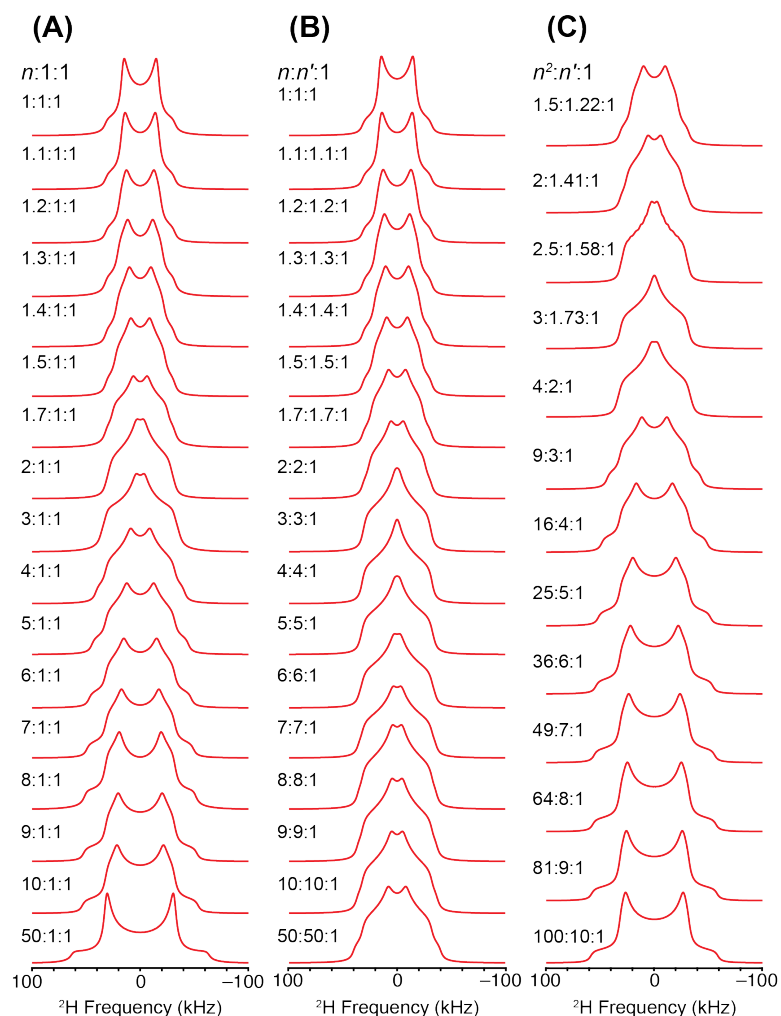


**Figure 5.5:** Simulated  $^2\text{H}$  SSNMR spectra for the (A)  $n:1:1$ , (B)  $n:n':1$ , and (C)  $n^2:n':1$  population models. The ratios represent the relative populations of the rotational states (*i.e.*, the populations of the  $0^\circ(180^\circ):60^\circ(240^\circ):120^\circ(300^\circ)$  states).

$60^\circ(240^\circ)$  and  $120^\circ(300^\circ)$  states are only sparsely populated; hence, the motion that occurs in this regime is equivalent to a two-fold exchange of deuterons in the  $0^\circ$  and  $180^\circ$  positions. As the temperature is incremented upwards, the  $60^\circ(240^\circ)$  and  $120^\circ(300^\circ)$  states become increasingly populated, and the exchange model now resembles that of a six-fold rotation, where any rotational state can exchange with a neighbouring state by making a  $60^\circ$  rotation. At room temperature, the population distribution is 1.3:1:1.

The  $n:1:1$  model for the rotational motion in **1-D** was confirmed at higher temperatures (**Figure 5.6**). This set of spectra was acquired at 9.4 T (as opposed to 4.75 T for the lower temperature data), and therefore, the effects of the CSA on the appearance of the spectra are increased, and are evident because of their asymmetry. Simulations of the high-temperature spectra were conducted using  $\Omega = 60$  ppm, which is consistent with the values previously reported for metal hydrides.<sup>52</sup> The orientation of the hydrogen chemical shielding tensor for **1** was predicted using DFT calculations and is shown in **Figure 5.1(C)**, with the calculated hydrogen chemical shielding parameters listed in **Table D2**. This is in contrast with the value determined by DFT calculations and this discrepancy between calculations and experiment is likely due to an improper choice of functional (*vide supra*) that does not accurately calculate CS tensors for this system.

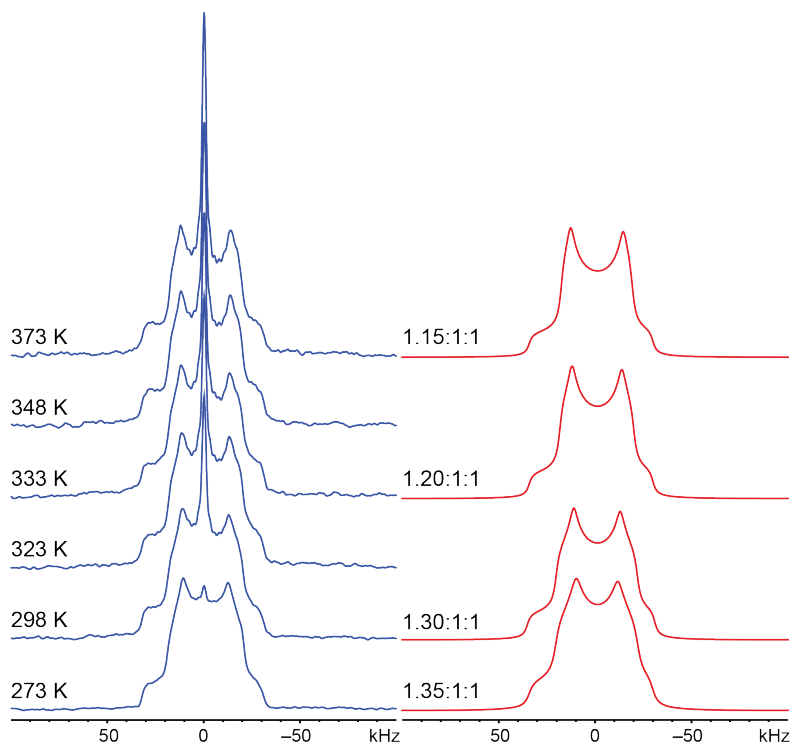


**Figure 5.6:** (A) VT  $^2\text{H}$  SSNMR spectra of **1-D** acquired at 9.4 T. (B) The accompanying simulations using the  $n:1:1$  rotational model. The simulations include the effects of  $^1\text{H}$  CSA.



### 5.4.1.3 Calculation of the Energy Landscape

This model was confirmed by first principles DFT calculations of an energy landscape (**Figure 5.7**). The Pt–H bond length was fixed at 1.657 Å (*i.e.*, the value obtained from DFT calculations), and the H–Pt–P angle was kept at 90°. The H–Pt–P–C torsion angle was varied in increments of 10° and the positions of the hydrides were fixed in positions exactly *trans* to one another. At each rotational step, a geometry optimization was performed in which the heavy atom framework was kept in place and the positions of the *tert*-butyl hydrogen atoms were relaxed.

The energy landscape is in agreement with the experimental NMR data. The landscape is symmetric about the global minima at 0° and 180°, corresponding to the hydride positions determined by XRD experiments (*i.e.*, the hydrides are eclipsed with respect to the P–C9 bonds (**Figure D1**)). Local minima are also observed when the hydrides are eclipsed with the P–C1 and P–C5 bonds (60° and 120°, 240° and 300°), confirming the three-site (or equivalently, six-site) rotation model with populations described by an *n*:1:1 ratio.

### 5.4.2 *trans*-D<sub>2</sub>Pt(P(NMe<sub>2</sub>)<sub>3</sub>)<sub>2</sub> (**2**)

Compound **2** consists of a H–Pt–H unit with *trans*-P(NMe<sub>2</sub>)<sub>3</sub> coordinated donor ligands. The crystal structure of **2** shows that the hydride ligands are in eclipsed positions with respect to the P–N bonds.<sup>44</sup> The Pt–H bond length is 1.667 Å, which is considerably longer than that observed in the crystal structure of **1**. The longer bond length suggests that either the hydrides are static or that a different mode of motion is occurring.

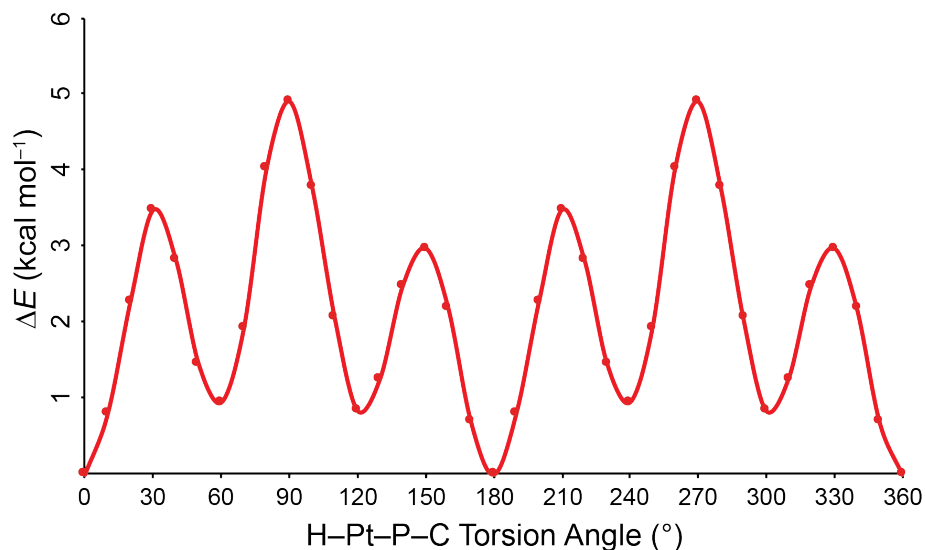


**Figure 5.7:** The energy landscape for **1** as determined by DFT calculations. The hydride positions were rotated about the P–Pt–P axis. Global minima are observed at H–Pt–P–C torsion angles of 0° and 180° (hydrides eclipsed with the P–C9 bonds) and local minima are observed at positions where the deuterides are eclipsed with the P–C1 and P–C5 bonds.

The VT  $^2\text{H}$  SSNMR spectra of **2-D** are shown in **Figure 5.8**. The spectrum acquired at 273 K was simulated with  $C_Q = 79(3)$  kHz and  $\eta_Q = 0.0(1)$ . The smaller  $C_Q$  value in comparison to that of **1-D** ( $C_Q = 88$  kHz) is consistent with the increased Pt–D bond length in **2-D**. Increasing the temperature does not result in any changes in the  $^2\text{H}$  powder patterns, suggesting two possibilities: (i) either no motions are occurring and the deuterides are fixed in or near the positions indicated by the SCXRD structure or (ii) the motions are occurring at rates in the FML and that increasing the temperature does not result in any further changes in the powder patterns. The calculated  $^2\text{H}$  EFG tensor parameters (**Table 5.2**) are in excellent agreement with those determined experimentally, suggesting that the first possibility is the most likely. *N.B.*, A two-site jump (*i.e.*, the deuterides rotating 180° and exchanging positions) in the FML cannot be completely

ruled out, as this motional model does not result in changes in the  $^2\text{H}$  powder patterns  
(Figure 5.4(A)).

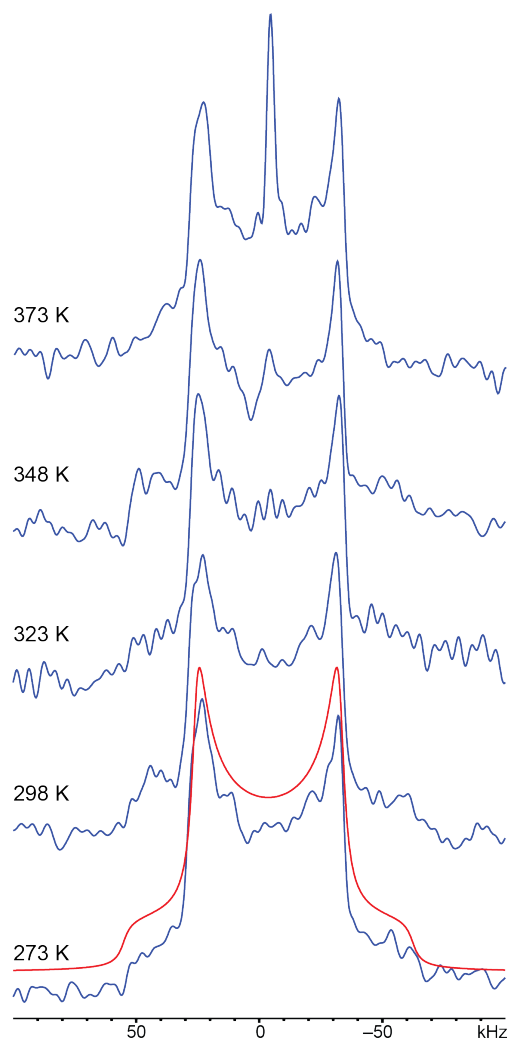


**Figure 5.8:** VT  $^2\text{H}$  SSNMR spectra acquired at 9.4 T for **2-D**. A simulation of the spectrum acquired at 273 K is shown as the red trace. The spectra do not change with temperature indicating that the motion is in the SML.

The structural differences between **1-D** and **2-D** (*i.e.*, the  $\text{P}(\text{tBu})_3$  ligands in **1-D** and the  $\text{P}(\text{NMe}_2)_3$  ligands in **2-D**) are likely the primary cause of different motions of the deuterides. For instance, an interaction between the lone pairs on the N atoms of the ligand in **2-D** and the deuterides, or differences in the degree of steric hindrance which

influence the rotation of the deuterides, may cause an increased barrier to rotation. A calculation of the energy landscape, similar to that of **1**, is necessary to determine the causes of the apparent lack of motion, but is beyond the scope of the current study.

#### 5.4.3 *trans*-D<sub>2</sub>Pt(P(Cy)<sub>3</sub>)<sub>2</sub> (**3**)

The crystal structure of **3** (or **3-D**) has not been reported herein nor in the literature; therefore, it is not possible to determine the approximate positions of the hydrides, which would aid at making suggestions about the presence and/or nature of hydride dynamics. However, based on the chemical similarity of **1** and **3** (*i.e.*, both have alkyl-phosphine donor ligands), it is posited that the hydrides are likely in the same positions and undergoing similar motion.

The VT <sup>2</sup>H SSNMR spectra for **3-D** are shown in **Figure 5.9**. The spectrum acquired at 173 K was simulated with  $C_Q = 42(1)$  kHz and  $\eta_Q = 0.0(1)$ . The value of  $C_Q$  that is observed for **3-D** is significantly smaller than that of **1-D** and **2-D** (both experimentally and computationally), indicating that either the Pt–D bond length is greater in **3-D** and there is no motion or the rotational motion is occurring in the FML at this temperature that produces a narrow pattern as in the high-temperature limit for **1-D** (*i.e.*, an effective  $C_Q$  is observed at this temperature resulting from  $V_{33}^{\text{eff}} = \frac{1}{2}V_{33}$ ). The former case is very unlikely, since this would correspond to a Pt–D bond length of greater than 2.0 Å (the  $C_Q$  approximate scales as the inverse cube of the Pt–D bond length). Increasing the temperature to 348 K does not result in any changes to the powder patterns, suggesting motions with rates in the FML at all temperatures. The spectra of **3** can be modelled using either the three- or four-site jump models, but without IMR data, the exact motional model cannot be determined. The observation that motions occur in

the FML at 173 K for **3-D** suggest that the activation barrier for rotation is lower than that determined for **1**; however, experiments conducted at lower temperature are required to confirm this.

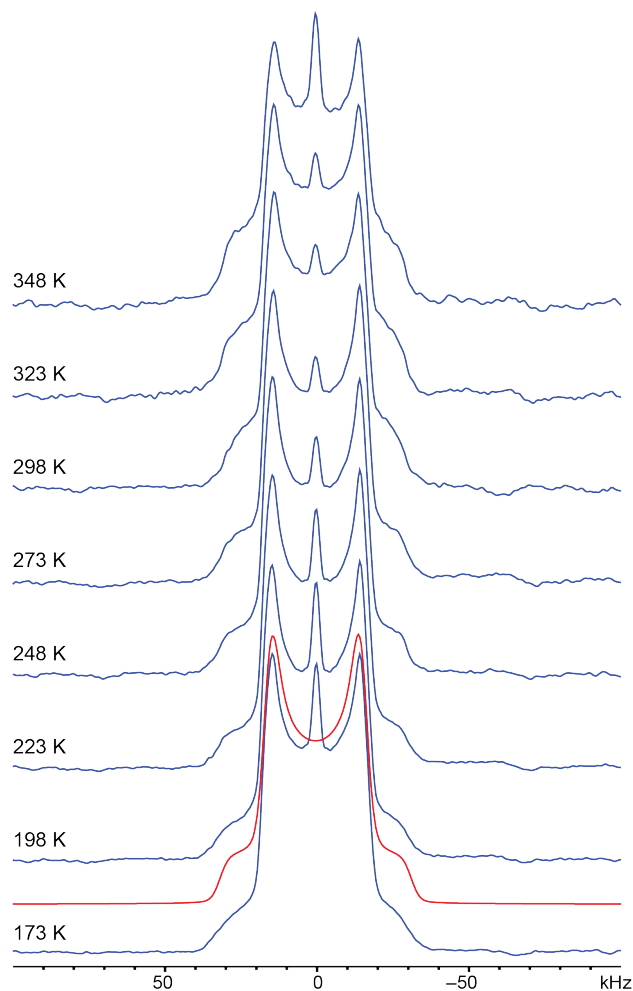


**Figure 5.9:** VT  $^2\text{H}$  SSNMR spectra of **3-D** acquired at 9.4 T. A simulation of the spectrum acquired at 173 K is shown as the red trace. The spectra do not change with temperature, indicating that the motion is in the FML (see text for details)

#### 5.4.4 *trans*- $\text{D}_2\text{Pt}(\text{iPr})_2$ (**4**)

According to the known crystal structure of **4** (Scheme 5.1(D)),<sup>53</sup> the *iPr* ligands are slightly staggered with respect to one another (a N–C–C–N torsion angle of  $42^\circ$ ), and Pt–H bond lengths in **4** are 1.704 and 1.962 Å. The long bond lengths could again suggest

the absence of motion in this system; however, there is a large difference between the two Pt–H distances, owing to the difficulties in accurately determining hydride positions using XRD. The apparent positions of the hydrides are staggered with respect to the *i*Pr ligands (**Figure D5(A)**).

The VT  $^2\text{H}$  SSNMR spectra of **4-D** are shown in **Figure 5.10**. The spectrum acquired at 223 K was simulated with  $C_Q = 77(4)$  kHz and  $\eta_Q = 0.0(1)$ . There are no appreciable changes in the powder patterns with increasing temperature, suggesting that there is no motion of the deuterides in **4**. At this point, it is not clear what structural or electronic factors are inhibiting the motion of the deuterides in this system and a more detailed computational study is needed.

#### 5.4.5 *trans*-DPt(*i*Pr) $_2$ (**5**)

The composition of **5** is similar to that of **4**, but with only one hydride ligand and a  $[\text{BARF}_4]^-$  anion to balance the excess positive charge resulting from the missing hydride. The carbene ligands are in slightly staggered positions, similar to **4**, but the apparent position of the hydride lies between the planes of the carbene ligands (**Figure D5(B)**). The Pt–H bond length is 1.518 Å, shorter than those reported for **2** and **4**, which suggests two possibilities: (i) the observed bond length is artificially short because of the “smearing” effect of rotational motion, or (ii) the observed bond length is short and should result in the observation of a large  $C_Q$  value in  $^2\text{H}$  SSNMR spectra acquired at low temperatures (*i.e.*, absence of motions or motions in the SML).

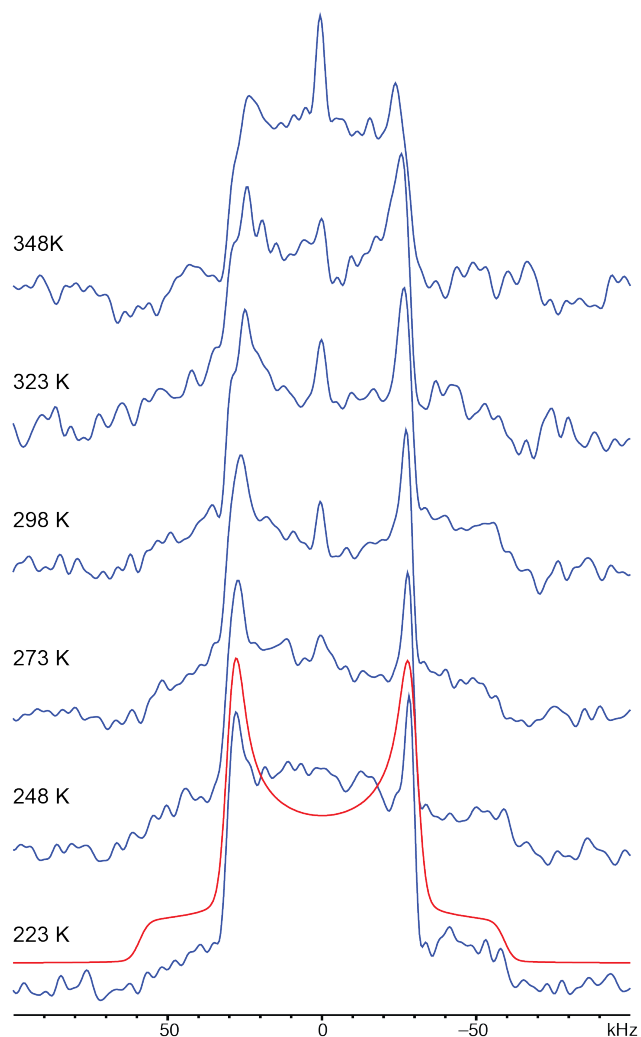


**Figure 5.10:** VT  $^2\text{H}$  SSNMR spectra of **4-D** acquired at 9.4 T. An analytical simulation of the spectrum acquired at 223 K is shown in red. The spectra do not change with temperature, indicating that the motion is in the SML (see text for details).

The VT  $^2\text{H}$  SSNMR spectra and corresponding simulations for **5-D** are shown in **Figure 5.11**. The spectrum acquired at 173 K was simulated with  $C_Q = 105(5)$  kHz and  $\eta_Q = 0.0(1)$ , which is in excellent agreement with those determined by DFT calculations. In addition, comparison of the bond lengths and  $C_Q$  values for **2** and **5**, and the assumption that the  $C_Q$  value scales as the inverse cube of the internuclear distance,

allows for the prediction of a Pt–H bond length of *ca.* 1.52 Å in very good agreement with the crystal structure.

Increasing the temperature produces drastic changes in the powder patterns, with the intensities of the horns decreasing, and an increase of intensity of a feature in the centre of the pattern. At 323 K, what may be the vestiges of an axially symmetric pattern are observed, but the combination of poor S/N and possible interfering signal from a thermally decomposed species make this assignment difficult. The spectra were simulated with the four-site jump model (**Figure 5.4(C)**), in which the deuteride is rotating between four positions separated by 90°.

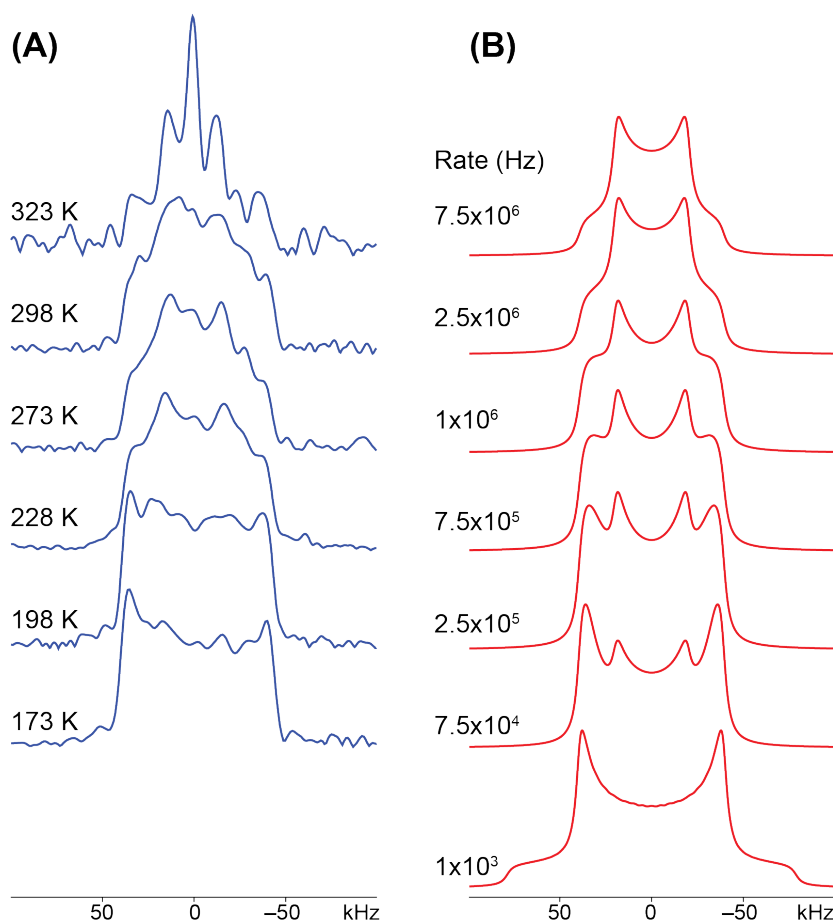


**Figure 5.11:** (A) VT <sup>2</sup>H SSNMR spectra of **5-D** acquired at 9.4 T. (B) Accompanying simulations using the four-site jump rotational model.



Despite the similar structures of **4-D** and **5-D**, the motion of the deuterides in these systems is strikingly different. A 90° rotation of the single deuteride ligand in **5** results in its occupation of a position similar to those occupied by the two deuteride ligands in **4-D**. It is likely that the energy barrier to rotation in **5** is significantly lower; however, the exact reasons for this difference in activation energy is currently not known. Interestingly, the higher onset temperature of motion, and the observation of rates in the IMR, suggest that the motion in **5** is more hindered than that observed for either **1** or **3**.

## 5.5 Conclusions

In this chapter, we have demonstrated that platinum-hydride compounds can function as low energy barrier molecular rotors in the solid state, and that the nature of the donor ligands greatly influences the rotational motion of the hydrides. SCXRD and <sup>195</sup>Pt SSNMR indicate that the deuterides in *trans*-D<sub>2</sub>Pt(P<sup>t</sup>Bu<sub>3</sub>)<sub>2</sub> (**1-D**) are dynamic; however, it is necessary to use <sup>2</sup>H SSNMR to elucidate the rates and modes of these motions. Simulation of the <sup>2</sup>H SSNMR spectra demonstrate that the deuterides exhibit a three-fold rotational motion in **1-D**, and that the populations of three well defined rotational states change with temperature. These results were confirmed using DFT calculations to produce an energy landscape, which reveals six-fold rotational motion with a very low activation energy, in good agreement with the experimental models. The motional models proposed for **1-D** provide a framework in which to discuss the dynamics of other platinum-deuteride compounds. Compounds **2-D** and **3-D** are structurally similar, but the former exhibits no motion over a temperature range from 273-373 K,

whereas the latter has motions with rates in the FML even at 173 K. Lastly, **4-D** and **5-D**, which differ in the absence of a deuteron and presence of a charge balancing anion in the latter, exhibit drastically different motions; the deuterides in **4-D** are static at high temperatures (akin to **2-D**), while those in **5-D** exhibit a four-fold rotation with rates in the IMR. The nature of the coordinating donor ligands clearly have a drastic effect on the deuteride motion; a more detailed computational study is needed to determine how the molecular-level structures can be designed with different components to influence the dynamics in terms of rotational modes and rates of motion. It is hoped that the methodologies outlined herein will allow for the rational design of solid-state molecular rotors with low energy barriers and finely-tuned motions.

## 5.6 References

- (1) Balzani, V.; Credi, A.; Raymo, F. M.; Stoddart, J. F. *Angew. Chem. Int. Ed.* **2000**, *39*, 3348–3391.
- (2) Badjic, J. D.; Balzani, V.; Credi, A.; Silvi, S.; Stoddart, J. F. *Science* **2004**, *303*, 1845–1849.
- (3) Bruns, C. J.; Stoddart, J. F. *Acc. Chem. Res.* **2014**, *47*, 2186–2199.
- (4) Shirai, Y.; Osgood, A. J.; Zhao, Y.; Kelly, K. F.; Tour, J. M. *Nano Lett.* **2005**, *5*, 2330–2334.
- (5) Kottas, G. S.; Clarke, L. I.; Horinek, D.; Michl, J. *Chem. Rev.* **2005**, *105*, 1281–1376.
- (6) Kelly, T. R.; De Silva, H.; Silva, R. A. *Nature* **1999**, *401*, 1995–1997.
- (7) Koumura, N.; Zijlstra, R. W. J.; Van Delden, R. A.; Harada, N.; Feringa, B. L. *Nature* **1999**, *401*, 152–155.
- (8) Bauer, E. B.; Ruwwe, J.; Hampel, F. A.; Szafert, S.; Gladysz, J. A.; Martín-Alvarez, J. M.; Peters, T. B.; Bohling, J. C.; Lis, T. *Chem. Commun.* **2000**, *6*, 2261–2262.
- (9) Shima, T.; Hampel, F.; Gladysz, J. A. *Angew. Chem. Int. Ed.* **2004**, *43*, 5537–5540.
- (10) Wang, L.; Hampel, F.; Gladysz, J. A. *Angew. Chem. Int. Ed.* **2006**, *45*, 4372–4375.
- (11) Nawara, A. J.; Shima, T.; Hampel, F.; Gladysz, J. A. *J. Am. Chem. Soc.* **2006**, *128*, 4962–4963.
- (12) Zeits, P. D.; Rachiero, G. Pietro; Hampel, F.; Reibenspies, J. H.; Gladysz, J. A. *Organometallics* **2012**, *31*, 2854–2877.

- (13) Nawara-Hultzsch, A. J.; Stollenz, M.; Barbasiewicz, M.; Szafert, S.; Lis, T.; Hampel, F.; Bhuvanesh, N.; Gladysz, J. A. *Chem. Eur. J.* **2014**, *20*, 4617–4637.
- (14) Krause, M.; Hulman, M.; Kuzmany, H.; Dubay, O.; Kresse, G.; Vietze, K.; Seifert, G.; Wang, C.; Shinohara, H. *Phys. Rev. Lett.* **2004**, *93*, 2–5.
- (15) Vogelsberg, C. S.; Garcia-Garibay, M. A. *Chem. Soc. Rev.* **2012**, *41*, 1892–1910.
- (16) Iwamura, H.; Mislow, K. *Acc. Chem. Res.* **1988**, *21*, 175–182.
- (17) Khuong, T. A. V.; Nunez, J. E.; Godinez, C. E.; Garcia-Garibay, M. A. *Acc. Chem. Res.* **2006**, *39*, 413–422.
- (18) Bracco, S.; Castiglioni, F.; Comotti, A.; Galli, S.; Negroni, M.; Maspero, A.; Sozzani, P. *Chem. Eur. J.* **2017**, *23*, 11210–11215.
- (19) Setaka, W.; Yamaguchi, K. *J. Am. Chem. Soc.* **2013**, *135*, 14560–14563.
- (20) Akutagawa, T.; Shitagami, K.; Nishihara, S.; Takeda, S.; Hasegawa, T.; Nakamura, T.; Hosokoshi, Y.; Inoue, K.; Ikeuchi, S.; Miyazaki, Y.; Saito, K. *J. Am. Chem. Soc.* **2005**, *127*, 4397.
- (21) Van Der Putten, D.; Diezemann, G.; Fujara, F.; Hartmann, K.; Sillescu, H. *J. Chem. Phys.* **1992**, *96*, 1748–1757.
- (22) Wang, X.; Beckmann, P. A.; Mallory, C. W.; Rheingold, A. L.; Dipasquale, A. G.; Carroll, P. J.; Mallory, F. B. *J. Org. Chem.* **2011**, *76*, 5170–5176.
- (23) Gray, G. M.; Duffey, C. H. *Organometallics* **1994**, *13*, 1542–1544.
- (24) Shima, T.; Bauer, E. B.; Hampel, F.; Gladysz, J. a. *Dalton Trans.* **2004**, *4*, 1012–1028.
- (25) Lewanzik, N.; Oeser, T.; Blümel, J.; Gladysz, J. A. *J. Mol. Catal. A Chem.* **2006**, *254*, 20–28.

- (26) O'Dell, L. A.; Schurko, R. W. *Chem. Phys. Lett.* **2008**, *464*, 117–130.
- (27) O'Dell, L. A.; Rossini, A. J.; Schurko, R. W. *Chem. Phys. Lett.* **2009**, *468*, 330–335.
- (28) O'Dell, L. A. *Solid State Nucl. Magn. Reson.* **2013**, *55–56*, 28–41.
- (29) Eichele, K.; Wasylishen, R. E. 2001.
- (30) Davis, J. H.; Jeffrey, K. R.; Bloom, M.; Valic, M. I.; Higgs, T. P. *Chem. Phys. Lett.* **1976**, *42*, 390–394.
- (31) van Gorkom, L. C. M.; Hook, J. M.; Logan, M. B.; Hanna, J. V.; Wasylishen, R. E. *Magn. Reson. Chem.* **1995**, *33*, 791–795.
- (32) Bielecki, A.; Burum, D. P. *J. Magn. Reson.* **1995**, *220*, 215–220.
- (33) Vold, R. L.; Hoatson, G. L. *J. Magn. Reson.* **2009**, *198*, 57–72.
- (34) Baerends, E. J. Z. T.; Autschbach, J. SCM, Theoretical Chemistry, Vrije Universiteit: Amsterdam.
- (35) Velde, G.; Bickelhaupt, F. M.; van Gisbergen, S. J. A.; Guerra, C. F.; Baerends, E. J.; Snijders, J. G.; Ziegler, T. *J. Comput. Chem.* **2001**, *22*, 931.
- (36) Hammer, B.; Hansen, L.; Nørskov, J. *Phys. Rev. B* **1999**, *59*, 7413–7421.
- (37) Perdew, J.; Burke, K.; Ernzerhof, M. *Phys. Rev. Lett.* **1996**, *77*, 3865–3868.
- (38) van Lenthe, E.; Snijders, J. G.; Baerends, E. J. *J. Chem. Phys.* **1996**, *105*, 6505–6516.
- (39) Schmidt, M. W.; Baldridge, K. K.; Boatz, J. A.; Elbert, S. T.; Gordon, M. S.; Jensen, J. H.; Koseki, S.; Matsunaga, N.; Nguyen, K. A.; Su, S. J.; Windus, T. L.; Dupuis, M.; Montgomery, J. A. *J. Comput. Chem.* **1993**, *14*, 1347–1363.
- (40) Gordon, M. S.; Schmidt, M. W. In *Theory and Applications of Computational*

- Chemistry, the first forty years*; Dykstra, C. E., Frenking, G., Kim, K. S., Scuseria, G. E., Eds.; Elsevier: Amsterdam, 2005; pp 1167–1189.
- (41) Ferguson, G.; Siew, P. Y.; Goe, A. B. *J. Chem. Res. Synop.* **1979**, *39*, 1495.
- (42) Robertson, G. B.; Tucker, P. A.; Wickramasinghe, W. A. *Aust. J. Chem.* **1986**, *39*, 1495–1507.
- (43) Owston, P. G.; Partridge, J. M.; Rowe, J. M. *Acta Crystallogr.* **1960**, *13*, 246–252.
- (44) Downs, E. L.; Zakharov, L. N.; Tyler, D. R. *Acta Crystallogr. Sect. E Crystallogr. Commun.* **2015**, *71*, m83–m84.
- (45) Goodfellow, R. J. In *Multinuclear NMR*; Mason, J., Ed.; Plenum Press: New York, 1987.
- (46) Widdifield, C. M.; Schurko, R. W. *Concepts Magn. Reson. Part A* **2009**, 91–123.
- (47) Lucier, B. E. G.; Reidel, A. R.; Schurko, R. W. *Can. J. Chem.* **2011**, *89*, 919–937.
- (48) Tang, J. A.; Kogut, E.; Norton, D.; Lough, A. J.; McGarvey, B. R.; Fekl, U.; Schurko, R. W. *J. Phys. Chem. B* **2009**, *113*, 3298–3312.
- (49) Autschbach, J.; Zheng, S. *Magn. Reson. Chem.* **2008**, *46*, S45–S55.
- (50) Chandrakumar, N. *Spin-1 NMR*; Springer: Berlin, 1996.
- (51) Schmidt-Rohr, K.; Spiess, H. W. *Multidimensional Solid-State NMR and Polymers*; Academic Press: New York, 1994.
- (52) Garbacz, P.; Terskikh, V. V.; Ferguson, M. J.; Bernard, G. M.; Kędziołek, M.; Wasylshen, R. E. *J. Phys. Chem. A* **2014**, *118*, 1203–1212.
- (53) Conjero, S. *Private communication to be published*

# Chapter 6: An Investigation of Chlorine Ligands in Transition-metal Complexes via $^{35}\text{Cl}$ SSNMR and DFT Calculations

## 6.1 Overview

Chlorine ligands in a variety of diamagnetic transition-metal (TM) complexes in common structural motifs were studied using  $^{35}\text{Cl}$  solid-state NMR (SSNMR), and insight into the origin of the observed  $^{35}\text{Cl}$  NMR parameters was gained through first-principles density functional theory (DFT) calculations. The WURST-CPMG pulse sequence and the variable-offset cumulative spectrum (VOCS) methods were used to acquire static  $^{35}\text{Cl}$  SSNMR powder patterns at both standard (9.4 T) and ultra-high (21.1 T) magnetic field strengths, with the latter affording higher signal-to-noise ratios (S/N) and reduced experimental times (*i.e.*, < 1h). Analytical simulations were performed to extract the  $^{35}\text{Cl}$  electric field gradient (EFG) tensor and chemical shift (CS) tensor parameters. It was found that the chlorine ligands in various bonding environments (*i.e.*, bridging, terminal-axial, and terminal-equatorial) have drastically different  $^{35}\text{Cl}$  EFG tensor parameters, suggesting that  $^{35}\text{Cl}$  SSNMR is ideal for characterizing chlorine ligands in TM complexes. A detailed localized molecular orbital (LMO) analysis was completed for  $\text{NbCl}_5$ . It was found that the contributions of individual molecular orbitals must be considered to fully explain the observed EFG parameters, thereby negating simple arguments based on comparison of bond lengths and angles. Finally, we discuss the application of  $^{35}\text{Cl}$  SSNMR for the structural characterization of  $\text{WCl}_6$  that has been

grafted onto a silica support material. The resulting tungsten-chloride surface species is shown to be structurally distinct from the parent compound.

## 6.2 Introduction

Group V and VI transition metals (TM) are commonly used to fabricate a wide range of complexes with various uses, such as reagents in redox reactions,<sup>1-4</sup> anti-tumour agents<sup>5-7</sup> and superconducting materials.<sup>8-10</sup> However, perhaps their most ubiquitous use is for the catalysis of reactions involving organic and organometallic species.<sup>11-16</sup> Their multiple oxidation states and relatively large atomic sizes allow for the coordination of a variety of ligands and the synthesis of catalysts that can be fine-tuned for specific purposes. Such complexes find use in both homogeneous and heterogeneous catalytic processes; the latter is widely thought to afford higher selectivity and efficiency.<sup>17,18</sup> As a result, the design and application of heterogeneous catalysts, which involves the chemical or physical immobilization of the TM species on high-surface area materials, represent burgeoning areas of research.<sup>19-21</sup>

Structural characterization of heterogeneous catalysts is often difficult, as the support materials are almost always disordered and insoluble, thereby limiting or preventing their analysis by conventional techniques such as X-ray diffraction (XRD) or solution-state NMR spectroscopy. Surface techniques such as X-ray photoelectron spectroscopy (XPS)<sup>22</sup> and IR spectroscopy<sup>23,24</sup> have previously been used to study immobilized species; however, the structural information is often limited. Solid-state NMR (SSNMR) spectroscopy is now widely used for molecular-level characterization of heterogeneous catalysts,<sup>25-28</sup> providing information on structural motifs, bonding, interatomic distances, symmetry and ground-state electronic distributions. Furthermore,



unlike XRD methods, SSNMR is capable of probing short-range order in systems lacking long-range order (*i.e.*, amorphous and/or disordered solids).

SSNMR experiments involving  $^1\text{H}$  and  $^{13}\text{C}$  are the most common for studies of heterogeneous catalysts.<sup>27,29–31</sup> However, our research group has shown that it may be possible to investigate such systems from the perspective of the TM nuclei; to date, we have characterized bulk metallocene complexes utilizing  $^{91}\text{Zr}$ ,  $^{47/49}\text{Ti}$ ,  $^{93}\text{Nb}$ , and  $^{139}\text{La}$  SSNMR.<sup>32–36</sup> The spectra of many of these nuclei are very broad, ranging from several hundred kHz to MHz in breadth; accordingly, S/N tends to be very poor in many of these spectra, which suggests limitations for studying the diluted, supported TM species in heterogeneous catalysts. However, recent developments in broadband excitation sequences and other signal enhancing techniques,<sup>37–39</sup> along with the increasing availability of higher magnetic field strengths and improved NMR probes and hardware, suggest that SSNMR of such systems may hold much promise. Unfortunately, for certain TM nuclei such as  $^{95/97}\text{Mo}$ ,  $^{103}\text{Rh}$ ,  $^{181}\text{Ta}$ , and  $^{183}\text{W}$ , probing the metal centre using SSNMR currently remains challenging due to their inherently unreceptive natures. In such cases, it is often more convenient and informative to conduct NMR experiments involving other nuclei on the ligands surrounding the metal centre, since their NMR parameters are likely to be sensitive to structural differences. A prime example of this is chlorine, which is found widely in many TM complexes.

Chlorine has two naturally occurring NMR-active isotopes,  $^{35}\text{Cl}$  and  $^{37}\text{Cl}$ , with natural abundances of 75.78 and 24.22%, respectively. Both have nuclear spins of  $I = 3/2$  and low gyromagnetic ratios (“low- $\gamma$ ”), with relatively small quadrupole moments of

$-8.165$  and  $-6.435 \text{ fm}^2$ .<sup>40</sup>  $^{35}\text{Cl}$  is the preferred target NMR nuclide due to its higher receptivity (*i.e.*, both its natural abundance and Larmor frequency are higher).

The  $^{35}\text{Cl}$  quadrupolar interaction (QI), which arises from coupling between the  $^{35}\text{Cl}$  nuclear quadrupole moment and local electric field gradients (EFGs) at the  $^{35}\text{Cl}$  nucleus, is very sensitive to subtle differences in structure. Accordingly, the quadrupolar coupling constant,  $C_Q$ , and the asymmetry parameter,  $\eta_Q$  (see **Table 6.1** for definitions), which are determined from simulations of the  $^{35}\text{Cl}$  SSNMR powder patterns, reflect variance in structure and bonding.  $^{35}\text{Cl}$  SSNMR spectra typically exhibit central transition (CT,  $+1/2 \leftrightarrow -1/2$ ) powder patterns that are strongly influenced by the second-order quadrupolar interaction (SOQI); the two satellite transition patterns (ST,  $\pm 3/2 \leftrightarrow \pm 1/2$ ) are predominantly broadened by the first-order quadrupolar interaction (FOQI), and are rarely observed in  $^{35}\text{Cl}$  SSNMR spectra (excepting in cases where the magnitude of  $C_Q$  is very small).

The majority of  $^{35}\text{Cl}$  SSNMR studies to date have focused on systems with the chlorine atoms at the centre of ground-state electronic distributions of high spherical or Platonic symmetry (*e.g.*,  $\text{Cl}^-$  ions weakly coordinated by water molecules and other ligands,  $\text{ClO}_4^-$ , etc.). Such environments are generally associated with small values of  $C_Q$  and have relatively narrow  $^{35}\text{Cl}$  CT powder patterns that can be acquired using conventional Hahn-echo experiments and high-power rectangular pulses.<sup>41–44</sup> Examples of such systems include metal-chloride salts, hydrochloride (HCl) salts of amino acids, and pharmaceuticals. The application of  $^{35}\text{Cl}$  SSNMR to systems in which Cl is involved in covalent bonding is very rare by comparison, since the values of  $C_Q$  are much larger and the powder patterns much broader. Some recent works include investigations of

group 13 chloride salts,<sup>45</sup> chlorine-containing metallocenes,<sup>46</sup> organometallic transition metal complexes<sup>47</sup> and organic compounds with covalent C-Cl bonds.<sup>48</sup> All of these studies report the use of high magnetic fields and specialized pulse sequences due to the exceptionally broad <sup>35</sup>Cl powder patterns associated with these systems. Such spectra, and the concomitant experiments necessary for their acquisition, fall under the classification of ultra-wideline (UW) NMR spectroscopy.<sup>49,50</sup>

Herein, we describe the application of <sup>35</sup>Cl SSNMR in conjunction with first-principles density functional theory (DFT) calculations to study diamagnetic inorganic chlorine-containing TM complexes (**Scheme 6.1**) that exhibit a variety of common structural motifs and are representative of several broader classes of TM complexes widely used in catalysis. All of these compounds have been previously characterized by <sup>35</sup>Cl NQR spectroscopy; this allows us to determine whether the values of  $C_Q$  extracted from simple analytical simulations under the high-field approximation (*i.e.*,  $\nu_0 > \nu_Q$ ) are valid, and to also accurately measure the values of  $\eta_Q$ , which are unavailable from NQR spectra of spin-3/2 nuclides. First, we demonstrate the application of the Wideband Uniform-Rate Smooth Truncation-Quadrupolar Carr-Purcell-Meiboom-Gill (WURST-CPMG) pulse sequence<sup>38,51</sup> for the rapid acquisition (*i.e.*, < 1h) of UW <sup>35</sup>Cl SSNMR spectra at both 9.4 and 21.1 T. In one case, the use of <sup>35</sup>Cl NMR and <sup>35</sup>Cl NQR experiments in tandem for the differentiation of polymorphs is explored. Second, quadrupolar parameters determined from simulations of these spectra are compared to those obtained from plane wave DFT calculations. This data, along with theoretically derived <sup>35</sup>Cl EFG tensor orientations, are used to propose relationships between the <sup>35</sup>Cl quadrupolar parameters and the nature of the chlorine structural environments (*i.e.*, the

identity of the metal (M), M-Cl bond lengths, geometric arrangements, etc.). Third, a full analysis of the contributions of the individual molecular orbitals to the principal components of the  $^{35}\text{Cl}$  EFG tensor for  $\text{NbCl}_5$  is presented, and utilized to explore the origins of the experimentally observed  $^{35}\text{Cl}$  quadrupolar parameters. Fourth, we present an example of an application of  $^{35}\text{Cl}$  SSNMR to a tungsten chloride species grafted onto a silica support material. Based on experimental and theoretical data on the bulk species presented herein, it is possible to make a rough structural interpretation of this result. Finally, we discuss the potential applications of this methodology for the study of heterogeneous TM chloride catalysts.

### 6.3 Experimental and Computational Details

#### 6.3.1 Sample Preparation

Compounds  $\alpha\text{-WCl}_6$ ,  $\text{NbCl}_5$ , and  $\text{TaCl}_5$  were purchased from Strem Chemicals, and compounds  $\text{WOCl}_4$  and  $\text{MoOCl}_4$  were purchased from Sigma-Aldrich Canada, Ltd. All samples were used without further purification or modification (phase purity was checked with powder XRD, *vide infra*).  $\beta\text{-WCl}_6$  was prepared by the slow sublimation of  $\alpha\text{-WCl}_6$  under a nitrogen environment.<sup>52</sup> All of the compounds were stored and packed under an inert nitrogen atmosphere in a dry glove box due to their air- and moisture-sensitive natures. All samples were finely ground and packed into shortened 5 mm outer diameter glass NMR tubes, then capped and sealed with Parafilm to limit their exposure to atmosphere for the duration of the experiments.

#### 6.3.2 Synthesis of $\text{WCl}_6\text{-SiO}_2$

A toluene solution of  $\text{WCl}_6$  was added to a toluene suspension of dehydroxylated silica (Degussa Aerosil 250, pretreated at  $700^\circ\text{C}$  under  $10^{-5}$  bar vacuum) and the resulting mixture was stirred overnight at room temperature. After filtration of the supernatant, the solid was washed three times with toluene, one time with pentane, and dried under vacuum ( $10^{-5}$  bar). The amount of tungsten in the sample is 5.48 wt%. HCl evolution was checked by IR spectroscopy as in a previous communication.<sup>53</sup>

### 6.3.3 Powder X-ray Diffraction (PXRD)

PXRD experiments were performed at 100 K on a Bruker Apex 2 Kappa Diffractometer using graphite monochromatized Mo  $K_\alpha$  radiation ( $\lambda = 0.7107 \text{ \AA}$ ). Theoretical PXRD patterns were simulated for all samples using the Powder Cell software package.<sup>54</sup>

### 6.3.4 $^{35}\text{Cl}$ SSNMR Spectroscopy

A Varian Infinity Plus Spectrometer equipped with a wide-bore Oxford 9.4 T magnet ( $\nu_0(^1\text{H}) = 400 \text{ MHz}$  and  $\nu_0(^{35}\text{Cl}) = 39.16 \text{ MHz}$ ) was used for the acquisition of static (*i.e.*, stationary samples)  $^{35}\text{Cl}$  SSNMR spectra for all samples. The experiments were conducted on a Varian Chemagnetics 5 mm triple-resonance (HXY) T3 MAS NMR probe. Spectra were also collected using a Bruker Avance II spectrometer with a 21.1 T ( $\nu_0(^{35}\text{Cl}) = 88.2 \text{ MHz}$ ) standard-bore magnet at the National Ultrahigh-field NMR Facility for Solids in Ottawa, Ontario, Canada. A home-built 4 mm double resonance probe was used for all experiments. The spectrum of  $\text{WCl}_6\text{-SiO}_2$  was acquired on a Bruker Avance III spectrometer with an 18.8 T standard-bore magnet using a 3.2 mm HX MAS probe at Université Lille Nord de France. Chemical shifts were referenced to 1 M NaCl (aq), with NaCl(s) ( $\delta_{\text{iso}} = 0 \text{ ppm}$ ) used as a secondary reference.

All  $^{35}\text{Cl}$  CT powder patterns were too broad to be uniformly excited with a single, rectangular, high-power pulse. Hence, the WURST-CPMG pulse sequence<sup>38,51</sup> was used with a 50  $\mu\text{s}$  WURST pulse swept over 2000 kHz (sweep rate of 40 MHz/ms) for experiments at 9.4 and 21.1 T whereas at 18.8 T, the WURST pulse was swept over 4000 kHz (sweep rate of 80 MHz/ms). The experiments at 18.8 T also used a continuous-wave  $^1\text{H}$  decoupling field of 30 kHz that was applied for the duration of the scan, including during the WURST pulses. A detailed list of the experimental parameters can be found in Appendix E (**Tables E1-E3**). Spectra were acquired using the variable offset cumulative spectrum (VOCS) technique<sup>55-57</sup> with each sub-spectrum acquired using a transmitter offset of 100 kHz. Sub-spectra were processed using the NUTS program from Acorn software. The free induction decays (FIDs) of the sub-spectra were processed with digital filtering, Fourier transformation, and a magnitude calculation. The individual sub-spectra were then co-added (9.4 T) or skyline projected (21.1 T) to produce the total spectrum. The spectra consist of a series of narrow lines, called *spikelets*, whose outer manifold is representative of the shape of the powder pattern. Analytical simulations of the spectra were generated using WSolids<sup>58</sup> (9.4 T) and QUEST<sup>59</sup> (21.1 T) software packages; precise values of the quadrupolar parameters are obtained by matching the positions of the key spectral discontinuities (*i.e.*, “shoulders” and “horns”), and not the positions of the individual spikelets. Uncertainties in the quadrupolar parameters were estimated by bidirectional variation of each parameter, and visual comparison of experimental and simulated spectra.

$^{35}\text{Cl}$  transverse relaxation time constants ( $T_2$ ) were measured using the CPMG pulse sequence. Echo trains were acquired by placing the transmitter at each of the

spectral discontinuities. The intensity of each echo train was then plotted as a function of time and fit to an exponential decay using the Origin software package.

### 6.3.5 $^{35}\text{Cl}$ NQR Spectroscopy

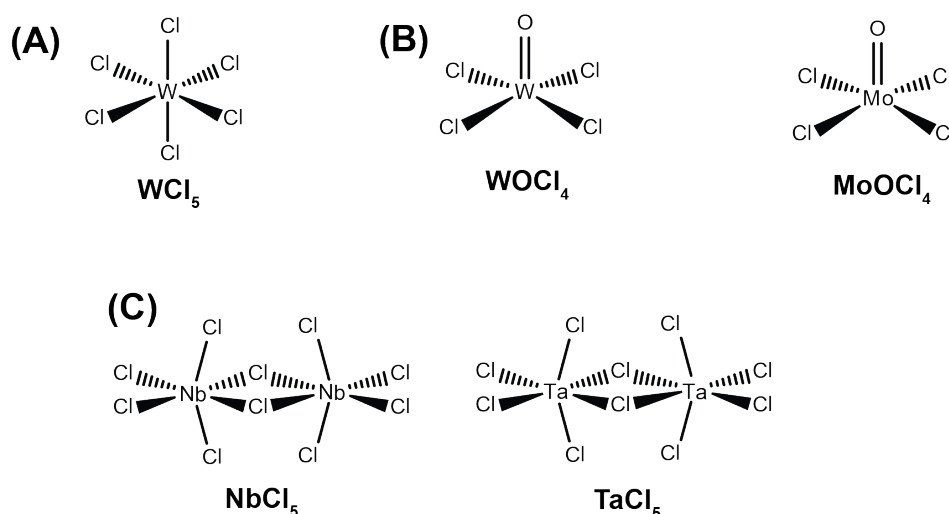
Experiments were conducted on a Varian Chemagnetics triple resonance (HXY) T3 MAS probe with a 5 mm coil and a Varian Infinity Plus console. The probe was placed as far away from the magnet as possible to limit the effects from the external magnetic field. The Hahn-echo pulse sequence was used with a  $3.5\ \mu\text{s}$   $90^\circ$  pulse width and a recycle delay of 0.5 s. Processing of the  $^{35}\text{Cl}$  NQR spectra was done using NUTS.

### 6.3.6 Plane-wave DFT Calculations

$^{35}\text{Cl}$  EFG and CS tensor parameters were calculated using the CASTEP<sup>60</sup> plane-wave density functional theory code in the Materials Studio 5.0 software package. Calculations employed the generalized gradient approximation (GGA), the gauge-including projector augmented wave (GIPAW) formalism and revised Perdew, Burke, and Ernzerhof (rPBE) functionals, with the core-valence interactions being described by on-the-fly pseudopotentials (**Table E4**). Integrals over the Brillouin zone were performed using a Monkhorst-Pack grid with a  $k$ -point spacing of  $0.07\ \text{\AA}^{-1}$ . Wavefunctions were expanded in plane waves with a kinetic energy cut-off of 300 eV. Crystal structures were obtained from the Inorganic Crystal Structure Database (ICSD) and calculations were completed both prior to and post geometry optimization of the structures (*i.e.*, all of the atomic positions were allowed to vary simultaneously while the cell parameters were fixed). All calculations were performed on the Shared Hierarchical Academic Research Computing Network (SHARCNET) using either 8 or 16 cores and 16 GB of memory per core.

### 6.3.7 $^{35}\text{Cl}$ Natural Bond Orbital/Natural Local Molecular Orbital Analysis of $\text{NbCl}_5$

All computations were performed using a developer's version of Amsterdam Density Functional (ADF)<sup>61</sup> package. Experimental single-crystal XRD crystal structures were used as starting structures for geometry optimization. For the computation of EFG tensor parameters and the geometry optimization routines, relativistic effects were included by utilizing the zeroth-order regular approximation (ZORA) in its scalar form.<sup>62</sup> All calculations were carried out using the revised Perdew-Burke-Ernzerhof (rPBE) functional.<sup>63,64</sup> The triple- $\zeta$  doubly polarized (TZ2P) all-electron Slater-type basis sets were used for Nb and Cl in all computations. Localized Molecular Orbital (LMO) analyses of  $^{35}\text{Cl}$  EFGs were performed as described previously.<sup>65</sup> LMOs were generated using the natural bond orbital (NBO) algorithm<sup>66</sup> implemented in a locally modified version of the NBO 5.0 program.<sup>67</sup> The set of "natural" LMOs generated by the NBO code was used for the EFG analysis.



**Scheme 6.1:** Schematic representations of (A) tungsten(VI) chloride ( $\text{WCl}_6$ ), (B) tetrachlorotungsten(VI) oxide ( $\text{WOCl}_4$ ) and tetrachloromolybdenum(VI) oxide ( $\text{MoOCl}_4$ ), (C) niobium(V) chloride ( $\text{NbCl}_5$ ) and tantalum(V) chloride ( $\text{TaCl}_5$ ).



## 6.4 Results and Discussion

For ease of discussion, all complexes have been grouped according to their structural similarities (**Scheme 6.1**). Some of the complexes exist as *polymorphs* in the solid state, which are pure substances that crystallize in more than one stable phase, with each having a distinct arrangement of atoms.<sup>68</sup> Powder X-ray diffraction (pXRD) patterns, which are useful for determining the presence of known crystalline phases, as well as for detecting for the presence of multiple polymorphs and crystalline impurities, were acquired for all of the samples (**Figures E7-E11**).

Before each group of systems is discussed in detail, it is useful to comment on some of the common features observed for all of the <sup>35</sup>Cl SSNMR spectra, as well as some of the aspects of the plane-wave DFT calculations of the <sup>35</sup>Cl EFG tensor parameters. First, all <sup>35</sup>Cl SSNMR spectra were acquired at both standard (9.4 T) and ultra-high magnetic field strengths (21.1 T). The higher field strength serves to increase S/N due to (i) a more favourable Boltzmann distribution and (ii) the reduction in the breadth of the SOQI-dominated CT pattern by an amount proportional to the inverse of  $B_0$ . Despite the general superiority of the 21.1 T data in terms of increased S/N, reduced experimental times and improved resolution, we note that the experiments completed at 9.4 T were crucial for parameterizing the experiments and optimizing our use of the 21.1 T spectrometer. The spectra acquired at 21.1 T are shown in this chapter, while those acquired at 9.4 T are presented in Appendix E. The only exception to this was  $\beta$ -WCl<sub>6</sub>, which was only studied at 9.4 T.

**Table 6.1:** Experimentally measured  $^{35}\text{Cl}$  NMR parameters for transition metal chlorides.

Sample	Site	$ C_Q ^a$	$\eta_Q^b$	$\delta_{\text{iso}}^c$	$\Omega^d$	$\kappa^e$	$\alpha^f$	$\beta$	$\gamma$
$\alpha\text{-WCl}_6$	1	21.00(10)	0.029(5)	800(40)	200(100)	1.0(2)	0(10)	0(10)	0(10)
$\beta\text{-WCl}_6$	1	21.00(10)	0.029(5)	800(40)	200(100)	1.0(2)	0(10)	0(10)	0(10)
$\text{WOCl}_4$	1	26.05(10)	0.115(5)	620(50)	550(150)	-1.0(4)	50(5)	15(10)	50(5)
$\text{MoOCl}_4$	1	30.50(10)	0.585(10)	650(50)	800(100)	1.0(2)	0(5)	90(5)	0(10)
	2	25.30(10)	0.510(5)	950(100)	800(150)	1.0(2)	0(5)	90(5)	90(5)
	3	25.00(10)	0.500(5)	800(50)	300(100)	1.0(3)	0(10)	90(10)	0(10)
	4	23.30(5)	0.540(20)	730(30)	235(50)	0.0(5)	0(20)	0(10)	0(20)
$\text{NbCl}_5$	1	25.30(5)	0.385(10)	250(150)	460(300)	1.0(2)	90(30)	0(10)	90(30)
	2	15.00(8)	0.081(7)	850(50)	200(200)	0.0(5)	0(20)	0(5)	0(30)
	3	14.70(9)	0.655(5)	990(40)	300(200)	0.0(3)	45(15)	0(20)	45(15)
$\text{TaCl}_5$	1	25.70(8)	0.430(10)	260(100)	250(200)	1.0(5)	90(30)	0(10)	90(30)
	2	15.65(15)	0.043(6)	640(50)	300(100)	1.0(3)	0(30)	0(5)	0(30)
	3	16.70(30)	0.480(20)	900(40)	700(50)	-1.0(3)	0(30)	90(5)	0(30)
$\text{WCl}_6\text{-SiO}_2$	1	25.98(5)	0.11(1)	450(30)	300(100)	-1.0(5)	50(10)	15(5)	50(10)

<sup>a</sup>  $C_Q = eQV_{33}/h$ , <sup>b</sup>  $\eta_Q = (V_{11} - V_{22})/V_{33}$ , <sup>c</sup>  $\delta_{\text{iso}} = (\delta_{11} + \delta_{22} + \delta_{33})/3$ , <sup>d</sup>  $\Omega = \delta_{11} - \delta_{33}$ , <sup>e</sup>  $\kappa = 3(\delta_{22} - \delta_{\text{iso}})/\Omega$ , <sup>f</sup> the Euler angles,  $\alpha$ ,  $\beta$  and  $\gamma$ , define the relative orientation of the EFG and CS tensors. The ‘‘ZZZ’’ convention for rotation is used herein, as described by Dye *et al.*,<sup>83</sup> and as implemented in the WSolids<sup>58</sup> software package.

Second, the breadth of each powder pattern is extremely large (700 to 1750 kHz) due to broadening of the CT by the SOQI. For all of the systems discussed herein, the SOQI has a much larger effect on the CT powder pattern than the chlorine chemical shift anisotropy (CSA); hence, the spectral features arise almost solely from the former. As such, the values obtained for the isotropic chemical shift ( $\delta_{\text{iso}}$ ), span ( $\Omega$ ), skew ( $\kappa$ ), and the Euler angles ( $\alpha$ ,  $\beta$  and  $\gamma$ ) describing the relative orientations of the EFG and CS tensors (see **Table 6.1** for definitions) have large uncertainties associated with them. The chlorine CS tensor parameters were calculated and the results are shown in Appendix E, along with a figure demonstrating that the inclusion of CSA has little effect on the appearance of the powder patterns (**Table E7**, **Figure E17**).

Third, the extreme breadths of the CT powder patterns make it difficult to distinguish chlorine environments that are chemically similar (*i.e.*, those with comparable bond lengths and angles) but crystallographically distinct. However, the specific types of bonding environment for chlorine (*i.e.*, bridging, terminal-axial, or terminal-equatorial, see **Scheme 6.2**) are easily discernable in the  $^{35}\text{Cl}$  SSNMR spectra. Furthermore, techniques such as  $^{35}\text{Cl}$  NQR and  $T_2$  editing of CPMG echo trains generally allow for the resolution of chemically similar environments and the accurate measurement of the NMR parameters.

Fourth, higher intensity than expected is always observed in the higher frequency range (*i.e.*, leftmost regions) of each spectrum in comparison to the low frequency (rightmost) range. This effect is more pronounced for certain samples in comparison to others probably due to effects such as  $T_2$  anisotropy and/or variation in probe/circuit characteristics over the broad range of acquisition frequencies (*vide infra*). Fifth, in some cases, it is possible to acquire signal extending past the edges of the CT in each powder pattern. This signal is attributed to the  $^{35}\text{Cl}$  satellite transition (ST) patterns (*i.e.*,  $-3/2 \leftrightarrow -1/2$  and  $+1/2 \leftrightarrow +3/2$ ), which are visible owing to the high abundance of chlorine in each complex. ST patterns are broadened immensely by the FOQI over a range of several MHz, and often are associated with  $T_2(^{35}\text{Cl})$  parameters that are distinct from those of the CT. In the case of  $^{35}\text{Cl}$ , the ST patterns result in minimal interference with the CT patterns. We note that the acquisition of the full ST powder pattern is generally unnecessary for UW SSNMR spectra, since the CT pattern provides information on all of the relevant NMR parameters. However, with quadrupolar parameters obtained from

simulations of the CT patterns, it is possible to rapidly locate the key discontinuities in the STs, and to potentially further refine the quadrupolar parameters.<sup>57</sup>

Despite the extreme breadths of the CT powder patterns, it was possible to attain high S/N, high-resolution spectra in relatively short time frames (*e.g.*, 32 s to 26 min at 21.1 T) owing to the broadband excitation of the WURST pulses, the long <sup>35</sup>Cl transverse relaxation times constants ( $T_2$ ) that favour CPMG-type experiments, and the high chlorine concentrations in these samples.

As mentioned, chlorine sites that are chemically very similar are not easily differentiated in the <sup>35</sup>Cl SSNMR spectra, and therefore, analytical simulations are representative of the convolution of the quadrupolar parameters of these sites. By fitting the simulations to the positions of the well-defined discontinuities of the spectra, it was possible to extract the <sup>35</sup>Cl EFG tensor parameters  $C_Q$  and  $\eta_Q$  (**Table 6.1**). <sup>35</sup>Cl NQR measurements have previously been conducted on all of the samples discussed herein. Since NQR measurements on spin-3/2 nuclei involve the measurement of a single transition, no values of  $\eta_Q$  are typically reported, which is a limitation of the NQR experiment.<sup>69,70</sup> Nonetheless, we see generally good agreement between our experimental values of  $C_Q$  and those from NQR measurements on <sup>35</sup>Cl nuclei possessing values of  $\eta_Q$  near to zero (*i.e.*, axially symmetric EFG tensors, **Table 6.2**).

**Table 6.2:** Experimental and calculated (using CASTEP)  $^{35}\text{Cl}$  EFG tensor parameters and comparison of predicted NQR frequencies obtained from  $^{35}\text{Cl}$  SSNMR data to those reported in literature. Calculation of the NMR parameters was completed both prior to and post geometry optimization of the structure.

Complex	Site	Experimental		Calculated				Predicted <sup>a</sup> $\nu_{\text{Q}}^{\text{NQR}}$ (MHz)	Reported <sup>10,21</sup> $\nu_{\text{Q}}^{\text{NQR}}$ (MHz)
		$ C_{\text{Q}} $ (MHz)	$\eta_{\text{Q}}$	pre-geometry optimization $C_{\text{Q}}$ (MHz)	$\eta_{\text{Q}}$	post-geometry optimization $C_{\text{Q}}$ (MHz)	$\eta_{\text{Q}}$		
$\alpha\text{-WCl}_6$	1	21.00	0.029	-15.62	0.06	-18.58	0.05	10.501	10.520
$\beta\text{-WCl}_6$	1	21.00	0.029	-16.39	0.01	-18.65	0.07	10.501	10.520
	2			-29.83	0.10	-18.60	0.07		10.525
	3			-8.001	0.01	-18.73	0.07		10.576
$\text{WOCl}_4$	1	26.05	0.115	-22.06	0.08	-23.39	0.14	13.054	13.076
$\text{MoOCl}_4$	1	30.50	0.585	-30.66	0.10	-24.07	0.31	16.096	15.658
	2	25.30	0.510	-15.64	0.94	-23.09	0.41	13.187	13.088
	3	25.00	0.500	-23.39	0.56	-25.50	0.44	13.010	12.904
	4	23.30	0.540	-26.44	0.33	-23.17	0.41	12.203	12.757
$\text{NbCl}_5$	1	14.70	0.655	-12.10	0.81	-12.72	0.77	7.858	7.612
	2	15.00	0.081	-11.92	0.14	-12.31	0.09	7.508	7.219
	3			-12.08	0.85	-12.95	0.77		7.365
	4			-11.76	0.10	-12.28	0.08		7.721
	5			-11.90	0.84	-12.80	0.77		
	6			-11.70	0.08	-12.35	0.07		
	7	25.30	0.385	24.29	0.28	23.90	0.27	12.959	13.058
	8			23.89	0.32	23.97	0.27		
	9			23.69	0.33	23.79	0.28		
$\text{TaCl}_5$	1	16.70	0.48	-13.58	0.71	-15.47	0.63	8.665	8.141
	2	15.65	0.043	-14.35	0.09	-15.29	0.06	7.827	7.598
	3			-13.88	0.72	-15.63	0.63		8.261
	4			-13.99	0.08	-15.34	0.06		7.641
	5			-13.66	0.74	-15.64	0.63		8.231
	6			-13.82	0.07	-15.38	0.05		7.663
	7	25.70	0.430	25.38	0.34	25.93	0.30	13.240	13.334
	8			25.52	0.32	25.98	0.31		13.356
	9			25.54	0.32	25.89	0.31		13.377

<sup>a</sup> The NQR frequencies were calculated from NMR parameters obtained from solid-state  $^{35}\text{Cl}$  SSNMR spectra using  $\nu_{\text{Q}}^{\text{NQR}} = (C_{\text{Q}}/2)\sqrt{(1+(\eta_{\text{Q}})^2/3)}$

The quadrupolar parameters determined from  $^{35}\text{Cl}$  NMR spectra, in conjunction with  $^{35}\text{Cl}$  EFG tensor parameters obtained from DFT calculations, were used to differentiate chlorine sites in distinct bonding arrangements (*i.e.*, bridging ( $\text{Cl}_{\text{br}}$ ), terminal-axial ( $\text{Cl}_{\text{ax}}$ ) and terminal-equatorial ( $\text{Cl}_{\text{eq}}$ ); **Scheme 6.2** and *vide infra*). No

consideration is given to the theoretical chlorine nuclear magnetic shielding tensors herein, since in most cases, the experimentally determined values of the chemical shift tensor parameters are associated with large uncertainties (as discussed above). The  $^{35}\text{Cl}$  EFG tensor parameters were calculated using CASTEP<sup>60</sup> both prior to and post-geometry optimization of each structure (**Table 6.2**). Geometry optimization of the structures resulted in small changes in bond lengths (**Table E5**), large changes in the computed EFG tensor parameters, and greatly reduced forces between atoms (**Table E6**). In all cases, it was found that terminal chlorines have negative values of  $C_Q$  whereas bridging chlorines have positive values. The theoretical magnitudes of  $C_Q$  are found to be consistently less than the experimentally measured values (**Figure 6.1**), similar to the observations of Rossini *et al.*<sup>46</sup> We note that the sign of  $C_Q$  cannot be measured directly from the  $^{35}\text{Cl}$  NMR spectra, but is readily determined by the calculations.

#### 6.4.1 Tungsten(VI) Chloride ( $\text{WCl}_6$ )

$\text{WCl}_6$  exists as one of two polymorphs,  $\alpha$  or  $\beta$ .  $\alpha\text{-WCl}_6$  form has one tungsten atom and one chlorine atom within the asymmetric unit (*i.e.*, there is one unique chlorine environment). There are six chlorine atoms arranged around a central tungsten atom in an octahedral arrangement (**Scheme 6.1**).  $\beta\text{-WCl}_6$  has two tungsten atoms and three chlorine atoms within the asymmetric unit. The three chlorine sites have similar W–Cl bond lengths (2.23, 2.26 and 2.34 Å) and comparable Cl–W–Cl bond angles (91.3, 91.6 and 90.3°), resulting in a slightly distorted octahedral arrangement of chlorine atoms about

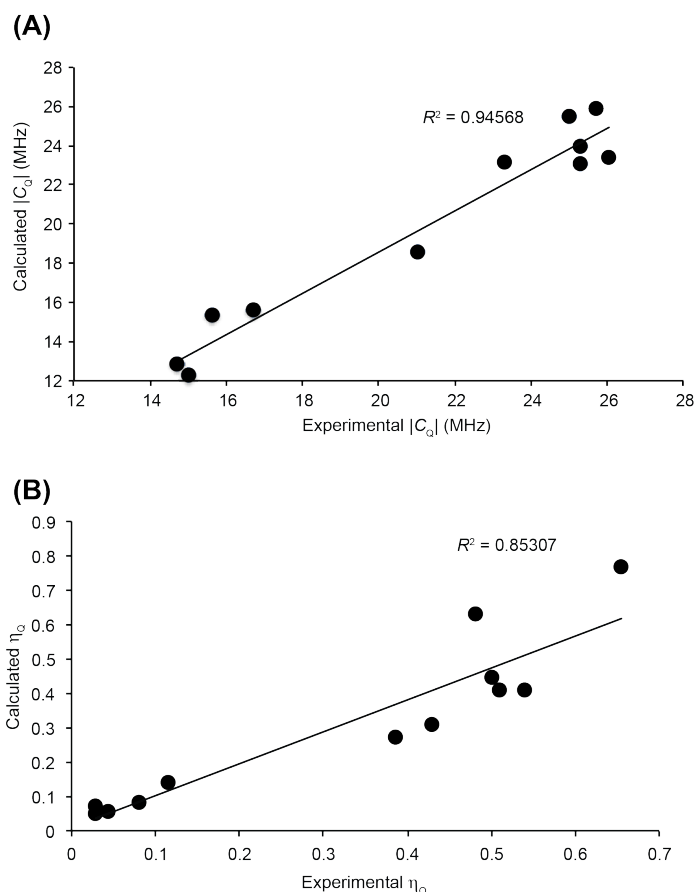


**Figure 6.1:** Comparison between the experimental and calculated values of (A)  $C_Q$  and (B)  $\eta_Q$  for all sites. All calculated values were obtained from  $^{35}\text{Cl}$  EFG tensor calculations completed on geometry optimized structures using CASTEP. The values of both  $C_Q$  and  $\eta_Q$  for the pseudo-bridging chlorine sites in  $\text{MoOCl}_4$  were omitted due to poor correlation between experiment and calculation.

the central tungsten atom.<sup>71</sup> Both forms feature hexagonal close packed lattices of chlorine atoms with tungsten ions filling the octahedral holes.  $\beta\text{-WCl}_6$  can be prepared from  $\alpha\text{-WCl}_6$  by the slow sublimation under  $\text{N}_2(\text{g})$ , or annealing a sample at a temperature greater than 200 °C (we chose the former procedure, see Section 6.3.1 for details).<sup>52</sup>

The  $^{35}\text{Cl}$  static SSNMR spectra of  $\alpha\text{-WCl}_6$  and  $\beta\text{-WCl}_6$  acquired at 21.1 T and 9.4 T, respectively, are shown in **Figure 6.2(A)** and **6.2(B)**. The latter compound was

synthesized after experiments on all other samples had been conducted at 21.1 T; for reasons described below, no high-field data for this compound is presented. The CT of  $\alpha$ - $\text{WCl}_6$  has a breadth of *ca.* 700 kHz and is characteristic of a powder pattern broadened by the second-order quadrupolar interaction. The discontinuities typical of such a spectrum are clearly visible and the overall manifold of the spikelet pattern is representative of a single distinct chlorine site. This spectrum was best simulated with one site,  $C_Q = 21.0$  MHz and  $\eta_Q = 0.029$  (**Table 6.1**). This result is consistent with  $\alpha$ - $\text{WCl}_6$ , which has one distinct chlorine environment. The CT of  $\beta$ - $\text{WCl}_6$  is *ca.* 1.5 MHz in breadth (due to the inverse dependence of the CT breadth on the applied external magnetic field strength). Despite the presence of multiple, magnetically and crystallographically distinct chlorine sites in  $\beta$ - $\text{WCl}_6$ , there appears to be only a single CT pattern, almost identical to the pattern acquired for  $\alpha$ - $\text{WCl}_6$  at 9.4 T (**Figure E12**). In fact, this pattern can be subjected to a similar one-site simulation, yielding identical quadrupolar parameters to those of  $\alpha$ - $\text{WCl}_6$  (within the limits of their uncertainties).

The benefit of ultra-wideline SSNMR experiments for rapidly acquiring spectra of anisotropically broadened powder patterns is tempered by their ability to resolve patterns arising from sites with very similar quadrupolar parameters. Even our attempts to acquire higher-resolution Hahn-echo spectra at key discontinuities failed to aid in clearly resolving the three unique chlorine sites in  $\beta$ - $\text{WCl}_6$  (**Figure 6.2 (C)**). In this case,  $^{35}\text{Cl}$  NQR is clearly very useful for trying to resolve the structurally similar sites in  $\beta$ - $\text{WCl}_6$ , as well as confirming the identity of each of these polymorphs. Both the  $\alpha$  and  $\beta$  forms



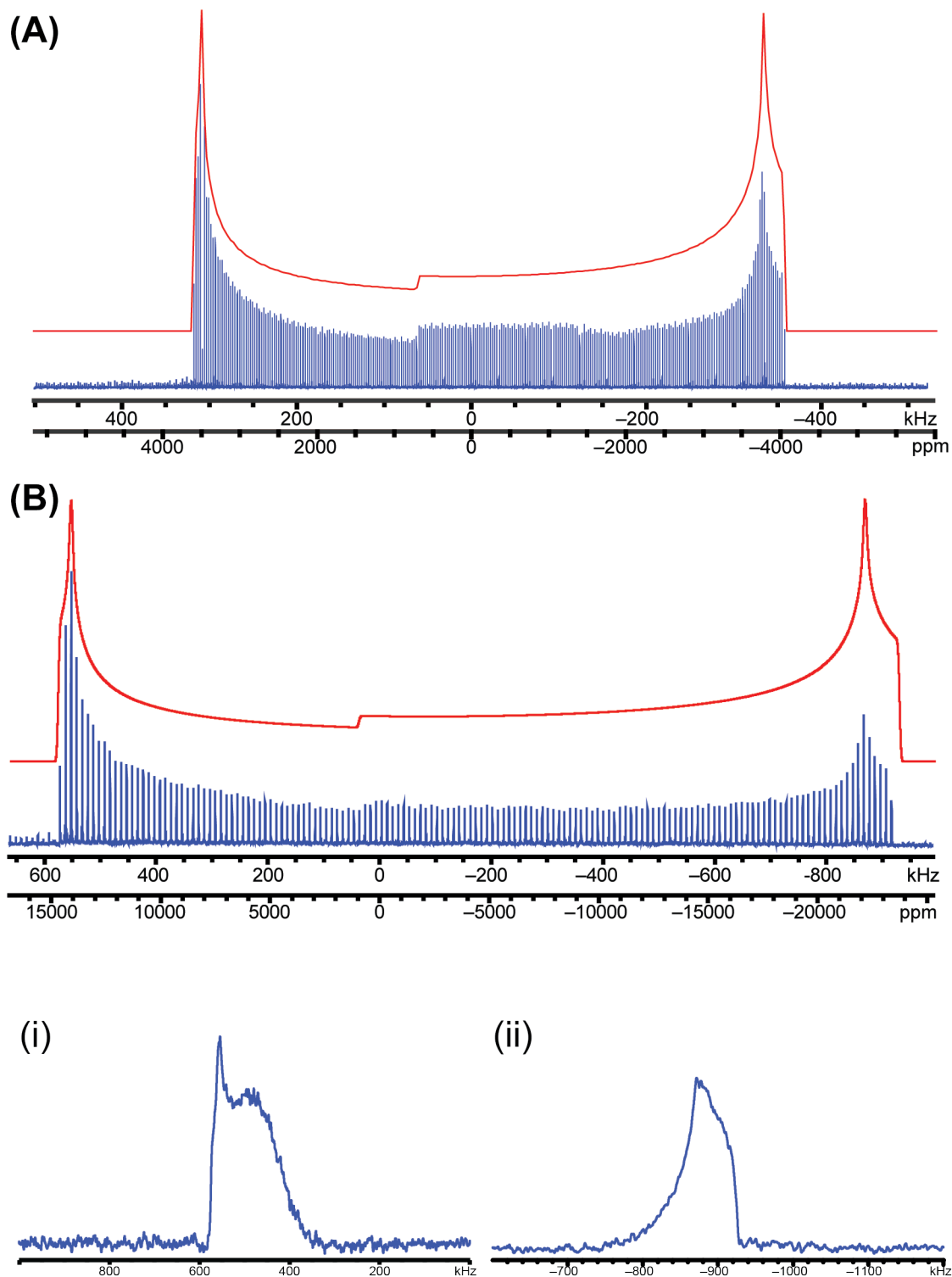


**Figure 6.2:** Static  $^{35}\text{Cl}$  SSNMR spectra acquired using frequency-stepped WURST-CPMG for (A)  $\alpha\text{-WCl}_6$  at 21.1 T and (B)  $\beta\text{-WCl}_6$  at 9.4 T with corresponding analytical simulations shown in red. (C) Hahn-echo experiments conducted on  $\beta\text{-WCl}_6$  at (i) the high and (ii) the low frequency discontinuities.

have previously been studied by  $^{35}\text{Cl}$  NQR spectroscopy. The  $^{35}\text{Cl}$  NQR spectrum of  $\alpha\text{-WCl}_6$  has a single peak corresponding to a frequency at  $\nu_Q^{\text{NQR}} = 10.520$  MHz, whereas that of  $\beta\text{-WCl}_6$  has three peaks ( $\nu_Q^{\text{NQR}} = 10.520, 10.525$  and  $10.576$  MHz).<sup>72</sup> The values of  $\nu_Q^{\text{NQR}}$  predicted from the experimentally determined  $^{35}\text{Cl}$  EFG tensor parameters obtained for  $\text{WCl}_6$  (**Table 6.2**), using the expression  $\nu_Q^{\text{NQR}} = (C_Q/2)(1+(\eta_Q^2/3))^{1/2}$ ,<sup>73</sup> are in good agreement with the previously reported NQR frequencies. Using the same NMR probe, we conducted our own  $^{35}\text{Cl}$  NQR experiments, and found a single peak at  $\nu_Q^{\text{NQR}} = 10.5154$  MHz for  $\alpha\text{-WCl}_6$  and three peaks at  $\nu_Q^{\text{NQR}} = 10.512, 10.519,$  and  $10.548$  MHz for  $\beta\text{-WCl}_6$  (**Figures 6.3(A)** and **(B)**), in excellent agreement with previous results. The quadrupolar parameters extracted for  $\beta\text{-WCl}_6$  from NQR experiments are so similar, that not even experiments at 21.1 T could effectively separate these patterns; hence, no further NMR experimentation was carried out.

It is clear that NMR and NQR are ideal partners for studying polymorphs, especially in cases where there is no *a priori* knowledge of the quadrupolar parameters. The specificity of the NQR experiment, while valuable for differentiating sites with similar quadrupolar parameters, is also a crutch, in that it results in tedious searches for NQR resonances over broad frequency ranges. However, the UW SSNMR experiments are capable of providing rapid and accurate determinations of quadrupolar parameters, allowing for the NQR experiment to be conducted in a frequency region of high specificity, and forgoing the monotonous, long “search periods” associated with conventional NQR experimentation.

In both  $\alpha$ - $\text{WCl}_6$  and  $\beta$ - $\text{WCl}_6$ , the  $C_Q$  values are at the lower end of the range of values reported for a chlorine directly bound to a transition metal.<sup>74</sup> As well, the values of  $\eta_Q$  are close to zero, indicating that the  $^{35}\text{Cl}$  EFG tensors are nearly axially symmetric in each case, and that the chlorine atoms are in environments of high cylindrical symmetry. This is expected for chlorine atoms that are in terminal bonding arrangements with respect to the central metal atom, and indicates that  $V_{33}$  is likely to be oriented directly along or close to the direction of the metal-chlorine bond (*vide infra*).

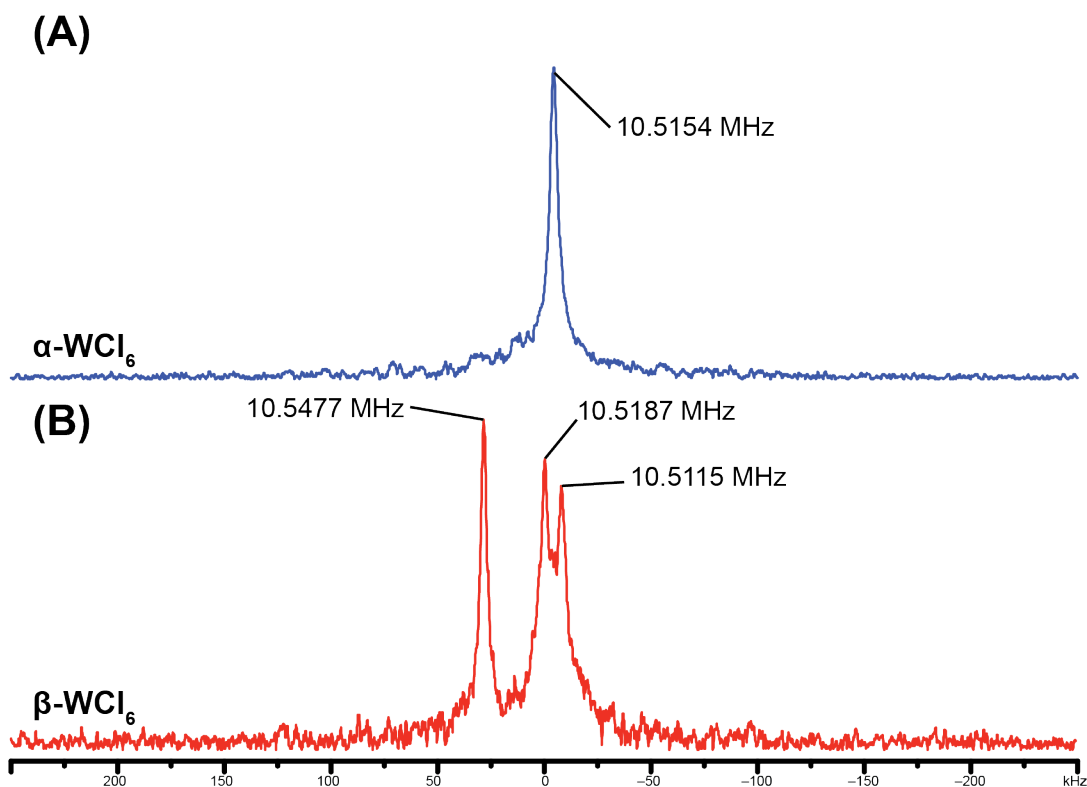


**Figure 6.3.**  $^{35}\text{Cl}$  NQR spectra for (A)  $\alpha$ - $\text{WCl}_6$  and (B)  $\beta$ - $\text{WCl}_6$ . The NQR frequencies ( $\nu_Q^{\text{NQR}}$ ) for each of the sites are shown in the figure. The spectra were acquired with a transmitter frequency of 10.52 MHz.

Plane-wave DFT calculations of the  $^{35}\text{Cl}$  EFG tensors for both  $\alpha$ - $\text{WCl}_6$  and  $\beta$ - $\text{WCl}_6$  are presented in **Table 6.2**. In both forms of the compound, the values of  $C_Q$  are

found to be negative (consistent with the terminal chlorine site) and consistently lower in magnitude than the experimental values. The values of  $\eta_Q$  are predicted to be near zero, also in agreement with experiment. The calculated  $^{35}\text{Cl}$  NMR parameters obtained prior to optimization of the structure are in poorer agreement with experiment, highlighting the need for geometry optimization of the structures. For example, in the set of calculations on model systems of  $\beta\text{-WCl}_6$  without geometry optimization, there is a large range of  $C_Q$  values predicted, which is not expected for chlorine environments that are chemically very similar. This suggests that the reported crystal structure of  $\beta\text{-WCl}_6$  may be inaccurate, as geometry optimization of the structure yields quadrupolar parameters that are more consistent with the  $^{35}\text{Cl}$  SSNMR data, and not subject to wild variations from site to site. It is also important to note that the predicted quadrupolar parameters are not ideal (*i.e.*, quite far from experimental values) for use as *a priori* starting points for the acquisition of NQR spectra; however, NQR experiments featuring the use of WURST pulses may be useful in this respect.<sup>75</sup>

The theoretically determined  $^{35}\text{Cl}$  EFG tensor orientations for  $\alpha\text{-}$  and  $\beta\text{-WCl}_6$  are shown in **Figures 6.4(A)** and **(B)**, respectively. In both cases, the largest principal components of each  $^{35}\text{Cl}$  EFG tensor,  $V_{33}$ , are oriented along, or nearly along the W–Cl bonds ( $\angle V_{33}\text{-Cl-W} = 178^\circ$  for  $\alpha\text{-WCl}_6$  and  $180^\circ$  for  $\beta\text{-WCl}_6$ ). The value of  $\eta_Q$  is close to zero in both forms, so the orientations of  $V_{11}$  and  $V_{22}$  are of little consequence, since  $V_{11} \approx V_{22}$ .

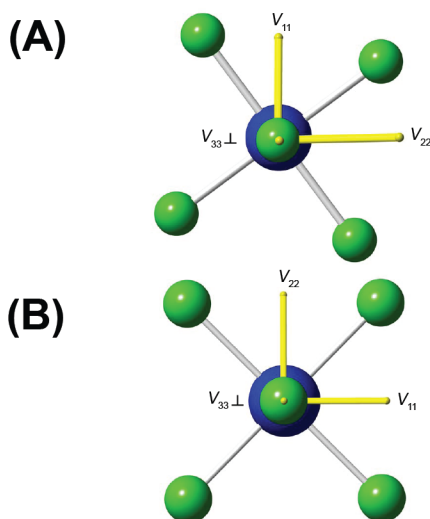


**Figure 6.4:** Theoretical  $^{35}\text{Cl}$  EFG tensor orientations in the molecular frames for (A)  $\alpha\text{-WCl}_6$  and (B)  $\beta\text{-WCl}_6$ , as determined from  $^{35}\text{Cl}$  EFG tensor calculations completed on geometry-optimized structures using CASTEP.

#### 6.4.2 Tetrachlorotungsten(VI) oxide ( $\text{WOCl}_4$ ) and tetrachloromolybdenum(VI) oxide ( $\text{MoOCl}_4$ )

The crystal structure of  $\text{WOCl}_4$  has one molecule in the asymmetric unit with four chlorine atoms in magnetically equivalent environments ( $r(\text{W-Cl}) = 2.285 \text{ \AA}$ ).<sup>76</sup> The molecule has a square pyramidal structure with an oxygen atom double bonded to the central tungsten atom at the apex (**Scheme 6.1**). The chlorine atoms sit in a square plane, which lies slightly below the plane of the tungsten atoms. Previous XRD studies of  $\text{WOCl}_4$  have suggested that the molecules are associated through weak interactions between the oxygen of one molecule and the tungsten of another. The molecules stack on top of one another to form linear arrays with asymmetric W–O–W bridges (the intramolecular W–O distance is  $1.737 \text{ \AA}$ , whereas the intermolecular W–O distance is  $2.258 \text{ \AA}$ ).

The local molecular structure of **MoOCl<sub>4</sub>** is similar to that of **WOCl<sub>4</sub>** (**Scheme 6.1**); however, their extended structures are strikingly different. Neutron and X-ray diffraction studies have shown that **MoOCl<sub>4</sub>** contains two molecules in the asymmetric unit with four chemically and magnetically distinct chlorine sites. The square pyramidal units do not form linear arrays, but instead, are associated through weak interactions between the chlorine atoms of one molecule and the molybdenum atom of another (the Mo–Cl bond length is *ca.* 2.3 Å, and the intermolecular Mo···Cl distance is 2.9 Å). These intermolecular interactions cause the molecules to form *quasi*-dimeric structures, with a single chlorine from each molecule forming the *pseudo*-bridge between adjacent pyramidal units.<sup>77</sup>

The <sup>35</sup>Cl SSNMR spectra for **WOCl<sub>4</sub>** and **MoOCl<sub>4</sub>** are shown in **Figures 6.5(A)** and **(B)**, respectively. The CT of the **WOCl<sub>4</sub>** pattern has a breadth of *ca.* 1075 kHz. The appearance of the discontinuities indicates that there is only one chlorine environment within the complex, in agreement with the aforementioned structure. The markedly different appearance of the <sup>35</sup>Cl SSNMR spectrum for **MoOCl<sub>4</sub>** clearly reflects the structural differences between the two complexes. The discontinuities in the **MoOCl<sub>4</sub>** spectrum are less well defined than those in the **WOCl<sub>4</sub>** spectrum, and it appears that there are at least four discernible patterns, three of which are very similar and overlapping with each other. The spectrum for **MoOCl<sub>4</sub>** has a much larger breadth (*ca.* 1750 kHz) than that of **WOCl<sub>4</sub>** and exhibits notable distortions, with greater intensity apparent in the high-frequency region of the spectrum.

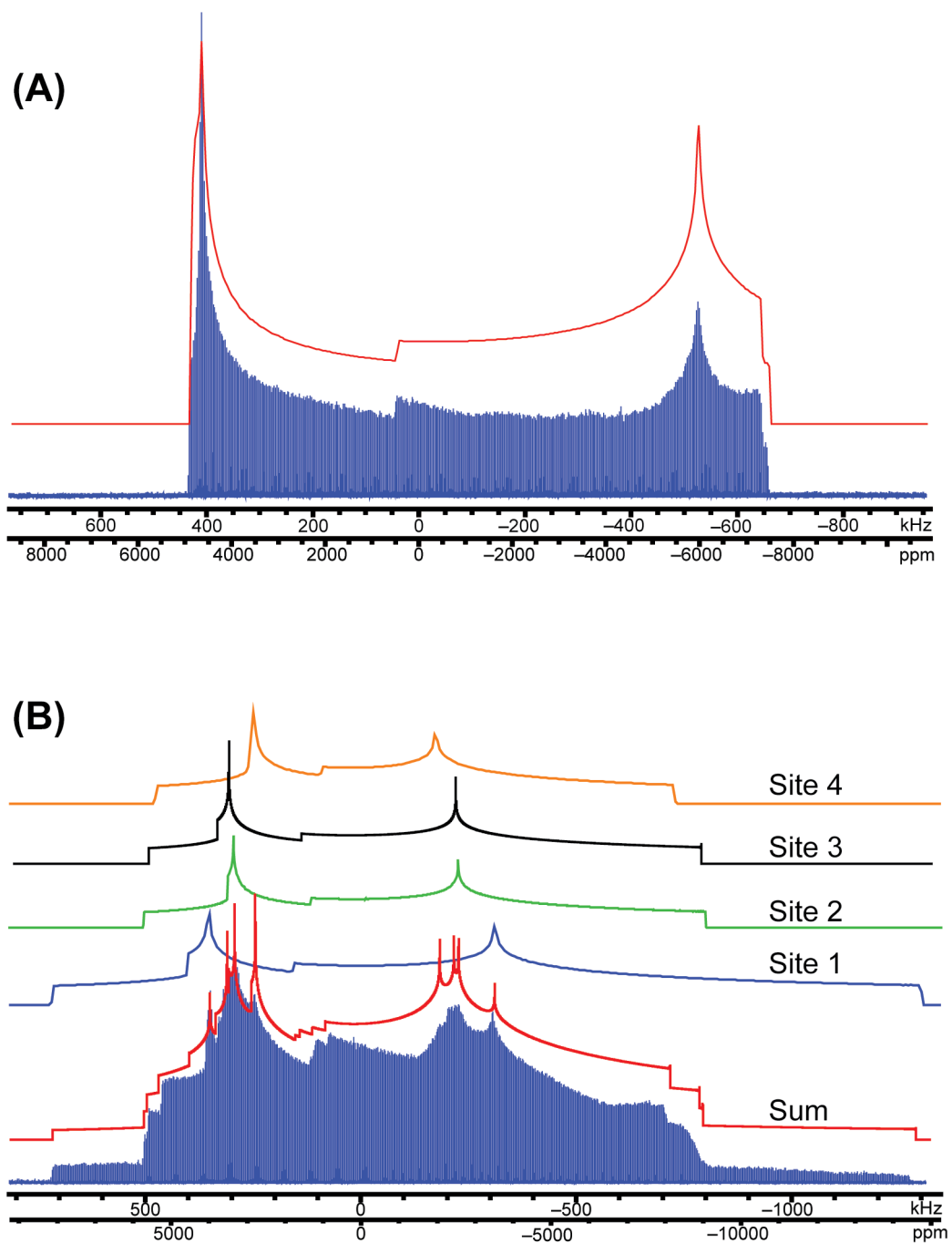


**Figure 6.5:** Static  $^{35}\text{Cl}$  SSNMR spectra acquired at 21.1 T for (A)  $\text{WOCl}_4$  and (B)  $\text{MoOCl}_4$ . Analytical simulations representative of the entire powder patterns are shown in red, while individual sites are shown in blue (C11), green (C12), black (C13) and orange (C14).

The **WOCl<sub>4</sub>** spectrum is best simulated with a single site  $C_Q = 26.05$  MHz and  $\eta_Q = 0.115$  (**Table 6.1**). The **MoOCl<sub>4</sub>** spectrum is simulated with four overlapping patterns of equal intensity arising from chlorine environments with distinct quadrupolar parameters (**Table 6.1**). Three of the patterns have values of  $C_Q$  and  $\eta_Q$  that lie within experimental error of one other, indicating that there are three chlorine sites with similar chemical environments. The resulting overlap of these three patterns causes broadening of the outer discontinuities.

The magnitudes of  $C_Q$  for **WOCl<sub>4</sub>** and **MoOCl<sub>4</sub>** are considerably larger than that of **WCl<sub>6</sub>**; it is not trivial to explain this difference, given the distinct modes of bonding in and different symmetries of these two sets of compounds. In particular, one must be cautious in looking for relationships between M-Cl bond lengths and magnitudes of  $C_Q$ . The natures of the M-Cl bonds in **WCl<sub>6</sub>** are likely to be very different from those in the **MOCl<sub>4</sub>** species, despite the very similar M-Cl bond lengths (*i.e.*, by natures, we mean the differences in bonds in terms of their covalent/ionic character, hybridization of *s* and *p* orbitals, and multiple bond characters).<sup>78</sup> Even the comparison of the structurally similar **WOCl<sub>4</sub>** and **MoOCl<sub>4</sub>** species does not reveal any simple explanation for the variation in values of  $C_Q$  (clearly the nature of the extended structure in the latter case plays a role in influencing the EFG tensor). The value of  $\eta_Q$  for **WOCl<sub>4</sub>** is comparable to that of **WCl<sub>6</sub>** and is consistent with previous observations for terminal chlorine environments. The values of  $\eta_Q$  for **MoOCl<sub>4</sub>** are all moderate, indicating non-axial EFG tensors, and reflecting the association of the molecules into dimeric structures. Indeed, a careful analysis of the contributions from individual molecular orbitals to the EFG tensors is necessary to account for differences in values of  $C_Q$ , as well as for examining the



relationships between intra- and intermolecular contacts and EFG tensor orientations and parameters (*vide infra*).<sup>65</sup>

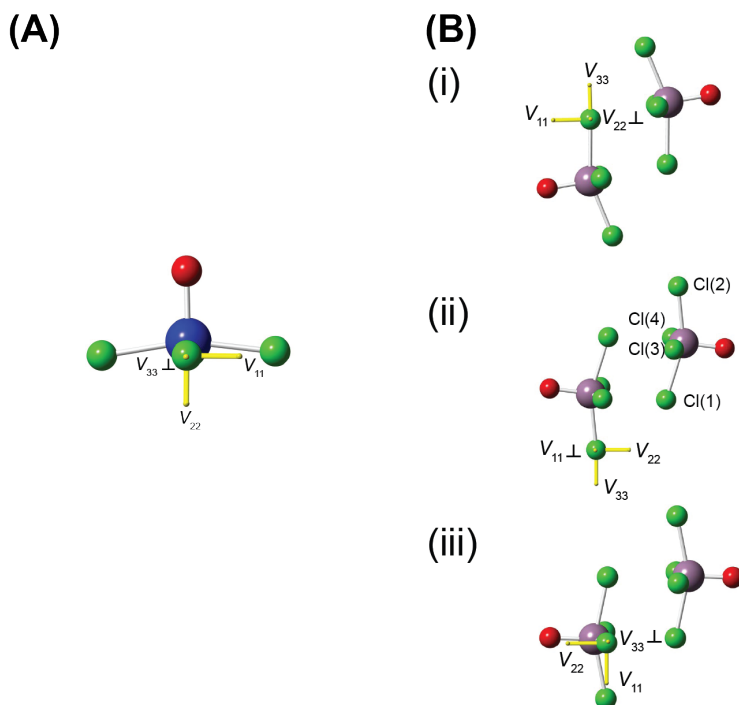


**Figure 6.6:** Theoretical  $^{35}\text{Cl}$  EFG tensor orientations for (A)  $\text{WOCl}_4$  and (B)  $\text{MoOCl}_4$  with (i) the pseudo-bridging chlorine sites (Cl1), (ii) the terminal chlorine sites opposite the pseudo-bridging sites (Cl2) and (iii) the terminal chlorine sites adjacent to the pseudo-bridging chlorine sites (Cl3 and Cl4). All pictured orientations were determined from  $^{35}\text{Cl}$  EFG tensor calculations completed on geometry-optimized models using CASTEP.

Both  $\text{WOCl}_4$  and  $\text{MoOCl}_4$  systems have previously been studied by  $^{35}\text{Cl}$  NQR spectroscopy and similar results regarding the types and multiplicities of chlorine environments were found. The NQR spectrum for the  $\text{WOCl}_4$  complex has a single peak corresponding to the single chlorine chemical environment, and the value of the NQR frequency is in good agreement with the experimentally determined value of  $C_Q$  (Table 6.2). The spectrum of the  $\text{MoOCl}_4$  complex has four NQR frequencies, three of which are very similar. The highest frequency resonance (ca. 3 MHz higher than the others) was

assigned to the chlorine atoms which act as the *pseudo*-bridge between the metal centres.<sup>72</sup> This is consistent with our findings discussed above.

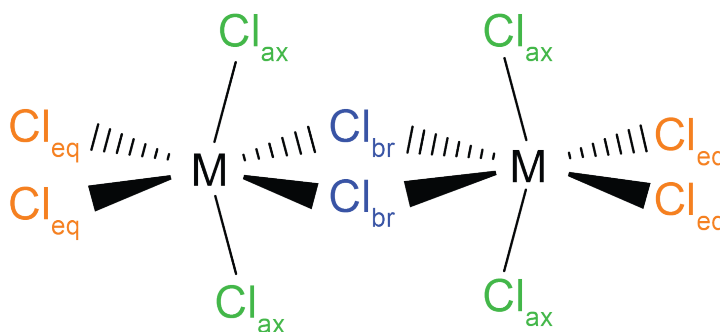
Plane-wave DFT calculations were performed for **WOCl<sub>4</sub>** and **MoOCl<sub>4</sub>** using structures obtained from the ICSD. The DFT calculations of the <sup>35</sup>Cl EFG tensors for **WOCl<sub>4</sub>** predict one magnetically distinct chlorine environment, as expected. The value of  $C_Q$  predicted from post-geometry optimized calculations is found to be negative, and  $\eta_Q$  close to zero, consistent with the chlorine atoms being in a terminal environment. The theoretical magnitudes of  $C_Q$  are considerably lower than the experimentally determined values, but the values of  $\eta_Q$  are more closely reproduced. <sup>35</sup>Cl DFT calculations completed for **MoOCl<sub>4</sub>** predict four chlorine environments, all with negative values of  $C_Q$  and moderate values of  $\eta_Q$ , consistent with our assignments above.

The <sup>35</sup>Cl EFG tensor orientations for **WOCl<sub>4</sub>** and **MoOCl<sub>4</sub>** are shown in **Figures 6.6(A)** and **(B)** respectively. Since the value of  $\eta_Q$  is near zero for the single chlorine site in **WOCl<sub>4</sub>**, this indicates that  $V_{33}$  is the distinct component in the <sup>35</sup>Cl EFG tensor and that the values of  $V_{11}$  and  $V_{22}$  are similar in magnitude. Due to the symmetry of the **WOCl<sub>4</sub>** molecule, the presence of the chlorine atoms in a plane below the tungsten atom, and the covalently bound O atom,  $V_{33}$  is not oriented exactly along the W–Cl bond (*i.e.*,  $\angle(V_{33}\text{-Cl-W} = 4.45^\circ)$ ). In **MoOCl<sub>4</sub>**, the three magnetically distinct chlorine sites (the pseudo-bridging chlorine atom (Cl1), the terminal chlorine atom opposite to the pseudo-bridge (Cl2), and the terminal chlorine atom adjacent to the pseudo-bridge (Cl3 and Cl4)) have distinct <sup>35</sup>Cl EFG tensor orientations. The designation *pseudo-bridging* refers to a chlorine atom that has a covalent bond with one metal centre, and a distant contact with a second metal centre from a neighbouring molecule. All three sites have moderate values

of  $\eta_Q$ , indicating that their  $^{35}\text{Cl}$  EFG tensors are not axially symmetric, which is indicative of an absence of cylindrical symmetry of the ground-state electron density about these chlorine sites. For Cl1,  $V_{33}$  is oriented near the Mo–Cl bond ( $\angle(V_{33}\text{-Cl-Mo} = 1.85^\circ)$ ) and the value of  $C_Q$  is negative, which is consistent with similar observations for terminal chlorine environments.<sup>45</sup> It has been shown that chlorine atoms which are involved in true bridging interactions between transition metal centres have  $^{35}\text{Cl}$  EFG tensor orientations in which  $V_{33}$  is oriented perpendicular (or approximately perpendicular) to the plane of the M–Cl–M bonding arrangement and positive values of  $C_Q$ .<sup>46</sup> Sites Cl2, Cl3 and Cl4 all have the  $V_{33}$  components directed near the direction of their respective Mo–Cl bonds ( $\angle(V_{33}\text{-Cl-Mo} = 5.67^\circ$  and  $12.95^\circ$ , respectively), as is typical of chlorines in terminal bonding arrangements.

#### 6.4.3 Niobium(V) chloride ( $\text{NbCl}_5$ ) and tantalum(V) chloride ( $\text{TaCl}_5$ )

The crystal structure of niobium pentachloride ( $\text{NbCl}_5$ ) has one molecule in the asymmetric unit with nine crystallographically distinct chlorine atoms. The complex forms a dimeric structure in which the chlorine atoms form two octahedra sharing a common edge, with the niobium atoms occupying the centres of the octahedra. This structure results in three specific bonding arrangements for the chlorine atoms: bridging ( $\text{Cl}_{\text{br}}$ ), terminal-axial ( $\text{Cl}_{\text{ax}}$ ), and terminal-equatorial ( $\text{Cl}_{\text{eq}}$ ) (**Scheme 6.2**). The average Nb–Cl bond distances are 2.555, 2.302, and 2.250 Å for  $\text{Cl}_{\text{br}}$ ,  $\text{Cl}_{\text{ax}}$ , and  $\text{Cl}_{\text{eq}}$ , respectively.<sup>79</sup> Tantalum(V) chloride ( $\text{TaCl}_5$ ) is isostructural to  $\text{NbCl}_5$ , and has average Ta–Cl bond lengths of 2.547, 2.307, and 2.225 Å for  $\text{Cl}_{\text{br}}$ ,  $\text{Cl}_{\text{ax}}$ , and  $\text{Cl}_{\text{eq}}$ , respectively.<sup>80</sup>



**Scheme 6.2:** Schematic representation of the different chlorine bonding environments in the bridging pentahalide species. Bridging chlorine atoms (Cl<sub>br</sub>) are shown in blue, terminal-axial (Cl<sub>ax</sub>) in green and terminal-equatorial (Cl<sub>eq</sub>) in orange.

The static <sup>35</sup>Cl SSNMR spectra of **NbCl<sub>5</sub>** and **TaCl<sub>5</sub>** are shown in **Figures 6.7(A)** and **(B)**, respectively. The CT patterns have breadths of *ca.* 1300 kHz (**NbCl<sub>5</sub>**) and *ca.* 1400 kHz (**TaCl<sub>5</sub>**). For each system, the outer manifolds of the spikelet patterns reveal several clearly defined discontinuities that indicate the presence of three distinct patterns, consistent with the presence of the Cl<sub>br</sub>, Cl<sub>ax</sub>, and Cl<sub>eq</sub> bonding environments (*vide infra*).

The analytical simulation for the entire powder pattern of **NbCl<sub>5</sub>** is shown in **Figure 6.7(A)** as the red trace, with the individual patterns shown as the blue ( $C_Q = 25.30$  MHz and  $\eta_Q = 0.385$ ), green ( $C_Q = 15.0$  MHz and  $\eta_Q = 0.081$ ), and orange ( $C_Q = 14.70$  MHz and  $\eta_Q = 0.655$ ) traces. We note that the patterns are simulated with 1:1:1 signal intensity (instead of the expected 1:2:2, Cl<sub>br</sub>:Cl<sub>ax</sub>:Cl<sub>eq</sub>) as the WURST-CPMG technique is non-quantitative (since each Cl site is likely to have a slightly different  $T_2$  constant) and the relative signal intensity does not accurately reflect the relative populations of the individual chlorine environments. Using results obtained via DFT calculations (*vide infra*), it is possible to assign the three patterns in the spectrum to the specific chlorine bonding environments. The pattern with the largest absolute magnitude of  $C_Q$

corresponds to the  $\text{Cl}_{\text{br}}$  environment, consistent with the results obtained for  $\text{Cp}^*\text{ZrCl}_3$  in the study by Rossini *et al.*,<sup>46</sup> but distinct from those for bridging chlorine sites in main group compounds.<sup>45</sup> This suggests that the value of  $C_Q$  for the bridging chlorine is strongly dependent on the nature of the metal to which it is bonded, as well as the overall structure of the complex. The  $\text{Cl}_{\text{br}}$  has a moderate value of  $\eta_Q$ , as is typical for this type of environment. The pattern with the value of  $\eta_Q$  close to zero is assigned to the  $\text{Cl}_{\text{ax}}$ , again consistent with high cylindrical symmetry about such terminal M–Cl bonds. The final pattern has a value of  $\eta_Q$  closest to unity and is assigned to the  $\text{Cl}_{\text{eq}}$ , which differs from results obtained by Rossini *et al.* where it was found that terminal chlorine environments had values of  $\eta_Q$  close to zero. Since the values of  $C_Q$  for the two types of terminal sites are almost identical, it is clear that  $\eta_Q$  is useful for their differentiation.

In a similar manner, analytical simulations of the entire  $^{35}\text{Cl}$  CT pattern, as well as the three contributing patterns, are shown in **Figure 6.7(B)** for  $\text{TaCl}_5$ . The site assignments are identical to those described for  $\text{NbCl}_5$ . The values for  $C_Q$  for all three sites of  $\text{TaCl}_5$  are larger than the corresponding values for  $\text{NbCl}_5$ . Since  $\text{NbCl}_5$  and  $\text{TaCl}_5$  are isostructural, and tantalum is one row below niobium in the periodic table, it is the relative size of the metal atom which appears to influence the magnitude of the quadrupolar interaction, with the larger central metal atom corresponding to a larger value of  $C_Q$ . Interestingly, the M–Cl bond lengths are very similar in these two systems, with the largest difference being 0.03 Å, again discouraging the invoking of simple correlations between bond length and  $C_Q$ .

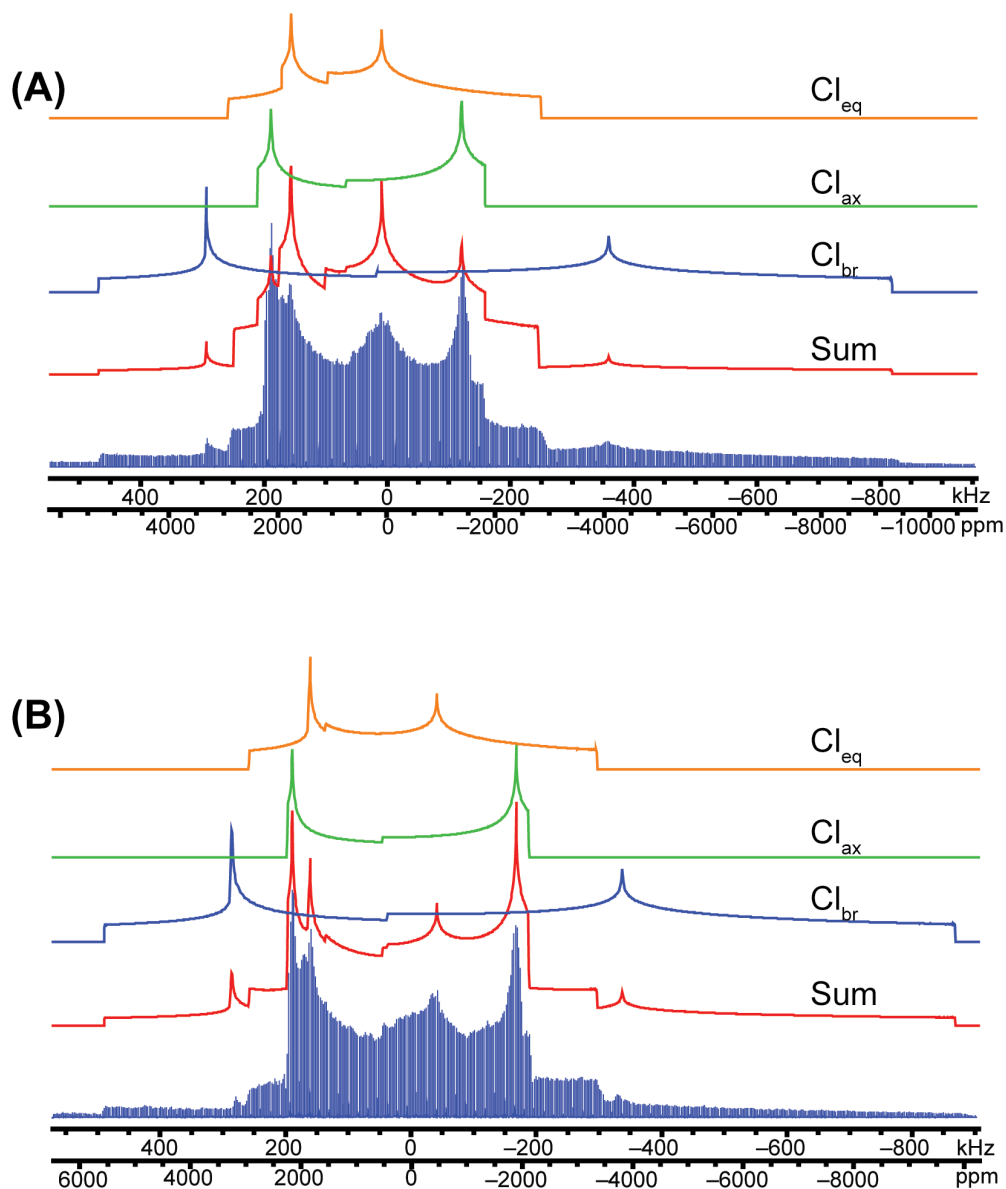


**Figure 6.7:** Static  $^{35}\text{Cl}$  SSNMR spectra acquired at 21.1 T for (A)  $\text{NbCl}_5$  and (B)  $\text{TaCl}_5$ . Corresponding analytical simulations representative of the entire powder patterns are shown in red and simulations of the individual sites are shown in blue ( $\text{Cl}_{\text{br}}$ ), green ( $\text{Cl}_{\text{ax}}$ ), and orange ( $\text{Cl}_{\text{eq}}$ ).

Both of these complexes were previously studied by  $^{35}\text{Cl}$  NQR spectroscopy, with the measured quadrupolar frequencies given in **Table 6.2**. The room temperature NQR study of  $\text{NbCl}_5$  reveals seven distinct sites, five of which have comparable NQR frequencies. The two remaining sites have substantially higher NQR frequencies, and are

assigned to  $\text{Cl}_{\text{br}}$ , which is consistent with our results.<sup>72</sup> Similar NQR results were found for  $\text{TaCl}_5$ ,<sup>81</sup> and are also consistent with this work.

Plane-wave DFT calculations of  $^{35}\text{Cl}$  EFG tensors were performed on  $\text{NbCl}_5$  and  $\text{TaCl}_5$  (**Table 6.2**). Calculated values of  $C_Q$  and  $\eta_Q$  distinguish bridging and terminal chlorine sites, not only by the absolute magnitudes of  $C_Q$ , but also by their signs: bridging and terminal chlorines have positive and negative values of  $C_Q$ , respectively. The CASTEP calculations for post-geometry optimized  $\text{NbCl}_5$  and  $\text{TaCl}_5$  models are in good agreement with experimental values of  $C_Q$  and reasonable agreement for values of  $\eta_Q$  (**Figure 6.1**).

The theoretical  $^{35}\text{Cl}$  EFG tensor orientations were determined for both complexes. Since they are isostructural, only the results for  $\text{NbCl}_5$  are shown in **Figure 6.8**. The  $\text{Cl}_{\text{br}}$  sites, which have moderate values of  $\eta_Q$ , have  $V_{33}$  components oriented nearly perpendicular ( $90.30^\circ$ ) to the M–Cl–M plane, which is consistent with observations by Rossini *et al.*<sup>46</sup> The moderate values of  $\eta_Q$  for these sites indicate that the  $^{35}\text{Cl}$  EFG tensor is non-axial (*i.e.*,  $V_{11} \neq V_{22}$ ), which is consistent with the local geometry of a  $\text{Cl}_{\text{br}}$  atom. The  $\text{Cl}_{\text{ax}}$  sites have values of  $\eta_Q$  close to zero, with  $V_{33}$  components oriented near the directions of the M–Cl bonds in each case, as expected. Finally, the  $\text{Cl}_{\text{eq}}$  sites have large values of  $\eta_Q$ , indicating that  $V_{11}$  is the distinct component of the  $^{35}\text{Cl}$  EFG tensor (*i.e.*, the absolute magnitudes of  $V_{22}$  and  $V_{33}$  are similar). In each system,  $V_{11}$  is oriented towards the bridging chlorine environments, and  $V_{33}$  is directed near the M–Cl bonds, in good agreement with previous studies.

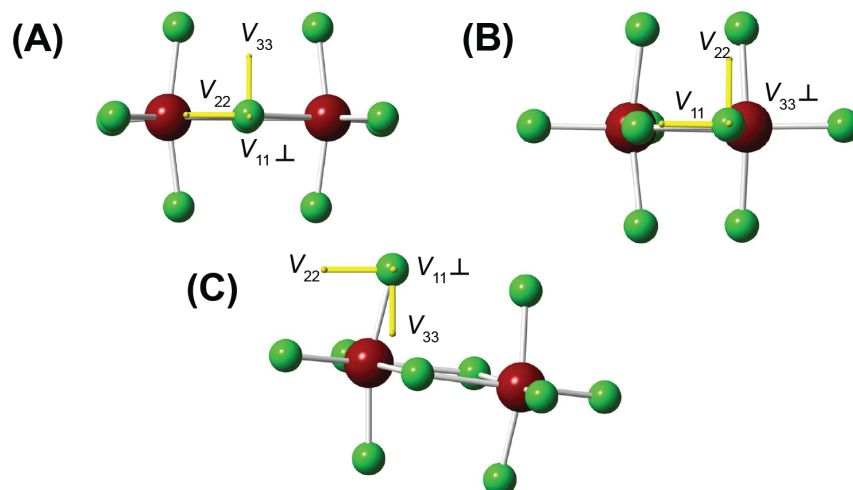


**Figure 6.8:** Theoretical  $^{35}\text{Cl}$  EFG tensor orientations in the molecular frame for the (A)  $\text{Cl}_{\text{br}}$ , (B)  $\text{Cl}_{\text{eq}}$ , and (C)  $\text{Cl}_{\text{ax}}$  environments in  $\text{NbCl}_5$ . Orientations were determined from  $^{35}\text{Cl}$  EFG tensor calculations completed on geometry-optimized models using CASTEP. Similar tensor orientations were found for the isostructural  $\text{TaCl}_5$  complex.

#### 6.4.4 $^{35}\text{Cl}$ Transverse Relaxation Time ( $T_2$ ) measurements

As mentioned above, the  $^{35}\text{Cl}$  SSNMR spectra obtained for each of the compounds investigated exhibit variations in spectral intensity that do not precisely match the intensities produced from analytical simulations. For example, higher intensity is consistently observed in the high-frequency (leftmost) regions of the spectra. While there are no detailed studies in literature that investigate this phenomenon, we have reported instances of this intensity variation in several other papers on ultra-wideline NMR of quadrupolar nuclei.<sup>47,82</sup> We speculate that it may be caused by two factors: (i) tuning limitations of the probe used that may cause uneven excitation/detection across the range of frequencies studied and/or (ii) variation of the transverse relaxation times across the breadth of the pattern, which we refer to as  $T_2$  anisotropy.

In order to investigate this further, we measured the transverse relaxation time constants across the patterns by placing the transmitter at frequencies corresponding to



different discontinuities of the patterns, and acquiring a series of echoes using a CPMG experiment. By plotting the echo intensity against the echo time and fitting the data to an exponential decay, the  $T_2$  values and their associated errors were determined. The process is shown for **WCl<sub>6</sub>** in **Figure 6.9** and the remaining data is shown in **Table E8**. We found that in most cases,  $T_2$  values measured at the low-frequency discontinuities are smaller than those measured at higher frequency. The overall differences in  $T_2$  values are not large, certainly well under an order of magnitude. At this time, it is unclear that the tuning characteristics of the probe are responsible for any of the intensity variation, since we have used the exact same probes and tuning configurations to acquire spectra where the intensity variations do not follow the patterns described above. Clearly, a more detailed study of this intensity variation is required; if  $T_2$  anisotropy is solely responsible for this phenomenon, some interesting physical models and chemical interpretations could arise in the future.

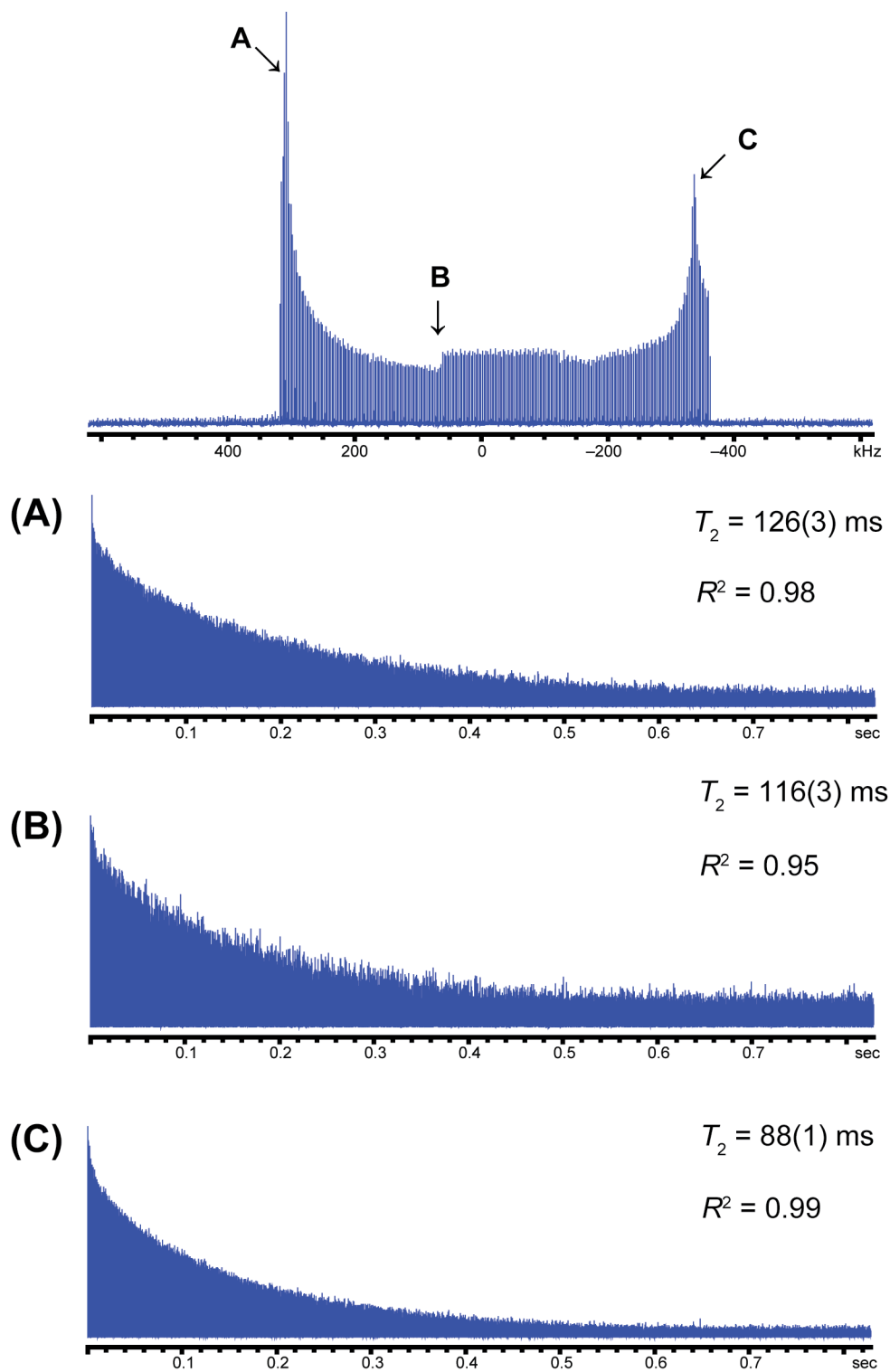


**Figure 6.9:**  $T_2$  relaxation time constants and corresponding CPMG echo trains from experiments on  $\alpha\text{-WCl}_6$  at (A) the high-frequency, (B) central and (C) low-frequency discontinuities.

#### 6.4.5 LMO Analysis of the $^{35}\text{Cl}$ EFG Tensors

Upon examining the results obtained for the dimer pentahalide species, certain questions arise: (i) why do the  $\text{Cl}_{\text{br}}$  sites have significantly larger values of  $C_Q$  compared to the terminal chlorines, and (ii) why do the  $\text{Cl}_{\text{eq}}$  sites have values of  $\eta_Q \approx 1$  when the  $\text{Cl}_{\text{ax}}$  have values of  $\eta_Q \approx 0$ ? In order to further probe the origins of the  $^{35}\text{Cl}$  EFG tensors for the various chlorine environments in the pentahalide species, we performed Localized Molecular Orbital (LMO) analysis, in which the contributions of each LMO to the  $^{35}\text{Cl}$  EFG tensors are determined.<sup>65</sup> The LMOs are quantum-mechanical representations of bonds and lone pairs as well as core shell electron pairs. For  $\text{Nb}_2\text{Cl}_{10}$ , there are also three-centre  $\mu$ -bonding LMOs centred on the bridging chlorine atoms. Here, we chose to conduct calculations and analysis upon the  $\text{Nb}_2\text{Cl}_{10}$  dimer, which possesses distinct types of terminal and bridging chlorine sites. We note that DFT MO calculations and concomitant LMO analyses were only conducted upon  $\text{Nb}_2\text{Cl}_{10}$  clusters, since these species are sufficiently isolated from surrounding lattice that  $^{35}\text{Cl}$  EFG tensors are not adversely affected by long-range electrostatic interactions. Compounds like  $\alpha\text{-WCl}_6$ ,  $\beta\text{-WCl}_6$  and  $\text{MoOCl}_4$  all feature shorter intermolecular contacts that may influence the  $^{35}\text{Cl}$  EFG tensors, so LMO analyses on isolated clusters from these systems were not conducted (a full study of inter- and intramolecular electrostatic effects on EFG tensors for all of these systems is beyond the scope of the current work).

The  $^{35}\text{Cl}$  EFG tensor parameters calculated using ADF and CASTEP are in good agreement with one another as well as the experimentally obtained parameters (**Table E10**). This indicates that the  $^{35}\text{Cl}$  EFG tensor parameters are highly dependent upon EFGs originating within the individual  $\text{Nb}_2\text{Cl}_{10}$  units, and almost independent of EFGs

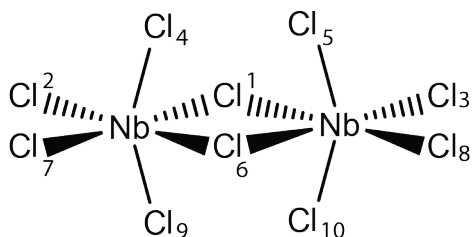
arising from intermolecular interactions within the solid. Furthermore, geometry optimization of the structure improves the agreement between the calculated parameters and those obtained experimentally.

The contribution of each LMO to the principal components of the  $^{35}\text{Cl}$  EFG tensors are tabulated in **Table 6.3**, and the atom labels for the  $\text{Nb}_2\text{Cl}_{10}$  unit are shown in **Figure 6.10(A)**. The individual LMOs that contribute to the EFGs are shown in **Figure 6.10(B)** as isosurfaces.<sup>65</sup> The calculations describe contributions from core, lone-pair (LP, with the  $\pi$  and  $\sigma$  referring to local symmetry with respect to the metal-chlorine bond axis), dative Nb-Cl  $\sigma$ -bonds,  $\pi$ -bonds, and 3-centred bridging  $\mu$ -bonds. Graphical representations of the  $^{35}\text{Cl}$  EFG tensors for the distinct chlorine environments ( $\text{Cl}_{\text{ax}}$ ,  $\text{Cl}_{\text{aeq}}$  and  $\text{Cl}_{\text{br}}$ ) in the form of polar plots (EFG in the direction of the electric field) are shown in **Figure 6.11**. The blue regions of the graphical representations correspond to positive EFGs and the orange regions represent negative EFGs.

The case of the  $\text{Cl}_{\text{ax}}$  environment is the most straightforward and agrees with previous findings in the literature for terminal chlorines.<sup>46</sup> The largest component of the EFG tensor,  $V_{33}$ , is positive and oriented roughly parallel to the Nb-Cl bond axis (**Figure 6.11(A)**), indicating a loss of electron density in this direction to the covalent Cl-Nb interactions. The  $\sigma(\text{Cl}_{\text{ax}}\text{-Nb})$  (**MO1**) and the  $\sigma$  LP  $\text{Cl}_{\text{ax}}$  (**MO2**) LMOs both make large negative contributions to the value of  $V_{33}$  (**Table 6.3**). The  $\pi$  LPs (**MO3** and **MO4**) make large positive contributions that outweigh those of the  $\sigma$  orbitals and therefore, the overall  $V_{33}$  for the  $\text{Cl}_{\text{ax}}$  is positive. The axial symmetry of the EFG tensor at the  $\text{Cl}_{\text{ax}}$ , with a value of  $\eta_{\text{Q}}$  close to 0, is due to the cylindrical electronic distribution about the nucleus caused

by contributions of **MO3** and **MO4** to  $V_{11}$  and  $V_{22}$  that are roughly equal in magnitude but opposite in sign.

**(A)**



**(B)**

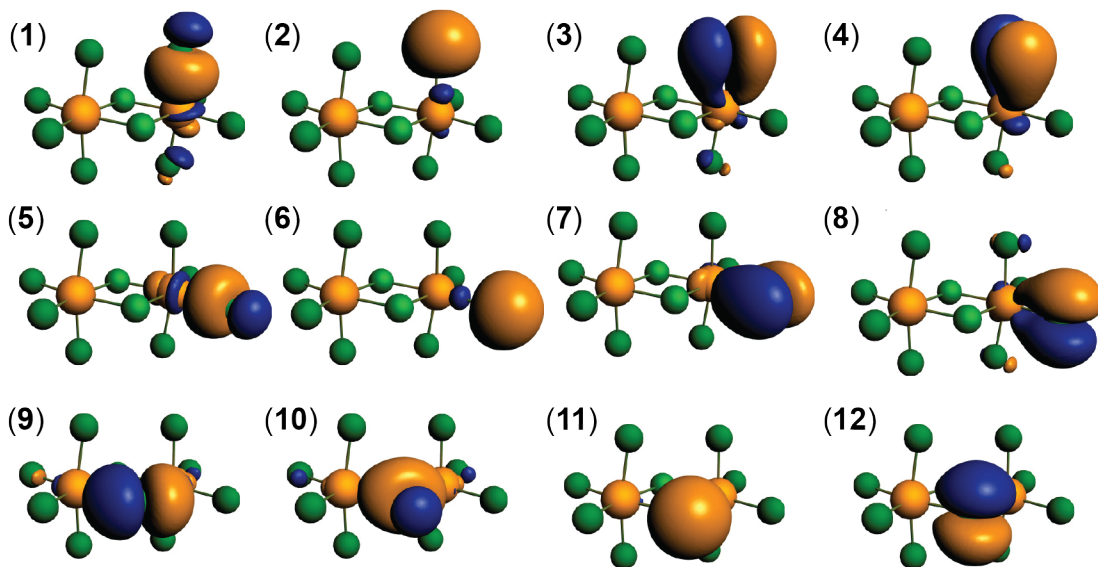


**Figure 6.10:** (A) Atom numbering of the  $\text{Nb}_2\text{Cl}_{10}$  unit used in the LMO analysis. (B) Isosurface representations of the LMOs (1)  $\sigma(\text{Cl}_{\text{ax}}\text{-Nb})$ , (2)  $\sigma$  LP  $\text{Cl}_{\text{ax}}$ , (3)  $\pi_x$  LP  $\text{Cl}_{\text{ax}}$ , (4)  $\pi_y$  LP  $\text{Cl}_{\text{ax}}$ , (5)  $\sigma(\text{Cl}_{\text{eq}}\text{-Nb})$ , (6)  $\sigma$  LP  $\text{Cl}_{\text{eq}}$ , (7)  $\pi(\text{Cl}_{\text{eq}}\text{-Nb})$ , (8)  $\pi_z$  LP  $\text{Cl}_{\text{eq}}$ , (9)  $\pi_x$  LP  $\text{Cl}_{\text{br}}$  (with some  $\mu$ -bonding character), (10)  $\mu(\text{Nb}\text{-Cl}\text{-Nb})$ , (11)  $\sigma$  LP  $\text{Cl}_{\text{br}}$  and (12)  $\pi_z$  LP  $\text{Cl}_{\text{br}}$ .

MO #	Orbital Type <sup>a</sup>	NLMO Composition <sup>b</sup>	Contributions to $V_{11}^c$		Contributions to $V_{22}^c$		Contributions to $V_{33}^c$	
			Cl <sub>ax</sub>	Cl <sub>eq</sub>	Cl <sub>ax</sub>	Cl <sub>br</sub>	Cl <sub>ax</sub>	Cl <sub>br</sub>
1	$\sigma(\text{Cl}_{\text{ax}}-\text{Nb})$	82 Cl (26 s, 74 p) 15 Nb (18 s, 1 p, 81 d)	2.81	0.01	2.85	0.01	-5.66	0.00
2	$\sigma \text{ LP Cl}_{\text{ax}}$	99 Cl (73 s, 27 p)	0.88	0.00	1.14	0.01	-2.02	0.01
3	$\pi_x \text{ LP Cl}_{\text{ax}}$	87 Cl (1 s, 99 p) 11 Nb (1 s, 1 p, 98 d)	-4.99	0.00	1.08	0.01	3.91	0.00
4	$\pi_y \text{ LP Cl}_{\text{ax}}$	87 Cl (100 p) 11 Nb (1 p, 99 d)	1.03	0.01	-5.31	0.00	4.28	0.01
5	$\sigma(\text{Cl}_{\text{eq}}-\text{Nb})$	78 Cl (25 s, 75 p) 22 Nb (20 s, 1 p, 79 d)	-0.01	1.13	0.01	2.80	0.00	-3.93
6	$\sigma \text{ LP Cl}_{\text{eq}}$	99 Cl (74 s, 26 p, 0.02 d)	-0.01	0.96	0.01	1.17	0.01	-2.13
7	$\pi(\text{Cl}_{\text{eq}}-\text{Nb})$	-	-0.01	-6.43	0.01	4.06	0.00	2.38
8	$\pi_z \text{ LP Cl}_{\text{eq}}$	89 Cl (100 p) 8 Nb (20 s, 1 p, 79 d)	-0.16	4.47	0.01	-8.93	0.01	0.09
9	$\pi_x \text{ LP Cl}_{\text{br}}(\mu)$	86 Cl (100 p) 6 Nb (18 s, 3 p, 79 d) 5 Nb (19 s, 3 p, 78 d)	0.01	-0.02	-0.01	0.01	0.00	0.01
10	$\mu(\text{Nb}-\text{Cl}-\text{Nb})$	84 Cl (30 s, 70 p) 6 Nb (15 s, 1 p, 83 d) 6 Nb (16 s, 1 p, 83 d)	0.00	-0.02	-5.39	0.00	0.00	0.01
11	$\sigma \text{ LP Cl}_{\text{br}}$	98 Cl (70 s, 30 p) 1 Nb (9 s, 1 p, 89 d)	0.00	-0.02	-2.66	0.01	1.33	0.01
12	$\pi_z \text{ LP Cl}_{\text{br}}$	94 Cl (100 p)	0.03	-0.01	4.59	0.00	4.60	0.01
-	$\pi(\text{Cl}_{\text{ax}}-\text{Nb})$	-	-0.01	-0.01	0.01	-0.01	0.01	0.02
-	$\pi \text{ LP Cl}_{\text{is}}$	-	0.02	-0.24	-0.11	0.18	0.10	0.15
-	$\sigma \text{ LP Cl}_{\text{is}}$	-	-0.02	-0.03	-0.01	-0.03	0.04	0.05
-	$\sigma(\text{Cl}_{\text{is}}-\text{Nb})$	-	0.00	0.00	0.03	-0.02	-0.01	0.01
-	Core Cl <sub>ax</sub>	100 Cl	-0.03	0.02	0.02	0.04	0.04	0.06
-	Core Cl <sub>eq</sub>	100 Cl	-0.05	-0.01	0.04	0.01	-0.06	0.04
-	Core Cl <sub>br</sub>	100 Cl	0.02	-0.03	0.05	0.01	0.11	0.01
-	Core Cl <sub>is</sub>	100 Cl	-0.11	-0.13	-0.01	-0.13	0.18	0.23
-	Core Nb	100 Nb	0.24	0.26	-0.07	0.28	-0.32	-0.52
Total calculated			-0.35	-0.09	0.40	0.92	0.71	0.81
Experimental			-	-	-	-	0.74	0.75
			-	-	-	-	1.32	1.32

<sup>a</sup>“Core” refers to non-bonding orbitals in the subshells below the valence shell,  $\pi$  LP denotes chlorine lone pairs which may participate in  $\pi$ -bonding,  $\sigma$  LP are lone pairs of  $\sigma$ -symmetry with respect to the Cl-Nb axis, and  $\pi$ ,  $\sigma$  and  $\mu$  represent orbitals with significant covalent nature. <sup>b</sup>The composition of an LMO with each number signifying percentages. The contributions from each atom as well as the atomic orbital character for selected LMOs are shown. <sup>c</sup>The contributions of each orbital towards  $V_{11}$ ,  $V_{22}$  and  $V_{33}$  are given in a.u.

**Table 6.3:** LMO contributions to the  $^{35}\text{Cl}$  EFG tensors of the various chlorine environments in  $\text{NbCl}_5$

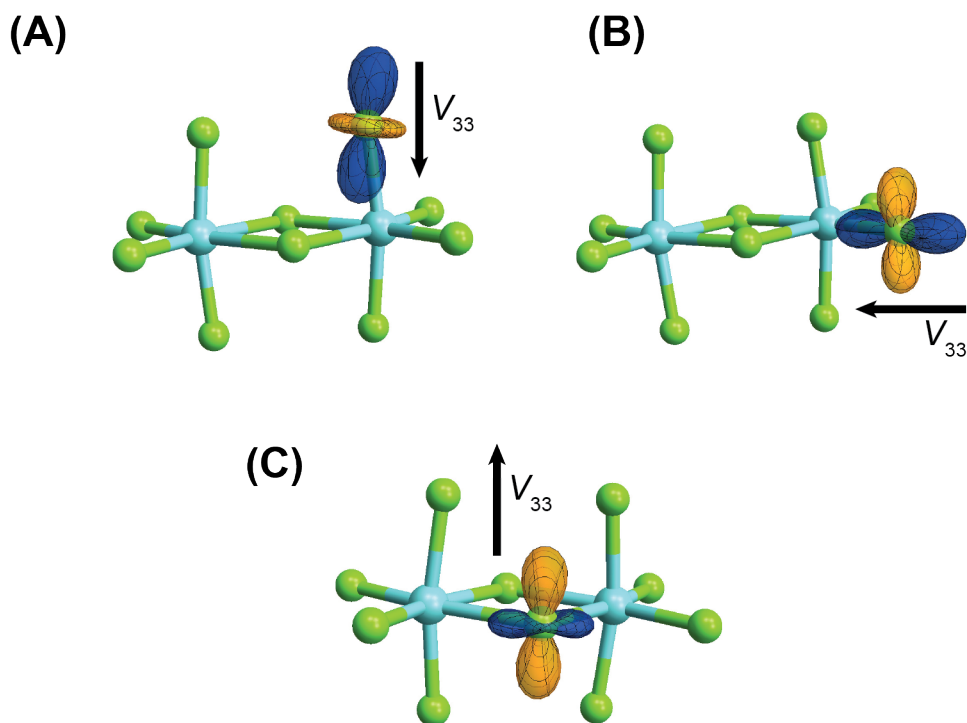


**Figure 6.11:** Graphical representations (polar plots) of  $^{35}\text{Cl}$  EFG tensors of  $\text{NbCl}_5$  for (A)  $\text{Cl}_{\text{ax}}$ , (B)  $\text{Cl}_{\text{eq}}$  and (C)  $\text{Cl}_{\text{br}}$  environments. The blue colour indicates a positive EFG while orange indicates a negative EFG. The values of  $V_{33}$  are +0.71, +0.81 and  $-1.32$  a.u., for (A) - (C) respectively.

Like the  $\text{Cl}_{\text{ax}}$ , the  $\text{Cl}_{\text{eq}}$  sites also have a positive  $V_{33}$ , which is oriented along the direction of the Nb-Cl bond (**Figure 6.11(B)**). The  $\sigma(\text{Cl}_{\text{eq}}\text{-Nb})$  (**MO5**) and  $\sigma$  LP  $\text{Cl}_{\text{eq}}$  (**MO6**) orbitals cause large negative contributions to  $V_{33}$ , in a similar manner to the terminal-axial chlorine atoms. The  $\pi(\text{Cl}_{\text{eq}}\text{-Nb})$  (**MO7**) and the  $\pi_z$  LP  $\text{Cl}_{\text{eq}}$  (**MO8**) orbitals make positive contributions to  $V_{33}$  that outweigh those of the  $\sigma$  orbitals, and results in an overall positive EFG. The  $\pi$  orbitals of the  $\text{Cl}_{\text{eq}}$  contribute quite differently to the values of  $V_{11}$  and  $V_{22}$ . **MO7** generates a negative contribution to  $V_{11}$  and a positive contribution to  $V_{22}$ , whereas **MO8** makes a positive contribution to  $V_{11}$  and an even larger negative

contribution to  $V_{22}$ . The unequal contribution to  $V_{11}$  and  $V_{22}$  of **MO7** and **MO8** is reflected in the large asymmetry parameter of the  $^{35}\text{Cl}$  EFG tensor ( $\eta_Q$  is near unity). This is contrasted to the case of the  $\text{Cl}_{\text{ax}}$ , in which equal involvement from the orbitals with  $\pi$  symmetry leads to an axially symmetric tensor with  $\eta_Q$  close to zero.

For the  $\text{Cl}_{\text{br}}$ ,  $V_{33}$  is oriented perpendicular to the equatorial plane formed by the two Nb atoms and the  $\text{Cl}_{\text{br}}$  atom (**Figure 6.11(C)**), as is typical for bridging chlorines.<sup>47</sup> The  $\text{Cl}_{\text{br}}$  environment consists of two equivalent, weakly covalent Nb- $\text{Cl}_{\text{br}}$  orbitals per Cl atom at an angle of  $102^\circ$  and two relatively “pure” LP orbitals. The orbitals in the plane of the Nb-Cl-Nb bond ( $\pi_x$  LP  $\text{Cl}_{\text{br}}$  (**MO9**),  $\mu(\text{Nb-Cl-Nb})$  (**MO10**) and  $\sigma$  LP  $\text{Cl}_{\text{br}}$  (**MO11**)) create positive contributions to  $V_{33}$ ; however, these contributions are outweighed by the enormous negative contribution made by the out-of-plane  $\pi_z$  LP  $\text{Cl}_{\text{br}}$  (**MO12**). **MO12** is almost entirely non-covalent in nature and therefore, contributes very strongly to the EFG. The result is a large, negative  $V_{33}$  at the  $\text{Cl}_{\text{br}}$  nuclei which is oriented in the direction of the lone-pair (**MO12**). The moderate value of  $\eta_Q$  for the  $\text{Cl}_{\text{br}}$  nuclei is caused by unequal contributions of the in-plane orbitals (**MO9**, **MO10**, and **MO11**) to  $V_{11}$  and  $V_{22}$ .

#### 6.4.6 $^{35}\text{Cl}$ SSNMR of $\text{WCl}_6$ supported on silica

$\text{WCl}_6$  has been grafted onto a silica support material, as described in the Experimental Section. Our aim in the current work was to see if it was possible to acquire a high quality spectrum of this sample in a reasonable time frame, and make comparisons between this new spectrum and some of the spectra of the tungsten chlorides discussed herein. Only two other attempts at acquiring  $^{35}\text{Cl}$  SSNMR spectra of such systems have been reported, by our group (silica-supported  $\text{TiCl}_4$ ),<sup>47</sup> and by Mania *et al.*



(silica-supported  $\text{TiCl}_4$ ).<sup>26</sup> The  $^{35}\text{Cl}$  SSNMR spectrum of this sample, acquired using the WURST-CPMG pulse sequence at a field of 18.8 T is shown in **Figure 6.12**. The spectrum was acquired in a single experiment (*i.e.*, no piecewise acquisitions), over a period of ca. 15.8 hours. It is noted that the long experimental times are a result of the low weight percentage of  $\text{WCl}_6$  loaded onto the silica support material (W wt% = 5.48%). The CT powder pattern spans a range of just over 1.2 MHz, which is far wider than that observed for the spectrum of pure  $\alpha\text{-WCl}_6$ , which spans only ca. 650 kHz at 21.1 T (it would span ca. 740 kHz at 18.8 T, **Figure E20**). Simulations of the spectrum of grafted  $\text{WCl}_6$  yield  $C_Q = 25.98(5)$  MHz and  $\eta_Q = 0.11(1)$ , which are far different values from those of pure  $\text{WCl}_6$  ( $C_Q = 21.0(1)$  MHz and  $\eta_Q = 0.029(5)$ ). In fact, this new set of quadrupolar parameters bears a striking resemblance to those of  $\text{WOCl}_4$  ( $C_Q = 26.05(10)$ ,  $\eta_Q = 0.115(5)$ ), which suggests that a major change in the structure and bonding of  $\text{WCl}_6$  has taken place. A full structural analysis and interpretation of this result is currently underway, and beyond the scope of the current work; however, we have again demonstrated that it is possible to acquire high quality ultra-wideline  $^{35}\text{Cl}$  SSNMR spectra of diluted, surface-bound species, and that such spectra are potentially very rich in structural information.

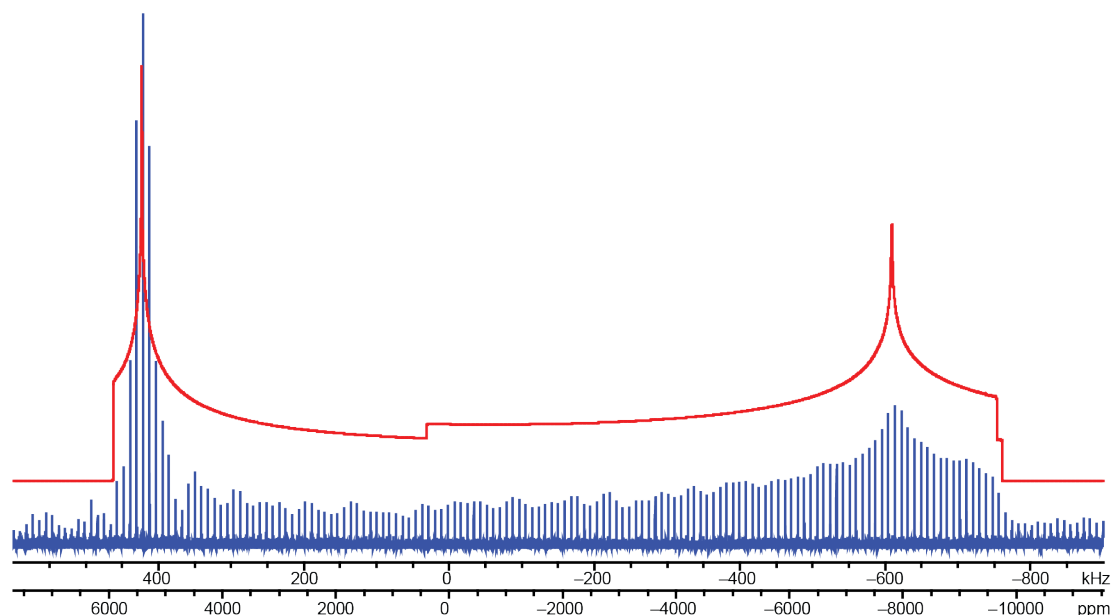


**Figure 6.12:** Static  $^{35}\text{Cl}$  SSNMR spectrum acquired using the WURST-CPMG pulse sequence at 18.8 T for  $\text{WCl}_6\text{-SiO}_2$  with corresponding analytical simulation shown in red.

## 6.5 Conclusions

Using the WURST-CPMG pulse sequence and the VOCS technique we have demonstrated it is possible to acquire broad  $^{35}\text{Cl}$  SSNMR powder patterns for diamagnetic chlorine-containing TM complexes exhibiting a variety of structural motifs. The experiments were conducted at both moderate (9.4 T) and ultra-high (21.1 T) magnetic field strengths, with the latter affording great reductions in experimental times due to increases in S/N ratios and reductions in CT pattern breadths. The  $^{35}\text{Cl}$  SSNMR spectra prove to be very useful as probes of structure, due to the sensitivity of the  $^{35}\text{Cl}$  EFG tensors to both subtle and significant differences in molecular geometry and chemical environment.

The  $^{35}\text{Cl}$  SSNMR spectra of  $\alpha\text{-WCl}_6$  and  $\beta\text{-WCl}_6$  were acquired, but were not of high enough resolution to differentiate the two polymorphic forms; however, the two polymorphs could be differentiated by  $^{35}\text{Cl}$  NQR experiments. This highlights the

efficacy of using SSNMR and NQR in tandem; the rapid acquisition of the SSNMR spectra provides an estimation of the quadrupolar parameters and substantially refines the frequency region in which to search for NQR signal. The effects of molecular packing in the solid state were also visible in the  $^{35}\text{Cl}$  SSNMR spectra of **WOCl<sub>4</sub>** and **MoOCl<sub>4</sub>**. The **WOCl<sub>4</sub>** molecules stack in symmetric linear arrays resulting in a single chlorine environment whereas the **MoOCl<sub>4</sub>** complex forms *quasi*-dimeric structures resulting in several distinct chlorine environments (*i.e.*, pseudo-bridging and terminal). In the dimeric pentahalide complexes, **NbCl<sub>5</sub>** and **TaCl<sub>5</sub>**, the individual chlorine environments were distinguished based on their values of  $C_Q$ . It was found that the  $\text{Cl}_{\text{br}}$  environments had larger values of  $C_Q$  when compared to the terminal chlorine environments. Furthermore, the two terminal chlorine environments,  $\text{Cl}_{\text{ax}}$  and  $\text{Cl}_{\text{eq}}$ , could be distinguished based on their values of  $\eta_Q$ , the former having values close to 0 and the latter having values close to unity. It was also observed that the tantalum complex had larger absolute magnitudes of  $C_Q$  for all chlorine environments, suggesting that the size of the metal centre influences the value of  $C_Q$ .

Plane-wave DFT calculations were completed for model structures of each complex. The  $^{35}\text{Cl}$  EFG tensor parameters were found to be in generally good agreement with experimental results, especially in systems in which intermolecular interactions have little influence on the  $^{35}\text{Cl}$  EFG. The theoretical  $^{35}\text{Cl}$  EFG tensor orientations reveal that  $V_{33}$  is directed either along or near the M-Cl bond for chlorine atoms in terminal bonding environments. Conversely, for chlorine atoms in bridging bonding environments,  $V_{33}$ 's are oriented approximately perpendicular to the M-Cl-M planes. An LMO analysis completed on the **NbCl<sub>5</sub>** system revealed that the  $^{35}\text{Cl}$  NMR parameters are determined

by the composition and relative orientations of the MOs participating in bonding to chlorine. The  $\eta_Q$  value close to zero for the  $\text{Cl}_{\text{ax}}$  arises from equivalent contributions of the  $\pi$  LP orbitals to  $V_{11}$  and  $V_{22}$  whereas the  $\pi$  orbitals for the  $\text{Cl}_{\text{eq}}$  do not contribute equivalently, leading to an  $\eta_Q$  close to unity. The large value of  $C_Q$  for the  $\text{Cl}_{\text{br}}$  arises from the large, negative contribution of the  $\pi_z$  LP orbital that is perpendicular to the Cl-M-Cl plane, because positive contributions from other orbitals centred on  $\text{Cl}_{\text{br}}$  are reduced due to the true Cl-Nb covalency.

We also demonstrated the application of  $^{35}\text{Cl}$  SSNMR to the study of a transition-metal catalyst that has been grafted onto a silica support material. The resulting spectrum is drastically different than the bulk species, indicating that the structure of the  $\text{WCl}_6$  species changes upon grafting. Given the rapidity with which the  $^{35}\text{Cl}$  SSNMR spectra can be acquired, and the fact that “focused” NQR experiments can be conducted in the wake of SSNMR experiments to examine site specificities, we believe that an enormous number of chlorinated transition-metal complexes can be structurally probed in both the bulk and supported forms. We hope to establish this protocol as a strong basis for the study of chlorine-containing transition-metal complexes, and extend this study to catalytic systems of increasing complexity, with the aim of studying immobilized heterogeneous catalysts with very dilute chlorine contents.

## 6.6 References

- (1) Ajiboye, S. I.; Iqbal, J.; Peacock, R. D.; Prouff, N.; Taylor, G. J.; Winfield, J. M.; Liu, X. *Fluor. Chem.* **1998**, *91*, 213–218.
- (2) Englert, U.; Pampaloni, G.; Puccini, F.; Volpe, M. *J. Organomet. Chem.* **2007**, *692*, 3144–3150.
- (3) Sim, A.; Cant, N. W.; Trimm, D. L. *Int. J. Hydrog. Energy* **2010**, *35*, 8953–8961.
- (4) Nguyen, A. I.; Blackmore, K. J.; Carter, S. M.; Zarkesh, R. A.; Heyduk, A. F. *J. Am. Chem. Soc.* **2009**, *131*, 3307–3316.
- (5) Mokdsi, G.; Harding, M. M. *J. Inorg. Biochem.* **2001**, *86*, 611–616.
- (6) Waern, J. B.; Harris, H. H.; Lai, B.; Cai, Z.; Harding, M. M.; Dillon, C. T. *J. Biol. Inorg. Chem.* **2005**, *10*, 443–452.
- (7) Köpf-Maier, P.; Klapötke, T. *J. Cancer Res. Clin. Oncol.* **1992**, *118*, 216–221.
- (8) Matthias, B. T.; Geballe, T. H.; Geller, S.; Corenzwit, E. *Phys. Rev.* **1954**, *95*, 1435.
- (9) Raub, C. J.; Sweedler, R.; Jensen, M. A.; Broadston, S.; Matthiasg, T. *Phys. Rev. Lett.* **1964**, *13*, 746–747.
- (10) Bukowski, Z.; Badurski, D.; Stepień-Damm, J.; Troc, R. *Solid State Commun.* **2002**, *123*, 283–286.
- (11) Nowak, I.; Ziolk, M. *Chem. Rev.* **1999**, *99*, 3603–3624.
- (12) Tanabe, K.; Okazaki, S. *Appl. Catal. A* **1995**, *133*, 191–218.
- (13) Wallace, K. C.; Liu, A. H.; Davis, W. M.; Schrock, R. R. *Organomet.* **1989**, *8*, 644–654.
- (14) Ushikubo, T.; Wada, K. *J. Catal.* **1994**, *148*, 138–148.
- (15) Schrock, R. R.; Hoveyda, A. H. *Angew. Chem. Int. Ed.* **2003**, *42*, 4592–4633.
- (16) Yandulov, D. V.; Schrock, R. R. *Science* **2003**, *301*, 76–78.
- (17) Balcar, H.; Čejka, J.; Sedláček, J.; Svoboda, J.; Zedník, J.; Bastl, Z.; Bosáček, V.; Vohlídal, J. *J. Mol. Catal. A* **2003**, *203*, 287–298.

- (18) Garrett, C. E.; Prasad, K. *Adv. Synth. Catal.* **2004**, *346*, 889–900.
- (19) Collman, J. P.; Hegedu, L. S.; Cooke, M. P.; Norton, J. R.; Dolcetti, G.; Marquardt, D. N. *J. Am. Chem. Soc.* **1972**, *94*, 1789–1790.
- (20) Dumont, W.; Poulin, J.; Dang, T.; Kagan, H. B. *J. Am. Chem. Soc.* **1973**, *95*, 8295–8299.
- (21) Maschmeyer, T.; Rey, F.; Sankar, G.; Thomas, J. M. *Nature* **1995**, *378*, 159–162.
- (22) Eisen, M. S.; Marks, T. J. *J. Am. Chem. Soc.* **1992**, *114*, 10358–10368.
- (23) Joubert, J.; Delbecq, F.; Sautet, P.; Le Roux, E.; Taoufik, M.; Thieuleux, C.; Blanc, F.; Copéret, C.; Thivolle-Cazat, J.; Basset, J.-M. *J. Am. Chem. Soc.* **2006**, *128*, 9157–9169.
- (24) Blanc, F.; Thivolle-Cazat, J.; Basset, J.-M.; Copéret, C.; Hock, A. S.; Tonzetich, Z. J.; Sinha, A.; Schrock, R. R. *J. Am. Chem. Soc.* **2007**, *129*, 1044–1045.
- (25) Blanc, F.; Basset, J.-M.; Copéret, C.; Sinha, A.; Tonzetich, Z. J.; Schrock, R. R.; Solans-Monfort, X.; Clot, E.; Eisenstein, O.; Lesage, A.; Emsley, L. *J. Am. Chem. Soc.* **2008**, *130*, 5886–5900.
- (26) Mania, P.; Verel, R.; Jenny, F.; Hammond, C.; Hermans, I. *Chem. Eur. J.* **2013**, *19*, 9849–9858.
- (27) Blanc, F.; Copéret, C.; Lesage, A.; Emsley, L. *Chem. Soc. Rev.* **2008**, *37*, 518–526.
- (28) Zhang, W.; Xu, S.; Han, X.; Bao, X. *Chem. Soc. Rev.* **2012**, *41*, 192–210.
- (29) Jezequel, M.; Dufaud, V.; Ruiz-Garcia, M. J.; Carrillo-Hermosilla, F.; Neugebauer, U.; Niccolai, G. P.; Lefebvre, F.; Bayard, F.; Corker, J.; Fiddy, S.; Evans, J.; Broyer, J. P.; Malinge, J.; Basset, J. M. *J. Am. Chem. Soc.* **2001**, *123*, 3520–3540.
- (30) Ahn, H.; Marks, T. J. *J. Am. Chem. Soc.* **2002**, *124*, 7103–7110.
- (31) Le Roux, E.; Chabanas, M.; Baudouin, A.; de Mallmann, A.; Coperet, C.; Quadrelli, E. A.; Thivolle-Cazat, J.; Basset, J.; Lukens, W.; Lesage, A.; Emsley, L. *J. Am. Chem. Soc.* **2004**, *126*, 13391–13399.
- (32) Hung, I.; Schurko, R. W. *J. Phys. Chem. B* **2004**, *108*, 9060–9069.
- (33) Lo, A. Y. H.; Bitterwolf, T. E.; Macdonald, C. L. B.; Schurko, R. W. *J. Phys. Chem. A* **2005**, *109*, 7073–7087.

- (34) Hamaed, H.; Lo, A. Y. H.; Lee, D. S.; Evans, W. J.; Schurko, R. W. *J. Am. Chem. Soc.* **2006**, *128*, 12638–12639.
- (35) Rossini, A. J.; Hung, I.; Schurko, R. W. *J. Phys. Chem. Lett.* **2010**, *1*, 2989–2998.
- (36) Rossini, A. J.; Hung, I.; Johnson, S. A.; Slebodnick, C.; Mensch, M.; Deck, P. A.; Schurko, R. W. *J. Am. Chem. Soc.* **2010**, *132*, 18301–18317.
- (37) Larsen, F. H.; Jakobsen, H. J.; Ellis, P. D.; Nielsen, N. C. *J. Magn. Reson.* **1998**, *131*, 144–147.
- (38) O’Dell, L. A.; Schurko, R. W. *Chem. Phys. Lett.* **2008**, *464*, 117–130.
- (39) Harris, K. J.; Lupulescu, A.; Lucier, B. E. G.; Frydman, L.; Schurko, R. W. *J. Magn. Reson.* **2012**, *224*, 38–47.
- (40) Harris, R. K.; Becker, E. D.; Menezes, S. M. C. D. E. *Pure Appl. Chem.* **2001**, *73*, 1795–1818.
- (41) Kentgens, A. P. M. *Geoderma* **1997**, *80*, 271–306.
- (42) Chapman, R. P.; Hiscock, J. R.; Gale, P. A.; Bryce, D. L. *Can. J. Chem.* **2011**, *89*, 822–834.
- (43) Bryce, D. L.; Gee, M.; Wasylishen, R. E. *J. Phys. Chem. A* **2001**, *105*, 10413–10421.
- (44) Hamaed, H.; Pawlowski, J. M.; Cooper, B. F. T.; Fu, R.; Eichhorn, S. H.; Schurko, R. W. *J. Am. Chem. Soc.* **2008**, *130*, 11056–11065.
- (45) Chapman, R. P.; Bryce, D. L. *Phys. Chem. Chem. Phys.* **2009**, *11*, 6987–6998.
- (46) Rossini, A. J.; Mills, R. W.; Briscoe, G. A.; Norton, E. L.; Geier, S. J.; Hung, I.; Zheng, S.; Autschbach, J.; Schurko, R. W. *J. Am. Chem. Soc.* **2009**, *131*, 3317–3330.
- (47) Johnston, K. E.; O’Keefe, C. A.; Gauvin, R. M.; Trébosc, J.; Delevoye, L.; Amoureux, J.-P.; Popoff, N.; Taoufik, M.; Oudatchin, K.; Schurko, R. W. *Chem. Eur. J.* **2013**, *19*, 12396–12414.
- (48) Perras, F. A.; Bryce, D. L. *Angew. Chem. Int. Ed. Engl.* **2012**, *51*, 4227–4230.
- (49) Schurko, R. W. In *Encyclopedia of Magnetic Resonance*; John Wiley and Sons, 2012; pp. 77–94.
- (50) Schurko, R. W. *Acc. Chem. Res.* **2013**, *46*, 1985–1995.

- (51) O'Dell, L. A.; Rossini, A. J.; Schurko, R. W. *Chem. Phys. Lett.* **2009**, *468*, 330–335.
- (52) Taylor, J. C.; Wilson, P. W. *Acta Crystallogr. Sect. B Struct. Sci.* **1974**, *30*, 1216–1220.
- (53) Popoff, N.; Espinas, J.; Gouré, E.; Boyron, O.; Le Roux, E.; Basset, J.-M.; Gauvin, R. M.; De Mallmann, A.; Taoufik, M. *Macromol. Rapid Commun.* **2011**, *32*, 1921–1924.
- (54) Kraus, W.; Nolze, G. PowderCell for Windows, 2000.
- (55) Massiot, D.; Farnan, I.; Gautier, N.; Trumeau, D.; Trokiner, A.; Coutures, J. P. *Solid State Nucl. Magn. Reson.* **1995**, *4*, 241–248.
- (56) Medek, A.; Frydman, V.; Frydman, L. *J. Phys. Chem. A* **1999**, *103*, 4830–4835.
- (57) Tang, J. A.; Masuda, J. D.; Boyle, T. J.; Schurko, R. W. *ChemPhysChem* **2006**, *7*, 117–130.
- (58) Eichele, K.; Wasylishen, R. E. WSolids: Solid-State NMR Spectrum Simulation Package, 2001.
- (59) Perras, F. A.; Widdifield, C. M.; Bryce, D. L. *Solid State Nucl. Magn. Reson.* **2012**, *45-46*, 36–44.
- (60) Clark, S. J.; Segall, M. D.; Pickard, C. J.; Hasnip, P. J.; Probert, M. I. J.; Refson, K.; Payne, M. C. *Z. Krist.* **2005**, *220*.
- (61) Baerends, E. J. Z. T.; Autschbach, J. Amsterdam Density Functional.
- (62) Van Lenthe, E.; Snijders, J. G.; Baerends, E. J. *J. Chem. Phys.* **1996**, *105*, 6505–6516.
- (63) Hammer, B.; Hansen, L.; Nørskov, J. *Phys. Rev. B* **1999**, *59*, 7413–7421.
- (64) Perdew, J.; Burke, K.; Ernzerhof, M. *Phys. Rev. Lett.* **1996**, *77*, 3865–3868.
- (65) Autschbach, J.; Zheng, S.; Schurko, R. W. *Concepts Magn. Reson.* **2010**, *36A*, 84–126.
- (66) Reed, A. E.; Weinhold, F. *J. Chem. Phys.* **1985**, *83*, 1736.
- (67) Glendening, E. D.; Badenhop, J. K.; Reed, A. E.; Carpenter, J. E.; Bohmann, J. A.; Morales, C. M.; Weinhold, F. NBO 5.0, 2001.



- (68) Harris, R. K. *Analyst* **2006**, *131*, 351–373.
- (69) Lucken, E. A. C. In *Nuclear Quadrupole Coupling Constants*; Academic Press: New York, 1969; pp. 34–45.
- (70) Das, T. P.; Hahn, E. L. In *Nuclear Quadrupole Resonance Spectroscopy*; Academic Press: New York, 1958; pp. 3–7.
- (71) Smith, D. K.; Landingham, R. L.; Smith, G. S.; Johnson, Q. *Acta Crystallogr. Sect. B Struct. Sci.* **1968**, *24*, 1563.
- (72) Pisarev, E. A.; Semin, G. K.; Drobot, D. V.; Kuznetsov, S. I.; Bryukhova, E. V. *Zh. Neorg. Khim.* **1974**, *23*, 1171–1182.
- (73) Suits, B. H. *Nuclear Quadrupolar Spectroscopy in Handbook of Applied Solid-State Spectroscopy*; Vij, D. R., Ed.; Springer: New York, 2006.
- (74) Widdifield, C. M.; Chapman, R. P.; Bryce, D. L. *Annu. Reports NMR Spectrosc.* **2009**, *66*, 195.
- (75) Rossini, A. J.; Hamaed, H.; Schurko, R. W. *J. Magn. Reson.* **2010**, *206*, 32–40.
- (76) Hess, H.; Hartung, H. *Z. Anorg. Chem.* **1966**, *344*.
- (77) Taylor, J. C.; Waugh, A. B. *Dalt. Trans.* **1980**, *10*, 2006–2009.
- (78) Lucken, E. A. C. In *Nuclear Quadrupole Coupling Constants*; Academic Press: New York, 1969; pp. 120–130.
- (79) Zalkin, A.; Sands, D. E. *Acta Crystallogr.* **1958**, *11*, 615–619.
- (80) Rabe, S.; Mueller, U. *Z. Krist. - New Cryst. Struc.* **2000**, *215*, 1–2.
- (81) Semin, G. K.; Kuznetsov, S. I.; Alimov, I. M.; Khotsianova, T. L.; Bryukhova, E. V.; Nisselson, L. A.; Tretyakova, K. V. *Inorg. Chim. Acta* **1974**, *13*, 181.
- (82) Lucier, B. E. G.; Tang, J. A.; Schurko, R. W.; Bowmaker, G. A.; Healy, P. C.; Hanna, J. V. *J. Phys. Chem. C* **2010**, *114*, 7949–7962.
- (83) Dye, J. L.; Ellaboudy, A. S.; Kim, J. *Solid State NMR of Quadrupolar Nuclei*; Marcel Dekker, Inc.: New York, 1991.

## Chapter 7: Conclusions and Future Outlook

### 7.1 General Overview

In this thesis, the structure, formations, and dynamics of porous materials were investigated. The numerous applications of porous materials, both potential and already realized, has resulted an intense area of research which aims to develop cleaner, more efficient means for their production. In addition, an intimate understanding of the structure-property relationships of porous materials is crucial for their rational design and fine-tuning of their properties.

As demonstrated herein, SSNMR is well-suited to the study of porous materials and provides detailed, molecular-level structural information and a means for unambiguously determining motional models for systems with dynamic components. The application of multinuclear SSNMR in tandem with both experimental techniques (*e.g.*, SCXRD and PXRD) and theoretical approaches (*i.e.*, DFT calculations) allows for the accurate description of many systems; however, in some instances, the information provided by SSNMR can stand alone for their full characterization. Furthermore, the details on structure and dynamics afforded by SSNMR are not available from any other characterization technique. Wherever possible, a multinuclear SSNMR approach was utilized, taking advantage of the fact that nearly every element on the periodic table has at least one NMR-active nuclide. This multinuclear SSNMR methodology, coupled with the development of NMR techniques for the study of unreceptive nuclides, is essential for ensuring the routine application of SSNMR to a wide variety of systems beyond those investigated herein.

## 7.2 Solid-state Synthesis of Cadmium-imidazolate Frameworks

In **Chapters 2** and **3**, two solid-state synthetic techniques (*i.e.*, accelerated aging reactions and mechanochemical synthesis) were utilized for the generation of cadmium-containing zeolitic imidazolate frameworks. Both of these synthetic approaches adhere to the Twelve Principles of Green Chemistry,<sup>1</sup> as they require little or no solvent, make use of readily available reagents, involve low energy inputs, and afford quantitative yields. Despite the great promise of these techniques for the synthesis of a wide range of materials, little is known about the underlying mechanisms that drive the chemical transformations. A detailed mechanistic understanding is essential so that these reactions can be optimized and to ensure clean and reproducible generation of the desired products.

In **Chapter 2**, accelerated aging reactions were used for the synthesis of a new cadmium-imidazole framework (CdIF) with an unknown structure. By varying the stoichiometry of the reagents, it was determined that the Cd:imidazole ratio in this CdIF is 1:3, instead of the typical 1:2 ratio found in most ZIFs. A combination of multinuclear SSNMR and PXRD were used to refine and elucidate its structure. It was determined that the structure of the CdIF consists of Cd atoms in four-coordinate, tetrahedral environments in a framework structure with a diamondoid topology. The multinuclear SSNMR experiments indicate that there is excess, unreacted 2-methylimidazole guest molecules within the pores of the framework structure. This demonstrates that the combination of SSNMR and PXRD, a technique known as *NMR-assisted crystallography*, is useful for elucidating the structures of new materials.

In Chapter 3, the mechanochemical formation of CdIFs was monitored using SSNMR and PXRD. SSNMR experiments reveal the presence of an intermediate that

undergoes chemical transformation *in situ* within the NMR rotor. PXRD identifies this intermediate as the previously reported CdIF-1 framework, and the SSNMR experiments suggest the presence of solvent and HMeIm molecules in the pores. It was observed that chemical transformations occur within the closed environments of the rotors and milling jars, but not in the XRD capillaries that are left open to the atmosphere. It is suggested that ball milling provides the activation energy required to initiate the reactions, but that aging processes drive the reactions to completion. Finally, a reaction pathway was proposed in which the reaction proceeds towards products of decreasing void volume and increasing thermodynamic stability, consistent with Ostwald's Rule of Stages.<sup>2,3</sup>

### 7.3 Future Work – Monitoring the Formation of Porous Materials

A full mechanistic understanding of the formation of porous materials using solid-state synthetic techniques has not been achieved to date. There is evidence to suggest that the sequential formation of products with lower densities and high thermodynamic stabilities follows Ostwald's rule of stages;<sup>2,3</sup> however, at this point, the exact nature of these transformations is unclear. The use of *in situ* multinuclear SSNMR experiments provide a more detailed understanding in this regard. Both accelerated aging reactions and mechanochemical syntheses use a catalytic protic salt, which is known to not only accelerate the reactions, but to play a role in determining the structures and compositions of final products; however, the exact role of the salt is not understood. The results of the <sup>15</sup>N MAS NMR in Chapter 3 suggests that there are NO<sub>3</sub><sup>-</sup> ions within the pores of the framework that possibly act as templating agents (a similar effect was observed by Friščić *et al.*).<sup>4</sup> Therefore, multinuclear SSNMR experiments on the products of reactions

conducted with different salts, especially those containing NMR-active nuclides (e.g.,  $\text{ND}_4\text{NO}_3$ ) could aid in the determination of reaction mechanisms. Monitoring the reaction processes at intermediate stages may also be of great value in this respect.

Mixed-linker MOFs and ZIFs have shown promise as porous materials whose properties can be tuned by varying the relative amounts of the constituent linker molecules.<sup>5-7</sup> There is currently no general theory that describes how the distribution of the linkers within the framework structure affect the bulk properties of the material. SSNMR has been shown to provide information on linker distributions in MOFs that have been synthesized using conventional solvothermal techniques.<sup>8,9</sup> The mechanisms of MOF and ZIF formation in solid-state synthetic techniques are certainly different than those of analogous solvothermal reactions; therefore, it is possible that mixed-linker MOFs and ZIFs made using these techniques may have different linker distributions or entirely different structures. In a preliminary study, our group synthesized a series of mixed-linker ZIFs using mechanochemical methods, and used SSNMR to characterize the resulting products. The  $^{111}\text{Cd}$  CP/MAS NMR spectrum of the mixed-linker species are drastically different than those of the single-linker species made using the same imidazole linkers, implying a rich and distinct set of chemistries that should be further investigated.

The majority of ZIFs feature Zn as the metal linker; hence, it would be of great interest to probe the formations and structures of Zn-containing ZIFs with  $^{67}\text{Zn}$  SSNMR (this is an especially attractive project due to the successes with  $^{111}\text{Cd}$  SSNMR described in this thesis).  $^{67}\text{Zn}$  is an unreceptive, quadrupolar nucleus with a nuclear quadrupole moment of moderate size ( $I = 5/2$ ;  $\nu_0(^{67}\text{Zn}) = 25.027$  MHz at 9.4 T; n.a. = 4.1%,  $Q = 15.0$

fm<sup>2</sup>). While there have been some preliminary explorations of <sup>67</sup>Zn SSNMR of MOFs by Huang and co-workers,<sup>10-12</sup> for the purpose of examining framework structures, there have been no generalized applications to the study of the formation of ZIFs, the monitoring of impurities and by-products, or the effects of molecular-level motions on host-guest chemistry. The application of <sup>67</sup>Zn SSNMR for these purposes is challenging due to the poor receptivity of <sup>67</sup>Zn; however, we plan to apply an arsenal of methods and hardware to make this possible. A combination of carefully calibrated WURST-CPMG pulse sequences, <sup>1</sup>H-<sup>67</sup>Zn BRAIN-CP NMR experiments under both static and MAS conditions, and the use of these UWNMR methods under DNP conditions (9.4 T at the Ames Lab) and at ultra-high magnetic fields (*i.e.*, the 36 T, 1.59 GHz series connected hybrid (SCH) NMR magnet at the National High Magnetic Field Laboratory (NHMFL) in Tallahassee, FL, will allow us to probe the molecular-level structures and dynamics of reaction mixtures, intermediate mixtures, and final products, both *ex situ* and *in situ*, under a variety of conditions.

The ability to determine three-dimensional structures of both crystalline and amorphous solids is a primary concern for chemists and materials scientists. The emerging field of NMR crystallography shows great promise for the characterization of such systems, by using the well-established “triumvirate of methods that include solid-state NMR spectroscopy, X-ray crystallography, and first-principles DFT calculations on periodic solids.”<sup>13-15</sup> The relationships between NMR observables and structure are at the heart of this method: if NMR interaction tensors can be calculated to reliably match those obtained experimentally, then it is possible to use these structure-property relationships for the refinement of known structures and the prediction of unknown structures. Our

group is currently pursuing this from the perspective of EFG tensors (e.g.,  $^{35}\text{Cl}$ ,  $^{14}\text{N}$ ,  $^{17}\text{O}$ ) associated with molecules in organic solids. We believe that a combination of CS and EFG tensor data from nuclides such as  $^{111}\text{Cd}$ ,  $^{67}\text{Zn}$ ,  $^{13}\text{C}$ ,  $^{14}\text{N}$ ,  $^{17}\text{O}$ , and  $^1\text{H}$  may prove invaluable in aiding in the prediction and refinement of structures of new ZIFs. Our first steps will be to optimize such calculations for Zn- and Cd-containing ZIFs with known crystal structures, and then to extend the optimized calculations to intermediate and final product states to probe structures and reaction pathways. Calculations on solids containing heavy atoms such as cadmium will likely require relativistic treatment of the electronic structure to obtain agreement with experimental results. Such calculations may also be able to predict hitherto unknown ZIFs, which may guide future rational preparations of these materials.

#### 7.4 Dynamics of Molecular Machines

The design and synthesis of molecular machines represents a “hot topic” in modern chemistry, especially in light of the awarding of the Nobel Prize in Chemistry to Stoddard, Sauvage, and Feringa for their contributions to this field. The current state of the materials being developed today still pale in comparison to those envisioned by Richard Feynman; however, complex systems, with increasingly intricate constructions and motions are constantly being synthesized.<sup>16–18</sup> SSNMR experiments are ideal to study the motions of simple molecular machines in the solid state (**Chapters 4 and 5**), and are able to provide correlations between the modes and rates of motions, and numerous chemical and physical factors, including electrostatic interactions, void spaces, steric hindrance, effects guest molecules, and temperature.

In **Chapter 4** the motions of crown ether (CE) rings incorporated into the framework structures of MOFs were investigated using  $^2\text{H}$  and  $^{13}\text{C}$  SSNMR. The CE rings mainly exhibit three types of rotational motions (*i.e.*, two-site jumps, partial rotation, and full rotation). CE rings of smaller sizes undergo more restricted rotational motions and the inclusion of bulky substituents on the rings also leads to hindered rotational motions. It was found that interactions between the framework structures and the CE rings also impedes motion and that reversible solvation/desolvation processes can be used to affect ring rotation. Lastly,  $^{13}\text{C}$  SSNMR experiments reveal that spatially-coherent shuttling motion of the CE rings is possible within the free volume of MOFs.

Multinuclear SSNMR experiments were also used to investigate the rotational motion in inorganic metal hydride rotors (**Chapter 5**). A detailed analysis was given for *trans*- $\text{D}_2(^t\text{Bu}_3\text{P})_2$ , and rotational motion was observed in the  $^2\text{H}$  SSNMR spectra acquired at temperatures as low as 75 K. Several motional models were proposed, but it was determined that the changes observed in the  $^2\text{H}$  SSNMR spectra are not due to the rates of the motions, but rather to differences in the populations of the various rotational states. A series of compounds with various coordinating donor ligands was then investigated using  $^2\text{H}$  SSNMR. The nature of the coordinating ligand has a drastic effect on the motion, and for some cases, no motion was observed over large temperature ranges.

## 7.5 Future Work – Molecular Machines

MOFs that use zirconium clusters as SBUs are stable under conditions of high temperatures and can withstand treatment with strong acids and bases.<sup>19–21</sup> Furthermore, they have very large void spaces, making them attractive for a wide range of applications.



Therefore, incorporating [2]rotaxanes into such framework structures offers the possibility of creating chemically switchable devices (*i.e.*, through protonation/deprotonation of recognition sites on the axles). However, due to the geometries of these MOFs, [2]rotaxane molecules must be doped into the structures (*i.e.*, usually in a 1:5 ratio with other organic linkers). The doping of [2]rotaxanes, combined with the low densities of these materials, lead to the dynamic components being very dilute. Preliminary  $^2\text{H}$  SSNMR investigations conducted on Zr-based MOFs with rotaxane ligands yield spectra with very low S/N, making simulation of the spectra difficult. The use of  $^2\text{H}$  MAS NMR could greatly increase the S/N of the NMR spectra of these dilute species; however, such spectra are significantly more challenging to simulate than their static counterparts. The a priori knowledge of motion provided by the static  $^2\text{H}$  SSNMR experiments will greatly facilitate the simulation of MAS spectra and allow for the study of more complex systems with dilute dynamic components.

Our research group is currently developing methods to improve the acquisition and interpretation of  $^2\text{H}$  SSNMR spectra under both static and MAS conditions. For static samples, plan to utilize optimal control theory (OCT) to develop pulses capable of broadband excitation that are superior to WURST pulse sequences. In this process, we plan to monitor the density matrices associated with the equilibrium and non-equilibrium states, and how they are influenced by frequency-swept pulses (like WURST) and OCT pulses that use WURST pulses as a starting condition. For MAS samples, we plan to utilize the WURST pulses for irradiation of single spinning sidebands within the  $^2\text{H}$  ST patterns, in the hoped that we will obtain high-resolution powder patterns with high that will aid in identification of chemical shifts, quadrupolar parameters, and the affects of

molecular dynamics. The combination of these two techniques is key for rapidly acquiring  $^2\text{H}$  SSNMR spectra and successfully modeling motions in complex molecular machines.

It may also be very interesting to probe the Zr metal-clusters in these MOFs via  $^{91}\text{Zr}$  SSNMR ( $I = 5/2$ ;  $\nu_0(^{91}\text{Zr}) = 37.185$  MHz at 9.4 T; n.a. = 11.22000%,  $Q = -17.6$  fm $^2$ ). This work can be done in concert with that on the much less receptive  $^{67}\text{Zn}$  nucleus discussed above, utilizing the aforementioned pulse sequences and hardware for similar purposes. Intriguingly, there are currently no  $^{91}\text{Zr}$  SSNMR studies of Zr clusters reported in the literature; hence, as a starting point, it may be of great value to study some simple molecular  $^{91}\text{Zr}$  clusters, in order to determine if structural or dynamical effects manifest in the second-order CT  $^{91}\text{Zr}$  powder patterns.

Lastly, the results of **Chapter 5** indicate that motion can occur in the solid state without having to incorporate dynamic components into a porous material. However, these systems were limited to very small rotators (*i.e.*, hydrides and deuterides), and therefore, the applications of these materials in their current forms are likely limited. By using very bulky stopper groups on the [2]rotaxanes, it can be envisioned that crystalline materials can be synthesized such that the free volume within the crystals will be sufficient to allow rotation of the crown ether rings. [2]rotaxanes have been synthesized which use bulky trityl stoppers, and preliminary  $^2\text{H}$  SSNMR studies reveal that these rotaxanes undergo dynamics over a wide temperature range. These results indicate that it is possible to achieve large amplitude dynamics in strictly organic materials.

Our group has recently obtained a 5 mm HX static NMR probe that is optimized for low-gamma use over a temperature range of 20 to 450 K. Not only will this probe be

of utility for some on-site investigations of the systems with unreceptive  $^{67}\text{Zn}$  and  $^{91}\text{Zr}$  nuclides described above, but it will serve a much grander purpose for the study of molecular-level dynamics over a temperature range from 20 to 120 K. This temperature range is often studied by physicists conducting NMR experiments on materials that exhibit superconducting phase transitions (in fact, these often go to ca. 1 K), but it is a range that is not often explored by chemists. The reason for this is that most SSNMR spectroscopy involves MAS NMR experiments on nuclides like  $^{13}\text{C}$  and  $^{15}\text{N}$  at rates of 4 kHz or higher. For such experiments to be conducted at low temperatures, very expensive hardware and sample holders are required. Fortunately, the collection of UWNMR techniques developed in our laboratory are applicable to stationary samples; given the enormous selection of NMR-active nuclides from across the periodic table at our disposal, there are amazing possibilities for investigation of static structures (corresponding to temperatures around 77 K, at which many crystal structures are determined) or low-temperature dynamic motions (*e.g.*, Me group rotations). With respect to the work in this thesis, projects will be pursued focused upon elucidating the low temperature motions of many of the molecular rotors described in Chapter 5; in particular, compound **3** (trans-D<sub>2</sub>Pt(PCy<sub>3</sub>)<sub>2</sub>), which appears to have a mobile rotor at temperatures greater than 173 K, is of great interest. Multinuclear SSNMR experiments on MOFs from the UWDM series described herein, and new MOFs that are currently designed, may also reveal much new information on structure and dynamics over this range of low temperatures.

## 7.6 Surface Supported Catalysts

The use of high magnetic fields and the WURST-CPMG pulse sequence allowed for the rapid acquisition of  $^{35}\text{Cl}$  SSNMR spectra for a series of transition-metal chloride compounds (**Chapter 6**). The compounds have molecular geometries commonly exhibited by organometallic catalysts, and the different bonding environments (*i.e.*, bridging, terminal axial, and terminal equatorial) could be distinguished using  $^{35}\text{Cl}$  SSNMR. A detailed analysis of the origin of the  $^{35}\text{Cl}$  EFG tensor parameters was provided by DFT calculations. These techniques were then applied to study a transition-metal compound supported onto a porous material (*i.e.*, silica). Despite the dilute nature of the surface supported species, it was possible to acquire a  $^{35}\text{Cl}$  SSNMR spectrum, and preliminary structural assignments were made.

## 7.7 Future Work – Ultra-wideline $^{35}\text{Cl}$ SSNMR

The  $^{35}\text{Cl}$  EFG tensor parameters are very sensitive to the bonding environments of Cl atoms, and to the oxidation states of the metals to which they are bound. While the acquisition of SSNMR spectra of paramagnetic materials is often challenging owing to very efficient paramagnetic relaxation, we have shown that such experiments are possible for simple transition metal halides.  $\text{MoCl}_5$  is isostructural to the pentahalide compounds studied in Chapter 6; however, the metal centres have a  $d^1$  electron configuration and the compound is paramagnetic. The  $^{35}\text{Cl}$  SSNMR spectrum has a single powder pattern and through the use of DFT calculations, the powder pattern was assigned to the terminal axial environments. These results suggest that  $^{35}\text{Cl}$  SSNMR could be used as a probe of unpaired spin density in transition-metal compounds.

Finally, our group recently demonstrated that it is possible to acquire  $^{35}\text{Cl}$  UW NMR experiments under DNP conditions, by utilizing the BRAIN-CP sequence for  $^1\text{H}$ - $^{35}\text{Cl}$  polarization transfer.<sup>22</sup> If the metal chlorides mentioned above (or derivatives thereof) can be stabilized on surfaces of porous materials via chemical grafting or physical confinement, there is certainly a major role for DNP  $^1\text{H}$ - $^{35}\text{Cl}$  SSNMR to play. The surfaces of silica and other porous materials provide an ample source of protons that should allow us to successfully use  $^1\text{H}$ - $^{35}\text{Cl}$  BRAIN-CP methods for CP from protons on the surface to  $^{35}\text{Cl}$  nuclides in the metal chlorides.<sup>23</sup> We plan to explore this from the perspectives of the choices of the best radicals, solvents, and loading levels of the metal chloride catalysts.

## 7.8 References

- (1) Anastas, P. T.; Werner, J. C. *Green Chemistry: Theory and Practice*; Oxford University Press: New York, 1998.
- (2) Nývlt, J. *Cryst. Res. Technol.* **1995**, *30*, 443–449.
- (3) Akimbekov, Z.; Katsenis, A. D.; Nagabhushana, G. P.; Ayoub, G.; Arhangel'skis, M.; Morris, A. J.; Friščić, T.; Navrotsky, A. *J. Am. Chem. Soc.* **2017**, *139*, 7952–7957.
- (4) Friščić, T.; Reid, D. G.; Halasz, I.; Stein, R. S.; Dinnebier, R. E.; Duer, M. J. *Angew. Chem. Int. Ed.* **2010**, *49*, 712–715.
- (5) Jayachandrababu, K. C.; Verploegh, R. J.; Leisen, J.; Nieuwendaal, R. C.; Sholl, D. S.; Nair, S. *J. Am. Chem. Soc.* **2016**, *138*, 7325–7336.
- (6) Eum, K.; Jayachandrababu, K. C.; Rashidi, F.; Zhang, K.; Leisen, J.; Graham, S.; Lively, R. P.; Chance, R. R.; Sholl, D. S.; Jones, C. W.; Nair, S. *J. Am. Chem. Soc.* **2015**, *137*, 4191–4197.
- (7) Grau-Crespo, R.; Aziz, A.; Collins, A. W.; Crespo-Otero, R.; Hernández, N. C.; Rodríguez-Albelo, L. M.; Ruiz-Salvador, A. R.; Calero, S.; Hamad, S. *Angew. Chem. Int. Ed.* **2016**, *55*, 16012–16016.
- (8) Kong, X.; Deng, H.; Yan, F.; Kim, J.; Swisher, J. A.; Smit, B.; Yaghi, O. M.; Reimer, J. A. *Science* **2007**, *342*, 882–885.
- (9) Krajnc, A.; Kos, T.; Zabukovec Logar, N.; Mali, G. *Angew. Chem. Int. Ed.* **2015**, *54*, 10535–10538.
- (10) Sutrisno, A.; Terskikh, V. V.; Shi, Q.; Song, Z.; Dong, J.; Ding, S. Y.; Wang, W.; Provost, B. R.; Daff, T. D.; Woo, T. K.; Huang, Y. *Chem. Eur. J.* **2012**, *18*, 12251–

12259.

- (11) He, P.; Lucier, B. E. G.; Terskikh, V. V.; Shi, Q.; Dong, J.; Chu, Y.; Zheng, A.; Sutrisno, A.; Huang, Y. *J. Phys. Chem. C* **2014**, *118*, 23728–23744.
- (12) Xu, J.; Lucier, B. E. G.; Sinelnikov, R.; Terskikh, V. V.; Staroverov, V. N.; Huang, Y. *Chem. Eur. J.* **2015**, *21*, 14348–14361.
- (13) Harris, R. K.; Wasylshen, R. E.; Duer, M. J. *NMR Crystallography*; John Wiley and Sons: Singapore, 2009.
- (14) Bryce, D. L. *IUCrJ* **2017**, *4*, 350–359.
- (15) Ashbrook, S. E.; McKay, D. *Chem. Commun.* **2016**, *52*, 7186–7204.
- (16) Shirai, Y.; Osgood, A. J.; Zhao, Y.; Kelly, K. F.; Tour, J. M. *Nano Lett.* **2005**, *5*, 2330–2334.
- (17) Badjic, J. D.; Balzani, V.; Credi, A.; Silvi, S.; Stoddart, J. F. *Science* **2004**, *303*, 1845–1849.
- (18) Coskun, A.; Banaszak, M.; Astumian, R. D.; Stoddart, J. F.; Grzybowski, B. A. *Chem. Soc. Rev.* **2012**, *41*, 19–30.
- (19) Kalidindi, S. B.; Nayak, S.; Briggs, M. E.; Jansat, S.; Katsoulidis, A. P.; Miller, G. J.; Warren, J. E.; Antypov, D.; Corà, F.; Slater, B.; Prestly, M. R.; Mart-Gastaldo, C.; Rosseinsky, M. J. *Angew. Chem. Int. Ed.* **2015**, *54*, 221–226.
- (20) Devautour-Vinot, S.; Maurin, G.; Serre, C.; Horcajada, P.; Paula Da Cunha, D.; Guillerm, V.; De Souza Costa, E.; Taulelle, F.; Martineau, C. *Chem. Mater.* **2012**, *24*, 2168–2177.
- (21) Lawrence, M. C.; Schneider, C.; Katz, M. J. *Chem. Commun.* **2016**, *52*, 4971–4974.

- (22) Hirsh, D. A.; Rossini, A. J.; Emsley, L.; Schurko, R. W. *Phys. Chem. Chem. Phys.* **2016**, *18*, 25893–25904.
- (23) Rossini, A. J.; Zagdoun, A.; Lelli, M.; Lesage, A.; Coperet, C.; Emsley, L. *Acc. Chem. Res.* **2013**, *46*, 1942–1951.



## Appendix A Supplementary Tables and Figures for Chapter 2

**Table A1:** Optimized recycle delays for  $^1\text{H}$  MAS experiments

Compound	Recycle Delay (s)
1	5
2	5
3	5
4	7.5

**Table A2:**  $^1\text{H}$ - $^{13}\text{C}$  CP/MAS contact times and recycle delays

Compound	Contact Time (ms)	Recycle Delay (s)
1	1	5
2	10	5
3	2	5
4	2	7.5
HMeIm	15	60

**Table A3:**  $^1\text{H}$ - $^{111}\text{Cd}$  CP contact times and recycle delays

Compound	Contact Time (ms)	Recycle Delay (s)
1	8	5
2	17	5
3	7	5
4	5	7.5

**Table A4:**  $^1\text{H}$ - $^{14}\text{N}$  BCP/WCPMG experimental parameters

Compound	Recycle Delay (s)	Contact Time (ms)	# of echoes	# of subspectra
1	1	20	40	15
HMeIm	30	20	80	26

**Table A5:** Selected bond lengths in the Cd-imidazole compounds with known structures

Compound	Bond	Length (Å)
2	Cd-N1	2.215
	Cd-N2	2.228
	Cd-N3	2.260
	Cd-N4	2.226
3	Cd1-N2	2.203
	Cd1-N3	2.198
	Cd1-N5	2.199
	Cd1-N6	2.258
	Cd1-N7	2.167
	Cd2-N1	2.201
	Cd2-N2	2.209
4	Cd-N1	2.401

**Table A6:** Selected bond angles in the Cd-imidazole compounds with known structures

Compound	Bond	Angle (°)
2	N1-Cd-N2	113.5
	N1-Cd-N3	115.2
	N1-Cd-N4	112.2
	N2-Cd-N3	96.66
	N2-Cd-N4	112.9
	N3-Cd-N4	105.3
3	N2-Cd1-N3	115.3
	N2-Cd1-N5	115.6
	N2-Cd1-N6	80.97
	N2-Cd1-N7	107.4
	N3-Cd1-N5	109.9
	N3-Cd1-N6	126.1
	N3-Cd1-N7	102.0
	N5-Cd1-N6	106.5
	N5-Cd1-N7	105.1
	N6-Cd1-N7	29.33
	N1-Cd2-N2	106.8
	N1-Cd2-N2	117.4
4	N1-Cd-N1	89.769
	N1-Cd-N1	90.231

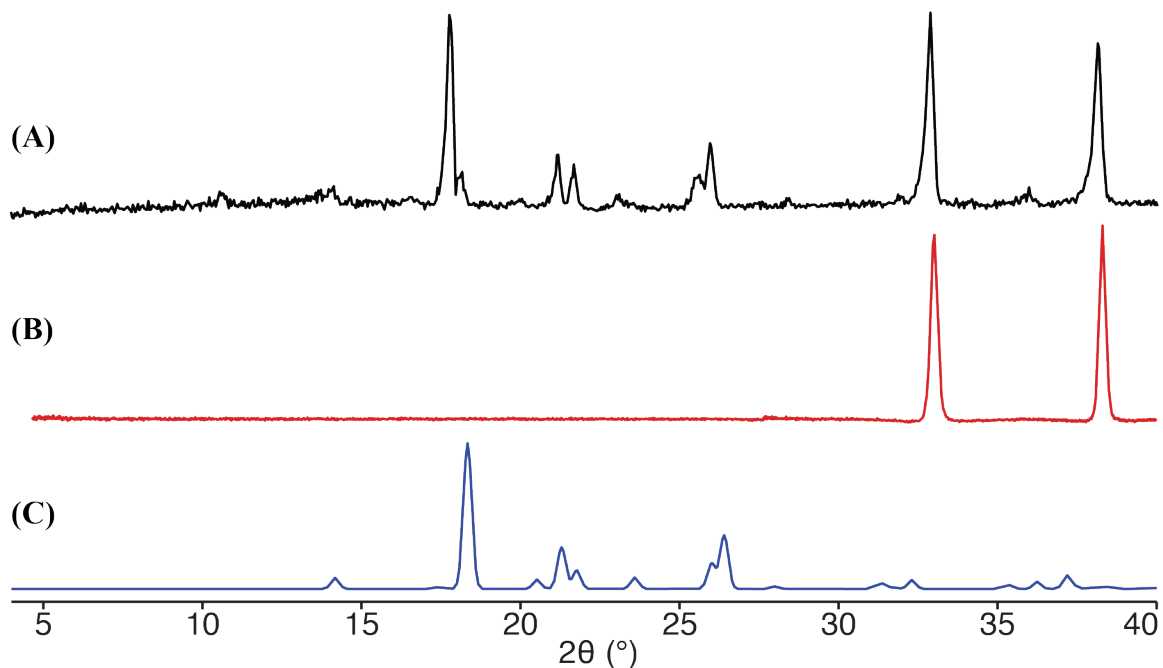


**Figure A1:** Experimental PXRD patterns for (A) the dry-milled reaction mixture before aging and (B) CdO. (C) Simulated PXRD pattern for HMeIm.

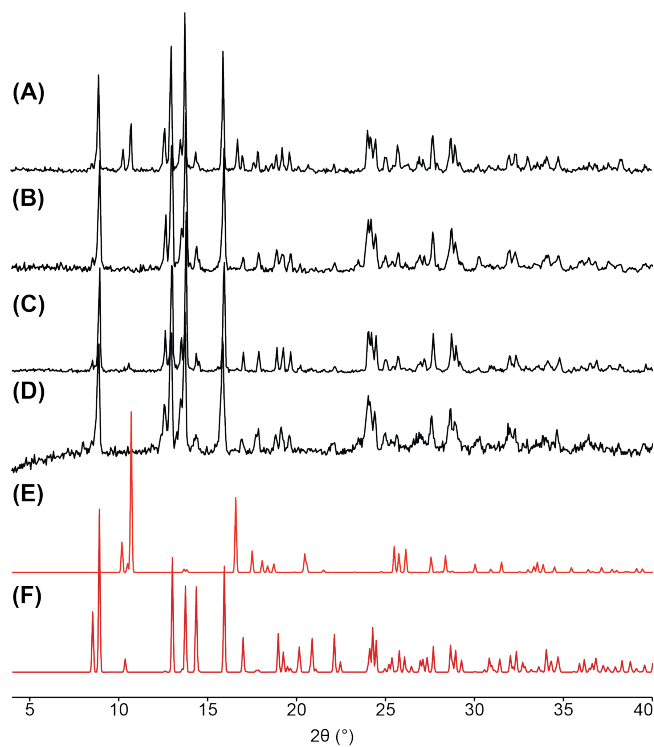


**Figure A2:** Experimental PXRD patterns for the products of the aging reaction treated with either  $(\text{NH}_4)_2(\text{SO}_4)$  after (A) one day and (B) seven days of aging, or  $\text{HCafHSO}_4$  after (C) one day and (D) seven days of aging. Simulated PXRD patterns from the crystal structures (E) 1 and (F) 3.

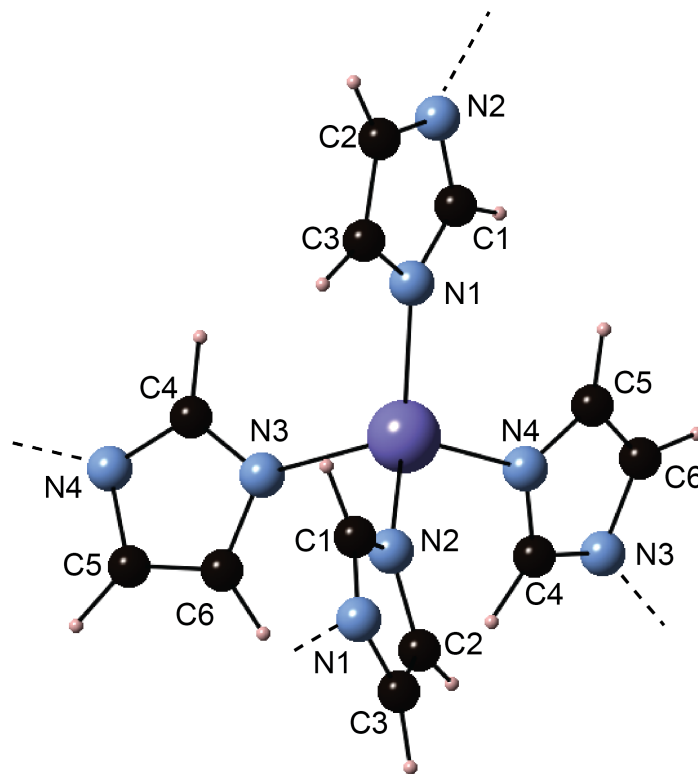


**Figure A3:** The coordination environment of the Cd atoms in *dia*-Cd[Im]<sub>2</sub> (**2**).

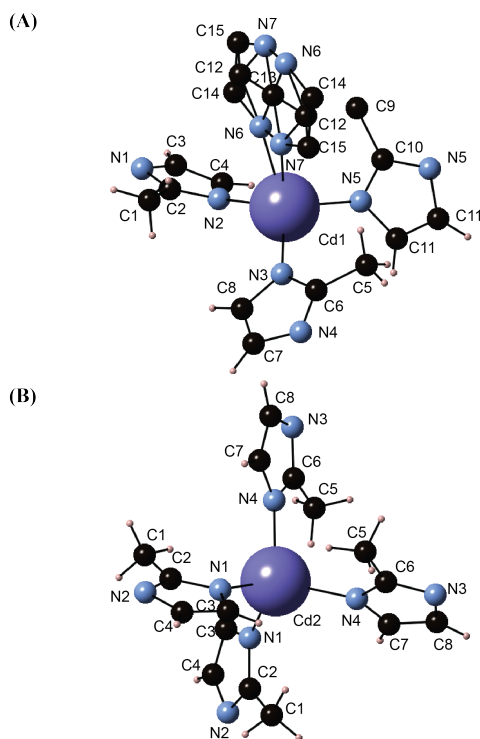


**Figure A4:** Coordination environment about (A) the Cd1 site, (B) the Cd2 site and atom labeling in thle *yqt1*-Cd[MeIm]<sub>2</sub> (**3**) framework. There is an apparent positional disorder of one of the MeIm-ligands at the Cd1 site.

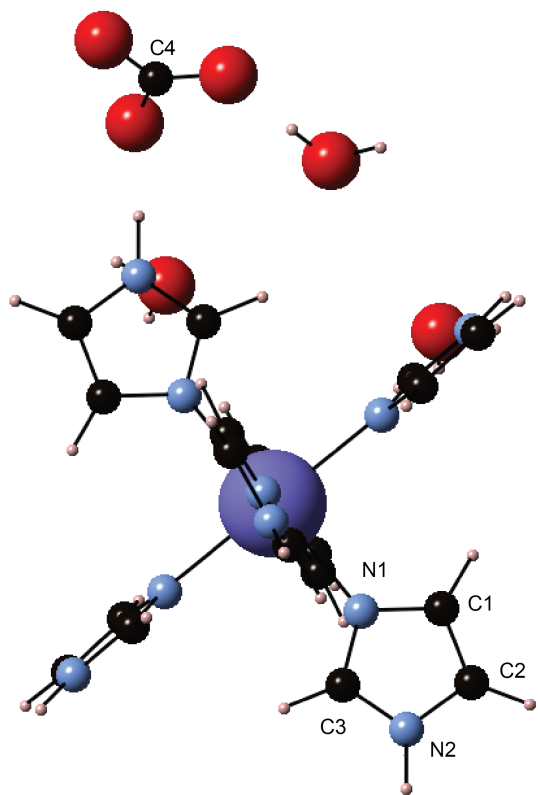


**Figure A5:** Coordination environment about the Cd atom and atom labelling in the  $\text{Cd}[\text{Im}]_6\text{CO}_3 \cdot 3\text{H}_2\text{O}$  (**4**) molecule.

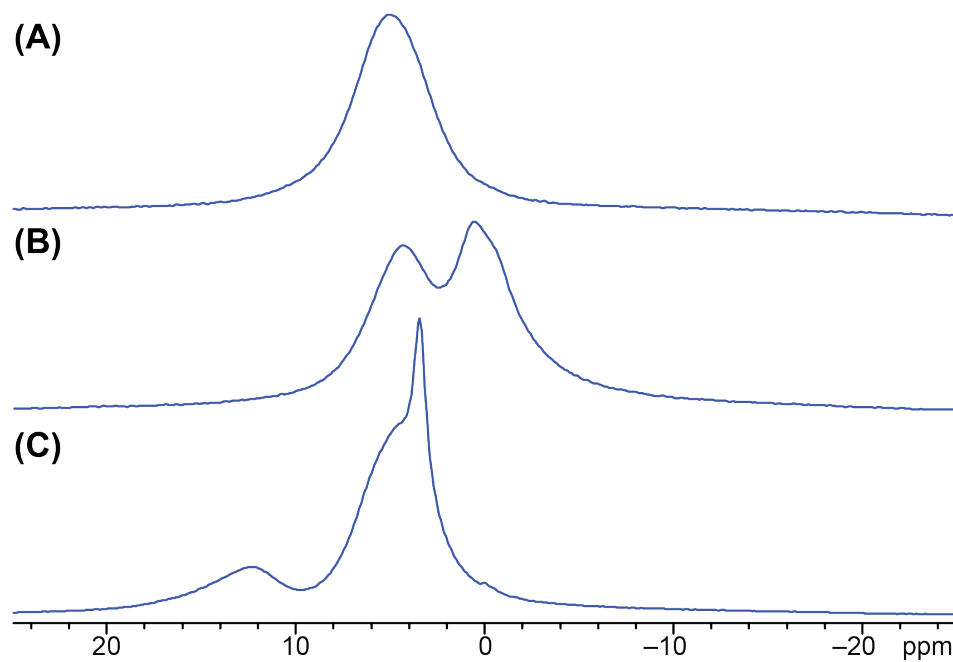


**Figure A6:**  $^1\text{H}$  MAS ( $\nu_{\text{rot}} = 16$  kHz) NMR spectra acquired at 9.4 T for (A) framework **2**, (B) framework **3**, and (C) compound **4**.

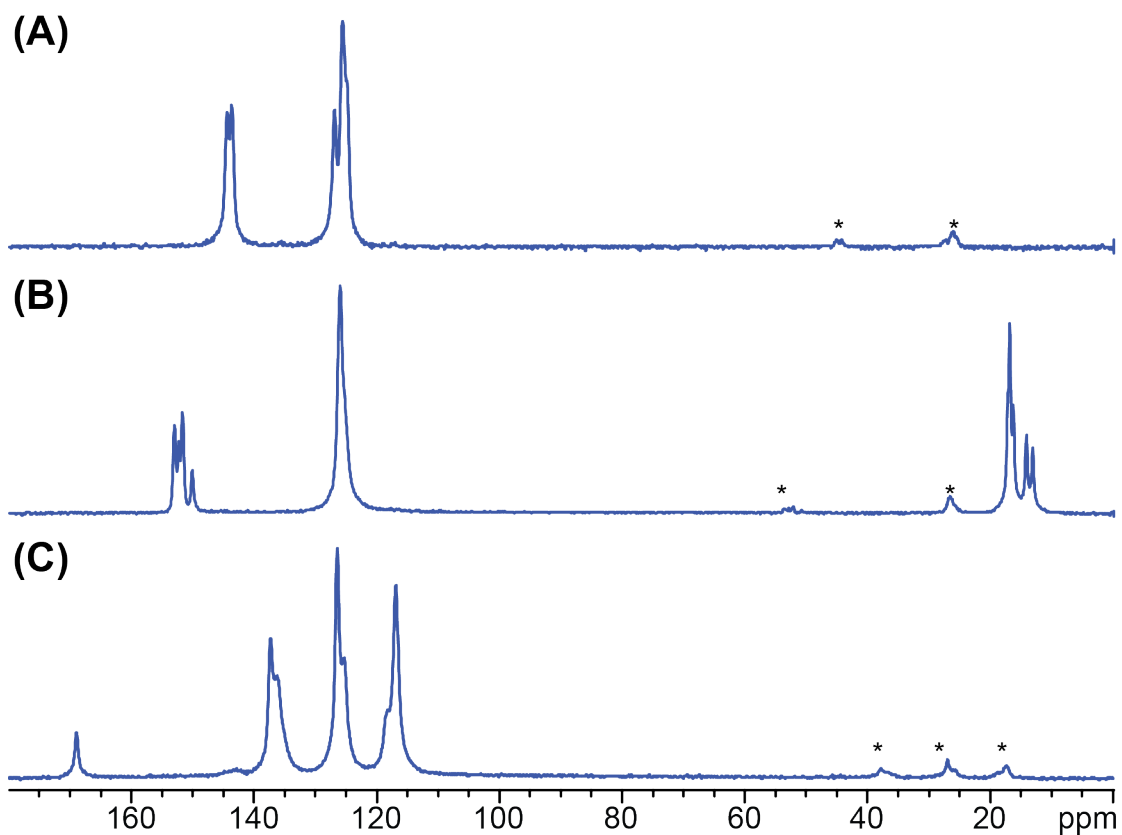


**Figure A7:**  $^1\text{H}$ - $^{13}\text{C}$  CP/MAS ( $\nu_{\text{rot}} = 10$  kHz) NMR spectra acquired at 9.4 T of (A) framework **2**, (B) framework **3**, and (C) compound **4**. The asterisks (\*) denoted spinning sidebands.

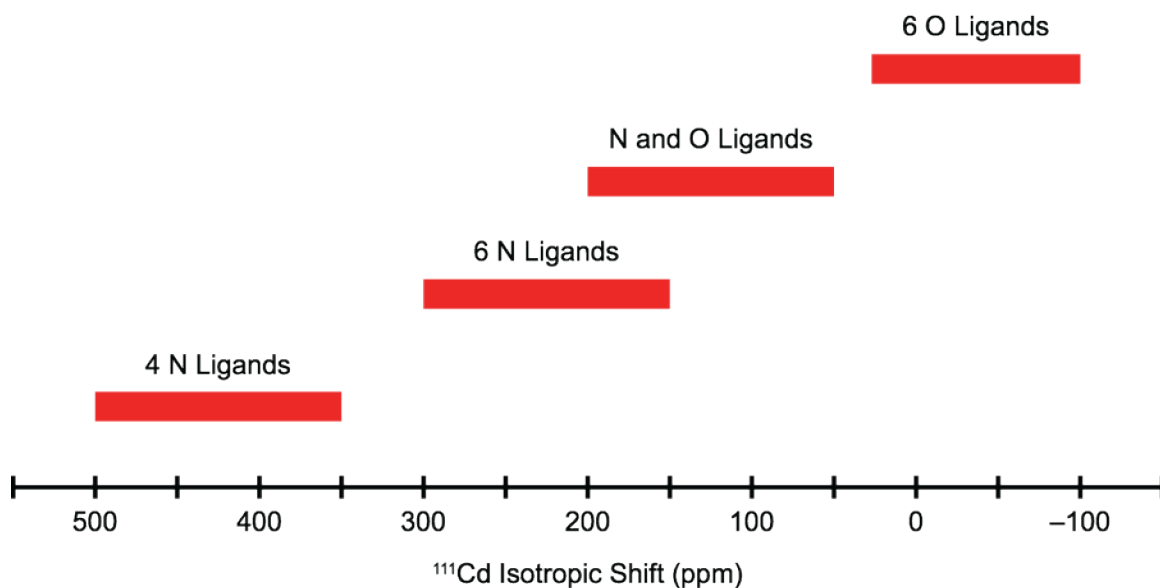


**Figure A8:** Proposed  $^{111}\text{Cd}$  isotropic chemical shift ranges based on the compounds investigated herein and on studies conducted by Ellis *et al.*

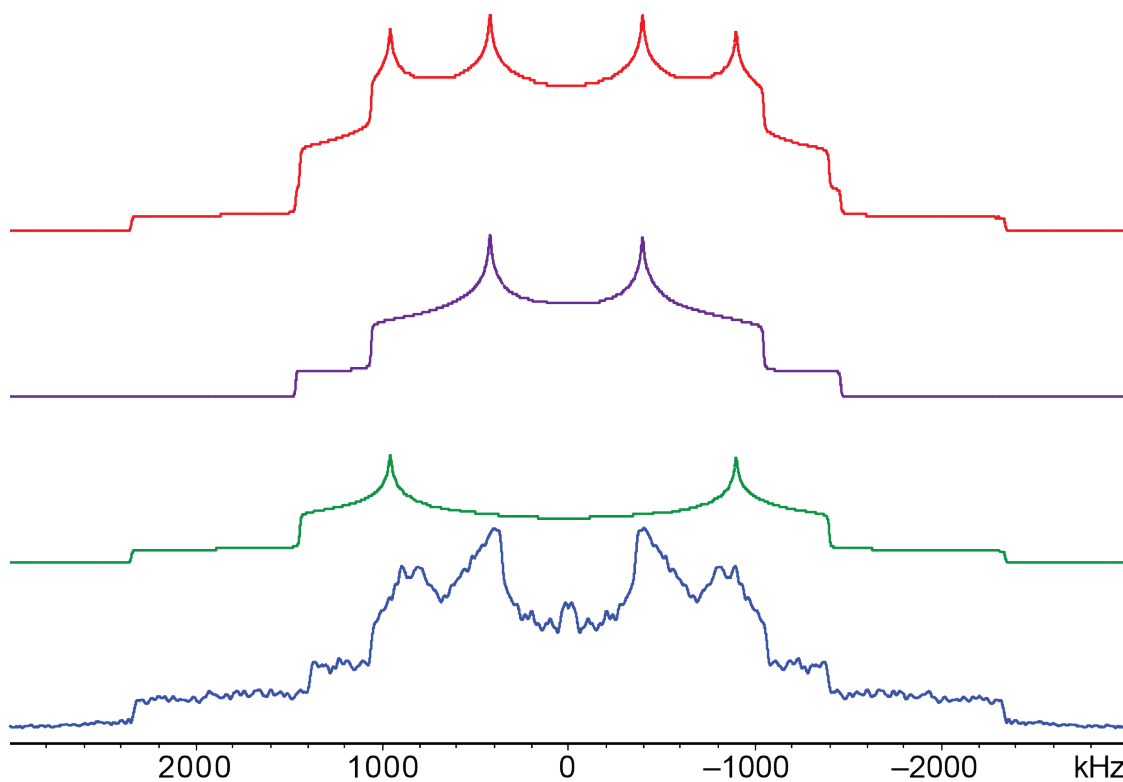


**Figure A9:**  $^1\text{H}$ - $^{14}\text{N}$  BRAIN-CP/WURST-CPMG spectrum of bulk HMeIm (blue trace) and simulation of the powder pattern (red trace). A deconvolution of the simulation into the two distinct powder patterns is also shown. The purple trace is the pattern corresponding to the N1 site ( $C_Q = 1.95(5)$  MHz,  $\eta_Q = 0.44(2)$ ) and the green trace is the pattern corresponding to the N2 site ( $C_Q = 3.13(5)$  MHz,  $\eta_Q = 0.21(2)$ ).

## Appendix B: Supplementary Tables and Figures for Chapter 3

**Table B1:**  $^1\text{H}$ - $^{111}\text{Cd}$  CP/MAS NMR contact times and recycle delays

Reaction Set/Compound	Contact Time (ms)	Recycle Delay (s)
<b>1</b>	10	1
<b>2</b>	10	1
<b>3</b>	10	1
<b>4</b>	10	1
<b>Amorphous framework</b>	10	1
<b>CdIF-1<sub>as</sub></b>	15	2.5
<b>CdIF-1<sub>dried</sub></b>	15	2.5
<b>CdIF-1<sub>HMeIm</sub></b>	15	2.5

**Table B2:** Calculated pore volumes for the Zn and Cd ZIFs.

Compounds	Void volume ( $\text{\AA}^3$ ) <sup>a</sup>	% of unit cell volume	$\Delta H_{\text{trans}}$ ( $\text{kJ mol}^{-1}$ )
<i>sod</i> -Zn[MeIm] <sub>2</sub>	1268.47	25.8	26.25
<i>a</i> -Zn[MeIm] <sub>2</sub>	--	--	19.38
<i>kat</i> -Zn[MeIm] <sub>2</sub>	12.30	0.3	17.95
<i>dia</i> -Zn[MeIm] <sub>2</sub>	0	0	15.61
<b>CdIF-1<sup>b</sup></b>	1859.21	31.2	--
<i>d</i> CdM <sup>c</sup>	235.06	14.6	--
<i>y</i> CdM	8.45	0.3	--

<sup>a</sup> Calculated using Mercury 3.9 with a 1.2  $\text{\AA}$  radius probe (*i.e.*, the volume of void spaces which can be occupied by a fictitious molecule with a 1.2  $\text{\AA}$  radius). <sup>b</sup> Water molecules were removed from the pores before the calculation. <sup>c</sup> HMeIm molecules were removed from the pores before the calculation.



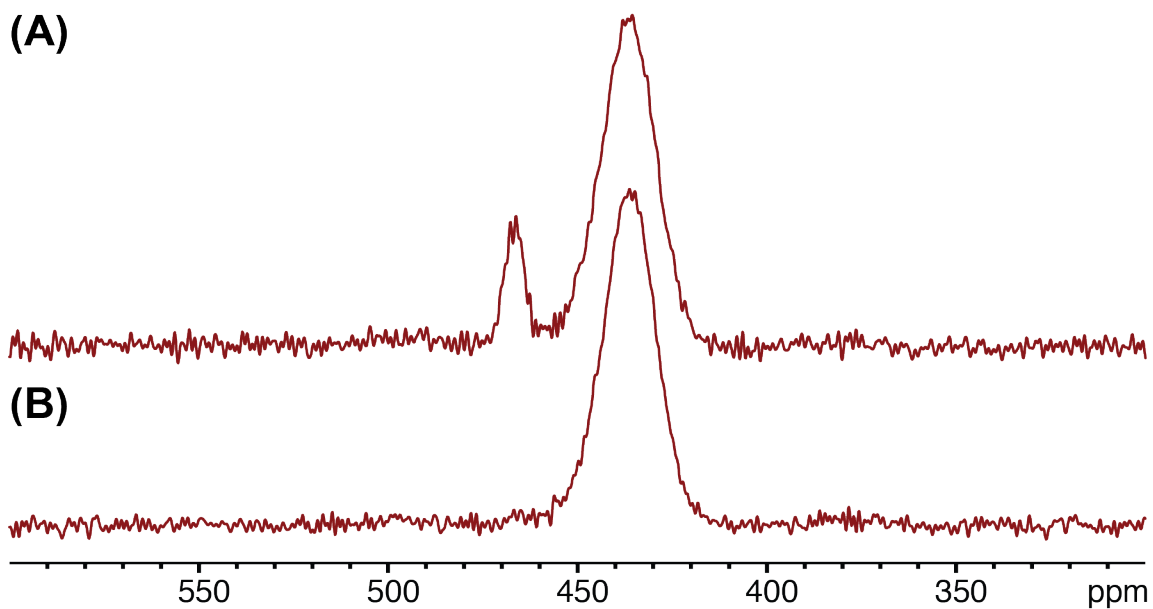


**Figure B1:** (A)  $^1\text{H}$ - $^{111}\text{Cd}$  CP/MAS NMR spectrum acquired for the products of **3** (twenty minute acquisition time). (B)  $^{111}\text{Cd}$  NMR spectrum of the same sample acquired for an additional twenty minutes (the two spectra are non-cumulative).

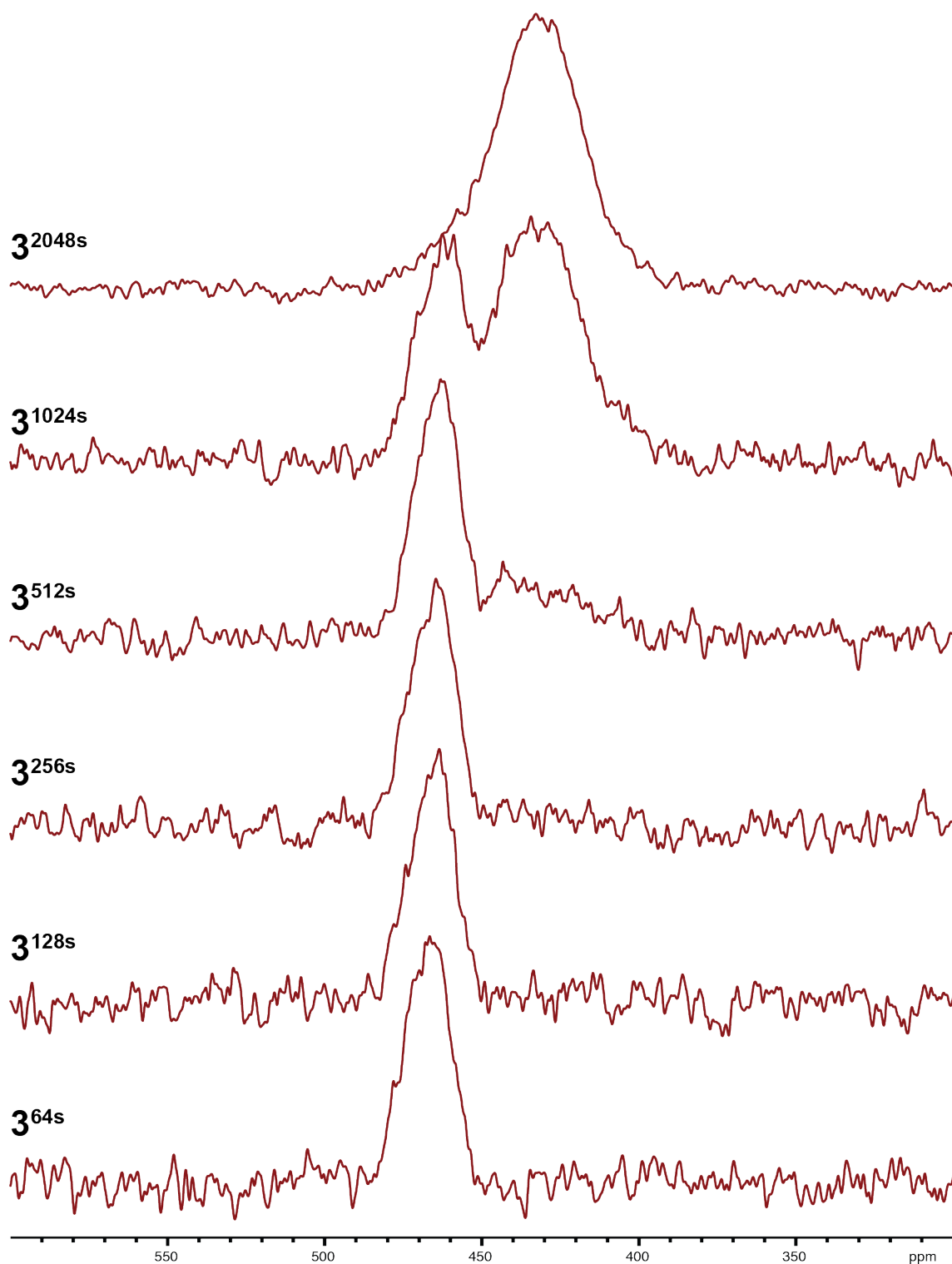


**Figure B2:**  $^1\text{H}$ - $^{111}\text{Cd}$  CP NMR spectra acquired under static conditions (*i.e.*, no sample rotation) for products **3** at different time intervals (the spectra are non-cumulative).

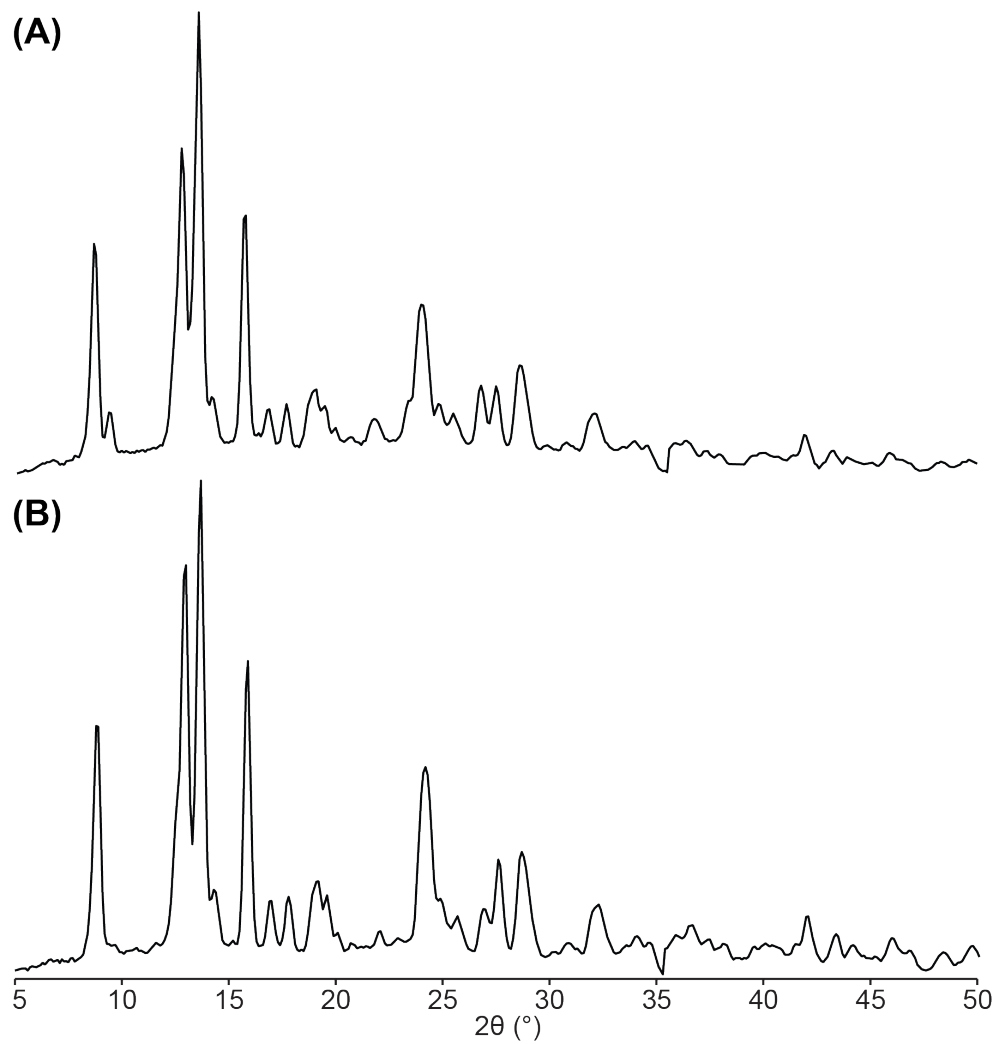


**Figure B3:** Experimental PXR D patterns obtained for (A)  $185m$  and (B)  $125m-a1h$ .

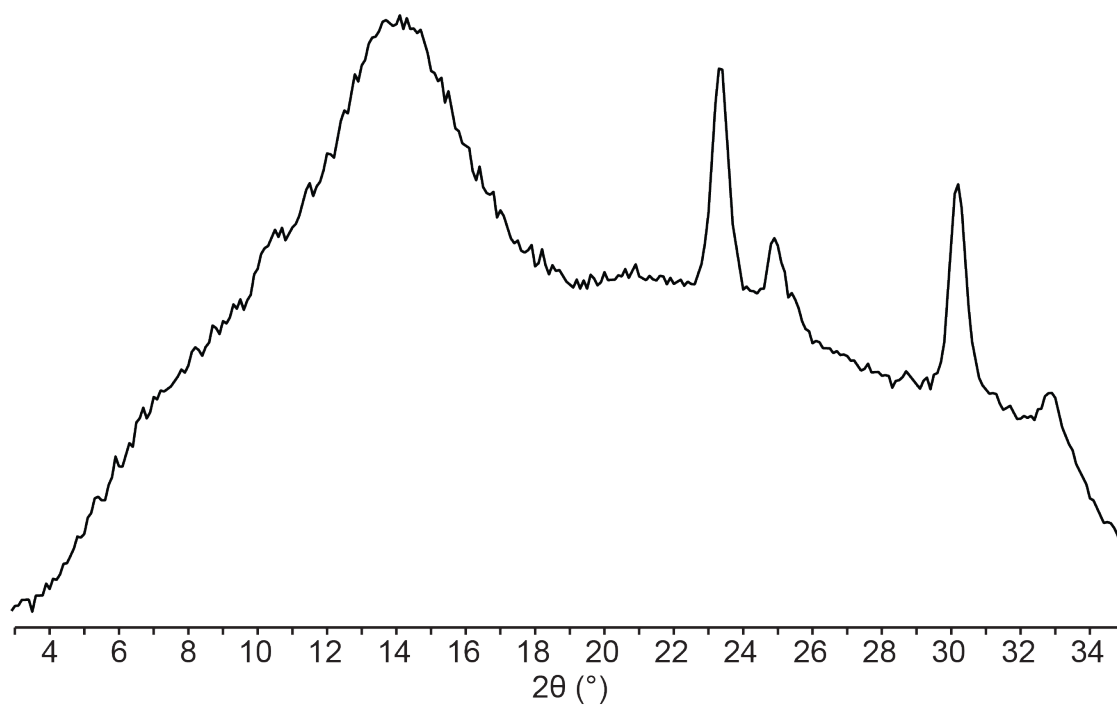


**Figure B4:** Experimental PXRD pattern acquired for *aCdM* that was synthesized by milling a sample of *γCdM* for three hours. The broad features confirm the amorphous nature of this material.

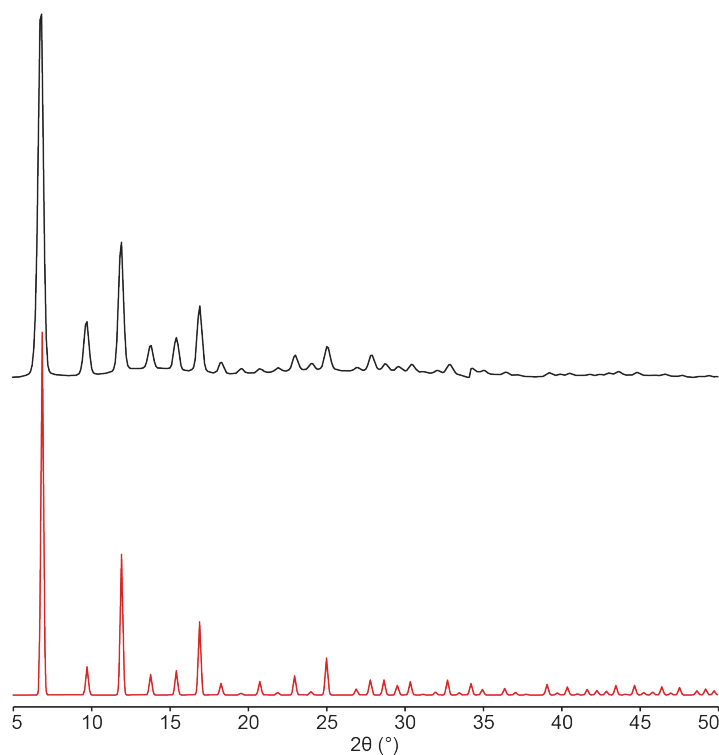


**Figure B5:** (A) Experimental PXRD pattern obtained for *CdIF-1*. (B) Simulated PXRD pattern of *CdIF-1* from the crystal structure reported by Tian *et al.*

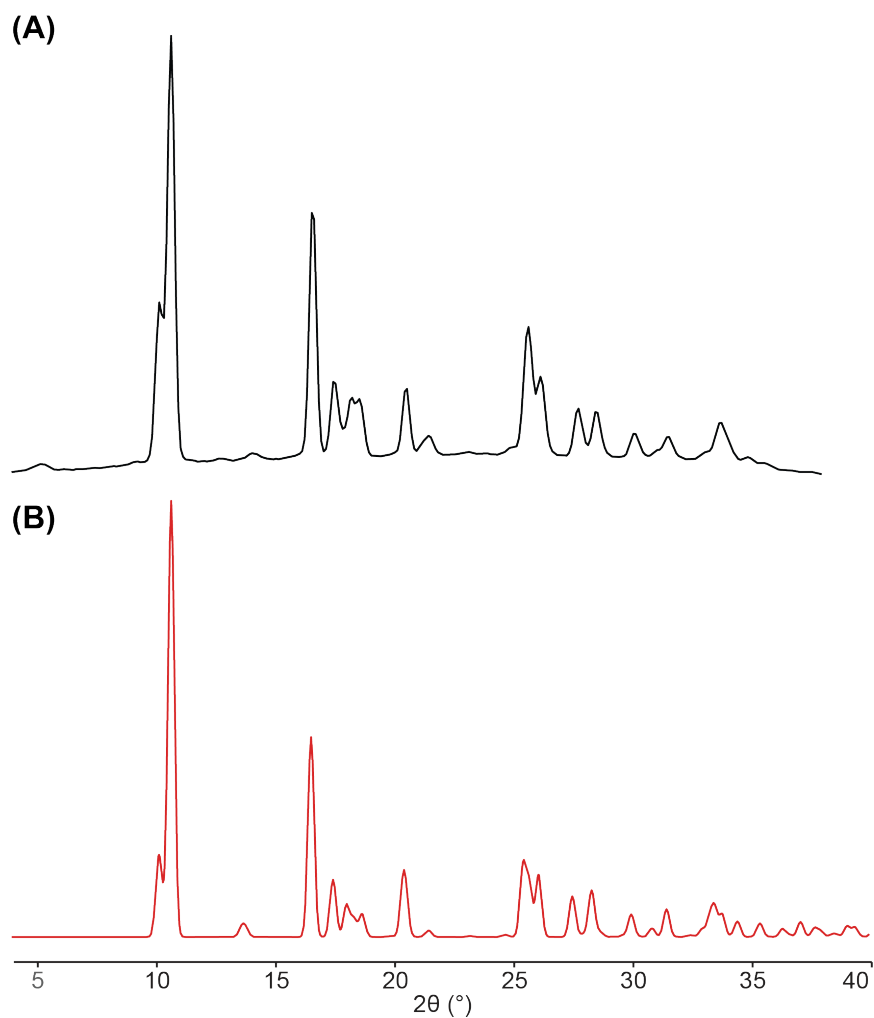


**Figure B6:** (A) Experimental PXRD pattern for **CdIF-1<sub>HMeIm</sub>**. (B) Simulated PXRD pattern from the crystal structure of *dCdM*.

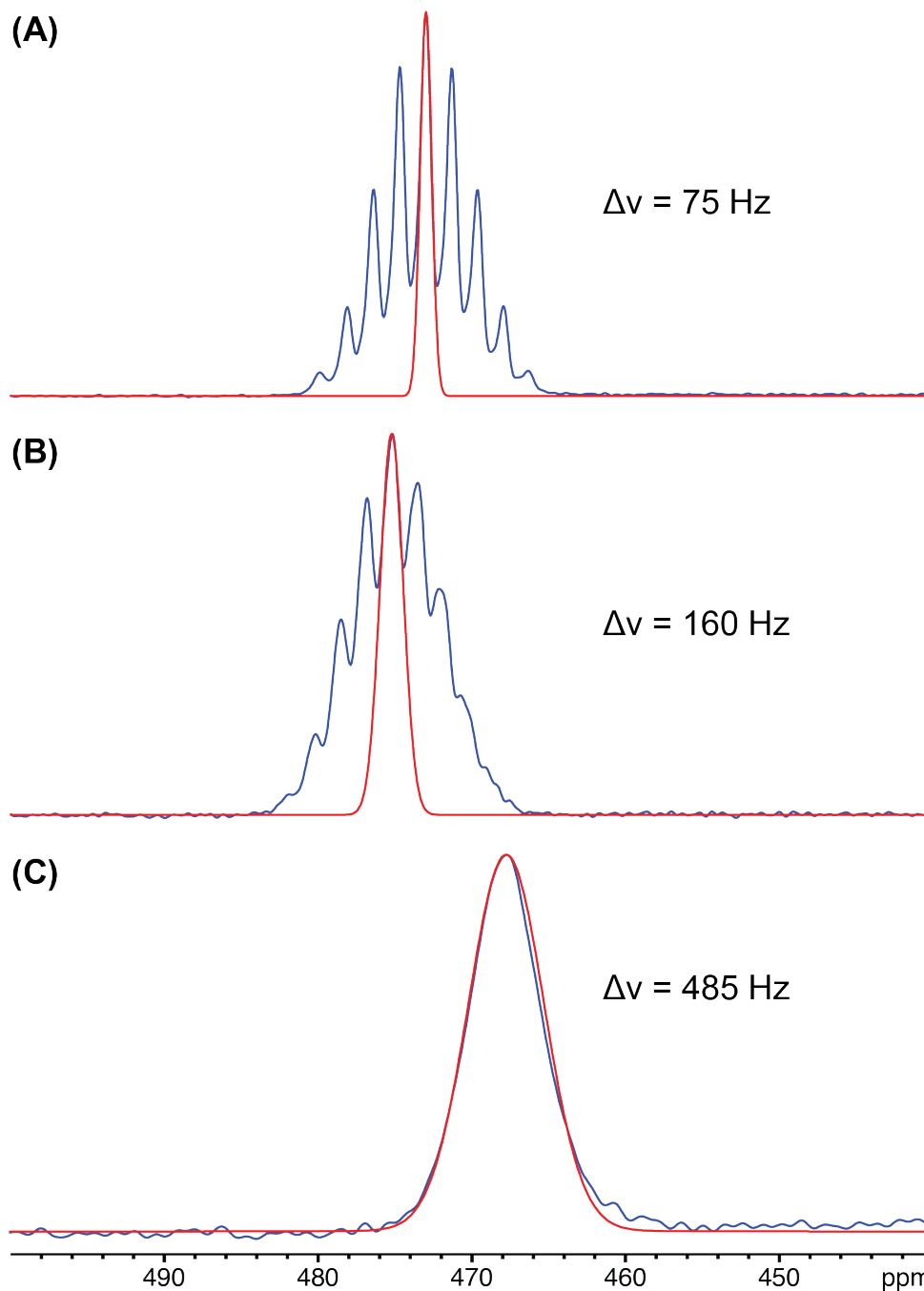


**Figure B7:** Comparison of the peak widths in the  $^{111}\text{Cd}$  NMR spectra of (A) **CdIF-1<sub>dried</sub>**, (B) **CdIF-1**, and (C) **1<sub>30s</sub>**. Experimental spectra are shown in blue and the corresponding simulations are shown as the red traces.

## Appendix C Synthetic Information and Supplementary Tables and Figures for Chapter 4

### Synthetic procedures:

#### Synthesis of **A**<sub>3</sub>:

The synthesis of **A**<sub>2</sub> has been reported in the literature.<sup>1</sup> **A**<sub>3</sub> was made in a similar fashion to **A**<sub>2</sub>, but using 2-methylpyridine-4-boronic acid instead of 4-pyridinylboronic acid.

#### Synthesis of **L**<sub>3</sub>:

*Meso*-tetra-(4-carboxyphenyl)porphine (250 mg, 0.3 mmol) and PdCl<sub>2</sub> (225 mg, 1.2 mmol) were added into a 80 mL microwave tube. DMF (25 mL) was added, the tube was placed inside the microwave reactor and heated at 155 °C for three cycles of 5 min. After cooling it down, THF (50 mL) was added and the reaction was filtered. The resultant organic layer was washed with water, centrifuged and filtered to yield a purple powder. Yield: 250 mg, 89 %. <sup>1</sup>H NMR (500 MHz, DMSO-d<sub>6</sub>, 298 K) δ (ppm) = 8.82 (s, 8H), 8.39 (d, *J* = 8.3 Hz, 8H), 8.32 (d, *J* = 8.3 Hz, 8H).

#### Synthesis of UWDM-P1:

Zn(NO<sub>3</sub>)<sub>2</sub>·6H<sub>2</sub>O (6 mg, 0.02 mmol), **A**<sub>2</sub> (30 mg, 0.04 mmol), and **L**<sub>3</sub> (9 mg, 0.01 mmol) were loaded into a 20 mL scintillation vial. DMF (2 mL) and HBF<sub>4</sub>·Et<sub>2</sub>O (1 drop) were added and the mixture sonicated for 1 minute. The mixture was heated in a programmable oven at 85 °C for 48 hours and cooled to room temperature over 6 hours.

Red plate crystals were collected by filtration and stored in fresh DMF. Yield based on porphyrin: 238 mg, 90%.

#### Synthesis of UWDM-P2:

Zn(NO<sub>3</sub>)<sub>2</sub>·6H<sub>2</sub>O (6 mg, 0.02 mmol), **A**<sub>2</sub> (30 mg, 0.04 mmol), and **L**<sub>3</sub> (9 mg, 0.01 mmol) were loaded into a 20 mL scintillation vial. DMF (2 mL) and HBF<sub>4</sub>·Et<sub>2</sub>O (1 drop) were added and the mixture sonicated for 1 minute. The mixture was heated in a programmable oven at 80 °C for 48 hours and cooled to room temperature over 6 hours. Red plate crystals were collected by filtration and stored in fresh DMF. Yield based on porphyrin: 210 mg, 80%.

#### Desolvation of UWDM-P1 and UWDM-P2:

UWDM-P1<sub>d</sub> and UWDM-P2<sub>d</sub> were made by soaking UWDM-P1 and UWDM-P2 in CH<sub>2</sub>Cl<sub>2</sub> for 8-10 hours, changing the solvent every 2 hours to exchange the DMF in the pores of the framework for CH<sub>2</sub>Cl<sub>2</sub>. The samples were then filtered and left to air dry to evaporate the CH<sub>2</sub>Cl<sub>2</sub>.

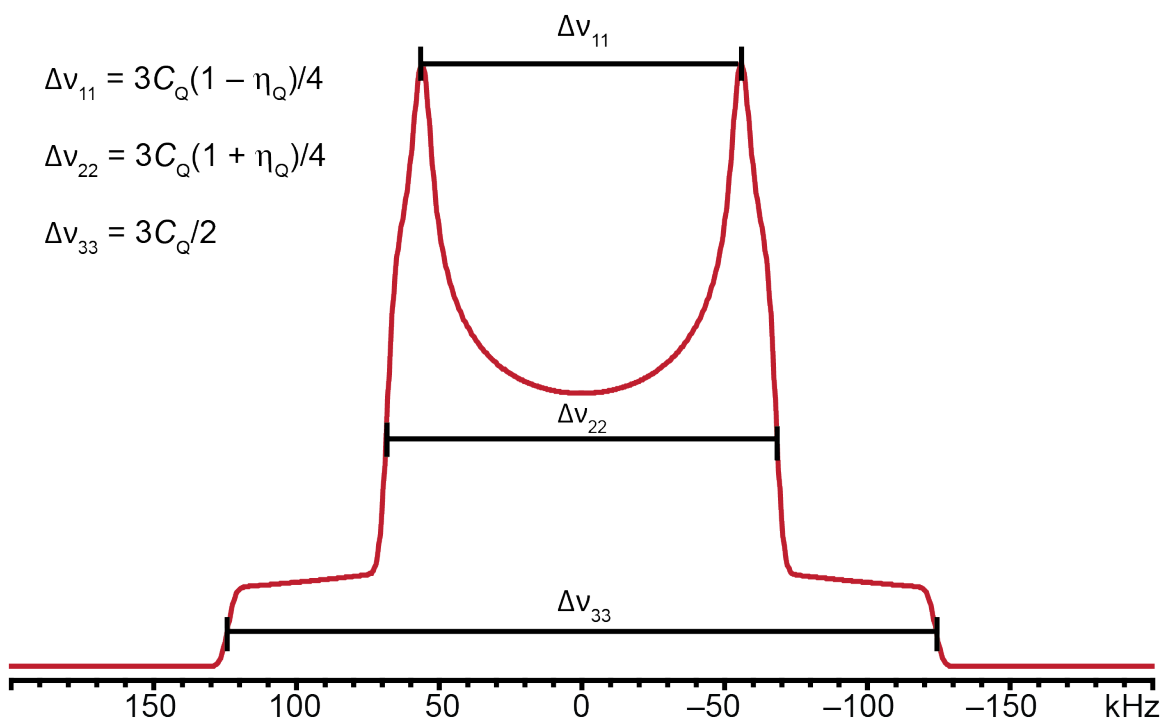
**Table C1:** Optimized recycle delays and 90° pulse lengths used in the acquisition of <sup>2</sup>H SSNMR spectra at 9.4 T.

Sample	Recycle delay (s)	90° pulse length (μs)
UWDM-1 <sub>(22)</sub>	0.1	3.25
UWDM-1 <sub>(B24)</sub>	0.05	3.25
UWDM-2	0.5	3.5
α-UWDM-3	0.5	3.25
β-UWDM-3	0.5	3.25
UWDM-P1	1	3.25
UWDM-P1 <sub>d</sub>	1	3.25
UWDM-P2	1	3.00
UWDM-P2 <sub>d</sub>	1	3.25

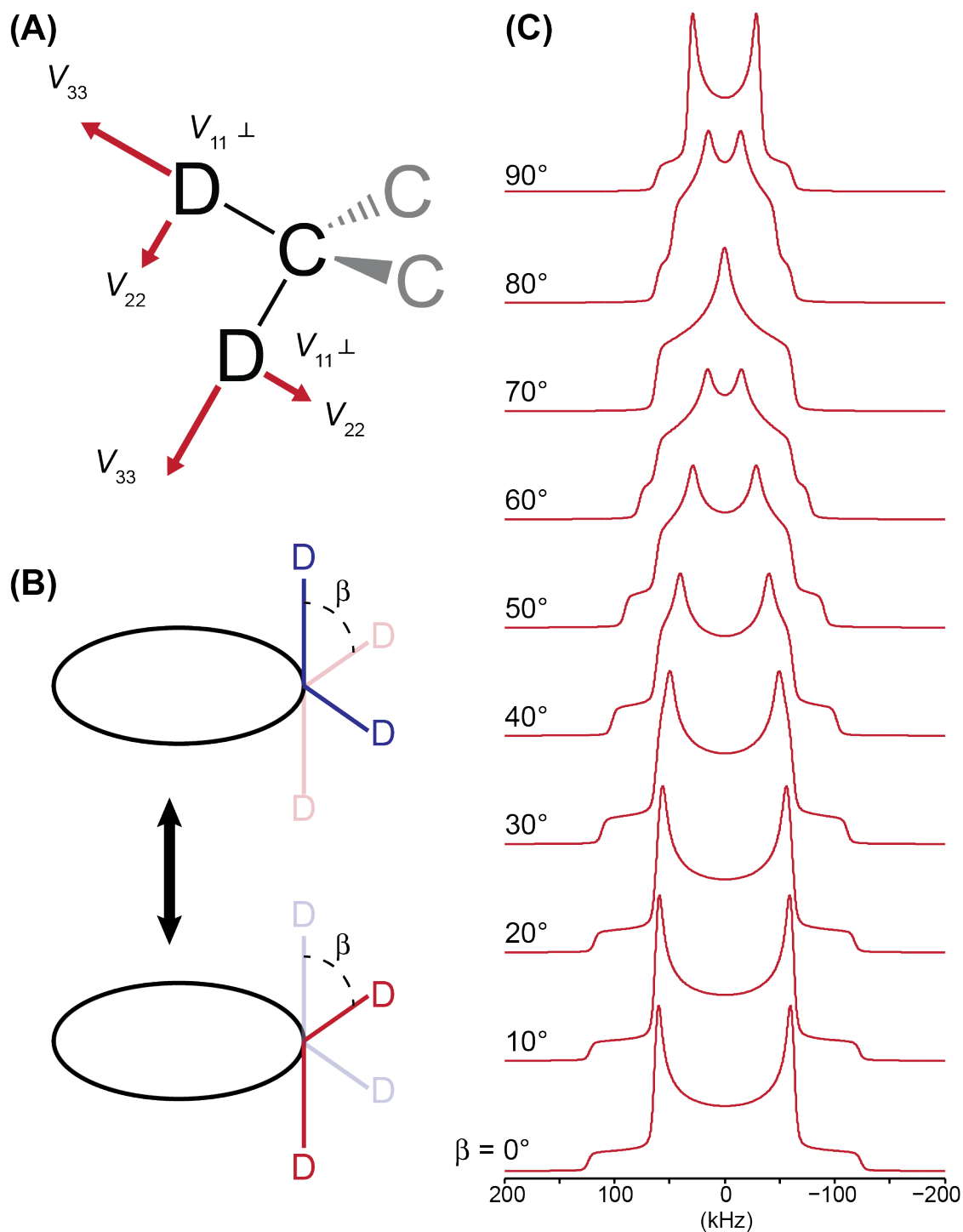


**Table C2:** Shuttling rates obtained from the simulation of solution-state  $^{13}\text{C}$  NMR data for the [2]rotaxane made from  $\text{A}_4$  and  $\text{CE}_4$ .

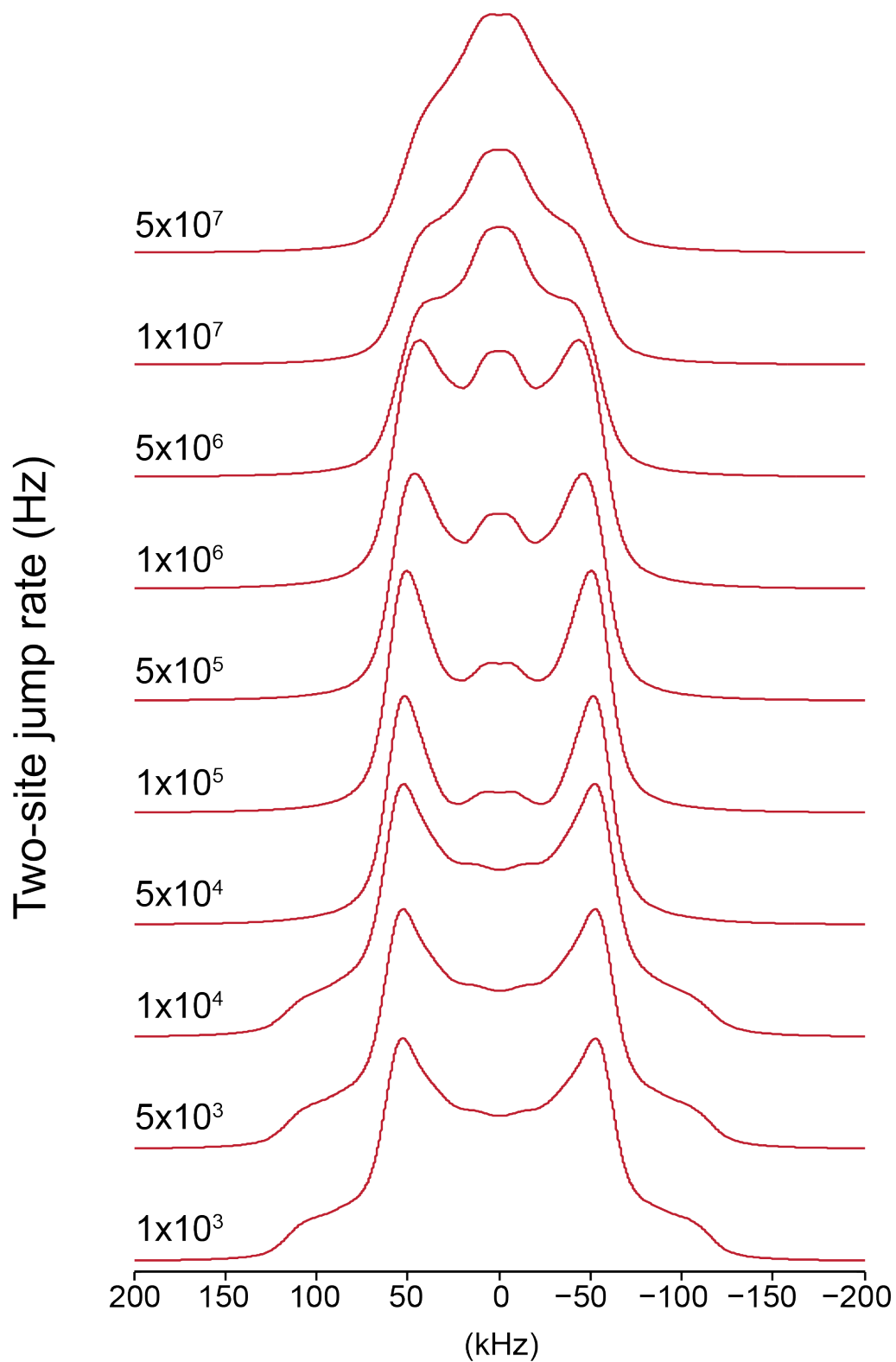
Temperature (K)	Rate (Hz)
210	565
213	830
218	2800
223	7000
228	13000
233	25000
238	65000
243	110000
253	310000
273	1400000
298	6900000



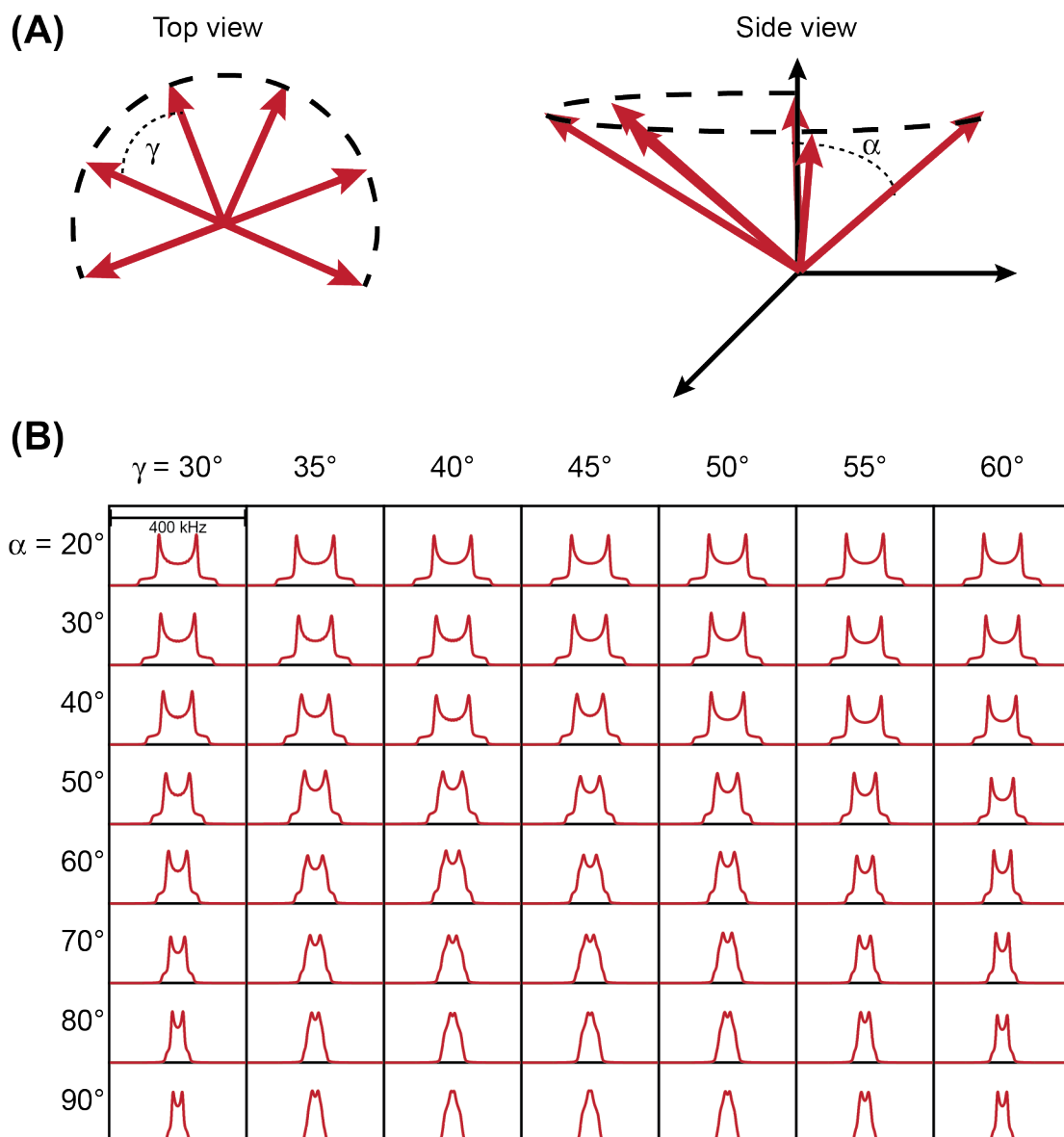
**Figure C1:** Simulation of a  $^2\text{H}$  SSNMR powder pattern showing the positions of the three sets of discontinuities (horns, shoulders and feet) and their respective frequency separations ( $\Delta v_{11}$ ,  $\Delta v_{22}$  and  $\Delta v_{33}$ ). Also shown are the relations between the positions of the discontinuities and the quadrupolar parameters ( $C_Q$  and  $\eta_Q$ ).



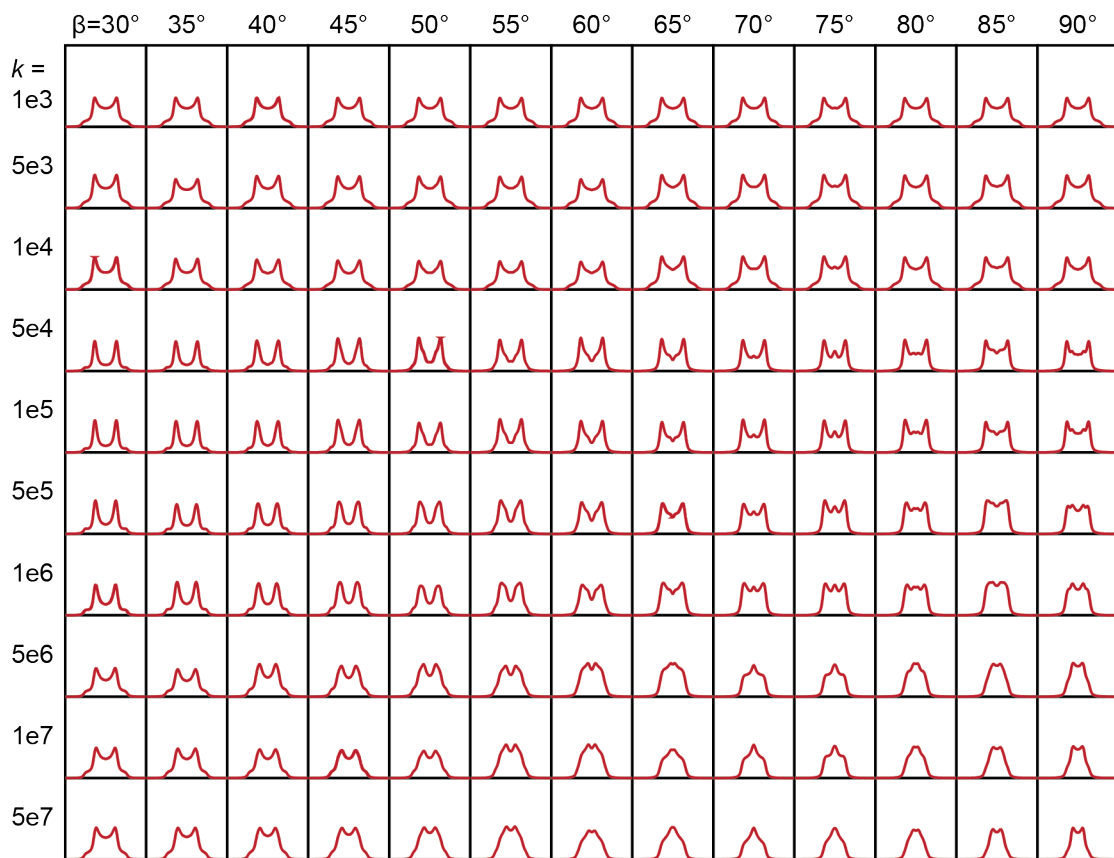
**Figure C2:** (A) Orientation of the <sup>2</sup>H EFG tensor for the deuterons in the alkyl region of the macrocycles in the MOF systems. (B) Depiction of the two-site jump motional model. The CH<sub>2</sub> group jumps through an angle  $\beta$  about an axis that is in the plane of the ring. (C) Simulated <sup>2</sup>H powder patterns for this motional model simulated in the FML with the corresponding values of  $\beta$ . The powder patterns were simulated using a SML EFG tensor with  $C_Q = 165$  kHz and  $h_Q = 0.0$ .



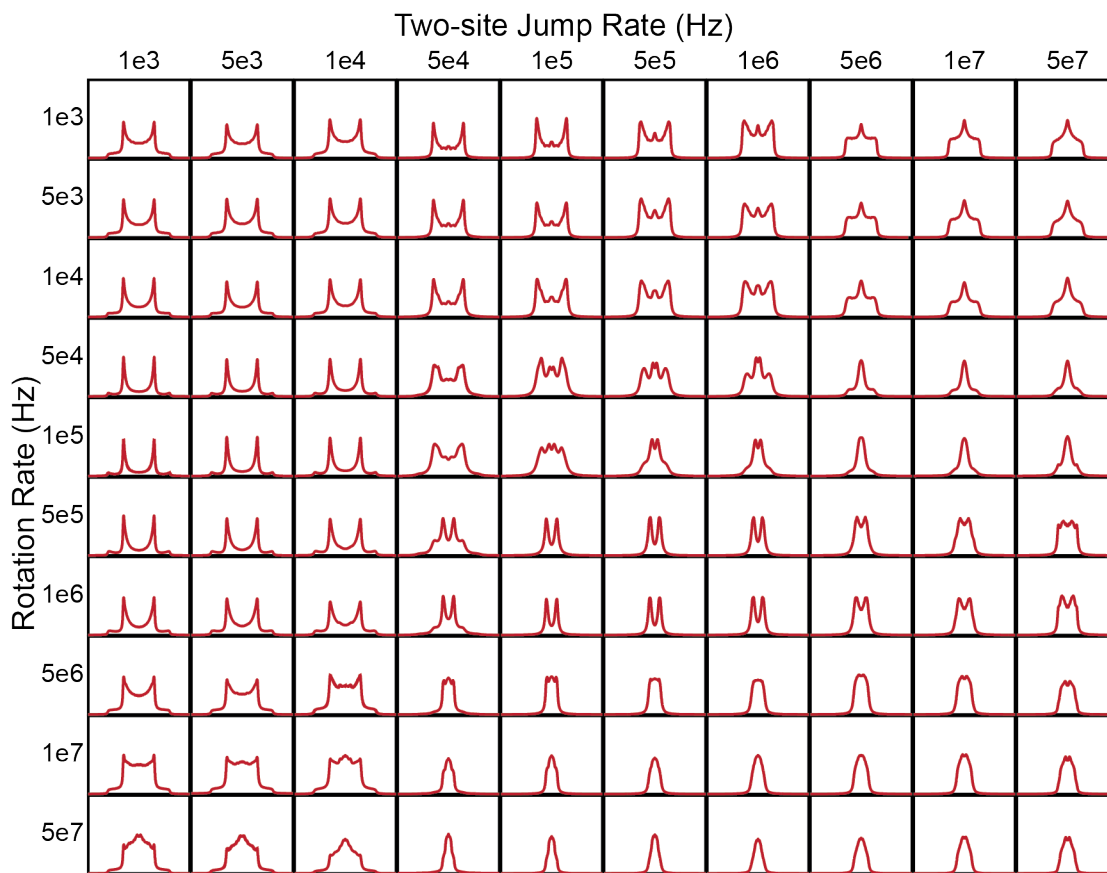
**Figure C3:** Simulated  $^2\text{H}$  SSNMR powder patterns for the two-site jump model with  $\beta = 77^\circ$  using rates within the three motional regimes. Rates in the SML are considered to be  $\leq 10^3$  Hz, IMR rates are between  $10^3$  and  $10^7$  Hz and FML rates are  $\geq 10^7$  Hz.



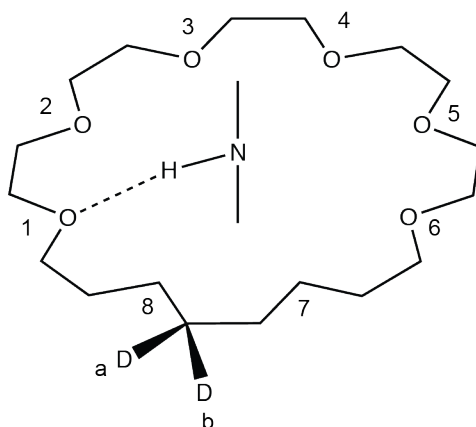
**Figure C4:** (A) Depiction of the partial rotation motional model. The  $V_{33}$  component of the EFG tensor is depicted with the red arrows and jumps between  $n$  sites separated by an angle  $\gamma$ . Jumps can only occur to adjacent sites. The sites that the deuteron can visit are offset from the rotation axis by the angle  $\alpha$ . (B) Simulated  $^2\text{H}$  powder patterns for this motional model simulated in the FML as a function of the angles  $\alpha$  and  $\gamma$  and by considering six rotational steps. The powder patterns were simulated using a SML EFG tensor with  $C_Q = 165$  kHz and  $\eta_Q = 0.0$ . It is noted that the right-most column represents the special case of full rotation.



**Figure C5:** Simulated  $^2\text{H}$  powder patterns using various rates ( $k$ ) for different two-site jump angles ( $\beta$ ). Simulations used a SML EFG tensor with  $C_Q = 165$  kHz and  $\eta_Q = 0.0$ .



**Figure C6:** Simulated  $^2\text{H}$  SSNMR powder patterns for a motional model consisting of two-site jumps through an angle of  $72^\circ$  combined with partial rotation where the ring jumps through an angle  $225^\circ$  in  $45^\circ$  steps.

**(A)****(B)**

$$K = \begin{pmatrix} -j-r-a & j & r & 0 & 0 & 0 & 0 & 0 & 0 & 0 & 0 & 0 & 0 & 0 & a & 0 \\ j & -j-r-a & 0 & r & 0 & 0 & 0 & 0 & 0 & 0 & 0 & 0 & 0 & 0 & 0 & a \\ r & 0 & -j-2r & j & r & 0 & 0 & 0 & 0 & 0 & 0 & 0 & 0 & 0 & 0 & 0 \\ 0 & r & j & -j-2r & 0 & r & 0 & 0 & 0 & 0 & 0 & 0 & 0 & 0 & 0 & 0 \\ 0 & 0 & r & 0 & -j-2r & j & r & 0 & 0 & 0 & 0 & 0 & 0 & 0 & 0 & 0 \\ 0 & 0 & 0 & r & j & -j-2r & 0 & r & 0 & 0 & 0 & 0 & 0 & 0 & 0 & 0 \\ 0 & 0 & 0 & 0 & r & 0 & -j-2r & j & r & 0 & 0 & 0 & 0 & 0 & 0 & 0 \\ 0 & 0 & 0 & 0 & 0 & r & j & -j-2r & 0 & r & 0 & 0 & 0 & 0 & 0 & 0 \\ 0 & 0 & 0 & 0 & 0 & 0 & r & 0 & -j-2r & j & r & 0 & 0 & 0 & 0 & 0 \\ 0 & 0 & 0 & 0 & 0 & 0 & 0 & 0 & r & j & -j-2r & 0 & r & 0 & 0 & 0 \\ 0 & 0 & 0 & 0 & 0 & 0 & 0 & 0 & 0 & r & 0 & -j-r-a & j & a & 0 & 0 \\ 0 & 0 & 0 & 0 & 0 & 0 & 0 & 0 & 0 & 0 & r & -j-r-a & j & -j-r-a & 0 & a \\ 0 & 0 & 0 & 0 & 0 & 0 & 0 & 0 & 0 & 0 & a & 0 & -j-2a & j & a & 0 \\ 0 & 0 & 0 & 0 & 0 & 0 & 0 & 0 & 0 & 0 & a & j & -j-2a & 0 & a & 0 \\ a & 0 & 0 & 0 & 0 & 0 & 0 & 0 & 0 & 0 & 0 & 0 & a & 0 & -j-2a & j \\ 0 & a & 0 & 0 & 0 & 0 & 0 & 0 & 0 & 0 & 0 & 0 & 0 & a & j & -j-2a \end{pmatrix} \begin{matrix} 1a \\ 1b \\ 2a \\ 2b \\ 3a \\ 3b \\ 4a \\ 4b \\ 5a \\ 5b \\ 6a \\ 6b \\ 7a \\ 7b \\ 8a \\ 8b \end{matrix}$$

**Figure C7:** (A) Schematic diagram showing the sites used in the simulation of  $\beta$ -UWDM-3. The numbered positions correspond to the rotational sites (1-6 are sites where the oxygen atoms on the ring form hydrogen bonds with the axle and sites 7 and 8 correspond to rotation through the alkyl portion of the ring). Sites *a* and *b* correspond to the two positions in the two-site jump model where the  $\text{CD}_2$  groups rotate about an axis in the plane of the ring. (B) Kinetic matrix used in the simulation of the high-temperature data for  $\beta$ -UWDM-3. *j* is the rate constant for the two-site jump motion, *r* is the rate constant for rotation between hydrogen-bonding positions and *a* is the rate constant for rotation through the alkyl portion of the ring.

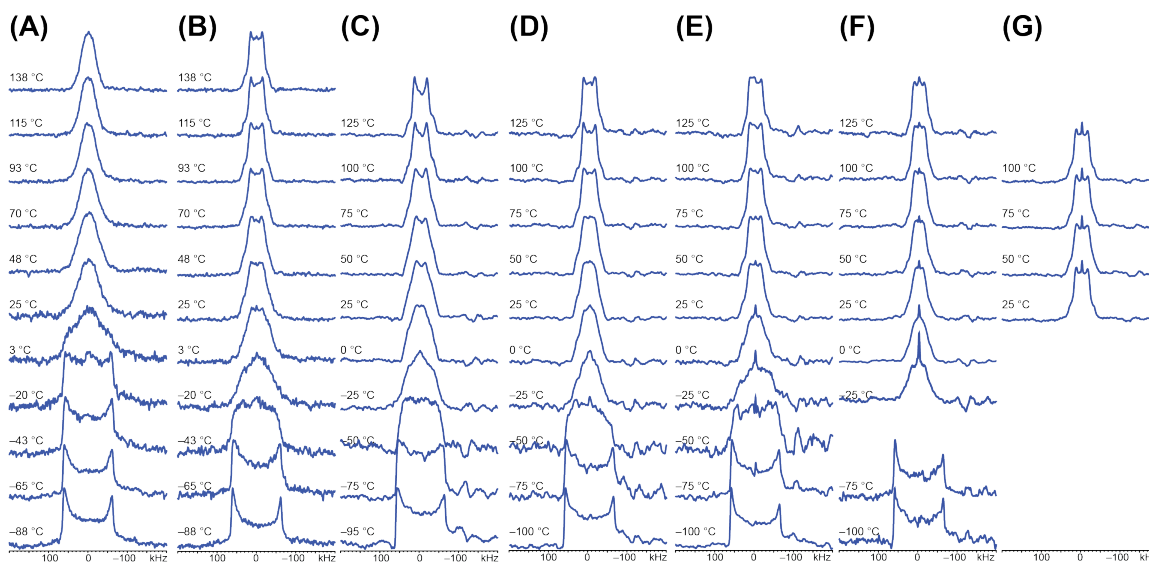


**Figure C8:** VT  $^2\text{H}$  SSNMR spectra of UWDM-P2 with (A) no solvent, or the addition of (B) dimethylformamide, (C) mesitylene, (D) dioxane, (E) 1-butanol, (F) ethylene glycol, or (G) triethylene glycol within the pores of the framework.

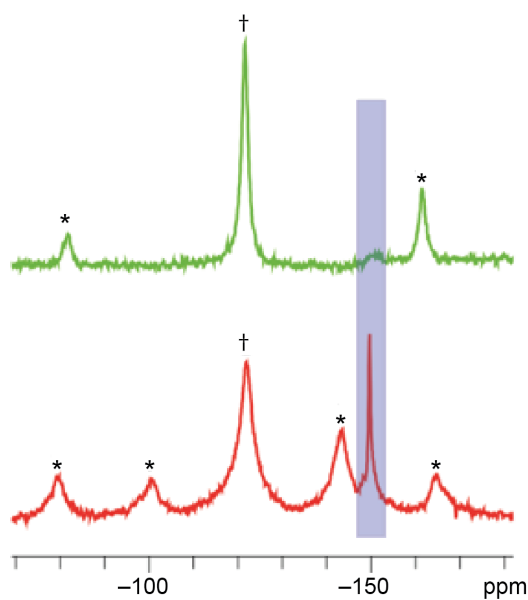


**Figure C9:**  $^{19}\text{F}$  MAS NMR spectra acquired for (A) UWDM-4 ( $\nu_{\text{rot}} = 18$  kHz) and (B) UWDM-4 $\cdot\text{HBF}_4$  ( $\nu_{\text{rot}} = 9.5$  kHz). The blue shaded region shows signal from the  $\text{BF}_4^-$  anion, † denote signal from the Teflon spacers and caps, and \* denote spinning sidebands of the Teflon signal.



UWDM3-neutral  $^{13}\text{C}$  VACP-MAS 8 kHz spinning speed processed with 50 Hz  
Gaussian broadening (0.3 offset) and two zero fills

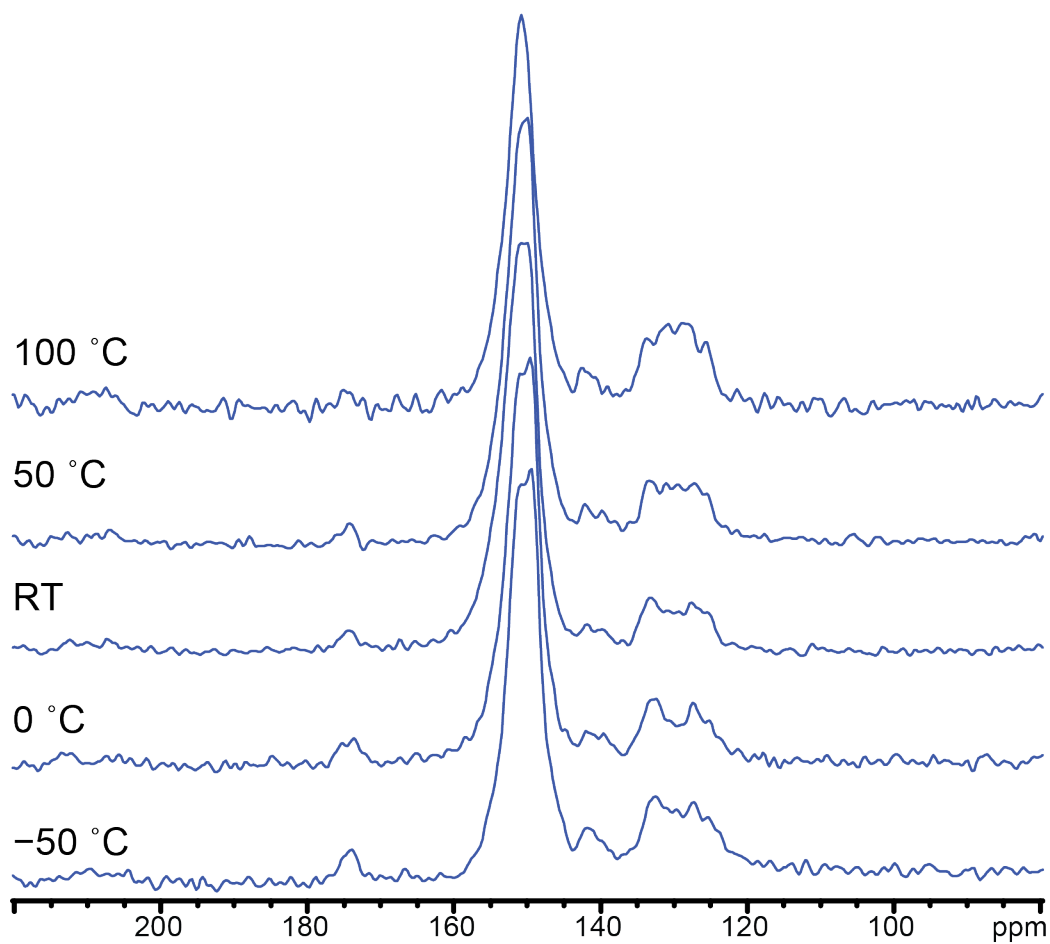


**Figure C10:**  $^1\text{H}$ - $^{13}\text{C}$  CP/MAS ( $v_{\text{rot}} = 8$  kHz) acquired at 9.4 T for neutral UWDM-4. The resolution of these spectra is too low to observe chemical exchange.

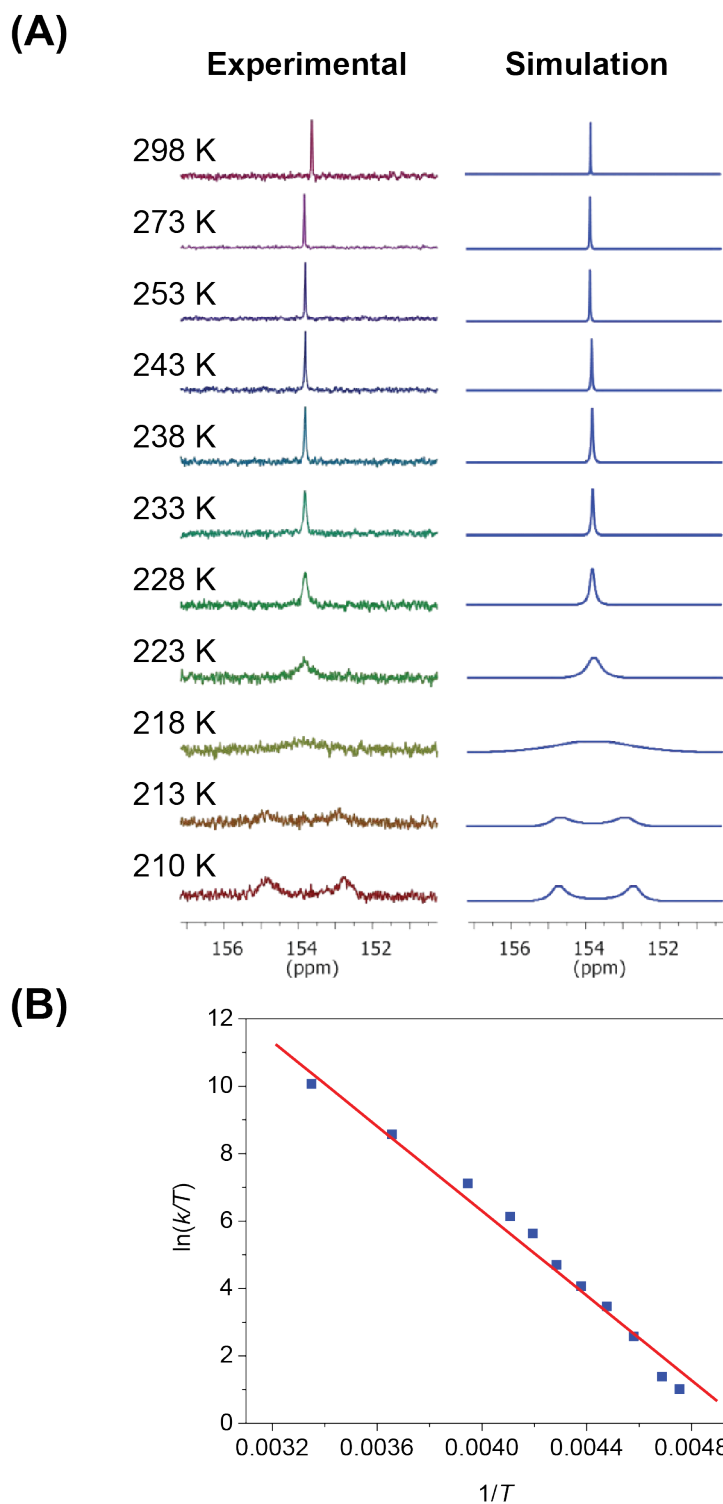


**Figure C11:** (A) Solution-state VT  $^{13}\text{C}$  NMR data of the [2]rotaxane made from **A<sub>4</sub>** and **CE<sub>4</sub>**. (B) The Eyring plot is generated from the  $^{13}\text{C}$  NMR data and used to calculate the thermodynamic parameters listed in **Table 4.12**.

## Appendix D Supporting Tables and Figures for Chapter 5

### Synthetic procedures:

#### Synthesis of (cod)PtCl<sub>2</sub>

(cod)PtCl<sub>2</sub> was synthesized using a modified literature procedure.<sup>1</sup> K<sub>2</sub>PtCl<sub>4</sub> (830 mg, 2.00 mmol) was dissolved in distilled H<sub>2</sub>O which was degassed with N<sub>2</sub>(g) in a round bottomed flask fitted with a condenser. 30 mL of an ethanol solution of 1,5-cyclooctadiene (0.267 M, 8.00 mmol) was added and the solution was refluxed at 100°C for 1 h. After 1 h, the reaction mixture was cooled in an ice bath. The white precipitate was collected by Millipore filtration, washed with H<sub>2</sub>O (3 x 5 mL) and Et<sub>2</sub>O (3 x 5 mL), and dried under high-vacuum to give pure (cod)PtCl<sub>2</sub> (620 mg, 83% yield).

#### Synthesis of 1-H

*trans*-H<sub>2</sub>Pt(P<sup>t</sup>Bu<sub>3</sub>)<sub>2</sub> was synthesized using a modified literature procedure.<sup>2</sup> A slurry containing (cod)PtCl<sub>2</sub> (112 mg, 0.300 mmol) and NaBH<sub>4</sub> (57.0 mg, 1.50 mmol) in 3.00 mL of dry toluene was prepared in a Pyrex bomb in a glove box under argon atmosphere. 600 μL of P<sup>t</sup>Bu<sub>3</sub> (1.00 M in toluene, 0.600 mmol) was added and the Pyrex bomb sealed. 500 μL of dry EtOH (13.8 mmol) was added using Schlenk line techniques under argon. The reaction was stirred overnight (15 h). The solvent was removed *in vacuo* and the crude product was extracted with dry toluene (3 x 2 mL) and filtered through a medium grain sintered filter. Slow evaporation of the filtrate under high-vacuum afforded colourless microcrystals of *trans*-H<sub>2</sub>Pt(P<sup>t</sup>Bu<sub>3</sub>)<sub>2</sub> (150 mg, 83.3% yield) which were collected and washed with dry hexanes (3 x 250 μL). Recrystallization from toluene/hexanes at -30°C gave single crystals suitable for X-ray crystallography.

## Synthesis of 1

A slurry containing (cod)PtCl<sub>2</sub> (100 mg, 0.267 mmol) and NaBD<sub>4</sub> (90.0 mg, 2.14 mmol) in 3.00 mL of dry toluene was prepared in a Pyrex bomb in a glove box under argon atmosphere. 535 μL of P<sup>t</sup>Bu<sub>3</sub> (1.00 M in toluene, 0.535 mmol) was added and the Pyrex bomb sealed. 500 μL of dry EtOD (13.5 mmol) was added using Schlenk line techniques under argon. The reaction was stirred overnight (15 h). The solvent was removed *in vacuo* and the crude products were extracted with dry toluene (3 x 2 mL) and filtered through a medium grain sintered filter. Slow evaporation of the filtrate under high-vacuum afforded colourless microcrystals composed of a mixture of *trans*-H<sub>2</sub>Pt(P<sup>t</sup>Bu<sub>3</sub>)<sub>2</sub> (**1-H**), *trans*-D<sub>2</sub>Pt(P<sup>t</sup>Bu<sub>3</sub>)<sub>2</sub> (**1**), *trans*-HDPt(P<sup>t</sup>Bu<sub>3</sub>)<sub>2</sub>, and *trans*-Pt(P<sup>t</sup>Bu<sub>3</sub>)<sub>2</sub> [150 mg, 93.8% yield], which was collected and washed with dry hexanes (3 x 250 μL).

**Table D1:** Recycle delays used in the acquisition of VT <sup>2</sup>H SSNMR spectra at 9.4 T

Compound	Recycle delay (s)
<b>1-D</b>	30
<b>2-D</b>	30
<b>3-D</b>	0.5
<b>4-D</b>	30
<b>5-D</b>	2.5

**Table D2:** Calculated hydrogen chemical shielding tensor parameters.

Compound	$\sigma_{\text{iso}}$	$\Omega$	$\kappa$
<b>1</b>	31.3	16.4	-0.19
<b>2</b>	32.7	23.2	-0.03
<b>4</b>	31.7	23.6	0.35
<b>5</b>	62.4	27.3	0.57

<sup>a</sup> Isotropic chemical shielding:  $\sigma_{\text{iso}} = (\sigma_{11} + \sigma_{22} + \sigma_{33})/3$ . <sup>b</sup> Span:  $\Omega = \sigma_{33} - \sigma_{11}$ . Skew:  $\kappa = 3(\delta_{\text{iso}} - \delta_{22})/\Omega$ . The shielding tensor parameters were not converted into chemical shift tensor parameters as a suitable reference compound for hydrogen shifts was not determined

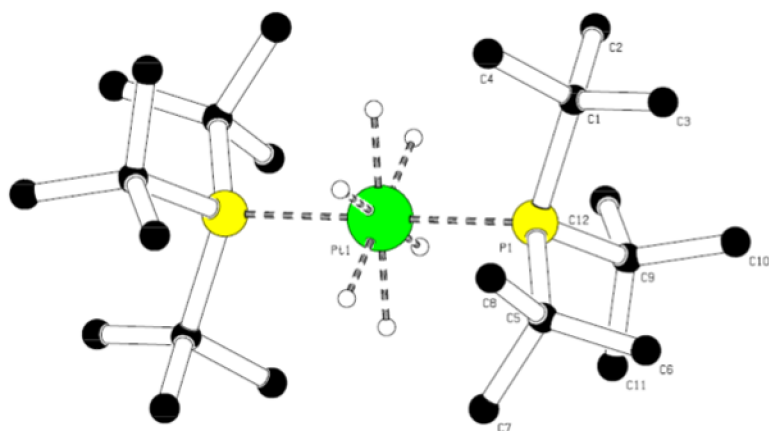


**Figure D1:** Crystal structure of **1-H** showing the disorder of the hydride ligands. Atom numbering is shown for one of the phosphine ligands.

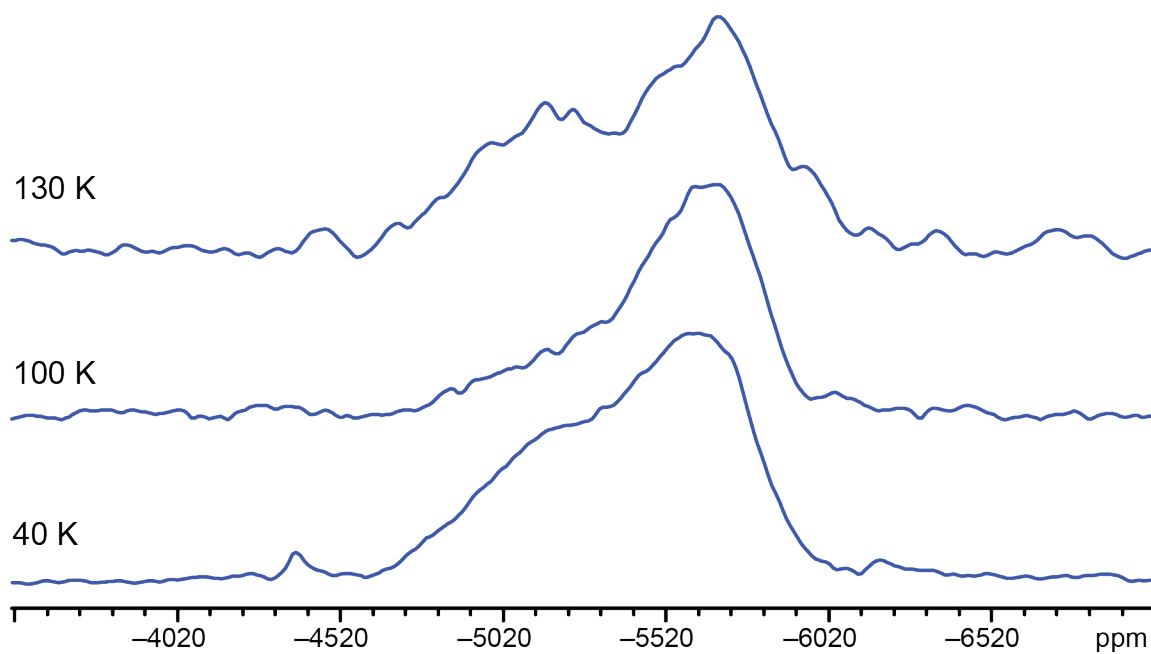


**Figure D2:** VT  $^{195}\text{Pt}$  SSNMR spectra for **1-H** acquired at 4.75 T. The low S/N is due to the long  $T_1(^{195}\text{Pt})$  at low temperatures and the experiments being run without  $^1\text{H}$  decoupling. The spectrum at 40 K was acquired with significantly more scans.

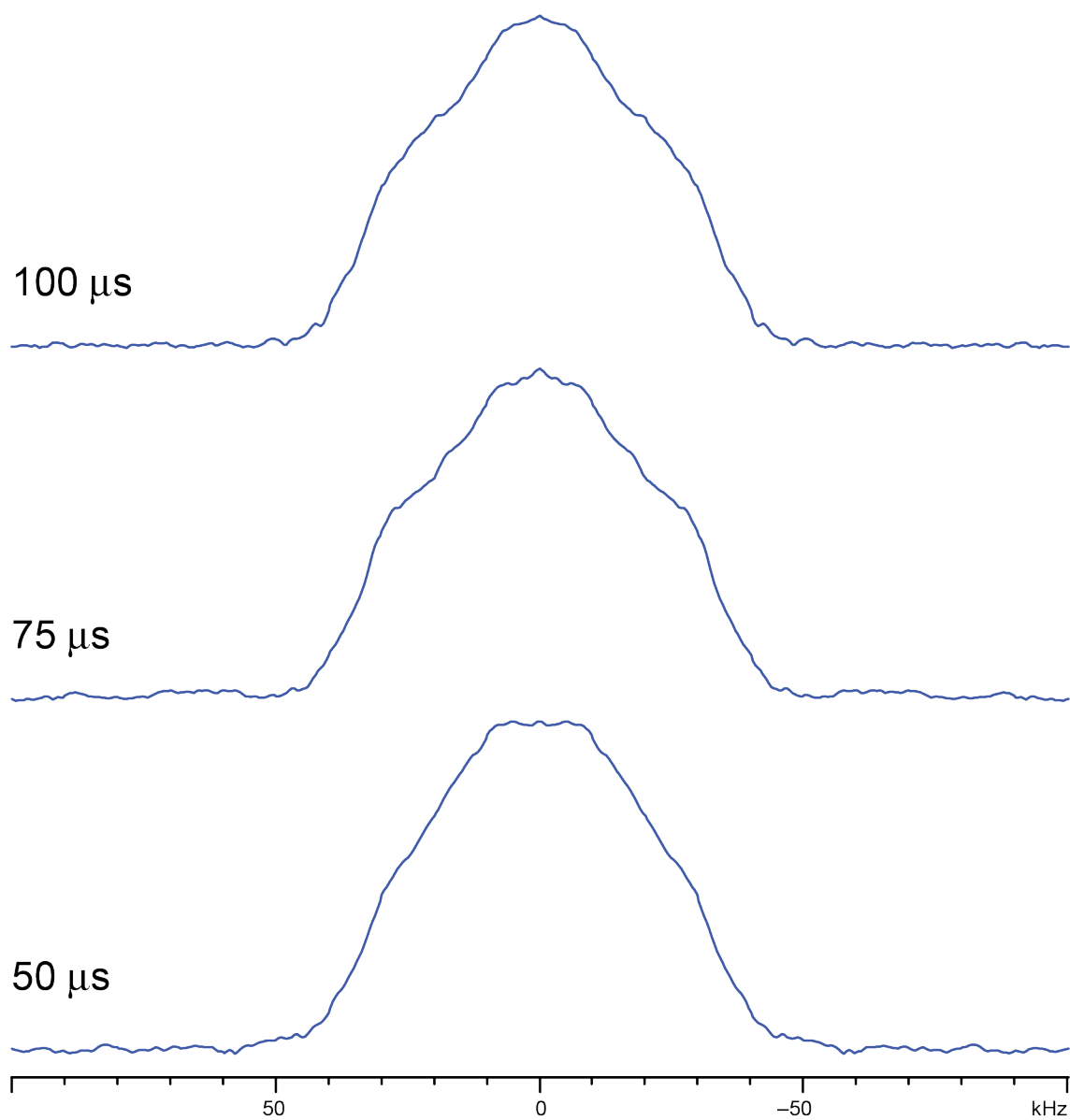


**Figure D3:**  $^2\text{H}$  SSNMR spectra acquired for **1-D** at 120 K with different values of the interpulse delay ( $\tau$ ). There are no appreciable differences in the spectra, indicating that the motion is occurring with rates in the FML.

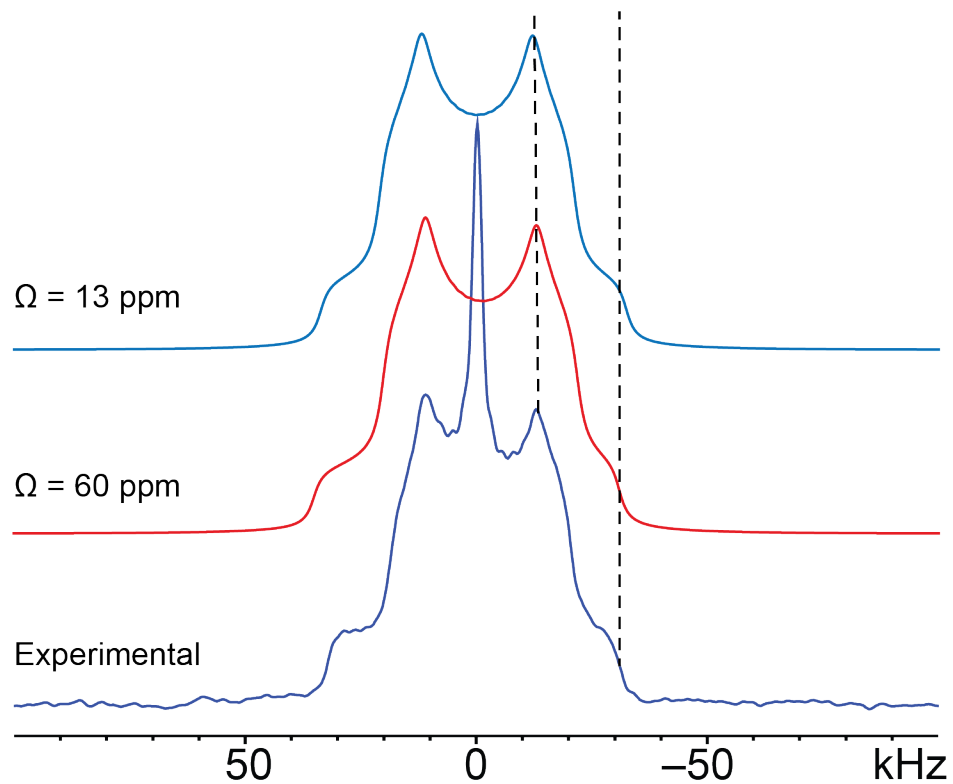


**Figure D4:** Simulations of the experimental  $^2\text{H}$  SSNMR for **1** pattern collected at 9.4 T and 298 K using  $\Omega = 60$  and 13 ppm. The latter value was obtained from DFT calculations. The dashed lines show the relative positions of the low-frequency discontinuities.

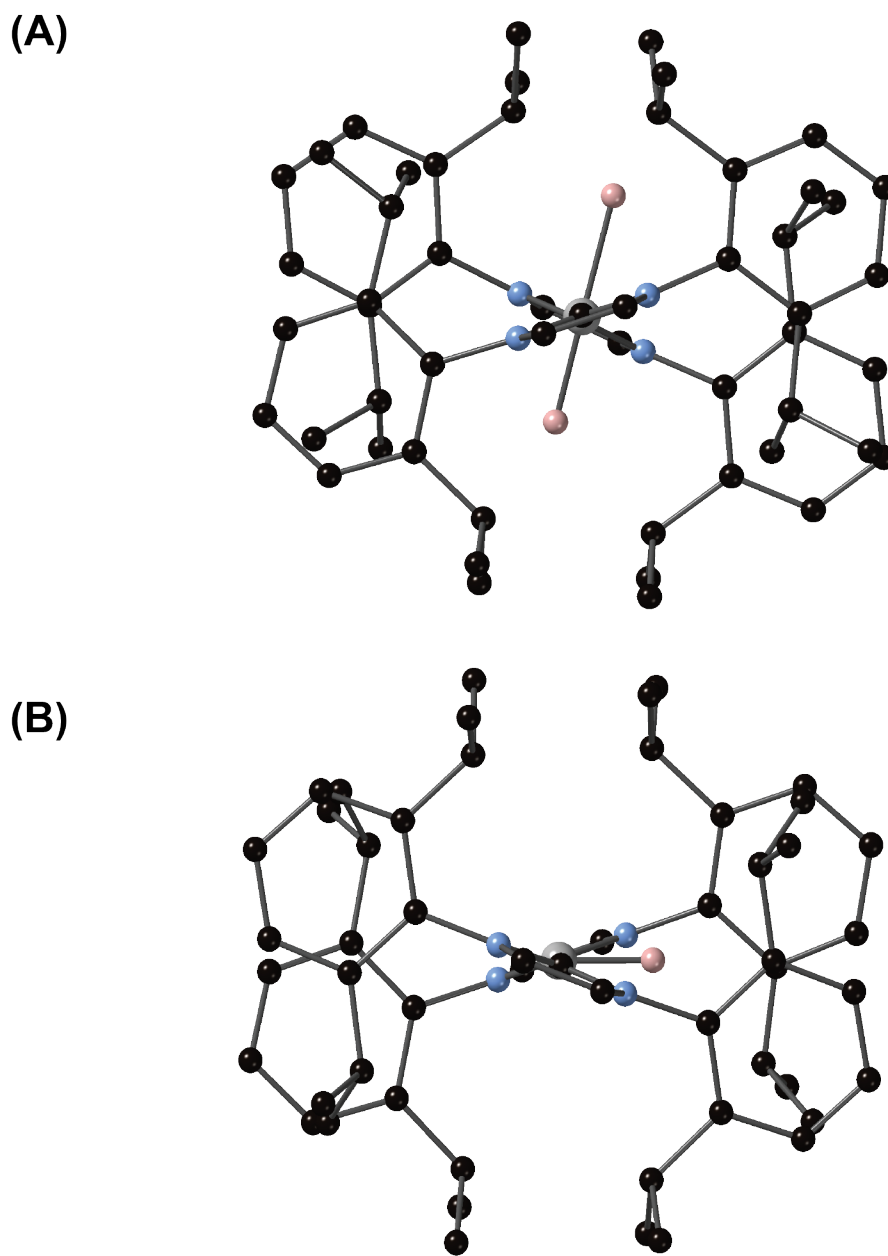


**Figure D5:** View along the C–Pt–C rotation axis showing the relative positions of the hydrides in (A) 4-H and (B) 5-H.

**References:**

- (1) Baker, M. V.; Brown, D. H.; Simpson, P. V.; Skelton, B. W.; White, A. H.; Williams, C. C. *J. Organomet. Chem.* **2006**, *691*, 5845–5855.
- (2) Goel, A. B.; Goel, S. *Inorg. Chim. Acta* **1982**, *65*, L77–L78.



## Appendix E Supplementary Information for Chapter 6

### Detailed discussion of NLMO analysis of NbCl<sub>5</sub>

For atom numbering refer to **Figure 6.10(A)**. Structural data are collected in **Table E9**. Selected LMOs in the Nb<sub>2</sub>Cl<sub>10</sub> complex are displayed in the form of isosurfaces in **Figure 6.10(B)** (see also **Figure E18**). Calculated and experimental EFG parameters are collected in **Table 6.2**. Graphical representations of the calculated EFG tensors are shown in **Figure 6.11**. An LMO analysis of the  $V_{33}$  for the different chlorine types is provided in **Table E11**. Further details about the composition of the most important LMOs are listed in **Table E12**. The discussion of the results refers frequently to the EFG paper by Autschbach, Zheng, and Schurko (AZS), Reference 64.

### The chlorine electronic environment

The EFGs are best discussed in reference to spherical Cl<sup>-</sup> ions, for which all components of the EFG tensor vanish identically. The LMOs representing the three lone pairs (LPs) of a Cl ligand, as calculated with the NBO program, are typically in the form of two  $\pi$  LPs and one  $\sigma$  LP, where  $\pi$  and  $\sigma$  refer to the local metal–Cl bond axis. In addition, one finds dative Cl $\rightarrow$ Nb  $\sigma$  bonds. The pattern is most obvious for the axial chlorines, Cl<sub>ax</sub>, and similar for the terminal equatorial chlorines Cl<sub>eq</sub> (**Figure 6.10(B)**). The Nb contributions in the  $\sigma$ (Cl–Nb) orbitals are 22% (Cl<sub>eq</sub>) and 15% (Cl<sub>ax</sub>), respectively, indicating that the bonds are only partially covalent.

In the sets of  $\pi$  LPs, there is also a significant degree of Cl–Nb covalency visible in the  $\pi$  LP orbitals. Since Nb(V) has no occupied 4*d* orbitals, one can indeed expect a degree of Cl $\rightarrow$ Nb  $\pi$  donation.

The bridging chlorines, Cl<sub>br</sub>, afford two formal lone pairs, and two LMOs that have 3-center bonding character (labeled as  $\mu$  in **Figure 6.10(B)**). When taking linear combinations of the 3-center LMOs, the Cl<sub>br</sub> environment is revealed as affording two partially covalent Cl–Nb bonding LMOs, one  $\sigma$  LP and one  $\pi$  LP.

### EFGs for the axial terminal chlorines

The case of the Cl<sub>ax</sub> appears to be most straightforward. Because the LPs are generated with local  $\pi$  and  $\sigma$  symmetry, we discuss the EFG based on an atomic hybridization model with two  $p_{\pi}$  lone pairs, and two  $sp^1$  hybrids, one of which is forming the Cl $\rightarrow$ Nb bond. The orientation of the EFG tensor for Cl<sub>ax</sub> is shown in **Figure 6.11**; the principal axis associated with the positive  $V_{33}$  is roughly parallel to the Cl–Nb axis. Without a covalent bond, and assuming that  $V_{33}$  lies exactly in the direction of the  $sp^1$  hybrids, the two  $\pi$  LPs would create relative contributions of +1 each to  $V_{33}$ , while each  $sp$  hybrid would contribute –1, resulting in a vanishing EFG. The LMO compositions in **Table E12** reveal that the  $\sigma$  LP is *s*-rich while  $\sigma$ (Cl–Nb) is *p*-rich. Sharing of electron density of the *p*-rich hybrid with Nb results, therefore, in a particularly strong loss of negative EFG at Cl (i.e.,  $V_{33} > 0$ ). However, the partially covalent nature of the  $\pi$  LPs simultaneously reduces their positive contributions to  $V_{33}$  as well. Therefore, the positive EFG for Cl<sub>ax</sub> is created by a balance between the  $\sigma$  and  $\pi$  donation from Cl to Nb, with the latter being weaker.

The numerical EFG analysis in **Table E11** fully supports the qualitative assessment. The imbalance between  $\sigma$ (Cl–Nb) and  $\sigma$  LP Cl(5) due to the *p*-rich character

of the former and the *s*-rich character of the latter is evident. If  $\sigma(\text{Cl-Nb})$  had 100% Cl *p* character and no Nb contributions, its negative contribution to  $V_{33}$  would be twice as large in magnitude as those from the  $\pi$  LPs (assuming that the latter also had no Nb character).

The relatively pure cylindrical symmetry of the  $\text{Cl}_{\text{ax}}$  environment is visible in the equal Nb character of 11% of the two  $\pi$  LP LMOs. The axial symmetry of the EFG tensor, with  $\eta$  close to zero, is a consequence of the approximately cylindrical electron distribution around the  $\text{Cl}_{\text{ax}}$ .

### EFGs for the equatorial terminal chlorines

The graphical representation of the  $\text{Cl}_{\text{eq}}$  EFG tensor in **Figure 6.11** immediately indicates the large asymmetry parameter. The  $V_{33}$  component is in the direction of the Cl-Nb bonds. The strong asymmetry of the tensor can be traced back to the non-equivalency of the formal Cl  $\pi$  LP orbitals. In fact, one of them (labeled  $\pi_y$ , with the Cl  $3p_y$  orbital lying in the equatorial plane), has a covalent Cl-Nb character of 18%, almost approaching that of the  $\sigma(\text{Cl}_{\text{eq}}\text{-Nb})$  LMO (22%), while the  $\text{Cl}_{\text{eq}} \pi_z$  LP has only 8% Nb character which is less than found for the  $\pi$  LPs of  $\text{Cl}_{\text{ax}}$ . The numerical EFG analysis shows that, indeed, the two  $\pi$  orbitals centered at  $\text{Cl}_{\text{eq}}$  contribute very differently to  $V_{33}$  at  $\text{Cl}_{\text{eq}}$ . The positive contribution from the partially bonding orbital is significantly lower than that of the  $\pi_z$  LP.

The EFG for the  $\text{Cl}_{\text{eq}}$  is positive overall. The reason is that the  $\sigma(\text{Cl-Nb})$  LMO has an even larger Nb character (22%) than the chlorine  $\pi$  orbitals. As a consequence, the negative  $V_{33}$  contribution from this orbital is particularly small in magnitude. Compare, for instance, the contribution of this orbital to  $V_{33}$ ,  $-3.9$  au, with the  $-5.7$  au generated by  $\sigma(\text{Cl-Nb})$  LMO at  $\text{Cl}_{\text{ax}}$ . Both orbitals have very similar  $3p$  character at Cl (75 and 74%, respectively), and therefore the difference in the EFG contributions must be due to the differences in the covalent Cl-Nb character. In comparison, the contributions from the  $\sigma$  LP orbitals at  $\text{Cl}_{\text{eq}}$  and  $\text{Cl}_{\text{ax}}$  are approximately equal. Both of these orbitals also have very similar chlorine  $3p$  characters of 26% and 27%, respectively.

The different nature of the EFG tensor, compared to that for the  $\text{Cl}_{\text{ax}}$ , with an asymmetry parameter much closer to unity and a positive EFG component in the direction of the Cl-Nb bond, can be understood with the help of an atomic hybrid orbital model. Assume a chlorine  $sp^1$  hybridization with the two  $sp$  hybrids along the *y* direction. The set of valence hybrid orbitals can be labeled  $p_x$ ;  $p_z$ ;  $sp_1$ ;  $sp_2$ . Furthermore, assume that  $sp_1$  is *p*-rich (75% *p* character) and  $sp_2$  is *s*-rich (25% *p* character). We assume populations of these Cl centered orbitals that reflect the partially covalent Cl-Nb bonding. For instance, consider a configuration  $(p_x)^{1.8}(p_z)^{1.9}(sp_1)^{1.6}(sp_2)^2$ , where  $sp_2$  is the  $\sigma$  LP hybrid. The setup approximately reflects the relative magnitudes of the Nb contributions in the LMOs according to **Table E11**. Next, evaluate the EFG tensor for such an atomic configuration (see the AZS paper for details and further examples). One obtains an  $\eta = 1$  tensor with Cartesian components (arbitrary units):

The small depopulation of the  $p_z$  orbital plays an important role in determining the balance between  $V_{22}$  and  $V_{33}$ , i.e., in which direction the largest-magnitude component lies. For example, for a configuration  $(p_x)^{1.8}(p_z)^2(sp_1)^{1.6}(sp_2)^2$ , the tensor would be

$$V = \begin{pmatrix} -5 & 0 & 0 \\ 0 & +20 & 0 \\ 0 & 0 & -25 \end{pmatrix}$$

in the same arbitrary units. The axis associated with  $V_{33}$  would now point in the  $z$  direction (the axial direction in the complex), and the second largest EFG tensor component would be along the Cl–Nb direction.

Without any bonding involving the Cl orbitals of local  $\pi$  symmetry, the EFG tensor would afford  $\eta = 1$ , with  $V_{33}$  positive and oriented along the Cl–Nb direction. Likewise, equal involvement of the  $\pi$  orbitals would create a tensor with  $\eta$  close to zero, as seen for the Cl<sub>ax</sub> environments. The experimentally determined large values for the asymmetry parameters for the terminal equatorial chlorine atoms can therefore be linked to the different involvement of orbitals with local  $\pi$  symmetry in the ligand–metal bonds.

### EFGs for the equatorial bridging chlorines

The case of the bridging chlorines, Cl<sub>br</sub>, is also very interesting. As the LMOs show, there are two equivalent weakly covalent Cl<sub>br</sub>–Nb bonds per Cl, along with relatively pure LP orbitals, one  $\pi$  (100% Cl 3*p*), and one  $\sigma$  (*s*-rich, about 70% Cl 3*s*). The largest-magnitude component of the EFG tensor points in the axial direction of the complex (along the  $z$  direction), as shown in **Figure 6.11**.

An understanding of why the tensor adopts this particular orientation in the complex derives from an atomic hybridization model for variable hybridization in the  $xy$  plane as previously adopted in the AZS paper. The set of hybrids formed from a set of  $s$ ;  $p_x$ ;  $p_y$ ;  $p_z$  atomic orbitals reads

$$(spn_1, spn_2, spn_3, p_z) = (s, p_x, p_y, p_z) \begin{pmatrix} -\gamma & -\frac{1}{\sqrt{2}}\sqrt{1-\gamma^2} & -\frac{1}{\sqrt{2}}\sqrt{1-\gamma^2} & 0 \\ \sqrt{1-\gamma^2} & -\frac{\gamma}{\sqrt{2}} & -\frac{\gamma}{\sqrt{2}} & 0 \\ 0 & -\frac{1}{\sqrt{2}} & \frac{1}{\sqrt{2}} & 0 \\ 0 & 0 & 0 & 1 \end{pmatrix}$$

where  $\gamma = \cot(\theta/2)$  goes from 1 to  $1/\sqrt{3}$  to zero, for an angle  $\theta = 90^\circ$  to  $\theta = 120^\circ$  to  $\theta = 180^\circ$ , respectively. The orbitals  $spn_2$  and  $spn_3$  form a set of bonding hybrids at an angle of  $\theta$ , whereas  $spn_1$  and  $p_z$  are considered lone pairs. For a  $90^\circ$  angle, one obtains a set of pure  $s$  and  $p$  orbitals, with  $spn_1$  being the  $s$  orbital, and  $spn_2$  and  $spn_3$  being two  $p$  orbitals pointing along the bonds at  $90^\circ$ . For an angle of  $120^\circ$ , one obtains an  $sp^2$  set, along with  $p_z$ . For an angle of  $180^\circ$ , one obtains two  $sp$  hybrids and two  $p$  orbitals. We refer to this set of hybrids as a variable- $n$   $sp^n$  set. The corresponding EFG tensor for populations of less than two for the bonding orbitals has been calculated previously<sup>4</sup> as:

$$\text{Configuration } (spn_1)^2(sp_n2)^{2\zeta}(sp_n3)^{2\zeta}(sp_n4)^2 \text{ with } 0 \leq \zeta \leq 1:$$

$$V = (1-\zeta) \begin{pmatrix} -(1-2\gamma^2) & 0 & 0 \\ 0 & (2-\gamma^2) & 0 \\ 0 & 0 & -(1+\gamma^2) \end{pmatrix}$$

For a bridging angle of  $102^\circ$ , as adopted in the  $\text{Nb}_2\text{Cl}_{10}$  complex (**Table E9**), the parameter in this model works out to be about 0.81, which gives a negative  $V_{33}$  in  $z$  direction (axial direction), and a positive  $V_{22}$  component in the  $xy$  plane perpendicular to the direction of Cl to the Nb–Nb midpoint. The EFG tensor for such an idealized atomic configuration is shown in **Figure E19** for  $\theta = 102^\circ$  and  $\zeta = 0.9$ . It is seen to be a suitable approximation of the calculated  $\text{Cl}_{\text{br}}$  EFG tensor for  $(\text{NbCl}_5)_2$  displayed in **Figure 6.11**. The fact that the  $\text{Cl}_{\text{br}}$   $\sigma$  LP orbital is  $s$ -rich is already incorporated in the model to a large degree. The idealized set of  $sp^n$  hybrids affords 66%  $s$  character for orbital  $spn_1$ . The actual  $s$  character of the  $\text{Cl}_{\text{br}}$   $\sigma$  LP LMO obtained from the DFT calculation and subsequent orbital localization is 70% (**Table E12**).

The numerical EFG analysis for  $\text{Cl}_{\text{br}}$  in **Table E11** supports the qualitative conclusions drawn from the atomic hybrid model: Since the  $V_{33}$  tensor component is perpendicular to the equatorial plane ( $V_{33}$  is along  $z$ , the axial direction), any depletion of chlorine electron density ‘in-plane’, relative to a spherical  $\text{Cl}^-$  ion, results in a negative  $V_{33}$ . The numerical data indeed shows that the positive in-plane EFG contributions at  $\text{Cl}_{\text{br}}$  are not capable of balancing the huge negative EFG from the Cl  $3p_z$ . The particularly large magnitude of  $V_{33}$  for the bridging chlorines may be attributed to two factors: (1) The  $3p_z$  orbital at Cl is not involved in covalent bonding and therefore fully contributes to the EFG. For the other chlorines in the complex, the analysis has shown that there is a partial cancellation of EFG contributions from orbitals with local  $\sigma$  and  $\pi$  symmetry. (2) The Nb– $\text{Cl}_{\text{br}}$ –Nb angle is only  $102^\circ$ , which means that the partially covalent bonds formed between Nb and Cl involve chlorine hybrids that are particularly  $p$ -rich. A loss in electron density from  $p$ -rich orbitals oriented perpendicular to a given axis ( $z$  in our case), as compared to an electron density loss from hybrids with higher  $s$  character, creates a particularly large EFG negative magnitude in the axis direction.

**Table E1:** Experimental times for the acquisition of  $^{35}\text{Cl}$  SSNMR spectra at 9.4 and 21.1 T.

Complex	Number of sub-spectra	9.4 T		Number of sub-spectra	21.1 T	
		Acquisition time per sub-spectrum (min)	Total acquisition time (hours)		Acquisition time per sub-spectrum (min)	Total acquisition time (hours)
<b>WCl<sub>6</sub></b>	21	13.5	4.7	2	0.27	0.01
<b>WOCl<sub>4</sub></b>	29	26.9	13	2	2.13	0.07
<b>MoOCl<sub>4</sub></b>	37	13.5	8.3	4	8.53	0.57
<b>NbCl<sub>5</sub></b>	33	13.5	7.4	3	8.53	0.43
<b>TaCl<sub>5</sub></b>	35	13.5	7.9	3	8.53	0.43



**Table E2:** WURST-CPMG acquisition parameters for  $^{35}\text{Cl}$  SSNMR spectra acquired at 9.4 T for all samples.

	<b>WCl<sub>6</sub></b>	<b>WOCl<sub>4</sub></b>	<b>MoOCl<sub>4</sub></b>	<b>NbCl<sub>5</sub></b>	<b>TaCl<sub>5</sub></b>
Pulse sequence	WURST-CPMG	WURST-CPMG	WURST-CPMG	WURST-CPMG	WURST-CPMG
Number of sub-spectra	76	29	37	33	69
Number of scans per sub-spectrum	1000	2000	1000	1000	1000
Recycle delay (s)	0.8	0.8	0.8	0.8	0.8
Meiboom-Gill loops [N]	40	40	40	40	40
Real points per loop	100	100	100	100	100
Acquisition length (number of points)	4000	4000	4000	4000	4000
Dwell ( $\mu\text{s}$ )	1.0	1.0	1.0	1.0	1.0
Sweep of WURST pulse (kHz)	2000	2000	2000	2000	2000
Sweep rate of WURST pulse (MHz/ms)	40	40	40	40	40
Spectral width (kHz)	1000	1000	1000	1000	1000
WURST pulse width ( $\mu\text{s}$ )	50	50	50	50	50
RF power (kHz)	21.7	21.7	21.7	21.7	21.7

**Table E3:** WURST-CPMG acquisition parameters for  $^{35}\text{Cl}$  SSNMR spectra acquired at 21.1 T for all samples.

	$\text{WCl}_6$	$\text{WOCl}_4$	$\text{MoOCl}_4$	$\text{NbCl}_5$	$\text{TaCl}_5$	$\text{WCl}_6\text{-SiO}_2$
Pulse sequence	WURST-CPMG	WURST-CPMG	WURST-CPMG	WURST-CPMG	WURST-CPMG	WURST-CPMG
Number of sub-spectra	2	2	4	3	3	1
Number of scans per sub-spectrum	16	128	512	512	512	56832
Recycle delay (s)	1	1	1	1	1	1
Meiboom-Gill loops [N]	160	160	320	320	160	360
Real points per loop	1600	1600	1600	1600	1600	200
Acquisition length (number of points)	256k	256k	512k	512k	256k	128k
Dwell ( $\mu\text{s}$ )	0.25	0.25	0.25	0.25	0.25	0.25
Sweep of WURST pulse (kHz)	2000	2000	2000	2000	2000	4000
Sweep rate of WURST pulse (MHz/ms)	40	40	40	40	40	80
Spectral width (kHz)	4000	4000	4000	4000	4000	4000
WURST pulse width ( $\mu\text{s}$ )	50	50	50	50	50	50
RF Power	35.7	35.7	35.7	35.7	35.7	35.7

**Table E4:** Pseudopotential information for CASTEP calculations.

<b>Atom</b>	<b>Pseudopotential String</b>
O	2 1.3 16.537 18.375 20.212 20UU:21UU(qc=7.5)[]
Cl	2 1.7 5.88 7.35 9.187 30UU:31UU:32LGG[]
Nb	3 2.2 2.2 1 7.7 8.8 10 40U=-2.145:50U=-0.145:41U=-1.27U=+0.25:42U=-0.1U=+0[]
Mo	3 2 2 2 8.9 10.1 11.7 40U=-2.365:50U=-0.15:41U=-1.415U+0.25:42U=-0.14U=+0.25[]
Ta	1 2.4 2.4 1.2 7 8.8 10 60U=-0.2U=+1.75:52U=-0.14U=+0[]
W	3 2.1 2.1 2.1 8.5 9.6 10.6 50U:60U:51UU:52UU[]



**Table E5:** Pre- and post-geometry optimization bond lengths.

<b>Complex</b>	<b>Bond</b>	<b>Pre-opt length (Å)</b>	<b>Post-opt length (Å)</b>
<b><math>\alpha</math>-WCl<sub>6</sub></b>	W1-Cl1	2.2374 ± 0.0568	2.2993
<b><math>\beta</math>-WCl<sub>6</sub></b>	W1-Cl1	2.2551 ± 0.0125	2.2998
	W1-Cl1	2.2551 ± 0.0103	2.2998
	W2-Cl2	2.5163 ± 0.0321	2.3007
	W2-Cl2	2.5170 ± 0.0328	2.3008
	W2-Cl3	2.0720 ± 0.0252	2.3005
	W2-Cl3	2.0728 ± 0.0240	2.3006
<b>WOCl<sub>4</sub></b>	W1-O1	1.8177 ± 0.1000	1.7369
	W1-O1	2.1773 ± 0.1000	2.2581
	W1-Cl1	2.2853 ± 0.0057	2.2971
<b>MoOCl<sub>4</sub></b>	Mo1-O1	1.6984 ± 0.0422	1.6638
	Mo1-Cl1	2.3952 ± 0.0999	2.2839
	Mo1-Cl2	2.2044 ± 0.0591	2.2956
	Mo1-Cl3	2.3517 ± 0.1307	2.3625
	Mo1-Cl4	2.3655 ± 0.0619	2.2941
	Mo1-Cl3	2.9913 ± 0.0389	3.1039
<b>NbCl<sub>5</sub></b>	Nb1-Cl1	2.5719 ± 0.0565	2.5678
	Nb1-Cl2	2.2587 ± 0.0737	2.2736
	Nb1-Cl3	2.3045 ± 0.1106	2.3197
	Nb2-Cl4	2.5691 ± 0.0555	2.5676
	Nb2-Cl5	2.2519 ± 0.0734	2.2760
	Nb2-Cl6	2.3027 ± 0.1159	2.3191
	Nb2-Cl7	2.5559 ± 0.0514	2.5662
	Nb2-Cl8	2.2560 ± 0.0736	2.2748
	Nb2-Cl9	2.3043 ± 0.1166	2.3203
<b>TaCl<sub>5</sub></b>	Ta1-Cl1	2.5437 ± 0.0104	2.5576
	Ta1-Cl2	2.2508 ± 0.0134	2.2902
	Ta1-Cl3	2.3123 ± 0.0217	2.3372
	Ta2-Cl4	2.5506 ± 0.0103	2.5580
	Ta2-Cl5	2.2520 ± 0.0132	2.2915
	Ta2-Cl6	2.3074 ± 0.0224	2.3376
	Ta2-Cl7	2.5475 ± 0.0103	2.5564
	Ta2-Cl8	2.2483 ± 0.0132	2.2921
	Ta2-Cl9	2.3024 ± 0.0223	2.3384

**Table E6:** Initial and post-optimization atomic forces in the structures.

<b>Complex</b>	<b>Atom</b>	<b>Pre-optimization Forces (eV/Å)</b>	<b>Post-optimization Forces (eV/Å)</b>
$\alpha$ -WCl <sub>6</sub>	Cl1	1.537072341	0.007916729
	Cl2	1.537072341	0.007916729
	Cl3	1.537072341	0.007916729
	Cl4	1.537077134	0.007916773
	Cl5	1.537077134	0.007916773
	Cl6	1.537077134	0.007916773
	Cl7	1.537075852	0.007918264
	Cl8	1.537075852	0.007918264
	Cl9	1.537075852	0.007918264
	Cl10	1.537072341	0.007916729
	Cl11	1.537072341	0.007916729
	Cl12	1.537072341	0.007916729
	Cl13	1.537077134	0.007916773
	Cl14	1.537077134	0.007916773
	Cl15	1.537077134	0.007916773
	Cl16	1.537075852	0.007918264
	Cl17	1.537075852	0.007918264
	Cl18	1.537075852	0.007918264
	W1	0	0
	W2	0	0
	W3	0	0
$\beta$ -WCl <sub>6</sub>	Cl1	1.098937213	0.005427053
	Cl2	0.881171831	0.004108832
	Cl3	4.224856502	0.003680666
	Cl4	1.098937213	0.005427053
	Cl5	0.881171831	0.004108832
	Cl6	4.224856502	0.003680666
	Cl7	1.098939076	0.005423099
	Cl8	0.881172545	0.004107761
	Cl9	4.22486116	0.003683653
	Cl10	1.098937213	0.005427053
	Cl11	0.881171831	0.004108832
	Cl12	4.224856502	0.003680666
	Cl13	1.098939076	0.005423099
	Cl14	0.881172545	0.004107761
	Cl15	4.22486116	0.003683653
	Cl16	1.098937213	0.005427053
	Cl17	0.881171831	0.004108832
	Cl18	4.224856502	0.003680666
	W1	0	0
	W2	7.88254	0.00658
	W3	7.88254	0.00658

<b>WOCl<sub>4</sub></b>	O1	2.26108	0.02615
	O2	2.26108	0.02615
	Cl1	0.246414192	0.032597715
	Cl2	0.246414192	0.032597715
	Cl3	0.246414192	0.032597715
	Cl4	0.246414192	0.032597715
	Cl5	0.246414192	0.032597715
	Cl6	0.246414192	0.032597715
	Cl7	0.246414192	0.032597715
	Cl8	0.246414192	0.032597715
	W1	2.027	0.02052
	W2	2.027	0.02052
<b>MoOCl<sub>4</sub></b>	O1	1.668418499	0.00342965
	O2	1.668418499	0.00342965
	Cl1	1.047502325	0.007060779
	Cl2	0.960480992	0.006229486
	Cl3	0.104390131	0.007912357
	Cl4	0.536009503	0.006370377
	Cl5	1.047502325	0.007060779
	Cl6	0.960480992	0.006229486
	Cl7	0.104390131	0.007912357
	Cl8	0.536009503	0.006370377
	Mo1	3.067000005	0.009570042
	Mo2	3.067000005	0.009570042
<b>NbCl<sub>5</sub></b>	Cl1	0.286530543	0.001447964
	Cl2	0.281517328	0.006154064
	Cl3	0.453164882	0.00643461
	Cl4	0.360999519	0.009185124
	Cl5	0.35690131	0.005401805
	Cl6	0.327939184	0.004142053
	Cl7	0.286530543	0.001447964
	Cl8	0.281517328	0.006154064
	Cl9	0.453164882	0.00643461
	Cl10	0.360999519	0.009185124
	Cl11	0.35690131	0.005401805
	Cl12	0.327939184	0.004142053
	Cl13	0.286530543	0.001447964
	Cl14	0.281517328	0.006154064
	Cl15	0.453164882	0.00643461
	Cl16	0.360999519	0.009185124
	Cl17	0.35690131	0.005401805
	Cl18	0.327939184	0.004142053
	Cl19	0.286530543	0.001447964

CI20	0.281517328	0.006154064
CI21	0.453164882	0.00643461
CI22	0.360999519	0.009185124
CI23	0.35690131	0.005401805
CI24	0.327939184	0.004142053
CI25	0.286530543	0.001447964
CI26	0.281517328	0.006154064
CI27	0.453164882	0.00643461
CI28	0.360999519	0.009185124
CI29	0.35690131	0.005401805
CI30	0.327939184	0.004142053
CI31	0.286530543	0.001447964
CI32	0.281517328	0.006154064
CI33	0.453164882	0.00643461
CI34	0.360999519	0.009185124
CI35	0.35690131	0.005401805
CI36	0.327939184	0.004142053
CI37	0.286530543	0.001447964
CI38	0.281517328	0.006154064
CI39	0.453164882	0.00643461
CI40	0.360999519	0.009185124
CI41	0.35690131	0.005401805
CI42	0.327939184	0.004142053
CI43	0.286530543	0.001447964
CI44	0.281517328	0.006154064
CI45	0.453164882	0.00643461
CI46	0.360999519	0.009185124
CI47	0.35690131	0.005401805
CI48	0.327939184	0.004142053
CI49	0.171257926	0.004525273
CI50	0.120437444	0.008294558
CI51	0.371876174	0.002959409
CI52	0.171257926	0.004525273
CI53	0.120437444	0.008294558
CI54	0.371876174	0.002959409
CI55	0.171257926	0.004525273
CI56	0.120437444	0.008294558
CI57	0.371876174	0.002959409
CI58	0.171257926	0.004525273
CI59	0.120437444	0.008294558
CI60	0.371876174	0.002959409
Nb1	0.387779713	0.003866614
Nb2	0.387779713	0.003866614
Nb3	0.387779713	0.003866614
Nb4	0.387779713	0.003866614
Nb5	0.387779713	0.003866614

	Nb6	0.387779713	0.003866614
	Nb7	0.387779713	0.003866614
	Nb8	0.387779713	0.003866614
	Nb9	0.28832	0.00532
	Nb10	0.28832	0.00532
	Nb11	0.28832	0.00532
	Nb12	0.28832	0.00532
<b>TaCl<sub>5</sub></b>	Cl1	0.912403647	0.002330536
	Cl2	0.558784658	0.007632876
	Cl3	0.932347808	0.003890578
	Cl4	0.677532468	0.009191175
	Cl5	1.021712316	0.006893976
	Cl6	0.763711531	0.007362228
	Cl7	0.912403647	0.002330536
	Cl8	0.558784658	0.007632876
	Cl9	0.932347808	0.003890578
	Cl10	0.677532468	0.009191175
	Cl11	1.021712316	0.006893976
	Cl12	0.763711531	0.007362228
	Cl13	0.912403647	0.002330536
	Cl14	0.558784658	0.007632876
	Cl15	0.932347808	0.003890578
	Cl16	0.677532468	0.009191175
	Cl17	1.021712316	0.006893976
	Cl18	0.763711531	0.007362228
	Cl19	0.912403647	0.002330536
	Cl20	0.558784658	0.007632876
	Cl21	0.932347808	0.003890578
	Cl22	0.677532468	0.009191175
	Cl23	1.021712316	0.006893976
	Cl24	0.763711531	0.007362228
	Cl25	0.912403647	0.002330536
	Cl26	0.558784658	0.007632876
	Cl27	0.932347808	0.003890578
	Cl28	0.677532468	0.009191175
	Cl29	1.021712316	0.006893976
	Cl30	0.763711531	0.007362228
	Cl31	0.912403647	0.002330536
	Cl32	0.558784658	0.007632876
	Cl33	0.932347808	0.003890578
	Cl34	0.677532468	0.009191175
	Cl35	1.021712316	0.006893976
	Cl36	0.763711531	0.007362228
	Cl37	0.912403647	0.002330536
	Cl38	0.558784658	0.007632876

CI39	0.932347808	0.003890578
CI40	0.677532468	0.009191175
CI41	1.021712316	0.006893976
CI42	0.763711531	0.007362228
CI43	0.912403647	0.002330536
CI44	0.558784658	0.007632876
CI45	0.932347808	0.003890578
CI46	0.677532468	0.009191175
CI47	1.021712316	0.006893976
CI48	0.763711531	0.007362228
CI49	0.310815588	0.004346596
CI50	0.222146514	0.005438318
CI51	0.24656556	0.002262145
CI52	0.310815588	0.004346596
CI53	0.222146514	0.005438318
CI54	0.24656556	0.002262145
CI55	0.310815588	0.004346596
CI56	0.222146514	0.005438318
CI57	0.24656556	0.002262145
CI58	0.310815588	0.004346596
CI59	0.222146514	0.005438318
CI60	0.24656556	0.002262145
Ta1	0.730966338	0.008209294
Ta2	0.730966338	0.008209294
Ta3	0.730966338	0.008209294
Ta4	0.730966338	0.008209294
Ta5	0.730966338	0.008209294
Ta6	0.730966338	0.008209294
Ta7	0.730966338	0.008209294
Ta8	0.730966338	0.008209294
Ta9	0.67992	0.00479
Ta10	0.67992	0.00479
Ta11	0.67992	0.00479
Ta12	0.67992	0.00479

---

**Table E7:** Calculated (using CASTEP)  $^{35}\text{Cl}$  CS tensor parameters. Calculation of the NMR parameters was completed both prior to and post geometry optimization of the structure.

Complex	Atom	Pre-optimization			Post-optimization		
		$\delta_{\text{iso}}$ (ppm)	$\Omega$ (ppm)	$\kappa$	$\delta_{\text{iso}}$ (ppm)	$\Omega$ (ppm)	$\kappa$
$\alpha\text{-WCl}_6$	C11	837.67	58.39	-0.057	899.92	69.83	0.593
$\beta\text{-WCl}_6$	C11	833.16	196.15	0.497	887.60	228.91	0.471
	C12	703.09	430.12	-0.277	884.81	248.47	0.435
	C13	960.76	337.20	0.868	899.30	217.62	0.450
$\text{WOCl}_4$	C11	767.43	305.65	-0.618	740.92	342.07	-0.868
$\text{MoOCl}_4$	C11	910.467	517.37	-0.427	886.95	660.23	-0.515
	C12	974.01	798.07	-0.521	921.73	695.72	-0.189
	C13	620.29	487.24	-0.398	604.14	419.02	-0.571
	C14	901.71	725.77	0.104	875.33	762.19	-0.050
$\text{NbCl}_5$	C11	983.63	986.15	0.228	963.76	1080.89	0.308
	C12	819.59	617.09	0.888	837.78	659.78	0.807
	C13	978.82	1012.70	0.216	983.04	1082.83	0.365
	C14	821.88	600.31	0.961	854.32	700.90	0.734
	C15	982.61	1005.64	0.229	998.06	1025.27	0.169
	C16	802.45	614.45	0.972	841.50	669.54	0.837
	C17	378.80	172.63	0.046	363.55	255.67	0.462
	C18	352.46	231.48	0.450	386.77	194.88	0.602
	C19	373.91	242.50	0.374	354.48	227.72	-0.079
$\text{TaCl}_5$	C11	893.95	856.60	0.306	928.36	955.42	0.293
	C12	710.42	502.02	0.853	734.55	540.63	0.927
	C13	890.23	864.97	0.280	931.61	927.24	0.286
	C14	711.71	490.51	0.902	742.93	558.12	0.884
	C15	894.66	856.47	0.277	927.06	930.19	0.349
	C16	705.12	509.10	0.862	735.30	571.27	0.844
	C17	310.50	217.23	0.228	323.33	251.67	0.529
	C18	302.39	214.81	0.311	334.30	189.24	0.306
	C19	306.71	216.35	0.260	338.56	214.42	0.428

**Table E8:**  $T_2$  measurements made by placing the transmitter on each of the discontinuities of the  $^{35}\text{Cl}$  SSNMR powder patterns.

Complex	Discontinuity <sup>a</sup>	Frequency (MHz)	$T_2$ (ms)
<b>WCl<sub>6</sub></b>	HF horn	88.484744	126(3)
	central	88.2361209	116(3)
	LF horn	87.8422801	88(1)
<b>WOCl<sub>4</sub></b>	HF horn	88.5861728	93(2)
	central	88.2163264	61(2)
	LF horn	87.6489894	62(1)
<b>MoOCl<sub>4</sub></b>	HF horn, large	88.5282208	53(1)
	HF horn, mid	88.4728915	51(1)
	HF horn, small	88.4240720	50(1)
	central	88.2792384	46(1)
	central 2	88.2515733	44(1)
	LF horn, small	87.9944541	42(1)
	LF horn, mid	87.9684169	41(1)
LF horn, large	87.8677108	42(1)	
<b>NbCl<sub>5</sub></b>	HF horn, large	88.4684169	66(3)
	HF horn, mid	88.3638598	76(1)
	HF horn, small	88.2329408	82(1)
	central	88.2320458	84(1)
	central 2	88.2108905	82(1)
	LF horn, small	88.1848523	86(1)
	LF horn, mid	88.0546653	79(1)
	LF horn, large	87.8203284	58(2)
<b>TaCl<sub>5</sub></b>	HF horn, large	88.4561412	13(1)
	HF horn, mid	88.3659350	33(1)
	HF horn, small	88.3364512	34(1)
	central	88.2229182	30(1)
	LF horn, small	88.1346461	30(1)
	LF horn, mid	88.0093982	27(1)
LF horn, large	87.8818843	26(1)	



**Table E9:** Structural parameters of (NbCl<sub>5</sub>)<sub>2</sub>. Selected averaged XRD and optimized (OPT)<sup>a</sup> bond distances (Å) and bond angles (°).

Bond	XRD	OPT
Nb-Cl <sub>ax</sub>	2.304	2.333
Nb-Cl <sub>eq</sub>	2.254	2.290
Nb-Cl <sub>br</sub>	2.563	2.604
Nb-Nb-Cl <sub>ax</sub>	84.3	84.9
Nb-Cl <sub>br</sub> -Nb	101.9	102.9

<sup>a</sup>XRD were used as starting geometries then optimized with scalar-ZORA/revPBE/TZ2P.

**Table E10:** Comparison of experimental (EXP) and calculated <sup>35</sup>Cl EFG tensor parameters (using ADF and CASTEP (CSP)) on a geometry optimized structure of NbCl<sub>5</sub>, as well as ADF calculations performed on non-optimized crystal structures (XRD).

Cl	$C_Q$ (MHz) <sup>a</sup>				$\eta_Q$ <sup>b</sup>				$V_{33}$ (au) <sup>c</sup>			
	EXP	ADF	CSP	XRD	EXP	ADF	CSP	XRD	EXP	ADF	CSP	XRD
2	14.30	-15.55	-12.61	-13.53	0.72	0.79	0.75	0.85	-0.75	0.81	0.66	0.71
3		-15.55	-12.61	-13.53		0.79	0.75	0.85		0.81	0.66	0.71
7		-15.54	-14.28	-13.31		0.79	0.80	0.85		0.81	0.74	0.69
8		-15.54	-14.28	-13.31		0.79	0.80	0.85		0.81	0.74	0.69
1	25.35	25.40	24.74	25.28	0.375	0.40	0.42	0.31	-1.32	-1.32	-1.29	-1.32
6		25.39	23.22	24.96		0.40	0.48	0.32		-1.32	-1.21	-1.30
4	14.25	-13.54	-13.24	-12.94	0.052	0.01	0.10	0.07	-0.74	0.71	0.69	0.67
5		-13.54	-13.24	-12.94		0.01	0.10	0.07		0.71	0.69	0.67
9		-13.40	-13.07	-12.87		0.01	0.17	0.07		0.70	0.68	0.67
10		-13.40	-13.07	-12.87		0.01	0.17	0.07		0.70	0.68	0.67

<sup>a</sup>  $C_Q = eQV_{33}/h$ , <sup>b</sup>  $\eta_Q = (V_{11} - V_{22})/V_{33}$ , <sup>c</sup>  $V_{33}$  is the largest component of the EFG tensor in its principal axis system.

**Table E11:** LMO contributions to the  $V_{33}$  component of equatorial (eq), bridging (br) and axial (ax) chlorides in the complex  $(\text{NbCl}_5)_2$ . All values are in au.

<b>LMO type</b>	<b>Cl<sub>eq</sub>(8)</b>	<b>Cl<sub>br</sub>(6)</b>	<b>Cl<sub>ax</sub>(5)</b>
core Cl(5)	0.03	-0.05	0.06
core Cl(6)	0.02	-0.16	0.01
core Cl(8)	0.08	0.01	0.04
core Cls	0.26	-0.17	0.23
core Nb	-0.57	0.40	-0.52
$\pi_x$ LP Cl(5)	0.00	-0.01	3.91
$\pi_y$ LP Cl(5)	0.01	-0.01	4.28
$\pi_x$ LP Cl(6)( $\mu$ )	0.01	3.89	0.00
$\mu(\text{Nb-Cl-Nb})$	0.01	2.71	0.00
$\pi_z$ LP Cl(6)	0.01	-9.19	0.01
$\pi$ LP Cl(8)	4.46	0.00	0.09
$\pi$ LP Cls	0.06	0.02	0.15
$\pi$ (Cl4-Nb)	0.02	-0.02	0.02
$\pi$ (Cl8-Nb)	2.38	0.01	0.00
$\sigma$ LP Cl(5)	0.01	-0.01	-2.02
$\sigma$ LP Cl(6)	0.01	1.32	0.01
$\sigma$ LP Cl(8)	-2.13	0.00	0.01
$\sigma$ LP Cls	0.05	-0.03	0.05
$\sigma$ (Cl5-Nb)	0.00	-0.01	-5.66
$\sigma$ (Cl8-Nb)	-3.93	0.00	0.00
$\sigma$ (Cls-Nb)	0.03	-0.02	0.01
$\Sigma$ Analysis	0.81	-1.33	0.69
Total Calculated	+0.81	-1.32	+0.71

Cl<sub>s</sub> = All other chlorides not listed in sites 5,6 or 8 of complex  $\text{NbCl}_5$ . LP = lone pair

**Table E12:** Bonds orders and compositions of selected chlorine-centered LMOs

Equatorial Cl	Bridging Cl	Axial Cl
WBI(Cl <sub>eq</sub> -Nb) = 1.17	WBI(Cl <sub>br</sub> -Nb) = 0.49 (ea.)	WBI(Cl <sub>ax</sub> -Nb) = 1.06
$\pi_y(\text{Cl}_{\text{eq}}\text{-Nb})$ 82 Cl s(1)p(99)d(0) 18 Nb s(1)p(0)d(99)	$\pi_x \text{ LP Cl}_{\text{br}} (\mu \text{ bonding})$ 86 Cl s(0)p(100)d(0) 6 Nb s(18)p(3)d(79) 5 Nb s(19)p(3)d(78)	$\pi_x \text{ LP Cl}_{\text{ax}}$ 87 Cl s(1)p(99)d(0) 11 Nb s(1)p(1)d(98)
$\pi_z \text{ LP Cl}_{\text{eq}}$ 89 Cl s(0)p(100)d(0) 8 Nb s(0) p(1) d(98)	$\mu(\text{Nb-Cl-Nb})$ 84 Cl s(30)p(70)d(0) 6 Nb s(15)p(1)d(83) 6 Nb s(16)p(1)d(83)	$\pi_y \text{ LP Cl}_{\text{ax}}$ 87 Cl s(0)p(100)d(0) 11 Nb s(0)p(1)d(99)
$\sigma \text{ LP Cl}_{\text{eq}}$ 99 Cl s(74)p(26)d(0.02)	$\pi_z \text{ LP Cl}_{\text{br}}$ 98 Cl s(0)p(100)d(0)	$\sigma \text{ LP Cl}_{\text{ax}}$ 99 Cl s(73)p(27)d(0)
$\sigma(\text{Cl}_{\text{eq}}\text{-Nb})$ 78 Cl s(25)p(75)d(0) 22 Nb s(20)p(1)d(79)	$\sigma \text{ LP Cl}_{\text{br}}$ 98 Cl s(70)p(30)d(0) 1 Nb s(9)p(1)d(89)	$\sigma(\text{Cl}_{\text{ax}}\text{-Nb})$ 82 Cl s(26)p(74)d(0) 15 Nb s(18)p(1)d(81)

All integers are in percent(%). ea. = each of the bridging chlorides

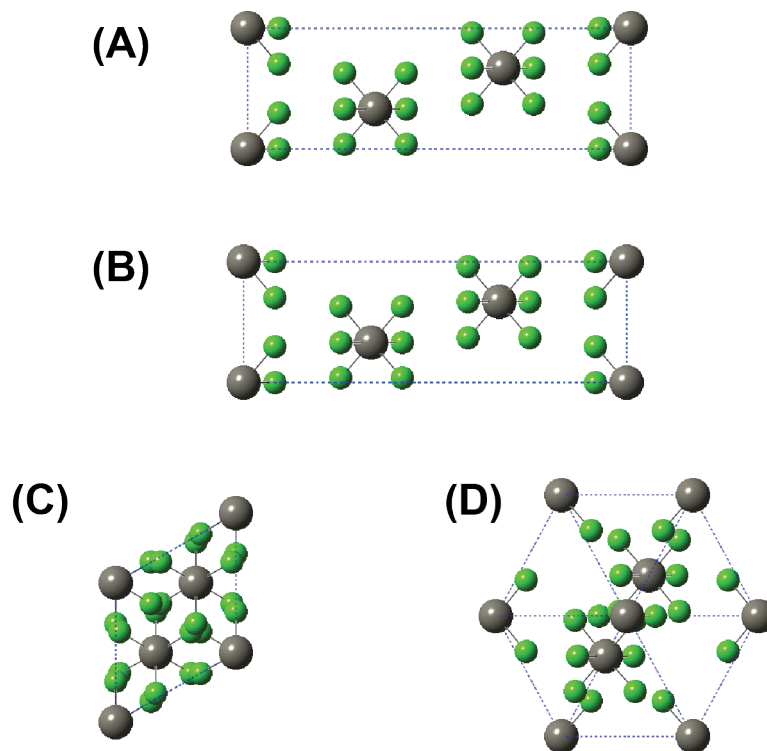


**Figure E1:** Depictions of the packing of atoms in the unit cell for  $\alpha\text{-WCl}_6$  with views along the crystallographic (A) *a*-axis, (B) *b*-axis, (C) *c*-axis and (D) [111] plane.

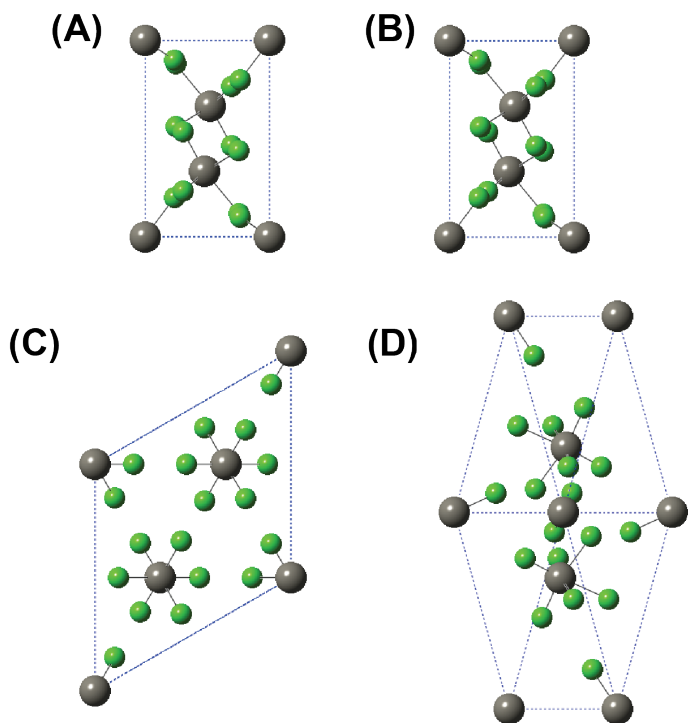


**Figure E2:** Deceptions of the packing of atoms in the unit cell for  $\beta\text{-WCl}_6$  with views along the crystallographic (A)  $a$ -axis, (B)  $b$ -axis, (C)  $c$ -axis and (D)  $[111]$  plane.

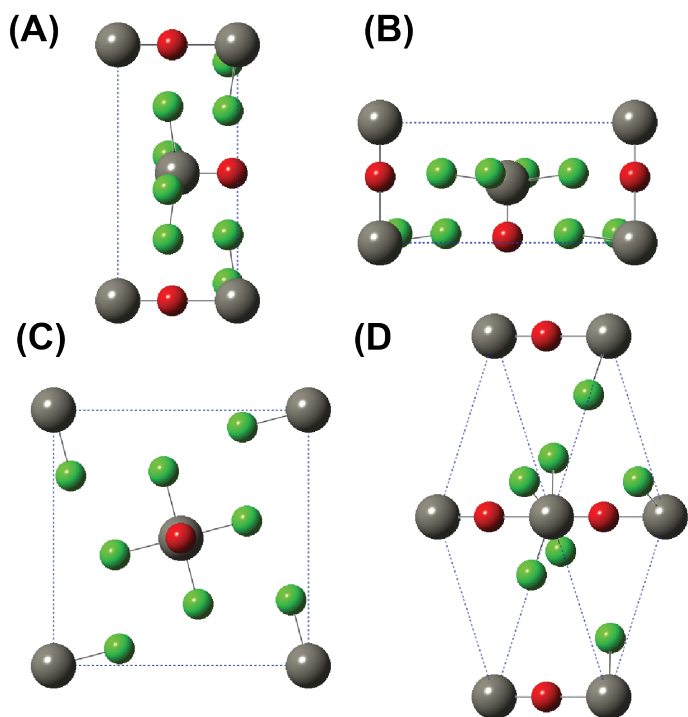


**Figure E3:** Deceptions of the packing of atoms in the unit cell for  $\text{WOCl}_4$  with views along the crystallographic (A)  $a$ -axis, (B)  $b$ -axis, (C)  $c$ -axis, and (D) the  $[111]$  plane.

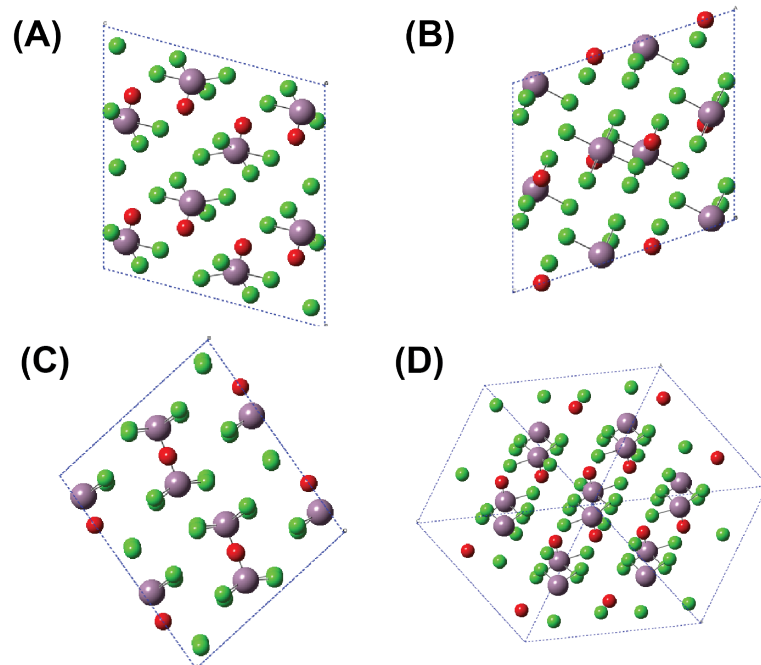


**Figure E4:** Deceptions of the packing of atoms in a  $2 \times 2 \times 2$  supercell for  $\text{MoOCl}_4$  with views along the crystallographic (A)  $a$ -axis, (B)  $b$ -axis, (C)  $c$ -axis, and (D)  $[111]$  plane.

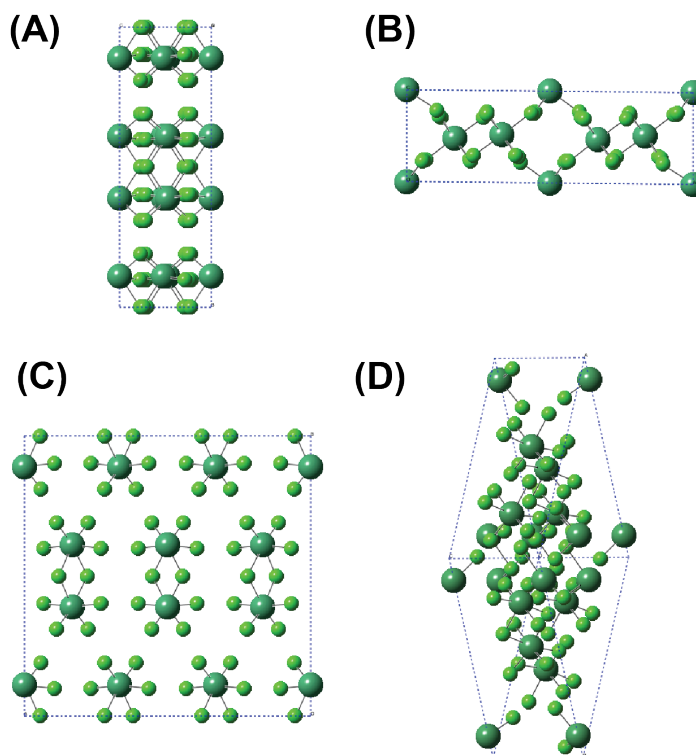


**Figure E5:** Deceptions of the packing of atoms in the unit cell for  $\text{NbCl}_5$  with views along the crystallographic (A)  $a$ -axis, (B)  $b$ -axis, (C)  $c$ -axis, and (D)  $[111]$  plane.

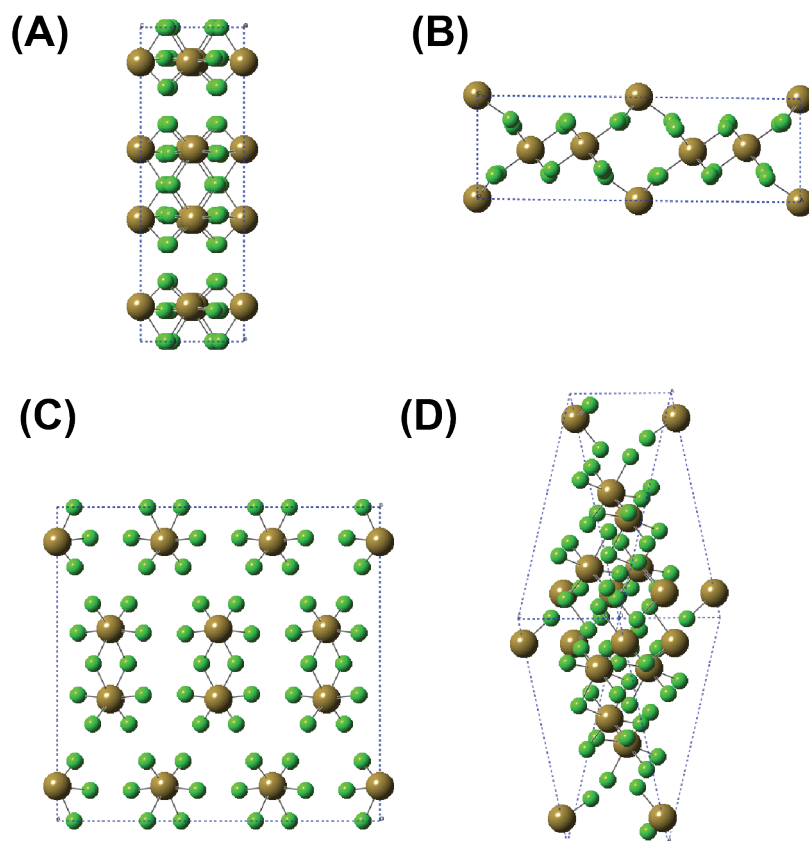


**Figure E6:** Depictions of the packing of atoms in the unit cell for **TaCl<sub>5</sub>** with views along the crystallographic (A) *a*-axis, (B) *b*-axis, (C) *c*-axis, and (D) [111] plane.

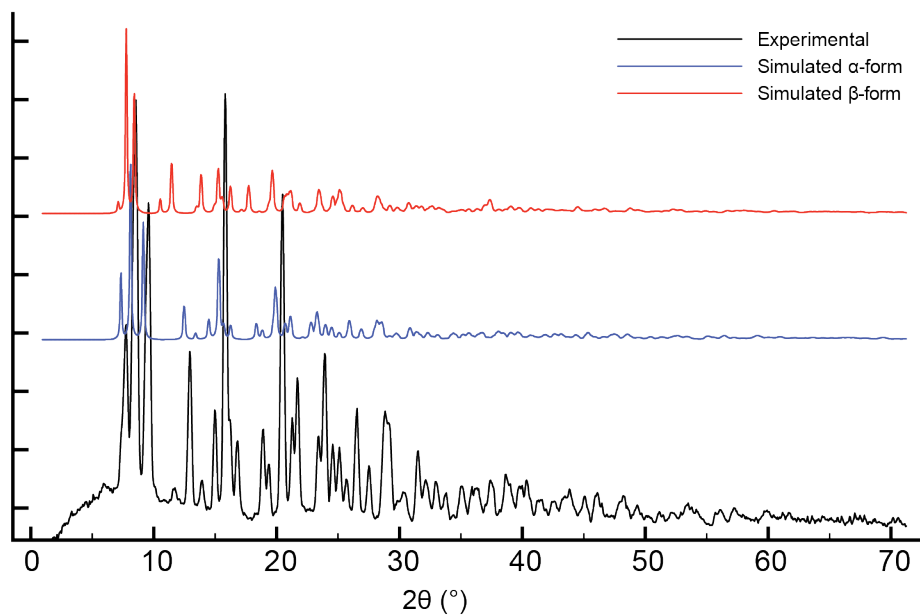


**Figure E7:** Experimental PXRD pattern for **WCl<sub>6</sub>** shown as the black trace. Simulated patterns for  $\alpha$ -**WCl<sub>6</sub>** (red trace) and  $\beta$ -**WCl<sub>6</sub>** (blue trace).

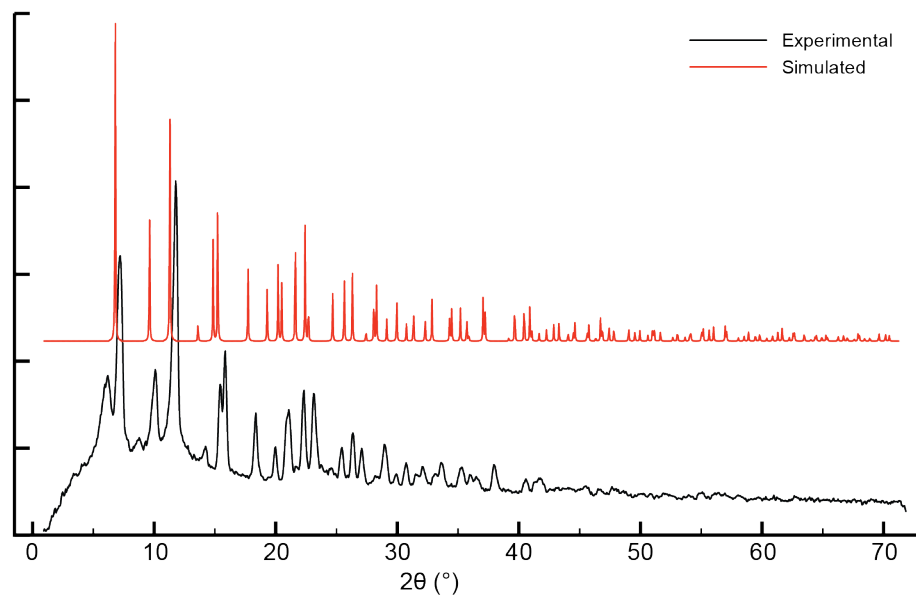


**Figure E8:** Experimental (black trace) and simulated (red trace) PXR D patterns for  $\text{WOCl}_4$ .

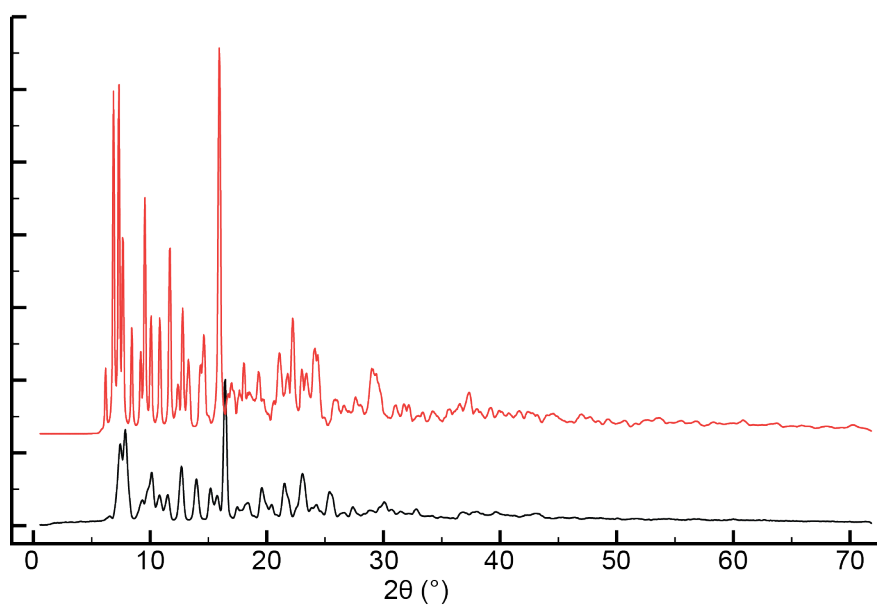


**Figure E9:** Experimental (black trace) and simulated (red trace) PXR D patterns for  $\text{MoOCl}_4$ .

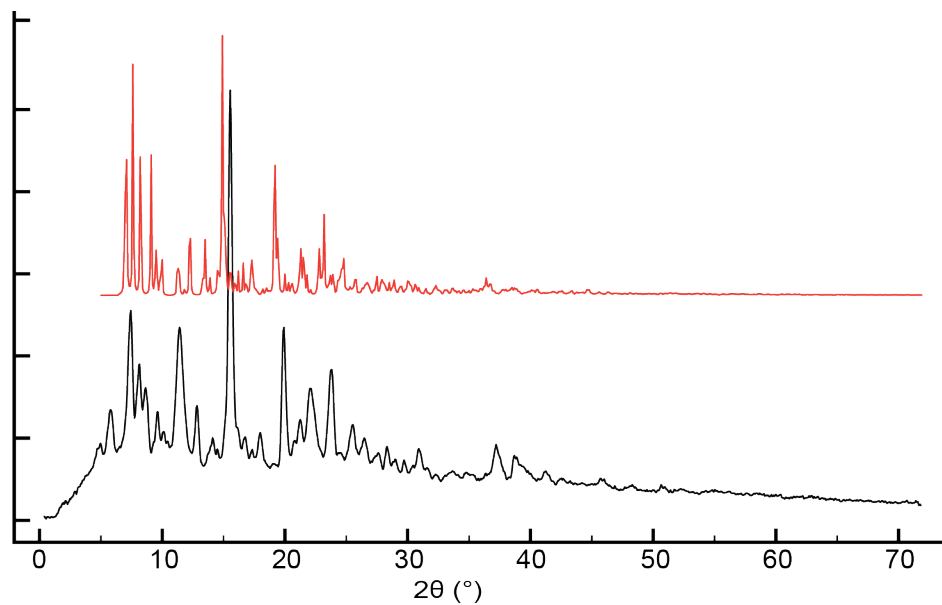


**Figure E10:** Experimental (black trace) and simulated (red trace) PXR D patterns for NbCl<sub>5</sub>.

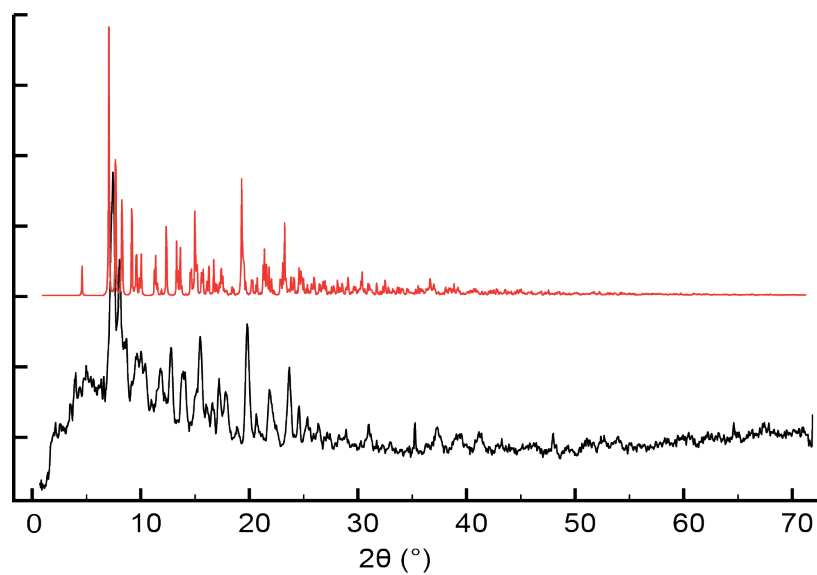


**Figure E11:** Experimental (black trace) and simulated (red trace) PXR D patterns for TaCl<sub>5</sub>.



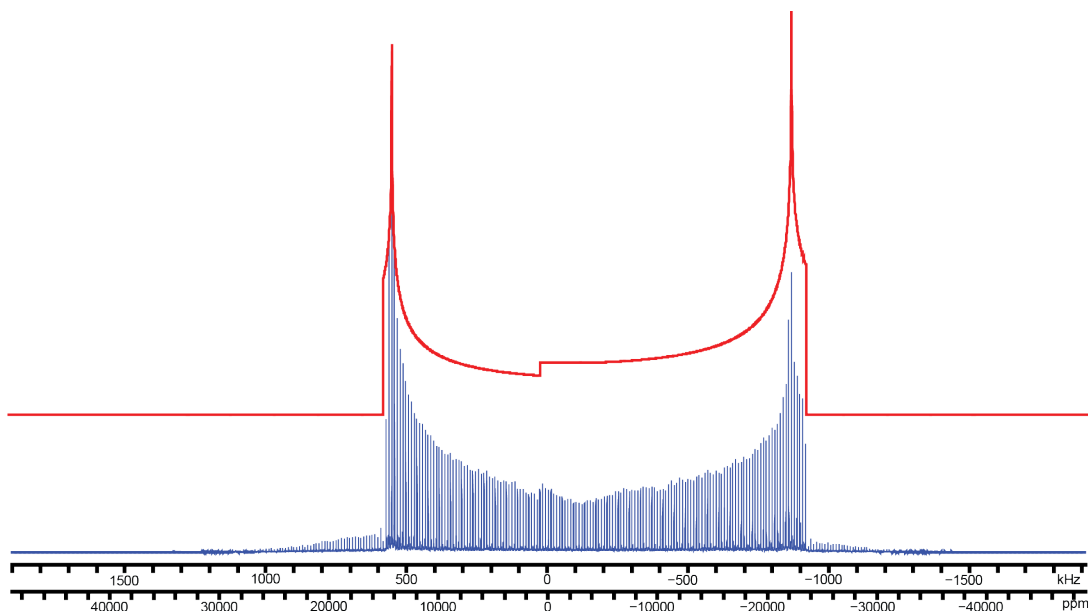


**Figure E12:** Static  $^{35}\text{Cl}$  SSNMR spectrum of  $\alpha\text{-WCl}_6$  acquired at 9.4 T with corresponding analytical simulation (red trace).

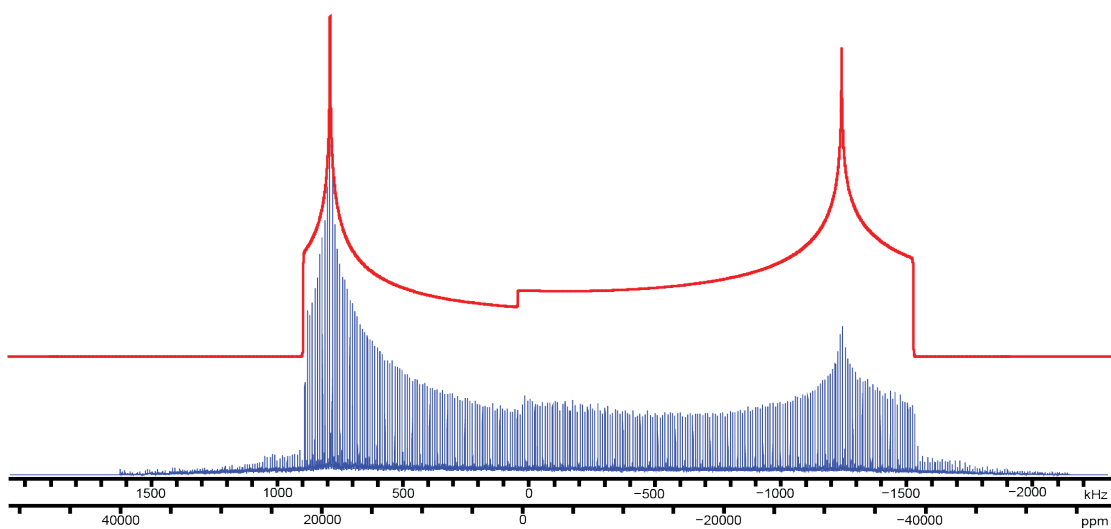


**Figure E13:** Static  $^{35}\text{Cl}$  SSNMR powder pattern for  $\text{WOCl}_4$  acquired at 9.4 T and corresponding analytical simulation (red trace).

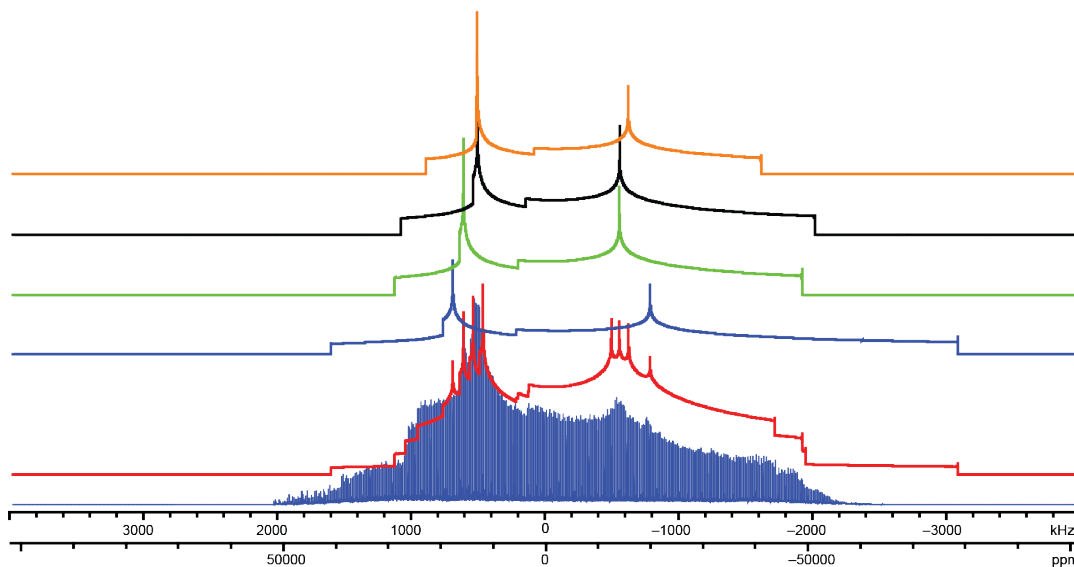


**Figure E14:** Static  $^{35}\text{Cl}$  SSNMR powder pattern for  $\text{MoOCl}_4$  acquired at 9.4 T. Analytical simulations for the individual sites are shown in blue, green, black, and orange. The red trace is an analytical simulation representative of the entire powder pattern.

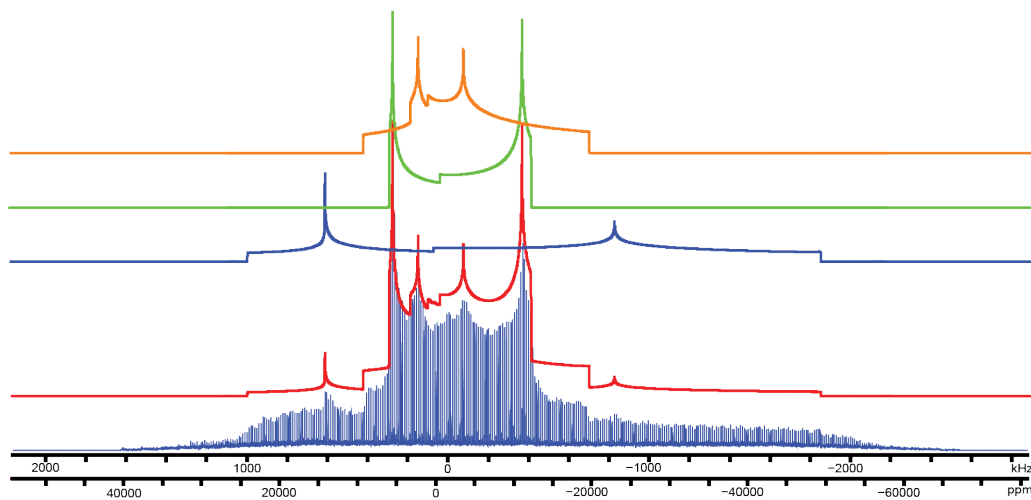


**Figure E15:** Static  $^{35}\text{Cl}$  SSNMR powder pattern for  $\text{NbCl}_5$ . Analytical simulations are shown in blue (bridging), green (terminal axial), and orange (terminal equatorial). The red trace is an analytical simulation representative of the entire powder pattern.

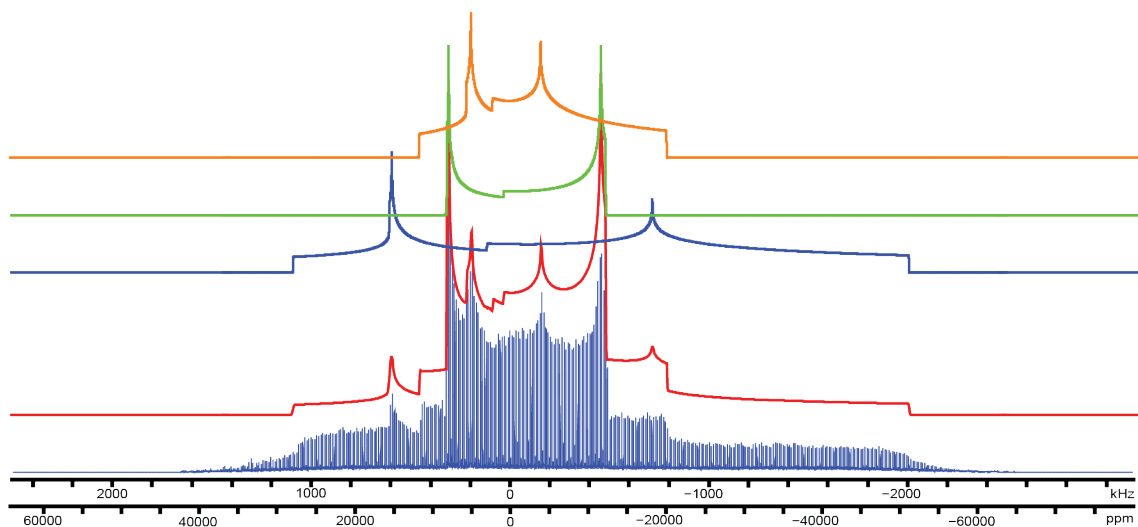


**Figure E16:** Static  $^{35}\text{Cl}$  SSNMR powder pattern for  $\text{TaCl}_5$ . Analytical simulations are shown in blue (bridging), green (terminal axial), and orange (terminal equatorial). The red trace is an analytical simulation representative of the entire powder pattern.

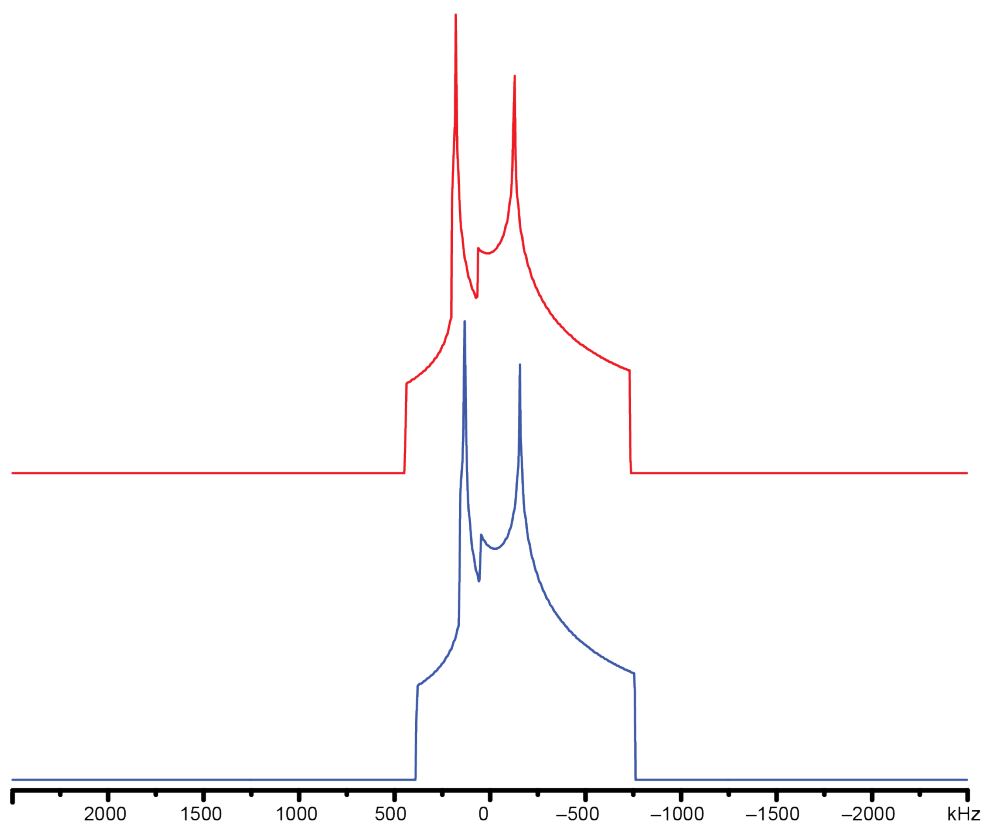


**Figure E17:** Simulation of the  $^{35}\text{Cl}$  SSNMR powder pattern for the terminal-equatorial site in  $\text{NbCl}_5$  including only the quadrupolar interaction (bottom trace) and both the quadrupolar and CSA interactions (top trace).

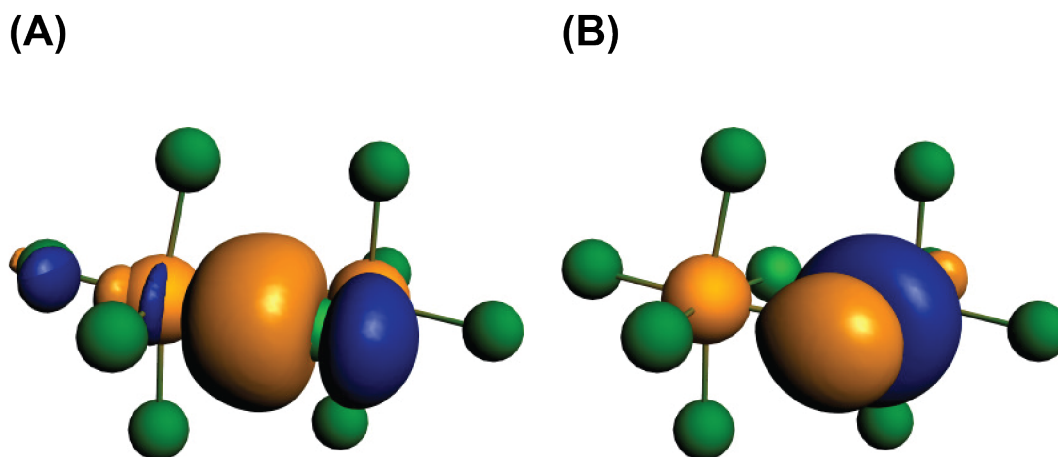


**Figure E18:** Dative (Cl→Nb) bonds in  $\text{NbCl}_5$ . Linear combinations of (A)  $(v+vi)/\sqrt{2}$  and (B)  $(v-vi)/\sqrt{2}$  of LMOs (v) and (vi) of **Figure 6.9(B)**.

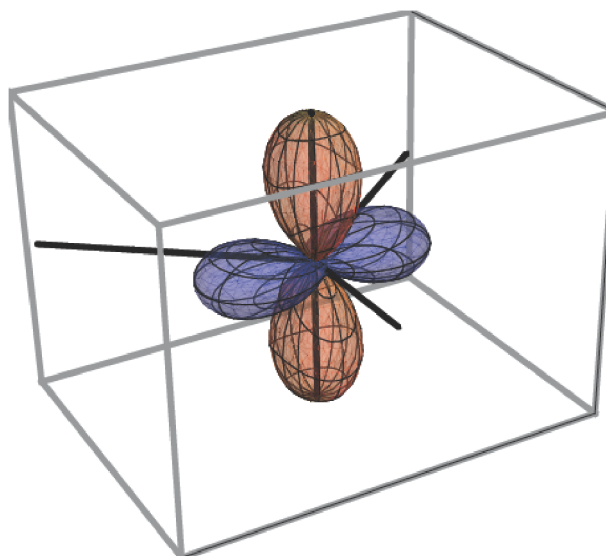


**Figure E19:** Graphical representation of the EFG related to the  $sp^n$  set of hybrid orbitals of Eq. (3). Electron configuration  $(spn_1)^2 (spn_2)^{1.8} (spn_3)^{1.8} (spn_4)^2$ . Angle  $\theta$  between  $spn_2$  and  $spn_3$ :  $102^\circ$ . The negative tensor component  $V_{33}$  (orange) is perpendicular to the plane spanned by the directional vectors of the two bonding hybrids with occupancy lower than two.

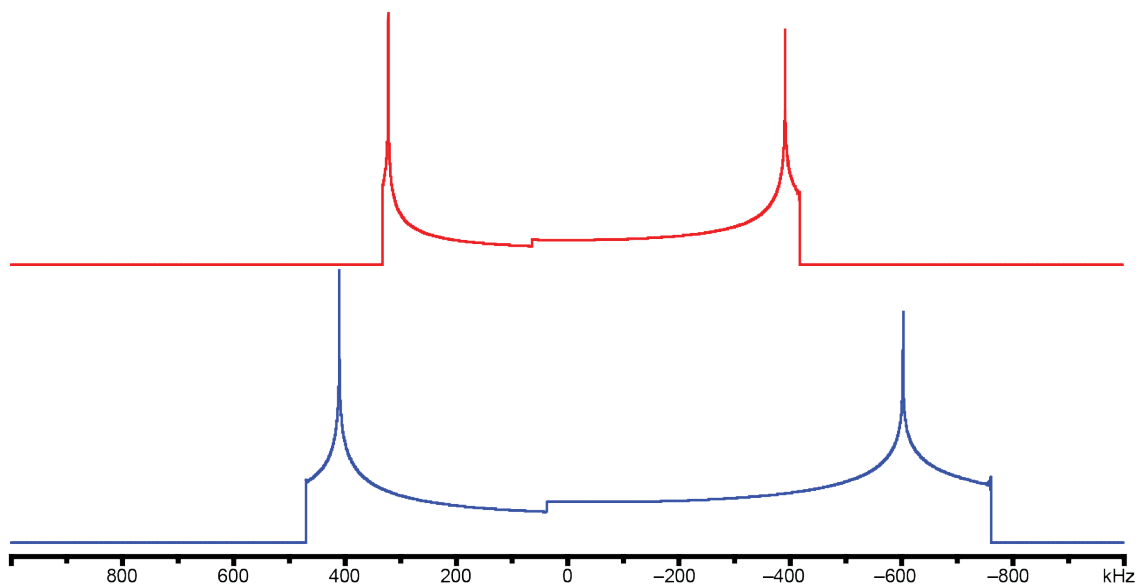


**Figure E20:** Analytical simulations of static  $^{35}\text{Cl}$  SSNMR spectra acquired at 18.8 T for  $\alpha\text{-WCl}_6$  (red trace) and  $\text{WCl}_6\text{-SiO}_2$  (blue trace).

## Vita Auctoris

<b>Name</b>	Christopher Andrew O’Keefe
<b>Year of Birth</b>	1989
<b>Place of Birth</b>	Windsor, ON
<b>Education</b>	Ph.D. Candidate (2017) University of Windsor, Ontario, Canada  B.Sc. Honours Chemistry (2012) University of Windsor, Ontario, Canada  St. Joseph’s Catholic High School (2007)